Steering cars toward natural gas *p. 538*

Challenges in valuing nature for conservation *p. 549*

Imaging a supervolcano's magma reservoir *p. 617*

Science

$10
31 OCTOBER 2014
sciencemag.org

AAAS

SPECIAL ISSUE

The aging brain

How cognitive function can flourish *p. 566*

CONTENTS

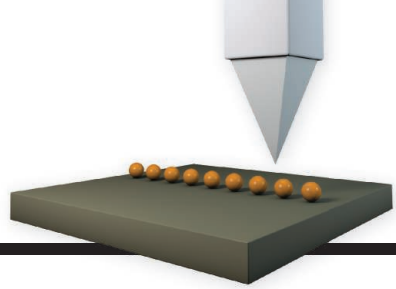

545 & 602

A glimpse at Majorana fermions via iron atoms

31 OCTOBER 2014 • VOLUME 346 • ISSUE 6209

NEWS

IN BRIEF

530 & 630

IN DEPTH

FEATURE

INSIGHTS

PERSPECTIVES

SCIENCE PRIZE ESSAY

SPECIAL SECTION

The aging brain

INTRODUCTION

NEWS

REVIEWS

SEE ALSO

▸ PERSPECTIVE P. 547
▸ *SCIENCE SIGNALING* RESEARCH ARTICLE BY W. M. PRYOR *ET AL.* (28 OCT. 2014)
▸ sciencemag.org/special/neuro2014

ON THE COVER

Myelin content (red, high; grayish purple, low) mapped on the cerebral cortex of a healthy adult, aged over 70 years, scanned for the Human Connectome Project, Lifespan supplement. Myelin maps provide useful markers for functionally distinct regions of the cerebral cortex, which vary in size between individuals. For more on the aging brain, see page 566. *Image: M. F. Glasser, D. C. Van Essen, and J. S. Elam for the WU-Minn Human Connectome Project consortium; http://humanconnectome.org*

Published by AAAS

CONTENTS

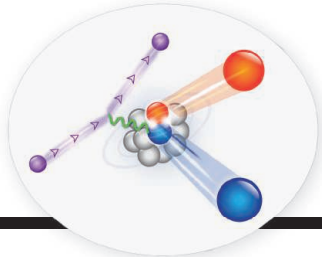

614
Probing the momentum of protons and neutrons

31 OCTOBER 2014 • VOLUME 346 • ISSUE 6209

SCIENCE (ISSN 0036-8075) is published weekly on Friday, except the last week in December, by the American Association for the Advancement of Science, 1200 New York Avenue, NW, Washington, DC 20005. Periodicals mail postage (publication No. 484460) paid at Washington, DC, and additional mailing offices. Domestic individual membership and subscription (51 issues): $153 ($74 allocated to subscription). Domestic institutional subscription (51 issues): $1282; Foreign postage extra: Mexico, Caribbean (surface mail) $55; other countries (air assist delivery) $85. First class, airmail, student, and emeritus rates on request. Canadian rates with GST available upon request, GST #1254 88122. Publications Mail Agreement Number 1069624. **Printed in the U.S.A.**
Change of address: Allow 4 weeks, giving old and new addresses and 8-digit account number. **Postmaster:** Send change of address to AAAS, P.O. Box 96178, Washington, DC 20090–6178. **Single-copy sales:** $10.00 current issue, $15.00 back issue prepaid includes surface postage; bulk rates on request.

Published by AAAS

Science
AAAS
1200 New York Avenue, NW, Washington, DC 20005
Bateman House, 82-88 Hills Road, Cambridge, UK CB2 1LQ

SUBSCRIPTION SERVICES For change of address, missing issues, new orders and renewals, and payment questions: 866-434-AAAS (2227) or 202-326-6417, FAX 202-842-1065. Mailing addresses: AAAS, P.O. Box 96178, Washington, DC 20090-6178 or AAAS Member Services, 1200 New York Avenue, NW, Washington, DC 20005

INSTITUTIONAL SITE LICENSES 202-326-6755 **REPRINTS:** Author Inquiries 800-635-7181 **COMMERCIAL INQUIRIES** 803-359-4578 **PERMISSIONS** 202-326-6765, permissions@aaas.org **AAAS Member Services** 202-326-6417 or http://membercentral.aaas.org/discounts

INFORMATION FOR AUTHORS See pages 680 and 681 of the 7 February 2014 issue or access www.sciencemag.org/about/authors

Published by AAAS

EDITORIAL

Planet at the crossroads

When we think of nature in 2014, chances are that protected areas come to mind: Amazonian rainforests teeming with wildlife, the sweeping plains of the Serengeti, or an Alpine lake surrounded by glaciers. But the world's protected areas are at a crossroads, and next month, when the International Union for Conservation of Nature (IUCN) convenes its once-in-a-decade World Parks Congress in Sydney, Australia, nations will discuss how to address the challenges in protecting ecosystems across the world for the benefit of humanity.

The good news is that the total number of protected sites has doubled since the last World Parks Congress in Durban, South Africa, in 2003. Today, there are more than 200,000 such areas, covering around 15% of land and 3% of the oceans, in national parks, marine reserves, World Heritage sites, and indigenous and community conserved areas. Since Durban, nearly 200 nations agreed at the 2010 Convention on Biological Diversity (CBD) on new global targets to achieve protection for at least 17% of terrestrial and 10% of marine environments by the year 2020.

"Protected areas remain the single most effective tool to conserve biodiversity..."

Protected areas remain the single most effective tool to conserve biodiversity, which is why recent reports are sobering. The IUCN Red List of Threatened Species reveals that all completely assessed species face severe risk of extinction, ranging from 13% of birds to 63% of cycads. The World Wide Fund for Nature's Living Planet Report confirmed a 52% drop in the global populations of mammals, birds, reptiles, amphibians, and fish between 1970 and 2010, whereas the CBD's Global Biodiversity Outlook 4 report concluded that international efforts to prevent wildlife and habitat loss will fail to meet the overall 2020 targets. There has been some progress toward protecting ecosystems on land, but we are not on track for oceans, despite the recent establishment of large marine protected areas in the Pacific Ocean and elsewhere. Another analysis indicates that the scale of policy and management response is far from commensurate with the magnitude of the challenge.*

Against this backdrop, what can we expect to emerge from the Sydney World Parks Congress? Species occurring sparsely in protected areas are sliding toward extinction twice as fast as those that are well protected. Therefore, countries must draw a line on activities that damage or degrade protected areas and must include important biodiversity areas in newly established protective areas. The congress will address the most egregious detrimental activities, including illegal logging and mining, but will also consider the delicate balancing act between conservation and development needs. Here, the scientific community can serve to fill the gaps in our current knowledge to better guide policy.

The congress will also examine the importance of long-term vision and accountability in ecosystem management.† Countries must adopt the principle of nonregression in environmental law, which requires that norms already adopted by states shall not be revised if the result weakens protections. Downgrading and even removing the official status of protected regions—as seen in both high- and low-income countries—threaten the ability of societies to address climate change, food and energy security needs, and sustainability.

The Sydney congress is a platform for government, business, indigenous and civil society leaders, and more than 4000 delegates from 168 countries to figure out how to get back on track toward the 2020 goals. The congress should also inspire a new generation of protected-area custodians. Societies must better understand how protected areas yield substantial benefits for people. These areas reduce the impact of disasters by providing natural coastal defenses, supply food and fresh water, improve physical and mental health, and provide jobs and livelihoods to millions of people around the world. Wise investments in the future of our planet require conserving our greatest natural assets: protected areas.

– Julia Marton-Lefèvre

Julia Marton-Lefèvre is the Director General of the International Union for Conservation of Nature, Gland, Switzerland. E-mail: julia.marton-lefevre@iucn.org

*D. P. Tittensor *et al.*, *Science* **346**, 241 (2014). †See the *Science* series on conservation (www.sciencemag.org/site/extra/conservation/).

10.1126/science.1261787

NEWS

> "The perfume ... is quite strong."
>
> **Kathrin Altwegg**, principal investigator for the Rosetta probe's spectrometer, on the "odor" given off by comet Churyumov-Gerasimenko, which emits hydrogen sulfide, ammonia, formaldehyde, and other pungent compounds.

IN BRIEF

New consortium aims to find structures for 200 membrane proteins.

Giving shapes to signaling proteins

Some 40% of all approved drugs target the proteins called G protein-coupled receptors (GPCRs), which relay signals across the cell membrane. But we know the 3D shapes of just 22 of the estimated 826 human GPCRs. This week, a trio of U.S. and Chinese academic institutions announced that they'll join forces over the next 5 years with three pharmaceutical companies to determine the structures of 200 more. Obtaining such structures has been difficult. The GPCRs solved to date all required adding small druglike molecules in order to stabilize them, says Raymond Stevens, a structural biologist at the University of Southern California (USC) in Los Angeles, who will lead the new consortium. Drug companies are well placed to supply such stabilizers, Stevens adds. In exchange for sharing their molecules, each of the companies—Amgen, Sanofi, and Ono—will get to recommend five GPCR targets per year. In addition to USC, the iHuman Institute at ShanghaiTech University in China and the Shanghai Institute of Materia Medica will participate.

http://scim.ag/GPCRstructures

AROUND THE WORLD

Chinese science funding revamp

BEIJING | The Chinese government is readying a major shake-up of how it doles out science funding. The Ministry of Science and Technology may hand control of the lion's share of research spending to as-yet-unidentified "independent institutes," reports the state-run *People's Daily*. In 2013, the ministry doled out $3.6 billion in R&D funding, primarily through its 863 high-tech development and 973 basic research programs. In an interview with China Radio, science minister Wan Gang welcomed the pending reform, saying that it's intended to "get rid of the shackles on technological innovation." Observers say that the National Natural Science Foundation of China could serve as a model for what may be a new agency or agencies for managing R&D spending.

http://scim.ag/Chineseoverhaul

Pause on virus studies protested

BETHESDA, MARYLAND | A U.S. government moratorium on certain risky virology studies has gone too far, researchers said at a 22 October meeting of the National Science Advisory Board for Biosecurity (NSABB). The 17 October pause halts new federal funding for so-called gain-of-function (GOF) studies that make influenza, MERS, or SARS more transmissible

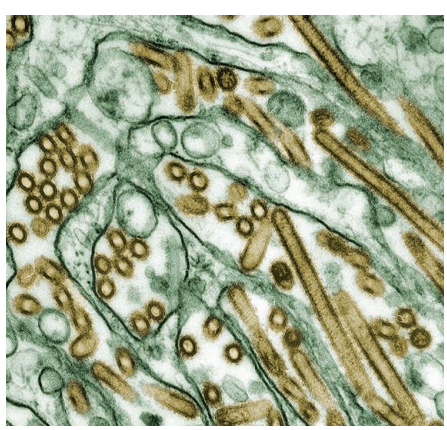

Risky studies on the H5N1 bird flu virus are on hold.

IMAGES: (LEFT TO RIGHT) V. ALTOUNIAN/*SCIENCE* BASED ON PROTEIN STRUCTURE FROM BRIAN KOBILKA; CYNTHIA GOLDSMITH/WIKIMEDIA COMMONS

BY THE NUMBERS

40%

The minimum cut in greenhouse gas emissions, compared with 1990 levels, that Europe should reach by 2030, according to an agreement E.U. leaders announced on 23 October.

$65 million

Largest ever gift to the University of California, Santa Barbara, from billionaire investor Charles Munger for a residence for visiting scholars at the Kavli Institute for Theoretical Physics.

35,000

Estimated number of African lions, compared with 76,000 in 1980, according to a U.S. Fish and Wildlife Service proposal to list the animal as a threatened species.

Alan Eustace dangling beneath an unseen helium-filled weather balloon before his free fall.

PHOTO: J. MARTIN HARRIS PHOTOGRAPHY/PARAGON SPACE DEVELOPMENT CORP.

Postcards from the edge of space

Computer scientist Alan Eustace, 57, a senior vice president at Google, last week broke the records for the world's highest and fastest free fall jump. At 41,419 meters above Earth's surface, Eustace jumped from 2374 meters higher than previous record-holder Felix Baumgartner, who made his leap in 2012. Eustace began his free fall at the upper edge of Earth's stratosphere. He plummeted for 4 minutes and 27 seconds and reached a top speed of 1321 kilometers per hour before deploying two parachutes. In addition to being low in oxygen, the stratosphere's air temperatures increase with altitude and therefore required careful engineering of Eustace's pressurized life-support suit to keep him cool and breathing. Other technologies that accompanied the VP on his sound barrier–breaking descent included cameras and a simple two-way radio to communicate with ground control. "It was a wild, wild ride," Eustace told *The New York Times*.

in mammals or more pathogenic. The idea is to provide a year for experts to work out a U.S. government-wide policy for reviewing the risks and benefits of GOF studies. But scientists told NSABB that the pause is sweeping up even routine influenza surveillance and vaccine work and halting efforts to develop a mouse model for MERS. White House officials said they are working with the National Institutes of Health to allow exceptions for research needed to protect public health.
http://scim.ag/pauseprotest

Creationist event stirs concerns

EAST LANSING, MICHIGAN | A creationist conference set for Michigan State University (MSU) is creating unease among some of the school's students and faculty, which includes prominent evolutionary biologists. The 1 November Origin Summit is sponsored by Creation Summit, an Oklahoma-based Christian group founded to "challenge evolution and all such theories predicated on chance." The event will include eight workshops, including one on why "the big bang is fake" and another targeting the work of MSU biologist Richard Lenski, who has led a major study of bacterial evolution. The organizers invited Lenski to participate in a debate, but he hasn't responded and is encouraging others to ignore the event. It "will be just another forgettable blip in the long history of antiscience, antievolution screeds," he predicts.
http://scim.ag/creationistsconf

Pakistan's polio program blasted

ISLAMABAD | Pakistan's polio eradication program is "a disaster" and needs new leadership, concludes the Independent Monitoring Board of the Global Polio Eradication Initiative in an October report. So far in 2014, more than 200 Pakistani children have become paralyzed, accounting for 80% of the world's polio cases, and the country has exported the virus to Afghanistan and the Middle East. Killings of vaccinators and a Taliban ban on polio vaccination in North Waziristan pose enormous challenges. But "[t]he government ... can reach its children if it wants to," the report says, calling on the prime minister to immediately move the program from the ministry of health to the National Disaster

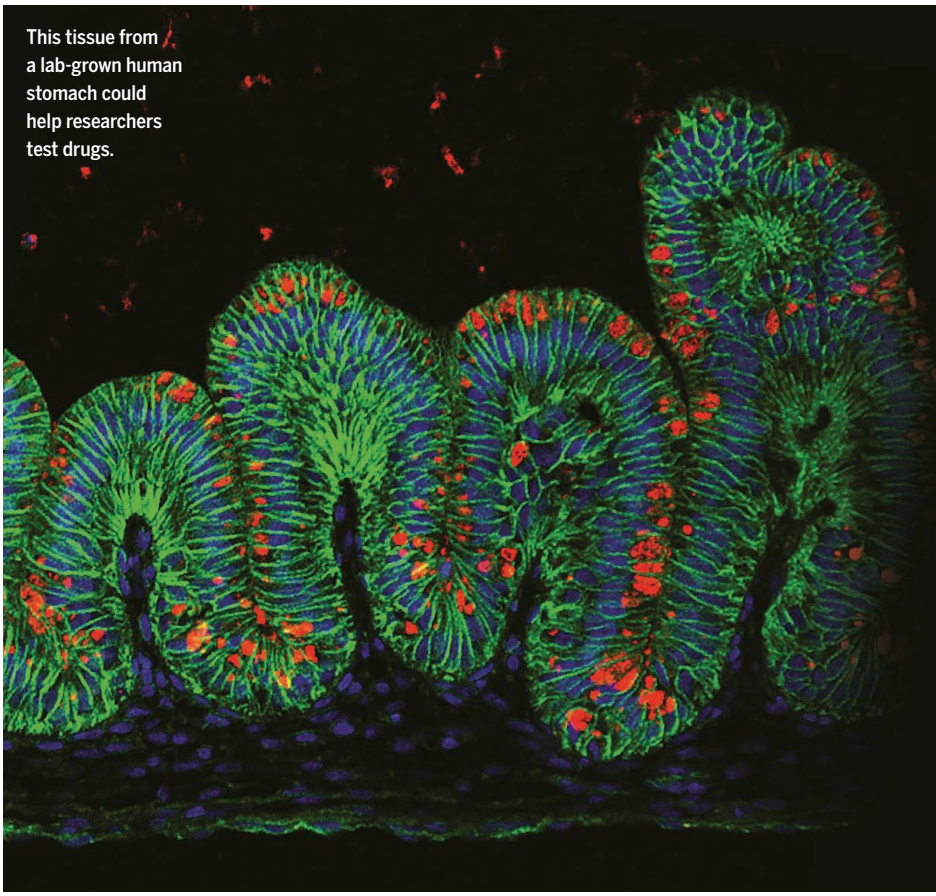

This tissue from a lab-grown human stomach could help researchers test drugs.

Tummy in a dish

The colorful snakelike image here is fluorescently labeled tissue from a stomach smaller than a pea. But the organ is not from a very small animal; it's a mini human stomach grown in a dish. The digestive systems of mice, flies, and other model organisms differ from those of humans, making them of limited use for studying human gut diseases. So researchers have turned to pluripotent stem cells—cells derived from embryos or reprogrammed adult cells that can potentially turn into any cell type—to grow digestive organs in the lab. Last week in *Nature Medicine*, one group unveiled a small intestine created from human stem cells. This week, a different team reports in *Nature* that they've coaxed both types of stem cells to form small spheres with all the properties of a functional stomach. When the researchers exposed the tiny stomachs to the bacterium *Helicobacter pylori*, which contributes to stomach ulcers and cancers, they saw the same cellular changes known to occur in life-size stomachs.

Management Authority. Without decisive action, "Pakistan is very likely to be the polio virus' last home on earth," it warns.

New ethics guidance for trials

WASHINGTON, D.C. | The federal Office for Human Research Protections (OHRP) is standing by its position that a study that gave some 1300 premature infants various levels of oxygen did not adequately inform parents of risks. The SUPPORT study, which ran from 2005 to 2009 at 23 institutions, has been criticized as unethical by the advocacy group Public Citizen and some bioethicists but defended by others and its funder, the National Institutes of Health. OHRP's comments were part of proposed guidance released last week that lays out a new ethics blueprint for clinical trials that include existing standard-of-care treatments.

Looming diabetes and TB link

BARCELONA, SPAIN | For reasons that remain murky, diabetes triples the risk of developing tuberculosis (TB), and a new report warns of this "looming co-epidemic." Nearly 400 million people had diabetes in 2013, a number projected to jump by 50% in the next 2 decades, notes the analysis released at the 45th Union World Conference on Lung Health by two disease advocacy groups. Some 9 million people developed TB last year, and one-third of the world's population lives with a latent form of the mycobacterium that causes the disease. Diabetes impairs immune responses against that microbe, and drugs for the two diseases can interfere with each other and exacerbate each one. The report calls for TB testing in all people with diabetes and increasing research to clarify the TB-diabetes link.

NIH awards 12 diversity grants

BETHESDA, MARYLAND | The National Institutes of Health (NIH) last week committed $240 million over 5 years to 12 projects that it hopes will eventually lead to more minority grant applicants. Previous NIH programs, with budgets one-tenth the size, have served a handful of minority undergraduates at individual institutions. In contrast, each of the new awards involves many institutions, targets hundreds rather than tens of students, and plans to extend beyond the campus into the public schools. NIH Director Francis Collins says previous efforts have left NIH "far short of where we need to be," although some program directors say that tight funding has limited the impact of successful approaches to training more minorities.

NEWSMAKERS

PubPeer comments draw lawsuit

A scientist who claims that anonymous comments on the peer-review website PubPeer cost him a lucrative job has filed a libel lawsuit against the anonymous posters. **Fazlul Sarkar**, a cancer researcher at Wayne State University in Detroit, Michigan, on 9 October also subpoenaed PubPeer in a bid to force it to disclose the posters' identities. The lawsuit, filed in a local court in Wayne County, Michigan, claims that the negative comments about Sarkar's work prompted the University of Mississippi Cancer Institute to withdraw its offer of a tenured position paying $350,000 annually. PubPeer moderators have said that they will oppose efforts to reveal the identities of their users, and the American Civil Liberties Union has offered to defend the website.
http://scim.ag/pubpeersuit

IMAGE: KYLE MCCRACKEN/*NATURE*

Endangered populations of fire salamanders in Europe have succumbed to a new fungus.

IN DEPTH

CONSERVATION BIOLOGY

The coming salamander plague

Already harming a European species, an Asian fungus could wreak havoc in North America

By **Erik Stokstad**

A new kind of amphibian apocalypse could be approaching. In the late 1980s, a deadly fungus called *Batrachochytrium dendrobatidis* (Bd) began to send more than 200 species of amphibians spiraling toward extinction. Although many groups suffered, frogs in Central American rainforests seemed especially ravaged. "It's a bitter pill to swallow when you think about what's gone," says herpetologist Joseph Mendelson III of Zoo Atlanta. Bd has been called the greatest disease threat to biodiversity.

Now, Mendelson and other researchers fear a related chytrid fungus could inflict further losses on salamanders. On page 630, researchers show that the recently described fungus, *Batrachochytrium salamandrivorans* (Bs), arose in Asia and migrated, likely via imported amphibians, to Europe, where it is killing endangered salamanders. North America, the global center of salamander diversity, could be next. The new threat is "extremely worrying," says Ariadne Angulo of the International Union for Conservation of Nature in Toronto, Canada.

Angulo and others hope advance warning of this salamander fungus will spur efforts to control the exotic pet trade. "You almost never get a second chance," says biologist Karen Lips of the University of Maryland, College Park. "If we can keep this thing out, we can do something huge for protecting salamander diversity in the United States."

In 2010, volunteers at a nature reserve near Maastricht, the Netherlands, noticed that the reserve's fire salamanders (*Salamandra salamandra*) were mysteriously dying. They brought some to An Martel, a veterinarian at Ghent University in Merelbeke, Belgium. She was alarmed by deep ulcers and sores on the animals, which are typical of Bd. DNA tests for the pathogen came up negative, but with a microscope, Martel saw a similar fungus. Her first reaction was amazement, she recalls. "Immediately after that, it was very scary."

Martel and her colleagues isolated, described, and named Bs. It killed healthy fire salamanders within a week, they reported in the *Proceedings of the National Academy of Sciences* in September 2013. By then, the reserve's small, endangered population of fire salamanders was nearly wiped out. Other researchers began keeping a wary eye on the fungus. "We thought: 'Uh oh, we have another one to worry about,' " Mendelson says.

> ***"If we can keep this thing out, we can do something huge for protecting salamander diversity."***
>
> **Karen Lips**, University of Maryland, College Park

To find out how far the fungus had spread, Martel and her colleagues asked researchers to send tissue samples, which had already been collected worldwide for studies of Bd. Ultimately, Martel's team screened nearly 5400 samples, representing about 150 kinds of amphibians from four continents. Those from the Americas were clean. So were European amphibians, except for the fire salamanders from the Netherlands and two populations in Belgium. But 4% of salamanders from Thailand, Vietnam, and Japan tested positive for Bs. The fungus was even found in a 150-year-old museum specimen of an Asian newt, adding to evidence that Bs originated in Asia.

The researchers also wanted to know how big a threat the fungus poses. Three species of Asian salamanders appear to be reservoirs of the disease; several individuals could beat back infections, although they shed fungal spores for at least 5 months. That worries researchers. Infected Asian salamanders brought to Europe or North America could become amphibian "Typhoid Marys," passing the fungus to native populations. Nine of 10 European salamander species tested were susceptible.

North America is an even greater worry, because it boasts about 190 species of salamanders. Lab experiments show that Bs can infect the lesser siren (*Siren intermedia*), a common species in the Southeast, although it does not get sick. (Four species of tested salamanders are resistant.) The fungus kills two kinds of newts, which are so abundant that, if infected, they could rapidly transmit the fungus to many other kinds of salamanders. If

PHOTO: STOCKPHOTOASTUR/ISTOCKPHOTO.COM

Bs reaches North America, Lips predicts, "the newts are going to be the tinder for a fire."

Bs is already spreading, having crossed from the Netherlands into Belgium. Its relative Bd is known to spread via amphibians or other animals, or simply by floating downstream. The key to preventing Bs from becoming another Bd, many researchers believe, is to clamp down on the small but often lucrative global trade in amphibians. An estimated 2.3 million Chinese fire belly newts (*Cynops orientalis*) were imported into the United States between 2001 and 2009, according to a recent study. In Europe, officials have some legal tools for regulating the trade, but rarely use them. A new E.U. animal health law, expected next year, could help, says geneticist Matthew Fisher of Imperial College London, who studies wildlife diseases. "It will be more aggressive," he predicts.

In the United States, no agency directly regulates imports of salamanders or other amphibians. "It's a clear example of why we need to modernize our laws," says Peter Jenkins, a consultant with the Center for Invasive Species Prevention in Washington, D.C. Congress is considering bills to give the U.S. Fish and Wildlife Service (FWS) more authority and tools, but antiregulation lawmakers have helped stall the proposals.

The pet trade is open to improved regulation, says Marshall Meyers of the Pet Industry Joint Advisory Council in Washington, D.C. He points out that the largest pet companies already treat imported amphibians with antimicrobial compounds to prevent the spread of Bd and other pathogens. The companies are also working with FWS officials to come up with ways to identify species, not yet in commerce, that might become invasive; this risk assessment could be a stopgap approach to screening out potential wildlife diseases and would "say to the pet trade: 'Beware—don't deal with these,' " Meyers says.

Lips and other scientists are afraid such strategies won't be good enough. They would like more details about exactly how companies do their testing and treatments. Under existing U.S. law, a company "could have 100% infected imports and there is nothing we can do," Lips says.

More broadly, researchers say the World Customs Organization should develop a tracking system for the amphibian trade, much as it monitors the movements of other goods. Mendelson, for one, says there's already enough evidence that North America should ban commercial salamander imports. Once the fungus arrives, it may be too late to prevent extinctions. "To do nothing," he says, "would be to ignore the lessons of the Bd disaster." ■

IMAGES: SRIVAS CHENNU

NEUROSCIENCE

An easy consciousness test?

EEG studies detect awareness in locked-in people

By **Emily Underwood**

After several weeks in a coma, most people either die or transition into a "vegetative state." They may sometimes open their eyes, but they seem unaware of themselves or their surroundings. Recent high-profile studies have shown, however, that many are far from unconscious. Researchers now estimate that roughly 40% of people deemed vegetative are partially or even fully conscious but unable to communicate because of severe damage to brain regions that control movement.

This past weekend, more than 100 neuroscientists, neurologists, philosophers, and ethicists crammed into a small New York University auditorium in Greenwich Village in New York City, intent on sparing future brain injury patients from such misdiagnosis. Although the initial studies revealing this problem relied on modern, and expensive, brain imaging techniques, many at the meeting agreed that the most practical screening tool could be the century-old electroencephalography (EEG) test. EEG techniques are still too crude to reliably detect low-to-intermediate levels of consciousness, but they could provide a useful screen for people who are "locked-in"—highly aware but unable to communicate with the outside world, says Adrian Owen, a neuroscientist at the University of Western Ontario in London, Canada. These people—roughly one in five of those who are misdiagnosed as vegetative—"can do everything that you can do except for move and speak," Owen says.

Unlike legal brain death, which can be diagnosed by testing basic brain stem responses, such as flinching in response to pain, "there is no gold standard" for discriminating between people in a vegetative state and those who are partly or fully conscious, explains Nicholas Schiff, a neurologist at Weill Cornell Medical College in New York City. In 2006, however, Owen's team demonstrated that it could communicate with a 23-year-old woman who had been diagnosed as vegetative, by asking her to imagine playing tennis while her brain was scanned with a functional magnetic resonance imaging (fMRI) machine. In response to Owen's discovery, the James S. McDonnell Foundation formed a consortium of researchers to generate inexpensive, portable methods for measuring borderline states of consciousness.

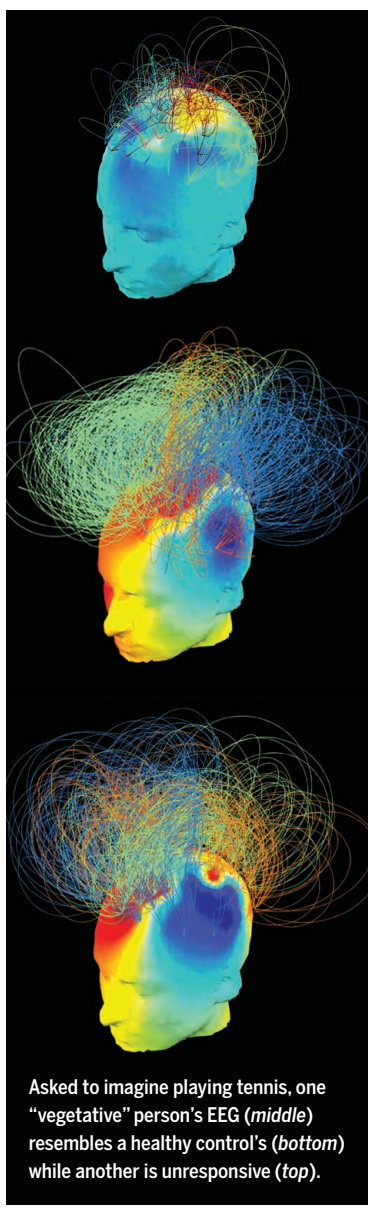

Asked to imagine playing tennis, one "vegetative" person's EEG (*middle*) resembles a healthy control's (*bottom*) while another is unresponsive (*top*).

The collaboration has at times been fractious—last year, for example, Schiff and several other members of the consortium went head-to-head with Owen over a paper his team published in 2011 in *The Lancet*. It claimed that conscious but locked-in patients could be spotted by instructing them to imagine opening and closing their right fist or moving their feet and monitoring their brains just with EEG, which measures electrical activity of the brain using simple sensors on the scalp.

At the meeting, however, Schiff and other participants presented their own data supporting an EEG screen for locked-in people.

In one study, also published online on 24 October in *Annals of Neurology*, Schiff and colleagues examined EEG recordings taken from 44 people who had severe brain injury and found that four patients who showed very little or no responsiveness nevertheless had EEG patterns that looked similar to those of healthy controls. When the researchers tested a subset of the people on an fMRI test similar to the tennis task used in Owen's original study, only the four who had more normal-looking EEGs were able to communicate.

Owen points to another recent study, on which he was a co-author, as support for the potential of EEG recordings. A research group led by Srivas Chennu of the University of Cambridge performed a complex mathematical analysis on the EEG signals of healthy and vegetative people to determine how well their different brain regions were working together. In three of the 32 brain-injured patients, the EEG analyses resembled those of healthy people, the team reported on 16 October in *PLOS Computational Biology*. Follow-up studies showed that all three of those patients were conscious and able to communicate with researchers through the fMRI technique that involves imagining playing tennis.

These findings suggest that EEG may work "much better" as a screening tool for locked-in patients than fMRI, which has been shown to miss telltale signs of awareness in many patients, Schiff says. Ultimately, he adds, the goal is to come up with a bedside EEG screening test that could be administered in just 30 minutes. If patients passed the EEG test, physicians might be able to help them communicate by monitoring their brain activity with fMRI, he says.

Cheap and practical solutions such as EEG "have to be the answer" in the long term, Owen agrees, although they will need refining to detect levels of consciousness that lie somewhere between a vegetative state and full awareness. One promising approach, he says, is to apply strong magnetic pulses to the brain and use EEG to measure the electrical "echo" that comes back. Marcello Massimini, a neuroscientist at the University of Milan in Italy, has recently found that these echoes are highly complex in healthy people. But in people with severe brain damage, the echoes often fail to propagate throughout the brain, or they create uniform "ripples" of activity that don't convey much information, "like dropping a stone in a pond," Massimini says.

As EEG proves its value as a diagnostic tool for locked-in patients, Schiff says that one advantage could be decisive: "You can get an EEG test anywhere in the world." ■

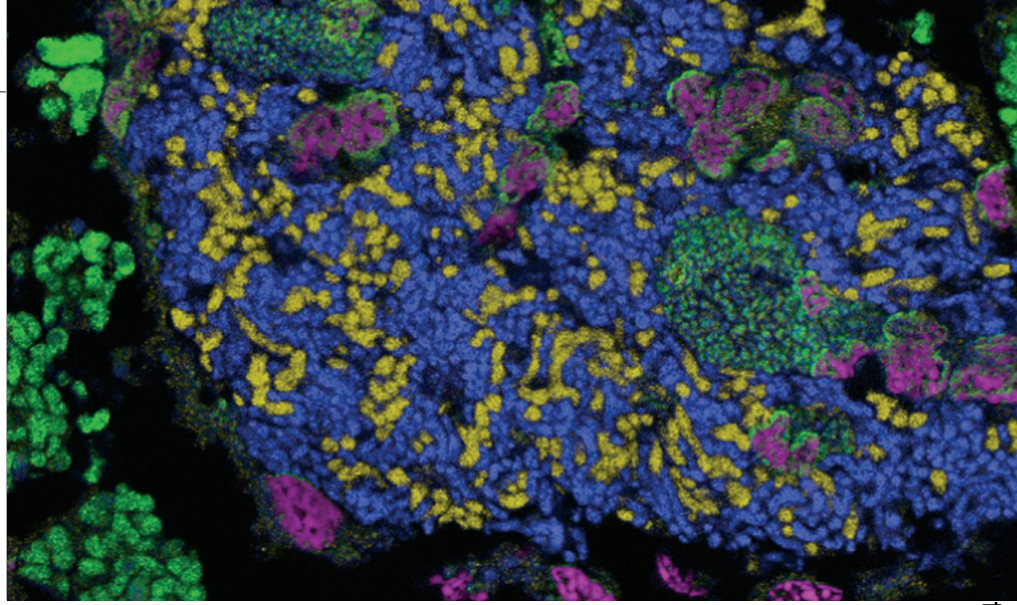

IMAGE: JAMES VAN LEUVEN AND JOHN MCCUTCHEON, PUBLISHED IN *CELL* 158:1270–1280

MICROBIOLOGY

Modern symbionts inside cells mimic organelle evolution

Long-term partnerships can result in extremes in genome reduction or expansion

By **Elizabeth Pennisi**, *in Irvine, California*

Some 2 billion years ago, primitive cells took in guests—and life was changed for good. A once free-living bacterium took up residence in a cell and gave rise to the organelles called mitochondria, which generate energy for their host cells by oxidizing sugars and also equipped some early life to survive Earth's increasing levels of oxygen. Another intracellular guest microbe became the ancestor of chloroplasts, the photosynthesizing organelles that made plants and algae possible.

Those momentous events, investigators are realizing, were not one-of-a-kind. Endosymbiosis, as a mutually beneficial relationship between an organism and a guest living inside its cells is called, is alive and well today, and has lessons to offer for how the process played out early in life history. "The line separating endosymbiont from organelle is very unclear indeed," said John McCutcheon, a biologist at the University of Montana, Missoula, earlier this month at "Symbioses becoming permanent," a meeting held here by the National Academy of Sciences and the Canadian Institute for Advanced Research.

At the meeting, biologists described how they are exploring those parallels. They are probing how insects such as cicadas and other multicellular organisms set up partnerships inside their cells with microbes that, like their ancient forerunners that became organelles, help provide essential nutrients and other services. Along the way, they are learning about the complex bargains host cells strike with their microbial partners—trade-offs that can explain some of the features of mitochondria and chloroplasts today.

Although DNA studies have convinced biologists that mitochondria evolved just once, from a type of microbe called an α-proteobacterium, the organelles have diversified wildly since then. Whereas modern free-living relatives of this bacterium harbor about 2000 genes across several million bases, its mitochondrial descendants all have far fewer genes—sometimes as few as three—and a wide range of genome sizes and shapes. The smallest mitochondrial genome is just 6000 bases long; human mitochondrial DNA stretches 16,000 bases. Some plants, in contrast, greatly expanded the genomes of their mitochondria, padding them with apparently inessential DNA: The biggest known, at 11 million bases, belongs to a flower called *Silene*, and it's divided into many circular chromosomes, some of which have no genes at all on them. Mitochondria have "been an endless reservoir of unconventional genomes," says David Smith, an evolutionary biologist at the University of Western Ontario in London, Canada. "They break all the rules."

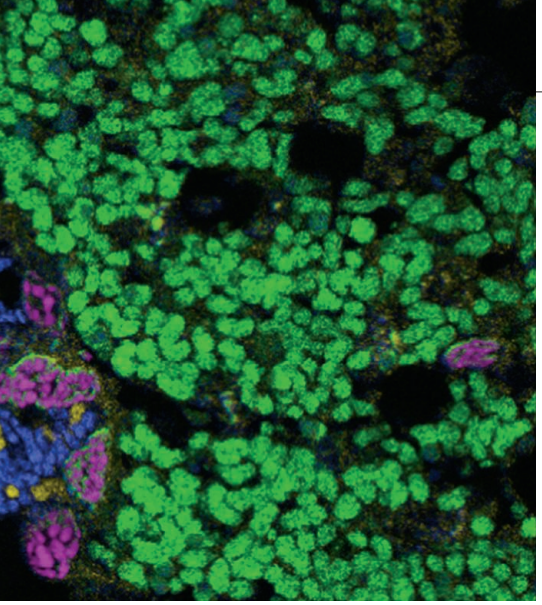

Inside a specialized cicada organ, one endosymbiotic microbe has split into two species (yellow and blue). They are surrounded by a third (green). Insect nuclei are purple.

But many modern endosymbionts break those same rules, McCutcheon noted at the meeting, drawing on his studies of cicadas. These sap-sucking insects derive amino acids missing from their diet from bacterial partners that reside in specialized cells. The cicada *Diceroprocta semicincta*, for example, harbors two such partners. One, called *Hodgkinia*, supplies the insect with two amino acids it cannot provide on its own, while the other, *Sulcia*, provides another eight. In another cicada species, however, *Hodgkinia* has doubled the amount of its DNA, diverged into two distinct genomes, and divided up the task of supplying the two amino acids, McCutcheon and his colleagues reported at the meeting and online on 28 August in *Cell*. One *Hodgkinia* provides some of the genes and the other fills in the gaps in amino acid production, making both "species" essential to the endosymbiosis.

McCutcheon's team has more recently looked at the endosymbionts of a *Magicicada* cicada, which emerges on a 13- or 17-year cycle and may harbor scores of distinct *Hodgkinia* genomes, some that seem to carry very few or no functional genes. The finding parallels what happened to the plant mitochondrial genome in *Silene*, McCutcheon suggests. It seems that in both these cases, unchecked mutation rates and DNA amplification led to greatly expanded but marginally functional, fragmented genomes. "When things go wonky, they really go wonky," Smith says.

The cicada's unusual lifestyle—long dormancy, followed by a brief burst of activity—may play a role in this "genomic insanity," McCutcheon proposes. The species with a single *Hogkinia* genome can take 3 years to fully develop, and the one with many *Hodgkinia* genomes can take 17. Although cicada nymphs are basically dormant during most of that long cycle, the endosymbionts might be free to replicate with no survival pressures acting to keep their genomes stable. "Some cicada life histories seem to allow slop and chance to take over, or maybe just slop," McCutcheon told the audience.

Investigators are also examining modern analogs to the complex evolution of the chloroplast, which seems to have emerged once, but then was lost and regained in different ways in various modern photosynthetic organisms. The photosynthetic organelle was originally a cyanobacterium that was engulfed by a eukaryote. Plant biologists have long recognized that in some branches of the plant and algal family tree, this initial chloroplast was lost, but a new one was acquired when a host cell swallowed up an alga that in turn had its own chloroplast.

At the meeting, Patrick Keeling, a protistologist at the University of British Columbia, Vancouver, in Canada, described his studies of a more recent example of this process, called tertiary endosymbiosis. Some dinoflagellates, single-cell aquatic protists, no longer have their original chloroplast, relegating some of its light-sensing apparatus to a cellular component dubbed an eyespot. But they have replaced it by taking in a diatom, a single-celled alga that has its own photosynthetic machinery. The dinoflagellate still carries the diatom's nucleus and mitochondria, but "I would challenge anyone to say this is not an organelle," Keeling says.

> ***"The line separating endosymbiont from organelle is very unclear indeed."***
>
> **John McCutcheon**, University of Montana, Missoula

The meeting highlighted other similarities between endosymbionts and organelles. Mitochondria are typically passed only from the mother to offspring, and some endosymbionts similarly depend on maternal transmission, dwelling in eggs and perhaps even promoting female progeny over male to perpetuate themselves, says Steve Perlman of the University of Victoria in Canada.

All these results "make organelles not so special," says W. Ford Doolittle, a molecular evolutionary biologist emeritus at Dalhousie University in Halifax, Canada. Embracing endosymbionts as good models for the evolution of organelles makes for "an interesting paradigm shift in the field." ■

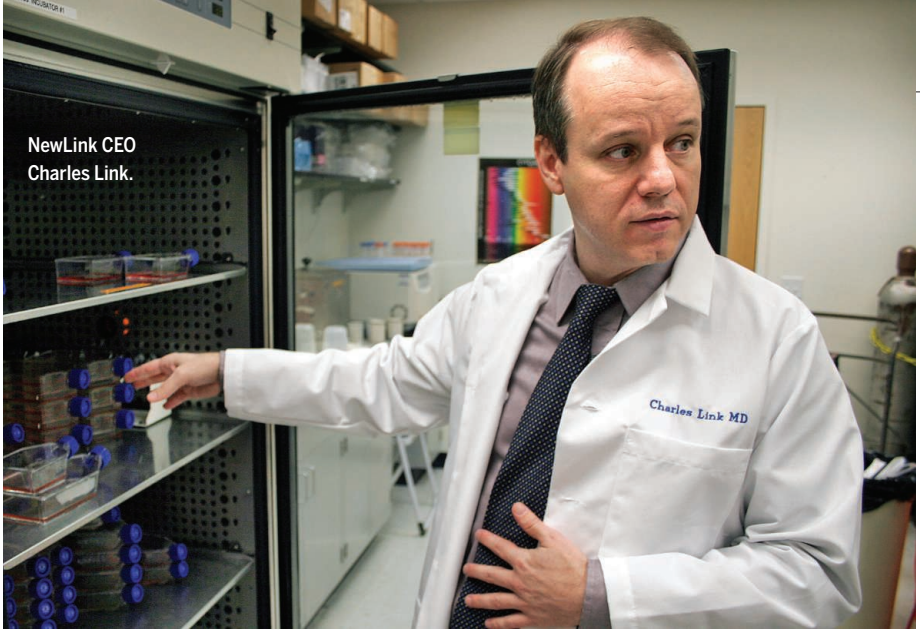

NewLink CEO Charles Link.

INFECTIOUS DISEASES

The Ebola vaccine underdog

NewLink Genetics says it might have enough doses ready by spring to vaccinate most people at risk

By **Jon Cohen**

In the race to develop an Ebola vaccine, little NewLink Genetics has been in the shadow of pharmaceutical giant GlaxoSmithKline (GSK).

Both companies have rushed experimental vaccines into small, early-stage trials. Hopes are high that the vaccines can be ready for large efficacy trials in hard-hit West Africa in January—and if they work, for real-world use in the spring. GSK's efforts have received extensive media attention, and, with its substantial manufacturing capacity and experience, the mammoth U.K.-based company is widely assumed to be in the lead. In contrast, NewLink, a cancer drug company based in Ames, Iowa, with just 120 employees, has until recently avoided media coverage and drawn criticism for delaying the launch of its studies.

But a different picture emerged after NewLink broke its media silence following a high-level meeting on Ebola vaccines held by the World Health Organization on 23 October. At the meeting, NewLink executives said that, under a best-case scenario, the company might have 12 million doses of vaccine by April. That number would far outstrip GSK's estimate of 230,000 doses by that date.

There are many caveats. If NewLink's vaccine requires a high dose to be effective, far fewer people could be immunized. And NewLink's vaccine, which combines an Ebola gene with a weakened vesicular stomatitis virus (VSV), a livestock pathogen, poses unique risks.

NewLink CEO Charles Link Jr., an oncologist who previously worked at the National Cancer Institute, spoke with *Science* about the charges of delay and why he is optimistic about the higher projections. This interview has been edited for brevity and clarity.

Q: You recently completed a $1 billion deal with Genentech to develop a cancer immunotherapy. Did those negotiations delay work on the Ebola vaccine and influence your decision to avoid media?
A: I really don't feel there were any delays. Things are moving so quickly that we're right on the edge of moving too quickly. There's a huge push and pull between wanting to do the right thing for humanity and needing to do things safely, scientifically, and ethically in healthy volunteers who are receiving the vaccine. Our view was we didn't want to hype anything. We just wanted to work on the project. Ebola came first, [the Genentech] negotiation came second, and PR came third. We've been trying to play it low-key, but it's difficult to play it low-key with all this attention.

Q: You licensed the vaccine from the Canadian government for a mere $200,000. Although you have received small contracts from the U.S. government to develop the vaccine, did you have trouble getting substantial funding to support the Ebola program?
A: No doubt. At first, the board didn't see much commercial potential in it. But when the crisis began to evolve, everybody was: "Let's go, let's make this happen." There was no hesitancy once the crisis began.

Q: What about your projection of 12 million doses available in April?
A: The key question is what is going to be the dose of the vaccine.

Q: Studies under way are looking at doses of 10^6 virus particles up to 10^8. The 12 million is based on 10^6, right?
A: Yes, so if a dose needs to be 10^6 or 10^5 virus particles, we're going to have plenty of vaccine for West Africa if it works.

Q: Why do you think the lower doses might suffice?
A: Even though this vaccine is based on an attenuated virus, it is replicating at least some in humans. In talking to experts who have worked with a lot of attenuated vaccines, you may only need 10^4 [virus particles] to create the immunologic effect—and we may amend our studies to look at those lower doses.

Q: Do you think the vaccines are going to be safe and effective?
A: In the primate model, such a wide variety of these vaccines work that I really believe one of them is going to be effective in humans. That is my hope and dream here—ours or someone else's.

Q: What about side effects? The VSV vaccine was used in 2009 to treat a lab worker who had a needlestick injury in Germany. What happened?
A: The woman developed a temperature of 38.5°[C]. I don't think you can have a vaccine that causes high fever in a significant portion of subjects, especially where fever is the first indication of Ebola. But she was given a dose of 5×10^7 [virus particles], based on an extrapolation from monkey studies. We're hoping that at the lower doses people might have low-grade fevers, but there won't be high-grade fevers.

Q: Is there a risk of VSV spreading from vaccinated people and infecting livestock?
A: It's a legitimate concern and we're looking at ways to evaluate that.

Q: Producing the vaccine in bulk will require large-scale manufacturing capacity. Have you considered linking with big pharma companies that know how to mass-produce vaccine, including putting it into vials?
A: We are in fact in active discussions with a big company about just that potential. ■

PHOTO: AP PHOTO/CHARLIE NEIBERGALL

GEOCHEMISTRY

Low oxygen stifled animals' emergence, study says

Rocks shed light on a billion years of stalled evolution

By **Carolyn Gramling**

Paleontologists call it the "boring billion." Between the appearance of complex cells 2.1 billion to 1.6 billion years ago and the explosive diversification of multicellular animals some 800 million years ago, not much happens in the fossil record. Evolution seems to have been mired. On page 635 in this week's issue of *Science*, a team analyzing geochemical tracers in ancient rocks offers new evidence to explain the long lag: Atmospheric oxygen during that period was anywhere from 10 to 100 times lower than believed.

The finding by a team led by Noah Planavsky of Yale University is "very exciting," says geochemist Sean Crowe of the University of British Columbia, Vancouver, in Canada. "There's been a tendency to shy away from changes in atmospheric or oceanic oxygenation as important for driving the evolution of animals. It's great to see that we now have a little more information pointing toward oxygen as an important driver."

Oxygen's rise in Earth's atmosphere used to have a simple story arc. For the first 2 billion years of the planet's history, scientists thought, the atmosphere was devoid of free oxygen; what oxygen existed was bound up in rocks. Then came the Great Oxygenation Event, sometime about 2.3 billion years ago, when cyanobacteria in the oceans began producing enough oxygen for the gas to accumulate in the atmosphere and the surface of the ocean.

What followed was the boring billion. Oxygen levels decreased (and possibly rose and fell again due to biogeochemical feedbacks such as decreased tectonic activity, weathering, and bacterial activity in the oceans). Previous estimates put oxygen at the time at anywhere from 1% to 40% of present-day levels. It wasn't until about 800 million years ago that oxygen again began to rise, causing reactions that triggered global cooling and then—about 542 million years ago—a rapid diversification of animals called the Cambrian Explosion.

"There's a conundrum associated with the observation that you have the emergence of eukaryotic organisms … and then this extremely long lag between that innovation and the emergence of complex multicellular organisms," says Christopher Reinhard, a geochemist at the Georgia Institute of Technology in Atlanta and a co-author of the new paper.

To resolve the puzzle, researchers need to know more about ancient oxygen levels. Recent studies have suggested that oxygen's rise was a lot bumpier than once thought—and some of the most surprising data come from chromium isotopes in ancient rocks. Chromium chemistry is highly sensitive to oxygen in the atmosphere: In an oxygen-free environment, the metal is bound up in rocks in one form, chromium(III). But even a whiff of oxygen is enough to oxidize another metal, manganese, which reacts with the chromium(III) and converts it to a new, easily weathered form, chromium(VI). Rain then washes the chromium(VI) into the ocean, where it is locked up in sediments. Just how much oxygen is present can be determined from the ratio of two chromium isotopes, chromium-53 and chromium-52. Because the heavier isotope is more likely to be oxidized and subsequently weathered away, the higher the ratio of 53 to 52, the more oxygen the new sediments once held.

In 2009, geochemist Robert Frei of the University in Copenhagen and his colleagues published the first study to use chromium as such a proxy for early oxygen levels, finding that the surface ocean already contained some oxygen 2.8 billion to 2.6 billion years ago. Even more surprisingly, they found, oxygen dropped off steeply about 1.8 billion years ago.

To add to that tantalizing data point, Planavsky, Reinhard, and colleagues focused on ironstones—sedimentary rocks containing grains of sand coated in hematite, an iron-rich mineral—which form in shallow seawater. The deep ocean was still anoxic during the boring billion, so to study what was happening in the atmosphere and shallow ocean, "we wanted something that was a nearshore setting where we were likely to track a terrestrial input," Planavsky says. They studied four ironstone samples from around the world, ranging in age from 1.7 billion to 0.9 billion years.

None of the ironstones showed any signs of chromium isotopic fractionation. And that, Planavsky says, sharply limits how much oxygen could have been in the atmosphere at those times. "We can have significant chromium oxidation at very low levels of oxygen, just 0.1%" of present atmospheric levels. That suggests Earth was not only oxygen-poor during the boring billion, Reinhard says, but also "perhaps more profoundly than people really appreciated."

Frei isn't fully convinced. "There's no doubt that these values tell you something about the composition of shallow waters in some basins at the time," he says, but whether they can be extrapolated to all shallow ocean waters isn't yet clear. "The puzzling thing is that we know that around 1.2 billion years ago there was the formation of gypsum deposits," which require oxygen to form in the ocean.

Reinhard says the study reemphasizes the role of oxygen in biological evolution. Recent studies have stressed genetic innovation over environmental factors, he says, but "we bring that back to the table." ■

An oxygen threshold

Chromium isotope ratios in rocks older than 800 million years (●) point to low atmospheric oxygen, in contrast to younger rocks (●). In an oxygenated world (//), multicellular organisms and other eukaryotes also rapidly diversified about 800 million years ago.

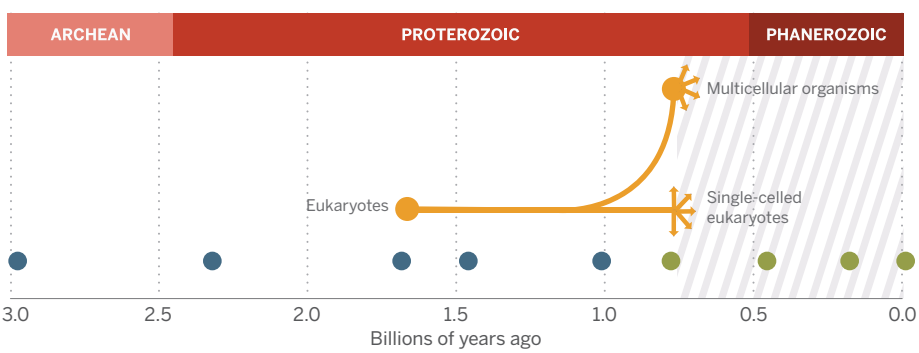

PHOTO: PLANAVSKY ET AL./*SCIENCE*

Giant balloons of uncompressed natural gas on buses in China in the 1980s underscore the challenge of using this low energy density fuel for transportation.

PHOTO: © LOUIE PSIHOYOS/CORBIS

STEPPING ON THE GAS

What would it take to put you behind the wheel of a methane-powered vehicle? Researchers are determined to find out

By **Robert F. Service**, *in Los Angeles, California*

Dane Boysen is a lousy salesman. Speaking at a conference on natural gas–powered vehicles here this month, Boysen, who heads a natural gas vehicle research program at the U.S. Department of Energy's Advanced Research Projects Agency-Energy (ARPA-E), says what industry stalwarts don't want to hear. "Honestly, natural gas is not that great of a transportation fuel." In fact, he adds, "it's a stupid fuel."

Some audience members respond with playful boos, but they know what he's talking about: energy density. A liter of gasoline will propel a typical car more than 10 kilometers down the road; a liter of natural gas at ambient temperature and pressure will take it 13 meters. Even when natural gas is chilled to make it liquid or jammed into a high-pressure tank—processes that cost both energy and money—it still can't match gasoline's range.

Nevertheless, Boysen's ARPA-E project, called Methane Opportunities for Vehicular Energy (MOVE), is in the middle of spending $30 million over 5 years to jump-start the development of natural gas–powered cars and light-duty trucks, a category that makes up nearly 60% of all vehicles on the road.

Why? Because, low energy density aside, natural gas has a lot to offer. It's abundant and cheap. The current fracking boom in the United States is producing so much natural gas that a volume of gas with the energy equivalent of a gallon of gasoline costs roughly half as much. And the United States has known gas reserves to last at least another century. Gas is also relatively clean. Natural gas–powered engines generate up to 30% less climate-warming CO_2 than gasoline engines do, as well as far lower volumes of the nitrogen oxide and sulfur oxide pollutants that contribute to urban smog.

What's more, those engines already exist. With a little tinkering, conventional gasoline or diesel engines can burn natural gas. According to NGVAmerica, an industry trade group in Washington, D.C., 15.2 million natural gas–powered vehicles are on the road worldwide. They include 142,000 in the United States, most of them heavy-duty trucks and transit buses. Some projections suggest that most trucks in the United States will be natural gas–powered by 2030.

For heavy-duty engines, economics is the driver. Even though trucks with natural gas engines cost tens of thousands of dollars more than their diesel counterparts, trucks use so much fuel—an average of more than 45,000 liters of diesel per year—that fuel savings offset the extra cost in as little as 2 or 3 years, says William Zobel, vice president of market development and strategy for Trillium CNG in Escondido, California, which builds compressed natural gas (CNG) fueling stations. Tightening pollution standards for trucks and buses are also driving the shift.

Now, Boysen and others want to see natural gas expand its reach to natural gas–powered light-duty cars and trucks. "It's right here," Boysen says, stretching out a hand to clutch an imaginary prize. "I absolutely believe [the technology] is going to take off," he says. Reynaldo Gonzalez, a transportation researcher at the California Energy Commission in Sacramento, agrees. "There is only one alternative vehicle technology with an economic advantage, and that's natural gas," he says.

But as Stephen Yborra, who directs market development for NGVAmerica, puts it, "there are an awful lot of hurdles to overcome." Honda, for example, already makes a natural gas version of its Civic sedan. But it has sold only 2000 of them in the United States, compared with more than 1.5 million gasoline-powered cars a year. Major improvements in fuel tanks, pumps, and infrastructure will be needed before natural gas vehicles rule the road.

As Boysen paces a small stage here at a conference center at the Port of Los Angeles, outside the window massive container ships are being unloaded with cars from Japan, TVs from Korea, and furniture from China. Those goods are moved out by some 8000 trucks every day, more and more of them fueled by natural gas to comply with the port's pollution standards. But Boysen is candid about the obstacles to expanding that revolution. He says he's free to speak openly, because he's leaving ARPA-E at the end of this month. One by one, he ticks off formidable technical challenges and the efforts engineers are making to solve them.

"Home refueling and low-pressure tanks would be major game changers for this industry."

Cherif Youssef, Southern California Gas Company

GAS TANK MATERIALS. The biggest problem goes back to the meager energy density of natural gas. At ambient temperature and pressure, it's a mere 40,000 joules per liter, slightly more than 1/1000 that of gasoline. To carry enough fuel, a car needs an oversized fuel tank, which eats into its cargo space. As a result, Honda's natural gas Civic has less than half the trunk volume of its gasoline counterpart. "Drivers hate this because they can't pick up people at the airport," Boysen says.

The fuel tanks also have to be pressurized—another source of headaches. Today's tanks compress gas to 250 bar, about 250 times atmospheric pressure. To handle the stresses, tanks must be made either from thick metal—which makes them heavy—or from lighter but expensive carbon fiber. Current tanks add an average of $3500 to the cost of natural gas vehicles. Boysen's MOVE project is aiming to reduce this premium to $2000, a number that in-

PHOTO: © RALPH D. FRESO/REUTERS/CORBIS

cludes the costs of any needed refueling equipment. "Two thousand dollars is really a major challenge," says Cherif Youssef, a technology development manager with Southern California Gas Company here.

One option is to fill storage tanks with porous materials that sponge up methane at modest pressure and release it when the pressure is reduced. That lower pressure would make tanks lighter and cheaper and could also reduce the cost of the compressors needed to refill them. In 2012, the U.S. Department of Energy set the target for methane absorbents at 263 cubic centimeters of volume of methane per volume of absorbent (v/v), equivalent to CNG at 250 bar at 25°C.

Activated carbon is one such sponge that continues to attract plenty of attention, because the material is cheap and is produced by the ton for a wide variety of industrial uses. But its theoretical maximum capacity is only 220 v/v. Materials called metal-organic frameworks (MOFs) have already beaten that number. Unlike activated carbons, which have a randomly oriented internal structure, MOFs are porous crystalline materials that are designed from the atomic scale up, and they can be tailored to grab on to methane molecules.

Researchers have already engineered hundreds of MOFs. The early methane storage leader was a copper-containing MOF known as HKUST-1. When pressurized to 35 bar, it has been reported to store as much as 220 v/v. But not all of that gas is released when the pressure drops. At 5 bar, HKUST-1 still holds on to a third of its methane, reducing its usable capacity to 149 v/v. Earlier this year, researchers led by chemist Omar Yaghi of the University of California, Berkeley, reported in the *Journal of the American Chemical Society* that they could do better. They created a MOF called MOF-519 that has less total volumetric capacity than HKUST-1 but a greater working capacity. Another promising MOF-like material called a porous polymer network, made by researchers at Texas A&M University, tops all other leading materials for total storage capacity but can't yet match their working capacity.

Still, it's one thing to make gram-scale quantities of MOFs in a lab, but another entirely to make it by the train car loads that would be needed to outfit millions of cars with 21st century fuel tanks. Here, too, there has been progress. The chemical company BASF has developed methods to synthesize ton-scale quantities of another MOF contender and is road-testing MOF-equipped delivery vans in Germany. Framergy, a startup company in College Station, Texas, says it can now make grams of other MOFs for just pennies, within sight of the ARPA-E target of less than $10 per kilogram.

That's all good news, Boysen says. But other "large challenges" remain before MOF-based storage will be practical—among them reaching DOE's target of a 263 v/v working capacity. "So there's still work to do here," he says.

GAS TANK SHAPES. Spongelike fuel storage at modest pressures might free engineers to build tanks in shapes other than the now-standard high-pressure cylinder. That's critical, notes Ellen Sun, who heads a next-generation tank project at the United Technologies Research Center (UTRC) in East Hartford, Connecticut, because in a car, a cylinder occupies a box as big as its largest dimension, wasting a lot of space. For heavy-duty trucks and buses, which don't have tight space constraints, an awkward tank shape is less of a problem. But it's a killer for passenger cars. A MOF-based tank could be shaped like a traditional—though large—gas tank.

UTRC and other companies are also using more conventional approaches to reengineer high-pressure tanks to ease the stresses on the tank material so it can be made to fit any desired shape. A company called REL Inc., for example, has created a tank prototype with two interpenetrating networks of channels to hold methane. Because it uses the full rectangular volume, it is 30% more space-efficient than a cylindrical tank of the same capacity. UTRC and a company called Otherlab in San Francisco, California, meanwhile, are developing technologies to create networks of small interconnected cylinders that can conform to any shape.

GASSING UP. Whatever sort of tanks wind up on the road, they will have to be refilled. Engineers are working to improve that technology, too. One challenge is the time it takes to fill up. Gasoline pumps can supply as much as 10 gallons (38 liters) of fuel per minute, an energy transfer rate equivalent to 20 megawatts of power. Today's CNG systems can fill the equivalent of a 15-gallon (57-liter) tank in 5 minutes. But they are expensive and primarily service trucks and specialized fleets.

Many advocates of natural gas cars dream of a low-pressure compressor that could be used for home refueling, as roughly half of U.S. homes—some 60 million—already have a natural gas line. If cars could be refueled at home, consumers would tolerate slower filling rates, as they do with electric vehicles. "Home refueling and low-pressure tanks would be major game changers for this industry," says Southern California Gas

How far a car can go on a liter of fuel

In meters, assuming fuel economy of 10.6 km/liter (25 mpg) of gasoline

10,600
Gasoline

7197
Liquefied natural gas

2968
Compressed natural gas (CNG) at 250 bar

2968
CNG with adsorbent at 35 bar (DOE goal)

2257
CNG with MOF-519 adsorbent (theoretical capacity)

13
Unpressurized natural gas

Crystalline metal-organic framework (MOF) materials under development at BASF. The company is working to scale up the production of MOFs to store natural gas.

Company's Youssef. One such compressor is already on the market, Boysen notes. But it costs $5500, a number the MOVE project is hoping to drop by more than 90%.

At the natural gas–powered vehicles conference, researchers reported a few steps in that direction. A group at Oregon State University, Corvallis, said it had designed a natural gas–burning engine that, at the flip of a switch, can turn one of its cylinders into a compressor and act as its tank's own pump. Meanwhile, researchers at the University of Texas, Austin, have created a simplified compressor with only one moving part: a piston that slides back and forth. They think it could be manufactured for $1500, not far from the MOVE target.

Like the MOFs, those prototypes still have a way to go to make it to market. Among the many challenges they'll have to deal with is filtering out water and other impurities from low-pressure gas lines so they don't accumulate in gas tanks. But with so few vehicles on the road, compressor manufacturers have been unwilling to invest in new technologies. As a result, says Bradley Zigler, a combustion researcher at the National Renewable Energy Laboratory in Golden, Colorado, "right now there is a valley of death between research progress and commercially available technologies."

INFRASTRUCTURE, INFRASTRUCTURE, INFRASTRUCTURE. Even if engineers do it all—come up with a cheap space-age crystal to hold gas in a low-pressure tank, a more efficient natural gas–burning engine to reduce the demand for a large tank, and a cheap new compressor—that still might not be enough. For drivers to gamble tens of thousands of dollars on a new kind of car, analysts say, they'll need all of these technologies to be widely available at the same time. "It has to be in a box," Youssef says. "To me, that's the biggest hurdle. I'm afraid we're not there yet."

Even then, Boysen notes, natural gas vehicles would face competition from a more-than-viable alternative: the gasoline- and diesel-powered cars that now make up 93% of passenger vehicles on the road. Drivers will need to be convinced that a natural gas car will work at least as well as current cars do. They will need to know they can buy fuel wherever and whenever they want. And they will need a nationwide network of mechanics and parts suppliers to fix things when they break. Gasoline-powered and electric cars already cover the whole menu, but would-be competitors have far to go.

This suite of demands is particularly acute for truly novel technologies, such as hydrogen-powered fuel cell vehicles. The lack of an existing fueling infrastructure for those cars makes it far less likely that drivers will embrace them. But the fact that such challenges are also proving daunting to natural gas–powered cars, with their sizable fuel cost advantage, underscores just how difficult it is to transform the way we drive. For Boysen and his colleagues, the allure of natural gas is stronger than ever. But they know reality can be unkind to even the most appealing technologies. ■

Weaving a new gas tank

Crisscrossing voids (false color) could enable engineers to build high-pressure tanks in any shape needed.

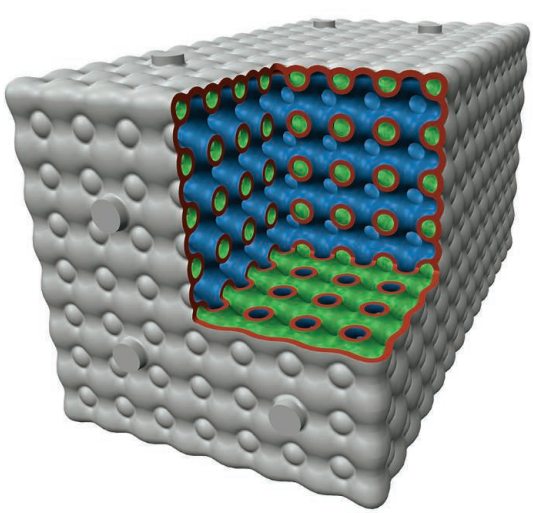

IMAGES: (TOP) BASF CORPORATION (2); (BOTTOM) REL INC.

The neurology of the undead *p. 557*

A coordinated eye on the prize *p. 554*

PERSPECTIVES

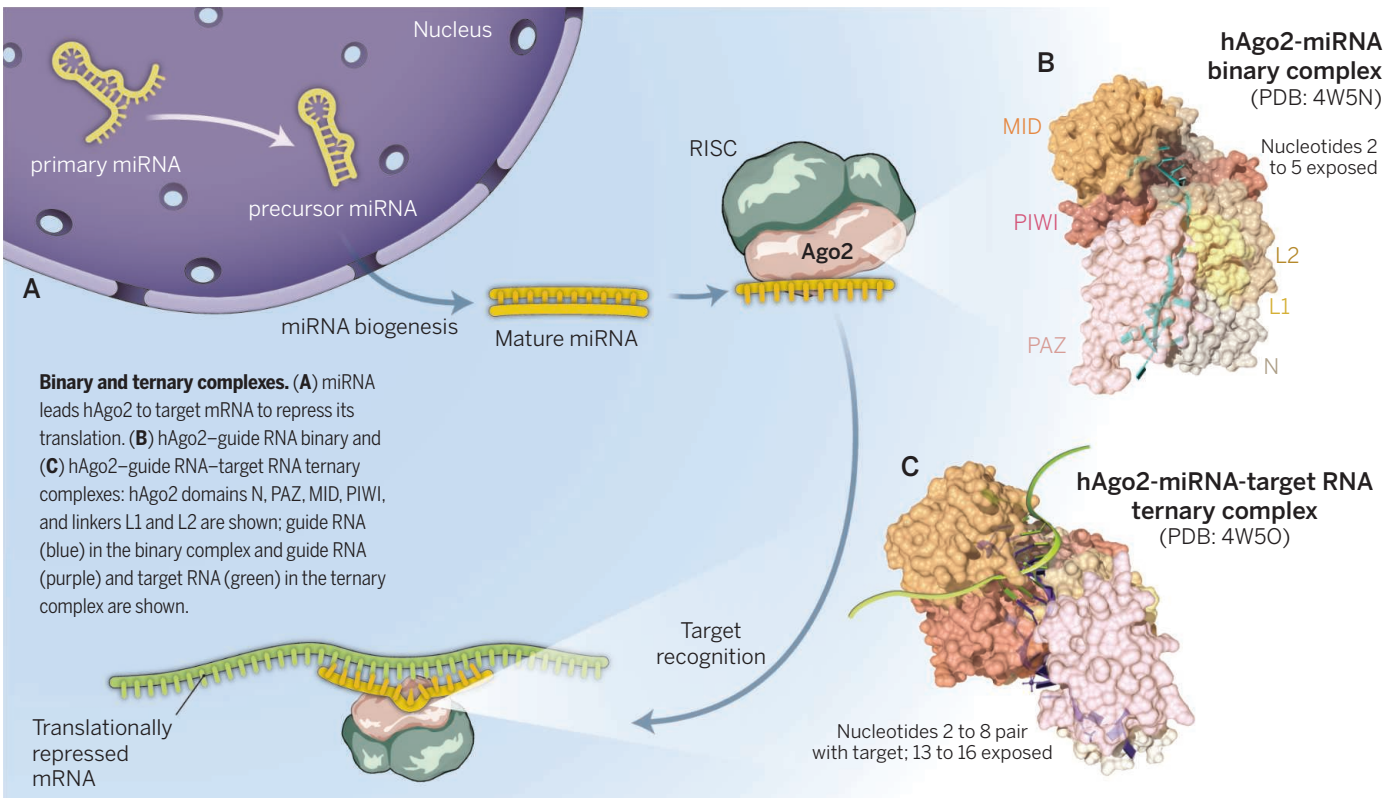

Binary and ternary complexes. (**A**) miRNA leads hAgo2 to target mRNA to repress its translation. (**B**) hAgo2–guide RNA binary and (**C**) hAgo2–guide RNA–target RNA ternary complexes: hAgo2 domains N, PAZ, MID, PIWI, and linkers L1 and L2 are shown; guide RNA (blue) in the binary complex and guide RNA (purple) and target RNA (green) in the ternary complex are shown.

RNA

Complete pairing not needed

Structures of microRNA-mRNA–human Argonaute reveal where and how intermolecular interactions are specified

By **Dinshaw J. Patel**

Gene expression can be silenced in eukaryotic cells by small noncoding RNAs that target mRNAs and prevent their translation into protein. These microRNAs (miRNAs) recruit a ribonucleoprotein complex called the RNA-induced silencing complex (RISC) and guide it to target mRNA, where miRNA-mRNA annealing allows RISC to execute translational repression (see the first figure, panel A). Argonaute (Ago) protein, a key component of RISC, is highly conserved from prokaryotes to eukaryotes and is essential for gene silencing (*1*). The mechanistic basis underlying the silencing initially emerged from x-ray crystallographic studies of prokaryotic Ago proteins bound as binary complexes to guide strands (DNA) and as ternary complexes with added target strands (RNA or DNA). These structural studies focused on small interfering RNA (siRNA)–mediated cleavage of target mRNA, whereas more recent studies of the same complexes in eukaryotes have focused on miRNA-mediated translational repression (*2*–*4*). On page 608 of this issue, major mechanistic insights are gleaned from structural studies by Schirle *et al.* (*5*) on binary and ternary complexes of human Argonaute 2 (hAgo2).

The Ago protein adopts a bilobal scaffold composed of N-terminal (N and PAZ domain) and C-terminal (MID and PIWI domain) lobes (*6*). The PIWI domain, which adopts a ribonuclease H (RNase H) fold, contains the catalytic acidic residues involved in siRNA-mediated target cleavage (*6*). Structural studies on the binary complex of *Thermus thermophilus* Ago (*Tt*Ago) with a bound guide strand (in this case, DNA) identified the nucleic acid binding channel between the two lobes, with the 5′-phosphorylated end of the guide anchored within the MID domain of Ago and the 3′-end anchored within the PAZ domain (*7*). Notably, nucleotides 2 to 6 of the bound guide were in a helical conformation with their base edges directed out-

CREDIT: V. ALTOUNIAN/*SCIENCE*

ward, available for pairing with target RNA. This configuration thus constitutes the nucleation step of target recognition.

Follow-up structural studies examined ternary complexes of *Tt*Ago bound to a DNA guide strand with an added target RNA (or DNA). These studies defined the pivot-like conformational changes associated with nucleation, propagation, and cleavage steps of the catalytic cycle (*8*). These structural studies used target strands of varying length complementary to the guide's seed segment (nucleotides 2 to 8), target-cleavage site (nucleotides 10 and 11), and the supplementary segment (nucleotides 12 to 19). The studies also defined the role of a pair of Mg^{2+} ions and acidic residues positioned within the PIWI domain of Ago in mediating the cleavage chemistry. From a functional viewpoint, both DNA- and RNA-guided prokaryotic Agos were shown to be involved in defense against mobile genetic elements (*9*, *10*).

Unlike siRNA-mediated cleavage of target mRNAs, which require perfect complementarity between guide and target, miRNAs require pairing of guide and target to primarily span the seed segment (nucleotides 2 to 8) of the target mRNA for translational repression and degradation (*4*, *11*). Two enzymes, Dicer and Ago, mediate miRNA biogenesis, converting precursor miRNA to mature miRNA that is then loaded onto Ago (*4*). To understand the principles underlying miRNA-mediated translational repression, structural studies on prokaryotic Ago (pAgo) complexes have been extended to their eukaryotic Ago (eAgo) counterparts. These include studies of binary complexes of hAgo2 (*12*, *13*) and budding yeast *Kluyveromyces polysporus* Ago (*Kp*Ago) (*14*) with bound guide RNA strands. The seed segments of guide RNAs—either mixed-sequence (*12*, *14*) or defined-sequence (*13*)—were anchored at both ends in the eAgo complexes, with nucleotides 2 to 5 directed outward and available for pairing with target RNA, similar to their prokaryotic counterparts. In addition, structural studies on *Kp*Ago binary complexes with guide RNA identified a key glutamic acid that inserted into the catalytic pocket of eAgo to complete a catalytic tetrad (composed of four acidic residues) associated with formation of a cleavage-competent conformation (*14*).

Extension of these studies to ternary complexes required Schirle *et al.* to generate and purify milligram amounts of hAgo2 bound to a defined-sequence guide RNA (*15*), which could then be used to generate ternary complexes in amounts sufficient for crystallization and structure determination. The structural analysis was aided by x-ray data sets (at 2.9 Å resolution) of hAgo2 binary complexes with 5′-phosphorylated guide RNA (21 nucleotides in length) (see the first figure, panel B) and ternary complexes with added target RNAs (11 nucleotides in length) that were complementary to nucleotides 2 to 7, 2 to 8, and 2 to 9 of the guide (at 1.8 to 2.5 Å resolution) (see the first figure, panel C).

Schirle *et al.* show that ternary complex formation involving hAgo2 is facilitated by shape complementarity between the minor groove of the guide-target duplex that spans seed nucleotides 2 to 7, and hydrophobic residues of the interacting Ago scaffold. This explains why mismatches between guide and target are not tolerated within this region of the seed segment. By contrast, there are no such intermolecular contacts with hAgo2 for the duplex spanning nucleotides 8 and 9, explaining why mismatches are tolerated at these positions. Earlier structural studies of binary eAgo complexes had identified a kink between nucleotides 6 and 7 of the guide as a result of insertion of an isoleucine residue from helix α7 of the protein (*12*–*14*). Strikingly, Schirle *et al.* show that upon ternary complex formation, nucleotides 6 and 7 adopt a stacked helical conformation, with α7 undergoing a 4 Å shift. This change is necessary for accommodating the guide-target duplex within the hAgo2 scaffold.

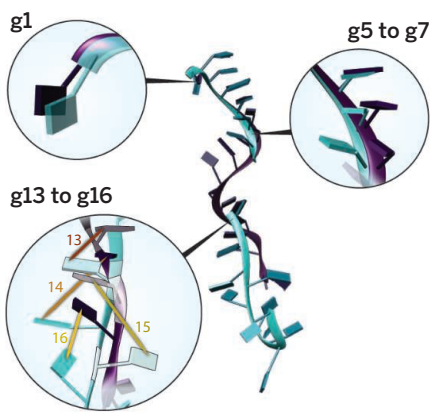

Superposition. The guide (g) RNA in binary (blue) (PDB: 4W5N) and ternary (purple) (PDB: 4W5O) complexes compares nucleotides 1, 5 to 7, and 13 to 16.

Another notable feature of the binary complex of hAgo2 with defined-sequence guide RNA is that in addition to the expected anchoring of both ends of the guide and the helical alignment adopted by the seed segment, the guide strand spanning nucleotides 14 to 18 could be traced for the first time. This segment is anchored within a narrow channel between the N and PAZ domains, with their base edges directed inward and unavailable for pairing. By contrast, upon formation of the ternary complex with target RNA, nucleotides 14 to 18 underwent a profound conformational change from an unstacked to a stacked state, whereby their base edges were directed outward and available for pairing.

These distinct conformational transitions within the guide strand upon proceeding from the hAgo2 binary to ternary complex formation (see the second figure) led Schirle *et al.* to propose a stepwise model for miRNA targeting, whereby the miRNA guide strand initially interrogates mRNAs to identify candidate target sites through pairing involving seed nucleotides 2 to 5. This, in turn, triggers a concerted conformational transition in hAgo2, involving helix α7 and the PAZ domain, which exposes seed nucleotides 6 to 8 and supplementary segment nucleotides 13 to 16 in a helical conformation with base edges available for additional target recognition. In this model, there is no pairing involving nucleotides 9 to 12, showing that annealing within this segment is not important for translational repression. Hence, guide-target recognition spanning nucleotides 2 to 8 and 13 to 16 by Ago2 avoids the topological constraints associated with complete pairing within its nucleic acid–binding channel.

Future research should examine longer target RNAs, so as to observe guide-target pairing in miRNA-mediated hAgo2 ternary complexes spanning not only nucleotides 2 to 8, but also 13 to 16. Also, the mechanistic basis underlying siRNA-mediated cleavage of perfectly complementary target mRNAs by hAgo2 (but not by the related hAgo1, hAgo3, and hAgo4) has yet to be addressed. Such cleavage by the RNase H fold of the PIWI domain requires pairing of the guide and target spanning nucleotides 10 and 11, as well as precise positioning of a pair of Mg^{2+} cations and a catalytic tetrad of histidine and three acidic residues (*8*) at the hAgo2 cleavage site. Additional structural studies will also be required to elucidate the contribution of the N domain of hAgo2 in siRNA-mediated slicing of mRNA. ■

Structural Biology Program, Memorial Sloan-Kettering Cancer Center, New York, NY 10065, USA. E-mail: pateld@mskcc.org

REFERENCES

1. G. Meister, *Nat. Rev. Genet.* **14**, 447 (2013).
2. D. C. Swarts *et al.*, *Nat. Struct. Mol. Biol.* **21**, 743 (2014).
3. C.-D. Kuhn, L. Joshua-Tor, *Trends Biochem. Sci.* **38**, 263 (2013).
4. M. Ha, V. N. Kim, *Nat. Rev. Mol. Cell Biol.* **15**, 509 (2014).
5. N. T. Schirle *et al.*, *Science* **346**, 608 (2014).
6. J. J. Song *et al.*, *Science* **305**, 1434 (2004).
7. Y. Wang *et al.*, *Nature* **456**, 209 (2008).
8. Y. Wang *et al.*, *Nature* **461**, 754 (2009).
9. D. C. Swarts *et al.*, *Nature* **507**, 258 (2014).
10. I. Olovnikov *et al.*, *Mol. Cell* **51**, 594 (2013).
11. D. P. Bartel, *Cell* **116**, 281 (2004).
12. N. T. Schirle, I. J. MacRae, *Science* **336**, 1037 (2012).
13. E. Elkayam *et al.*, *Cell* **150**, 100 (2012).
14. K. Nakanishi *et al.*, *Nature* **486**, 368 (2012).
15. C. F. Flores-Jasso *et al.*, *RNA* **19**, 271 (2013).

10.1126/science.1262123

PHYSICAL CHEMISTRY

Clarifying the structure of carbonic acid

Discrepancies in the reported structures of the difficult-to-isolate solid form of a common acid have been resolved

By **Götz Bucher**[1] *and* **Wolfram Sander**[2]

For many decades, carbonic acid (H_2CO_3)—formed from CO_2 and water—was regarded as a "nonexisting" free molecule that only existed in equilibrium with its deprotonated ions, bicarbonate (HCO_3^-) and carbonate (CO_3^{2-}), in solution. Both H_2O and CO_2 are very stable, and any covalently bound product of these two molecules will be thermodynamically less stable. However, theoretical work in the late 1970s suggested that kinetic barriers could prevent H_2CO_3 decomposition (*1*), and in 1987, H_2CO_3 was shown to have a finite lifetime in gas-phase experiments (*2*). In the 1990s, two independent syntheses of solid H_2CO_3 were published, but the two solids had rather different spectroscopic properties (*3*, *4*). In a series of publications (*5*–*7*), these two forms of carbonic acid were assigned to polymorphic structures that, upon sublimation, were claimed to produce different structures in the gas phase. A recent, very elegant study by Reisenauer *et al.* (*8*) resolves these discrepancies and demonstrates that there is only one form of solid H_2CO_3. The second "polymorph" was identified as the methyl ester of carbonic acid.

The hunt for the "free" carbonic acid began after quantum-chemical calculations that showed that the dissociation of H_2CO_3 into H_2O and CO_2, while highly exothermic, is prevented by a large activation barrier (>40 kcal/mol) (*1*). This result suggested that H_2CO_3 should be kinetically stable at room temperature and that there should be a realistic chance to isolate this molecule in the gas phase or even in condensed phases. However, the caveat of kinetic stabilization is that it depends entirely on the reaction pathway. Solvents, surfaces, and other constituents in solution might act as catalysts and reduce the activation barrier toward decomposition. Indeed, the decomposition of H_2CO_3 is strongly catalyzed by water, and even a single water molecule interacting with H_2CO_3 diminishes the barrier toward decomposition (*9*). In aqueous solution, H_2CO_3 can be produced by ultrafast protonation of HCO_3^-, but its lifetime (for the deuterated isotopomer D_2CO_3) is only 300 ns (*10*).

Three different methods have been used to synthesize the free carbonic acid: thermolysis of a suitable molecular precursor, high-energy irradiation of mixtures of CO_2 and H_2O, and protonation of HCO_3^- at very low temperatures. The first method was described by Schwarz and co-workers in 1987 to generate H_2CO_3 in the gas phase (*2*). By simply heating ammonium bicarbonate (NH_4HCO_3), small amounts of H_2CO_3 are released that were detected with sophisticated mass spectrometric methods.

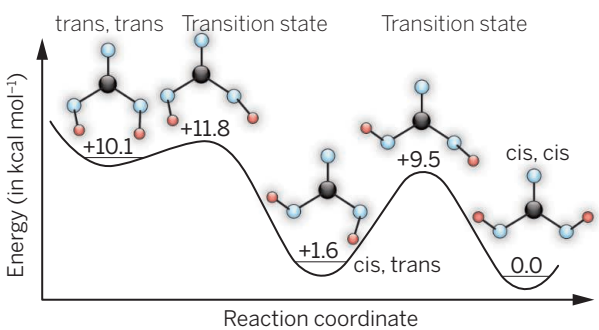

Carbonic acid conformers. The three conformers of carbonic acid (H_2CO_3) and the transition states connecting them, as calculated with density functional theory. Reisenauer *et al.* showed that solid H_2CO_3 forms only the two most stable conformers, cis,cis and cis-trans. Figure adapted with permission from (*8*).

Although these experiments demonstrated the existence of H_2CO_3 as stable species in the gas phase, many of the structural and spectroscopic characterization methods needed for further study of this molecule required solid samples. One way to synthesize H_2CO_3 in the solid state is to apply high-energy irradiation to mixtures of CO_2 and H_2O at very low temperature. Moore and Khanna reported in 1991 that proton irradiation of CO_2/H_2O ice at 20 K produced H_2CO_3 as a solid film after evaporating excess CO_2 and H_2O at 250 K in a vacuum system (*3*). Evidence for the formation of H_2CO_3 was a strong infrared (IR) absorption at 1705 cm^{-1} assigned to the carbonyl stretching vibration. Later, it was shown that H_2CO_3 is formed also by other means of irradiation—for example, with ultraviolet light. This finding is of great interest to astrochemistry, because CO_2 and H_2O in planetary and cometary ices are likely photolyzed to produce solid H_2CO_3.

Shortly after this finding, Mayer and coworkers (*4*) reported an alternative route to solid H_2CO_3 by protonation of HCO_3^- with hydrochloric acid (HCl) at very low temperatures. Small droplets of solutions of HCO_3^- and HCl in methanol (CH_3OH) solvent were codeposited on a surface cooled to 78 K. At this temperature, CH_3OH forms a solid glass that traps and immobilizes HCO_3^- and HCl. Warming this glass to temperatures above 140 K softened it and allowed the trapped species to diffuse so that HCO_3^- could be protonated by HCl. A new species with a strong IR absorption at 1730 cm^{-1} was assigned to carbonic acid.

Obviously, the IR data for solid H_2CO_3 produced by these two independent methods do not agree, and this difference was initially attributed to the formation of polymorphic crystal structures under different experimental conditions: β-H_2CO_3 is formed by high-energy irradiation of CO_2/H_2O ices, and α-H_2CO_3 by low-temperature protonation of bicarbonate in CH_3OH glasses. It was later shown that β-H_2CO_3 is also formed by low-temperature protonation of HCO_3^-, if instead of methanolic solutions of HCO_3^- and HCl, aqueous solutions are used in the experiments (*5*). Additional experiments by the Mayer group revealed that α-H_2CO_3 can be sublimed, and condensation from the gas phase reproduces the same α-polymorph (*6*). Bernard *et al.* recently found that the β-polymorph of H_2CO_3 can also be sublimed, but it recondenses as the β-polymorph (*7*). This disturbing finding was rationalized by attibuting different composition of the gas phase obtained by sublimation of the two polymorphs.

In the gas phase, three distinct conformers of H_2CO_3 exist that differ by the position of the OH hydrogen atoms: the most stable cis-cis, the slightly less stable cis-trans, and the least stable trans-trans conformer (see the figure). However, it is expected that these isomers, and also their dimers, rapidly equilibrate, and thus sublimation of different polymorphs of H_2CO_3 should result in the same crystalline phase, in contradiction to the experimental finding.

[1]*School of Chemistry, University of Glasgow, Glasgow G12 8QQ, UK.* [2]*Lehrstuhl für Organische Chemie II, Ruhr-University Bochum, 44780 Bochum, Germany. E-mail: wolfram.sander@rub.de*

To obtain clear spectra of the conformers of H_2CO_3, Reisenauer *et al.* developed a very clean source: the pyrolysis of esters of H_2CO_3 (*8*). This method had been demonstrated to produce carboxylic acids and also suggested, but not proven experimentally, to produce H_2CO_3 (see the scheme) (*11*). The products of the pyrolysis were trapped in solid argon at extremely low temperature (8 K), and characterization by IR spectroscopy revealed that the more stable cis,cis and the cis,trans conformers were formed. The spectra perfectly matched the spectra obtained by sublimation of β-H_2CO_3 and trapping the products in solid argon, but markedly differed from those of α-H_2CO_3

These results suggested that β-H_2CO_3 indeed is solid H_2CO_3, whereas α-H_2CO_3 has a different constitution. Reisenauer *et al.* also showed that "α-H_2CO_3" is actually its monomethyl ester, $CO(OH)(OCH_3)$. By using acidic CH_3OH for the protonation, the classic conditions for esterification of carboxylic acids, the monomethyl ester instead of the free carbonic acid is formed.

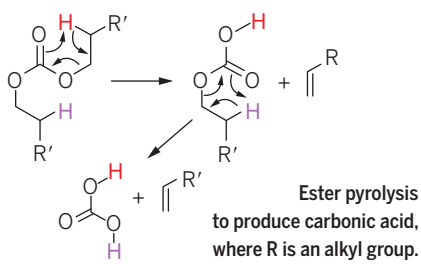

Ester pyrolysis to produce carbonic acid, where R is an alkyl group.

This finding also explains why aqueous HCl and HCO_3^- in the absence of CH_3OH produced solid H_2CO_3 as expected, which was formerly identified as the β-polymorph. Thanks to the clean synthesis of H_2CO_3 via ester pyrolysis, the fog has lifted, and we can now look forward to a clearer exploration of the chemical landscape of this fascinating compound. ■

REFERENCES

1. B. Jonsson *et al.*, *J. Am. Chem. Soc.* **99**, 4628 (1977).
2. J. K. Terlouw, C. B. Lebrilla, H. Schwarz, *Angew. Chem. Int. Ed. Engl.* **26**, 354 (1987).
3. M. H. Moore, R. K. Khanna, *Spectrochim. Acta A Mol. Biomol. Spectrosc.* **47**, 255 (1991).
4. W. Hage, A. Hallbrucker, E. Mayer, *J. Am. Chem. Soc.* **115**, 8427 (1993).
5. W. Hage, A. Hallbrucker, E. Mayer, *J. Mol. Struct.* **408-409**, 527 (1997).
6. W. Hage, K. R. Liedl, A. Hallbrucker, E. Mayer, *Science* **279**, 1332 (1998).
7. J. Bernard, R. G. Huber, K. R. Liedl, H. Grothe, T. Loerting, *J. Am. Chem. Soc.* **135**, 7732 (2013).
8. H. P. Reisenauer, J. P. Wagner, P. R. Schreiner, *Angew. Chem. Int. Ed.* **53**, 11766 (2014).
9. T. Loerting *et al.*, *Angew. Chem. Int. Ed.* **39**, 891 (2000).
10. K. Adamczyk, M. Prémont-Schwarz, D. Pines, E. Pines, E. T. J. Nibbering, *Science* **326**, 1690 (2009).
11. G. Bucher, *Eur. J. Org. Chem.* **2010**, 1070 (2010).

10.1126/science.1260117

PHYSICS

Seeking out Majorana under the microscope

A chain of iron atoms on lead may reveal a signature of the elusive Majorana particle

By **Patrick A. Lee**

The Dirac equation was initially developed to give a quantum mechanical description of particles such as electrons, but ended up predicting the existence of positrons—the antiparticle of the electron. A year before he disappeared under mysterious circumstances in 1938, the young Italian physicist Ettore Majorana discovered a solution to the Dirac equation that implied the existence of particles, or states of matter, that are their own antiparticles. This finding was contrary to Dirac's solution, in which particles (electrons) and their antiparticles (positrons) are distinct. It has long been suspected, but not proven, that neutrinos are Majorana particles (*1*). In the past several years, the Majorana state has attracted the attention of the condensed matter physics community, but a definitive sighting has remained elusive. On page 602 of this issue, Nadj-Perge *et al.* (*2*) report considerable progress toward creating the Majorana state in the laboratory.

There are a number of reasons why this seemingly esoteric problem of creating and confirming Majorana particles is of interest to condensed matter physicists. First, the quasi-particles in a superconductor are natural candidates for Majorana physics, because they constitute a quantum mechanical admixture of particles and holes. If the admixture has equal amplitude, the antiparticles and particles become identical. Second, it was pointed out by Kitaev (*3*) that Majorana bound states (MBSs) form at the ends of a superconductor chain if the wave function of the electron pair formed in the superconductor is antisymmetric (called p-wave), as opposed to symmetric (s-wave) in conventional superconductors. The MBS wave functions are localized at each end of the chain and are exactly at zero energy. They hybridize to form a conventional quasi-particle (complex fermion) with energy $E_o \approx \exp(-L/\xi)$, where L is the length of the chain and ξ is the coherence length of the superconductor. In the limit $L >> \xi$, $E_o \rightarrow 0$ and the addition or removal of the quasi-particle costs no energy; that is, the MBSs become part of the ground-state manifold. More generally, the presence of $2N$ MBSs far apart implies the existence of N low-energy quasi-particles, each of which can either be empty or occupied, leading to a ground-state degeneracy of 2^N. It is as if each complex fermion has been split into two real MBSs that are spatially far apart.

Because the association of MBS pairs into quasi-particles is a matter of choice, the following phenomenon occurs. Suppose we have four MBSs (see the figure, panel A) and the MBS pairs (**1**, **2**) and (**3**, **4**) form quasi-particles, which are both occupied. If we exchange the positions of MBSs **2** and **3**, the state will change to a different state, in this case a linear superposition of states where the two quasi-particles are both occupied or both empty. For conventional particles, the exchange of their positions can only lead to a sign change (for fermions) or in certain cases a change in the phase of the wave function (for so-called anyons). But now we end up with a different state entirely. The MBSs obey what is referred to as non-Abelian statistics—an exotic possibility that has not been observed experimentally. Apart from being a fascinating example of quantum weirdness, the ability to spatially decompose quasi-particle states has been proposed to be the basis of a fault-tolerant quantum computer and memory (*3*).

Superconductors with p-wave pairing are rare in nature; forming a one-dimensional chain out of them presents a formidable task. Fortunately, it may be possible to create structures with the desired properties using conventional s-wave superconductors. Starting with the proposal of Fu and Kane (*4*) to couple the newly discovered surface state of topological insulators to conventional superconductors by the proximity effect, many schemes have been proposed to build structures using a variety of more or less conventional materials, and the race to create MBS in the laboratory is on.

Up to now, the most convincing sighting of MBS used a scheme that places a semiconducting nanowire on top of a superconductor (*5*). A zero-bias peak was observed in the tunneling conductance under conditions consistent with theoreti-

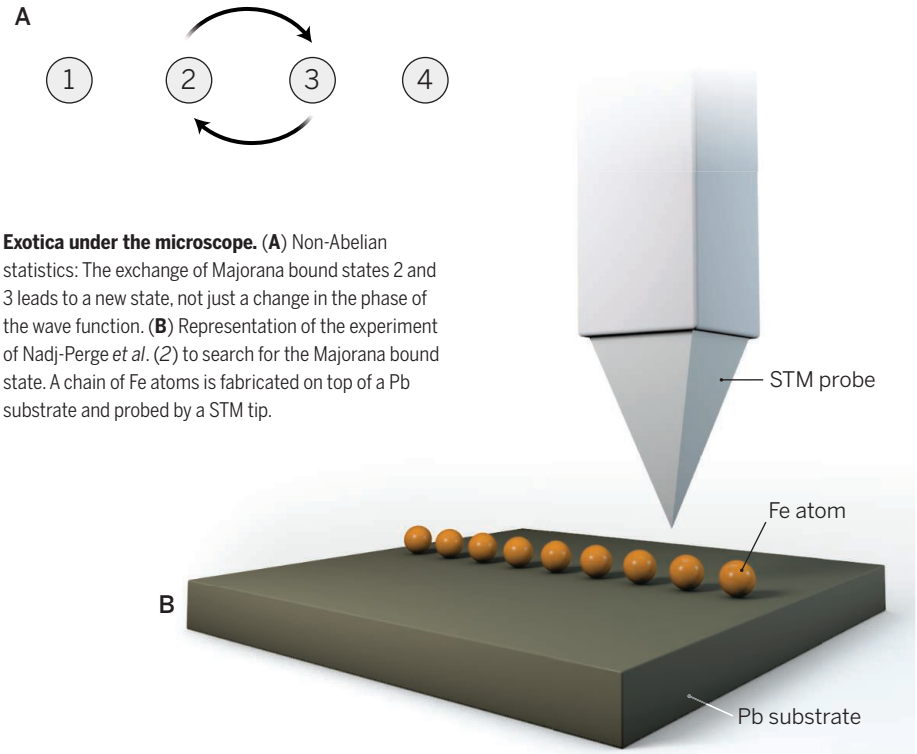

Exotica under the microscope. (**A**) Non-Abelian statistics: The exchange of Majorana bound states 2 and 3 leads to a new state, not just a change in the phase of the wave function. (**B**) Representation of the experiment of Nadj-Perge *et al*. (*2*) to search for the Majorana bound state. A chain of Fe atoms is fabricated on top of a Pb substrate and probed by a STM tip.

cal predictions. However, the energy scale of the spin-orbit coupling—a key parameter responsible for the formation of the MBS—is very small (~0.05 meV) in the semiconductor nanowire and raises the question of whether disorder or other conventional effects may give alternative explanations of the zero-bias peak (*6*, *7*). Additional experiments are clearly desirable.

Nadj-Perge *et al.* report the observation of Majorana fermions in a chain of iron (Fe) atoms on the surface of superconductive lead (Pb) (see the figure, panel B). Remarkably, the Fe chains grow out of a central island along atomic rows on the crystalline Pb surface. If the chain of Fe is ferromagnetic, theory predicts that the strong spin-orbit coupling in Pb will lead to an effective p-wave component in the induced superconductivity in the Fe chain and hence a realization of the Kitaev model. Indeed, using a scanning tunneling microscope (STM), the group discovered zero-bias peaks at the end of the chains, but not in the middle. The wave function of the state is localized near the chain end to a surprising degree, so that the zero-bias peaks disappear over a distance of 10 Å—a signature consistent with MBSs.

The Fe chain system has an advantage over the semiconductor nanowire: Because we are dealing with atomic-scale devices, the energy scales are several orders of magnitude higher. For example, the spin-orbit coupling is estimated to be 100 meV (versus 0.05 meV), and the spin splitting due to exchange is 900 meV (versus a few meV) from the magnetic field in the nanowire system. Thus, there are reasons to believe that the MBSs are more robust.

The experiment is clearly a tour de force combining the fabrication of structures on an atomic scale and the ability to probe the electronic structure with high energy and spatial resolution. Unlike the earlier experiment, the spatial location of the zero-bias state is clearly identified. However, there are still a number of loose ends to contend with. The energy gap of the induced superconductivity on the Fe chain is estimated to be very small: 0.2 meV, 20% of the Pb bulk gap. This corresponds to about 2 K, not much higher than the temperature where the experiment is carried out, 1.4 K. As a result, no clear gap structure is seen and the tunneling conductance shows only a modest reduction of no more than 50% at low energies. The zero-bias peak is a small structure on top of this large background. All the interesting phenomena associated with MBSs require the state to be well isolated from the quasi-particle excitations—a condition that is far from being satisfied in this experiment. A second problem is that the chain length is short, about 300 Å. On the other hand, the superconductivity coherence length is expected to be much longer because of the small energy gap. Thus, we are in the opposite limit, where $L << \xi$ and the MBSs are expected to strongly hybridize to form a conventional fermion, which lies at an energy E_o. This expectation seems at variance with the experimental observation of a rapid decay of the end-state wave function. This short-distance physics is not yet fully understood, but the long-distance behavior must still be controlled by the coherence length.

To make further progress, it is important to go to the lower temperature to resolve the finite energy splitting of the fermion. Currently the upper bound on the splitting is estimated to be 0.15 meV, which is comparable to the estimated induced superconductivity gap of 0.2 meV. The temperature limitation may be a technical issue, which will be overcome by future experiments, but the limitation of chain length may be more difficult to overcome. This may mean that the most fascinating phenomena associated with Majorana bound states, such as non-Abelian statistics that require the limit $L >> \xi$, may be beyond the reach of the atomic chain system. On the other hand, there are other interesting phenomena, such as the crossed Andreev effect (*8*) and noise correlation between leads attached to opposite ends or a chain (*9*), that require a voltage and temperature smaller than the energy splitting. It will be exciting to see whether the next generation of experiments capable of reaching much lower temperature will reveal these and other features of Majorana bound states. Meanwhile, other schemes that may be more scalable to long lengths are being pursued. Notable among them is a return to the original Fu-Kane scheme using a new type of two-dimensional topological insulators fabricated out of semiconductor heterostructures (*10*, *11*). The story of the search for Majorana particles is far from over. ■

Physics Department, Massachusetts Institute of Technology, Cambridge, MA 02139, USA. E-mail: palee@mit.edu

REFERENCES AND NOTES

1. F. Wilczek, *Nat. Phys.* **5**, 614 (2009).
2. S. Nadj-Perge *et al.*, *Science* **346**, 602 (2014).
3. A. Kitaev, *Ann. Phys.* **303**, 2 (2003).
4. L. Fu, C. L. Kane, *Phys. Rev. Lett.* **100**, 096407 (2008).
5. V. Mourik *et al.*, *Science* **336**, 1003 (2012).
6. J. Liu, A. C. Potter, K. T. Law, P. A. Lee, *Phys. Rev. Lett.* **109**, 267002 (2012).
7. H. O. H. Churchill *et al.*, *Phys. Rev. B* **87**, 241401 (2013).
8. J. Nilsson, A. R. Akhmerov, C. W. Beenakker, *Phys. Rev. Lett.* **101**, 120403 (2008).
9. J. Liu, F. C. Zhang, K. T. Law, *Phys. Rev. B* **88**, 064509 (2013).
10. L. Du, I. Knez, G. Sullivan, R. R. Du, http://arxiv.org/abs/1306.1925 (2013).
11. V. S. Pribiag *et al.*, http://arxiv.org/abs/1408.1701 (2014).

ACKNOWLEDGMENTS

I thank K. T. Law for discussions. Supported by the John Templeton Foundation and U.S. Department of Energy grant DE-FG-02-03-ER46076.

10.1126/science.1260282

CREDIT: V. ALTOUNIAN/*SCIENCE*

MENTAL HEALTH

Adolescent mental health—Opportunity and obligation

Emerging neuroscience offers hope for treatments

By **Francis S. Lee,[1] Hakon Heimer,[2,3] Jay N. Giedd,[4] Edward S Lein,[5] Nenad Šestan,[6] Daniel R. Weinberger,[7,8] B. J. Casey[1]***

The adolescent brain is more "plastic" than it will ever be again, capable of remarkable adaptability in light of the many social, physical, sexual, and intellectual challenges that this developmental phase brings. This is also a peak time for clinical onset of most mental illnesses (see the chart) (*1*). One in five adolescents have a mental illness that will persist into adulthood (*2*). Mental illnesses that emerge before adulthood impose a 10-fold higher cost than those that emerge later in life (*3*). Mental health costs are the highest single source of global economic burden in the world (*4*).

POLICY

The chronicity of adolescent-onset disorders is powerful motivation for early interventions to improve quality of life and reduce burdens on society. Yet, studies of interventions' economic effect have not demonstrated consistent benefits, which may be due, in part, to assessment of treatments that are not biologically based and/or do not consider how neurodevelopmental changes affect long-term effectiveness (*5*).

Understanding neurodevelopmental changes and their roles in both emergence of mental disorders and how they affect treatment efficacy is imperative. Yet, we estimate that less than 1% of the budget of the U.S. National Institutes of Health (NIH) was directed toward adolescent brain research in fiscal year 2014 (*6*). We highlight opportunities and priorities for more developmentally informed research to translate basic knowledge of adolescence toward clinical applications to treat mental illness.

ADOLESCENT BRAIN DYNAMICS. Adolescence is characterized by heightened emotional reactivity, sensitivity to peer influence, impulsivity, and novelty seeking, with a seemingly limited capacity to engage self-control to override these emotions and actions (*7*). These behavioral attributes are paralleled by hormonal and neurobiological changes that target specific brain regions and cell populations (see the graph) (*8*).

Studies in nonhuman primates show that this period is associated with overproduction, followed by selective stabilization and elimination, of principally excitatory synapses in the cortex (*9*) that may alter an excitatory/inhibitory balance in individual neurons and circuits. Regional changes in synaptic morphology, dendritic arborization, patterns of cortical cell firing, and availability of neurochemicals and their receptors all occur during adolescence. Changes in white matter during this time likely influence conduction of electrical impulses across the brain and (axonal) transport of cargoes essential for neurotransmission, cell metabolism, and survival.

Human-imaging studies have shown an analogous pattern in which low-level sensory and motor cortices develop earlier than do association cortices involved in rational thought and regulation of behavior (*10*). These regional neurochemical, structural and functional changes across development have been posited to lead to transient imbalances in functional brain circuitry during adolescence, underlying dysregulation of emotions and actions (*11*). Exacerbations in these imbalances by biological, environmental, and genetic factors may contribute to a risk for mental illness. A priority will be to delineate dynamics of brain development preceding, during, and following adolescence to understand the increase in mental illness during this time and how these neurobiological changes affect the type and timing of treatment of these disorders. Too often, pharmacological and behavioral treatments designed for the adult brain are imposed on the developing brain with little consideration for how neurobiological changes across time may impact the effectiveness of these treatments.

TECHNOLOGICAL ADVANCES FOR MAPPING BRAIN AND BEHAVIOR. We have unprecedented opportunities to advance understanding of the brain with novel technologies and data. These must be applied to both developing and developed brains. Techniques such as in vivo imaging of synaptic activity in deep brain structures, whole-brain clearing and imaging, and optogenetics are illuminating brain circuit dynamics in animal and cell model systems and may shed light on dysfunctional circuitry in brain disorders (*12*, *13*).

One example in human research is the NIH Brain Research through Advancing Innovative Neurotechnologies (BRAIN) Initiative. This focuses largely on techniques, not yet feasible in humans, for understanding intricate workings of the brain in nonhumans. Another promising initiative is the NIH Human Connectome Project, which focuses on how brain connections underlie complex behavior (*14*). A priority of these efforts should be to focus on developing brain structures, connections, and functions to delineate how developmental changes,—whether fetal, infant, child, or adolescent—affect the risk for mental disorders that emerge during adolescence. Priority should be given to how these changes

Emergence and peak in mental disorders during adolescence

One in five adolescents have a mental illness that will persist into adulthood

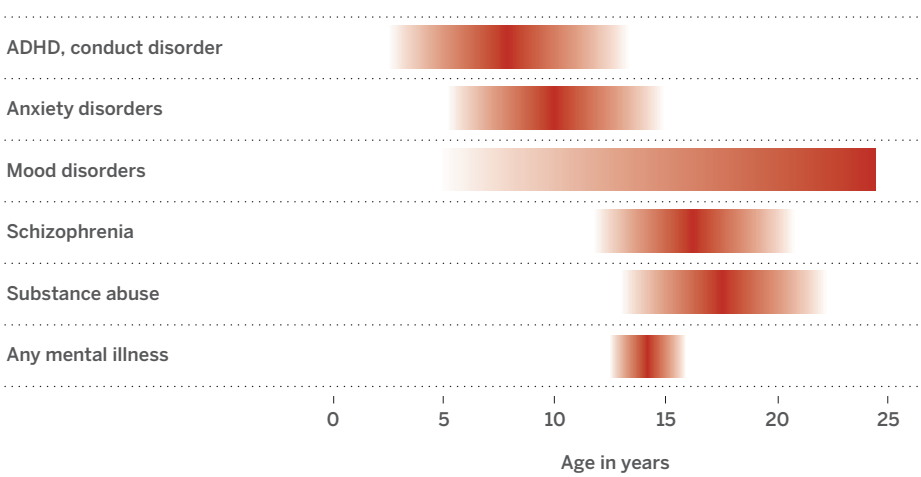

affect the type and timing of treatment of these disorders during these stages.

We are in an era of tremendous access to large, human-imaging data sets, novel imaging tools, and bioinformatics to guide us. Collaborative "big neuroscience" projects to map the structural and functional landscape of the human brain have been proposed and initiated around the world, but should emphasize the developing brain and changes that adolescence brings. Initiatives are under way or in conceptual stages to collect or merge large data sets in healthy and at-risk developmental populations that include psychosocial, clinical, behavioral, imaging, and/or genetic data (*15*). It is essential to exploit new knowledge through rigorous hypothesis-driven behavioral and brain testing. This will require support of scientific inquiries that bridge and integrate basic nonhuman and human investigations for deployment of new diagnostic tools and treatments.

In parallel with brain-imaging innovations and large data sets, systematic profiling of gene expression across regions and time points of the developing and adult human brain has revealed unforeseen spatiotemporal dynamics of the human brain transcriptome. Dramatic changes in gene expression are associated with the development of distinct brain regions and with developmental periods. Analysis of developmental transcriptome data is critical for interpreting the mechanism by which noncoding disease-associated mutations translate into clinical syndromes and for providing insights into the biology of mental illness (*16*). We anticipate the expansion of public data sets based on RNA sequencing of the human brain across developmental stages. A priority will be to characterize these transcriptional changes across development and translate these basic discoveries to direct novel treatments based on the age and genetic makeup of the individual.

A final example of technological developments is mobile devices. These may be used to measure fluctuations in autonomic function and arousal, location, and self-reported emotion, allowing objective assessment of individuals in the real world, in real time (*17*). This is in contrast to current methods that typically require individuals to self-report by reflecting back over an extended period, typically many weeks, which often does not reflect the person's true level of functioning. The long-term potential of these technologies could provide remote anticipation of critical mental health events such as suicidality. A priority will be to optimize this technology for different age groups and integrate these data with imaging and genetic data sets to link biology with the social and physical environment to develop and deploy diagnostics and treatments.

TREATING DEVELOPING VERSUS DEVELOPED BRAINS. Adolescence is a delimited window of development when the environment has a strong influence on brain and behavior. Understanding the timetable of behavioral and brain changes could uncover patterns of potential therapeutic relevance, guiding treatments that may vary by age, and informing public health strategies and policies for modifying the environment for lasting salutary effects.

Too often, children and adolescents are lumped together in large clinical trials with little consideration for how dynamic changes in the brain across development will impact the effectiveness of treatments. This is often compounded by treatments being based on evidence from the adult brain or from one sex without appreciation for differences between the developing and developed brain or female and male brain.

Characterizing sensitive periods may allow us to apply precision medicine, directing the timing and type of interventions at the level of an individual. For example, evidence is emerging on treatment for anxiety disorders, the most common form of mental illness in young people, affecting as many as 1 in 10 (*1*, *2*). A core symptom is difficulty recognizing when situations that have been experienced as dangerous are now safe. Exposure-based cognitive behavioral therapy is the most common treatment, based on basic principles of fear extinction learning, whereby a person is desensitized to fearful triggers through repeated exposures in a safe context.

Recent mouse and human studies indicate that adolescents have diminished fear extinction relative to younger or older age groups (*18*). This suggests that exposure therapies in clinical practice that build on principles of fear extinction may be less effective during adolescence than during childhood or adulthood (*19*). This illustrates the importance of age as a potential predictor of treatment response and even a target for novel treatments. A priority for future research will be to delineate treatments targeted to the biological state of the developing brain to maximize effectiveness.

OPPORTUNITY AND OBLIGATION. There is a tremendous opportunity to understand how sensitive windows may shift, constrict, or expand in an individual at different points in development. In parallel, it is essential that we bridge discoveries in humans and animal model systems at genetic,

Developmental course of brain maturation during adolescence

Behavioral attributes are paralleled by hormonal and neurobiological changes that target specific brain regions and cell populations

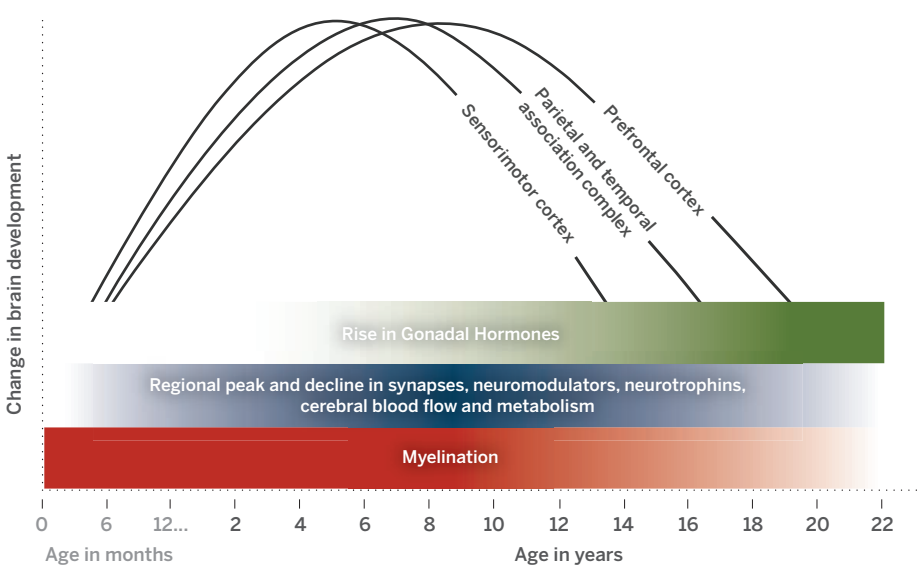

[1]Sackler Institute, Department of Psychiatry, Weill Cornell Medical College, New York, NY 10065, USA. [2]Schizophrenia Research Forum, Brain and Behavior Research Foundation, Providence, RI 02906, USA. [3]Banbury Center, Cold Spring Harbor Laboratory, Cold Spring Harbor, NY 11724, USA. [4]Division of Child and Adolescent Psychiatry, University of California, San Diego, CA 92123, USA. [5]Allen Institute for Brain Science, Seattle, WA 98103, USA. [6]Department of Neurobiology and Psychiatry, Kavli Institute for Neuroscience, Yale School of Medicine, New Haven, CT 06510, USA. [7]Lieber Institute for Brain Development, Baltimore, MD 21205, USA. [8]Department of Psychiatry, Neurology, Neuroscience, and the Institute of Genomic Medicine, Johns Hopkins School of Medicine, Baltimore, MD 20215, USA. *E-mail: bjc2002@med.cornell.edu

molecular, circuit, and behavioral levels to guide novel interventions. Together, these efforts will enhance our capacity to develop and target treatments by age, sex, and genetic makeup of the individual.

Despite the moral imperative and long-term economic benefit of improved diagnosis and treatment of mental disorders in adolescence, there has not been commensurate investment in research to bring them about. The NIH budget has not kept pace with inflation and is threatened by cutbacks. Increased commitment and resources are needed to help address our social obligation to reduce the unacceptably high burden of mental illness on youth today and to ensure a healthier tomorrow. ■

REFERENCES AND NOTES

1. T. Paus, M. Keshavan, J. N. Giedd, *Nat. Rev. Neurosci.* **9**, 947–957 (2008).
2. R. C. Kessler *et al.*, *Arch. Gen. Psychiatry* **62**, 593–602 (2005).
3. World Health Organization (WHO), *Economic Aspects of Mental Health in Children and Adolescents* (WHO, Geneva, 2007).
4. D. E. Bloom *et al.*, *The Global Economic Burden of Non-communicable Diseases* (World Economic Forum, Geneva, 2011).
5. J. Beecham, *J. Child Psychol. Psychiatry* **55**, 714–732 (2014).
6. These numbers were generated from NIH RePORTER, the publicly available database on NIH-funded research, using the search terms "adolescent" and "brain" and "development"; all active grants from 1 October 2013 to 30 September 2014 (FY 2014) were searched, based on a total NIH budget of $30.1 billion.
7. L. Spear, *The Behavioral Neuroscience of Adolescence* (W.W. Norton, New York, 2010).
8. B. J. Casey, N. Tottenham, C. Liston, S. Durston, *Trends Cogn. Sci.* **9**, 104–110 (2005).
9. P. Rakic, J. P. Bourgeois, P. S. Goldman-Rakic, *Prog. Brain Res.* **102**, 227–243 (1994).
10. N. Gogtay *et al.*, *Proc. Natl. Acad. Sci. U.S.A.* **101**, 8174–8179 (2004).
11. B. J. Casey, S. Getz, A. Galvan, *Dev. Rev.* **28**, 62–77 (2008).
12. M. L. Andermann *et al.*, *Neuron* **80**, 900–913 (2013).
13. K. Deisseroth *et al.*, *J. Neurosci.* **26**, 10380–10386 (2006).
14. E. R. Kandel, H. Markram, P. M. Matthews, R. Yuste, C. Koch, *Nat. Rev. Neurosci.* **14**, 659–664 (2013).
15. These include the Pediatric Imaging, Neurocognition, and Genetics (PING) study; the Philadelphia Neurodevelopmental Cohort (PNC) study; the National Consortium on Alcohol and Neurodevelopment in Adolescence (NCANDA); The Human Connectome Project Lifespan Pilot Study; the Adolescent Brain Cognitive Development (ABCD) study; and the Tokyo Teen Cohort.
16. A. T. Tebbenkamp, A. J. Willsey, M. W. State, N. Sestan, *Curr. Opin. Neurol.* **27**, 149–156 (2014).
17. G. F. Dunton *et al.*, *Health Psychol.* **33**, 255–263 (2014).
18. S. S. Pattwell *et al.*, *Proc. Natl. Acad. Sci. U.S.A.* **109**, 16318–16323 (2012).
19. A. T. Drysdale *et al.*, *Biol. Psychiatry* **75**, e19–e20 (2014).

ACKNOWLEDGMENTS

The ideas in this article were generated during a December 2013 Cold Spring Harbor Laboratory Banbury meeting on the adolescent brain, supported by the Allen Institute for Brain Science, The Lieber Institute for Brain Development, the National Institute on Alcohol Abuse and Alcoholism, and the National Institute of Mental Health, www.cshl.edu/banbury-center/banbury-reports/the-adolescent-brain-and-mental-disorders.html. The organizers and authors thank participants for contributions to the meeting and comments on this article.

10.1126/science.1260497

PHOTO: NIALL CORBET/HTTPS://FLIC.KR/P/BURRKF

Phulchoki Mountain Forest, Nepal. In this and many other ecosystems, different ecosystem services are rarely optimized simultaneously by management, requiring choices to be made.

CONSERVATION

The value of valuing nature

Valuing nature in economic terms is not always beneficial for biodiversity conservation

By **W. M. Adams**

The complex ways in which humans depend on their natural environment are increasingly expressed in terms of ecosystem services, which are often assigned economic values to assist decision-making. The key attraction of the ecosystem services concept to conservationists lies in the potential for win-win outcomes (*1*), where the value of an ecosystem service depends on high biological diversity and cannot be increased by modifying it. Such outcomes are possible. For example, in Costa Rican coffee plantations, retention of forest patches doubled pest control of coffee berry borer beetle by birds, with substantial economic benefits to coffee farmers (*2*). However, attention to ecosystem services does not automatically lead to the conservation of biodiversity (*3*). A series of factors challenge the creation of synergies between ecosystem services and biodiversity conservation (see the figure).

CONSERVATION SERIES

PROCESSES AND SERVICES. First, challenges arise in the relationship between ecological processes and the delivery of ecosystem services. The question of how many species (and how much genetic diversity) can be lost from an ecosystem before it ceases to provide services is critical to understanding the relationship between biodiversity and benefits from ecosystem services, but it is not easy to answer (*4*). Both biotic and abiotic processes are involved in the delivery of many ecosystem services—for example, wave attenuation in coastal defense (*5*). Relationships among biodiversity, biophysical processes, and the provision of ecosystem services are intricate and poorly understood (*6*).

Even if it is possible to identify which biophysical processes and ecosystem components underpin specific ecosystem services, a focus on those that deliver particular services is likely to affect other components of the ecosystem (such as rare species). For example, in Maryland, USA, stream channels were reengineered to provide particular services from streams (storm water management for flood control and sediment and nutrient storage). This approach causes the aquatic fauna and flora characteristic of stream ecosystems to be replaced by terrestrial and wetland species, and loss of healthy riparian trees (*7*).

Similarly, a focus on ecosystem services may lead to management aimed at controlling processes with substantial negative social impacts (e.g., disease, flood, or fire). These biophysical processes may be essential in supporting ecosystem components of

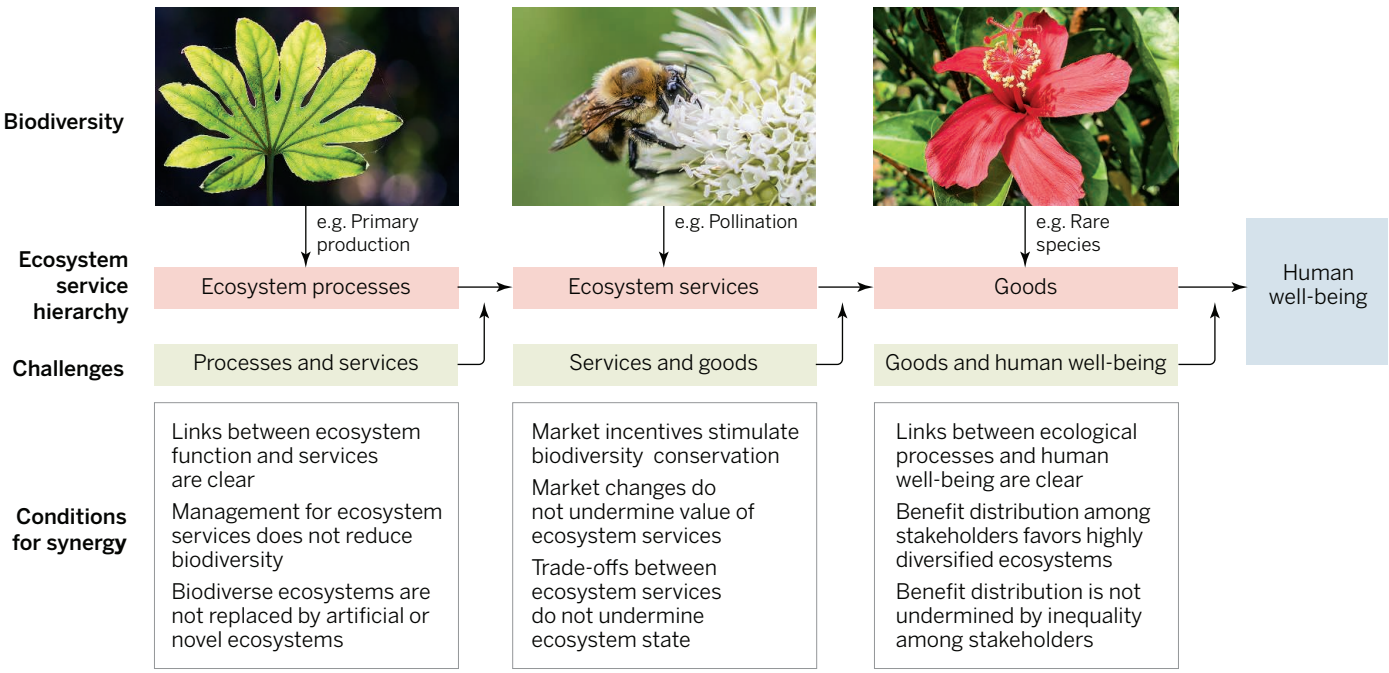

Finding synergies. Biodiversity can regulate fundamental ecosystem processes and ecosystem services, as well as constitute goods that contribute to human welfare (*4*). Challenges to the creation of synergies between ecosystem services and conservation arise in relationships among ecosystem processes, services, goods, and human well-being. These challenges define the conditions under which synergies arise or can be created.

interest to conservation, such as threatened habitats or species (*3*). Management aimed at providing valuable services may lead to support for artificial or novel ecosystems, non-native species, and organisms shaped by synthetic biology. Thus, services such as carbon sequestration may in future be provided by ecosystems that retain little of their original diversity (*8*). Such ecosystems are likely to deliver little value in terms of biodiversity conservation.

SERVICES AND GOODS. The second category of challenges relates to the links between ecosystem services and goods. First, there is the problem of missing markets. Some ecosystem services are produced and consumed in ways that make them amenable to economic valuation (for example, products such as food or timber), but others (such as soil formation and nutrient cycling) are not, although their value can be expressed through the directly valued services that they support (*9*). There are rarely effective markets to stimulate the conservation or restoration of biodiversity that provides regulating services (such as pollination by wild species), or for noncharismatic species as a cultural ecosystem service.

In principle, economic incentives can be created to support conservation of many ecosystem elements, including charismatic rare species—for example, in payments for ecosystem services (PES) schemes, where the users of services pay those who supply them (*1*). A PES scheme across the Brazilian Atlantic Forest biome could, for instance, provide cost-effective incentives for landowners to set aside land for forest, with benefits for biodiversity and ecosystem services (*10*). However, many PES-like payment schemes do not fulfill the criteria of markets (commoditization, conditionality, and voluntary exchange) and require support from taxes or charitable giving (*1*).

A related concern is that as market prices change over time, so too will the value ascribed to ecosystem services. Although the value of rare species may rise as populations fall, that of other ecosystem services may be more variable. For example, Mexican free-tailed bats (*Tadarida brasiliensis mexicana*) control pests in U.S. cotton production by predating on moths. The value of this ecosystem service to U.S. cotton production fell by 79% between 1990 and 2008 (*11*) as many farmers began to plant a cotton genetically modified with the bacterium *Bacillus thuringiensis* (*Bt*) that is toxic to insect pests. In future, pest resistance to *Bt* cotton may cause the value of bat moth predation to rise again. In the face of such relatively rapid shifts in market conditions and agricultural technology, it would be hard to make a watertight case for bat conservation on the basis of the ecosystem service they provide.

It also matters whether ecosystem services are considered and measured together ("bundled") or separately. The act of categorization and analysis of ecosystem services implies that different components can be separated (*7*). Yet, different services are coproduced. They may interact synergistically (so that more of one service means more of another) or may compete (such that there is a trade-off between one service and another). A study of ecosystem services in the watershed of the Panama Canal found that timber production and carbon sequestration increased synergistically. However, contrary to managers' expectations, both competed with water supply, such that no form of reforestation would increase water flow in the dry season, although this relationship varied with site-specific variables such as slope, soil properties, and forest species (*12*).

GOODS AND HUMAN WELL-BEING. The third category of challenges relates to the links between the provision of goods from ecosystem services and human well-being. Birch *et al.* used a site-based ecosystem assessment toolkit in the Phulchoki Mountain Forest in Nepal (see the photo) to compare the values of different services under community forest management with those from state-managed forest and land cleared for agriculture (*13*). Community forestry proved favorable for biodiversity but for most services, for most stakeholders, and at most scales, but ecosystem services were not all maximized simultaneously, leading to choices and trade-offs among services.

It is not enough to identify the net benefits of ecosystem services: It also mat-

Department of Geography, University of Cambridge, Downing Place, Cambridge CB2 3EN, UK. E-mail: wa12@cam.ac.uk

ters who gets them. Ecosystems tend to be owned by somebody, either privately or by the state (exceptions being deep oceans, the atmosphere, and Antarctica). Management decisions tend to reflect the interests of the owners, and where services demand other forms of capital (such as agricultural infrastructure), the supply of services depends on the availability of financial capital from owner, state, bank, donor, or investor. For example, in the Panama basin example discussed above (*12*), timber production and carbon sequestration increase or decrease together, but the two services have different beneficiaries in different locations. Landowners have a direct interest in the private benefits from either timber harvesting or livestock grazing, whereas carbon sequestration is a global public good. Choices about ecosystem management often involve such trade-offs between one service and another and between beneficiaries.

"...a monetary valuation of nature should be accepted only where it improves environmental [and] socioeconomic conditions..."

LOSERS AND WINNERS. Trade-offs among stakeholders in their access to ecosystem service benefits is a particular problem where there are differences in wealth and power. In the example of the Phulchoki Forest (Nepal) discussed above, community control of forest gave the local community the benefits of clean water, tourism, and harvested wild goods but restricted poor people's access to forest products, particularly those from certain "untouchable" castes. This created hardship, illegal use, and impacts on other areas (*13*).

Patterns of winners and losers from ecosystem services (and associated payment schemes) reflect prevailing patterns of wealth and power. Unequal access to ecosystem service benefits, including those experienced locally and at a distance, can lead to conflict, institutional failure, and ecosystem degradation. Institutional transparency, access to information, and secure resource tenure are fundamental to equitable outcomes.

CONSERVATION/ECOSYSTEM SERVICES. The identification and valuation of ecosystem services are valuable for sustainable environmental planning. Win-win outcomes are possible in cases where valuable ecosystem services increase support for biodiversity conservation. Although areas of high biodiversity and those providing ecosystem services do not always overlap, improved conservation planning could help identify opportunities for win-win outcomes (*14*). However, the ecosystem service approach is not itself a conservation measure. There is a risk that traditional conservation strategies oriented toward biodiversity may not be effective at protecting ecosystem services, and vice-versa. Analysis using political ecology and ecological economics suggests that a monetary valuation of nature should be accepted only where it improves environmental conditions and the socioeconomic conditions that support that improvement (*15*).

The challenges described here suggest that considering conservation in economic terms will be beneficial for conservation when management for ecosystem services does not reduce biotic diversity or lead to substitution of artificial or novel ecosystems, when effective market-based incentives stimulate and sustain the conservation or restoration of biodiversity, and when the distribution of services among stakeholders favors high-diversity ecosystem states and is not undermined by inequality.

In a world run according to an economic calculus of value, the survival of biotic diversity depends on its price. Sometimes calculation of ecosystem service values will favor conservation; sometimes it will not. Conservationists must plan for both outcomes, rather than hoping that recourse to economic valuation will automatically win the argument for biodiversity. Ultimately conservation is a political choice (*16*), and ecosystem service values are just one argument for the conservation of nature. ■

REFERENCES

1. R. Muradian *et al.*, *Conserv. Lett.* **6**, 274 (2013).
2. D. S. Karp *et al.*, *Ecol. Lett.* **16**, 1339 (2013).
3. K. H. Redford, W. M. Adams, *Conserv. Biol.* **23**, 785 (2009).
4. G. M. Mace, K. Norris, A. H. Fitter, *Trends Ecol. Evol.* **27**, 19 (2012).
5. I. Möller, J. Mantilla-Contreras, T. Spencer, A. Hayes, *Estuar. Coast. Shelf Sci.* **92**, 424 (2011).
6. P. A. Harrison *et al.*, *Ecosyst. Serv.* **9**, 191 (2014).
7. M. A. Palmer, S. Filoso, R. M. Fanelli, *Ecol. Eng.* **65**, 62 (2014).
8. K. H. Redford, W. M. Adams, R. Carlson, G. M. Mace, B. Ceccarelli, *Oryx* **48**, 10.1017/S0030605314000040 (2014).
9. D. J. Abson, M. Termansen, *Conserv. Biol.* **25**, 250 (2011).
10. C. Banks-Leite *et al.*, *Science* **345**, 1041 (2014).
11. L. López-Hoffman *et al.*, *PLOS ONE* **9**, 0087912 (2014).
12. S. Simonit, C. Perrings, *Proc. Natl. Acad. Sci. U.S.A.* **110**, 9326 (2013).
13. J. C. Birch *et al.*, *Ecosyst. Serv.* **8**, 118 (2014).
14. J. Cimon-Morin, M. Darveau, M. Poulin, *Biol. Conserv.* **166**, 144 (2013).
15. G. Kallis, E. Gómez-Baggethun, C. Zografos, *Ecol. Econ.* **94**, 97 (2013).
16. R. Muradian, L. Rival, *Ecosyst. Serv.* **1**, 93 (2012).

10.1126/science.1255997

NEUROSCIENCE

The atoms of neural computation

Does the brain depend on a set of elementary, reusable computations?

By **Gary Marcus,[1] Adam Marblestone,[2] Thomas Dean[3]**

The human cerebral cortex is central to a wide array of cognitive functions, from vision to language, reasoning, decision-making, and motor control. Yet, nearly a century after the neuroanatomical organization of the cortex was first defined, its basic logic remains unknown. One hypothesis is that cortical neurons form a single, massively repeated "canonical" circuit, characterized as a kind of a "nonlinear spatiotemporal filter with adaptive properties" (*1*). In this classic view, it was "assumed that these...properties are identical for all neocortical areas." Nearly four decades later, there is still no consensus about whether such a canonical circuit exists, either in terms of its anatomical basis or its function. Likewise, there is little evidence that such uniform architectures can capture the diversity of cortical function in simple mammals, let alone characteristically human processes such as language and abstract thinking (*2*). Analogous software implementations in artificial intelligence (e.g., deep learning networks) have proven effective in certain pattern classification tasks, such as speech and image recognition, but likewise have made little inroads in areas such as reasoning and natural language understanding. Is the search for a single canonical cortical circuit misguided?

Although the cortex may appear, at a coarse level of anatomical analysis, to be largely uniform across its extent, it has been known since the seminal work of neurologist Korbinian Brodmann a century ago that there are substantial differences between cortical areas. At a finer grain, the brain has hundreds of different neuron types, and individual synapses contain hundreds of different proteins (*3*). Duplication and divergence shape brain evolution (*4*), just as they do in biology more generally.

What would it mean for the cortex to be diverse rather than uniform? One pos-

sibility is that neuroscience's quarry should be not a single canonical circuit, but a broad array of reusable computational primitives—elementary units of processing akin to sets of basic instructions in a microprocessor—perhaps wired together in parallel, as in the reconfigurable integrated circuit type known as the field-programmable gate array.

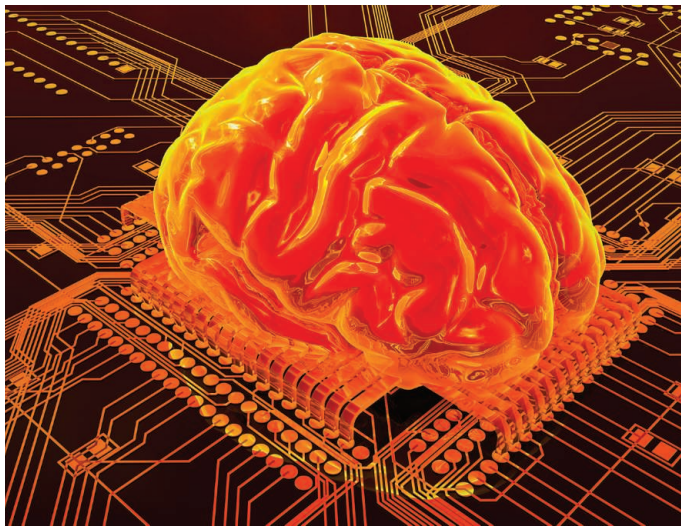

Candidate computational primitives might include circuits for shifting the focus of attention (*5*), for encoding and manipulating sequences, and for normalizing the ratio between the activity of an individual neuron and a set of neurons (*6*). These might also include circuits for switching or gating information flow between different parts of cortex (*7*), and for working memory storage, decision-making, storage and transformation of information via population coding and the manipulation (*2*) and encoding of variables (*8*, *9*), alongside machinery for hierarchical pattern recognition. Thus, cortical regions would differ not only in terms of their inputs, but also as a function of their inherent structures. The sensory cortex, for example, might be rich in circuits that underlie computational primitives useful for hierarchical pattern recognition and for mediating the effects of attention, whereas the prefrontal cortex might rely heavily on circuits supporting sequence production, decision-making, and variable binding.

Especially important in this regard (*2*, *10*) is a greater understanding of the neural underpinnings of variable binding—the transitory or permanent tying together of two bits of information: a variable (such as an *X* or *Y* in algebra, or a placeholder like *subject* or *verb* in a sentence) and an arbitrary instantiation of that variable (say, a single number, symbol, vector, or word). Such processes appear to be outside the scope of uniform pattern recognition systems, yet are likely to be central both in language (e.g., in interpreting sentences that combine words in novel ways) and deductive reasoning. Variables likely figure prominently in other domains, as well, such as navigation, motor control, and higher-level vision (*2*, *10*, *11*).

Several candidate neural mechanisms for variable binding have been proposed. These range from temporal synchrony among neural ensembles (*12*), to multiplication of vectors encoded by neural populations (*9*), to precisely controlled recurrent interactions between the prefrontal cortex and basal ganglia (*8*). Possible mechanisms also include interlinked systems of anatomically defined registers (groups of neurons defining temporary memory stores) with diverse encoding schemes (*2*, *11*) that could be implemented through the combination of neurobiologically well-established processes (*11*), such as Hebbian learning (the idea that connections between two neurons are strengthened if the neurons are active simultaneously), gating, and attentional spotlights.

Relatively little experimental work, however, has focused on choosing among these possibilities, in part because earlier techniques (e.g., brain imaging studies) were too coarse-grained. Emerging techniques like optogenetics, which allows for the pinpoint control of individual neurons, in conjunction with activity mapping and scalable comprehensive maps of neuronal connections, give hope that specific questions about the microcircuitry of variable binding might soon be addressed. For example, it might be possible to identify microcircuitry involved in behavioral tasks that require the neural circuitry of variable binding (such as complex comparisons of multiple elements parsed from visual scenes), and then to perturb that circuitry through optogenetic techniques, yielding causal clues into the neural organization of the computational units underlying variable binding. Ultimately, an adequate account of the mechanisms of variable binding may be indispensable for drawing firm connections between neurons and higher-level cognitive processes.

Several recently discovered biological mechanisms could underwrite the development of a diverse set of computational building blocks, differentially arrayed across the cortex. For example, there are systematic differences in gene expression between cortical areas, with differences between areas increasing as a function of their physical distance (*13*). Other molecular mechanisms, such as the alternative splicing of neurexins (proteins that help to orchestrate the formation of neuronal synaptic connections) (*14*), provide potential pathways by which seemingly subtle molecular differences could guide important qualitative variations in synaptic connectivity. Further, even within narrowly defined cell types (e.g., layer 5 pyramidal cells), molecularly defined combinatorial cues correlate with distinct patterns of wiring (*15*).

Neuroscience must develop precisely the sorts of experimental tools, detailed brain maps, and computational infrastructures that today's brain initiatives aim to support, but also a new set of intellectual tools for understanding how, even in principle, systems might bridge from neuronal networks to symbolic cognition. Toward that end, an interdisciplinary quest to construct a taxonomy and phylogeny of cortically instantiated computational primitives would advance our understanding toward the ultimate goal of deciphering how assemblies of such elements underlie behavior. ■

[1]*Departments of Psychology and Center for Neural Science, New York University, New York, NY 10003, USA.* [2]*Media Lab, Massachusetts Institute of Techonology, Cambridge, MA 02139, USA.* [3]*Google, Mountain View, CA 94043, USA. E-mail: gary.marcus@nyu.edu*

REFERENCES AND NOTES

1. O. D. Creutzfeldt, *Naturwissenschaften* **64**, 507 (1977).
2. G. F. Marcus, *The Algebraic Mind: Integrating Connectionism and Cognitive Science* (MIT Press, Cambridge, MA, 2001).
3. N. A. O'Rourke, N. C. Weiler, K. D. Micheva, S. J. Smith, *Nat. Rev. Neurosci.* **13**, 365 (2012).
4. D. H. Geschwind, P. Rakic, *Neuron* **80**, 633 (2013).
5. B. A. Olshausen, C. H. Anderson, D. C. Van Essen, *J. Neurosci.* **13**, 4700 (1993).
6. M. Carandini, D. J. Heeger, *Nat. Rev. Neurosci.* **13**, 51 (2011).
7. V. Mante, D. Sussillo, K. V. Shenoy, W. T. Newsome, *Nature* **503**, 78 (2013).
8. T. Kriete, D. C. Noelle, J. D. Cohen, R. C. O'Reilly, *Proc. Natl. Acad. Sci. U.S.A.* **110**, 16390 (2013).
9. C. Eliasmith *et al.*, *Science* **338**, 1202 (2012).
10. C. R. Gallistel, A. P. King, *Memory and the Computational Brain: Why Cognitive Science Will Transform Neuroscience* (Wiley, Sussex, UK, 2009).
11. K. J. Hayworth, *Front. Comput. Neurosci.* **6**, 73 (2012).
12. C. von der Malsburg, *Curr. Opin. Neurobiol.* **5**, 520 (1995).
13. M. J. Hawrylycz *et al.*, *Nature* **489**, 391 (2012).
14. D. D. Krueger, L. P. Tuffy, T. Papadopoulos, N. Brose, *Curr. Opin. Neurobiol.* **22**, 412 (2012).
15. S. A. Sorensen *et al.*, *Cereb. Cortex* 10.1093/cercor/bht243 (2013).

ACKNOWLEDGMENTS

We thank R. Yuste, X.-J. Wang, R. Granger, B. Aguera y Arcas, N. de Costa, C. Reid, E. Lein, S. Mihalas, A. Bernard, D. Amodei, and T. Poggio for helpful discussions; J. Goldman, D. Heeger, S. Seung, C. Koch, C. Eliasmith, S. Hill, R. Gallistel, K. Kording, S. Olsen, J. Freeman, S. Pinker, E. Davis, A. Vouloumanos, and D. Bemis for detailed comments; and S. Olsen, T. Movshon, J. Goldman, and E. Boyden for many useful references.

10.1126/science.1261661

ESSAY

NEUROSCIENCE

Shortcuts and checkpoints on the road to skilled movement

Coordinating intricate motor circuits

By **Eiman Azim**

A split second late or a few inches off the mark, and few would remember. Instead, running with his back to the ball, Willie Mays extended his arm and placed his glove squarely under the 420-foot center field drive. The New York Giants win Game 1 of the 1954 World Series, and Mays, his glove, and "The Catch" earn their place in history.

Few of our limb movements will ever gain such immortality, but what we accomplish every day is remarkable, nonetheless. When we catch a tipped wineglass or launch a dart toward a bullseye, hardly a second thought is given to the intricacy of neural circuits that orchestrate such precise movements.

How do these circuits control skilled behaviors? Because rodent limb movements are strikingly similar to those of primates (*1*), and mice provide a means of manipulating neuronal subtypes selectively (*2*), as a postdoc with Tom Jessell I reasoned that a detailed quantification of mouse reaching, together with a genetic dissection of spinal circuits, might help disentangle core features of mammalian skilled motor control (*3*).

Reaching appears simple, but deceptively so. Motor neurons fire, propelling the arm to target. Yet reaching does not arise from an isolated burst of motor output; rather, motor neuron activity is continually tweaked to shape appropriate limb kinematics (*4*–*6*). One strategy for updating motor output is to use proprioceptive feedback from muscles to evaluate outcome and correct course. But sensory information is slow in its trek from the periphery to the brain, creating at least two challenges for motor systems: how to achieve faster feedback for rapid movements, and how to prevent sensory feedback delays from destabilizing the limb (*7*) (see the figure, panel A).

INTERNAL COPIES PROVIDE FEEDBACK. Rapid movements unfold before sensory information arrives (*8*), implying the need for a faster source of information to refine motor output. One long-held idea argues that when motor commands direct arm movement, internal copies of these commands are conveyed to the cerebellum and help predict movement outcome to permit rapid course correction (*7*–*9*). Nevertheless, it is unclear whether putative internal copy pathways have any influence on motor output. Traditional experimental approaches such as electrical stimulation tend to perturb command and copy simultaneously, emphasizing the need for more-selective access to internal copy circuits.

Propriospinal neurons (PNs) in the cervical spinal cord have been implicated in the control of reaching in cats and primates and have the potential to transmit both motor and internal copy signals. They receive descending motor input and extend bifurcating axonal branches both to forelimb motor neurons and to the lateral reticular nucleus (LRN), a major input to the cerebellum (*10*) (see the figure, panel B). Manipulating the LRN-directed branch could therefore provide insight into the contribution of internal feedback to skilled movement.

We first needed to resolve whether PNs exist in mice. Collaborating with Bror Alstermark, we combined in vivo electrophysiology with viral labeling to show that PNs are present and, more tellingly, that they represent a subpopulation of V2a neurons (*11*), one of the cardinal interneuron subtypes involved in motor control (*2*). This genetic insight made it possible to ablate cervical V2a interneurons, revealing a severe and behaviorally selective perturbation of reaching movements. The similarity of these reaching deficits across species (*10*) supports the view that PNs have evolved to direct specific features of mammalian forelimb movement (*12*).

But ablating PNs does not resolve whether the internal copy branch alone can influence

Grand Prize Winner: Eiman Azim

Eiman Azim received undergraduate degrees from Stanford University and a Ph.D. from Harvard University. As a postdoctoral fellow at Columbia University, Dr. Azim has been exploring the neural basis of skilled movement using molecular, electrophysiological, and behavioral approaches in the mouse to identify and characterize feedback pathways that control goal-directed reaching.

Finalist: Allyson Friedman

Allyson Friedman received her undergraduate degree from Barnard College at Columbia University and her Ph.D. from Mount Sinai School of Medicine. Dr. Friedman is currently a postdoctoral fellow at Mount Sinai where she is conducting research on the ionic and neural circuit mechanisms of susceptibility and resilience to major depressive disorder to identify novel targets for treatment.

Finalist: Ho Ko

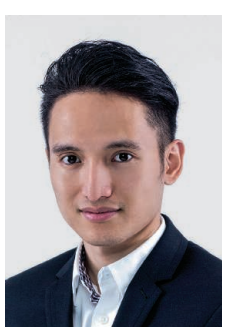

Ho Ko received his undergraduate degree from the Chinese University of Hong Kong and a Ph.D. from University College London. He is currently pursuing clinical training while conducting research studying the neural basis of motor control and visual information processing, as well as planning collaborative work with engineers to develop novel biomedical engineering technology.

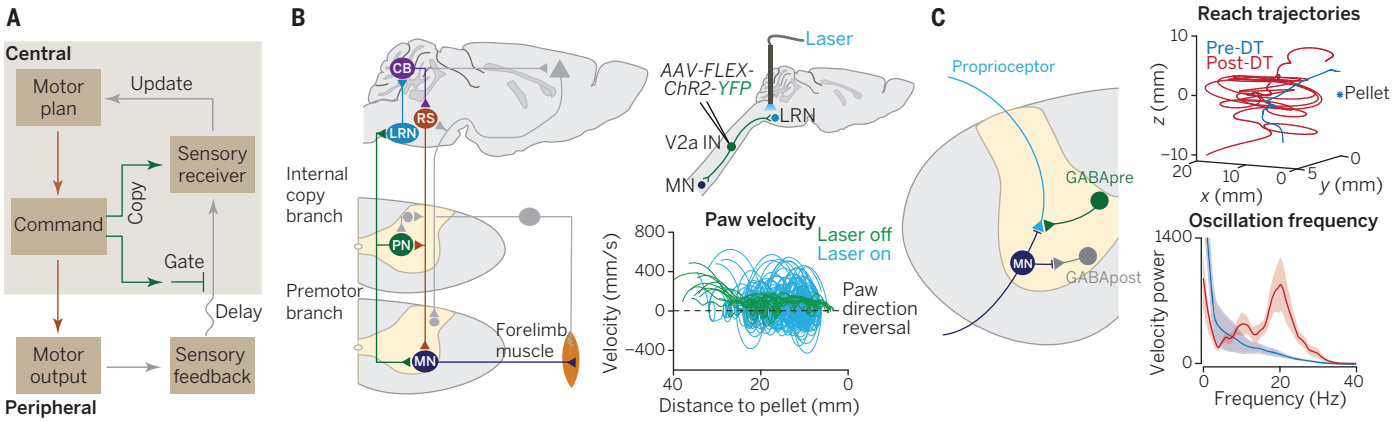

Internal copies and sensory gating in forelimb motor control. (**A**) During limb movement, motor commands elicit motor neuron activation and muscle contraction, generating proprioceptive sensory feedback. Temporal delays in peripheral feedback imply a need for i) a more rapid internal feedback mechanism (copy); and ii) a means to constrain sensory feedback gain (gate). (**B**) Cervical PNs receive input from descending pathways, including the reticulospinal (RS) tract. Bifurcating PN axons innervate forelimb motor neurons (MN; premotor branch) and the lateral reticular nucleus (LRN; internal copy branch), which projects to the cerebellum (CB). Colored neurons trace a putative cerebellar-motor loop. A conditional viral approach (*AAV-FLEX-ChR2-YFP*) was used to express ChR2 in cervical V2a interneurons, and ChR2+ PN terminals in the LRN were photostimulated to activate the PN internal copy branch selectively, resulting in a severe disruption of reaching kinematics (blue). (**C**) Presynaptic inhibitory (GABApre) neurons form axo-axonic contacts onto proprioceptive afferent terminals, in contrast to the far more abundant GABApost neurons, which form direct postsynaptic inhibitory contacts. Diphtheria toxin (DT)–mediated genetic ablation of cervical GABApre neurons uncovered severe limb oscillations during reaching of consistent ~20 Hz frequency (red). [(B) adapted from (*11*); (C) adapted from (*18*)]

reaching. To explore this issue, we expressed the light-gated cation channel ChR2 in cervical V2a interneurons and found that photostimulation of PN axon terminals within the LRN activates the internally directed PN branch without affecting the premotor branch. Intriguingly, activation of this copy pathway excites forelimb motor neurons through a rapid polysynaptic circuit, disrupting reach accuracy (figure, panel B). Moreover, these motor responses were substantially diminished by severing LRN projections to the cerebellum, implicating a fast cerebellar-motor feedback loop in forelimb control (figure, panel B). Thus, PN internal feedback, and likely motor copy circuits more generally, can serve to calibrate movement.

GAIN-CONTROL FOR SMOOTH MOVEMENT. What if Mays needed to wait for the announcer to relay the ball's location? Despite his best efforts, he would likely have undershot. By analogy, the spinal cord is similarly sensitive to outdated information. Delayed sensory feedback can push the system off equilibrium into an unstable state (*7*).

Like a volume knob adjusting feedback strength, a gating mechanism that limits the impact of delayed sensory information might maintain motor stability (*13*). For decades it has been appreciated that spinal sensory feedback can be inhibited presynaptically (*14*, *15*) (figure, panel C), yet pharmacological approaches have been unable to manipulate presynaptic and postsynaptic inhibition separately, leaving presynaptic inhibition as a phenomenon in search of a function.

> ***"Reaching appears simple, but deceptively so."***

Inhibitory neurons are not created equal, and thus molecular differences could provide a means of selective interneuron manipulation. Using the GABA-synthetic gene *Gad2* to gain selective access to neurons that contact sensory terminals (*16*, *17*), Andrew Fink combined ChR2-based activation with in vitro electrophysiology to establish that *Gad2*-expressing neurons mediate presynaptic inhibition at sensory-motor synapses (*18*). More strikingly, we found that eliminating these neurons unleashes severe limb oscillations during reaching that are absent at rest (figure, panel C), implicating proprioceptive feedback as the trigger. With Larry Abbott, we found that the core features of these reaching deficits can be accounted for by a model of the limb in which sensory feedback gain is high. Thus, a mix of molecules, manipulation, and modeling has uncovered presynaptic inhibition as a sensory gain-control mechanism critical for smooth limb movement.

Whether refined or routine, in the World Series or on backyard bases, movement defines our interaction with the world. Deciphering how intention is converted into action calls for a greater appreciation of the causal link between motor circuits and behavior. Through a reductionist approach in mice, in essence dismantling circuits one neural element at a time, plausible substrates for internal and external feedback control are emerging. Exploring how these and other motor circuits are conserved and modified across species should lead to a clearer understanding of our impressive—on occasion even Mays-like—repertoires of skilled behavior.■

Departments of Neuroscience and Biochemistry and Molecular Biophysics, Howard Hughes Medical Institute, Kavli Institute for Brain Science, Mortimer B. Zuckerman Mind Brain Behavior Institute, Columbia University, New York, NY

REFERENCES AND NOTES

1. I. Q. Whishaw, S. M. Pellis, B. P. Gorny, *Behav. Brain Res.* **47**, 59–70 (1992).
2. M. Goulding, *Nat. Rev. Neurosci.* **10**, 507–518 (2009).
3. A. Miri, E. Azimi, T. M. Jessell, *Neuron* **80**, 827–834(2013).
4. J. Messier, J. F. Kalaska, *Exp. Brain Res.* **125**, 139–152 (1999).
5. E. Todorov, M. I. Jordan, *Nat. Neurosci.* **5**, 1226–1235 (2002).
6. S. H. Scott, *Nat. Rev. Neurosci.* **5**, 532–546 (2004).
7. D. M. Wolpert, R. C. Miall, **9**, 1265 (1996).
8. D. M. Wolpert, R. C. Miall, M. Kawato, *Trends Cogn. Sci.* **2**, 338–347 (1998).
9. R. Shadmehr, J. W. Krakauer, *Exp. Brain Res.* **185**, 359–381 (2008).
10. B. Alstermark, T. Isa, *Annu. Rev. Neurosci.* **35**, 559–578 (2012).
11. E. Azim, J. Jiang, B. Alstermark, T. M. Jessell, *Nature* **508**, 357–363 (2014).
12. A. N. Iwaniuk, I. Q. Whishaw, *Trends Neurosci.* **23**, 372–37 (2000).
13. R. B. Stein, M. N. Oğuztöreli, *Biol. Cybern.* **22**, 147–157 (1976).
14. K. Frank, M. Fuortes, *Fed. Proc.* **16**, 49 (1957).
15. J. C. Eccles, R. M. Eccles, F. Magni, *J. Physiol.* **159**, 147–166 (1961).
16. D. I. Hughes *et al.*, *Proc. Natl. Acad. Sci. U.S.A.* **102**, 9038–9043 (2005).
17. J. N. Betley *et al.*, *Cell* **139**, 161–174 (2009).
18. A. J. Fink *et al.*, *Nature* **509**, 43–48 (2014).

ACKNOWLEDGMENTS

I thank mentors and collaborators T. M. Jessell, B. Alstermark, A. Fink, J. Jiang, L. Abbott, K. Croce, and Z. J. Huang. This work was supported by the Helen Hay Whitney Foundation, the Howard Hughes Medical Institute, the National Institutes of Health (NIH), Umeå University, the Swedish Research Council, the G. Harold and Leila Y. Mathers Foundation, and Project A.L.S.

10.1126/science.1260778

BOOKS *et al.*

NEUROSCIENCE

BRAAAAINS

By **Steven C. Schlozman**

When I was asked to review *Do Zombies Dream of Undead Sheep*, by neuroscientists Timothy Verstynen and Bradley Voytek, my opinions, admittedly, were not without bias. Having published my own zombie novel in 2011 (*1*), I think the shambling ghouls that George Romero introduced back in 1968 with *Night of the Living Dead* can serve as lovely, surprisingly accurate, and firmly tongue-in-cheek pedagogies displaying complicated principles of neurobiology.

Still, I can be objective. This new book is smart, informative, historically riveting, well referenced, and, like all good zombie stories, wonderfully fun. While some may argue that this kind of book is not the proper purview of respected neuroscientists like Verstynen and Voytek, I'd argue fervently that it is the perfect mechanism through which anyone might, um, "consume" neuroscience.

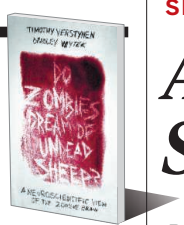

Do Zombies Dream of Undead Sheep?
A Neuroscientific View of the Zombie Brain
Timothy Verstynen and Bradley Voytek
Princeton University Press, 2014. 271 pp.

Among the many phenomena covered (from the neural correlates of lumbering to the infamously insatiable appetite of the undead), let's examine one example from the book. To appreciate it, you must be familiar with this popular zombie trope: When someone turns into a zombie, she can see you, but she can't see the *you* that makes *you* unique. All she can see is lunch. How do Verstynen and Voytek deal with this neurobiological conundrum? By diagnosing the zombie in question with "acquired prosopagnosia," a real condition in which individuals cannot recognize familiar people from their faces. They further localize her abnormality as a defect in the fusiform gyrus of the cerebral cortex. If you'll pardon the pun, that's pretty brainy stuff for a book about zombies.

ILLUSTRATION: HALF MAN TUBE/ISTOCKPHOTO

The reviewer is in the Department of Psychiatry at Massachusetts General Hospital at Harvard Medical School, Boston, MA 02114, USA. E-mail: sschlozman@mgh.harvard.edu

Zombie discussions are by definition intertextual. Those who choose to write about zombies are aware that they are engaging in the outlandish and therefore openly admit their conceit even as they make clear their theses. The authors stay true to this fine tradition, and the results are delightful.

If you want a sophisticated primer of neuroscience, coupled with a Halloween spin, then there can be no other book. Just remember that zombies are not real—yet.

REFERENCES AND NOTES

1. S. C. Schlozman, *The Zombie Autopsies: Secret Notebooks from the Apocalypse* (Hachette Book Group, New York, 2011).

10.1126/science.1261500

SPORTS SCIENCE

Advantage: Science

By **Pamela J. Hines**

The star pitcher hurls his fastball, only to watch it hit the dirt short of the plate. The pitch that worked for him on the smaller field of Little League baseball is useless on the bigger field of high school baseball. The coveted pitching spot is going to a different boy this year, one who never played baseball before but whose rotational strength and spring-loaded elbow bring just the right mix of biomechanics and endurance.

In Faster, Higher, Stronger, journalist Mark McClusky takes us into the world of athletics, looking at what differentiates winners from losers in elite competitions, from the Olympics to Formula One auto racing. The focus on extremes of excellence and performance at the margins of human capability makes a great read. The casual sportsman is not forgotten, as McClusky touches back on his own golf game to help weekend athletes relate. Marginal gains, trainability, and best fit run through the book, which is filled with engaging stories of athletes reaching the podium or missing by a hair.

The reviewer is on staff at Science *magazine, AAAS, Washington, DC 20005, USA. E-mail: phines@aaas.org*

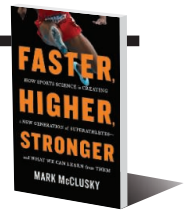

Faster, Higher, Stronger
How Sports Science Is Creating a New Generation of Superathletes—and What We Can Learn from Them
Mark McClusky
Hudson Street Press, 2014. 288 pp.

Throughout the book, McClusky shows us how seemingly inconsequential details can have surprising effects on athletic performance. In tennis, one more centimeter of height gives the server access to four more centimeters of the opposing court. The youngster who matures late but spent her youth competing against larger, stronger opponents gains skills useful on the adult playing field.

The variety of interacting factors that give an edge is eye-opening, including physical resources that the athlete brings and external resources brought by training and environment. Effective oxygen processing is crucial, but only some athletes can improve their abilities to process oxygen by training. Even the size of the town the athlete grew up in matters. If too small, the community doesn't have the infrastructure to support competitions; if too large, the system doesn't have the flexibility to allow athletes to find their way.

McClusky also discusses performance-enhancing drugs. Interestingly, the advantages accrued from legal and illegal enhancement can sometimes be the same—taking erythropoietin or training at a high altitude will both afford you more red blood cells, for example. Why is one practice grounds for disqualification, while the other is condoned? In a world where pharmaceutical enhancements are readily available and often difficult to detect, he encourages us to hold on to our sense of fair play.

There must be a good deal of resilience and persistence involved in bringing an individual athlete to the top—a topic the book could have explored in greater detail. How can those traits be trained or supported? How much room is there for marginal gains in the mental game?

Have athletes reached the limits of human performance? For some sports, that may be the case. With arm rotations up to 9000 degrees per second, pitchers may be reaching a biomechanical limit. For others participating in golf, tennis, and skiing, better clubs, slower balls, and new skis open up an edge for marginal gains. McClusky shows us how the right athlete competing in the right sport and informed by science will forge new records.

10.1126/science.1261142

Published by AAAS

LETTERS

Edited by **Jennifer Sills**

Venezuelan science in dire straits

Barrios (slums) in Venezuela.

IT IS HARD to find words that adequately describe the tragic state of Venezuelan science. The government's policies seem specifically designed to sabotage research and innovation. Based on data from the Science Citation Index and Scopus, from 1998 to 2008, there was a consistent increase in scientific production, which coincided with the highest crude oil prices per barrel ever recorded in Venezuela's history. This honeymoon period ended in May 2009 when former President Hugo Chávez, during a national broadcast, stated: "Researchers should stop working on obscure projects, and instead should go into the barrios (slums) to make themselves useful" (*1*).

Shortly after Chavez's words, Venezuelan scientists started facing budget cuts and ever-increasing pressure from government institutions trying to politicize funding. Several notable researchers and professors were blacklisted, threatened, and even fired (*2*), while thousands of young talents were forced to emigrate because of lack of work opportunities, in what is considered the largest brain drain ever recorded in Venezuela's history (*3*). This, along with a devastating economic landscape caused by a sudden decrease in oil prices (which has endured), initiated an accelerated decay in scientific production, as evidenced by various publication indexes (*4*).

After the historical peak in publications in 2008, publications indexes started to reveal a rampant decrease in peer-reviewed manuscripts, which has become more noticeable in the past 2 years, dropping by 24.9% in the Science Citation Index and by 21.12% in Scopus. For a comparison, by 1998 Venezuela had published 69% more than its neighboring country of Colombia as per Index Medicus/Medline records; however, for 2013 Colombia had surpassed by 222% the scientific production of Venezuela (*5*). This dire situation of Venezuelan science has worsened considerably as a product of a combination of factors, which include the lack of scientific training and background of government authorities, the politicization of science, and an unprecedented economic crisis. Venezuela is the only South American nation whose scientific output is declining, and it ranks among the lowest current citation impact weighted by research field in the region (*6*). For the year 2000, according to the World Intellectual Property Organization database, Colombian residents submitted 75 patent applications, whereas Venezuela had only filed 56. Strikingly, this gap increased in 2011 with Colombia filing 183 requests in contrast to Venezuela, which filed 33.

Because of the drop in oil prices and rising government debt, the Venezuelan economy has fallen into a downward spiral of problems, including a state of hyperinflation and extreme shortages of goods. Accessing foreign currency in Venezuela has become a complicated task because of the government's stringent currency exchange control system, which embraces an intricate scheme of different "official" rates (*7*). This has left local laboratory equipment and reagent suppliers and importers with no other option than selling their products at prices determined by the reticent and illegal black market rates, making prices inaccessible to the already constrained budgets of most research laboratories.

Our internal stocks of reagents have dried up, and the unbridled insecurity and violence that have taken over the country have precluded foreign commercial providers from complying with their maintenance and repair contracts, leading to a massive deterioration of Venezuela's research infrastructure. Because of the intimate historical relations between medical research laboratories and the health care system in Venezuela, this situation has also affected patient care. Diagnostics are most affected, but treatment is as well. Failure to access reagents and other consumables has led to a collapse in many public health programs (*8*). The health system is struggling with the chikungunya epidemic, because of the lack of reagents for serological testing and primers for PCR-based diagnosis.

Most research laboratories in Venezuela are surviving today thanks to regional and cross-continental collaborations and networking with other groups around the globe. However, most basic science programs in Venezuela are currently destined to disappear.

Despite the ominous ongoing public health and medical research crisis, the government has failed to call for an emergency plan or to prioritize the importation of scientific and research materials. There is no evidence of a sound commitment to scientific freedom. What will be the fate of science in Venezuela? It remains to be seen.

***Alberto E. Paniz-Mondolfi*[1,2]** and Alfonso J. Rodríguez-Morales*[3]**

[1]Department of Pathology and Laboratory Medicine, Hospital Internacional, Barquisimeto, 3023, Venezuela. [2]Laboratory of Biochemistry, Instituto de Biomedicina, Caracas, 1010A, Venezuela. [3]Public Health and Infection Research Group, Faculty of Health Sciences, Universidad Tecnológica de Pereira, Pereira, Risaralda, 660001 Colombia.

*Corresponding author.
E-mail: Alberto.paniz-mondolfi@yale.edu

REFERENCES

1. B. Casassus, *Science* **324**, 1126 (2009).
2. P. Gunson, *Science* **325**, 1190 (2009).
3. A. Petherick, *Nature* **459**, 898 (2009).
4. P. Mayta-Tristán, A. Dulanto-Pizzorni, J. J. Miranda, *Lancet* **371**, 1577 (2014).
5. L. F. Benavides, A. F. López-Isaza, A. J. Rodríguez-Morales, *Invest Clin.* **55**, 289 (2014).
6. R. Van Noorden, *Nature* **510**, 202 (2014).
7. "Of oil and coconut water," *The Economist*, 20 September 2014.
8. A. J. Rodríguez-Morales, A. E. Paniz-Mondolfi, *Lancet* **384**, 663 (2014).

PHOTO: ISTOCKPHOTO/EOPITZ

Population growth: Peak probability

IN THEIR REPORT "World population stabilization unlikely this century" (10 October, p. 234; published online 18 September), P. Gerland *et al.* used a United Nations (UN) 2012 assessment to support their claim that the population will not peak this century, despite our earlier work indicating that it will (*1*–*3*).

The UN assumptions used by Gerland *et al.* are mainly based on statistical extrapolation, whereas our approach is based on substantive reasoning and assessments of alternative arguments (*4*). For example, a changing education structure means that young Nigerian women are more educated than their elders, implying likely near-term fertility declines. The UN assumes constant fertility at 6.0 for 2010 to 2015, but the newest Demographic and Health Survey shows that it has already decreased to 5.5 in 2010 to 2013. The population increase for Nigeria from today's 160 million to 914 million in 2100 expected by the UN is thus unrealistic. For China, the UN assumes that fertility will only increase in the future. We assume, like many Chinese scientists and institutions (*5*), that it will decline and stay low in the coming decades. On balance, we therefore still expect the end of world population growth this century.

Wolfgang Lutz,* William Butz, Samir KC, Warren Sanderson, Sergei Scherbov

World Population Program, International Institute for Applied Systems Analysis (IIASA), A-2361 Laxenburg, Austria.

*Corresponding author. E-mail: lutz@iiasa.ac.at

REFERENCES

1. W. Lutz, W. C. Sanderson, S. Scherbov, *Nature* **387**, 803 (1997).
2. W. Lutz, W. C. Sanderson, S. Scherbov, *Nature* **412**, 543 (2001).
3. W. Lutz, W. C. Sanderson, S. Scherbov, *Nature* **451**, 716 (2008).
4. W. Lutz, W. Butz, S. KC, Eds., *World Population and Human Capital in the 21st Century* (Oxford Univ. Press, Oxford, 2014).
5. National Health and Family Planning Commission of China (2013); www.nhfpc.gov.cn/jczds/s3578/201311/f852a9d6833d4c1eb79b9e67f1885416.shtml.

Population growth: Limits of food supply

IN THEIR REPORT "World population stabilization unlikely this century" (10 October, p. 234; published online 18 September), P. Gerland *et al.* omit one of the major determinants of population growth: the food supply. More than 200 years ago, Malthus (*1*) famously asserted that the growth of a population will always outrun its ability to feed itself. Yet, in their projections of world population growth, Gerland *et al.* use as their independent variables only measures of fertility, life expectancy, and age at death. They conclude that "the projected population of Africa [is] between 3.1 and 5.7 billion with probability 95% by the end of the century," with no mention of agricultural limits. In fact, much of the continent's area is desert or rain forest (where nutrients are largely stored in living biomass rather than in the soil) and could not be made arable. The agricultural soils that do exist are relatively infertile compared with those of other inhabited continents.

Robert R. Holt

Truro, MA 02666, USA. E-mail: capebobholt@comcast.net

REFERENCES

1. T. R. Malthus, "An essay on the principle of population (1798)," *Oxford World's Classics* (Oxford Univ. Press, Oxford, 1999).

TECHNICAL COMMENT ABSTRACTS

Comment on "Control profiles of complex networks"

Colin Campbell, Katriona Shea, Réka Albert

■ Ruths and Ruths (Reports, 21 March 2014, p. 1373) find that existing synthetic random network models fail to generate control profiles that match those found in real network models. Here, we show that a straightforward extension to the Barabási-Albert model allows the control profile to be "tuned" across the control profile space, permitting more meaningful control profile analyses of real networks.

Full text at http://dx.doi.org/10.1126/science.1256492

Response to Comment on "Control profiles of complex networks"

Justin Ruths and Derek Ruths

■ Campbell, Shea, and Albert propose an adaptation of the Barabási-Albert model of network formation that permits a level of tuning of the control profiles of these networks. We point out some limitations and generalizations of this method as well as highlight opportunities for future work to refine formation mechanisms to provide control profile tuning in synthetic networks.

Full text at http://dx.doi.org/10.1126/science.1256714

TECHNICAL COMMENT

NETWORK MODELS

Comment on "Control profiles of complex networks"

Colin Campbell,[1,2]* Katriona Shea,[2] Réka Albert[1,2]

Ruths and Ruths (Reports, 21 March 2014, p. 1373) find that existing synthetic random network models fail to generate control profiles that match those found in real network models. Here, we show that a straightforward extension to the Barabási-Albert model allows the control profile to be "tuned" across the control profile space, permitting more meaningful control profile analyses of real networks.

Ruths and Ruths (*1*) present a statistic for characterizing the control nodes within a network. The measures η_s, η_e, and η_i are respectively defined as the fraction of a network's control nodes that arise from source nodes, external dilations, and internal dilations. The authors show that several existing synthetic networks are dominated by η_s (i.e., $\eta_s \gg \eta_i + \eta_e$).

Here, we show that with the addition of a single parameter, the Barabási-Albert (BA) model (*2*) may be modified to be dominated by any of the three types of control nodes introduced in (*1*). We first note that the BA model in its original form generates an undirected network. As such, two considerations are raised when modifying the BA model to generate directed networks. First, the preferential node selection may be based on total node degree, in-degree, or out-degree. Second, new edges may be directed either to or away from new nodes as they are added to the network. We consider here preferential attachment based on total node degree, which reduces to the undirected BA model when disregarding edge directionality; i.e., it generates networks with total node degree distributions that obey power laws.

The second consideration—that is, the choice of edge directionality—may be used to "tune" the control profile of the generated networks to be dominated by any of η_s, η_e, and η_i, as seen in real networks. Consider a time step in the BA model where an existing node x has been preferentially selected based on its total degree and is being connected to a new node y. We introduce the parameter p such that the directed edge $x \rightarrow y$ is assigned with probability p; directed edge $y \rightarrow x$ is thus assigned with probability $(1 - p)$. This modified BA model is therefore defined by three parameters: n, the number of nodes in the network; m, the number of edges to be connected to each new node; and p, the probability of new edges running out from the existing network to new nodes as the network is built.

Because the lowest-degree nodes are the most abundant in BA networks, the extremal values of $p = 0$ and $p = 1$ result in networks that are characterized by many source nodes (η_s domination) and many sink nodes (η_e domination), respectively. A moderate value of p reduces the uneven distribution between source nodes and sink nodes and introduces a heterogeneous flow structure to the networks, which results in the emergence of internal dilations (η_i domination).

We show the distribution of η_s, η_e, and η_i as a function of p for $n = 1000$, $m = 3$ in Fig. 1, and project the same data to a ternary plot, in the style of figure 3 from (*1*), in Fig. 2. Notably, the ternary plot of Fig. 2 shows that the control profile "travels," as a function of p, across the perimeter of the control profile space, suggesting that mixed control profiles constitute a forbidden region (*1*) of the state space for this model. This matches well with the control profiles of the real networks reported in (*1*), although the persistence of some number of source and sink control nodes prevents the model from generating networks with $\eta_i \approx 1$. We note, however, that a post hoc mechanism that eliminates all source and

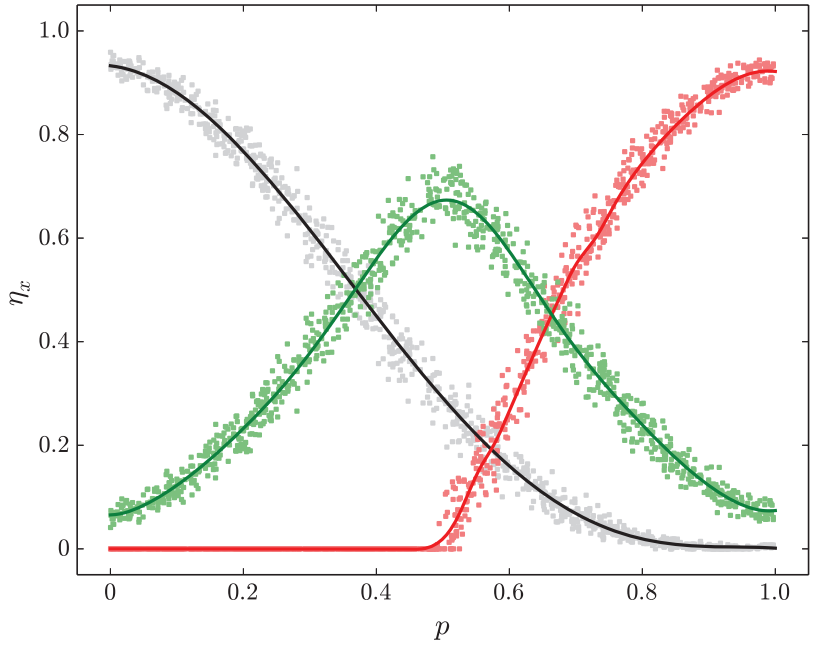

Fig. 1. The abundance of η_s (black squares), η_e (red squares), and η_i (green squares) in the modified Barabási-Albert model. The figure shows 1000 networks with $n = 1000$, $m = 3$, and p randomly sampled from the interval [0,1]. Colorized curves represent fits to the data.

Fig. 2. The data of Fig. 1 projected onto a ternary plot. Coloring corresponds to the largest value of η (black, η_s; green, η_i; red, η_e). As p increases from 0 to 1, the networks move clockwise across the control profile space, from η_s to η_i to η_e.

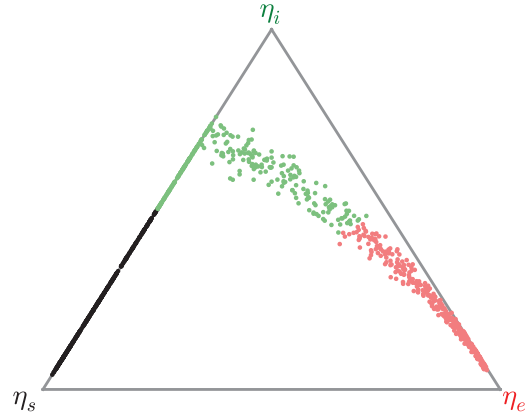

[1]Department of Physics, Pennsylvania State University, 122 Davey Laboratory, University Park, PA 16802, USA.
[2]Department of Biology, Pennsylvania State University, 208 Mueller Laboratory, University Park, PA 16802, USA.
*Corresponding author. E-mail: cec220@psu.edu

sink nodes (e.g., by adding edges $x \rightarrow$ source and sink $\rightarrow x$ for preferentially selected nodes x) successfully moves the control profile to $\eta_i = 1$ while maintaining a degree distribution that approximately obeys a power law.

Random network models offer insight into the mechanisms by which real networks form. In (*1*), the authors show that the control profile of real networks differs from existing models of random networks. In this Comment, we have shown that controlling the directionality and heterogeneity of a random network's edges can substantially affect the network control profile. These findings have implications for the development of new and modified network models that will greatly improve our ability to understand, control, defend, and protect a wide range of real networks.

REFERENCES AND NOTES

1. J. Ruths, D. Ruths, *Science* **343**, 1373–1376 (2014).
2. A.-L. Barabási, R. Albert, *Science* **286**, 509–512 (1999).

ACKNOWLEDGMENTS

This work was supported by NSF grant DMS-1313115.

27 May 2014; accepted 19 September 2014
10.1126/science.1256492

Entrepreneurs plan to use this abandoned shrimp farm in Puerto Rico to grow algae that will be converted into biofuel.

PHOTO: MARIO VELASCO/JORGE GASKINS

Can algae make the big time in renewable energy?

Researchers in Puerto Rico see a promising future for algae-based biofuel, though economic and regulatory questions remain

By **Kathy Wren**, *in San Juan*

Sugarcane plantations used to dominate the coastal landscape around Dorado, Puerto Rico, about 20 miles west of San Juan. But agriculture on the island declined in the mid–20th century, and then saltwater crept into the water table here. Now, a company called Bio-Lípidos de Puerto Rico Inc./Replenish Energy wants to use this area for what it hopes will become a major part of the island's energy portfolio: algae.

The company plans to grow single-celled, marine "microalgae," whose oil will be extracted to form the feedstock for biodiesel and other types of fuel. The dried remains will be used in a variety of products, from plastics to beauty products. Some of the algae will also become food for cultured shrimp and tilapia, whose waste, in turn, will be used to fertilize the algae.

A 320-acre pilot project on an abandoned shrimp farm is now shovel-ready, and more than half of the funding is in place. The company has received multiple investment offers pending a successful field trial, according to co-founder Jorge Gaskins. The biggest challenge ahead, he said at the annual meeting of the AAAS Caribbean Division, is that the Puerto Rican government has yet to clarify many elements of its biofuel policy, including which agencies would promote and regulate the industry and how available EPA tax incentives would be implemented.

Despite this uncertainty, Gaskins and other speakers at the meeting believe that marine algae represents an important opportunity for renewable energy in Puerto Rico and other countries with an abundance of sunlight, warm temperatures, and coastal waters. They made their case at the 20 September meeting, which drew roughly 100 scientists, students, and educators to the University of Turabo. Founded in 1985, the AAAS Caribbean Division serves as a hub for AAAS members in all of the islands and countries in the Caribbean region.

"Puerto Rico could produce a significant fraction of our total energy requirements using marine biomass if we make reasonable reductions in total energy consumption," said Gary Gervais, a research associate in the Department of Environmental Sciences at the University of Puerto Rico's Río Piedras campus.

As the effects of climate change mount, the need for renewable energy sources has become clear, especially in Puerto Rico, where as of 2012 only 1% of its electricity came from renewable sources, according to the U.S. Energy Information Administration. The government has adopted a policy requiring 20% of net electricity sales to come from renewable energy resources by 2035.

Compared to other sources of biofuel, such as corn, soybeans, or sugarcane, algae have a lot to offer. They grow quickly, especially in the consistently warm Caribbean; they are relatively efficient oil producers; and they don't require irrigation. Many species are also good multitaskers; Catalina Dávila, a postdoctoral student at the University of Puerto Rico, has identified a *Botryococcus* species in Puerto Rico's brackish

waters whose fatty acid profile makes it a good candidate for biofuel. And, because it efficiently removes nutrients from water, this microalgae may also be useful in wastewater treatment.

Macroalgae, or seaweeds, are also potential biofuel sources, although further research will be necessary to understand the ecological effects of farming seaweed. For example, blocking sunlight at the surface will likely impact life in deeper waters, said Agnerys Rodriguez-Santos, a technician in Gervais' lab.

Perhaps the most appealing thing about growing algae for biofuel is they don't require land that would otherwise be used for growing food, a key drawback for other biofuel crops. In Puerto Rico, however, large-scale algae cultivation would compete with the tourism industry for valuable coastal real estate. "The idea of a marine farm is very hard to talk about" with local land-use and regulatory agencies, said Gervais, who suggested that other Caribbean islands or the Caribbean coastline of Central or South American countries may be more practical locations for algae farming if the industry does scale up.

In the meantime, researchers are working to determine the most environmentally friendly and cost-effective ways to turn algae into fuel. Many involve extracting oils or synthesizing biocrude oil from raw biomass. And Gervais has developed a system for producing biogas from seaweed via anaerobic digestion in an oxygen-free bioreactor.

None of these approaches has yet been able to offer a means for making algae biofuel competitive with petroleum, however. For example, Arnulfo Rojas-Pérez, a graduate student at the University of Puerto Rico, is studying an approach called hydrothermal liquefaction, which uses hot, pressurized water instead of a chemical solvent to produce biocrude. This method is appealing because it doesn't require drying the algae, but even so, it has not been used in a successful commercial operation yet.

That may change soon, as the industry continues to progress. A 2013 report by the National Alliance for Advanced Biofuels and Bioproducts, a consortium of U.S. national laboratories, universities, and corporations, identified several technological advances in the last 3 years that have the potential to bring the price of algae-based biocrude down to $7.50 per gallon. Next, significant reductions in capital and operational expenditures will be needed to bring the cost down to $2.00 per gallon, making it more competitive with petroleum, the report concludes. ■

Ebola crisis reveals gaps in public health response

As health care workers have struggled to stop the disease, they have been hampered by a lack of infrastructure and training

By **Sarah Zielinski**

West Africa was already lacking in trained health care workers, but the 2014 Ebola crisis has devastated their small number. Melvin Korkor, an attending physician at a hospital in remote Bong County in Liberia, was one of the survivors. Nine of his colleagues, including five nurses, became infected and died early in the outbreak. "I was so compassionate in my profession to the extent that I had to touch one of the nurses," he said. A few days after she died, Korkor fell sick. "I isolated myself from my family," he said.

By the time he recovered, his hospital was closed but still had a lot of patients needing care. "We're going to reopen our hospital," he pledged, "but we're going to need to stop the transmission of Ebola."

The Ebola crisis has quickly grown into the most difficult health security problem faced by the modern world, but it is also providing opportunities to better prepare nations for future health emergencies, said speakers at a conference on global health security.

"We need to capitalize on this moment. As deep and humanly unsettling as this moment is, shame on us if we can't build from it," said Laura Holgate, senior director for weapons of mass destruction terrorism and threat reduction for the White House National Security Council.

Holgate and others gathered in Washington, D.C., on 25 September for a conference addressing the role of nongovernmental organizations in the Global Health Security Agenda (GHSA), which was held at the Milken Institute School of Public Health at George Washington University and co-sponsored by AAAS, the Nuclear Threat Initiative, CORDS: Connecting Organizations for Regional Disease Surveillance, the UPMC Center for Health Security, the Elizabeth R. Griffin Research Foundation, and the CSIS Global Health Policy Center.

The conference preceded the release of 11 "action packages" by GHSA to focus international discussion and efforts to prevent, rapidly detect, and effectively respond to infectious disease threats. Representatives of 44 nations and institutions, including the World Health

Hygienists at the Ebola treatment unit at Island Clinic in Monrovia wash health workers' scrubs at the new clinic, which opened 21 September and was filled to capacity a day later.

PHOTO: FLICKR/MORGANA WINGARD FOR USAID

Laura Holgate, Keiji Fukuda, and J. Stephen Morrison of the Center for Strategic and International Studies said that the Ebola crisis offers an opportunity to strengthen the global health response. Improving support and training for first responders such as Liberian physician Melvin Korkor (above) will be critical.

Organization, met on 26 September at the White House to discuss implementation of the action plans.

The outbreak has revealed vulnerabilities in health care infrastructure, training, and technology, speakers said. For instance, there is no quick and cheap diagnostic test for Ebola yet, which slowed the first identification of the disease in West Africa. "If there had been rapid diagnostics at any of many points of intervention between December, when the first case occurred, and March, when it was finally diagnosed…it could have had an incredible impact," said Thomas Inglesby, director of the UPMC Center for Health Security.

If new tests are developed, they will have to work in environments that may lack electricity, clean water, and sanitation facilities. These same deficits are already hindering care in West African hospitals, said Patty Olinger, the director of global programs at the Elizabeth R. Griffin Research Foundation, at a panel discussion organized by AAAS's Center for Science, Technology, and Security Policy. When Olinger visited the region's clinics, she found that water was collected in some cases from a river and lighting sometimes came from kerosene lanterns. At one hospital, laundry from infectious patients was mixed with everyone else's, she said.

Ebola has overwhelmed the public health systems in West Africa and left those with non-Ebola diseases without any place to go. "We have no idea—I don't know if we ever will—how many people have died of non–Ebola-related causes," said Joseph Fair, a virologist and senior advisor to Fondation Mérieux, which is dedicated to fighting infectious diseases. "We've seen a complete breakdown in an already vulnerable public health infrastructure."

That infrastructure is only now starting to develop after more than a decade of civil conflict in West Africa. The legacy of that conflict also has contributed to a mentality that "run and flee" is the best response to a crisis, Fair said. Past Ebola outbreaks have been contained because it was possible to identify and segregate infected individuals, then trace and track anyone with whom they may have come in contact. That has not happened in Guinea, Sierra Leone, and Liberia.

Educating West Africans about disease and sanitation is crucial, and the messages must be tailored to the people who are to receive it, noted several speakers. The region also needs more trained medical workers, but there are no dedicated academic institutions or programs that are able to research and train the multidisciplinary specialists needed to respond to disasters such as Ebola, said Laud Boateng, a public health physician from Ghana who is currently a Mandela Washington Fellow working on an Ebola education campaign for African youth.

"The Ebola outbreak highlights where we are vulnerable and what remains to be done," said Keiji Fukuda, assistant director-general for health security at the World Health Organization.

Science and *Science Translational Medicine* have made their collection of research and news articles on Ebola freely available to researchers and the general public at www.sciencemag.org/site/extra/ebola/. ■

AAAS Council Reminder

The next meeting of the AAAS Council will take place during the 2015 AAAS Annual Meeting in San Jose, California, and will begin at 9:00 a.m. on 15 February 2015 in the Almaden Ballroom of the Hilton San Jose.

Individuals or organizations wishing to present proposals or resolutions for possible consideration by the council should submit them in written form to AAAS Chief Executive Officer Alan I. Leshner by 1 December 2014. This will allow time for them to be considered by the Committee on Council Affairs at its winter meeting.

Items should be consistent with AAAS's objectives and be appropriate for consideration by the council. Resolutions should be in the traditional format, beginning with "Whereas" statements and ending with "Therefore be it resolved."

Late proposals or resolutions delivered to the AAAS Chief Executive Officer in advance of the February 2015 open hearing of the Committee on Council Affairs will be considered, provided that they deal with urgent matters and are accompanied by a written explanation of why they were not submitted by the 1 December deadline. The Committee on Council Affairs will hold its open hearing at 2:30 p.m. on 14 February 2015 in the Santa Clara Room of the Hilton San Jose.

PHOTOS: RICK REINHARD/GEORGE WASHINGTON UNIVERSITY

A couple defies the years at the Luckenbach, Texas, dance hall.

THE AGING Brain

By **Peter Stern**, **Pamela J. Hines**, *and* **John Travis**

Should we consider aging a natural part of life or an illness? When it comes to the brain, research has tended to focus on the negative side of aging—Alzheimer's disease, for example. Yet all of us know individuals who continue to be mentally sharp their whole lives. And history repeatedly offers proof—Titian, Socrates, da Vinci, and so on—that great creativity and insight can come with maturity.

This special issue of *Science* therefore looks at the mechanisms and contexts of successful brain aging. The developmental trajectory of the brain through the entire life span is affected by genetic, physical, and psychological factors. One thing we know already is that our mental lives benefit when we lead lives that are not only physically healthy but also intellectually challenging and socially engaged (Lindenberger, p. 572).

As we age, our brains constantly reorganize in response to new experiences. Even after adverse physical or psychosocial events, such as a stroke or a loved one's sudden death, there is an astonishing level of flexibility in the brain that enables an individual to compensate and adjust (Gutchess, p. 579). Indeed, the language systems of the brain, responsible for some of the richest human interactions, have an inbuilt resilience that ensures that they remain largely robust across the life span (Shafto and Tyler, p. 583).

Although many researchers are closely watching how individuals age cognitively (Underwood, p. 568), aging populations have global implications for economies and societies (Harper, p. 587). These demographic transformations have to be much more widely discussed if societies are to become well prepared, both mentally and on an institutional level, for the challenges they present.

PHOTO: ROBB KENDRICK

INSIDE

RELATED ITEMS

- **PERSPECTIVE P. 547**
- ***SCIENCE SIGNALING* RESEARCH ARTICLE BY W. M. PRYOR *ET AL.* (28 OCT. 2014)**
- **sciencemag.org/special/neuro2014**

Starting young

Decades-old IQ test records from Scottish children have opened a unique window on how the brain ages

By **Emily Underwood**

On 4 June in 1947, just before being released for the summer holiday, 11-year-old Sheila McGowan sat down at her desk with a pencil and paper to take an intelligence test at a state-run school in Glasgow, Scotland. It began easily enough, with simple analogies: "A man is to skin as what—coat, animal, bird, skin or cloth—is to fur?" for example. The test quickly progressed to more difficult challenges: spatial puzzles, arithmetic, and decoding cyphers. There were 71 questions in all, with only 45 minutes to finish.

More than 70,000 other 11-year-olds took the same test that day, as part of one of the first efforts to measure the intelligence of an age cohort across an entire nation. Called the Scottish Mental Surveys, the tests, including an earlier survey administered in 1932, were originally aimed at determining how many children were too "mentally defective" to benefit from schooling and to address fears that the average Scottish intelligence was dropping as professional families had fewer children.

McGowan remembers the test "very well," because her mother was gravely ill when she took it. After her mom died the following April, McGowan lived alone with her father, who had to work night shifts at the local shipyard to make ends meet. She had scored high on the intelligence test, but like many poor Scottish teenagers at

PHOTO: DOUGLAS ROBERTSON/UNIVERSITY OF EDINBURGH CENTRE FOR COGNITIVE AGEING AND COGNITIVE EPIDEMIOLOGY

Published by AAAS

In April, psychologist Ian Deary (*front*, *center*) gathered surviving members of the Lothian Birth Cohorts to hear about how their brains are aging.

the time, McGowan did not finish school. She went to work at 16, as a Glasgow shop assistant.

Decades passed. McGowan married and had two daughters, became a teacher at a college for the deaf, and earned a bachelor's degree in psychology. Then, in 2003, a leaflet arrived at her door asking if she had taken the 1947 mental test. The note was from cognitive psychologist Ian Deary and his colleagues at the University of Edinburgh in the United Kingdom. He wanted McGowan to take the same test again and participate in an ongoing study to determine whether she had maintained her girlhood sharpness or was showing signs of cognitive decline.

"It took a little bit of courage" to agree to join the study, she says. Indeed, several of McGowan's old schoolmates opted not to participate because they didn't relish the idea of scientists tracking their mental downswing, she says.

But Deary and colleagues did persuade more than 1000 of McGowan's contemporaries in the Lothian region of the Scottish lowlands, as well as more than 500 participants from the 1932 survey, to sign up for what is now a decade's worth of follow-up studies. This April, Deary gathered as many surviving participants as possible—the 1947 and 1932 cohorts are now 78 and 93 years old, respectively—to the Church of Scotland's Assembly Hall on the Mound in Edinburgh for a sneak preview of the most recent results. Roughly 400 elderly Scots attended, with one well-behaved golden retriever in tow.

Standing before a podium under the Assembly Hall's vaulted ceilings, Deary regaled the group with the fruits of their participation in the study, a unique look at how childhood cognitive abilities fare across a lifetime. It has yielded more than 250 scientific publications, based on more than 20,000 hours of cognitive tests and brain scans, done at roughly 2- to 3-year intervals. And, most significantly, it offers the beginnings of an answer to a long-debated question: Why do some healthy people maintain their cognitive sharpness as they age, whereas others lose their edge?

After studying the Lothian cohorts' test scores on dozens of cognitive tests, sampling their genes, scanning their brains, and documenting their lifestyles and health in painstaking detail for more than 10 years, Deary has found one factor that appears to predict late-life cognitive ability better than any other single measure. It's not exercise, education, or any other virtuous activity, but rather simply an individual's level of intelligence at age 11. As Deary likes to say about old age, quoting Fred Astaire, "To make a success of it, you've got to start young."

LIKE MANY COUNTRIES, Scotland's population is aging rapidly, with the number of people over the age of 65 projected to increase by roughly 60% over the next 20 years. Dozens of aging studies worldwide are tracking seniors such as McGowan, looking for clues about how to stave off cognitive decline and dementia. But the Lothian Birth Cohort studies remain unique thanks to an unexpected windfall.

In 1997, Deary and colleagues discovered records from the Scottish Mental Surveys stashed away in a University of Edinburgh basement. Boxes upon boxes of documents—containing information painstakingly analyzed in the predigital age by tabulation machines that relied on punch cards and needles—had piled up in government and university archives, collecting dust. As they sifted through the data, Deary and psychiatrist Lawrence Whalley realized they'd stumbled on a gold mine. "This will change our lives," Whalley recalls Deary telling him at the time.

Although a handful of longitudinal aging studies can look back to IQ tests or other records of cognitive ability from age 19 to 22 or so, "it's very rare that we have any information about the cognitive abilities of these people at earlier ages," notes Timothy Salthouse, a psychologist at the University of Virginia in Charlottesville.

Deary was well-suited to exploiting the trove of documents, having spent decades studying the cognitive and biological basis of differences in people's intelligence. He also had a personal connection to the study: His uncle, Richard Deary, had participated in the 1932 Scottish Mental Survey, but died in World War II at age 21, when his submarine struck a mine in the Mediterranean Sea.

After unearthing the national survey data, Deary and colleagues received U.K. charitable and government funding to launch their new study of the participants. Financial realities made it impractical to recontact all the survivors of the roughly 160,000 children who took the Scottish Mental Surveys in 1932 and 1947, but for one representative sample they reached out to the nearly 5000 who lived in the Lothian region near Edinburgh.

As participants rolled in, ultimately numbering 1641 from the two cohorts, they were retested on the original assessment used in the Scottish Mental Survey—a measure of IQ that has proven to be reliable and well-validated in both childhood and older age, Deary says. The researchers also administered a range of other cognitive and physical tests and took DNA samples, hoping to detect genetic variations that would help explain differences in how the participants' mental abilities were changing with time. In 2005, Deary's research group "upped their game," he says, after persuading the Age UK research charity to fund "The Disconnected Mind," an effort to perform MRI scanning studies on 1000 of the Lothian participants. (Unlike many aging studies, the Edinburgh team has no guaranteed funding, so Deary says he must find new

The great divergence

How Lothian study participants fared with age on the Scottish Mental Survey test; at age 11, all scores are set to zero, while gains or losses at age 70 are from the mean score of the group.

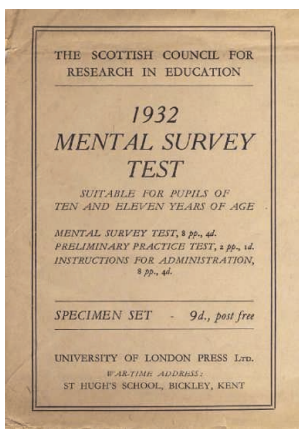
THE SCOTTISH COUNCIL FOR RESEARCH IN EDUCATION

1932 MENTAL SURVEY TEST

SUITABLE FOR PUPILS OF TEN AND ELEVEN YEARS OF AGE

MENTAL SURVEY TEST, 8 pp., 4d.
PRELIMINARY PRACTICE TEST, 2 pp., 1d.
INSTRUCTIONS FOR ADMINISTRATION, 8 pp., 4d.

SPECIMEN SET - 9d., post free

UNIVERSITY OF LONDON PRESS Ltd.
WARTIME ADDRESS:
ST HUGH'S SCHOOL, BICKLEY, KENT

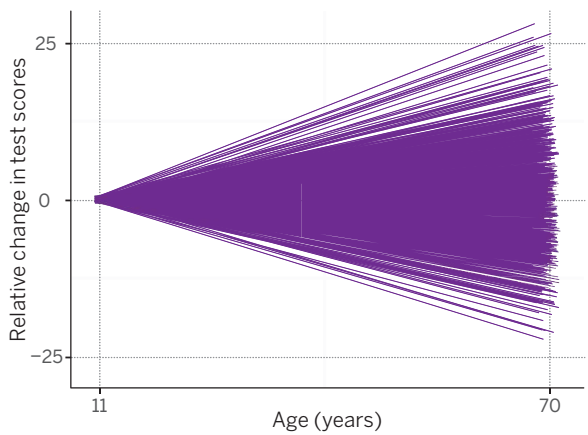

CREDITS: (PHOTO) IAN DEARY; (GRAPH) STUART RITCHIE AND IAN DEARY

sources for each wave of data collection. "It takes up a lot of my time.")

So far, the work has supported a clear conclusion: A large part of participants' differences in cognitive ability during these senior years, as measured in relation to their peers, depends on where they stood at 11. The participants' scores at age 11 can predict about 50% of the variance in their IQs at age 77, Deary and his colleagues estimate.

A few studies elsewhere have also demonstrated the importance of early cognitive ability to maintaining one's faculties with age, says Paul Thompson, a neuroscientist at the University of Southern California (USC) in Los Angeles. In the Nun Study of Aging and Alzheimer's Disease at the University of Minnesota, for example, researchers examined autobiographical essays written by Roman Catholic sisters at the time of induction at about age 22. They found that the linguistic complexity in the writing was a strong indicator of how the nuns would fare in later life. Compared with nuns whose essays "looked like Cicero, with wonderful, florid prose," nuns whose writing was laconic and brief were substantially more likely to have poor cognitive function and Alzheimer's disease 58 years later, Thompson says.

By having an intelligence measure from even earlier in life, the Lothian studies are helping distinguish glitter from gold in the vast literature on factors correlated with cognition. A good recent example is Deary's analysis of the potential benefits of drinking, Thompson says. A smattering of correlational studies suggest that drinking small amounts of wine has positive effects on cognition late in life—indeed, Deary initially found a similar result when he first looked for a relationship between alcohol consumption and cognitive performance in the Lothian cohort. When he accounted for the participants' IQ scores on the Scottish Mental Survey, however, the perceived benefit dissolved. Rather than gaining cognitive benefit from drinking wine when they were older, "people who drank more were already likely to be smart," Deary says.

The Lothian cohort has similarly challenged other reported influences on cognition, such as diet, body mass index, and caffeine consumption. None of those factors seems to have any effect on cognitive skills in the Lothian cohort when childhood intelligence is accounted for, Deary says. Even the effects of social and intellectual activity disappeared when he took into account how bright children were at age 11, possibly because those children are more likely to end up being socially and intellectually engaged.

Deary's work is "very elegant," says Pamela Greenwood, a psychologist at George Mason University in Fairfax, Virginia, but she cautions that it does not mean mental function in old age is foreordained, with no hope for interventions that can help boost or preserve one's brainpower. Although it's still early days for research into cognitive training, Greenwood says there is growing evidence that activities that improve specific abilities, such as the ability to control attention, may have practical benefits for reasoning and problem-solving.

Indeed, although childhood IQ may be the largest factor in late-life intelligence, the Lothian study suggests it accounts for just half the variation—which means that other factors must account for the remaining 50%. Regardless of how smart they were as children, people in the Lothian cohort who did not smoke, were physically fit, bilingual, or had more education enjoyed slightly better cognitive test scores in old age than their early life scores would have predicted, he says. And Deary is convinced that other factors, both genetic and environmental, must also play a role in explaining how some people whose intelligence ranked quite low as children made impressive strides as adults, while others "start out at a high level, and end up quite low."

THIS SPRING, WHEN DEARY SPOKE to the study participants under the Assembly Hall's vaulted ceilings, he began by teasing them. Gazing out over a sea of white hair and wool cardigans, he said, "I've decided to mix it up today, and pit the 1921s against the 1936s." The two groups looked around the auditorium, trying to determine who belonged in which group. Few of the 550 people who took the Scottish Mental Survey in 1932 and enrolled in the study more than 60 years later were present—they are now 93 years old—but the attendance of 78-year-olds from the larger 1947 test cohort was more robust. "You can't tell who is who, can you?" Deary joked.

He shared the good news first. Over the past decade of testing, both cohorts had held up well on tests of memory and knowledge, such as remembering a paragraph-long story and pronouncing words, though likely in part because of their growing familiarity with the test, Deary says. In skills that required abstract problem-solving, fast thinking, and speedy reaction times, however, all groups showed some decline with age from results in previous years. A task that required a person to quickly discriminate between two lines of different lengths as they flashed on a screen was particularly challenging for all the participants and elicited a widespread

After taking an intelligence exam at age 11, Margaret Lawson is now among the 1641 Scots being studied for clues to how the brain ages.

PHOTOS: (LEFT TO RIGHT) KAREN KASMAUSKI; THE WELLCOME LIBRARY

Tracking healthy aging

Other studies of aging have taken various approaches to tracking cognitive change.

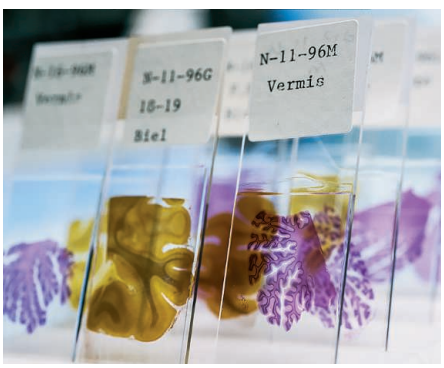

THE NUN STUDY 1986
Archived autobiographical essays written when women joined an order of Catholic nuns at age 22 provide an early cognitive measure for this long-term study. Many of the 600 sisters have agreed to donate their brains to research (above) after death.

SWEDISH ADOPTION/TWIN STUDY OF AGING 1984
Like several other twin studies worldwide, this study of more than 2000 identical and nonidentical twins reared in separate homes looks at the role of genes versus environment in cognitive decline.

OKINAWA CENTENARIAN STUDY 1976
In the world's longest running study of centenarians, including more than 900 people, researchers look for both genetic and lifestyle contributors to the unusual longevity and lucidity of the residents of Okinawa, Japan.

BALTIMORE LONGITUDINAL STUDY OF AGING 1958
More than 1000 healthy people between 20 and 60 years old are now enrolled in this study of aging over the past half-century, returning to Baltimore every 2 years for cognitive and physical tests.

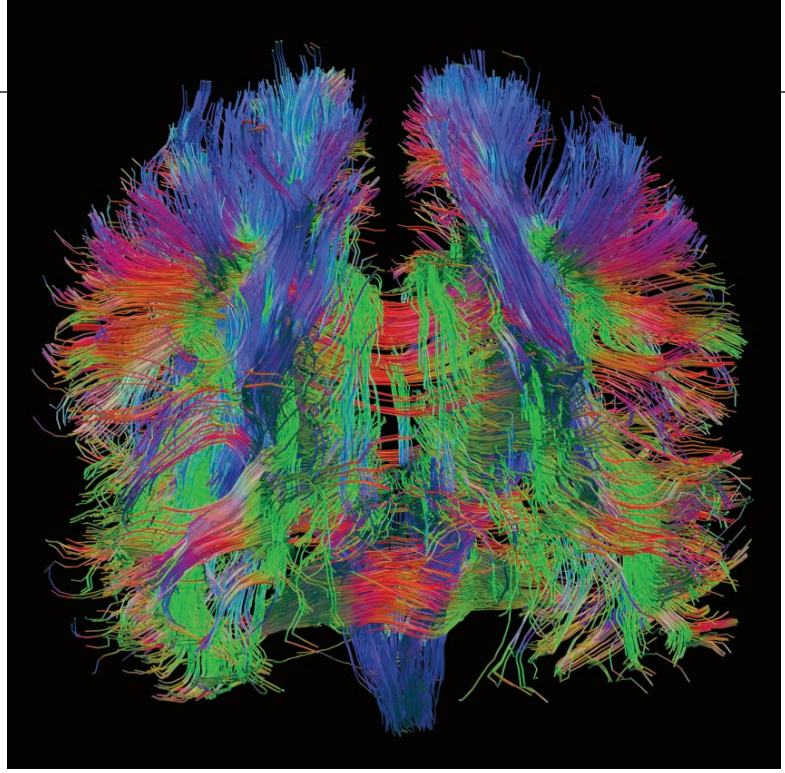

Maps of white matter connections in the Lothian cohorts, such as this one, of a 73-year-old participant, suggest that better neuronal wiring in old age is linked to higher cognitive function.

groan when Deary named it. That all participants seem to be struggling at this task suggests age may take a particular toll on the ability to quickly and efficiently sample sensory information, says Stuart Ritchie, one of Deary's postdoctoral students. "A fascinating thing is that decline in this simple sensory speed measure tracks decline in complex thinking skills as the cohort ages," Deary says.

Although the averages of the Lothian cohort reveal intriguing trends, Deary's true passion is for the study of individual divergence. He flipped to a slide that displayed how the cohorts' test scores on all the tests had fanned out as people hit their 70s and 80s, with many straying far from the average. "What I'm trying to do with my colleagues is study why the mean does not tell you the full story," he told the elderly Scots.

Brain scans of these volunteers show that aging takes a vastly different toll on each person, notes Joanna Wardlaw, a neuroradiologist at the University of Edinburgh who collaborates with Deary. Using a technique called diffusion tensor imaging, which tracks how water molecules move throughout the brain's white matter tracts, Wardlaw and colleagues have found that roughly 10% of the differences in general cognitive function in the Lothian participants depends on the integrity of neuronal connections.

Certain blotchy patches of abnormal white matter, called hyperintensities, are known to signal damage to blood vessels, surrounding cells, and the connections between neurons. The hyperintensities generally increase with age but can vary drastically from person to person, Wardlaw says. An important goal of the Lothian study is to determine how hyperintensities interfere with cognition, and why some people seem to be more susceptible to them, whereas for others they seem to represent harmless "wrinkles" on the brain—the neural equivalent of crow's-feet or frown lines, she adds. What causes hyperintensities is still poorly understood, but research from the Lothian cohort and other groups suggests that they are "pretty tightly linked" to high levels of cortisol, a hormone released in response to stress, USC's Thompson notes.

Why the cerebral cortex tends to shrink in normal aging is another mystery that scans from the Lothian cohort may help unravel, says Sherif Karama, a psychiatrist at McGill University in Montreal, Canada. People with Alzheimer's disease have an undeniable thinning of the cerebral cortex, but this region, which is involved in nearly all the brain's higher level cognitive processes, such as thinking and decision-making, shrinks in "normal" aging, too, he explains. Historically, scientists have assumed that when healthy older people complained of cognitive deficits, their cortex shrinkage was to blame, or at least reflected a neurodegenerative process, he says. But earlier this year, Karama used Lothian data to show that the people with a relatively thinner cortex in old age also had a lower IQ both as adults and in childhood. That suggests, he says, that those who appear to be losing brain mass along with their cognitive abilities may simply have started out with less gray matter. Deary and colleagues have recently begun collecting the donated brains of Lothian participants after they die, in order to further explore structural and anatomical differences that might explain why some people age better than others.

Toward the end of his presentation this April, Deary unfolded a slip of paper and read a question about aging submitted by the audience: "So, are you just lucky or unlucky with the brain you've got?" it asked.

At least for now, "the short answer to that question appears to be 'yes,' " says Nicholas Martin, a geneticist at QIMR Berghofer Medical Research Institute in Herston, Australia, who is not involved in the studies. He says the growing body of data from the Lothian Birth Cohort studies and other aging research supports a theory that some describe irreverently, and a little brutally, as the "water tank hypothesis": The better put-together your brain is early on, thanks to good genes and, to some extent, a favorable early life environment, the more cognitive reserves you have to lose to neurodegeneration. In other words, Martin says, "the more you start out with in the tank, the longer it takes to draw down."

Pinpointing the genes that determine how full the tank is and how fast it empties will take studies much larger than Deary's. Neuroscientists and geneticists "have learned the hard way," Thompson notes, that hundreds of thousands of DNA samples are required to make even minor inroads toward identifying how different genetic variants affect the brain and how such variants interact with environment to affect behavior.

In 2009, the Lothian studies took a first step, joining a consortium of 70 separate institutions in 33 countries called ENIGMA, which seeks to ramp up the search for genetic variants that affect the brain. With access to brain scans and DNA from hundreds of thousands of people from regions as diverse as Brazil, the United States, Cambodia, and Siberia, researchers are already finding clusters of genes that play a role in notoriously complex disorders such as schizophrenia, says Thompson, who this month received an $11 million grant from the U.S. National Institutes of Health to establish a Center of Excellence for the ENIGMA project at USC. The same approach may also help untangle the genetic factors that affect cognitive aging—for example, why some people's brains age faster than others when exposed to high levels of stress hormones, he adds.

Sheila McGowan, for her part, has taken Deary's study as a call to action to make the best of her aging brain. A longtime art lover, she has taken up painting again and hopes to exhibit her work one day. At age 75, after joining the Lothian cohort, she began taking online university courses focused on philosophy and art history. Confronting the reality of her own aging brain "catapulted me out of my lethargy—I'm trying to buck the change," she says. ■

IMAGE: MARK BASTIN AND DAVE LIEWALD, BRAIN RESEARCH IMAGING CENTRE, UNIVERSITY OF EDINBURGH

REVIEW

Human cognitive aging: *Corriger la fortune?*

Ulman Lindenberger[1,2]

Human cognitive aging differs between and is malleable within individuals. In the absence of a strong genetic program, it is open to a host of hazards, such as vascular conditions, metabolic syndrome, and chronic stress, but also open to protective and enhancing factors, such as experience-dependent cognitive plasticity. Longitudinal studies suggest that leading an intellectually challenging, physically active, and socially engaged life may mitigate losses and consolidate gains. Interventions help to identify contexts and mechanisms of successful cognitive aging and give science and society a hint about what would be possible if conditions were different.

Around the world, the older segment of the adult population is increasing in size, proportion, or both. Advances in medicine and public health measures, rising standards of living, and improvements in education and nutrition have lengthened the human life span. Demographic evidence suggests that the debilitating effects of senescence are not being stretched out in time but delayed to later ages (*1*). Cognitive development in adulthood and old age follows a similar pattern. Longitudinal studies show that the onset of average decline in cognitive abilities occurs at considerably later ages than suggested by cross-sectional studies, which confound effects of age and birth cohort (*2*, *3*).

Comparisons across countries and of birth cohorts within countries (*1*), coupled with findings from cognitive neuroscience (*4*, *5*) and developmental psychology (*6*), indicate that adult cognitive development is variable across and malleable within persons (*7*). Evolutionary theories propose that human senescence reflects evolved limitations in somatic maintenance, resulting in a buildup of damage (*8*). In the absence of programmed aging, modifiers and modulators come to the fore, and individual differences abound. Hence, the shape and course of adult cognitive development is best conceived as a range of potential developmental trajectories that reflect person-specific endowments and environmental opportunities and constraints (*7*, *9*) (Fig. 1). Actual paths through life are sampled from this range and depend, in part, on the choices that people make. Readers hoping to reach a ripe old age with grace inevitably ask the question, what will become of their own cognitive abilities and what can be done to maintain them. Leading an intellectually challenging, physically active, and socially engaged life bodes well for enhanced cognitive stability and growth and may serve as a hedge against cognitive decline (*7*). However, invoking the impression that cognitive aging is under personal control would be just as wrong as claiming that its course cannot be altered, to some extent, through experience and goal-directed action. Life-span development is inherently probabilistic (*10*, *11*), and the range of potentially available developmental trajectories is likely to differ from person to person (*12*).

Neuroscience and, in particular, neuroepigenetics offer mechanistic explanations for the influence of common genetic variation, environmental conditions, and lifestyles on adult cognitive development. Multiple factors associated with vascular and metabolic risk, inflammation, stress, and deposition of iron and beta-amyloid accelerate brain aging (*7*, *13*). At the same time, the continued potential for neuroplasticity helps to maintain the viability of neural structures and postpone the onset of cognitive decline (*7*, *9*, *14*, *15*). Epigenetics has begun to identify mechanisms through which earlier experiences influence genome expression, which affects later development (*16*). Animal models have been proposed to capture the path dependency of cognitive development (*10*).

In the following, key features of human cognitive aging will be summarized from the combined perspectives of life-span psychology and the cognitive neuroscience of aging.

Fluid and crystallized cognitive abilities

Mechanisms related to maturation and senescence shape the course of cognitive development from conception to old age (*6*). In adulthood and old age, human brains show increasing marks of aging. At the same time, they accumulate knowledge about the world and continue to express potential for new learning. The life-span trajectories of cognitive abilities reflect dynamic equilibria of these interacting forces and form the empirical basis of two-component theories of intellectual development (*17*). Such theories distinguish between experience-based "crystallized" abilities, such as vocabulary, and "fluid" abilities that are less supported by acquired knowledge, such as reasoning and working memory, but are helpful in acquiring that knowledge in the first place.

As a summary observation, the ages at which cognitive skills reach their peak are likely to reflect a balance among competing processes of knowledge accumulation and deterioration of the supporting neural infrastructure. For instance, in correspondence chess tournaments, where players have 3 days to make each move, players achieve the title of world correspondence champion at a mean age of 46, which is about 10 years later than the mean age for becoming the world chess champion at tournaments, where players have an average of 3 min or less to make a move (*18*).

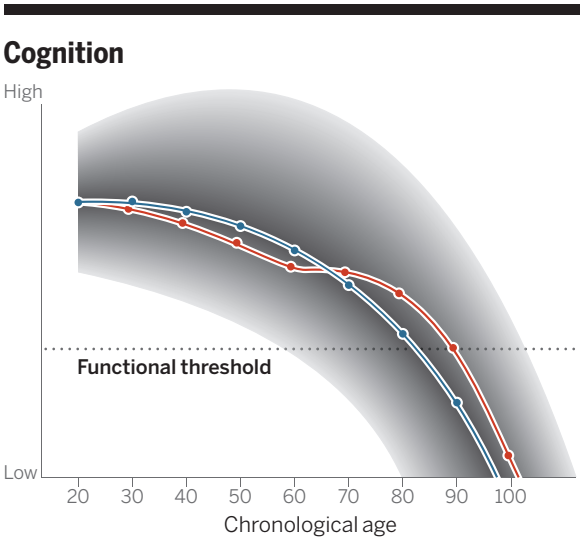

Fig. 1. An individual's range of possible cognitive developmental trajectories from early to late adulthood. The blue curve shows the most likely developmental path under normal circumstances. The fading of the background color indicates that more extreme paths are less likely. The functional threshold represents a level of functioning below which goal-directed action in the individual's ecology will be severely compromised. The red curve represents the hope that changes in organism-environment interactions during adulthood move the individual onto a more positive trajectory. Beneficial changes may consist in the mitigation of risk factors, such as vascular conditions, metabolic syndrome, or chronic stress; the strengthening of enhancing factors, such as neuroplasticity; or both. [Modified from (*7*)]

The senescent brain

A plethora of correlated processes contribute to human brain senescence, resulting in decreasing differentiation and integration of brain function and behavior (*19*, *20*). Senescence cumulatively affects the neurochemistry and anatomy of the human brain (*13*). Many neurotransmitters show marked age-related differences in concentration and receptor density. Dopaminergic

[1]Center for Lifespan Psychology, Max Planck Institute for Human Development, Lentzeallee 94, 14195 Berlin, Germany. [2]Max Planck University College London Centre for Computational Psychiatry and Ageing Research, London WC1B 5EH, UK. **E-mail: seklindenberger@mpib-berlin.mpg.de**

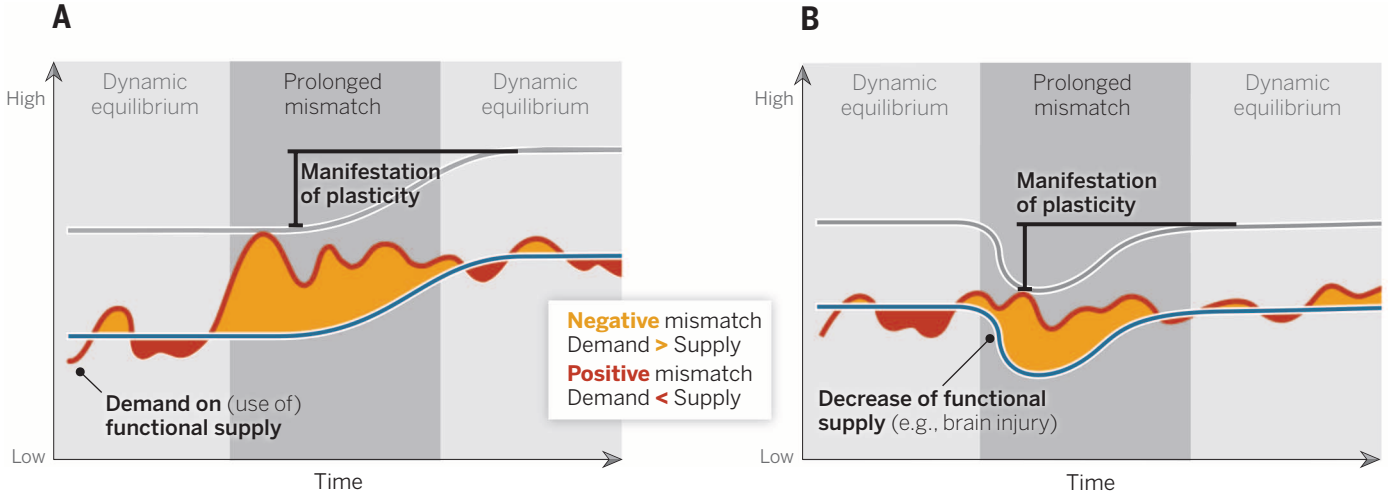

Fig. 2. The supply-demand mismatch model of adult cognitive plasticity. The mismatch between functional supply and experienced environmental demands can be caused by primary changes in demand (**A**) or functional supply (**B**). Functional supply denotes structural constraints imposed by the brain on function and performance, and permits a given range of performance and functioning. Flexibility denotes the capacity to optimize the brain's performance within this range. Deviations in functional demand that are within the available range of functional supply constitute the impetus for plasticity. Mismatches between supply and demand need to be prolonged to overcome the inertia and sluggishness of plasticity and to push the system away from its current dynamic equilibrium. [Adapted from (9)]

neuromodulation has received particular attention (*21*–*23*). Originating in the midbrain, dopamine neurons reach various subcortical and cortical regions. Positron emission tomography and single-photon emission computed tomography show a pronounced age-related decrease in dopaminergic neuromodulation in healthy older adults. Converging evidence from patient studies, animal research, pharmacological intervention, and molecular genetics indicates that dopamine plays a critical role in cognitive functioning (*21*, *22*). Longitudinal work (*24*) is needed to better understand the correlative triad among adult age, dopamine, and cognition (*22*).

Postmortem studies document age-related differences in various morphological aspects of the brain, such as reduced size and weight, expansion of cerebral ventricles and sulci, deformation and loss of myelin sheathing, region-specific loss of dendritic arborization and neuronal bodies, rarefication of cerebral vasculature, and reduced synaptic density (*13*). Magnetic resonance imaging (MRI) permits the study of age differences and age changes in vivo, yielding indicators of gray and white matter volume and integrity, neural activity, and metabolites. Increasing adult age is associated with markedly smaller volumes of gray and white matter. Polymodal cortical regions display greater volume reductions than other neocortical areas, whereas primary visual cortices show relatively little volume loss (*25*, *26*). Cross-sectional age trends are less clear for hippocampal volume, with some but not all studies suggesting accelerating shrinkage with advancing age. This inconsistency in results is likely to reflect sample differences in the admixture of preclinical pathology and the extent to which positive selection correlates with age. Longitudinal studies, which permit the efficient and unbiased assessment of change and of individual differences in change, report that hippocampal shrinkage accelerates with age and is exacerbated by vascular factors (*25*).

Diffusion tensor imaging (DTI) and T2-weighted (spin-spin relaxation) MRI imaging are increasingly used to study age changes and differences in the integrity of white matter. White matter hyperintensities, which reflect ischemic lesions, microbleeds, demyelination, and expansion of perivascular spaces, increase from middle to late adulthood and show associations with vascular risk and genetic variants related to inflammation (*27*). DTI indices point to decreasing white matter integrity with advancing adult age (*28*, *29*). The same holds true for life-span differences and changes in white matter volumes, which may reflect either the pruning of cortical connections in the course of maturational or experience-dependent plasticity, or alterations due to senescence and pathology.

Animal models help to identify mechanisms of age-related cognitive decline at the cellular level. In nonhuman primates, the degeneration of thin synaptic spines in dorsolateral prefrontal cortex, as well as synaptic alterations in the dentate gyrus of the hippocampus, contribute to age-related losses in memory (*30*). Rodent models indicate that normal aging alters excitatory synaptic transmission in hippocampal granule cells and in CA3 and CA1 pyramidal cells (*31*).

Individual differences in change

The extent of age-related differences and changes in brain and behavior varies markedly across individuals. The brains of adults differ reliably in the onset and degree of age-related volume losses. Lateral prefrontal cortex, prefrontal white matter, and the hippocampus are among the regions that show particularly large individual differences in age-related shrinkage (*25*). Rates of shrinkage are increased by risk factors such as treated hypertension and metabolic syndrome (*25*, *32*). The adverse effects of vascular and metabolic factors on brain health are not confined to individuals with a diagnosis of cardiovascular disease or diabetes. Instead, these risks operate well within the healthy range of functioning (*33*).

Adults who maintain high levels of general cognitive ability into very old age stand in sharp contrast to age peers whose cognitive resources are waning or depleted by later adulthood. Longitudinal studies reveal that individual differences in cognitive performance increase from early to late adulthood and old age (*34*, *35*). Both genetic and environmental factors contribute to individual differences in change (*36*, *37*). To some extent, the age-related increase in heterogeneity is absorbed by age-related increments in the prevalence of pathological conditions such as dementia (*38*). The remaining, ever more positively selected individuals who qualify as "generally healthy" or "normal" represent a continuously decreasing proportion of the aging population (*39*). But even within this positively selected segment, individual differences in various aspects of brain and behavior increase with advancing age.

Attempts to establish the dimensionality of cognitive aging help identify environmental, epigenetic, and genetic factors that impair or promote cognition in old age. If age-related changes are indeed correlated across different cognitive abilities, searching for factors with generalized effects on cognitive functioning seems worthwhile. Cross-sectional studies are inadequate for uncovering the covariance dynamics of change (*40*, *41*). Multivariate longitudinal panel studies are more informative because they allow researchers to examine whether between-person differences in age-related change are correlated across different aspects of brain and behavior. At the anatomical level, studies reporting such covariance information are rare. One study found that shrinkage of prefrontal white matter correlated with shrinkage of lateral prefrontal cortex (r = 0.71)

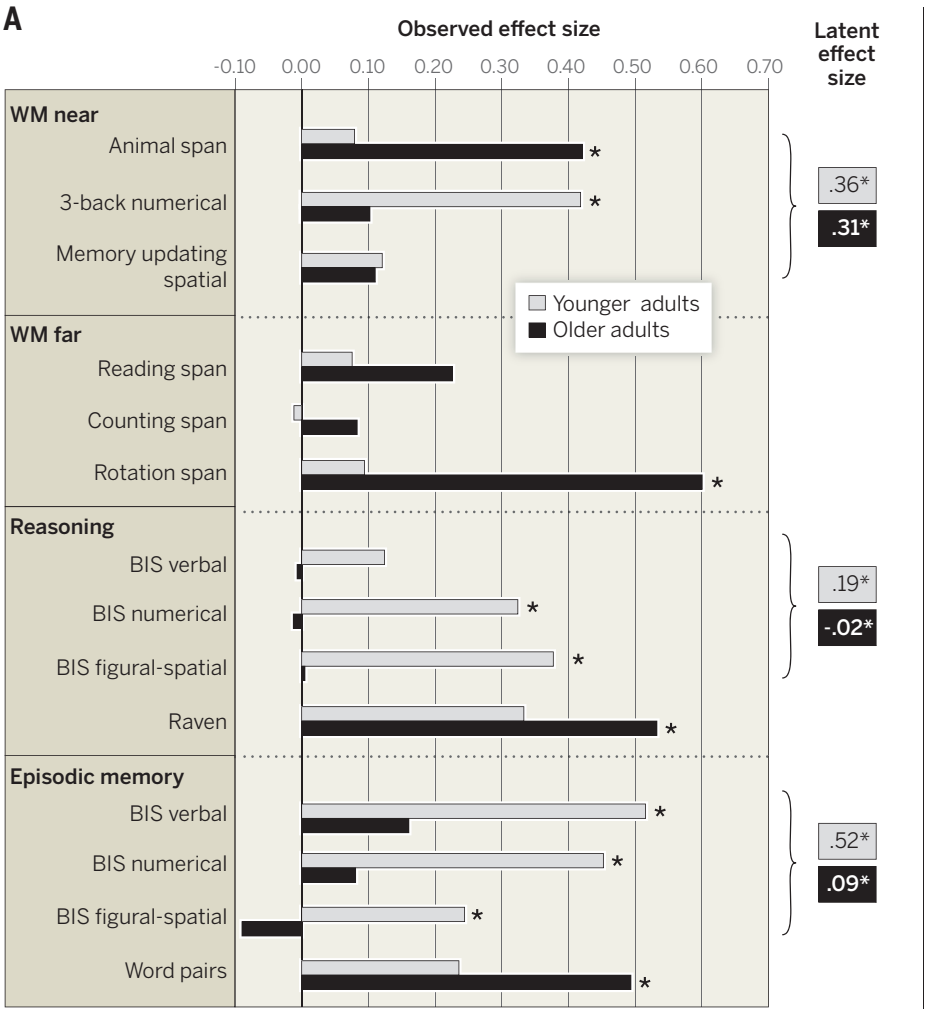

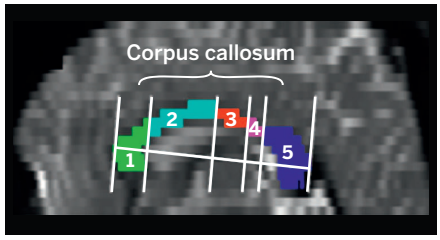

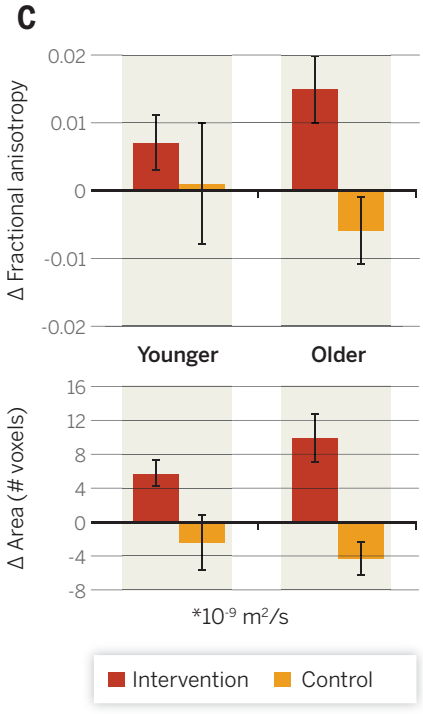

and with shrinkage of hippocampal volumes (r = 0.70), indicating that volume losses in the frontal lobes and in medial-temporal cortex are interdependent (*25*). Such structural interdependencies are in good agreement with studies showing that deficits in both prefrontal and hippocampal activation patterns contribute interactively to adult age differences in associative episodic memory (*42*).

Behaviorally, several longitudinal studies show that human cognitive aging has a strong general component. One study analyzed 20-year longitudinal data of 6203 middle-aged to very old adults (*43*). Participants were assessed up to eight times on 20 tasks of fluid intelligence, perceptual speed, memory, and vocabulary. Notably, 66% of the variance in cognitive change was shared across tasks. In another study, 39% of individual differences in change were shared across all tasks, and 33% were shared at the level of general cognitive abilities (*44*).

These findings support an early plea by Salthouse (*45*) to overcome "issue isolationism" and search for age-related mechanisms with general effects on adult cognition. Promising candidate mechanisms with some degree of empirical support are decrements in dopamine availability in striatal and cortical brain regions (*21*–*23*); anatomical changes in medial-temporal (*46*) and prefrontal (*47*) areas; structural and functional connectivity decrements due to white matter alteration (*27*, *48*, *49*); a compromised dynamic range of neural activation (*50*); and deficient synchronization of oscillatory activity within and across fast and slow frequencies (*51*). The lead-lag relations and reciprocal interdependencies among these and additional putative drivers of age-related declines in adult cognition are largely unknown. This lack of knowledge about the cascade of events associated with maintained or impaired cognition in late life points to the dire need for launching and sustaining multivariate longitudinal studies with a comprehensive range of ages, imaging techniques, and behavioral assessments (*52*, *53*).

There are reliable associations of individual differences in cognition at 11 years of age with late-life individual differences in cognition (*54*), brain status (*55*), and somatic health (*56*). Individuals with lower cognitive abilities are more likely to engage in behaviors that carry risks for late-life cognition, such as smoking (*57*). Also, the genetic contributions to individual differences in cognition overlap with those observed for socioeconomic status and education (*58*, *59*), underscoring the inadequacy of making unidirectional causal attributions on the basis of cross-sectional or short-term longitudinal data.

Although specific genetic variants play only a modest role in determining how long individuals live (*60*), they may influence age-related differences in cognition. The effects of common genetic polymorphisms on cognition are expected to increase with advancing adult age if the function that relates brain resources to behavior is assumed to be sigmoid rather than linear (*61*). Larger effects on episodic memory performance in samples of older adults than in samples of younger adults have been observed for variants in the brain-derived neurotrophic factor (BDNF) gene (*62*), the dopamine D2 receptor and transporter genes (*63*), and the dopamine and glutamate receptor genes (*64*). Similar effects on forgetting rates have been observed for D2 and D3 receptor genes and the DA transporter gene (*65*) and on response inhibition for dopamine D2 receptor genes (*66*). These results are consistent with the long-standing observation that broad heritability increases from early to late adulthood (*67*). However, the observed associations between variations at specific gene loci and individual differences in cognition are small, and causal accounts of the heritability of complex behavioral traits are "still

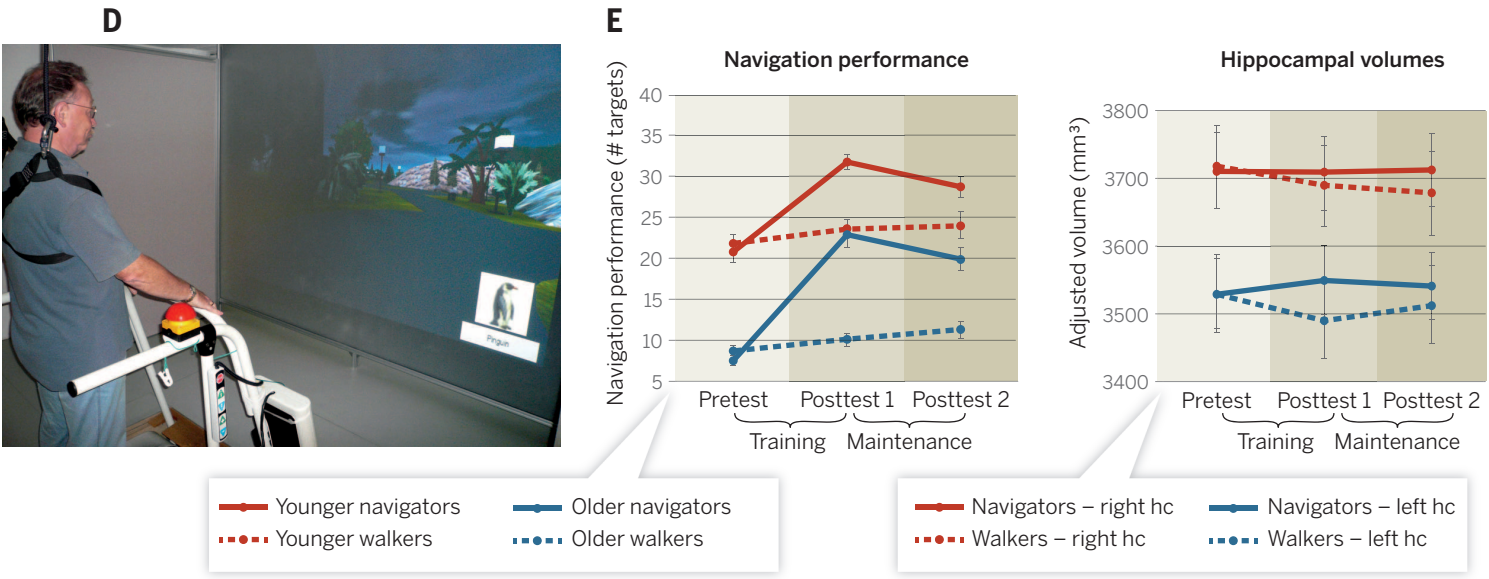

Fig. 3. Experience-dependent cognitive plasticity subsists into later adulthood. (**A** to **C**) In the COGITO study (*76*), 101 younger and 103 older adults practiced six tests of perceptual speed, three tests of working memory, and three tests of episodic memory over a period of 6 months for 101 daily 1-hour sessions. Transfer effects were assessed with unpracticed cognitive tests administered before and after training. (A) Effect sizes (ES) (standardized changes in the experimental group minus standardized changes in the control group), separately for younger adults (gray bars) and older adults (black bars). Statistically significant ES correspond to reliable interactions (*$p < 0.05$) between group (experimental versus control) and occasion (pretest versus posttest). Observed ES refer to individual tests, latent ES to cognitive abilities estimated with structural equation modeling. At the level of cognitive abilities, younger and older adults show transfer of training to working memory (WM); in addition, younger adults also show transfer to reasoning and episodic memory. (B) A midsagittal slice of a mean diffusivity data set, with the corpus callosum segmented into five different regions. The first region refers to the genu, which connects the prefrontal cortices. (C) Changes in fractional anisotropy and area of the genu assessed in subsamples of younger and older COGITO participants. Changes differ reliably between intervention and control groups but not by adult age (*78*). (**D** and **E**) In the SPACE study (*80*), healthy younger and older men performed a cognitively demanding spatial navigation task every other day over 4 months. The training group navigated in a virtual environment while walking on an exercise treadmill (D); a walk-time-yoked control group walked on a treadmill without the virtual environment. (E) Navigators show navigation-related gains in performance (middle panel) and stable hippocampal (hc) volumes that are maintained 4 months after termination of training (right panel). Error bars, mean ± SEM. Control groups show volume decrements in line with longitudinal estimates of age-related decline.

missing" (*68*). Cognitive abilities and their associated endophenotypes are highly polygenic; given the multitude of interactions among genes and environments, and the path-dependent nature of epigenetic effects, this renders it unlikely that individual allelic variations will account for a sizeable portion of phenotypic variance.

Experience-dependent plasticity in adulthood

Experience-dependent plasticity of brain and behavior subsists into late adulthood (*15*). Adults respond to a variety of challenges with structural changes in task-relevant brain areas. Similarly, physical exercise programs induce plasticity at neural and behavioral levels of analysis, effects that tend to be more pronounced among older sedentary adults, and presumably reflect the attenuation of vascular and metabolic risk factors (*69*).

According to one model (*9*), plastic changes are elicited by a mismatch between environmental demand and organismic supply, provided that the organism possesses the potential for a plastic response. The central tenet of this model is the distinction between plasticity and flexibility. Whereas flexibility refers to the capacity for variations in behavioral repertoire that do not require reorganization of brain structures and connections, plasticity refers to changes in behavior that do. Mismatches between supply and demand need to be prolonged to overcome the inertia and sluggishness of plasticity and to push the system away from its current dynamic equilibrium (Fig. 2).

Older brains accumulate an increasingly large behavioral repertoire, and plastic reorganization of the brain is metabolically costly (*30*, *70*). Presumably for both of these reasons, the brains of healthy older adults are less likely, and may have less need, to react to environmental challenges with a plastic response than the brains of children and adolescents. In other words, older adults have a richer model of the world that enables deployment of established behavioral repertoires. Down-regulating plasticity during adulthood may favor the emergence of stable social structures, which in turn may facilitate the deployment of plastic potential in the next generation [for a related but distinct line of reasoning, see (*71*)].

Are adult plastic changes elicited by intervention studies sufficiently large and persistent to improve cognitive competence in everyday life? One indicator of practical relevance is transfer of training: Does improvement on the trained tasks generalize to untrained tasks that tap into the same cognitive ability or to tasks measuring affiliated cognitive abilities? The experimental design and statistical analysis procedures of most intervention studies to date are not well suited to answer this question (*72*). The most common threat to validity concerns the distinction between task-specific effects and improvements at the ability level. Positive transfer to multiple indicators of a given cognitive ability is a necessary condition for claiming that the intervention has led to improvements at that level. Latent factor models (*73*) are an effective method for estimating intervention-induced changes at the ability level and for comparing observed transfer gradients with theoretical predictions (*74*–*76*).

In one exceptionally extensive intervention study (Fig. 3), transfer of training to cognitive abilities was observed, but transfer effects were reduced in scope (*76*) and maintenance (*77*) in older relative to younger adults. In both younger and older adults, the intervention was associated with improved white matter integrity in the anterior part of the corpus callosum (*78*) and reduced age-related shrinkage in the cerebellum (*79*). In another study (Fig. 3), 4 months of spatial navigation training protected the hippocampus against age-related shrinkage (*80*), both in younger

and older adults. However, training-related cortical thickening in the left precuneus and paracentral lobule was observed in younger adults alone (*81*). These results provide some reason to hope that cognitive interventions may ameliorate the course of cognitive aging but also suggest that plasticity decreases from early to late adulthood.

The increasing importance of environmental support

Thirty years ago, Craik *et al.* (*82*) placed findings on adult age differences in memory on a continuum ranging from self-initiated processing to environmental support. Memory performance is particularly impaired when retrieval depends on self-generated cues and active control processes. By contrast, when retrieval cues (e.g., hints, reminders, and contextual reinstatement) are provided by the environment, age-related deficits decrease or disappear altogether. Accordingly, the effect sizes of the performance advantage of younger over older adults are large for free recall, moderate for recognition memory, and small for associative and item priming (*83*).

Self-initiated processing and constructive cue generation require maintenance of task representations through recurrent connections between prefrontal and more posterior brain regions (*84*). The ability to hold task representations in mind declines with age (*85*), as reflected by impairments in a variety of cognitive functions such as attention, working memory, and executive control (*86*, *87*). We recently proposed that the resulting greater reliance on environmental control is not confined to memory but forms a general developmental trend (*88*). In perception, learning and remembering, and action management, older adults tend to rely more on external information than younger adults do, probably both as a direct reflection and indirect adaptation to difficulties in internally triggering and maintaining cognitive representations.

If greater reliance on the environment were always a direct reflection of weakened internal representations, the performance of older adults would suffer as soon as environmental support is eliminated. This is not always the case—removal of environmental sources of information may sometimes even benefit the performance of older adults (*89*, *90*). Such findings are inconsistent with the notion that increasing environmental control is a direct mirror image of waning internal control. Rather, the greater reliance of older adults on the environment may reflect a long-term adaptation to a cognitive system that is generally—but not necessarily in every specific instance—less capable of directing behavior in a top-down, internally regulated manner (*5*, *91*). There is thus a certain amount of slack between deficits in self-initiated processing and reliance on environmental support, such that aging individuals remain capable, in some situations at least, of reducing their degree of reliance on the environment when they need to do so. Therefore, direct and indirect pathways from the waning of top-down control to a greater reliance on environmental support likely coexist, but little is known about their relative importance and developmental interdependence.

When they have reached old age, individuals have acquired a relatively stable behavioral repertoire that is likely to match the regularities and affordances of the environments in which they live. The tendency of older adults, both automatic and deliberate, to outsource control to the environment may be inefficient at times but cost-effective in the long run if the cuing structure of the environment corresponds to their goals and needs.

Mechanisms of successful cognitive aging

Cognitive aging is highly individualized, and information based on between-person differences or averages may misrepresent the individual aging process to some degree (*92*, *93*). Hence, attempts at promoting successful cognitive aging (*94*) should also be directed toward the physical and social environment of the aging individual. In particular, assistive adaptive technology (*95*) provides individuals with cuing structures that connect properties of the environment to their personal action goals. However, both risks and opportunities need to be kept in mind. Chronic reliance on technological aids may deplete brain resources through disuse of skills and abilities, undermine motivation, and engender loss of autonomy. Conversely, assistive adaptive technology may foster cognitive maintenance and plasticity by combining support with challenges, thereby enhancing motivation (*96*), social participation, and a sense of autonomy, with positive repercussions on cognitive development in old age (*7*).

Turning toward aging individuals' brain and behavior, a number of general mechanisms have been linked to more favorable aging trajectories (*4*, *5*, *14*, *52*, *97*–*99*). These mechanisms are not mutually exclusive, and their viability and reciprocal relations remain to be determined. Animal models of individual differences in adult development play an important role in this effort (*10*, *30*, *100*).

Maintenance

As a general observation, older adults with more "youth-like" brain structure and functional brain responses show higher levels of cognitive performance than older adults whose brain structure and function deviates markedly from that of younger adults (*52*, *101*) (Fig. 4). This observation holds true cross-sectionally (*101*–*104*) and longitudinally (*105*). Brains with relatively well preserved anatomy and neurochemistry are more likely to generate functional activation patterns that resemble those of younger adults and that are germane to proficient performance. An important implication is that cognitive interventions should aim at preserving or, at least partially, restoring youth-like brain physiology.

Compensation

High levels of cognitive functioning in old age may reflect instances of successful compensation (*5*, *106*). According to one definition (*107*, *108*), compensation in the context of normal aging refers to structural or functional reorganization of the brain that evolves in response to aging-induced losses in brain functioning. Other than maintenance and restoration, compensation does not consist in preserving or reestablishing the substrate or function that was lost but in creating something alternative in response to a loss. Compared with discrete damaging events, such as a stroke, cerebral senescence is a process without clear boundaries in space and with no clear onset in time. Rather, the gradual loss in functional capacity in normal aging is distributed over many different brain areas, networks, and neurotransmitter systems. Compensatory reactions to normal aging may evolve differently and arguably less often than compensatory reactions to discrete damaging events. Brain circuitry potentially capable of compensating for a loss may itself be particularly vulnerable to normal aging. Compensatory recruitment of the prefrontal cortex may attenuate the adverse effects of aging on other areas of the brain (*4*), given its pivotal role for the organization of behavior (*109*). However, far from being spared by senescence, prefrontal areas and associated corticostriatal circuits show early and precipitous age-related decline (*22*, *25*). Hence, although the frontal lobes are increasingly needed, they are decreasingly able to counteract the adverse consequences of senescence on sensory, perceptual, and motor aspects of behavior (*98*).

Selection

A potentially powerful but rarely considered mechanism in the context of successful brain aging is selection. Younger adults' brains can execute a given task in more than one way (*110*, *111*). Different brain implementations of a given behavior may be differentially vulnerable to aging because some brain areas, circuits, and activation patterns are more resilient than others. More robust brain processing routes and areas with advancing adult age may signal selective survival due to differential robustness rather than compensatory development of alternate functional activation patterns. Individuals with a larger pool of available processing routes in early adulthood may draw on a greater cognitive reserve (*14*) or functional cerebral space (*112*) that provides a modicum of protection against the adverse effects of normal and pathological age-related changes on behavior because it offers a greater choice set for selection.

Multimodal longitudinal and experimental evidence is needed to probe the relative importance of maintenance, compensation, and selection as mechanisms of successful cognitive aging.

Outlook

Cognitive development in adulthood and old age differs substantially from person to person and is malleable within individuals. Maintaining cognitive abilities into old age and postponing or preventing pathologies leading to a diagnosis of dementia late in life are key aims for science and society. Exploring and exploiting the continued potential for cognitive maintenance and plasticity are major means to these ends. In the absence of strong genetic control, the course of human cognitive aging is open to a host of risk and protective or enhancing factors.

Beneficial lifestyle choices may attenuate partially modifiable risks, such as vascular and metabolic conditions, and promote changes that are likely to enhance cognition, such as angiogenesis, synaptogenesis, and neurogenesis. The developmental dependencies between risk and protective factors, and their modulation by behavior, are not well understood. Regions of the brain that are particularly plastic and provide the substrate for new learning and plasticity, such as the hippocampus, are also particularly vulnerable to risk factors such as stress and vascular conditions, suggesting that modifiability comes at a price (*12*, *113*, *114*). Nevertheless, interventions that attenuate the adverse effects of risk factors, such as physical exercise, extensive cognitive interventions (Fig. 3), and intellectually stimulating lifestyles, inspire cautious optimism about mitigating age-related declines (*7*).

Although maturation and senescence operate continuously throughout life, their relative importance and interactions change from childhood to old age. Direct experimental comparisons between children, younger adults, and older adults are particularly informative in this regard, as they point to the ways in which brain-behavior mappings reorganize during ontogeny. For instance, medial-temporal and prefrontal regions of the brain contribute differently to working memory and episodic memory in childhood and old age, presumably because medial-temporal lobe maturation progresses more rapidly than that of the frontal lobes, whereas both regions of the brain show signs of decline with advancing adult age (*115*, *116*).

Research on neuroepigenetics (*16*) is likely to lead to a better understanding of the effects of early life events and choices on adult cognitive development. Animal models of emerging individuality will play a pivotal role in this endeavor (*10*). Combining pharmacological (*117*) and behavioral interventions may reopen "windows of plasticity" in adulthood and old age (*118*). If the relevant molecular mechanisms are function-specific and can be brought under control, they may provide a basis for regulating plasticity in adulthood and old age (*119*).

Advances in understanding how behavior influences brain aging, and how brain aging influences behavior, are facilitated by taking a life-span perspective that conceptually integrates evidence across time scales, age periods, functional domains, and levels of analysis. Neurocomputational models are a powerful tool for theory development, because they bridge the gaps that hinder integration (*23*, *120*) and elucidate the constraints on what the brain can and cannot do. In this context, the connections between short-term variability and long-term change (*121*) deserve special attention, because they point to mechanisms and allow prediction. For instance, lack of processing robustness at an earlier point in time predicts longitudinal cognitive decline in old age (*122*).

To effectively foster cognitive health in old age, we need to better understand the malleable causes of individual differences in human cognitive aging. This requires long-term, multivariate, longitudinal

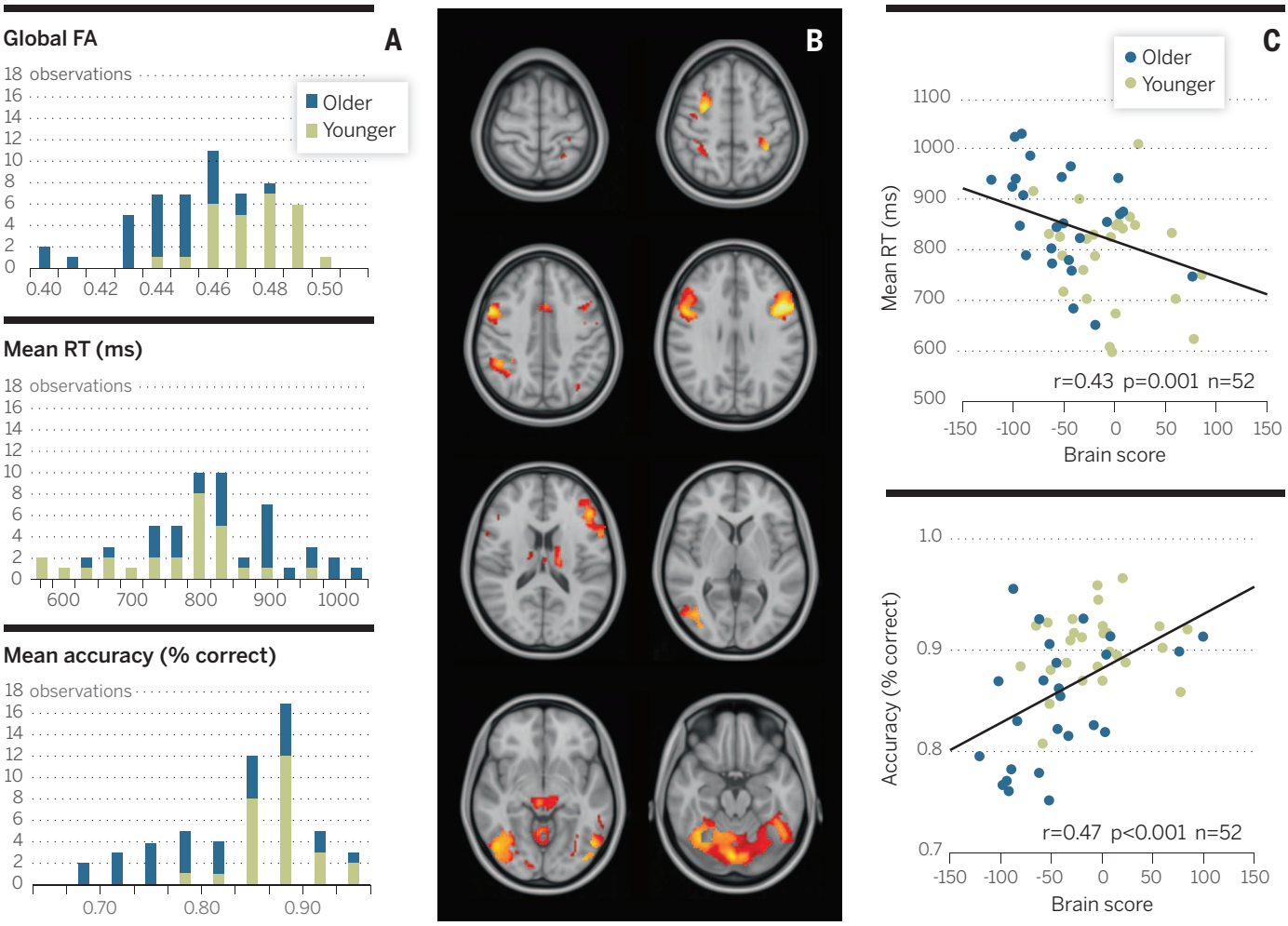

Fig. 4. A scaffold for efficiency in the human brain: Associations among white matter microstructure, task-related gray matter activation, and working memory performance in younger and older adults. (**A**) Overlap between age groups in white matter microstructural integrity, indexed by global fractional anisotropy (FA) of the diffusion tensor, task reaction time (RT), and task accuracy. (**B**) Higher FA values in most major white matter tracts are negatively related to the blood oxygenation level–dependent (BOLD) signal on task in task-positive gray matter regions. (**C**) Associations between working memory performance and a structure-function brain score representing higher FA values and a lower task-related BOLD signal. Higher brain scores are associated with faster RT and higher accuracy, regardless of age. [Modified from (*102*)]

studies of brain and behavior. When planning such studies, design factors such as the number and the spacing of measurement occasions, the number of participants, the number of indicators per construct, and measurement reliability need to be chosen with care (*123*). These choices influence the likelihood of correct identification of individual differences and mean trends in the age of onset, the functional form, and the rate of age-graded changes in adult cognition. In addition, longitudinal observations should be augmented by interventions to induce positive deviations from the modal path that help to identify contexts and mechanisms of successful aging and give science and society a hint about what would be possible if conditions were different. A more thorough understanding of mitigating, protective, and enhancing factors may provide the foundation for individualized interventions that promote successful cognitive development in adulthood and old age (*9*).

REFERENCES AND NOTES

1. J. W. Vaupel, *Nature* **464**, 536–542 (2010).
2. M. Rönnlund, L. Nyberg, L. Bäckman, L.-G. Nilsson, *Psychol. Aging* **20**, 3–18 (2005).
3. K. W. Schaie, *Intellectual Development in Adulthood: The Seattle Longitudinal Study* (Cambridge Univ. Press, New York, 1996).
4. C. Grady, *Nat. Rev. Neurosci.* **13**, 491–505 (2012).
5. D. C. Park, P. Reuter-Lorenz, *Annu. Rev. Psychol.* **60**, 173–196 (2009).
6. P. B. Baltes, U. Lindenberger, U. M. Staudinger, in *Handbook of Child Psychology: Vol 1. Theoretical Models of Human Development*, W. Damon, R. M. Lerner, Eds. (Wiley, New York, 2006), chap. 11, pp. 569–664.
7. C. Hertzog, A. F. Kramer, R. S. Wilson, U. Lindenberger, *Psychol. Sci. Public Interest* **9**, 1–65 (2009).
8. T. B. L. Kirkwood, *Cell* **120**, 437–447 (2005).
9. M. Lövdén, L. Bäckman, U. Lindenberger, S. Schaefer, F. Schmiedek, *Psychol. Bull.* **136**, 659–676 (2010).
10. J. Freund *et al*., *Science* **340**, 756–759 (2013).
11. P. C. M. Molenaar, D. I. Boomsma, C. V. Dolan, *Behav. Genet.* **23**, 519–524 (1993).
12. J. Belsky *et al*., *Mol. Psychiatry* **14**, 746–754 (2009).
13. N. Raz, K. M. Rodrigue, *Neurosci. Biobehav. Rev.* **30**, 730–748 (2006).
14. D. Barulli, Y. Stern, *Trends Cogn. Sci.* **17**, 502–509 (2013).
15. M. Lövdén, E. Wenger, J. Mårtensson, U. Lindenberger, L. Bäckman, *Neurosci. Biobehav. Rev.* **37** (9 Pt B), 2296–2310 (2013).
16. J. D. Sweatt, *Neuron* **80**, 624–632 (2013).
17. U. Lindenberger, in *International Encyclopedia of the Social and Behavioral Sciences*, N. J. Smelser, P. B. Baltes, Eds. (Elsevier Science, Oxford, 2001), vol. 13, pp. 8848–8854.
18. E. A. Bosman, N. Charness, in *Perspectives on Cognitive Change in Adulthood and Aging*, F. Blanchard-Fields, T. H. Hess, Eds. (McGraw-Hill, New York, 1996), pp. 428–453.
19. J. Park, J. Carp, A. Hebrank, D. C. Park, T. A. Polk, *J. Neurosci.* **30**, 9253–9259 (2010).
20. P. B. Baltes, U. Lindenberger, *Psychol. Aging* **12**, 12–21 (1997).
21. A. F. Arnsten, M. J. Wang, C. D. Paspalas, *Neuron* **76**, 223–239 (2012).
22. L. Bäckman, L. Nyberg, U. Lindenberger, S.-C. Li, L. Farde, *Neurosci. Biobehav. Rev.* **30**, 791–807 (2006).
23. S.-C. Li, U. Lindenberger, S. Sikström, *Trends Cogn. Sci.* **5**, 479–486 (2001).
24. N. Nevalainen *et al*., *Brain Res.* **2014**, 10.1016/j.brainres.2014.09.010 (2014).
25. N. Raz *et al*., *Cereb. Cortex* **15**, 1676–1689 (2005).
26. A. Pfefferbaum *et al*., *Neuroimage* **65**, 176–193 (2013).
27. N. Raz, Y. Yang, C. L. Dahle, S. Land, *Biochim. Biophys. Acta* **1822**, 361–369 (2012).
28. A. Z. Burzynska *et al*., *Neuroimage* **49**, 2104–2112 (2010).
29. L. T. Westlye *et al*., *Cereb. Cortex* **20**, 2055–2068 (2010).
30. J. H. Morrison, M. G. Baxter, *JAMA* **71**, 835–837 (2014).
31. S. N. Burke, C. A. Barnes, *Trends Neurosci.* **33**, 153–161 (2010).
32. Z. S. T. Tan *et al*., *Diabetes Care* **34**, 1766–1770 (2011).
33. K. B. Walhovd, A. B. Storsve, L. T. Westlye, C. A. Drevon, A. M. Fjell, *Neurobiol. Aging* **35**, 1055–1064 (2014).
34. C. M. de Frias, M. Lövdén, U. Lindenberger, L.-G. Nilsson, *Intelligence* **35**, 381–392 (2007).
35. B. J. Small, R. A. Dixon, J. J. McArdle, *J. Gerontol.* **66B** (suppl. 1), i153–i161 (2011).
36. I. J. Deary *et al*., *Nature* **482**, 212–215 (2012).
37. D. Finkel, N. Pedersen, M. McGue, *Psychol. Aging* **10**, 437–446 (1995).
38. R. S. Wilson, S. E. Leurgans, P. A. Boyle, D. A. Bennett, *Arch. Neurol.* **68**, 351–356 (2011).
39. U. Lindenberger, T. Singer, P. B. Baltes, *J. Gerontol. B* **57**, P474–P482 (2002).
40. S. M. Hofer, B. P. Flaherty, L. Hoffman, *Multivar. Behav. Res.* **41**, 165–187 (2006).
41. U. Lindenberger, T. von Oertzen, P. Ghisletta, C. Hertzog, *Psychol. Aging* **26**, 34–47 (2011).
42. Y. Fandakova, U. Lindenberger, Y. L. Shing, *Cereb. Cortex* **24**, 1832–1844 (2014).
43. P. Ghisletta, P. M. A. Rabbitt, M. Lunn, U. Lindenberger, *Intelligence* **40**, 260–268 (2012).
44. E. M. Tucker-Drob, *Dev. Psychol.* **47**, 331–343 (2011).
45. T. A. Salthouse, *A Theory of Cognitive Aging* (North Holland, Amsterdam, 1985).
46. Y. L. Shing *et al*., *Front. Aging Neurosci.* **3**, 2 (2011).
47. N. Raz *et al*., *Cereb. Cortex* **18**, 718–726 (2008).
48. J. R. Andrews-Hanna *et al*., *Neuron* **56**, 924–935 (2007).
49. G. Bartzokis, *Neurobiol. Aging* **32**, 1341–1371 (2011).
50. D. D. Garrett *et al*., *Neurosci. Biobehav. Rev.* **37**, 610–624 (2013).
51. M. Werkle-Bergner, R. Freunberger, M. C. Sander, U. Lindenberger, W. Klimesch, *Neuroimage* **60**, 71–82 (2012).
52. L. Nyberg, M. Lövdén, K. Riklund, U. Lindenberger, L. Bäckman, *Trends Cogn. Sci.* **16**, 292–305 (2012).
53. N. Raz, U. Lindenberger, *Psychol. Bull.* **137**, 790–795 (2011).
54. I. J. Deary, M. C. Whiteman, J. M. Starr, L. J. Whalley, H. C. Fox, *J. Pers. Soc. Psychol.* **86**, 130–147 (2004).
55. M. C. Valdés Hernández *et al*., *Neurobiol. Aging* **34**, 2740–2747 (2013).
56. R. Möttus, M. Luciano, J. M. Starr, I. J. Deary, *J. Psychosom. Res.* **75**, 275–278 (2013).
57. J. Corley, A. J. Gow, J. M. Starr, I. J. Deary, *J. Psychosom. Res.* **73**, 132–138 (2012).
58. D. Falkstedt, K. Sorjonen, T. Hemmingsson, I. J. Deary, B. Melin, *PLOS ONE* **8**, e82031 (2013).
59. R. E. Marioni *et al*., *Intelligence* **44**, 26–32 (2014).
60. K. Christensen, T. E. Johnson, J. W. Vaupel, *Nat. Rev. Genet.* **7**, 436–448 (2006).
61. U. Lindenberger *et al*., *Front. Neurosci.* **2**, 234–244 (2008).
62. S.-C. Li *et al*., *J. Cogn. Neurosci.* **22**, 2164–2173 (2010).
63. S.-C. Li, C. Gratton, M. Fabiani, R. T. Knight, *Neurobiol. Aging* **34**, 477–488 (2013).
64. G. Papenberg *et al*., *Neurobiol. Aging* **35**, 1213.e3–1213.e8 (2014).
65. G. Papenberg *et al*., **25**, 571–579 (2013).
66. L. S. Colzato, W. P. van den Wildenberg, B. Hommel, *Neuropsychologia* **51**, 1377–1381 (2013).
67. G. E. McClearn *et al*., *Science* **276**, 1560–1563 (1997).
68. E. Turkheimer, *Res. Hum. Dev.* **8**, 227–241 (2011).
69. L. Bherer, K. I. Erickson, T. Liu-Ambrose, *J. Aging Res.* **2013**, 657508 (2013).
70. C. W. Kuzawa *et al*., *Proc. Natl. Acad. Sci. U.S.A.* **111**, 13010–13015 (2014).
71. R. J. Moran, M. Symmonds, R. J. Dolan, K. J. Friston, *PLOS Comput. Biol.* **10**, e1003422 (2014).
72. H. Noack, M. Lövdén, F. Schmiedek, *Psychol. Res.* 2014, 10.1007/s00426-014-0564-6 (2014).
73. J. J. McArdle, *Annu. Rev. Psychol.* **60**, 577–605 (2009).
74. J. J. McArdle, J. J. Prindle, *Psychol. Aging* **23**, 702–719 (2008).
75. T. S. Redick *et al*., *J. Exp. Psychol. Gen.* **142**, 359–379 (2013).
76. F. Schmiedek, M. Lövdén, U. Lindenberger, *Front. Aging Neurosci.* **2**, 27 (2010).
77. F. Schmiedek, M. Lövdén, U. Lindenberger, *Dev. Psychol.* **50**, 2304–2310 (2014).
78. M. Lövdén *et al*., *Neuropsychologia* **48**, 3878–3883 (2010).
79. N. Raz *et al*., *Brain Cogn.* **82**, 171–180 (2013).
80. M. Lövdén *et al*., *Neurobiol. Aging* **33**, 620.e9–620.e22 (2012).
81. E. Wenger *et al*., *Neuroimage* **59**, 3389–3397 (2012).
82. F. I. M. Craik, D. a. Routh, D. E. Broadbent, *Philos. Trans. R. Soc. London Ser. B* **302**, 341–359 (1983).
83. D. La Voie, L. L. Light, *Psychol. Aging* **9**, 539–553 (1994).
84. S. Ardid, X.-J. Wang, A. Compte, *J. Neurosci.* **27**, 8486–8495 (2007).
85. M. Wang *et al*., *Nature* **476**, 210–213 (2011).
86. A. Gazzaley, in *Principles of Frontal Lobe Function*, D. T. Stuss, R. T. Knight, Eds. (Oxford Univ. Press, New York, 2013), pp. 593–608.
87. L. Hasher, R. T. Zacks, *Psychol. Learn. Motiv.* **22**, 193–225 (1988).
88. U. Lindenberger, U. Mayr, *Trends Cogn. Sci.* **18**, 7–15 (2014).
89. D. H. Spieler, U. Mayr, S. LaGrone, *Psychon. Bull. Rev.* **13**, 787–793 (2006).
90. D. R. Touron, E. T. Swaim, C. Hertzog, *J. Gerontol. B* **62**, P149–P155 (2007).
91. A. M. Freund, P. B. Baltes, in *Control of Human Behavior, Mental Processes, and Consciousness*, W. J. Perrig, A. Grob, Eds. (Lawrence Erlbaum Associates, Mahwah, NJ, 2000), pp. 35–58.
92. A. Brose, F. Schmiedek, M. Lövdén, U. Lindenberger, *Emotion* **12**, 605–617 (2012).
93. M. C. Voelkle, A. Brose, F. Schmiedek, U. Lindenberger, *Multivariate Behav. Res.* **49**, 193–213 (2014).
94. J. W. Rowe, R. L. Kahn, *Science* **237**, 143–149 (1987).
95. U. Lindenberger, M. Lövdén, M. Schellenbach, S.-C. Li, A. Krüger, *Gerontology* **54**, 59–68 (2008).
96. L. L. Carstensen, J. A. Mikels, M. Mather, in *Handbook of the Psychology of Aging*, J. Birren, K. W. Schaie, Eds. (Academic Press, San Diego, CA, 2006), pp. 343–362.
97. G. Kempermann, *Nat. Rev. Neurosci.* **13**, 727–736 (2012).
98. U. Lindenberger, A. Z. Burzynska, I. E. Nagel, in *Principles of Frontal Lobe Function*, D. T. Stuss, R. T. Knight, Eds. (Oxford Univ. Press, New York, 2013), pp. 609–627.
99. A. Gutchess, *Science* **346**, 579–582 (2014).
100. R. P. Haberman, C. Colantuoni, M. T. Koh, M. Gallagher, *PLOS ONE* **8**, e83674 (2013).
101. E. Düzel, H. Schütze, A. P. Yonelinas, H.-J. Heinze, *Hippocampus* **21**, 803–814 (2011).
102. A. Z. Burzynska *et al*., *J. Neurosci.* **33**, 17150–17159 (2013).
103. S. Duverne, S. Motamedinia, M. D. Rugg, *Cereb. Cortex* **19**, 733–744 (2009).
104. I. E. Nagel *et al*., *J. Cogn. Neurosci.* **23**, 2030–2045 (2011).
105. J. Persson *et al*., *Cereb. Cortex* **22**, 2297–2304 (2012).
106. R. Cabeza, N. A. Dennis, in *Principles of Frontal Lobe Function*, D. T. Stuss, R. T. Knight, Eds. (Oxford Univ. Press, New York, 2013), pp. 628–652.
107. L. Bäckman, R. A. Dixon, *Psychol. Bull.* **112**, 259–283 (1992).
108. P. B. Baltes, M. M. Baltes, in *Succcessful Aging: Perspectives from the Behavioral Sciences*, P. B. Baltes, M. M. Baltes, Eds. (Cambridge Univ. Press, New York, 1990), pp. 1–34.
109. J. Duncan, E. K. Miller, in *Principles of Frontal Lobe Function*, D. T. Stuss, R. T. Knight, Eds. (Oxford Univ. Press, New York, 2013), pp. 292–301.
110. G. M. Edelman, *Neural Darwinism. The Theory of Neuronal Group Selection* (Basic Books, New York, 1987).
111. J. Lautrey, in *Models of Intelligence: International Perspectives*, R. J. Sternberg, J. Lautrey, T. I. Lubart, Eds. (American Psychological Association, Washington, DC, 2003), pp. 117–131.
112. M. Kinsbourne, R. E. Hicks, in *Attention and Performance VII*, J. Requin, Ed. (Lawrence Erlbaum Associates, Hillsdale, New Jersey, 1978), pp. 345–362.
113. N. Raz, *Neuropsychology* **21**, 676–677, discussion 680–683 (2007).
114. P. Rakic, *Science* **227**, 1054–1056 (1985).
115. M. C. Sander, U. Lindenberger, M. Werkle-Bergner, *Neurosci. Biobehav. Rev.* **36**, 2007–2033 (2012).
116. Y. L. Shing *et al*., *Neurosci. Biobehav. Rev.* **34**, 1080–1091 (2010).
117. R. Chowdhury *et al*., *Nat. Neurosci.* **16**, 648–653 (2013).
118. J. Gervain *et al*., *Front. Syst. Neurosci.* **7**, 102 (2013).
119. A. E. Takesian, T. K. Hensch, *Prog. Brain Res.* **207**, 3–34 (2013).
120. K. E. Stephan, C. Mathys, *Curr. Opin. Neurobiol.* **25**, 85–92 (2014).
121. J. R. Nesselroade, in *Visions of Aesthetics, the Environment and Development: The Legacy of Joachim F. Wohlwill*, R. M. Downs, L. S. Liben, D. S. Palermo, Eds. (Laurence Erlbaum, Hillsdale, NJ, 1991), pp. 213–240.
122. M. Lövdén, S.-C. Li, Y. L. Shing, U. Lindenberger, *Neuropsychologia* **45**, 2827–2838 (2007).
123. T. von Oertzen, *Br. J. Math. Stat. Psychol.* **63**, 257–272 (2010).

ACKNOWLEDGMENTS

U.L. thanks R. Dolan, M. Lövdén, N. Raz, and F. Schmiedek for providing valuable comments on an earlier version of this article, and the Max Planck Society for continued research support. Parts of the research described in this article were financed by a Gottfried Wilhelm Leibniz Award 2010 of the German Research Foundation (DFG) to U.L. and a grant from the Federal Ministry of Education and Research ("The Berlin Aging Study II").

10.1126/science.1254403

REVIEW

Plasticity of the aging brain: New directions in cognitive neuroscience

Angela Gutchess[1,2]*

Cognitive neuroscience has revealed aging of the human brain to be rich in reorganization and change. Neuroimaging results have recast our framework around cognitive aging from one of decline to one emphasizing plasticity. Current methods use neurostimulation approaches to manipulate brain function, providing a direct test of the ways that the brain differently contributes to task performance for younger and older adults. Emerging research into emotional, social, and motivational domains provides some evidence for preservation with age, suggesting potential avenues of plasticity, alongside additional evidence for reorganization. Thus, we begin to see that aging of the brain, amidst interrelated behavioral and biological changes, is as complex and idiosyncratic as the brain itself, qualitatively changing over the life span.

Cognitive neuroscience altered how researchers think about normal cognitive aging. Although some prior research considered preservation or even functional gains in later life, much of the emphasis was on losses accrued with aging: poorer vision and hearing, increased forgetfulness, slower information processing, and more difficulty filtering relevant from irrelevant information. Even though the magnitude of these losses may vary across individuals, differences typically emerge when comparing groups of older adults (here, 60 years and older) to young adults (usually college-aged). With the advent of functional magnetic resonance imaging (fMRI), a noninvasive imaging method that assesses activity in regions of the brain based on measurement of blood flow, cognitive neuroscience research highlighted the plasticity of the aging brain, with changes and reorganization occurring throughout the life span. Although fMRI studies converged with behavioral work to show some losses with age, such as neural regions less active in older adults than in young, it also revealed that older adults could recruit regions of the brain to support cognitive functions in ways unlike young adults (*1*). Whereas regions such as the left frontal cortex may be specialized in young adults to manipulate large amounts of verbal information in working memory—for example, rehearsing a phone number—older adults exhibited less specialization in their recruitment of neural regions. Although young adults primarily drew on the left frontal cortex for these tasks, older adults also recruited the right frontal cortex, a region typically specialized for visuospatial information, such as remembering a map. Findings of bilateral activation (of both hemispheres of the brain, rather than just one) in older adults, and greater engagement of frontal cortex rather than middle or posterior brain regions, generated much interest in how the brain adapts to aging.

Cognitive neuroscience reveals plasticity to an extent that was not expected on the basis of behavioral research. Here, the term "plasticity" represents the potential for flexible recruitment of the brain, reflecting structural and functional changes, sometimes as a response to learning and experiences. One mechanism that could contribute to plasticity is neurogenesis, the growth of new neurons. Reports of neurogenesis occurring throughout adulthood (*2*) coincided with the emergence of the field of cognitive neuroscience of aging. Although it is uncertain to what extent neurogenesis supports plasticity with age, behaviors such as learning have been shown to increase the survival of new neurons (*3*). Neurogenesis is not the only mechanism that contributes to the sculpting of the brain with age, and a number of factors have been shown to modify plasticity with age (Fig. 1).

This Review highlights two new directions in the field of aging research with implications for plasticity. The first is the development of new tools to stimulate neural regions. Although cognitive neuroscience methods illustrate how brain activity changes in unexpected ways with aging, manipulation of neural activity is necessary to determine causality. That is, to determine whether patterns of neural activity are critical for cognition, specific brain regions must be able to be stimulated or suppressed. The second section will consider the extent to which these same mechanisms of plasticity extend to social and emotional domains. Although far less studied,

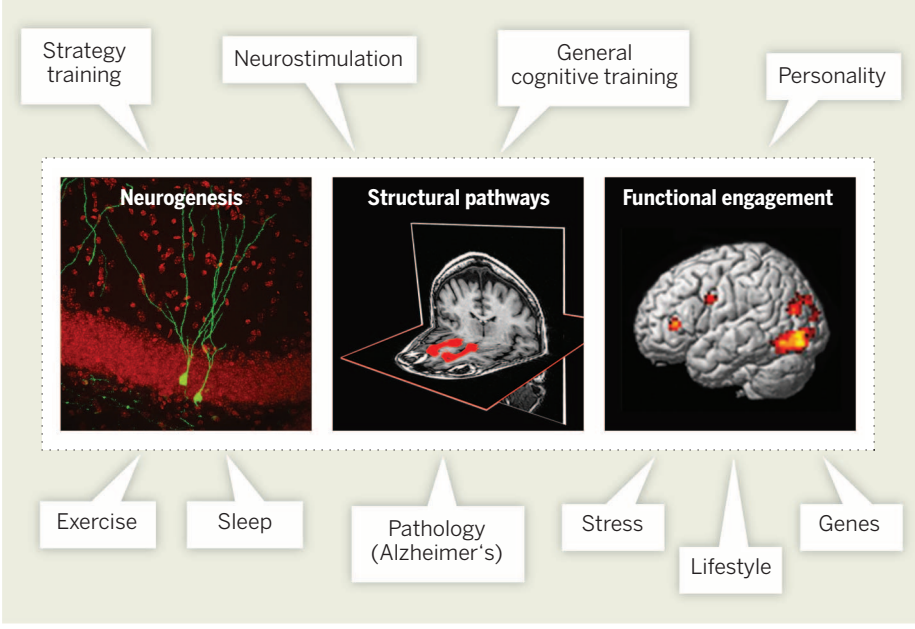

Fig. 1. Mechanisms of neuroplasticity and moderating factors that affect memory with age. The figure depicts three mechanisms (in boxes) through which neuroplasticity could affect memory, and lifestyle factors and interventions (in text balloons) that may modulate some or all of the mechanisms. Neurogenesis—growth of new neurons—may be one mechanism supporting plasticity. (Left) The development of new neurons (in green) in the dentate gyrus in an adult mouse brain. Structural pathways, such as the corticostriatal white matter tracts in the human brain (middle), may be altered through selective pruning or strengthening of connections. Additional structural mechanisms include increases or decreases in volume, as well as the reorganization of existing pathways. Changes in functional engagement include task-based neural activity, such as the regions activated during the encoding of pictures into memory (identified with fMRI of the human brain, right) as well as resting-state neural activity and differential weighting of regions within a network. Although plasticity may be reduced with age (*38*), a number of factors, such as exercise and stress, have been demonstrated to affect one or more mechanisms of plasticity. [Images adapted from, left to right, (*39*), (*34*), and (*40*), with permission.]

[1]Department of Psychology and Volen National Center for Complex Systems, Brandeis University, Waltham, MA, USA. [2]Massachussetts General Hospital, Athinoula A. Martinos Center for Biomedical Imaging, Charlestown, MA, USA.
*Corresponding author. E-mail: gutchess@brandeis.edu

they are equally important for health and well-being in old age. Together, these two topics reflect the potential for externally administered interventions and internally motivated information processing to capitalize on plasticity in the aging brain.

Manipulation of brain function

Two noninvasive methods of brain stimulation are used to study cognition. Repetitive transcranial magnetic stimulation (rTMS) operates by applying brief electrical pulses to the brain via a coil held over a specific region of a participant's head. Depending on the pulse sequences that are administered, rTMS activates or inhibits neural activity in a region located under the coil (*4*, *5*). Transcranial direct current stimulation (tDCS) (*4*) uses a battery to administer a small amount of current through two electrodes attached to the scalp (Fig. 2). Both rTMS and tDCS are safe for human participants when operated according to guidelines.

The effects of stimulating the brain can be short-lived or persist for some period of time after stimulation (*6*, *7*). Despite the inability to target small, spatially circumscribed regions or those deep in the brain, these methods hold promise, and applications for healthy and clinical populations are being tested. For example, particular rTMS protocols have been approved in the United States by the U.S. Food and Drug Administration for treating medication-resistant depression. The potential of neurostimulation in cognitive enhancement is particularly promising for cognitive aging. An emerging body of research with healthy young adults establishes that modulating specific brain regions with TMS and tDCS can improve cognitive abilities such as attention, perception, and memory, as shown by faster reaction times and greater accuracy (*6*, *7*). rTMS has the additional potential to improve performance by inhibiting regions that interfere with task performance, such as regions mediating top-down conceptual knowledge that compete with bottom-up perceptual processes (*7*).

Neurostimulation with age

There are few studies investigating neuromodulation of cognitive abilities in older adults. Stimulating a region can enhance memory performance for older adults, as shown by a study that applied tDCS to the temporoparietal cortex during the learning of objects and their locations on a map (*8*). The stimulation had no immediate effect on learning. On a follow-up test 1 week later, however, recall of the information was improved when older adults had received tDCS during learning, compared with when they had not. Neuromodulation studies also support the proposition that higher-performing older adults tend to recruit both hemispheres more often than do lower-performers (*9*, *10*), an idea originating from fMRI research.

Results are mixed from the few studies directly comparing the effects of neurostimulation across age groups. Some studies found that older adults can benefit more from neurostimulation than can younger adults. Name recall for faces was enhanced with tDCS stimulation of the anterior temporal lobes for both younger and older adults, although older adults improved more than did young adults (*11*). The authors interpreted this as reflecting the possibility that aging weakens cortical connections supporting access to semantic information, such as names, and that tDCS enhanced neuronal firing in a weakened system. Neurostimulation can also disproportionately benefit older adults' learning of motor sequences (*12*). On this motor task, behavioral training alone may have maximally benefitted young adults, so that tDCS could not further enhance their performance.

Other studies caution that older adults may be more constrained in the benefits from neurostimulation. Whereas young adults' memory performance improves with tDCS stimulation of left or right hemisphere frontal and parietal regions during word retrieval, only left hemisphere stimulation enhanced older adults' (*13*). Differences in cognitive abilities or life experiences could affect who benefits from neurostimulation with age. For example, older adults with higher levels of education benefitted from tDCS stimulation during a working memory task, whereas those with lower levels of education did not (*14*). Further investigation of individual differences, such as education or other factors that affect cognitive reserve, may help to resolve inconsistencies across studies.

Neurostimulation can enhance abilities other than memory. Administering tDCS over the dorsolateral prefrontal cortex in the right hemisphere increased older adults' conscious awareness of error commission (*15*), which is consistent with a role for this region in supporting metacognition, or awareness of task performance, in patients. This approach has translational potential; people may be able to better monitor task performance and correct errors across a variety of different cognitive abilities. To realize this potential, neurostimulation must be studied in conjunction with functional neuroimaging and behavioral research in order to elucidate the cognitive abilities and neural regions that are engaged.

Neuromodulation approaches can be combined with other cognitive neuroscience methods in order to investigate the ways in which neural regions operate together as a network. For example, by targeting a region such as dorsolateral prefrontal cortex with rTMS, one can investigate the impact of disrupting activity in that region on other regions, such as the hippocampus, that constitute the memory network. A study combining TMS and fMRI compared neural engagement when words were encoded with a deep, meaning-based encoding strategy versus a shallow, perceptual encoding strategy (*16*). Older adults received theta-burst stimulation over the left inferior prefrontal cortex, followed by an fMRI scan. The application of TMS enhanced activity in this region as well as in ventral visual regions—implicated in word recognition—selectively during deep encoding trials. Thus, results establish that TMS not only affects the activity in local regions that are being stimulated, but also in regions with which they are functionally connected during a task. Another study extended the investigation of connectivity under task-independent conditions. In a study of semantic word generation, older adults exhibited impaired task performance and higher levels of activity in neural regions implicated in the task (*17*). tDCS ameliorated older adults' neural activity to be in line with that of young adults, and task performance improved to the level of young adults (Fig. 2). To assess the effects of tDCS on the connectivity of the brain, the investigators used resting-state fMRI, which assesses spontaneous fluctuations in brain activity to investigate which regions co-activate during periods of rest rather than during tasks. Whereas anterior regions of the brain exhibited hyperconnectivity for older adults, applying tDCS

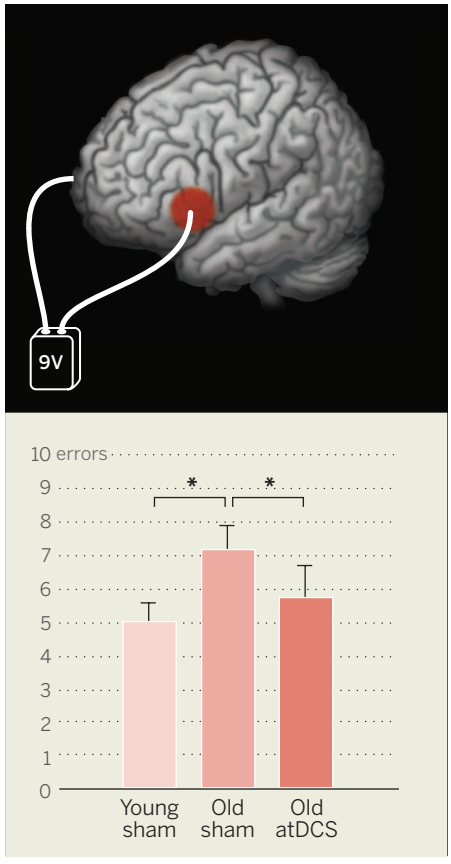

Fig. 2. Administration and effectiveness of tDCS. To administer tDCS, anodal and cathodal electrodes are placed on the scalp (top image depicts the underlying interface with the human brain) and connected to a source of direct current, much like a 9-V battery. When direct current is administered, it can stimulate the underlying region (here, the red circle denotes left ventral inferior frontal gyrus) and improve task performance. (Bottom) With anodal tDCS (atDCS) stimulation, older adults' number of errors on a word generation task is reduced from their performance under sham stimulation and reaches the level of young adults (statistically significant differences denoted by asterisks). [Data published with permission from (*17*).]

reduced the level of connectivity in these regions, while heightening it in posterior regions. These results suggest that tDCS repaired some age-related changes thought to be disruptive for cognitive tasks.

Limitations and future directions

Despite the potential for neurostimulation studies to advance understanding of which brain regions are causally implicated in cognitive changes with age, few studies investigate aging, and even fewer directly compare younger and older adults. More studies are needed that incorporate multiple age groups, especially from midlife, and converge with findings from other studies to substantiate the effects established thus far. The methods are also limited spatially, in terms of their ability to precisely target localized regions or reach neural regions deep within the brain, such as the hippocampus. TMS cannot be tolerated by participants in all scalp locations, including the forehead, because of twitching and sensitivity.

Neurostimulation holds potential for use as a cognitive enhancer to improve failing memory due to age or disease. For these methods to have real-world impact, critical tests of the time course and longevity of effects are needed. Effects must last longer than experimental sessions in order to be effective at enhancing cognition in everyday life. There are promising results from young adults, with effects persisting over 3 months when tDCS is combined with a five-session motor-skill training regime (*18*). The time course of the effects may be more limited for older adults as compared with young, posing challenges for extending benefits to cognitively vulnerable populations. For example, administering tDCS before or during a task was equally effective for young adults, but only administration during the task facilitated reaction times for older adults on a picture-naming task (*19*).

Ultimately, neurostimulation may prove most effective combined with other methods. Long-term cognitive training may be important to combine with neurostimulation protocols. For example, benefits from face-name training persisted for 6 months in patients with mild to moderate Alzheimer's disease, but these effects primarily reflected the memory strategy training program, with no additional benefit from tDCS (*20*). It is also possible that training in effective cognitive strategies could be enhanced with other recent neuroimaging approaches, such as neurofeedback. Patients with Parkinson's disease can be trained to increase neural activity in motor regions by using an imagery task with real-time feedback from fMRI (*21*). If successful memory strategies can be identified through behavioral training and corresponding neural regions can be established by using neurostimulation methods, it may be possible to extend neurofeedback approaches to train more complex memory strategies. It would also be important to directly compare internally guided recruitment of regions through strategies to external stimulation in order to identify the most effective approaches to engage neural regions. Considerations of future directions are provided in Box 1.

Extensions to emotional, social, and motivational domains

Whereas neurostimulation has a fundamentally exogenous influence on plasticity, emotional, social, and motivational situations may represent endogenous influences. Socioemotional processes may rely on neural systems distinct from cognition for which little is known about the effects of aging, making fMRI and other studies of neural engagement important for understanding age-related changes in these domains. Given some evidence for age-invariant performance, the aging brain may be more plastic for socioemotional than cognitive domains.

For emotion, there is mixed evidence for whether specialized brain regions, such as the amygdala, atrophy more or less than do other regions with age. Evidence is more consistent for age-related changes in functional engagement and connectivity (*22*). As with cognitive processes, there is a shift to greater engagement of frontal—more than posterior—regions with age (*23*). Social abilities—including mentalizing about others (what someone

Box 1. Consideration of future directions.

Questions in neurostimulation and aging

What is the time period over which effects can persist?
Is cognitive training necessary to elicit long-term changes?
Is neurostimulation more effective for some networks or regions than others?
What precise neural regions are targeted with different sites of stimulation, and how does this affect networks?
Can performance monitoring, based on training with neurofeedback, be as effective as external stimulation?
Who benefits the most, and under which conditions? How does this change across the life span?
How does aging affect which regions should be targeted, in isolation or as part of a network?

Questions in socioemotional cognition and aging

How distinct are neural regions and processes that mediate socioemotional cognition from other cognitive systems?
Does aging affect these systems in the same way as other cognitive systems?
How much do age differences reflect the use of different strategies, rather than changes in the neural systems per se?
How do social and emotional motivations compare with the predominantly economic motivations studied thus far?
Which individual difference factors predict better outcomes with age? Do gender, personality, or culture affect outcomes?
How can neurostimulation be used to probe these systems, which consist predominantly of regions that are not amenable to current methods?

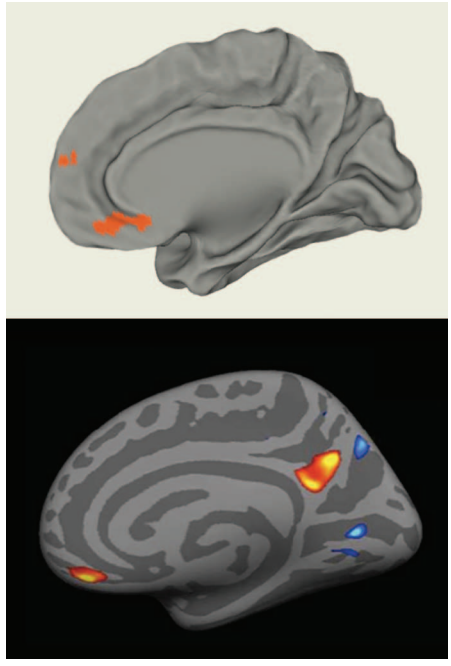

Fig. 3. Age comparisons of social processes. Whereas some studies find that age differences in neural activity in the human brain extend to social tasks, other studies find reduced age differences for socially relevant information. Moran and colleagues (*26*) reported age differences in medial prefrontal cortex during moral judgments of stories with negative outcomes compared with a control condition (top; orange areas represent age differences). Cassidy and colleagues (*25*), however, identified convergence across younger and older adults in a similar region when making socially relevant judgments about other people and their behaviors compared with a nonsocial control condition (bottom; orange areas represent commonalities with age). It is possible that motivational differences contribute to these discrepancies, with negatively valenced information inducing age differences but personally meaningful tasks bolstering neural activity for older adults [as discussed in (*29*)]. [Images adapted from (*26*, *25*) with permission.]

is thinking or feeling), pondering the self, or forming impressions—are only beginning to be investigated with aging. Although some studies indicate that neural regions may be engaged more similarly for younger and older adults on social tasks (*24*, *25*), others find age differences much like other domains (*26*) (Fig. 3).

It may be most important to understand qualitative differences across age groups in motivation or goals and how these affect neural engagement. Compared with younger adults, older adults prefer positive over negative information, perhaps reflecting a motivation to prioritize feeling good in the time remaining in life (*27*). Prioritization of positive over negative emotional information with age affects the conditions under which prefrontal cortex is engaged (*28*, *29*). It is also possible that social tasks can be performed more flexibly, making them amenable to different strategies, with corresponding differences in neural regions, across age groups.

Personality could also be important in understanding how age groups differ in their motivations and goals, in that it affects how people construct their environments. For example, neurotic individuals experience stress through high levels of negative emotion (*30*). Personality also shapes brain development across the life span. Higher levels of conscientiousness are associated with positive outcomes (larger brain volumes, less volumetric decline), whereas higher levels of neuroticism are associated with poorer outcomes (*31*) when comparing across different age groups. Education, occupation, leisure activities, and high-quality social interactions offer protective effects on behavior with age (*30*, *32*), and presumably also affect the trajectory of brain aging.

The study of motivation and aging largely focuses on economic tasks, involving rewards and losses. Neurotransmitters such as dopamine and serotonin are implicated in economic behavior, and age may reduce the ability to modulate these systems. These neurotransmitters affect the activation of particularly frontal and striatal regions that respond to rewards, risky situations, and delay (thought to discount the value of rewards) (*33*). Age-related impairments may be greater for losses than gains, which is consistent with the reduced emphasis on negative emotions (*27*). The integrity of white-matter connections between regions may be particularly important. Better integrity of thalamocorticostriatal pathways is associated with better reward learning and accounts for age differences on the task (*34*).

Future work can incorporate methods capable of targeting specific neurotransmitter systems [such as positron emission tomography (PET) or pharmacological interventions] to uncover biological causes for other changes in economic behavior with age, such as reduced risk-taking (*33*, *35*). One study using a multimodal imaging approach found that the levels of midbrain dopamine (measured with PET) had opposite effects for younger and older adults on the activation of regions of prefrontal cortex (measured with fMRI). More midbrain dopamine synthesis was related to higher levels of prefrontal activation for young adults, but less prefrontal activation for older adults (*36*). This study illustrates the complex relationships between these systems, with baseline age differences in the dopamine system potentially changing the very relationship between dopamine uptake and neural activation.

Conceptualizing motivation more broadly, including consideration of differences in emotional and social goals as well as exploring the response of the motivational system for rewarding social and emotional experiences, will be necessary to understand age-related changes and potential plasticity in these domains (*37*). These fields have progressed independently, emphasizing different neural regions. Furthermore, there are inherent limitations in studying social processes with cognitive neuroscience methods. Realistic social interaction is limited when movement contaminates data acquisition and participants are tested in a MR scanner. Current neurostimulation methods are not able to reach regions deep within the brain, such as those implicated in many socioemotional processes, although it may be possible to target these regions indirectly through other regions in the network. In studying the effects of neurostimulation, the study of socioemotional processes with age will continue to lag behind the study of cognition. Promising directions are described in Box 1.

Final thoughts

Recent findings of malleable patterns of activation, improved task performance through neurostimulation, and potential preservation in socioemotional domains highlight the plasticity available in the aging brain. Despite this promise, conclusively identifying the conditions that maximally benefit performance will be a challenge when studying such a dynamic and interrelated system. For example, perhaps an effective memory-training program paired with neurostimulation could increase gray-matter thickness and thus affect the functional activation patterns. Improved memory could reduce stress, improving mood and sleep and perhaps even facilitating social interactions and levels of activity. These changes could alter structural pathways and functional engagement of brain regions. In addition, these changes likely operate bidirectionally, dynamically influencing each other in complex ways. We have very little understanding of how these processes affect brain plasticity, let alone the combination of multiple factors and influences that have yet to be identified. Given the qualitative differences in the patterns of neural activity in older compared with younger adults, it is important to investigate these processes across age groups because results from one group are unlikely to translate to others. Last, experiences at different time points throughout the life span could affect later outcomes with aging, making life span and longitudinal studies, in which the same individual is studied over years, crucial to unravel how and when plasticity is available in the aging brain. Just as the advent of cognitive neuroscience increased appreciation of the malleability of the brain in old age, the study of aging can change thinking about the brain by highlighting the cascading effects of life experiences on plasticity.

REFERENCES AND NOTES

1. D. C. Park, P. Reuter-Lorenz, *Annu. Rev. Psychol.* **60**, 173–196 (2009).
2. P. S. Eriksson *et al.*, *Nat. Med.* **4**, 1313–1317 (1998).
3. D. M. Curlik 2nd, T. J. Shors, *J. Cogn. Neurosci.* **23**, 2159–2170 (2011).
4. M. Zimerman, F. C. Hummel, *Front. Aging Neurosci.* **2**, 149 (2010).
5. C. Freitas, F. Farzan, A. Pascual-Leone, *Front. Neurosci.* **7**, 42 (2013).
6. B. A. Coffman, V. P. Clark, R. Parasuraman, *Neuroimage* **85**, 895–908 (2014).
7. B. Luber, S. H. Lisanby, *Neuroimage* **85**, 961–970 (2014).
8. A. Flöel *et al.*, *Neurobiol. Aging* **33**, 1682–1689 (2012).
9. M. Zimerman, K. F. Heise, C. Gerloff, L. G. Cohen, F. C. Hummel, *Cereb. Cortex* **24**, 1030–1036 (2014).
10. R. Manenti, M. Cotelli, C. Miniussi, *Behav. Brain Res.* **216**, 153–158 (2011).
11. L. A. Ross, D. McCoy, H. B. Coslett, I. R. Olson, D. A. Wolk, *Front. Aging Neurosci.* **3**, 16 (2011).
12. M. Zimerman *et al.*, *Ann. Neurol.* **73**, 10–15 (2013).
13. R. Manenti, M. Brambilla, M. Petesi, C. Ferrari, M. Cotelli, *Front. Aging Neurosci.* **5**, 49 (2013).
14. M. E. Berryhill, K. T. Jones, *Neurosci. Lett.* **521**, 148–151 (2012).
15. S. Harty *et al.*, *J. Neurosci.* **34**, 3646–3652 (2014).
16. D. Vidal-Piñeiro *et al.*, *Brain Stimulat.* **7**, 287–296 (2014).
17. M. Meinzer, R. Lindenberg, D. Antonenko, T. Flaisch, A. Flöel, *J. Neurosci.* **33**, 12470–12478 (2013).
18. J. Reis *et al.*, *Proc. Natl. Acad. Sci. U.S.A.* **106**, 1590–1595 (2009).
19. A. Fertonani, M. Brambilla, M. Cotelli, C. Miniussi, *Front. Aging Neurosci.* **6**, 131 (2014).
20. M. Cotelli *et al.*, *Front. Aging Neurosci.* **6**, 38 (2014).
21. L. Subramanian *et al.*, *J. Neurosci.* **31**, 16309–16317 (2011).
22. K. Nashiro, M. Sakaki, M. Mather, *Gerontology* **58**, 156–163 (2012).
23. P. L. St Jacques, B. Bessette-Symons, R. Cabeza, *J. Int. Neuropsychol. Soc.* **15**, 819–825 (2009).
24. A. H. Gutchess, E. A. Kensinger, D. L. Schacter, *Soc. Neurosci.* **2**, 117–133 (2007).
25. B. S. Cassidy, J. Y. Shih, A. H. Gutchess, *Soc. Neurosci.* **7**, 552–564 (2012).
26. J. M. Moran, E. Jolly, J. P. Mitchell, *J. Neurosci.* **32**, 5553–5561 (2012).
27. A. E. Reed, L. L. Carstensen, *Front. Psychol.* **3**, 339 (2012).
28. C. M. Leclerc, E. A. Kensinger, *Soc. Neurosci.* **5**, 560–576 (2010).
29. B. S. Cassidy, E. D. Leshikar, J. Y. Shih, A. Aizenman, A. H. Gutchess, *Soc. Neurosci.* **8**, 462–473 (2013).
30. W. S. Kremen, M. E. Lachman, J. C. Pruessner, M. Sliwinski, R. S. Wilson, *J. Gerontol. A Biol. Sci. Med. Sci.* **67**, 760–765 (2012).
31. J. Jackson, D. A. Balota, D. Head, *Neurobiol. Aging* **32**, 2162–2171 (2011).
32. Y. Stern, *Neuropsychologia* **47**, 2015–2028 (2009).
33. P. N. Mohr, S. C. Li, H. R. Heekeren, *Neurosci. Biobehav. Rev.* **34**, 678–688 (2010).
34. G. R. Samanez-Larkin, S. M. Levens, L. M. Perry, R. F. Dougherty, B. Knutson, *J. Neurosci.* **32**, 5333–5337 (2012).
35. R. Mata, A. K. Josef, G. R. Samanez-Larkin, R. Hertwig, *Ann. N. Y. Acad. Sci.* **1235**, 18–29 (2011).
36. J. C. Dreher, A. Meyer-Lindenberg, P. Kohn, K. F. Berman, *Proc. Natl. Acad. Sci. U.S.A.* **105**, 15106–15111 (2008).
37. T. S. Braver *et al.*, *Cogn. Affect. Behav. Neurosci.* **14**, 443–472 (2014).
38. A. Pascual-Leone *et al.*, *Brain Topogr.* **24**, 302–315 (2011).
39. C. Zhao, E. M. Teng, R. G. Summers Jr., G. L. Ming, F. H. Gage, *J. Neurosci.* **26**, 3–11 (2006).
40. A. H. Gutchess *et al.*, *J. Cogn. Neurosci.* **17**, 84–96 (2005).

ACKNOWLEDGMENTS

I thank J. Jackson and B. Cassidy for helpful feedback and suggestions.

10.1126/science.1254604

REVIEW

Language in the aging brain: The network dynamics of cognitive decline and preservation

Meredith A. Shafto* and Lorraine K. Tyler

Language is a crucial and complex lifelong faculty, underpinned by dynamic interactions within and between specialized brain networks. Whereas normal aging impairs specific aspects of language production, most core language processes are robust to brain aging. We review recent behavioral and neuroimaging evidence showing that language systems remain largely stable across the life span and that both younger and older adults depend on dynamic neural responses to linguistic demands. Although some aspects of network dynamics change with age, there is no consistent evidence that core language processes are underpinned by different neural networks in younger and older adults.

Understanding and producing language are crucial and complex human behaviors, essential for effective communication, that underpin almost all our social interactions. They are so important for daily life that real or perceived communication problems are assumed to reflect lower intelligence or pathological conditions like dementia (*1*).

Although aging is associated with specific impairments in language production, most comprehension abilities remain stable as we age, and word knowledge even improves across much of the adult life span, declining only in very old age [(*2*), see (*3*) for review]. This pattern of impaired and spared language functions challenges models that propose age-related reductions in general cognitive resources and predict universal cognitive declines, including those in language functions (*4*). Moreover, the widespread changes in brain structure associated with aging raise the question of why much of language comprehension is preserved as we age, whereas aspects of production decline. These variable age effects make language an ideal model system for investigating the relation between age-related structural and functional brain changes and their behavioral consequences.

As a background to discussing research on the neurobiology of language and aging, we begin this review by highlighting the importance of moving away from a focus on the functional role of individual brain regions to understanding the network dynamics that characterize the effects of aging on cognition. In particular, we discuss claims that age-related neural decline leads to compensatory neural recruitment to support good performance and consider different uses of the term "compensation" (*5*). We then selectively review how age affects language performance. In the final section we describe, in the context of neurobiological models of the language system, two key examples of age-related language preservation and loss: (i) syntactic processing during comprehension, which is preserved with age, and (ii) phonological access during production, which shows age-related impairments. We highlight the challenges in determining whether age-related neural changes signify deterioration of specialized subcomponents of the language system, reorganization of language processes, or changing dynamics between language and other cognitive domains.

Centre for Speech, Language and the Brain, Department of Psychology, University of Cambridge, Cambridge CB2 3EB, UK.
*Corresponding author. E-mail: mshafto@csl.psychol.cam.ac.uk

The aging brain: Structure, function, and performance

Typical aging is associated with widespread gray- and white-matter brain changes (*6*), which show considerable regional variation across the brain in the timing and rate of declines. However, there is no simple correspondence between the degree of neural change and cognitive performance (*7*), perhaps partly because of age-related compensatory neural recruitment: Older adults with relatively preserved performance in cognitive domains that typically decline with age (e.g., episodic or working memory) show increases in neural activity, particularly in prefrontal regions (*8*). This recruitment often involves bilateral activation in conditions where younger adults only activate the right hemisphere, which suggests functional reorganization, wherein recruited left-hemisphere regions take on right hemisphere processing functions. However, there has been little systematic effort to test whether contralateral regions perform the same functions as the original system. Moreover, increased frontal activity is often accompanied by decreased activity in more posterior regions such as occipitotemporal cortex (*9*), which suggests that prefrontal cortex may be a general neural "resource" that flexibly supports performance (*5*). However, many experimental tasks involve executive or attentional processes that also rely on frontal function, which raises the issue of whether recruitment reflects age-related increases in the effect of task demands rather than changes in cognitive functions per se (*10*).

Recent studies focusing on age-related changes in network dynamics rather than individual brain regions suggest that prefrontal cortex may be important for compensation in a variety of cognitive contexts because of its involvement in a wide range of functional networks underpinning different cognitive processes [e.g., (*11, 12–14*)]. Networks are formed from multiple coactivating brain regions and are thought to be functionally specialized by virtue of their interregional connectivity. Each region may be involved in multiple networks, as seems to be the case for frontal cortex. Functional networks have largely been identified in resting-state data by using independent components analysis (ICA), seed-based connectivity, and graph theory methods, where synchronized activity across different regions is thought to reflect intrinsic connectivity. In younger adults, brain-wide networks have an optimized modular organization, with highly integrated local networks and weak connectivity between networks (*13*). Data from resting state and task-based studies (*11–13*) suggest that aging disrupts this organization, reduces integration within networks, and increases connectivity between them. Age-related reduced neural specificity, or "dedifferentiation," resulting from biological brain aging (*15*) may lead to age-related declines in the modularity of brain-wide network organization, an example of regional dedifferentiation in association with dedifferentiation at a network level (*11*). Given the evidence for compensatory bilateral recruitment (*8*), increased between-network connectivity may reflect attempts to compensate for within-network disruption, and this compensation may not always be successful (*14*). In the following sections, we describe core language processes that are typically either preserved or impaired with age and consider whether there is evidence that older adults' performance is underpinned by age-related changes in network dynamics.

Language functions across the adult life span: Evidence from behavioral studies

Spoken language comprehension involves a variety of processes operating in parallel over different time scales that transform the speech input into intermediate levels of representation, including speech sounds (acoustic-phonetic and phonology) and words (lexical semantic and syntactic properties), in the online development of a syntactically coherent and meaningful utterance. A key constraint in understanding this complex set of processes and their interactions is that they must occur very rapidly, as speech consists of a fast-fading input, which requires the listener to keep pace with the speaker in order to interpret the input effectively and to avoid an overload of uninterpreted auditory input. This system has been termed optimally efficient, because listeners process the speech input at around 200 ms delay, constructing high-level representations millisecond-by-millisecond (*16*).

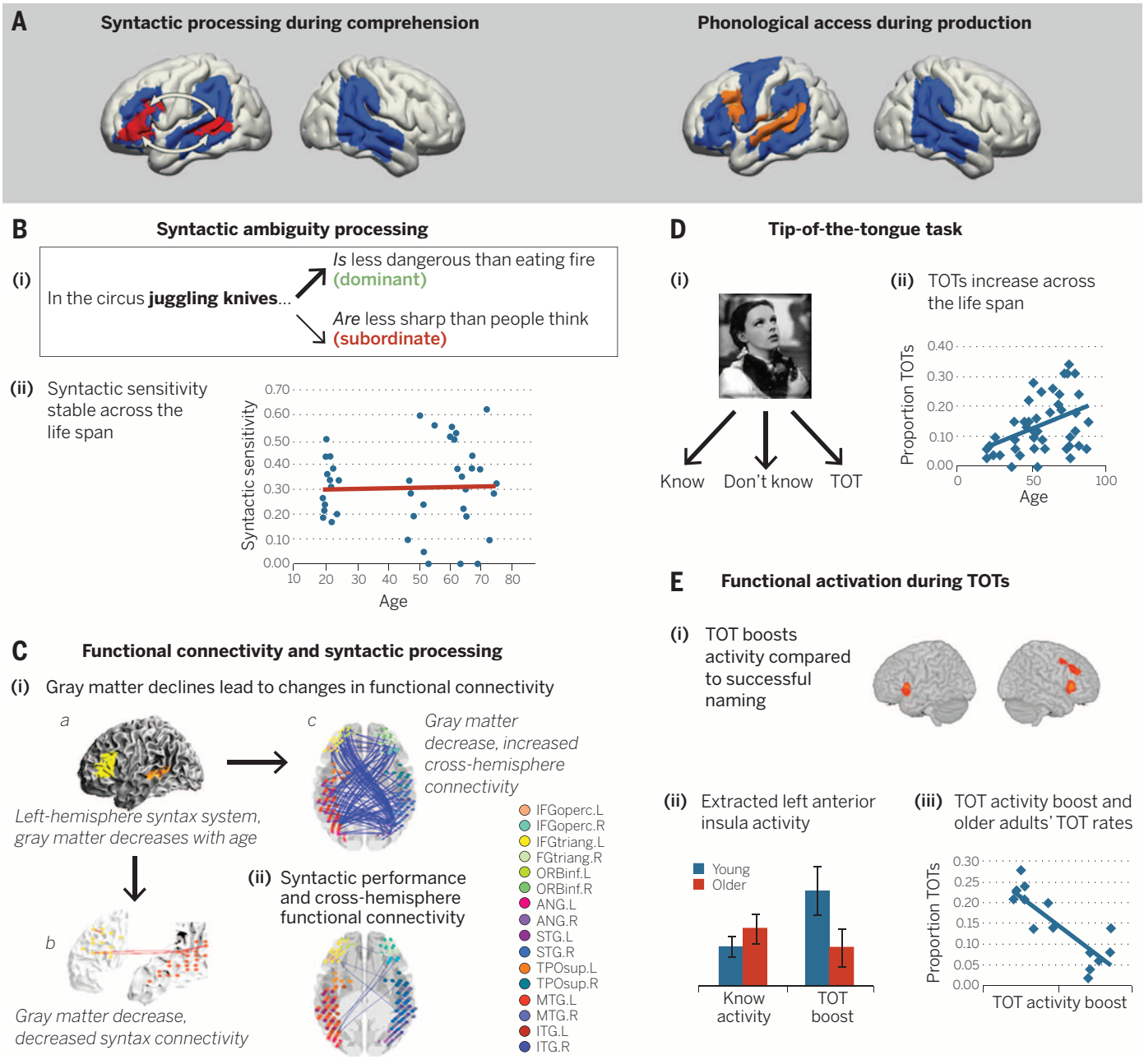

Fig. 1. Age-related changes in behavioral and neural measures during syntactic comprehension and word production. (**A**) Comprehension and production systems (blue) with (left) left hemisphere syntactic processing network (red), including key white matter pathways (white arrows); and (right) left hemisphere regions associated with phonological access and encoding during word production (orange). (**B**) Syntactic processing paradigm (*14*), where (i) participants in an fMRI scanner naturally listen to sentences containing syntactically ambiguous phrases (e.g., "...juggling knives...") with a strong bias toward a dominant interpretation and a weak bias toward a subordinate interpretation. (ii) Age does not affect sensitivity to syntactic ambiguity as measured in a task performed outside the scanner. Participants hear sentences up to the disambiguating word ("is" or "are") and indicate whether the sentence is acceptable. They more often reject subordinate compared with dominant resolutions, and this difference reflects syntactic sensitivity. (**C**) Changes to functional connectivity in relation to gray matter and performance. Graph theory measures of functional connectivity during sentence comprehension were calculated using the weighted correlation method. (i) (a) Within the key regions of the left hemisphere syntax system represented here, (b) red lines show decreasing functional connectivity accompanying decreasing gray matter integrity. (c) Blue lines show cross-hemisphere functional connectivity that increases with decreasing gray matter integrity. Finally, (ii) blue lines show cross-hemisphere functional connectivity that increases with decreasing syntactic sensitivity. (**D**) Example of a TOT-inducing paradigm where (i) participants see pictures of public figures and indicate whether they Know, Don't Know, or are having a TOT for the name (*51*). (ii) TOT rates increase with age across the life span (*51*). (**E**) Neural activity and performance in response to TOTs (*55*), where (i) TOTs boost activity relative to successful naming in bilateral regions, including inferior frontal, left anterior insula, right middle frontal, and anterior cingulate cortices. (ii) Within regions of TOT-related activity, representative activity extracted from left anterior insula is similar for younger and older adults for successful naming, but the boost of activity during a TOT is weaker for older adults (*55*). In whole-brain contrasts, older adults did not reliably activate any of the regions that younger adults engaged in response to TOTs. However, TOT-related activity was relevant for older adults' performance as (iii) older adults with more TOT-related activity have lower TOT rates.

Despite the multiple rapid computations required, core aspects of speech comprehension are well-preserved across the life span, including the automatic access of lexical representations and the online construction of syntactic and semantic representations (*3*, *17*). Older adults perform worse than younger adults when speech occurs rapidly or in noisy environments (*18*), although age differences are smaller when words occur in context (*17*, *18*). It remains unclear whether sensory deficits affect language comprehension directly or indirectly by taxing central cognitive processes.

Age-related changes in language comprehension are also affected by the experimental tasks used to assess performance. For example, when tasks tap real-time processing, increased syntactic complexity does not differentially affect older adults' comprehension (*19*–*21*). In contrast, age-related differences for syntactically complex sentences emerge when tasks probe later, more explicit processes requiring overt responses, such as plausibility or gender judgments, which may involve domain-general processes over and above core language processes (*22*). Similarly, older adults retain their ability to use online sentential context to support word recognition (*23*), despite some evidence for age-related delays in processing sentential context using off line comprehension judgments (*24*).

In sum, although debate continues about which measures of language comprehension decline with age, the weight of behavioral evidence suggest that real-time sentential processing is preserved in older adults (*23*). We consider in the next section whether neural data provides any evidence that preserved online syntactic processing is supported by compensatory recruitment.

Producing language begins with the speaker's intention to construct a meaningful utterance. Similar to comprehension, this generates a set of rapid, overlapping representations at semantic, syntactic, lexical, phonological, and articulatory levels (*25*), which are used in constructing structured sequences according to the rules of the language (*26*). These processes occur rapidly in time: in picture-naming tasks, semantic access is under way by 200 ms after viewing an object, phonological retrieval occurs at around 300 ms, and articulation between 400 and 600 ms (*26*, *27*).

In contrast to many comprehension processes, language production shows reliable age-related declines. Older adults produce propositionally and syntactically simpler speech than younger adults in natural contexts (*28*), use more vague terms, have more frequent and more empty pauses (*29*), and are slower to access phonological information in experimental contexts (*30*). This is consistent with findings that older adults have more difficulty with word finding both during naturalistic speech (*28*) and in experimental tasks focusing on single-word production. Normal aging leads to slower and less accurate picture naming and increases in "tip of the tongue states" (TOTs), where the meaning of a word is available, but the form is frustratingly out of reach (*3*, *31*). Older adults worry that TOTs indicate serious memory problems (*32*), but research suggests they are not caused by difficulties in accessing meanings, but by selective deficits in accessing phonological representations (*33*, *34*).

The network dynamics of language and aging

Syntactic processing: A case of age-related preservation

Language comprehension involves bilateral frontal, temporal, and parietal cortices (*35*). Functional activity within this extensive system is modulated by different aspects of language processing (phonological, semantic, and syntactic) instantiated in overlapping networks, although the specific details of the regions involved in these networks continue to be debated. As discussed above in the context of behavioral findings, this may be because tasks vary widely in their relevance to natural language processing; because task-related and language-related activations are not always differentiated, task-related activations may be included in models of language functions (*10*, *36*). These caveats notwithstanding, there is broad agreement that auditory processing typically involves a swathe of bilateral superior temporal activity (*37*, *38*), whereas the processes involved in constructing sentential semantic representations involve a bilateral network including superior and middle temporal gyri, as well as angular gyri (*39*). Syntactic processing, in contrast, involves a strongly left-lateralized network of inferior frontal and middle temporal regions, directly connected by the arcuate fasciculus and extreme capsule fiber pathways (see Fig. 1A) (*40*). The precise subregions of frontal and temporal cortices vary across studies (*41*), but data from brain-damaged patients shows that Broca's areas (BAs) 45 and 44 in inferior frontal cortex and left posterior middle temporal gyrus are the essential regions involved in syntactic processing (*42*). Within this network, during spoken language processing, syntactic information initially flows from left middle temporal to left inferior frontal cortex (*43*). The frontal cortices per se are not functionally specific, but rather engage in multiple functions including competition, selection (*44*), or integration (*45*) during speech processing, depending on the inputs they receive.

The integrity of the left fronto temporal syntax network declines with age, and these changes may be associated with increased right hemisphere frontal activity, even in paradigms with low tasks demands (*23*). This right hemisphere involvement does not seem to reflect compensatory reorganization to a bilateral system, as, even when performance is preserved in older adults, it is not related to the degree of right hemisphere activity (*23*).

Graph theory analyses of functional networks support a similar conclusion: Age-related declines in the integrity of the left hemisphere syntax network are associated with decreased connectivity within that network and widespread interhemispheric connectivity (Fig. 1, B and C) (*14*). This increased interhemispheric connectivity in older adults is consistent with age-related dedifferentiation in that it is associated with decreased gray matter (*15*) (Fig. 1C), poorer performance, and reduced network efficiency, as determined by graph theory measures. However, there is no evidence that the syntax system suffers from dedifferentiation in the sense of becoming less functionally specialized. The function of increased right hemisphere activation remains unclear. It may reflect cross-hemisphere disinhibition after structural decline in the left hemisphere syntax network, diffuse activity as a result of reduced efficiency, or attempted but unsuccessful compensatory activity (*46*).

Under some circumstances, increased bilateral activity may reflect task demands. As discussed earlier, experimental tasks often engage executive or attentional processes. A recent functional magnetic resonance imaging (fMRI) study shows that, during syntactic processing, age-related increases in prefrontal recruitment only occur when participants perform a task, not during task-free natural listening (*10*). The potential contribution of task demands is in keeping with findings that, although activity outside the left hemisphere syntax network does not support online syntactic processes during natural listening (*14*, *23*), compensatory recruitment supports older adults' performance on offline comprehension tasks. For example, older adults with better performance on offline tasks generate increased activity in bilateral regions associated with working memory when processing complex syntax (*22*, *47*). Thus, as with behavioral studies, domain-general cognitive processes appear to support offline performance measures rather than online syntactic processing.

If recruitment outside the left hemisphere language network does not support online syntactic processing, how do older adults largely retain the ability to carry out syntactic computations? A recent study of patients with left hemisphere brain damage showed that even when the left hemisphere syntax system was damaged, there were no regions in either hemisphere that compensated by performing the same syntactic computations as those carried out by the left hemisphere system (*48*). The degree to which patients' syntactic processing abilities were intact correlated only with the residue of the left hemisphere fronto-temporal network. A similar explanation may hold for older adults, given that age-related declines in the structural integrity of the left hemisphere syntax system are a matter of degree, not absolute. Therefore, like patients with left hemisphere damage, older adults' syntactic processing may rely solely on the residue of the normal syntax network in normal conversational settings.

In sum, the online syntactic processing during natural language comprehension does not conform to frameworks of aging where preserved cognitive performance is underpinned by compensatory functional reorganization (*5*). Although functional connectivity analyses suggest that age affects the organization of functional networks underpinning syntactic processing (*14*), the residue of the left hemisphere syntax system may normally be sufficient to enable syntactic

computations when sentences occur in typical, contextually rich environments.

Word production: A case of age-related impairment

Most neural models of language production focus on single-word production. Accessing word meaning engages bilateral middle temporal cortex (*38*), whereas accessing phonological representations involves primarily left-lateralized posterior superior temporal and left inferior frontal cortices (see Fig. 1A) (*26*). Generating overt speech involves interactions between left-lateralized posterior temporal and parietal regions and more anterior regions, including inferior frontal, anterior insula, and motor cortex involved in word planning and articulation (*49*). As with comprehension, these processes occur rapidly, with phonological access during picture naming typically under way within 600 ms of seeing an object (*26*).

Word production is often examined using picture-naming or TOT-inducing tasks, and in these paradigms, both younger and older adults experience occasional problems accessing phonological representations, which leads to dysfluencies and errors, slower naming, or TOTs (*3*). Normal aging weakens phonological access, making problems more frequent or more severe for older adults. Aging has only limited effects on successful phonological retrieval, for example, reducing phonological facilitation during picture naming (*50*) or delaying phonological access when making judgments about picture names (*30*). However, weaker phonological activation also leads to more retrieval failures for older adults, including higher TOT rates and decreased picture naming accuracy (Fig. 1D) (*31*).

Neural models of language and aging do not yet provide a mechanism for why phonological access is more vulnerable to aging than other language processes [but see (*3*, *4*) for discussion of cognitive accounts]. However, age-related increases in TOTs are associated with reduced integrity in left anterior insula and left arcuate fasciculus (*51*, *52*), which are involved in language production. Despite age-related structural declines, older and younger adults' functional responses are similar in response to incomplete phonological retrieval, engaging a domain-general cognitive control system that supports recovery: In younger adults, picture-naming errors and TOTs elicit activity in bilateral regions associated with cognitive control, including anterior insula, middle and inferior frontal and anterior cingulate cortices (Fig. 1E) (*53*–*55*). Similar activity is not found in TOT tasks when participants simply don't know the correct name, which indicates that partial phonological activation is necessary to trigger support from this cognitive control system (*55*). A recent MEG study of TOTs likewise suggests that cognitive control is recruited in response to weak phonological retrieval: During the time frame of phonological access (around 300 ms post stimulus), TOTs elicit a weaker response compared to successful naming in left inferior frontal and temporal regions (*56*). It is only at later time points, after 700 ms, that TOTs generate a stronger response compared with successful naming in regions associated with cognitive control, including left middle and right inferior frontal cortex.

Like younger adults, older adults respond to production problems by activating regions involved in cognitive control, but their weaker phonological activation appears to affect both when this recruitment is necessary and when it is possible. During successful picture naming, better-performing older adults show greater activation compared to younger adults, both within occipital, temporal, and frontal regions typically active during object naming, and within regions associated with cognitive control, including anterior cingulate, bilateral inferior frontal, and insular cortices (*57*). Older adults' activity during successful object naming is similar to that of younger adults during TOTs, which suggests that older adults need to use cognitive control to overcome reduced phonological activation and maintain performance. However, during retrieval failures like TOTs, older adults' phonological activation is often too weak to trigger cognitive control support. Although better-performing older adults have TOT-related activity similar to younger adults, older adults on average do not reliably show TOT-related recruitment (*55*). Consistent with this, during TOTs younger adults often report partial phonological information (like the first sound or letter of a word), although older adults more often cannot, reporting instead that their mind just "goes blank" (*31*). Thus, the current evidence suggests that weaker phonological activation initially leads to increased recruitment of cognitive control in older adults but will lead to less recruitment relative to younger adults when phonological activation is very weak. This pattern is consistent with the suggestion from other cognitive domains that with increasing task difficulty older adults initially "over-recruit" relative to younger adults but then "under-recruit" when they reach the limits of declining neural systems (*58*).

In summary, as with syntactic processing, current findings from word production suggest that although older adults "over-recruit" regions associated with cognitive control to maintain good performance in challenging situation (*57*), the network dynamics underpinning good performance do not fundamentally change with age: Both younger and older adults experience phonological retrieval problems and, provided sufficient partial activation, they both recruit cognitive control to support recovery.

Outlook

Our brief review of language in the aging brain underlines a key theme in the cognitive neuroscience of aging: Understanding the neural mechanisms of cognitive aging requires grappling with the dynamic interactions within and between the neural networks underlying cognition. Although aging affects network dynamics during language production and comprehension, these changes do not provide robust evidence for age-related reorganization of core language processes or fundamental changes in how language and domain-general processes interact. Well-preserved abilities like syntactic processing are enabled by the residue of highly connected specialized subnetworks and not by widespread neural compensation. Even in the case of production failures there is little evidence that recruitment reflects age-specific reorganization, as both younger and older adults recruit similar systems in response to naming difficulty. Furthering our current understanding of how aging affects language networks and their interactions with other neural networks requires future research to overcome a number of challenges. Chief among these is disentangling the overlapping and interacting networks involved in complex language processing and characterizing the contribution of networks outside the core language system.

Conclusion

The message from current research on language and aging is that, despite brain-wide changes in structure, older adults' brains remain responsive and capable of flexible network interactions. Moreover, the evidence suggests that good language performance is largely underpinned by the same processes across the adult life span. However, further research is needed to understand the complex relations between changes in network organization and performance and to determine whether the language functions discussed in this review extend more widely to other components of the language system.

REFERENCES AND NOTES

1. T. R. La Tourette, S. Meeks, *J. Lang. Soc. Psychol.* **19**, 463–473 (2000).
2. P. Verhaeghen, *Psychol. Aging* **18**, 332–339 (2003).
3. D. M. Burke, M. A. Shafto, in *The Handbook of Aging and Cognition*, F. I. M. Craik, T. A. Salthouse, Eds. (Psychology Press, New York, ed. 2, 2008), pp. 373–443.
4. D. M. Burke, D. G. MacKay, L. E. James, in *Models of Cognitive Aging*, T. J. Perfect, E. A. Maylor, Eds. (Oxford Univ. Press, Oxford, 2000), pp. 204–237.
5. D. C. Park, P. Reuter-Lorenz, *Annu. Rev. Psychol.* **60**, 173–196 (2009).
6. C. D. Good *et al*., *Neuroimage* **14**, 21–36 (2001).
7. N. Raz, K. M. Rodrigue, *Neurosci. Biobehav. Rev.* **30**, 730–748 (2006).
8. R. Cabeza, *Psychol. Aging* **17**, 85–100 (2002).
9. S. W. Davis, N. A. Dennis, S. M. Daselaar, M. S. Fleck, R. Cabeza, *Cereb. Cortex* **18**, 1201–1209 (2008).
10. S. W. Davis, J. Zhuang, P. Wright, L. K. Tyler, *Neuropsychologia* **63C**, 107–115 (2014).
11. L. Geerligs, R. J. Renken, E. Saliasi, N. M. Maurits, M. M. Lorist, *Cereb. Cortex* 10.1093/cercor/bhu012 (2014).
12. L. Geerligs, N. M. Maurits, R. J. Renken, M. M. Lorist, *Hum. Brain Mapp.* **35**, 319–330 (2014).
13. D. Meunier, S. Achard, A. Morcom, E. Bullmore, *Neuroimage* **44**, 715–723 (2009).
14. D. Meunier, E. A. Stamatakis, L. K. Tyler, *Neurobiol. Aging* **35**, 42–54 (2014).
15. P. B. Baltes, U. Lindenberger, *Psychol. Aging* **12**, 12–21 (1997).
16. W. Marslen-Wilson, *Nature* **244**, 522–523 (1973).
17. R. Thornton, L. L. Light, in *Handbook of the Psychology of Aging*, J. E. Birren, K. W. Schaie, Eds. (Elsevier, San Diego, CA, 2006).
18. P. A. Tun, *Psychol. Aging* **13**, 424–434 (1998).
19. G. DeDe, D. Caplan, K. Kemtes, G. Waters, *Psychol. Aging* **19**, 601–616 (2004).
20. G. S. Waters, D. Caplan, *Psychol. Aging* **16**, 128–144 (2001).

21. L. K. Tyler, H. Cobb, N. Graham, *Spoken Language Comprehension: An Experimental Approach to Disordered and Normal Processing* (MIT Press, Cambridge, MA, 1992).
22. J. E. Peelle, V. Troiani, A. Wingfield, M. Grossman, *Cereb. Cortex* **20**, 773–782 (2010).
23. L. K. Tyler *et al.*, *Cereb. Cortex* **20**, 352–364 (2010).
24. K. D. Federmeier, C. Van Petten, T. J. Schwartz, M. Kutas, *Psychol. Aging* **18**, 858–872 (2003).
25. D. Foygel, G. S. Dell, *J. Mem. Lang.* **43**, 182–216 (2000).
26. P. Indefrey, W. J. M. Levelt, *Cognition* **92**, 101–144 (2004).
27. W. J. M. Levelt, P. Praamstra, A. S. Meyer, P. Helenius, R. Salmelin, *J. Cogn. Neurosci.* **10**, 553–567 (1998).
28. S. Kemper, A. Sumner, *Psychol. Aging* **16**, 312–322 (2001).
29. H. Bortfeld, S. D. Leon, J. E. Bloom, M. F. Schober, S. E. Brennan, *Lang. Speech* **44**, 123–147 (2001).
30. Y. Neumann, L. K. Obler, H. Gomes, V. Shafer, *Aphasiology* **23**, 1028–1039 (2009).
31. D. M. Burke, D. G. MacKay, J. S. Worthley, E. Wade, *J. Mem. Lang.* **30**, 542–579 (1991).
32. E. A. Lovelace, P. T. Twohig, *Bull. Psychon. Soc.* **28**, 115–118 (1990).
33. E. S. Cross, D. M. Burke, *Brain Lang.* **89**, 174–181 (2004).
34. L. E. James, D. M. Burke, *J. Exp. Psychol. Learn. Mem. Cogn.* **26**, 1378–1391 (2000).
35. M. Bozic, L. K. Tyler, D. T. Ives, B. Randall, W. D. Marslen-Wilson, *Proc. Natl. Acad. Sci. U.S.A.* **107**, 17439–17444 (2010).
36. P. Wright, B. Randall, W. D. Marslen-Wilson, L. K. Tyler, *J. Cogn. Neurosci.* **23**, 404–413 (2011).
37. S. K. Scott, R. J. S. Wise, *Cognition* **92**, 13–45 (2004).
38. G. Hickok, D. Poeppel, *Nat. Rev. Neurosci.* **8**, 393–402 (2007).
39. J. R. Binder, R. H. Desai, W. W. Graves, L. L. Conant, *Cereb. Cortex* **19**, 2767–2796 (2009).
40. T. Rolheiser, E. A. Stamatakis, L. K. Tyler, *J. Neurosci.* **31**, 16949–16957 (2011).
41. A. D. Friederici, S. A. Rüschemeyer, A. Hahne, C. J. Fiebach, *Cereb. Cortex* **13**, 170–177 (2003).
42. L. K. Tyler *et al.*, *Brain* **134**, 415–431 (2011).
43. L. K. Tyler, T. P. L. Cheung, B. J. Devereux, A. Clarke, *Front. Lang. Sci.* **4**, 271 (2013).
44. J. Zhuang, L. K. Tyler, B. Randall, E. A. Stamatakis, W. D. Marslen-Wilson, *Cereb. Cortex* **24**, 908–918 (2014).
45. P. Hagoort, *Neuroimage* **20** (suppl. 1), S18–S29 (2003).
46. R. Cabeza, N. A. Dennis, in *Principles of Frontal Lobe Function*, D. T. Stuss, R. T. Knight, Eds. (Oxford Univ. Press, Oxford, ed. 2, 2012), pp. 628–652.
47. M. Grossman *et al.*, *Neuroimage* **15**, 302–317 (2002).
48. P. Wright, E. A. Stamatakis, L. K. Tyler, *J. Neurosci.* **32**, 8149–8157 (2012).
49. G. Hickok, *Phys. Life Rev.* **6**, 121–143 (2009).
50. J. K. Taylor, D. M. Burke, *Psychol. Aging* **17**, 662–676 (2002).
51. M. A. Shafto, D. M. Burke, E. A. Stamatakis, P. P. Tam, L. K. Tyler, *J. Cogn. Neurosci.* **19**, 2060–2070 (2007).
52. E. A. Stamatakis, M. A. Shafto, G. Williams, P. Tam, L. K. Tyler, *PLOS ONE* **6**, e14496 (2011).
53. S. Abel *et al.*, *Neurosci. Lett.* **463**, 161–171 (2009).
54. A. Maril, A. D. Wagner, D. L. Schacter, *Neuron* **31**, 653–660 (2001).
55. M. A. Shafto, E. A. Stamatakis, P. P. Tam, L. K. Tyler, *J. Cogn. Neurosci.* **22**, 1530–1540 (2010).
56. M. Lindín, F. Díaz, A. Capilla, T. Ortiz, F. Maestú, *Neuropsychologia* **48**, 1757–1766 (2010).
57. C. E. Wierenga *et al.*, *Neurobiol. Aging* **29**, 436–451 (2008).
58. K. A. Cappell, L. Gmeindl, P. A. Reuter-Lorenz, *Cortex* **46**, 462–473 (2010).

ACKNOWLEDGMENTS

Preparation of this review was supported by grants to L.K.T. from the Biotechnology and Biological Sciences Research Council (grant number BB/H008217/1) and the European Research Council under the European Community's Seventh Framework Programme (FP7/2007-2013)/ ERC Grant agreement no. 249640. The authors thank W. Marslen-Wilson, M. G. Shafto, and S. Shafto for helpful comments on an early draft and D. Samu and D. Meunier for help with figure preparation.

10.1126/science.1254404

REVIEW

Economic and social implications of aging societies

Sarah Harper

The challenge of global population aging has been brought into sharper focus by the financial crisis of 2008. In particular, growing national debt has drawn government attention to two apparently conflicting priorities: the need to sustain public spending on pensions and health care versus the need to reduce budget deficits. A number of countries are consequently reconsidering their pension and health care provisions, which account for up to 40% of all government spending in advanced economies. Yet population aging is a global phenomenon that will continue to affect all regions of the world. By 2050 there will be the same number of old as young in the world, with 2 billion people aged 60 or over and another 2 billion under age 15, each group accounting for 21% of the world's population.

By the end of the 21st century, demographic trends will converge with declining births, stabilization in population size, and aging populations across the globe (*1*). The age composition of the world's population will alter as median ages rise and a proportionate shift from younger to older people continues. At the turn of the millennium, there were more people over 60 than under 15 in Europe. North America will follow by 2030, Latin America and Asia by 2040. In terms of absolute numbers, the Asian/Pacific region is already the oldest, and by the middle of the century will hold two-thirds of the world's then 2 billion elders (aged 60 years or over). The worldwide numbers of those aged 80 and above will show an even greater rate of increase, rising from 69 million to 379 million by 2050, when nearly 10% of the developed world will be over 80 (*1*) (Fig. 1).

Europe's demographic structure in particular is predicted to age substantially. By 2060, those under 15 in the EU27 countries (European Union members, 2007–2013) will be around 14%. There will be nearly twice that proportion over 65, as this age group will increase from 87.5 million in 2010 to 152.6 million by 2060. Perhaps most striking of all, those aged 80 and over will constitute around 12% of the European population; this group is expected to almost triple in size, from 23.7 million in 2010 to 62.4 million in 2060. The demographic outlier is Africa, which will continue to grow and remain young, with one-third of its population still under 15 by the middle of the century (*1*).

Drivers

The conventional belief is that population aging is driven by falling mortality rates and increasing longevity. Although this is an important component of the process, it is widely accepted that the major driver is falling fertility, which fundamentally alters the subsequent age structure of a population and, if sustained, leads to increasing median ages and demographic aging (*2*).

Falling fertility or childbearing

Two-thirds of the world's countries now have childbearing rates or total fertility rates (*3*) near or below replacement level, crudely defined as 2.1. These are diverse and drawn from most world regions, including Asia (for example, Hong Kong,

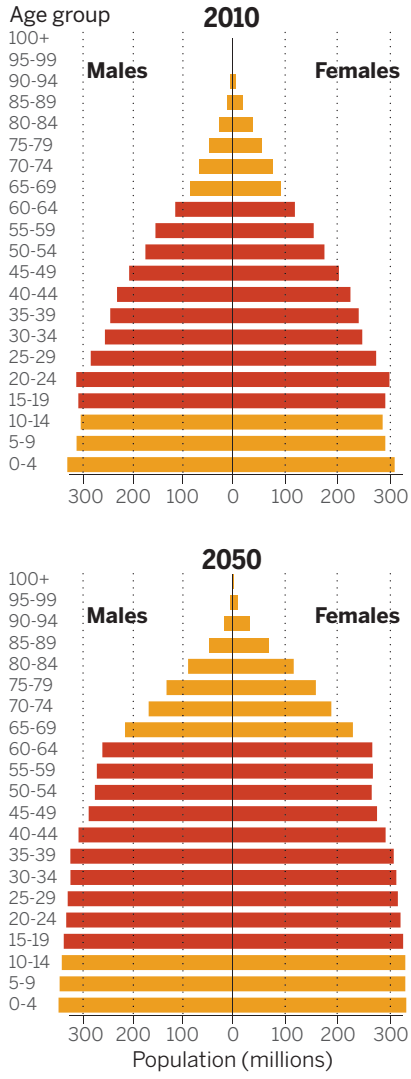

Fig. 1. World population pyramids. Population age structure for 2010 and projections for 2050 are shown. The working-age proportion is shown in red. Source: (*1*).

Oxford Institute of Population Ageing, University of Oxford, Oxford OX2 6PR, UK. **E-mail: sarah.harper@ageing.ox.ac.uk**

Singapore, Korea, Japan, Thailand, Myanmar, and Vietnam), the Americas (Argentina, Chile, Canada, and the United States), the Middle East and Africa (Mauritius, Iran, Tunisia), and Europe (every EU27 country, with a EU average of 1.6) (*4*) (Fig. 2).

Such low fertility may be due to technological advances and changes in the labor market that have altered the costs and rewards of marriage and child rearing (*5*–*7*). It may be that ideational changes have accompanied increased affluence, leading to a focus on individual autonomy and self-realization (*8*, *9*). Some demographers argue that the evolutionary link between sexual activity and procreation has been broken through the introduction of modern contraception, and that reproduction is now merely a function of individual preferences and culturally determined norms (*10*, *11*).

Some Asian and European countries may well be in a so-called low-fertility trap (*12*). This can result from both demographic and sociological factors: Fewer potential mothers in the future will result in fewer births, while ideal family size is declining among younger generations as a consequence of the lower childbearing they see in previous generations (*12*, *13*).

Falling mortality

A second key driver is falling mortality or death rates. Until recently, declines in mortality were focused on infant and child deaths. As more and more young people survived, the average life expectancy of the population increased. In advanced economies throughout the 20th century, there was a steady reduction in mortality across the life course. In mid-19th-century England, for example, half the population had died before their mid-40s. Today, half the English population can expect to survive until their mid-80s.

The drivers of life extension appear to be fourfold: healthy living, disease prevention and cure, age retardation or senescence prevention, and regenerative medicine. The first two brought us gains in life expectancy from birth seen over the past 150 years. They now promise to extend life expectancy for many in the advanced economies to over 100 this century (*14*).

Will increases in life expectancy be accompanied by increases in life extension, or will we see a compression of longevity after age 100? In countries such as Japan where there are sufficient numbers of very old people, the distribution of deaths above the mode is sliding to higher ages. This "shifting mortality" scenario suggests that with an increase in centenarians we should also expect to see an increase in supercentenarians. However, successful age retardation and regenerative medicine may be needed to achieve real radical extension of human life (*15*).

Implications

It has long been recognized that population aging has implications for societies and economies (*16*). It affects labor markets, patterns of saving and consumption, families and households, networks and social interaction, health and welfare services, housing and transport, and leisure and community behavior. In addition, the knowledge of both longer lives and the aging of the population influences not only social and economic policy and political decisions, but also the attitudes and behaviors of individuals (*17*, *18*). Are the financial and health institutions and programs designed for the demographic structure of the 20th century appropriate for the 21st century? Of particular interest is the capacity of individuals and households to make the relevant adjustments (e.g., to savings behavior, labor productivity, family and intergenerational transfers, and investment in their own human capital) and the capacity of 21st-century institutions to make the relevant adjustments to facilitate this.

As discussed above, the aging of populations is caused by two distinct trends: Older people are living longer, and at the same time younger people are having fewer children. The resulting challenges can be grouped into those that arise from (i) persistent below-replacement fertility and the changing age structure of the population, (ii) the increasing longevity of the older population, and (iii) the interaction of the two. Decreased fertility leads to demographic deficits and labor market concerns, in particular over reduced economic growth and the ability of nations to finance public welfare programs at a time when the number and percentage of those who are economically active are declining. Increased longevity raises concerns about the capacity of nations to finance and reconfigure health and long-term care provision, in advanced as well as emerging economies. Emerging economies will still be tackling acute and infectious diseases and relatively high levels of infant and child mortality, while at the same time addressing a growing number of frailer older adults who require long-term care. The interaction of the two trends creates challenges around issues of inter- and intragenerational fairness—that is, fairness and equity within and between different generations.

Demographic deficits and labor market concerns

Declining and aging populations are often viewed as having negative effects on economic growth and employment (*19*, *20*). These concerns are encompassed in the notion of the "demographic deficit" (*21*). This relates to the age-structural transition approach that examines the cohort composition of a population, considering the proportion of old and younger dependents in relation to productive adults, and how this will alter over time. In general, productive capacity varies across the life course, flowing from a period of childhood dependency through high productive potential in adulthood, then returning to a decrease in productive capacity in old age. The macroeconomic effects will differ depending on the age composition of the population. The decline in the proportion of younger people in a population is perceived as leading to a reduction in economic activity, whereas an increase in the proportion of older people is perceived as resulting in an economic burden through the higher requirement for pensions and health care.

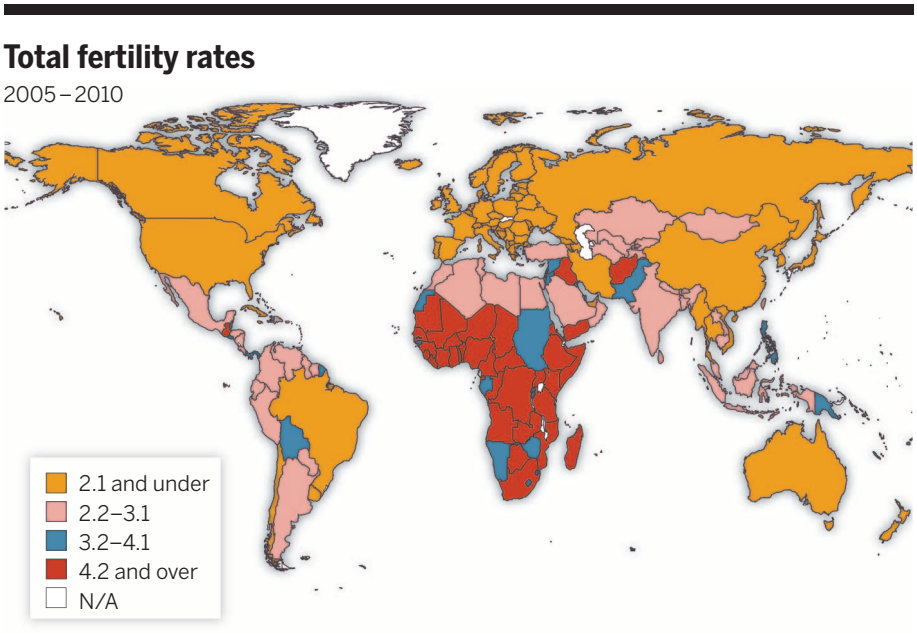

Fig. 2. Map of total fertility rates, 2005–2010. Total fertility rate, expressed as number of children per woman, represents the average number of children a hypothetical cohort of women would have at the end of their reproductive period if they were subject during their whole lives to the fertility rates of a given period and if they were not subject to mortality. Source: (*1*).

Much of this concern arises from an assumption that the older labor forces of the future will be less productive and less innovative, and that an older population will have lower rates of consumption. These preconceptions, however, are contested by arguments that future cohorts with higher levels of education, skills, and training will be able to maintain high levels of productivity given supportive and conducive working environments (*21*). In addition is the concern that older people will be recipients of publicly funded pensions for an increasing length of time, and will also draw down on savings accumulated in both private and national accounts (*22*).

In terms of the proportion of old and younger dependents in relation to productive adults, most industrialized countries will experience a rapid shift toward increased elderly dependency ratios [EDRs, defined as the number of persons of working age (aged 15 to 64) per person aged 65 or over] over the coming decades (Fig. 3). For example, the EU25 (European Union members, 2004–2006) (*23*) EDR is set to reach 51% by 2050, as the working-age population (15 to 64 years) decreases by 48 million between now and 2050, and the number of those of working age per older person 65+ will halve from 4 to 2 (*24*). Outside Europe, Japan and Korea will also age notably. Korea, the most rapidly aging country, will move from being the third youngest country in the Organisation for Economic Co-operation and Development (OECD) to the second oldest after Japan by 2050, when Japan will have one of the highest total dependency ratios (number of persons aged 15 to 64 per person outside that range) in the world at 74% in 2050.

Addressing the demographic deficit

At the macro level, many governments are exploring policies to compensate for, or even to alter, the age composition of the population by encouraging changes in fertility and migration rates. Another approach is to tackle the labor market directly, and to extend both the economic activity and the general productivity of the older population for as long as possible. This both reduces the need for social security provision for some, and enables further financing of those who are no longer able to remain economically active. In addition, there is a growing recognition that many labor markets have the potential to increase productivity through technological innovation.

Increase childbearing

The two main demographic solutions to the dependency balance are to increase childbearing and to increase migration. Although increasing fertility rates can have a strong influence on altering old-age dependency ratios, very few countries are currently pursuing an active fertility promotion policy. However, there is recognition that "family-friendly" policies, aimed at supporting both child and parents, can allow women to have the number of children they desire, which in most OECD countries tends to be higher than the actual number of achieved births (*25*–*27*). These policies include affordable child care, parental leave, financial transfers, and tax provisions.

Increase immigration

Alternatively, immigration is seen as a valid policy approach (*28*). Because of the relatively young age structure (and thus the labor potential) of immigrants, immigration has the potential to prevent population decline, maintain the size of the labor force (and thus the support ratio), and slow population aging. There are also the indirect effects of migration on innovation, economic growth, employment, and welfare. Immigration can affect the sustainability gap of public finances as it increases the number of potential taxpayers, even if the migrants' contributions to the present budget are negative (*29*). However, research has suggested that even a considerable expansion of immigration will do little to alter the predicted major capital shortages, tax increases, and reductions in real wages that can be expected as countries progress through the demographic transition (*30*).

Immigration can improve competitiveness and productivity through new trade and international linkages, encourage new investment, and increase innovation and entrepreneurship. In advanced aging economies, migrant workers fill the demand for both highly skilled workers and unskilled employment, particularly in the growing personal care sector.

Change dependency ratios by working longer

In many advanced economies, the rising elderly dependency ratios and the upcoming skills shortage have already led to reconsideration of retirement policies, leading to longer working lives and a more gradual entry into retirement (*31*). New cohorts of highly educated, skilled, and increasingly healthy populations are delaying retirement (*32*). This is in part a response to government social security changes, but is also due to the increased health status of these older generations. Future generations of older adults may have even higher levels of human capital—in terms of education, skills, and abilities—and better health profiles, and this will enable them to remain active, productive, and contributory for far longer, given supportive and conducive working environments (*2*). This has ergonomic and human resource implications for improving physical and psychological working environments. It also raises important questions around the growing need for skills and training across the life course, and of who will pay for this—individuals, employers, or governments. In addition, the substantial contribution made by older adults via the informal sector through providing family and community support and care is now increasingly being recognized (*33*).

Finance and reconfigure health and long-term care provisions

Population aging heralds a series of challenges for economies and societies in relation to the provision of health and social care (*34*).

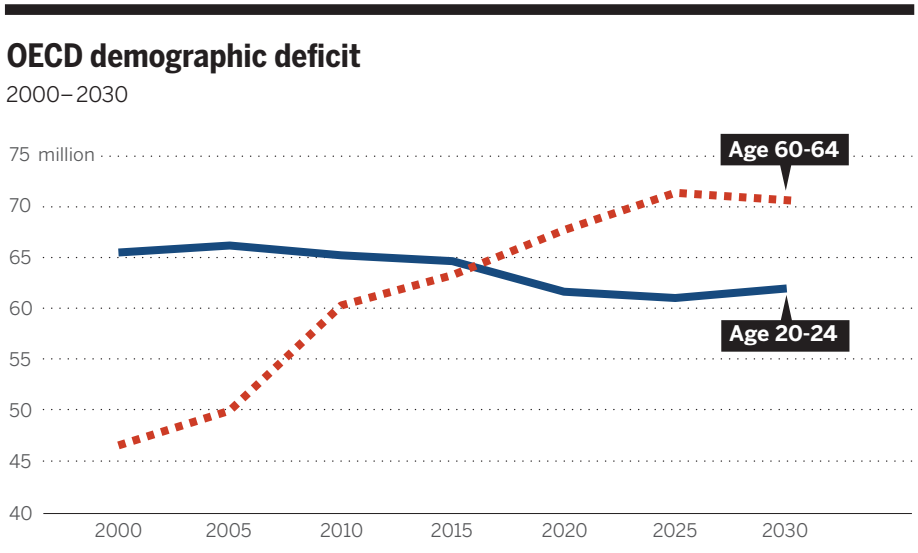

Fig. 3. Demographic deficit in OECD member nations. Observed and projected size of the incoming (20–24) and outgoing (60–64) working-age cohorts in OECD countries, 2000–2030. Source: OECD figures, Oxford Institute of Population Ageing, 2012.

(i) The total amount of ill health and disability in the population will rise because as societies improve their population life expectancy, the proportion of the population with serious health problems will increase unless there is a considerable improvement in the health of successive birth cohorts (which would manifest as a decrease over time in age-specific prevalence rates). This has been termed "epidemic of frailty" (*35*).

(ii) Changes in the type of ill health will arise from the shift from acute infectious disease to complex chronic long-term ill health and disability. This has been termed the chronic disease burden (*36*, *37*) and will exert pressure for a major shift in the allocation of health care resources and the configuration of services.

Therefore, even if population aging does not exert pressure for additional resources to be channeled into the health care system, it is likely to exert pressure for the development and improvement of services for people with complex health needs, and this may require a large shift in the allocation of resources as well as large-scale organizational change.

(iii) Population aging will affect a society's capacity to provide workers to care for the older population, as well as its ability to generate income to finance this. The changes in the dependency ratios discussed earlier will particularly affect the health care sector. In addition, demographic change will reduce informal family care through a reduction in the availability of younger family members to provide such care. This will increase the demand for formal care services, at a time when the provision of overseas migrants providing health care is reduced as their own societies start to age. This will also occur at a time when the epidemiological transition is toward labor-intensive chronic disease care.

Addressing the health and social care challenge

One approach is to maintain health among older populations for as long as possible, thus reducing the requirement to provide and finance long-term health and social care. A second approach focuses on the economic relationship between changing age structure and health care costs, and how this might evolve with changing population age structures.

Postponement of frailty and disability

Will declines in mortality be accompanied by declines in morbidity (i.e., disease and disability)? There is currently evidence that through healthy living and disease prevention, the onset of disability is being pushed back into our 80s (*38*). Will these gains in healthy years continue as we increasingly turn to science and technology to extend our lives? The "compression of morbidity" hypothesis (*39*, *40*) suggests that disability and frailty are compressed toward the end of life at a faster pace than death rates. Therefore, people are expected to live not only longer, but also in better health. Alternatively, the "expansion of morbidity" hypothesis (*41*–*43*) claims that the decline in mortality is largely due to the decreasing death rate of diseases, rather than due to a reduction in their incidence. As a result, falling mortality is accompanied by an increase in morbidity and disability. The "dynamic equilibrium" hypothesis (*44*) suggests a counterbalancing effect between the decreasing prevalence/incidence of chronic diseases and the decreasing fatality rates of such diseases. This is leading to longer periods of living with disability toward the end of one's life.

The evidence is equally mixed. Studies from the United States suggest that younger cohorts of elderly persons are living longer in better health (*45*); studies from Japan, the world's oldest country, suggest that as life expectancy reaches very high ages, most of the gained years are lived in poor health (*46*). For now we can conclude that although both life expectancy and healthy, disability-free life expectancy may be increasing, disability as a proportion of life after age 65 is also slowly increasing (*47*). Science, technology, and medicine—the modern drivers of longevity—are not only increasing our life expectancy but are also enabling us to live longer at the end of our lives with disease, disabilities, and frailties (Fig. 4).

Health care costs

Over the past 40 years, health care costs in most advanced countries have been rising on average between 1 and 2% faster than GDP (*48*). The age structure of a population is seen to be an important determinant of health care costs. Costs are high for infant and maternal care, and rise again as we age, from around age 55 for men and 60 for women. Yet, although per capita health spending does increase quite steeply once people reach their 60s, repeated analyses of age-related data on health spending have shown that proximity to death is more important than age per se as a predictor of the consumption of health resources (*49*–*51*). In other words, health care spending is heavily concentrated in the last few years of life, so much so that some analysts have argued that aging per se has virtually no effect on the way that the consumption of health care resources increases with age (*52*). However, in many advanced economies, aging of the large cohorts born in the middle of the 20th century will over the coming decades increase the proportion of the population in close proximity to their death and will inevitably increase health care consumption.

Although a number of cross-national studies have considered the determinants of health care costs, only one has found that the proportion of population aged 65 and over is the explanatory factor (*53*). Indeed, in advanced economies at least, per capita health care costs for those aged 65 years and over have increased at the same rate as for those aged less than 65 (*54*). In many countries, per capita spending on health care is reduced after age 85. This is partly due to the view still held in many societies that spending should be directed to the young when resources are limited; partly due to the lack of research, and thus innovation, in treatments for the very old; and partly due to the lower demands made by these cohorts relative to working-age adults. All three factors are likely to change as the more demanding younger cohorts reach old-old age.

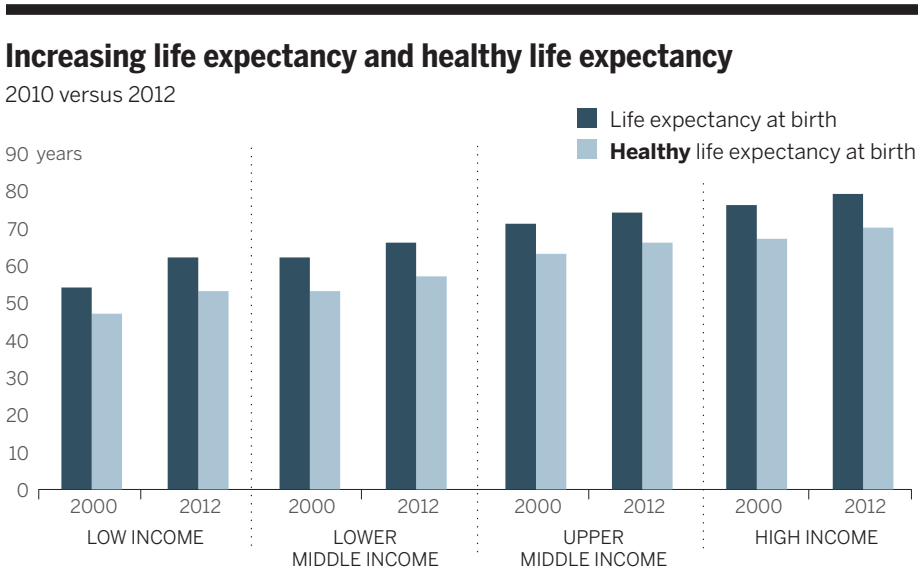

Fig. 4. Life expectancy versus healthy life expectancy. Source: Life expectancy data by World Bank income group; World Health Organization, Global Health Observatory Data Repository (http://apps.who.int/gho/data/view.main.700?lang=en).

It is the wider effects of income, lifestyle characteristics, and new technology, alongside the effects of environmental factors, that are driving up the demand for new advanced medical applications. Indeed, technological change in health care delivery has been the main driver, with up to half of the increase in health care spending in advanced economies over the past 50 years arising from medical technology (*55*). In addition, medical innovations now allow for the treatment of previously untreatable conditions, which also increases medical costs (*56*).

Addressing the social challenge

Change in age composition is altering the structure of families and the life course. Such change also brings into question the traditional contract between the generations, and raises queries around the reconfiguration of social institutions to deal with issues of inter- and intragenerational fairness that may arise as a result of population aging. In particular, inequalities in access to health, economic, and social resources—both between and within generations—are likely to remain a pressing concern over the coming decades.

Changing family structures

Changes in fertility and mortality are leading to a decrease in the number of living relatives within each generation (*16*, *57*). As fertility falls, and as the intervals between the generations increase because of late first childbearing, we may well see a contraction in the number of family generations alive at one time. Longevity is increasing the duration spent in certain kinship roles, such as spouse, parent of nondependent child, and sibling. Falling fertility has reduced the duration of others, such as parent of dependent child, or even the opportunity for some roles, such as sibling.

Delaying life transitions

Paradoxically, while public and legal institutions are generally lowering the age threshold into full legal adulthood, individuals are choosing to delay many of the transitions into full adulthood—full economic independence from parents, formal adult union through marriage or committed long-term cohabitation, and parenting—with a continued increase of age at first marriage, at leaving the parental home, and at first childbirth. Within the family, delayed transitions in younger life lead to subsequent transition delay for both the individual and other kin members. For example, delayed birth of a first child may lead to a long intergenerational interval and a later transition to both parenthood and grandparenthood. Similarly, extended economic dependence on parents not only delays the individual's full transition to independent adulthood, but also delays the experience of the empty-nest syndrome for the parents themselves. Awareness of ever-lengthening life spans may have given individuals at all ages the time and the liberty to delay these transitions as they progress through adulthood (*16*, *18*).

Inter- and intragenerational fairness and the changing intergenerational contract

The question of intergenerational fairness raises the issue of ensuring that both those generations who are working and those who are now retired will benefit from the proceeds of any economic growth. These factors need to be addressed together with intragenerational inequalities, which arise through differential access to education and employment opportunities.

There is also some questioning of the traditional contract between the generations, which has been based historically on a system of intergenerational reciprocity. Adults provide for young dependents (children) and in return, when those young dependents become adults, they provide for older dependents. This is maintained in most societies both directly at the familial level and at a societal level, with adults within the labor market providing via public transfers for both older and younger dependents. The question for an aging population is whether successful cohorts (in terms of both fertility and mortality reduction) pass the cost of such success onto future cohorts via the traditional intergenerational contract or a renegotiated one. This latter contract would require older cohorts to bear the costs of their longer lives, through (for example) higher postretirement contributions to their own welfare and/or a longer working life.

Conclusion

A variety of new policies are now being developed in the light of population aging, including broad, coherent, and integrated multi-pillar approaches to labor markets, health, and social security (*58*). These should enable and promote longer working lives through life long training, education and skills updating, and the provision of appropriate working environments for older workers. They should further ensure that private family or household transfers are integrated into old-age security systems where possible; promote well-being and enable healthy active living to reduce chronic illness and health care costs and support active contributory life for as long as possible; and provide access to education across the life course to ensure that all individuals are prepared physically, mentally, socially, and financially to cope with increasing individual responsibility for old age.

Moreover, it should be recognized that the major concerns listed above are dynamics of current cohorts and current behaviors. They are not fixed. Europe, which has had more than 100 years to prepare for its aging population, is still struggling with these questions. Yet the greatest challenges of global population aging may not be in Europe, but rather in the rapidly changing demography of Asia and Latin America—regions that are moving from being predominantly young to being predominantly old within just 25 years.

REFERENCES AND NOTES

1. United Nations, *World Population Prospects: The 2012 Revision* (medium variant) (2013); http://esa.un.org/wpp.
2. D. E. Bloom, D. Canning, G. Fink, *Oxf. Rev. Econ. Policy* **26**, 583–612 (2010).
3 Total fertility rate is the conventional annual measure of the birth rate, calculated as the average number of children per woman implied by current birth rates of women of all ages in a given year.
4. Eurostat, "Total fertility rate" (Publications of the European Communities, 2013); http://epp.eurostat.ec.europa.eu/tgm/table.do?tab=table&init=1&language=en&pcode=tsdde220&plugin=1.
5. H. P. Blossfeld, E. Klijzing, M. Mills, K. Kurz, *Globalization, Uncertainty and Youth in Society: The Losers in a Globalizing World* (Routledge, New York, 2005).
6. M. Kreyenfeld, *Eur. Sociol. Rev.* **26**, 351–366 (2010).
7. T. Sobotka, V. Skirbekk, D. Philipov, *Popul. Dev. Rev.* **37**, 267–306 (2011).
8. J. C. Caldwell, *Popul. Dev. Rev.* **6**, 225–255 (1980).
9. M. Mills, R. R. Rindfuss, P. McDonald, E. te Velde, *Hum. Reprod. Update* **17**, 848–860 (2011).
10. S. P. Morgan, H. Rackin, *Popul. Dev. Rev.* **36**, 91–118 (2010).
11. M. Iacovou, L. P. Tavares, *Popul. Dev. Rev.* **37**, 89–123 (2011).
12. W. Lutz, V. Skirbekk, M.R. Testa, The low fertility trap hypothesis: Forces that may lead to further postponement and fewer births in Europe. *Vienna Yearb. Popul. Res.* **4**, 167–192 (2006); www.iiasa.ac.at/publication/more_XJ-06-027.php.
13. S. Basten, L. Lutz, S. Scherbov, *Demogr. Res.* **28**, 1145–1166 (2013).
14. J. W. Vaupel, *Nature* **464**, 536–542 (2010).
15. K. Howse, Policy-making for a new generations of interventions in age-related disease and decline. In *Enhancing Human Capacities*, J. Savelscu, R. ter Meulen, G. Kahane, Eds. (Wiley-Blackwell, Oxford, 2011).
16. S. Harper, *Ageing Societies: Myths, Challenges and Opportunities* (Hodder Arnold, London, 2006).
17. S. Harper, *Families in Ageing Societies* (Oxford Univ. Press, Oxford, 2004).
18. S. Harper, A diverse world. In *People and the Planet* (Royal Society, 2012), chap. 2; www.interacademies.net/File.aspx?id=25028.
19. J. C. Chesnais, *Rev. Popul. Soc. Policy* **7**, 83–101 (1998).
20. L. Fina-Sanglas, Europe's population and labour market beyond 2000: Main issues and policy implications. In *Europe's Population and Labour Market Beyond 2000, Population Studies, 33*, A. Punch, D. L. Pearce, Eds. (Council of Europe, 2000), pp. 43–111.
21. R. Lee, A. Mason, *Eur. J. Popul.* **26**, 159–182 (2010).
22. R. Lee, A. Mason, *Population Aging and the Generational Economy: A Global Perspective* (Edward Elgar, Cheltenham, UK, 2011).
23. EU25 data are available for this measure, rather than EU27.
24. Eurostat, "Projected old-age dependency ratio" (Publications of the European Communities, 2013); http://epp.eurostat.ec.europa.eu/tgm/table.do?tab=table&init=1&plugin=1&language=en&pcode=tsdde511.
25. A. C. D'Addio, M. Mira d'Ercole, *Trends and Determinants of Fertility Rates in OECD Countries: The Role of Policies* (Organisation for Economic Cooperation and Development, Paris, 2005).
26. A.C. D'Addio, M. Mira d'Ercole, *Policies, Institutions and Fertility Rates: A Panel Data Analysis for OECD Countries* (Organisation for Economic Cooperation and Development, Paris, 2005).
27. OECD, *Babies and Bosses—Reconciling Work and Family Life: A Synthesis of Findings for OECD Countries* (Organisation for Economic Cooperation and Development, Paris, 2007).
28. C. Dustmann, T. Frattini, C. Halls, *Fiscal Stud.* **31**, 1–41 (2010).
29. H. Brücker, "Can international migration solve the problems of European labour markets?" (United Nations Economic Commission for Europe, 2002); www.unece.org/fileadmin/DAM/ead/sem/sem2002/papers/Brucker.pdf.
30. H. Fehr, S. Jokisch, S. Kotlikoff, "The role of immigration in dealing with the developed world's demographic transition" (NBER Working Paper 10512, National Bureau of Economic Research, 2004); www.nber.org/papers/w10512.
31. S. Harper, *Int. Soc. Secur. Rev.* **63**, 177–196 (2010).
32. D. E. Bloom, A. Boersch-Supan, P. McGee, A. Seike, "Population aging: Facts, challenges, and responses" (Program on the Global Demography of Ageing Working Paper 71, Harvard Initiative for Global Health, 2011); http://cdn1.sph.harvard.edu/wp-content/uploads/sites/1288/2013/10/PGDA_WP_71.pdf.
33. K. Haberkern, M. Szydlik, *Ageing Soc.* **30**, 299–323 (2010).
34. K. Howse, *Perspect. Pub. Health* **132**, 171–177 (2012).
35. J. M. Robine, C. Jagger, *Ageing Horizons* **3**, 14–21 (2005).
36. E. Nolte, C. M. McKee, *Health Aff.* **27**, 58–71 (2008).
37. D. Stuckler, *Milbank Q.* **86**, 273–326 (2008).
38. J. M. Robine, Y. Saito, C. Jagger, *Exp. Gerontol.* **38**, 735–739 (2003).
39. J. F. Fries, *N. Engl. J. Med.* **303**, 130–135 (1980).
40. J. F. Fries, *Milbank Q.* **67**, 208–232 (1989).
41. R. M. Gruenberg, *Milbank Mem. Fund Q.* **55**, 3–24 (1977).
42. L. Verbrugge, *Milbank Mem. Fund Q.* **62**, 475–519 (1984).
43. S. J. Olshansky, M. A. Rudberg, B. A. Carnes, C. K. Cassel, J. A. Brody, *J. Aging Health* **3**, 194–216 (1991).
44. K. G. Manton, *Milbank Q.* **60**, 183–244 (1982).
45. K. G. Manton, *Annu. Rev. Public Health* **29**, 91–113 (2008).
46. V. Yong, Y. Saito, *Demogr. Res.* **20**, 467–494 (2009).
47. C. Jagger *et al*., *Age Ageing* **38**, 319–325 (2009).
48. E. Jenkner, A. Leive, *Health Care Spending Issues in Advanced Economies* (International Monetary Fund, Washington, DC, 2010).
49. K. Howse, "What kinds of policy challenge does population ageing generate for healthcare systems?" (IARU Working Paper, Oxford Institute of Population Ageing, 2010).
50. P. Zweifel, S. Felder, A. Werblow, *Geneva Pap. Risk Insur. Issues Pract.* **29**, 652–666 (2004).
51. M. Seshamani, A. Gray, *Age Ageing* **33**, 556–561 (2004).
52. P. Zweifel, S. Felder, M. Meiers, *Health Econ.* **8**, 485–496 (1999).
53. G. W. Leeson, "Cost effectiveness and interventions" (Working Paper WP204, Oxford Institute of Population Ageing, 2004); www.ageing.ox.ac.uk/files/workingpaper_204.pdf.
54. M. Seshamani, A. Gray, *Appl. Health Econ. Health Policy* **2**, 9–16 (2003).
55. S. Smith, J. P. Newhouse, M. S. Freeland, *Health Aff.* **28**, 1276–1284 (2009).
56. F. Breyer, J. Costa-Font, S. Felder, *Oxf. Rev. Econ. Policy* **26**, 674–690 (2010).
57. V. L. Bengtson, *J. Marriage Fam.* **63**, 1–16 (2001).
58. S. Harper, K. Hamblin, *International Handbook on Ageing and Public Policy* (Edward Elgar, Cheltenham, UK, 2014).

10.1126/science.1254405

RESEARCH

Dissecting the microRNA messenger RNA repression complex
Schirle et al., *p. 608*

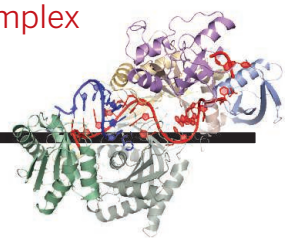

IN *SCIENCE* JOURNALS

Edited by **Stella Hurtley**

Lake Toba, northern Sumatra

VOLCANOLOGY

Imaging before an unimaginable eruption

Volcanic super-eruptions eject thousands of times the volume of the largest documented eruptions over human history. Several "supervolcanoes" capable of this type of unimaginable devastation dot the surface of Earth today. Jaxybulatov *et al*. use seismic background noise to estimate the size and maturity of one of the world's largest volcanic reservoirs, the Toba caldera in northern Sumatra. Magma storage under the caldera occurs slowly over time, in the form of horizontal layers of magma injected into the crust. These magmatic sills are documented to 20 kilometers below the surface, but more sills could exist even deeper. The characterization of magma storage in large volcanic systems may help us to prepare for future volcanic super-eruptions. — BG

Science, this issue p. 617

EARTH HISTORY

Low oxygen limited the rise of animals

Oxygen levels in Earth's early atmosphere had an important influence on the evolution of complex life. Planavsky *et al*. analyzed the isotopic signature of chromium in sedimentary rocks from across the globe—a proxy for past oxygen levels. Oxygen levels in the mid-Proterozoic (1.6 billion to 900 million years ago) were very low: less than 0.1% of the modern atmosphere. These low levels were probably below the minimum oxygen requirements for the earliest animals, delaying their emergence and diversification. — NW

Science, this issue p. 635

NUCLEAR PHYSICS

Scattering electrons off nuclear targets

Atomic nuclei consist of fermions—protons and neutrons—bound together by interactions. Because two identical fermions cannot occupy the same quantum state, both protons and neutrons have a broad range of momenta inside the nucleus. Hen *et al.* scattered electrons off nuclei of varying sizes to study the distribution of the protons' and neutrons' momenta. Protons formed high-momentum pairs with neutrons much more frequently than with other protons. Thus, surprisingly, the average momentum of a neutron was lower than that of a proton, even in nuclei with a larger number of neutrons than protons. — JS

Science, this issue p. 614

EARLY SOLAR SYSTEM

History recorded in asteroid's water

Astronomers know that interstellar water is abundantly available to young planetary systems—our blue planet collected (or accreted) plenty of it. Still, the details of water's movement in the inner solar system are elusive. Sarafian *et al.* measured water isotopes in meteorite samples from the asteroid Vesta for clues to the timing of water accretion. Their samples have the same isotopic fingerprint of volatiles as both Earth and carbonaceous chondrites, some of the most primitive meteorites. The findings suggest that Earth received most of its water relatively early from chondrite-like bodies. — MMM

Science, this issue p. 623

WILDLIFE DISEASE

A new, yet old, threat to amphibians

Globally, populations of amphibians have been severely affected by a disease caused by the fungus *Batrachochytrium dendrobatidis*. Recently, some European salamander populations were decimated by the emergence of a new, related chytrid fungus, *B. salamandrivorans*. Martel *et al.* screened amphibians across continents. This newly emerging threat seems to have originated in Asia and traveled to Europe with salamanders transported as part of the pet trade. Asian salamanders have evolved resistance to the pathogen, but salamanders from other parts of the world are highly susceptible. — SNV

Science, this issue p. 630

Published by AAAS

NEURODEGENERATION

Hunting for the effects of huntingtin

Huntington's disease (HD) is associated with a mutant form of the protein huntingtin (Htt). HD-associated symptoms are alleviated by inhibition of the kinase mTOR, which activates protein synthesis when amino acids are plentiful. In mouse striatal neurons, Pryor *et al.* found that wild-type Htt stimulated amino acid–induced mTOR signaling by enhancing its interaction with an activating protein. Mutant Htt promoted this interaction even when amino acid availability was not increased. In a mouse model of HD, activating mTOR in striatal neurons accelerated the onset of symptoms. — LKF

Sci. Signal. **7**, ra103 (2014).

PLANT GENETICS

Y male plants affect female development

Although most plants have both male and female organs within a single flower, some produce separate male and female plants. In some cases, such as persimmons, males are determined by a Y chromosome. Akagi *et al.* examined the gene transcript differences between male and female persimmons. A gene on the Y chromosome regulated a non–sex chromosome–linked small RNA that suppresses female organ development. This small RNA was localized to male flowers and could affect female development in other plant species. The evolutionary history of these genes suggests that they are tied to the origin of the separation of sexes in the persimmon family. — LMZ

Science, this issue p. 646

Persimmons separate the sexes

BEHAVIORAL ECONOMICS

How to increase charitable donations

Charities could raise more money from more people if they were to announce that a startup grant had been used to defray overhead expenses. Gneezy *et al.* told 40,000 potential donors that an initial donation (half of the target amount) would be used as seed money, as a source of matching funds, or for covering administrative and fundraising costs. When the money was assigned to cover administration, twice as many people made donations. — GJC

Science, this issue p. 632

NANOMEDICINE

Nanoparticles for molecular cancer imaging

Tiny particles can be coated with antibodies or peptides to target a molecule specific to cancer, improving diagnostic accuracy and patient stratification. Yet these decorated nanoparticles have been slow in making it to clinical trials. Now, Phillips *et al.* describe the translation of ultrasmall (<10 nm) inorganic nanoparticles, called "C dots," from animals to patients. The nanoparticles were not toxic in a small group of five patients with metastatic melanoma and were excreted intact via the kidneys and bladder. In contrast, larger or uncoated particles often get lodged in the liver. Many more studies in patients will be needed to confirm lack of toxicity and to optimize tumor targeting, but now that such ultrasmall nanoparticles can be tested in people, a new era of molecular cancer imaging has begun. — MLF

Sci. Transl. Med. **6**, 260ra149 (2014).

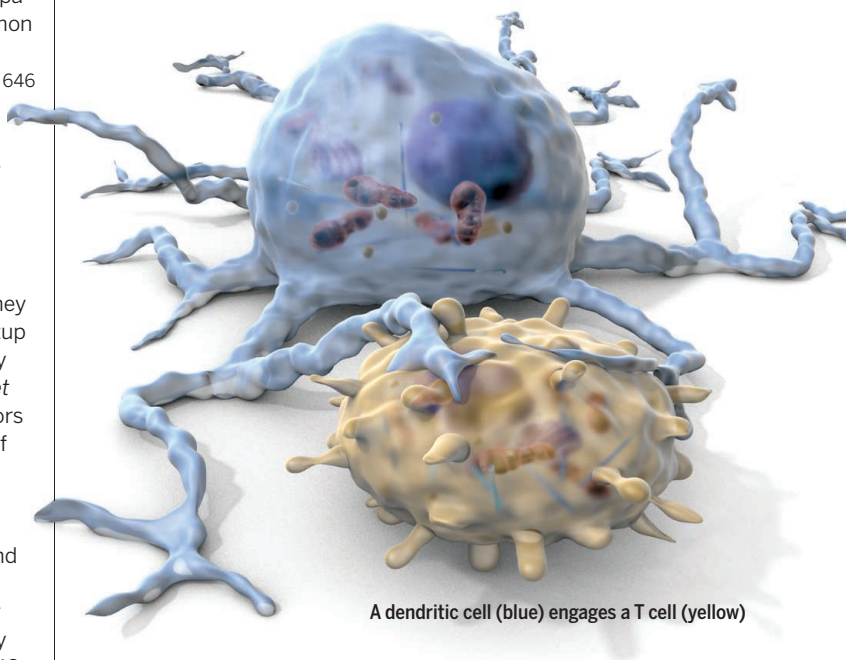

A dendritic cell (blue) engages a T cell (yellow)

CANCER IMMUNOLOGY

A dendritic cell target for immunotherapy

Cancer immunotherapies work by activating T cells to kill tumors. Antigen-presenting cells (APCs), such as dendritic cells and macrophages, activate T cells by engaging protein receptors on the T cell surface. This then tells the T cells to attack the tumors. But T cells typically cannot attack tumors because the immunosuppressive microenvironment of tumors keeps APCs from turning these signals on. Broz *et al*. now report, however, that low numbers of dendritic cells capable of activating T cells exist in tumors in mice. T cell–mediated clearance of tumors depended on these cells. In humans, an increased genetic signature of these cells correlated with better outcomes in a variety of tumor types. — KLM

Can. Cell 10.1016/j.ccell.2014.09.007 (2014).

GEOCHEMISTRY

Monitoring the mineral-water interface

At a microscopic level, mineral-water interfaces are vast, ever-changing landscapes. Individually, these interfaces have a trivial influence on the environment, but on a global scale they help drive important geochemical reactions such as the uptake of CO_2 from the atmosphere during chemical weathering. Siebecker *et al.* used fast-resolved x-ray absorption spectroscopy to monitor real-time mineral growth and dissolution on Al-rich pyrophyllite clay in a flowing Ni-rich solution. Not only did precipitation of mixed Ni-Al layered hydroxides occur on extremely fast time scales, but it occurred as a consequence of the rapid release of Al from the simultaneously dissolving pyrophyllite. — NW

Nat. Comm. 10.1038/ncomms6003 (2014).

ALSO IN *SCIENCE* JOURNALS

Edited by **Stella Hurtley**

NANOMATERIALS

Supported nanoparticles make the reaction faster

Several techniques now allow surface structures used as catalysts to be probed during exposure to reactive gases, as opposed to under vacuum conditions. Divins *et al.* used near-ambient-pressure x-ray photoelectron spectroscopy to compare the effect of reaction gases on unsupported palladium-rhodium nanoparticles versus ones on a reducible cerium oxide support. For the reaction of ethanol with steam to produce hydrogen, the supported nanoparticles were more reactive and less prone to reduction and surface rearrangement. — PDS

Science, this issue p. 620

TOPOLOGICAL MATTER

A possible sighting of Majorana states

Nearly 80 years ago, the Italian physicist Ettore Majorana proposed the existence of an unusual type of particle that is its own antiparticle, the so-called Majorana fermion. The search for a free Majorana fermion has so far been unsuccessful, but bound Majorana-like collective excitations may exist in certain exotic superconductors. Nadj-Perge *et al.* created such a topological superconductor by depositing iron atoms onto the surface of superconducting lead, forming atomic chains (see the Perspective by Lee). They then used a scanning tunneling microscope to observe enhanced conductance at the ends of these chains at zero energy, where theory predicts Majorana states should appear. — JS

Science, this issue p. 602; see also p. 547

CONSERVATION

How to achieve win-win outcomes for biodiversity

Ecosystems serve many functions, such as helping to guard against flooding or ensuring pollination by wild bees. Can efforts to conserve biodiversity rely on the economic benefits from such "ecosystem services"? In a Perspective, Adams argues that win-win outcomes are possible where economic and conservation benefits align. He cautions, however, that the ecosystem service concept is not a conservation measure in itself and that numerous conditions must be met for ecosystem service values to favor conservation. — JFU

Science, this issue p. 549

MEMBRANE TRAFFICKING

You've got to pick a Golgi tether or two

The inside of the cell contains a large variety of different membrane transport vesicles, each of which needs to find and fuse with its correct target destination. The detailed mechanism specifying which vesicle can fuse with which target membrane has been the subject of an enormous amount of research. An additional layer of specificity in intracellular membrane trafficking across the Golgi complex is thought to involve particular membrane "tethers." However, the importance of these tethers has been unclear. Wong and Munro used a clever trick to reveal how specific tethers can indeed ensure correct vesicle destination. Tether proteins experimentally expressed on mitochondria hijacked different transport vesicles and diverted them from their normal destination to the mitochondria. — SMH

Science, this issue p. 601

GENE REGULATION

Repressing the right (and not the wrong) mRNA

MicroRNAs (miRNAs) are small noncoding RNAs that regulate gene expression by targeting a repressor complex to specific messenger RNAs (mRNAs). Schirle *et al.* determined structures of a miRNA bound to both the central component of the repressor complex, the protein Argonaute-2 (Ago2), and a target mRNA (see the Perspective by Patel). The miRNA in the complex first recognizes a short region of complementary sequence in the mRNA. This initial interaction promotes structural changes that allow the complex to bind additional target sequences. The authors suggest that in the absence of extensive miRNA-mRNA pairing, the repressor complex active site is rendered inactive, preventing repression of nontarget mRNAs. — GR

Science, this issue p. 608; see also p. 542

NEURODEVELOPMENT

Making dendritic arbors during development

Developing axons are known to compete for limiting, target-derived neurotrophins for survival and growth in the peripheral nervous system. Joo *et al.* suggest that an additional, reciprocal model is involved in the development of dendritic arbors of cerebellar Purkinje cells. Working in mice, the authors show that growing dendrites of Purkinje neurons require presynaptic partner-derived neurotrophins during competitive dendritic growth in the central nervous system. — PJH

Science, this issue p. 626

CHEMICAL BIOLOGY

Epigenetics: It's all about the individual

The bromodomain and extraterminal domain (BET) proteins are a family of epigenetic regulators that affect transcription through interactions with acetylated chromatin. These proteins have attracted interest as drug targets because of their roles

in human diseases, including cancer. Parsing out the biological functions of individual family members is important for drug development but has been challenging because of the proteins' shared structural domains. In a proof-of-concept study, Baud *et al*. used a chemical genetics strategy to design a highly selective small-molecule probe that inhibits the chromatin binding activity of one family member. Extension of this approach may help elucidate the function of individual BET proteins and prioritize them as drug targets. — PAK

Science, this issue p. 638

CELL ADHESION

Pulling me apart only makes me stronger

Tension transmitted between neighboring cells can exert profound effects on cell proliferation, differentiation, and tissue organization. Exactly how intercellular mechanical tension is sensed at the molecular level is unknown. One attractive hypothesis is that a linkage between the cell-cell adhesion molecule E-cadherin, its binding partners α- and β-catenin, and actin filaments may act as a tension sensor. However, how this linkage is established at the molecular level is not known. Buckley *et al.* used optical tweezers to determine how mechanical load influences interactions of the cadherin/catenin complex with single actin filaments. The data support a model in which force shifts the interaction from a force-independent, weakly bound state to a highly force-sensitive, strongly bound state. The findings may explain how cells maintain tissue integrity while still being able to move and change shape. — SMH

Science, this issue p. 600

INNATE IMMUNITY

Overcoming staph infections is hardwired

Several evolutionarily conserved components of antistaphylococcal immunity have been identified, using *Drosophila* as a model organism. However, no vertebrate ortholog has been identified for the Toll ligand Spaetzle, which plays a key role in controlling gram-positive infection in flies. Hepburn *et al.* have now identified NGF-β as a functional equivalent to Spaetzle in vertebrates. NGF-β acts as a paracrine "alarmin" orchestrating macrophage and neutrophil responses to *S. aureus* infection. People with deleterious mutations in genes encoding NGF-β or its high-affinity receptor TRKA are predisposed to recurrent and severe staph infections. *S. aureus* proteins selectively trigger macrophage production of NGF-β, which enhances uptake and superoxide-dependent killing of *S. aureus*, stimulates proinflammatory cytokine production, and promotes neutrophil recruitment. Moreover, TrkA silencing in vivo increases susceptibility to *S. aureus*. Thus, the NGF-β–TRKA pathway is a critical, evolutionarily conserved component of vertebrate immunity to *S. aureus* infection. — SMH

Science, this issue p. 641

NEURODEGENERATION

Hunting for the effects of huntingtin

Huntington's disease (HD) is associated with a mutant form of the protein huntingtin (Htt). HD-associated symptoms are alleviated by inhibition of the kinase mTOR, which activates protein synthesis when amino acids are plentiful. In mouse striatal neurons, Pryor *et al.* found that wild-type Htt stimulated amino acid–induced mTOR signaling by enhancing its interaction with an activating protein. Mutant Htt promoted this interaction even when amino acid availability was not increased. In a mouse model of HD, activating mTOR in striatal neurons accelerated the onset of symptoms. — LKF

Sci. Signal. **7**, ra103 (2014).

PLANT GENETICS

Y male plants affect female development

Although most plants have both male and female organs within a single flower, some produce separate male and female plants. In some cases, such as persimmons, males are determined by a Y chromosome. Akagi *et al.* examined the gene transcript differences between male and female persimmons. A gene on the Y chromosome regulated a non–sex chromosome–linked small RNA that suppresses female organ development. This small RNA was localized to male flowers and could affect female development in other plant species. The evolutionary history of these genes suggests that they are tied to the origin of the separation of sexes in the persimmon family. — LMZ

Science, this issue p. 646

Persimmons separate the sexes

BEHAVIORAL ECONOMICS

How to increase charitable donations

Charities could raise more money from more people if they were to announce that a startup grant had been used to defray overhead expenses. Gneezy *et al.* told 40,000 potential donors that an initial donation (half of the target amount) would be used as seed money, as a source of matching funds, or for covering administrative and fundraising costs. When the money was assigned to cover administration, twice as many people made donations. — GJC

Science, this issue p. 632

NANOMEDICINE

Nanoparticles for molecular cancer imaging

Tiny particles can be coated with antibodies or peptides to target a molecule specific to cancer, improving diagnostic accuracy and patient stratification. Yet these decorated nanoparticles have been slow in making it to clinical trials. Now, Phillips *et al.* describe the translation of ultrasmall (<10 nm) inorganic nanoparticles, called "C dots," from animals to patients. The nanoparticles were not toxic in a small group of five patients with metastatic melanoma and were excreted intact via the kidneys and bladder. In contrast, larger or uncoated particles often get lodged in the liver. Many more studies in patients will be needed to confirm lack of toxicity and to optimize tumor targeting, but now that such ultrasmall nanoparticles can be tested in people, a new era of molecular cancer imaging has begun. — MLF

Sci. Transl. Med. **6**, 260ra149 (2014).

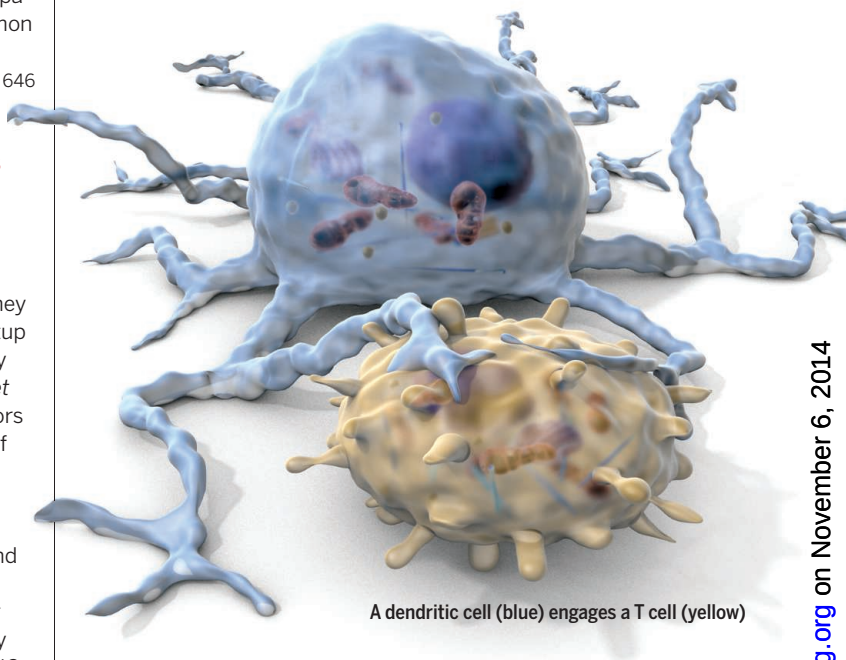

A dendritic cell (blue) engages a T cell (yellow)

CANCER IMMUNOLOGY

A dendritic cell target for immunotherapy

Cancer immunotherapies work by activating T cells to kill tumors. Antigen-presenting cells (APCs), such as dendritic cells and macrophages, activate T cells by engaging protein receptors on the T cell surface. This then tells the T cells to attack the tumors. But T cells typically cannot attack tumors because the immunosuppressive microenvironment of tumors keeps APCs from turning these signals on. Broz *et al.* now report, however, that low numbers of dendritic cells capable of activating T cells exist in tumors in mice. T cell–mediated clearance of tumors depended on these cells. In humans, an increased genetic signature of these cells correlated with better outcomes in a variety of tumor types. — KLM

Can. Cell 10.1016/j.ccell.2014.09.007 (2014).

GEOCHEMISTRY

Monitoring the mineral-water interface

At a microscopic level, mineral-water interfaces are vast, ever-changing landscapes. Individually, these interfaces have a trivial influence on the environment, but on a global scale they help drive important geochemical reactions such as the uptake of CO_2 from the atmosphere during chemical weathering. Siebecker *et al.* used fast-resolved x-ray absorption spectroscopy to monitor real-time mineral growth and dissolution on Al-rich pyrophyllite clay in a flowing Ni-rich solution. Not only did precipitation of mixed Ni-Al layered hydroxides occur on extremely fast time scales, but it occurred as a consequence of the rapid release of Al from the simultaneously dissolving pyrophyllite. — NW

Nat. Comm. 10.1038/ncomms6003 (2014).

The Colosseum in February 2012, during a cold wave that swept across Europe.

CLIMATE SCIENCE

Sea-ice loss behind Eurasia's chills

Severe winters, such as the deadly cold wave from January to February 2012 that blanketed Europe with snow, are becoming more frequent across Eurasia. Some scientists contend that Arctic sea-ice loss is responsible, but modelers haven't pinpointed a climate link. Mori *et al*. identified two circulation patterns that drove winter temperatures in Eurasia from 1979 to 2013: the Arctic Oscillation (which confines colder air to the polar latitudes) and a pattern dubbed "Warm Arctic and Cold Eurasia" (WACE), which correlated both to sea-ice loss in the Barents-Kara Sea and to particularly cold winters; its impact has more than doubled the probability of severe winters in central Eurasia. But by the end of the century, the Arctic Oscillation could overpower WACE's cooling effect, bringing temperatures back up. — CG

Nat. Geosci., 10.1038/ngeo2277 (2014).

QUANTUM PHYSICS

Making a measure of quantum coherence

The notion that particles have properties of waves lies at the heart of quantum mechanics. When quantum systems interact, their interaction can be described in terms of interfering waves, whose coherence is of utmost importance in working out how these waves ultimately interfere. Determining how much coherence there is in a system or how much is required for a particular process is difficult to quantify, though. Baumgratz *et al.* present a rigorous mathematical framework for the quantification of coherence and identify intuitive and easily computable measures that can be used to compute it. They argue that having such a quantifiable metric will have important implications for describing energy transfer processes or transferring quantum information between quantum elements. — ISO

Phys. Rev. Lett. 10.1103/PhysRevLett.113.140401 (2014).

AGING

A drug fights off ravages of aging in mice

Interested in a pill to extend life span and delay the onset of age-related diseases? The answer may lie in targeting the enzyme NAD-dependent deactylase sirtuin 1 (SIRT1): Animals with enhanced activity of SIRT1 show some of these effects. To study the effects of long-term SIRT1 activity, Mercken *et al*. fed mice a synthetic activator of SIRT1 from 6 months of age for the rest of their (~3-year) life span. The treated mice had 5% and 10% increases in maximum and mean life span, respectively. They also resisted many problems associated with human aging. The mice had more stable blood glucose levels, better muscle endurance and balance, less fat, and suppressed inflammatory responses. — LBR

Aging Cell 10.1111/acel.12220 (2014).

ASTRONOMY

A surprise window to the early universe

Less than a billion years after the Big Bang, black holes at the cores of distant quasars had already reached millions of times the Sun's mass, implying a puzzlingly rapid growth rate. To understand the process, astronomers look for their predecessors at even greater distances, but such objects may be cloaked in dust and gas that thwart optical and x-ray detection. Gallerani *et al.* recently detected a millimeter emission line (J = 17 to 16) of the molecule CO in one luminous quasar (J1148) that cuts through dust unabated. If the earliest ancestors of supermassive black holes indeed exist in such thick cocoons, long-wavelength emission lines may offer a way to look at sources that would otherwise lie invisible. — MMM

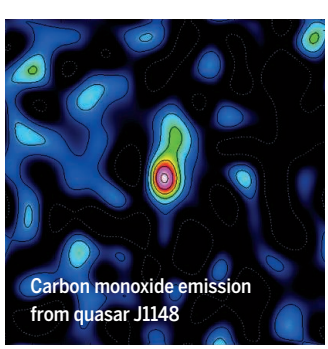

Carbon monoxide emission from quasar J1148

Mon. Not. R. Astron. Soc. 10.1093/mnras/stu2031 (2014).

CANCER GENOMICS

Cancer's deadly mutational tug of war

As cancers grow, they mutate, which allows their continued growth and metastasis. Mutations are either driver mutations—required for tumors to progress—or passenger mutations—additional random mutations that result from such rapid adaptation. How do passenger mutations affect tumors? McFarland *et al*. found that passenger mutations are 100 times more common than driver mutations and have smaller effects on tumors, but the effects are often deleterious. Thus driver and passenger mutations are in a "tug of war" that determines whether a tumor will progress. A better understanding of how passenger mutations accumulate could explain the success of current treatments or provide additional avenues to explore for therapeutic benefit. — LMZ

Proc. Natl. Acad. Sci. U.S.A. 10.1073/pnas.1404341111 (2014).

GENOME EDITING

Dissecting an RNA that dissects genomes

By adapting the immune defense system found in many species of bacteria, scientists can now edit the genome of any organism at will. In this system (called type II CRISPR Cas), a small RNA—the single guide RNA (sgRNA)—guides the enzyme Cas9 to DNA complementary sequences, which Cas9 then cleaves. Looking for how the sgRNA targets Cas9 to DNA, Briner *et al*. identified several structural modules in the sgRNA that determine Cas9 targeting. Some of these motifs also determined which species variant of Cas9 would be targeted. These results may inform the design of more compact and versatile genome editing systems. — GR

Mol. Cell 10.1016/j.molcel.2014.09.019 (2014).

Published by AAAS

RESEARCH ARTICLE SUMMARY

CELL ADHESION

The minimal cadherin-catenin complex binds to actin filaments under force

Craig D. Buckley,* Jiongyi Tan,* Karen L. Anderson, Dorit Hanein, Niels Volkmann, William I. Weis,† W. James Nelson,† Alexander R. Dunn†

INTRODUCTION: Cadherins are an ancient class of transmembrane proteins that are essential for the formation of multicellular tissues in metazoans. Cadherins link intercellular adhesions to the cellular cytoskeleton, but how they are connected specifically to actin filaments is a hotly debated issue. Genetic and cell culture experiments indicate that E-cadherin, β-catenin, and the actin filament binding protein αE-catenin form a minimal cadherin-catenin complex that binds to the actin cytoskeleton directly in epithelial tissues. However, experiments with purified proteins showed that a stable cadherin-catenin complex can be reconstituted, but it does not bind strongly to actin filaments in solution. Nevertheless, cell culture experiments indicated that the cadherin-catenin complex is under constitutive actomyosin-generated tension and that this connection is required for mechanotransduction at cadherin-based adhesions. Here, we tested the hypothesis that tension is required to stabilize a linkage between the cadherin-catenin complex and actin filaments, and clarify how the cadherin-catenin complex could interact directly with the actin cytoskeleton in cells.

RATIONALE: We developed an optical trap–based assay to measure the lifetime of cadherin-catenin complex/actin filament bonds under tension. An actin filament was attached to two optically trapped beads and suspended above purified cadherin-catenin complexes immobilized on a glass coverslip surface that was precoated with glass microspheres. The coverslip was mounted on a motorized stage. This spatial arrangement was informed by electron tomography of cell-cell junctions, which showed actin filaments parallel to the plasma membrane. Tension was applied to cadherin-catenin complex/actin bonds by moving the sample stage back and forth parallel to the actin filament; if the immobilized cadherin-catenin complexes bound the actin filament, the attached beads were displaced from the optical trap. The lifetime of the bond was measured from the time series of the force exerted on the trapped beads. Kinetic models were fit to bond lifetime distributions with respect to applied force.

RESULTS: We observed robust, reproducible cadherin-catenin complex/actin filament binding under force in optical trap–based experiments. Bond lifetime distributions had a biphasic dependence on force. The mean lifetimes increased from ~60 ms at low force to ~1.2 s at ~10 pN, after which they decreased. A two-state catch bond model is consistent with the biphasic mean lifetime distribution and the presence of two distinct lifetime subpopulations. In this model, bonds between a cadherin-catenin complex and an actin filament form in a weakly bound state and quickly dissociate, but rapidly transition to a strongly bound state as applied force increases. Long lifetimes are achieved in this state until higher forces accelerate dissociation from the strongly bound state (see the figure).

ON OUR WEB SITE

Read the full article at http://dx.doi.org/10.1126/science.1254211

CONCLUSION: Our data and kinetic model reconcile previous in vitro and in vivo work by demonstrating that the cadherin-catenin complex binds robustly to actin filaments under force. Thus, it seems that direct cadherin-catenin complex/actin filament binding was not detected in previous solution-based assays because bonds were not strengthened by tension. The two bound states in our model may correspond to different conformational states of αE-catenin, consistent with previous observations that αE-catenin may undergo changes in conformation in response to actomyosin-generated cytoskeletal tension. Our model of cadherin-catenin complex/actin filament bond dissociation, combined with previous evidence of cooperative binding of αE-catenin to actin filaments, indicates that the linkage is self-reinforcing and that its stability is dynamically regulated by mechanical force during tissue development and maintenance. ■

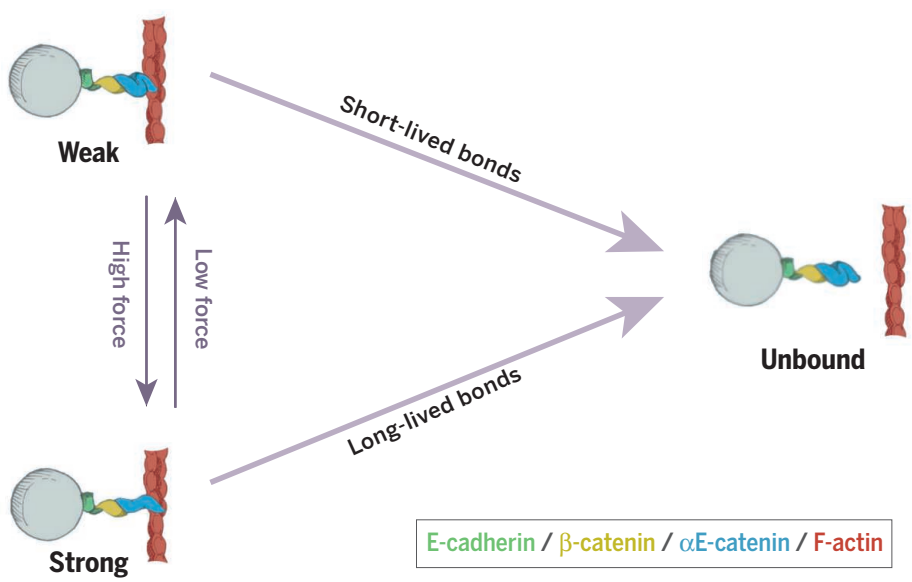

Two-state catch bond model of cadherin-catenin/F-actin interactions. Force stabilizes the cadherin-catenin/F-actin bond by shifting it from a weakly to a strongly bound state. The force dependence of the connection between the cadherin-catenin complex and actin filaments may explain the mechanosensitivity of cadherin-mediated intercellular adhesions.

The list of author affiliations is available in the full article online.
*These authors contributed equally to this work.
†Corresponding author. E-mail: alex.dunn@stanford.edu (A.R.D.); wjnelson@stanford.edu (W.J.N.); bill.weis@stanford.edu (W.I.W.)
Cite this article as C. D. Buckley *et al.*, *Science* **346**, 1254211 (2014). DOI: 10.1126/science.1254211

RESEARCH ARTICLE

CELL ADHESION

The minimal cadherin-catenin complex binds to actin filaments under force

Craig D. Buckley,[1]* Jiongyi Tan,[2]* Karen L. Anderson,[3] Dorit Hanein,[3] Niels Volkmann,[3] William I. Weis,[2,4,5]† W. James Nelson,[5,6]† Alexander R. Dunn[1,2,7]†

Linkage between the adherens junction (AJ) and the actin cytoskeleton is required for tissue development and homeostasis. In vivo findings indicated that the AJ proteins E-cadherin, β-catenin, and the filamentous (F)–actin binding protein αE-catenin form a minimal cadherin-catenin complex that binds directly to F-actin. Biochemical studies challenged this model because the purified cadherin-catenin complex does not bind F-actin in solution. Here, we reconciled this difference. Using an optical trap–based assay, we showed that the minimal cadherin-catenin complex formed stable bonds with an actin filament under force. Bond dissociation kinetics can be explained by a catch-bond model in which force shifts the bond from a weakly to a strongly bound state. These results may explain how the cadherin-catenin complex transduces mechanical forces at cell-cell junctions.

Epithelia serve as barriers between the organism and its environment. A defining feature of these tissues is adhesion between cells at specialized intercellular junctions. The mechanical connection at these junctions imparts shape, organization, and structural integrity to the tissue and enables morphogenetic changes such as the movement of epithelial sheets and the formation of tubes during development (*1*, *2*). Dysregulation of cell-cell junctions is common in cancer metastasis, which is characterized by loss of contact inhibition, epithelial-to-mesenchymal transitions, and abnormal cell invasiveness (*3*).

Classical cadherins and their cytoplasmic binding partners play a central role in intercellular adhesion in many tissues (*4*). In epithelial tissues, the extracellular domain of cadherin forms adhesive contacts between neighboring cells, and its cytoplasmic domain binds β-catenin, which in turn binds the F-actin binding protein αE-catenin (*5*), the most widely expressed of the three α-catenin family members (*6*). αE-catenin binds strongly to the E-cadherin/β-catenin complex [dissociation constant (K_d) ~1 nM] (*7*, *8*) but more weakly to F-actin (K_d ~1 μM) (*9*–*11*). Cell biological studies led to the hypothesis that αE-catenin directly links the E-cadherin/β-catenin complex to F-actin, consistent with its role in force transmission between cadherins and the actin cytoskeleton (*12*). However, in vitro binding of αE-catenin to the cadherin cytoplasmic domain/β-catenin complex further weakens the affinity of αE-catenin for F-actin by at least a factor of 20, to a level that would not be useful for transmitting force between E-cadherin and the actin cytoskeleton (*8*, *10*, *13*).

These biochemical studies, performed with proteins from *Mus musculus* (*Mm*; mouse) and *Danio rerio* (*Dr*; zebrafish), cast doubt on the simple model that αE-catenin directly links the cadherin/catenin complex to the actin cytoskeleton. Other proteins, including vinculin (*14*–*18*), epithelial protein lost in neoplasm (EPLIN) (*19*), α-actinin (*20*), and afadin (*21*, *22*), bind to both αE-catenin and F-actin and could be a link between the cadherin-catenin complex and F-actin. Notably, force exerted on the cadherin-catenin complex appears to recruit vinculin to cell junctions (*15*, *23*–*26*). However, it is unclear how the changes in αE-catenin conformation required for vinculin binding (*14*, *27*) can be induced by force if αE-catenin does not link the E-cadherin/β-catenin complex to F-actin.

Given the importance of actomyosin-generated tension in cell-cell adhesion (*12*, *15*, *25*), we posited that tension stabilizes a direct link between the minimal cadherin-catenin complex and F-actin. Therefore, we developed a single-molecule, optical trap–based assay that replicated the geometry of the adherens junction (AJ) and mechanical forces between cadherin-catenin complexes and actin filaments. We found that the application of physiological, pN-level forces increased the lifetime of normally transient bonds between cadherin-catenin complexes and an actin filament. This behavior is indicative of a catch bond, in which the dissociation rate decreases with applied force (*28*, *29*), rather than the more typical slip bond in which the dissociation rate increases exponentially with increasing applied force. We show that a two-state catch-bond model (*30*) fits the distribution of lifetimes of cadherin-catenin complex/F-actin bonds under force. In this model, the cadherin-catenin complex and an actin filament interact in a short-lived, weakly bound state under low forces and transition to a stable, strongly bound state at higher forces. Thus, our data reveal that the cadherin-catenin complex is a force-sensitive, direct linker to the actin cytoskeleton, and our model offers a kinetic basis for understanding mechanotransduction at AJs.

Experimental approach

To replicate in vitro the spatial organization of the cadherin-catenin complex and F-actin, we examined electron tomographic reconstructions of cell-cell contacts in Caco-2 cells (*31*), which are derived from human intestinal epithelia. These images showed dense arrays of actin filaments parallel to the plasma membrane (Fig. 1, A and B, and fig. S1). Although the centerline distance between cell-cell contacts and the F-actin arrays averaged between 0.5 and 1.5 μm, there were regions where the edges of the parallel F-actin arrays were in close proximity to the cell-cell contacts (see the supplementary text), and in other areas a less dense organization of actin filaments was present between the actin arrays and plasma membrane. Cell-cell contacts are dynamic (*8*, *32*), and therefore these images represent only a temporal snapshot of the proximity of junctions and the underlying actin filament bundles. Parallel actin arrays tended to appear at cell-cell contacts tens of nm above the extracellular matrix (ECM) interface, whereas nonparallel actin networks were spatially correlated with the basal membrane near the ECM contact. These observations are consistent with previous super-resolution microscopy data, which revealed actin filaments parallel to intercellular junctions in simple epithelia (*9*).

Without applied tension, cadherin-catenin complex/F-actin bonds are much weaker than αE-catenin homodimer/F-actin bonds (*8*, *10*, *13*). This difference was apparent in time-lapse movies of tetramethylrhodamine-labeled actin filaments diffusing in solution near the surface of coverslips coated with either 1 μM *Mm* green fluorescent protein (GFP)–E-cadherin/β-catenin/αE-catenin or 2 μM *Mm* GFP–αE-catenin homodimer (K_d for F-actin is ~1 μM) (Fig. 1, C and D). Actin filaments bound stably to *Mm* GFP–αE-catenin homodimers for at least 30 seconds, whereas actin filaments did not bind stably to the reconstituted *Mm* cadherin-catenin complex. Thus, these results replicate previous bulk sedimentation binding assays (*13*, *19*).

To apply tension on transient cadherin-catenin complex/F-actin bonds, we replicated the orientation of actin filaments and cadherin-catenin complexes observed at intercellular junctions in cells (Fig. 1). A single actin filament was optically trapped and extended above *Mm* or *Dr* cadherin-catenin complexes immobilized on a coverslip surface precoated with glass microspheres (*31*) (Fig. 1, E and F). The glass microspheres acted as spacers to prevent the surface of the coverslip from interfering with force measurements. The coverslip was mounted on a stage that moved

[1]Department of Chemical Engineering, Stanford University, Stanford, CA 94305, USA. [2]Biophysics Program, Stanford University, Stanford, CA 94305, USA. [3]Bioinformatics and Structural Systems Biology Program, Sanford-Burnham Medical Research Institute, La Jolla, CA 92037, USA. [4]Department of Structural Biology, Stanford University, Stanford, CA 94305, USA. [5]Department of Molecular and Cellular Physiology, Stanford University, Stanford, CA 94305, USA. [6]Department of Biology, Stanford University, Stanford, CA 94305, USA. [7]Stanford Cardiovascular Institute, Stanford University, Stanford, CA 94305, USA.
*These authors contributed equally to this work. †Corresponding author. E-mail: alex.dunn@stanford.edu (A.R.D.); wjnelson@stanford.edu (W.J.N.); bill.weis@stanford.edu (W.I.W.)

back and forth parallel to the actin filament. Upon formation of cadherin-catenin complex/F-actin bonds, the motion of the stage was transmitted to the trapped beads, and the displacement of beads within the optical trap caused a restoring force that was applied to the cadherin-catenin complex/F-actin bonds (Fig. 2A). The amount of applied force and the rate of its application were controlled by adjusting the frequency and amplitude of the stage oscillation. Because an optical trap works like a simple spring, the magnitude of this force was calculated from the stiffness of the trap and the displacement of the trapped beads caused by this force (*31*).

The cadherin-catenin complex binds to F-actin under tension

Mm cadherin-catenin complexes, added at a concentration of 1 μM to the flow cell, bound an actin filament when the stage was driven back and forth by sine waves with 150-nm amplitudes and frequencies of up to 150 Hz (6.7-ms period) (Fig. 2B). The stage motion was transmitted to the optically trapped beads whenever cadherin-catenin complexes bound to the suspended actin filament (Fig. 2A). We observed many changes in the force experienced by the trapped beads as a function of time, indicating the formation of robust *Mm* cadherin-catenin complex/F-actin bonds (Fig. 2, B and C).

Binding of the cadherin-catenin complex to F-actin required αE-catenin (Fig. 2D and supplementary text). The observed unbinding events were most likely caused by the dissociation of the intact cadherin-catenin complex from the suspended actin filament, rather than dissociation of αE-catenin from the E-cadherin/β-catenin heterodimer. In solution (without applied tension), the αE-catenin monomer binds strongly to E-cadherin/β-catenin (K_d = 1 nM) but binds more weakly by a factor of at least 1000 to F-actin (*7*–*9*, *13*). At the concentrations in our experiments, any αE-catenin molecules that detached from the surface-bound cadherin-catenin complex would occupy a negligible number of binding sites on the actin filament (*31*). Thus, it is unlikely that αE-catenin molecules attached to the actin filament could generate reversible binding events with surface-bound E-cadherin/β-catenin heterodimers. In contrast, the actin filament provided a very large number of binding sites for αE-catenin in the platform-bound cadherin-catenin complexes. Moreover, if αE-catenin separated from the E-cadherin/β-catenin complex during every actin filament-binding event, αE-catenin would most likely dissociate quickly from the actin filament and be irreversibly lost (this assumes a reasonably high off-rate, consistent with the weak affinity of monomeric αE-catenin for F-actin). This scenario would rapidly depopulate a platform of active cadherin-catenin complexes, whereas we observe tens to hundreds of binding events per glass microsphere platform (see, for example,

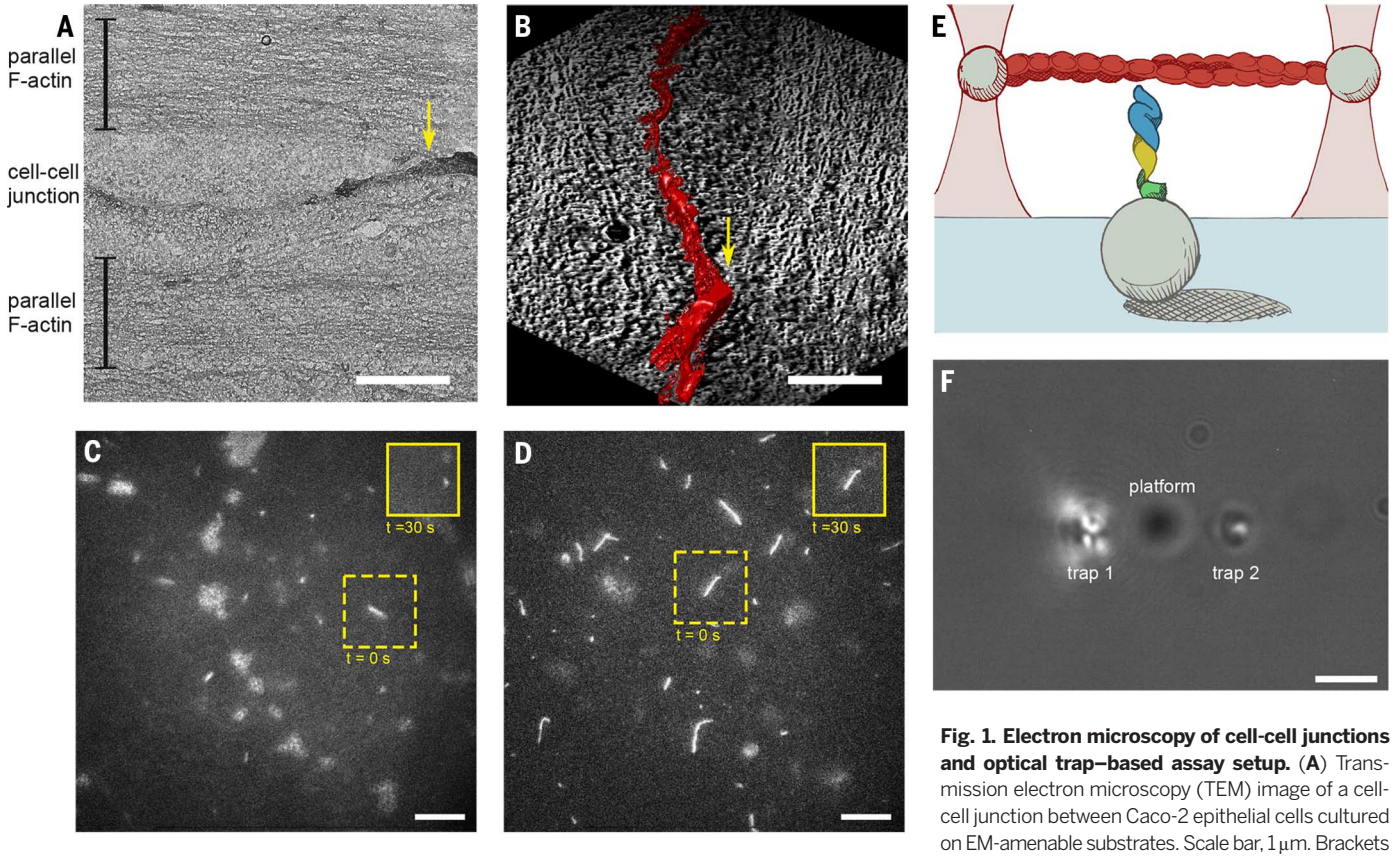

Fig. 1. Electron microscopy of cell-cell junctions and optical trap–based assay setup. (**A**) Transmission electron microscopy (TEM) image of a cell-cell junction between Caco-2 epithelial cells cultured on EM-amenable substrates. Scale bar, 1 μm. Brackets label actin filament arrays parallel to the junction, and the yellow arrow marks where the actin arrays were in close proximity to cell-cell contacts. (**B**) Three-dimensional electron tomography reconstruction of the same region shown in (A) rotated 90° clockwise and then tilted 45° around the horizontal axis. The cell-cell junction is highlighted in red. Yellow arrow marks the same region as in (A). Scale bar, 1 μm. (**C** and **D**) Fluorescence time-lapse micrographs of tetramethylrhodamine (TMR)–labeled F-actin (white lines) at the surface of a coverslip coated with either 1 μM *Mm* cadherin-catenin complex (C) or 2 μM *Mm* αE-catenin homodimer (D). Insets in solid yellow lines show the corresponding images for regions bounded in the dashed yellow lines after 30 s had elapsed; actin filaments remained stably bound to coverslips coated with *Mm* αE-catenin homodimer, whereas actin filaments diffused away from coverslips coated with the *Mm* cadherin-catenin complex within seconds. Out-of-focus features are glass microsphere platforms. Scale bars, 10 μm. (**E**) Illustration of a cadherin-catenin complex and actin filament reconstituted in the optical trap assay (not to scale). GFP–E-cadherin cytoplasmic tail (green), β-catenin (yellow) and αE-catenin (blue) are immobilized on a coverslip. Glass microspheres (1.5-μm diameter) on the coverslip act as platforms such that cadherin-catenin complexes can contact the actin filament. A single biotinylated, TMR-phalloidin-coated actin filament (red) extends between two 1-μm diameter streptavidin-coated beads held in optical traps (pink). (**F**) Top view of the assay in bright field. Beads attached to the actin filament (not visible) are held in traps 1 and 2, and the platform bead is positioned between the traps and below the filament. Scale bar, 2 μm.

Fig. 2C). In any case, the key finding remains that the cadherin-catenin complex bound the actin filament under tension.

Cadherin-catenin complex/F-actin binding was observed more frequently at intermediate stage oscillation speeds (150-nm amplitude, 50-Hz frequency) than at either lower or higher speeds (Fig. 2E). At these intermediate oscillation speeds, the majority of binding events started shortly

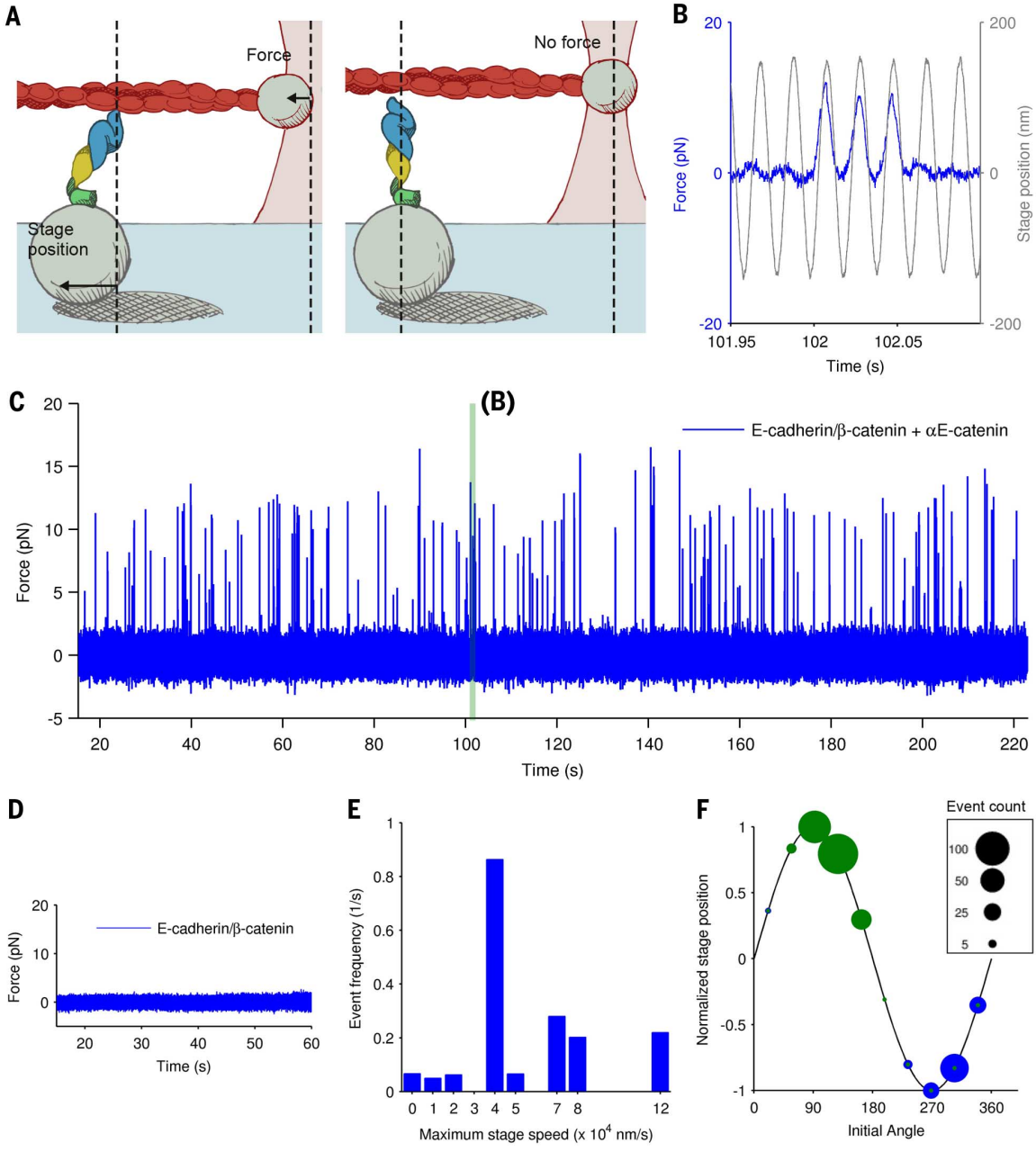

Fig. 2. *Mm* cadherin-catenin complexes bound actin filaments in oscillating-stage experiments. (**A**) The illustrations show that upon binding, the motion of the stage was transmitted to the trapped beads, and the force exerted on them was correlated with the motion of the stage, as shown in the time series in (B). The trapped beads stopped moving along with the stage when the surface-bound cadherin-catenin complex detached from the actin filament. (**B**) Part of a representative time series of force exerted on one of the two optically trapped beads attached to an actin filament (blue). About 1 μM *Mm* cadherin-catenin complex was purified and added to the flow cell. The stage was driven by a 150-nm amplitude, 50-Hz frequency sine wave (gray). (**C**) Full force time series from which the binding events in (B) came (shaded in teal). Peaks in the series are individual binding events, most of which lasted for about one half-period of the sine wave used to drive the stage. (**D**) Force time series from a negative control experiment in which ~1 μM *Mm* E-cadherin/β-catenin complex was purified without *Mm* αE-catenin and added to the flow cell. Oscillation amplitude and frequency of the sine wave used to drive the stage were the same as in (B). (**E**) Frequency of observed *Mm* cadherin-catenin complex/F-actin binding as a function of maximum stage speed (amplitude × angular frequency); n = 297 binding events; bin width is 10^4 nm/s. Event frequency is the number of binding events divided by the total time sampled. (**F**) Sine histogram of the number of *Mm* cadherin-catenin complex/F-actin binding events that started in each angle bin (legend shows counts; n = 235 binding events; bin width is 36°; binding events from trap 1 are in blue, and those from trap 2 are in green). All events were from the 4 × 10^4 nm/s bin shown in (E). The glass microsphere platform (A) was farthest from trap 1 when it was at +1, and from trap 2 when the stage position was at –1. Stage position was normalized by the maximum amplitude of the wave.

after the stage had changed direction and was in the slowest part of the sine cycle (Fig. 2F). This indicates that some minimum contact time was necessary to establish *Mm* cadherin-catenin complex/F-actin bonds before they were subjected to increasing tension. The observation that more events occurred at intermediate rather than low loading rates further indicated that the load stabilized the transient initial bonds. These results motivated us to examine the mechanism by which force might modulate the lifetime of the cadherin-catenin complex bond to F-actin.

Force regulates cadherin-catenin complex dissociation from F-actin

To investigate how force modulated the dissociation kinetics of individual cadherin-catenin complex/F-actin bonds, we modified our optical trap–based assay to observe the detachment of cadherin-catenin complexes from the actin filament under constant force. In these experiments, a signal drove the stage 100 nm back and forth at a constant rate of 1×10^4 nm/s (1.5×10^3 pN/s). Before reversing direction, the stage paused for 150 ms and the forces exerted on the trapped beads were measured. If these forces surpassed a user-defined threshold that indicated binding of cadherin-catenin complexes to the trapped actin filament, then the stage paused until complete detachment of all cadherin-catenin complex/F-actin bonds returned the trapped beads to their zero-force baselines. In these experiments, we used αE-catenin and β-catenin from *Dr* rather than *Mm*. *Mm* αE-catenin forms homodimers (*13*) whose potential presence during the preparation of the flow cell or during the assay could complicate the interpretation of cadherin-catenin complex/F-actin binding events. Importantly, *Dr* αE-catenin is a monomer and, like *Mm* αE-catenin, its affinity for F-actin decreases by a factor of 20 upon binding *Dr* β-catenin (*10*).

When we reconstituted cadherin-catenin complexes with 10 nM *Dr* αE-catenin [in these experiments, *Dr* β-catenin and E-cadherin were preabsorbed onto the coverslip and glass microspheres (*31*)], we observed stepwise changes in the forces exerted on the trapped beads (Fig. 3, A and B), indicating that several cadherin-catenin complexes were initially bound to the actin filament and that they unbound sequentially. The number of stepwise changes scaled with the

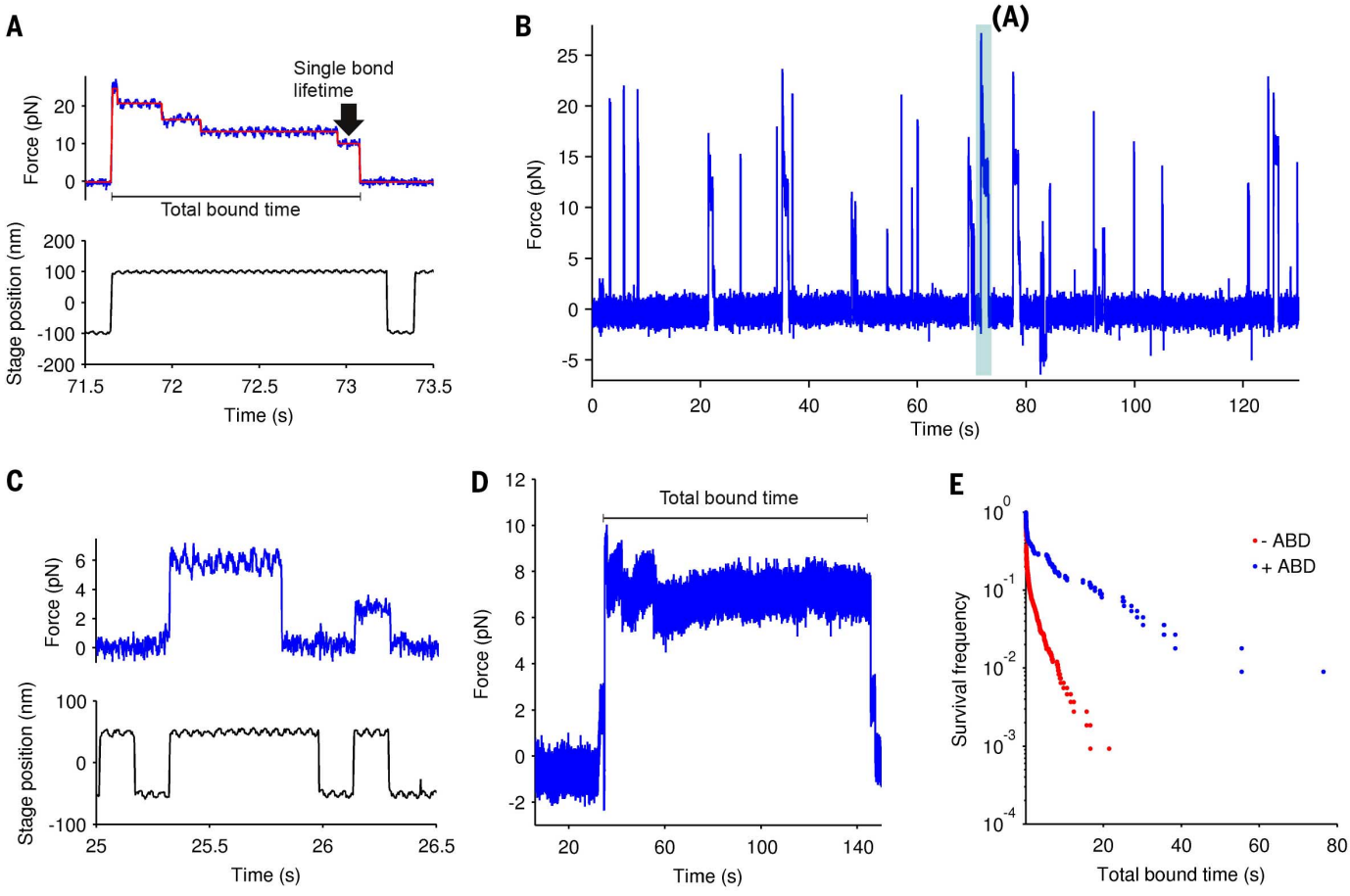

Fig. 3. Measurement of *Dr* cadherin-catenin complex/F-actin bond lifetimes in constant-stage-position experiments. (**A**) An actin filament binding event representative of those observed in the presence of cadherin-catenin complexes reconstituted with 10 nM of added *Dr* αE-catenin. The stage was driven using a wave in the shape of a trapezoid with a 100-nm height and 1×10^4 nm/s slope (top, force time series in blue; bottom, stage position time series in black). Piecewise-constant fit of the force signal is shown in red, and the black arrow points to the segment whose duration and magnitude are the lifetime of the last *Dr* cadherin-catenin/F-actin bond and the force exerted on it, respectively. The black bar underneath the trace represents the total bound time of the entire event. (**B**) A representative force time series, with the event in (A) shaded in teal. (**C**) Representative single-molecule force time series showing binding between a surface-bound *Dr* cadherin-catenin complex and an actin filament in the presence of 100 nM *Mm* αE-catenin ABD. Flow cell was prepared using 1 nM of added *Dr* αE-catenin. (**D**) Force time series showing an actin-binding event measured for multiple surface-bound *Dr* cadherin-catenin complexes and 100 nM *Mm* ABD. The black bar above the trace represents the total bound time of the entire event. Flow cell was prepared using 5 nM of added *Dr* αE-catenin. (**E**) Survival frequency of total bound times, as marked by the black bars in (A) and (D), measured in experiments using flow cells prepared with 5 nM of added *Dr* cadherin-catenin complex (red, no *Mm* ABD present, and $n = 412$ binding events; blue, 100 nM *Mm* ABD, and $n = 107$ binding events). The survival frequency at time t is the fraction of complexes that remain bound for durations greater than t.

concentration of *Dr* αE-catenin used to reconstitute the complexes, but the binding frequency decreased abruptly when less than 10 nM *Dr* αE-catenin was added to the flow cell (table S1). The lowest concentration of *Dr* αE-catenin that still resulted in binding activity was ~5 nM. Even at this minimal concentration, however, unbinding events still comprised a few stepwise changes (similar to Fig. 3A), indicating that binding by several complexes was favored over binding by a single complex (table S1).

To investigate whether multiple cadherin-catenin complexes might bind F-actin more readily than a single, isolated complex, we introduced the actin-binding domain (ABD) of αE-catenin into the reaction buffer. Because ABD binds cooperatively to F-actin but does not bind to β-catenin (*9*), we reasoned that the presence of ABD would mimic the effect of having many αE-catenin molecules bound to F-actin. When we prepared flow cells with 1 nM *Dr* αE-catenin to reconstitute the cadherin-catenin complex, none of the microsphere platforms interacted with the actin filament. However, when we included 100 nM of ABD in the assay buffer, we observed many binding interactions that dissociated in a single step (Fig. 3C), indicative of the interaction of a single cadherin-catenin complex with the actin filament. Under these conditions, approximately 1 in 10 platforms interacted with the actin filament, providing further evidence that the large majority of the platforms contained at most one active cadherin-catenin complex (supplementary text). These observations indicate that addition of ABD was sufficient to replicate the presence of multiple cadherin-catenin complexes interacting with the actin filament. Additionally, because we could observe unbinding of single cadherin-catenin complexes reliably only in the presence of ABD, we conclude that multiple cadherin-catenin complexes may be required for actin filament binding to occur at an observable rate. The increased on-rates for individual complexes in the presence of ABD may be due to changes in the actin filament induced by cooperative binding of ABD as reported previously (*9*), although further experiments are needed to show this unequivocally.

We next asked how the presence of ABD might alter the interaction of the actin filament with many surface-bound cadherin-catenin complexes.

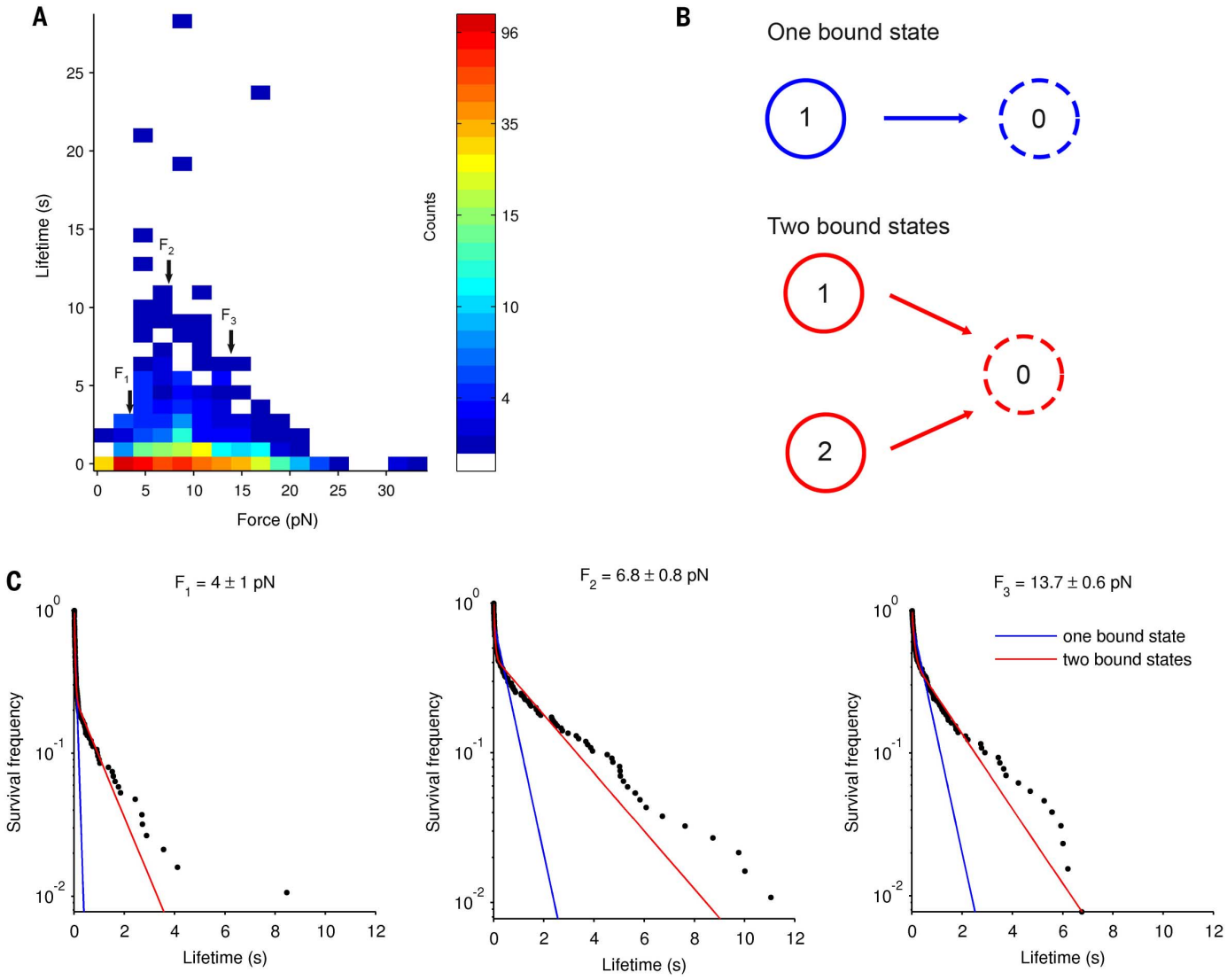

Fig. 4. Force-lifetime distribution of *Dr* cadherin-catenin complex/F-actin bonds and lifetime survival analysis. (**A**) Two-dimensional histogram of *Dr* cadherin-catenin complex/F-actin bond force-lifetime values measured from the last piecewise constant segment in multistep unbinding events, as shown in Fig. 3A. Tick labels on the color bar are bin counts (17 force bins, 32 lifetime bins, and n = 803 observations). (**B**) Kinetic schemes representing dissociation from either one bound state (blue) or two bound states (red). (**C**) Survival frequencies of *Dr* cadherin-catenin complex/F-actin bond lifetimes from three force bins indicated in Fig. 4A (black arrows, n = 188 observations in bin F_1, 185 in F_2, and 129 in F_3; errors are SEM). Red lines are least-square fits of a biexponential function (two bound states), and blue lines are those of a single exponential function (one bound state). $R^2 > 0.90$ for the biexponential function in all force bins, and the additional parameters of the biexponential function are justified ($P \sim 0$ in F test). Additional force bins are shown in fig. S2A.

Remarkably, in experiments using 5 nM of *Dr* αE-catenin to reconstitute the cadherin-catenin complex, addition of ABD greatly increased the total bound times of the cadherin-catenin complex/F-actin bonds (Fig. 3, D and E). This observation indicates that cooperative interactions between neighboring cadherin-catenin complexes and the actin filament enhanced the load-bearing capacity of cadherin-catenin/F-actin bonds by substantially extending their total bound time (Fig. 3D).

Two bound states in force-lifetime distributions

The duration of the last segment of stepwise unbinding events (black arrow in Fig. 3A) represented the lifetime of a single cadherin-catenin complex/F-actin bond, and the displacement from baseline represented the load experienced by the bond. The distribution of lifetimes of the last segment in multistep unbinding events revealed the existence of at least two bound states: a subpopulation of short-lived events at all forces and a subpopulation of long-lived events (up to 25 s) at forces between 5 pN and 10 pN (Fig. 4A).

These results formed the basis for testing several models to explain the distribution of cadherin-catenin complex/F-actin bond lifetimes. Models in which dissociation occurs from a single bound state (state 1) result in a bond survival probability that is described by a single exponential function. In contrast, dissociation from two distinct bound states (states 1 and 2) results in a survival probability that is described by a biexponential function, with a separate exponential decay rate corresponding to each bound state (Fig. 4B). In both of these models, state 0 represents the unbound state.

Bond survival probabilities over a broad range of forces were better fit by a biexponential function than a single exponential function; the improved fit was not due to chance ($P \sim 0$ in F test) (Fig. 4C and fig. S2). Furthermore, the biexponential function fits identified 24% of the lifetimes in the 4-pN bin as long-lived, 43% in the 6.8-pN bin, and 45% in the 13.7-pN bin. Based on this analysis, we conclude that (i) a model with a single bound state did not explain the distribution of cadherin-catenin complex/F-actin bond lifetimes, and (ii) models with two-bound states must recapitulate how the ratio of short-lived to long-lived lifetimes depended on force.

Two-state catch-bond model

Several quantitative models have been developed to account for the effect of force on how fast a bond dissociates. Most models are based on the Bell equation (*33*–*35*):

$$k_{ij}(F) = k_{ij}^{0} \exp(F x_{ij}/k_B T)$$

In this equation, $k_{ij}(F)$ is the rate of transition from state i to state j at force F, k_{ij}^{0} the rate constant, x_{ij} the distance to the transition state, k_B Boltzmann's constant, and T the absolute temperature. As formulated, the Bell equation fits the behavior of slip bonds, in which dissociation rates

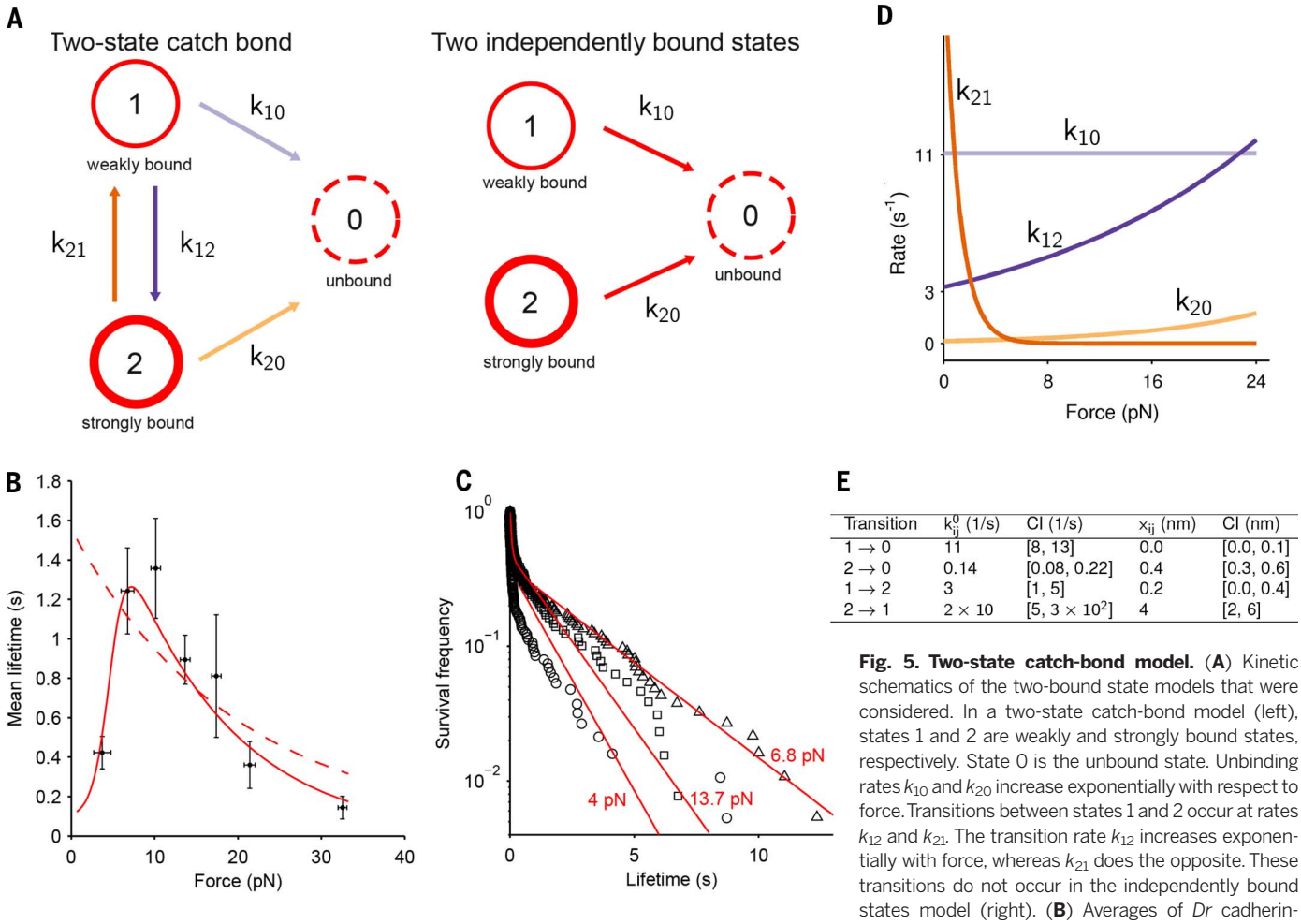

E

Transition	k_{ij}^{0} (1/s)	CI (1/s)	x_{ij} (nm)	CI (nm)
$1 \rightarrow 0$	11	[8, 13]	0.0	[0.0, 0.1]
$2 \rightarrow 0$	0.14	[0.08, 0.22]	0.4	[0.3, 0.6]
$1 \rightarrow 2$	3	[1, 5]	0.2	[0.0, 0.4]
$2 \rightarrow 1$	2×10	$[5, 3 \times 10^2]$	4	[2, 6]

Fig. 5. Two-state catch-bond model. (**A**) Kinetic schematics of the two-bound state models that were considered. In a two-state catch-bond model (left), states 1 and 2 are weakly and strongly bound states, respectively. State 0 is the unbound state. Unbinding rates k_{10} and k_{20} increase exponentially with respect to force. Transitions between states 1 and 2 occur at rates k_{12} and k_{21}. The transition rate k_{12} increases exponentially with force, whereas k_{21} does the opposite. These transitions do not occur in the independently bound states model (right). (**B**) Averages of *Dr* cadherin-catenin complex/F-actin bond lifetimes binned by force (black dots, error bars are SEM, and $n = 803$ bond force–lifetime measurements). The red curves show the mean lifetime distributions predicted by the two-state catch-bond model (solid red) and a two independently bound states model (dashed red). Model parameters were computed using maximum likelihood estimation. (**C**) Survival frequencies of *Dr* cadherin-catenin complex/F-actin bond lifetimes from Fig. 4C, compared with survival probability curves predicted by the two-state catch-bond model (red lines, $R^2 > 0.90$ for all bins except for the 4 pN bin, $R^2 = 0.67$). (**D**) Two-state catch-bond model dissociation rates as functions of force. (**E**) Table of maximum likelihood–estimated parameters of the two-state catch-bond model and their 95% confidence intervals determined by parametric bootstrapping.

increase exponentially with respect to applied tension. On the other hand, the equation with a negative exponential argument has been used in catch-bond models that include transitions in which rates decrease exponentially with respect to applied tension (*29*).

Based on the requirements determined by survival analysis of cadherin-catenin complex/F-actin bond lifetimes, we considered a two-state catch-bond model, which has been proposed to explain FimH adhesion (*30*, *36*), and a two independently bound states model (Fig. 5A). In the two-state catch-bond model, bonds at low force prefer a weakly bound state (state 1) and dissociate quickly (k_{10}) to an unbound state (state 0). As force increases to an intermediate value, bonds transition (k_{12}) into a strongly bound state (state 2) and remain in that state because force opposes transitions (k_{21}) back to the weakly bound state (state 1). In this intermediate force regime, dissociation from the strongly bound state (k_{20}) is not appreciably accelerated, resulting in long bond lifetimes. As force increases further, unbinding occurs directly from the strongly bound state. In a two independently bound states model (Fig. 5A), transitions between states 1 and 2 are not allowed, and bonds remain in the weakly (state 1) or strongly (state 2) bound state in which they originally formed until the cadherin-catenin complex dissociates (k_{10} or k_{20}) from the actin filament to an unbound state (state 0).

We found that the two-state catch-bond model was consistent with mean lifetime distributions and bond survival frequencies from our data (Fig. 5, B and C). We used maximum likelihood estimation to calculate the parameters of the two-state catch-bond model most likely to generate our unbinned, bond force-lifetime distributions (n = 803 bond force–lifetime measurements) (supplementary text; Fig. 5, D and E; fig. S3; and table S2). The estimated parameters predicted a mean bond lifetime curve that agreed well with the mean lifetime distribution (R^2 = 0.86) (Fig. 5B). Predicted survival probabilities also agreed well with survival frequencies of bond lifetimes in all force bins (R^2 > 0.90), except for the lowest force bin (F = 4 pN, R^2 = 0.61) in which the model underestimated the fraction of short-lived bonds (Fig. 5C). The most likely explanation for this discrepancy is that bond lifetimes at low forces were undersampled, because our assay cannot detect events that were both short lived (less than ~5 ms) and low force (less than ~1 pN). The two independently bound states model, in which the bond is not allowed to transition between bound states, did not fit the mean lifetime distribution (Fig. 5B), emphasizing the importance of force-dependent transitions in the bound states in the two-state catch-bond model.

Discussion

Our data and kinetic model reconcile previous in vitro and in vivo studies of the interaction between the cadherin-catenin complex and the actin cytoskeleton. The cadherin-catenin complex/F-actin linkage could not be reconstituted in solution using purified proteins (*8*, *13*, *19*) because, as shown here, force needed to be applied to the αE-catenin/F-actin interface to form a stable bond between F-actin and the cadherin-catenin complex.

In our experiments, the duration of direct bonds between the cadherin-catenin complex and an actin filament was sensitive to load, such that at moderate loads (~8 pN) the lifetime of the bonds dramatically increased relative to those observed at lower forces. These data were explained better by a two-state catch-bond model than any of the alternative models that we tested (supplementary text). In the two-state catch-bond model, force shifts the equilibrium from a weakly to a strongly bound state. Our model predicts that cadherin-catenin complex/F-actin bonds formed in the weakly bound state ~90% of the time. This probability was derived from the assumption that bound state transitions reached equilibrium before the application of force, which resulted in a model that was more consistent with our results than those that assumed different initial conditions, including those that incorporated force-loading history (*30*, *37*–*39*) (supplementary text and figs. S4 to S6).

In the two-state catch-bond model, cadherin-catenin complexes in the weakly bound state rapidly dissociate from actin filaments (k_{10}). Force accelerates the transition into the strongly bound state (k_{12}), from which cadherin-catenin complexes dissociate from actin filaments at a rate of ~0.1 s^{-1} at zero force (k_{20}), a reduction by a factor of 70 compared with the dissociation rate from the weakly bound state (k_{10}). Importantly, the transition from the strongly bound to weakly bound state is greatly decreased by tension (k_{21}): In effect, tension locks the complex in the strongly bound state. Finally, forces greater than 10 pN are sufficient to accelerate the dissociation of cadherin-catenin complexes from the strongly bound state (k_{20}), leading to a decrease in bond lifetimes at high forces.

The force-dependent distance parameters obtained from the model may be related to changes in protein structure that accompany the transition between the weakly and strongly bound states. In particular, the large value of x_{21}, 4 nm, suggests that the αE-catenin/F-actin linkage undergoes a large decrease in length between the strongly and weakly bound states. This putative conformational change underpins catch-bond behavior, because force that opposes this change maintains the bond in the strongly bound state. Previous work indicated that αE-catenin has multiple flexible domains that could be capable of mediating such a transition (*14*, *16*, *21*, *27*, *40*–*43*). At present, however, the precise structural changes in αE-catenin that accompany the transition between the weakly and strongly F-actin–bound states are unknown.

Catch-bond models have been used to describe the bonds formed by integrins, selectins, FimH, and myosin (*28*, *30*, *44*–*47*). Interestingly, the homophilic contacts between cadherin extracellular domains have also been shown to exhibit catch-bond behavior (*48*, *49*), indicating that the cadherin complex may be regulated by force on multiple levels. Although a two-state catch-bond model is a kinetic model that fits our data quantitatively, alternative models considering molecular details, such as the sliding-rebinding, deformation, and hydrogen bond network models that have been applied previously to selectins (*50*–*52*), may also describe the interaction between the cadherin-catenin complex and F-actin. Structural information about how αE-catenin, in a complex with β-catenin, binds F-actin will help establish the molecular basis of the kinetics observed in our experiments.

In summary, our study demonstrates that a strong interaction between the reconstituted cadherin-catenin complex and F-actin requires force and is best described by a two-state catch-bond model. Catch-bond behavior provides a possible explanation for how cells transduce mechanical signals through cadherin-based adhesions, as observed in cell culture and in vivo studies (*12*, *15*, *23*–*26*, *53*). Given the evidence for force-dependent conformational changes in αE-catenin (*15*, *16*), the two-state catch-bond model may also correspond to distinct conformational states of αE-catenin. In addition, changes in the structure of actin protomers within filaments observed in the presence of αE-catenin ABD (*9*) indicate that structural changes in the actin filament may also contribute to enhancing αE-catenin/F-actin interactions. Tension-stabilized states have been shown to regulate αE-catenin binding to vinculin, another actin-binding protein (*15*, *16*). Thus, tension may not only shift the cadherin-catenin complex into a strongly bound state but also promote binding of vinculin, thereby creating a self-reinforcing system for strong linkage of the complex to the actin cytoskeleton. The experiments described here provide an approach to address this possibility directly.

REFERENCES AND NOTES

1. B. M. Gumbiner, Regulation of cadherin-mediated adhesion in morphogenesis. *Nat. Rev. Mol. Cell Biol.* **6**, 622–634 (2005). doi: 10.1038/nrm1699; pmid: 16025097
2. C. M. Niessen, D. Leckband, A. S. Yap, Tissue organization by cadherin adhesion molecules: Dynamic molecular and cellular mechanisms of morphogenetic regulation. *Physiol. Rev.* **91**, 691–731 (2011). doi: 10.1152/physrev.00004.2010; pmid: 21527735
3. V. Vasioukhin, Adherens junctions and cancer. *Subcell. Biochem.* **60**, 379–414 (2012). doi: 10.1007/978-94-007-4186-7_16; pmid: 22674080
4. M. Takeichi, Dynamic contacts: Rearranging adherens junctions to drive epithelial remodelling. *Nat. Rev. Mol. Cell Biol.* **15**, 397–410 (2014). doi: 10.1038/nrm3802; pmid: 24824068
5. W. Meng, M. Takeichi, Adherens junction: Molecular architecture and regulation. *Cold Spring Harb. Perspect. Biol.* **1**, a002899 (2009). doi: 10.1101/cshperspect.a002899; pmid: 20457565
6. B. Janssens *et al.*, αT-catenin: A novel tissue-specific β-catenin-binding protein mediating strong cell-cell adhesion. *J. Cell Sci.* **114**, 3177–3188 (2001). pmid: 11590244
7. S. Pokutta, H. J. Choi, G. Ahlsen, S. D. Hansen, W. I. Weis, Structural and thermodynamic characterization of cadherin·β-catenin·α-catenin complex formation. *J. Biol. Chem.* **289**, 13589–13601 (2014). doi: 10.1074/jbc.M114.554709; pmid: 24692547
8. S. Yamada, S. Pokutta, F. Drees, W. I. Weis, W. J. Nelson, Deconstructing the cadherin-catenin-actin complex. *Cell* **123**, 889–901 (2005). doi: 10.1016/j.cell.2005.09.020; pmid: 16325582
9. S. D. Hansen *et al.*, αE-catenin actin-binding domain alters actin filament conformation and regulates binding of nucleation and disassembly factors. *Mol. Biol. Cell* **24**, 3710–3720 (2013). doi: 10.1091/mbc.E13-07-0388; pmid: 24068324

10. P. W. Miller *et al*., *Danio rerio* αE-catenin is a monomeric F-actin binding protein with distinct properties from *Mus musculus* αE-catenin. *J. Biol. Chem.* **288**, 22324–22332 (2013). doi: 10.1074/jbc.M113.458406; pmid: 23788645
11. D. L. Rimm, E. R. Koslov, P. Kebriaei, C. D. Cianci, J. S. Morrow, α 1(E)-catenin is an actin-binding and -bundling protein mediating the attachment of F-actin to the membrane adhesion complex. *Proc. Natl. Acad. Sci. U.S.A.* **92**, 8813–8817 (1995). doi: 10.1073/pnas.92.19.8813; pmid: 7568023
12. N. Borghi *et al*., E-cadherin is under constitutive actomyosin-generated tension that is increased at cell-cell contacts upon externally applied stretch. *Proc. Natl. Acad. Sci. U.S.A.* **109**, 12568–12573 (2012). doi: 10.1073/pnas.1204390109; pmid: 22802638
13. F. Drees, S. Pokutta, S. Yamada, W. J. Nelson, W. I. Weis, α-catenin is a molecular switch that binds E-cadherin-β-catenin and regulates actin-filament assembly. *Cell* **123**, 903–915 (2005). doi: 10.1016/j.cell.2005.09.021; pmid: 16325583
14. H. J. Choi *et al*., αE-catenin is an autoinhibited molecule that coactivates vinculin. *Proc. Natl. Acad. Sci. U.S.A.* **109**, 8576–8581 (2012). doi: 10.1073/pnas.1203906109; pmid: 22586082
15. S. Yonemura, Y. Wada, T. Watanabe, A. Nagafuchi, M. Shibata, α-Catenin as a tension transducer that induces adherens junction development. *Nat. Cell Biol.* **12**, 533–542 (2010). doi: 10.1038/ncb2055; pmid: 20453849
16. M. Yao *et al*., Force-dependent conformational switch of α-catenin controls vinculin binding. *Nat. Commun.* **5**, 4525 (2014). doi: 10.1038/ncomms5525; pmid: 25077739
17. R. B. Hazan, L. Kang, S. Roe, P. I. Borgen, D. L. Rimm, Vinculin is associated with the E-cadherin adhesion complex. *J. Biol. Chem.* **272**, 32448–32453 (1997). doi: 10.1074/jbc.272.51.32448; pmid: 9405455
18. E. E. Weiss, M. Kroemker, A. H. Rüdiger, B. M. Jockusch, M. Rüdiger, Vinculin is part of the cadherin-catenin junctional complex: Complex formation between α-catenin and vinculin. *J. Cell Biol.* **141**, 755–764 (1998). doi: 10.1083/jcb.141.3.755; pmid: 9566974
19. K. Abe, M. Takeichi, EPLIN mediates linkage of the cadherin catenin complex to F-actin and stabilizes the circumferential actin belt. *Proc. Natl. Acad. Sci. U.S.A.* **105**, 13–19 (2008). doi: 10.1073/pnas.0710504105; pmid: 18093941
20. K. A. Knudsen, A. P. Soler, K. R. Johnson, M. J. Wheelock, Interaction of α-actinin with the cadherin/catenin cell-cell adhesion complex via α-catenin. *J. Cell Biol.* **130**, 67–77 (1995). doi: 10.1083/jcb.130.1.67; pmid: 7790378
21. S. Pokutta, F. Drees, Y. Takai, W. J. Nelson, W. I. Weis, Biochemical and structural definition of the l-afadin- and actin-binding sites of α-catenin. *J. Biol. Chem.* **277**, 18868–18874 (2002). doi: 10.1074/jbc.M201463200; pmid: 11907041
22. K. Tachibana *et al*., Two cell adhesion molecules, nectin and cadherin, interact through their cytoplasmic domain-associated proteins. *J. Cell Biol.* **150**, 1161–1176 (2000). doi: 10.1083/jcb.150.5.1161; pmid: 10974003
23. F. Twiss *et al*., Vinculin-dependent cadherin mechanosensing regulates efficient epithelial barrier formation. *Biol. Open* **1**, 1128–1140 (2012). doi: 10.1242/bio.20122428; pmid: 23213393
24. S. Huveneers *et al*., Vinculin associates with endothelial VE-cadherin junctions to control force-dependent remodeling. *J. Cell Biol.* **196**, 641–652 (2012). doi: 10.1083/jcb.201108120; pmid: 22391038
25. Q. le Duc *et al*., Vinculin potentiates E-cadherin mechanosensing and is recruited to actin-anchored sites within adherens junctions in a myosin II-dependent manner. *J. Cell Biol.* **189**, 1107–1115 (2010). doi: 10.1083/jcb.201001149; pmid: 20584916
26. A. K. Barry *et al*., α-catenin cytomechanics: Role in cadherin-dependent adhesion and mechanotransduction. *J. Cell Sci.* **127**, 1779–1791 (2014). doi: 10.1242/jcs.139014; pmid: 24522187
27. E. S. Rangarajan, T. Izard, The cytoskeletal protein α-catenin unfurls upon binding to vinculin. *J. Biol. Chem.* **287**, 18492–18499 (2012). doi: 10.1074/jbc.M112.351023; pmid: 22493458
28. B. T. Marshall *et al*., Direct observation of catch bonds involving cell-adhesion molecules. *Nature* **423**, 190–193 (2003). doi: 10.1038/nature01605; pmid: 12736689
29. W. E. Thomas, V. Vogel, E. Sokurenko, Biophysics of catch bonds. *Annu Rev Biophys* **37**, 399–416 (2008). doi: 10.1146/annurev.biophys.37.032807.125804; pmid: 18573088
30. W. Thomas *et al*., Catch-bond model derived from allostery explains force-activated bacterial adhesion. *Biophys. J.* **90**, 753–764 (2006). doi: 10.1529/biophysj.105.066548; pmid: 16272438
31. Materials and methods are available as supplementary materials on *Science* Online.
32. S. Yamada, W. J. Nelson, Localized zones of Rho and Rac activities drive initiation and expansion of epithelial cell-cell adhesion. *J. Cell Biol.* **178**, 517–527 (2007). doi: 10.1083/jcb.200701058; pmid: 17646397
33. G. I. Bell, Models for the specific adhesion of cells to cells. *Science* **200**, 618–627 (1978). doi: 10.1126/science.347575; pmid: 347575
34. E. Evans, Probing the relation between force—lifetime—and chemistry in single molecular bonds. *Annu. Rev. Biophys. Biomol. Struct.* **30**, 105–128 (2001). doi: 10.1146/annurev.biophys.30.1.105; pmid: 11340054
35. H. A. Kramers, Brownian motion in a field of force and the diffusion model of chemical reactions. *Physica* **7**, 284–304 (1940). doi: 10.1016/S0031-8914(40)90098-2
36. D. Bartolo, I. Derényi, A. Ajdari, Dynamic response of adhesion complexes: Beyond the single-path picture. *Phys. Rev. E Stat. Nonlin. Soft Matter Phys.* **65**, 051910 (2002). doi: 10.1103/PhysRevE.65.051910; pmid: 12059596
37. E. Evans, A. Leung, V. Heinrich, C. Zhu, Mechanical switching and coupling between two dissociation pathways in a P-selectin adhesion bond. *Proc. Natl. Acad. Sci. U.S.A.* **101**, 11281–11286 (2004). doi: 10.1073/pnas.0401870101; pmid: 15277675
38. V. Barsegov, D. Thirumalai, Dynamics of unbinding of cell adhesion molecules: Transition from catch to slip bonds. *Proc. Natl. Acad. Sci. U.S.A.* **102**, 1835–1839 (2005). doi: 10.1073/pnas.0406938102; pmid: 15701706
39. B. T. Marshall, K. K. Sarangapani, J. Lou, R. P. McEver, C. Zhu, Force history dependence of receptor-ligand dissociation. *Biophys. J.* **88**, 1458–1466 (2005). doi: 10.1529/biophysj.104.050567; pmid: 15556978
40. J. Yang, P. Dokurno, N. K. Tonks, D. Barford, Crystal structure of the M-fragment of α-catenin: Implications for modulation of cell adhesion. *EMBO J.* **20**, 3645–3656 (2001). doi: 10.1093/emboj/20.14.3645; pmid: 11447106
41. E. S. Rangarajan, T. Izard, Dimer asymmetry defines α-catenin interactions. *Nat. Struct. Mol. Biol.* **20**, 188–193 (2013). doi: 10.1038/nsmb.2479; pmid: 23292143
42. S. Pokutta, W. I. Weis, Structure of the dimerization and β-catenin-binding region of α-catenin. *Mol. Cell* **5**, 533–543 (2000). doi: 10.1016/S1097-2765(00)80447-5; pmid: 10882138
43. N. Ishiyama *et al*., An autoinhibited structure of α-catenin and its implications for vinculin recruitment to adherens junctions. *J. Biol. Chem.* **288**, 15913–15925 (2013). doi: 10.1074/jbc.M113.453928; pmid: 23589308
44. F. Kong, A. J. García, A. P. Mould, M. J. Humphries, C. Zhu, Demonstration of catch bonds between an integrin and its ligand. *J. Cell Biol.* **185**, 1275–1284 (2009). doi: 10.1083/jcb.200810002; pmid: 19564406
45. K. K. Sarangapani *et al*., Low force decelerates L-selectin dissociation from P-selectin glycoprotein ligand-1 and endoglycan. *J. Biol. Chem.* **279**, 2291–2298 (2004). doi: 10.1074/jbc.M310396200; pmid: 14573602
46. B. Guo, W. H. Guilford, Mechanics of actomyosin bonds in different nucleotide states are tuned to muscle contraction. *Proc. Natl. Acad. Sci. U.S.A.* **103**, 9844–9849 (2006). doi: 10.1073/pnas.0601255103; pmid: 16785439
47. A. M. Clobes, W. H. Guilford, Loop 2 of myosin is a force-dependent inhibitor of the rigor bond. *J. Muscle Res. Cell Motil.* **35**, 143–152 (2014). doi: 10.1007/s10974-014-9375-z; pmid: 24500136
48. S. Rakshit, Y. Zhang, K. Manibog, O. Shafraz, S. Sivasankar, Ideal, catch, and slip bonds in cadherin adhesion. *Proc. Natl. Acad. Sci. U.S.A.* **109**, 18815–18820 (2012). doi: 10.1073/pnas.1208349109; pmid: 23112161
49. K. Manibog, H. Li, S. Rakshit, S. Sivasankar, Resolving the molecular mechanism of cadherin catch bond formation. *Nat. Commun.* **5**, 3941 (2014). doi: 10.1038/ncomms4941; pmid: 24887573
50. J. Lou, C. Zhu, A structure-based sliding-rebinding mechanism for catch bonds. *Biophys. J.* **92**, 1471–1485 (2007). doi: 10.1529/biophysj.106.097048; pmid: 17142266
51. T. A. Springer, Structural basis for selectin mechanochemistry. *Proc. Natl. Acad. Sci. U.S.A.* **106**, 91–96 (2009). doi: 10.1073/pnas.0810784105; pmid: 19118197
52. S. Chakrabarti, M. Hinczewski, D. Thirumalai, Plasticity of hydrogen bond networks regulates mechanochemistry of cell adhesion complexes. *Proc. Natl. Acad. Sci. U.S.A.* **111**, 9048–9053 (2014). doi: 10.1073/pnas.1405384111; pmid: 24927549
53. D. Cai *et al*., Mechanical feedback through E-cadherin promotes direction sensing during collective cell migration. *Cell* **157**, 1146–1159 (2014). doi: 10.1016/j.cell.2014.03.045; pmid: 24855950

ACKNOWLEDGMENTS

The authors thank S. Pokutta, J. Bianchini, and P. Miller for help with protein purification and biochemistry. C.D.B. thanks J. Sung and S. Nag for assistance with optical trapping instrumentation. D.H. and N.V. thank W. Ochoa, M. Rodriguez Lee, and C. Page for their contribution to the study, and H. Freeze and F. Levine for advice and discussion. The data reported in this paper are further detailed in the supplementary materials. This work was supported by NSF predoctoral fellowships (C.D.B. and J.T.), Stanford Bio-X predoctoral fellowships (C.D.B. and J.T.), a Burroughs Wellcome Career Award at the Scientific Interface (A.R.D.), the NSF (EFRI 1136790 to W.I.W., W.J.N., and A.R.D.), and the NIH (New Innovator Award 1DP2OD007078 to A.R.D., GM35527 to W.J.N., GM56169 to W.I.W., P01GM098412 to D.H. and N.V., and UO1GM094663 to W.J.N., W.I.W., D.H., and N.V.).

SUPPLEMENTARY MATERIALS

www.sciencemag.org/content/346/6209/1254211/suppl/DC1
Materials and Methods
Supplementary Text
Figs. S1 to S6
Tables S1 and S2
References (*54*–*72*)

1 April 2014; accepted 24 September 2014
10.1126/science.1254211

RESEARCH ARTICLE SUMMARY

MEMBRANE TRAFFICKING

The specificity of vesicle traffic to the Golgi is encoded in the golgin coiled-coil proteins

Mie Wong *and* Sean Munro*

INTRODUCTION: The eukaryotic cell contains membrane-bound organelles with distinct functionality and composition. Preservation of organelle identity depends on the highly selective transfer of proteins and lipids between compartments. Central to this are transport carriers called vesicles. Mechanisms are required not only for the selective incorporation of specific cargos into vesicles as they bud off a donor organelle but also for the correct delivery to an acceptor organelle. SNARE proteins on the vesicle and destination organelle drive membrane fusion after arrival and have been implicated in contributing to specificity in choice of organelle. However, upstream of the fusion step, a process called tethering is thought to initially attach the vesicle to the destination organelle and then bring it close to allow the SNARE proteins on opposite membranes to interact. The importance of tethering in conferring specificity to membrane traffic is currently unclear.

RATIONALE: To study the contribution of tethering to specificity in membrane trafficking, we focused on the Golgi apparatus. The Golgi complex is a multicompartment organelle at the intersection of secretory and endocytic trafficking pathways and so receives vesicles from a range of destinations. A family of well-conserved large coiled-coil proteins on the Golgi, the golgins, have been suggested to function as vesicle tethers at the Golgi. However, mild phenotypes of golgin mutants have presented a challenge for elucidating their in vivo roles. We thus used a relocation strategy to test for their sufficiency rather than necessity in vesicle tethering. Ten mammalian golgins that are conserved outside of vertebrates and found on different regions of the Golgi were ectopically expressed at the mitochondria through attachment to a mitochondrial transmembrane domain in place of their C-terminal Golgi targeting domain. We then used the distribution of cargo-laden vesicles originating from different locations as a readout for the golgins' tethering activity.

ON OUR WEB SITE

Read the full article at http://dx.doi.org/10.1126/science.1256898

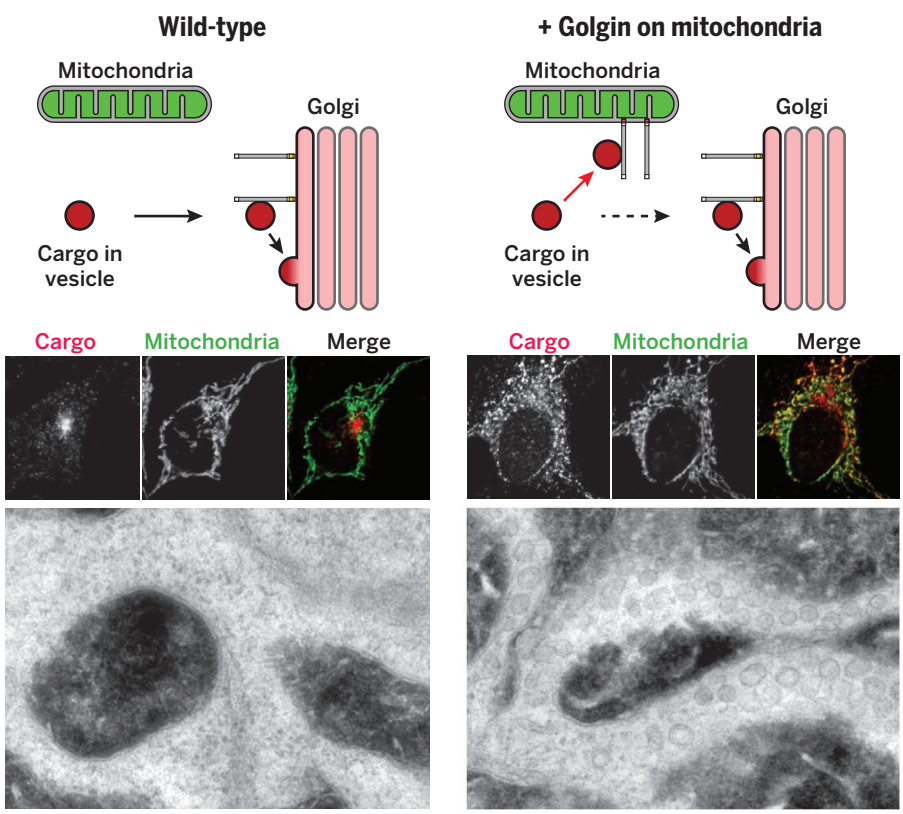

Golgins are sufficient to capture specific classes of vesicle. We hypothesized that if the golgins tether vesicles destined for the Golgi, then their relocation to mitochondria should result in ectopic capture of specific classes of vesicle. Immunofluorescence demonstrates that the presence of a single golgin on mitochondria results in the ectopic capture of a specific cargo. Electron microscopy reveals that vesicles accumulate around these mitochondria.

RESULTS: We demonstrate that subsets of golgins are capable of redirecting particular endogenous or exogenous cargo destined for the Golgi to an ectopic site, the mitochondria. Specifically, golgin-97, golgin-245, and GCC88 were able to capture endosome-to-Golgi cargos; GM130 and GMAP210 were able to capture endoplasmic reticulum (ER)–to-Golgi cargos; and golgin-84, TMF, and GMAP210 were able to capture Golgi resident proteins. Furthermore, electron microscopy yielded ultrastructural evidence for the accumulation of vesicular membranes around mitochondria decorated with specific golgins. These data suggest that not only do the golgins capture vesicles, they also exhibit specificity toward vesicles of different origins—from the endosomes, from the ER, or from within the Golgi itself.

CONCLUSION: We have been able to demonstrate that relocation of specific golgins is sufficient to reroute specific classes of transport vesicles to an ectopic site. Thus, most golgins are sufficient to nucleate a specific tethering process, and hence they are likely to make a major contribution to the specificity of vesicle traffic arriving at the Golgi. In addition, this relocation system may be a useful tool for isolating specific transport vesicles that are normally short-lived, hence providing a route to further understanding of specificity in membrane traffic. ■

MRC Laboratory of Molecular Biology, Cambridge CB2 0QH, UK.
*Corresponding author. E-mail: sean@mrc-lmb.cam.ac.uk
Cite this article as M. Wong, S. Munro, *Science* **346**, 1256898 (2014). DOI: 10.1126/science.1256898

RESEARCH ARTICLE

MEMBRANE TRAFFICKING

The specificity of vesicle traffic to the Golgi is encoded in the golgin coiled-coil proteins

Mie Wong and Sean Munro*

The Golgi apparatus is a multicompartment central sorting station at the intersection of secretory and endocytic vesicular traffic. The mechanisms that permit cargo-loaded transport vesicles from different origins to selectively access different Golgi compartments are incompletely understood. We developed a rerouting and capture assay to investigate systematically the vesicle-tethering activities of 10 widely conserved golgin coiled-coil proteins. We find that subsets of golgins with distinct localizations on the Golgi surface have capture activities toward vesicles of different origins. These findings demonstrate that golgins act as tethers in vivo, and hence the specificity we find to be encoded in this tethering is likely to make a major contribution to the organization of membrane traffic at the Golgi apparatus.

The functionality of the membrane-bound organelles of eukaryotic cells is determined by their constituent proteins and lipids. A major determinant of organelle composition in the endomembrane system is the highly selective transfer of cargo-laden vesicles between compartments. Not only must the correct cargo be collected at the origin, the transport vesicle must be selectively delivered to the correct destination. SNARE proteins on the vesicle and destination organelle assemble to drive membrane fusion (*1*). The diversity of cellular SNAREs, their differential localization, and their selective pairwise interactions implicate them in contributing specificity to membrane traffic (*2*–*4*). However, the relatively small size of SNAREs means that they can only interact after a vesicle is closely apposed to its potential destination. A process called tethering is thought to attach the vesicle to the organelle before SNARE complex assembly (*5*–*7*). The degree to which organelle tethers confer specificity rather than efficiency to membrane traffic is currently unclear.

To investigate this problem, we focused on the Golgi apparatus, the central sorting station in the endomembrane system (*8*). The Golgi is a stack of distinct cisternae arranged from cis to trans, and particular vesicles appear to preferentially fuse with different cisternae within the stack. For example, vesicles derived from the endoplasmic reticulum (ER) deliver cargo to the cis face of the Golgi, whereas those from the endocytic pathway deliver cargo to the trans face of the Golgi. Moreover, vesicles mediate selective transfer of contents between Golgi cisternae. Thus, providing spatial cues to vesicles arriving at the Golgi is critical for endomembrane traffic and represents an ideal system for investigating the basis of vesicle targeting specificity.

The golgins, large well-conserved coiled-coil proteins anchored to the membrane via their C termini (*9*–*11*), have been suggested to act as vesicle tethers, but in vivo evidence for this role is lacking (*12*, *13*). In addition, other roles have been proposed for some golgins, such as recruiting kinases or cytoskeletal regulators (*14*, *15*). Golgin mutants typically have mild or tissue-specific phenotypes, leaving their function uncertain (*16*, *17*). We hypothesized that the golgins have overlapping functions in tethering, which may obscure their function when any one is missing. We therefore developed methods to test their sufficiency, rather than necessity, in selective vesicle tethering.

Experimental strategy

Our strategy was to attach golgins to a different structure in the cell and then test whether this was sufficient to redirect Golgi-bound carriers to the ectopic destination (Fig. 1A). We chose mitochondria because they display a distinctive localization, are distributed throughout the cell, and do not normally capture transport vesicles. We tested 10 mammalian golgins chosen for their conservation outside of vertebrates and spatial distribution in different Golgi regions (Fig. 1B). Ectopic golgin localization was accomplished by either direct or induced attachment to a mitochondrial transmembrane domain in place of the C-terminal Golgi targeting domain (Fig. 1C). The direct fusion approach was more straightforward (Fig. 1D and fig. S1), whereas the induced targeting strategy provided tight temporal control (Fig. 1, C and E). The golgins GM130 and GCC185 are known to bind soluble cytosolic proteins [p115 and CLASP, respectively (*14*, *18*)], and in both cases, relocation of the golgin resulted in the binding partner being found on the mitochondria as well as the Golgi; this suggested that relocation had not grossly perturbed the structure of the golgin (fig. S2). For two of the golgins (GM130 and GMAP-210), a high expression level of the mitochondrial form caused the Golgi to become fragmented, which could be due to their titrating away factors that contribute to Golgi integrity (such as p115) or due to the effect of their relocation on ER-to-Golgi traffic (see below).

Vesicles originating from different locations were analyzed for localization upon ectopic expression of individual golgins. The identity of originating vesicles was marked by either endogenous or exogenous cargo selective to that site. Analysis of all combinations of originating vesicles with each of the 10 golgins was anticipated to provide a comprehensive view of their capacity to provide landmarks for vesicular traffic. We present these findings by successively analyzing transport vesicles of endosomal, ER, and intra-Golgi origin.

Capture of endosome-to-Golgi carriers

One of the best-characterized cargos that traffics from endosomes back to the Golgi is the cation-dependent mannose 6-phosphate receptor (CD-MPR) that delivers newly made lysosomal hydrolases to endosomes and then returns to the Golgi (*19*). At steady state, most of this receptor is in the Golgi apparatus, but mitochondrial forms of three of the golgins caused endogenous CD-MPR to accumulate on mitochondria (Fig. 2A). These were golgin-97, golgin-245, and GCC88, three of the four golgins that share a C-terminal GRIP domain that mediates binding to Arl1, a G protein of the trans side of the Golgi (*9*, *11*). In each case, CD-MPR distribution was the sum of the Golgi and mitochondrial distribution, and quantitation confirmed that the effect was seen in most of the transfected cells (Fig. 2B). The remaining seven golgins had no detectable effect on the distribution of the CD-MPR (Fig. 1A). The same three golgins could also induce a redistribution of the SNARE protein Vti1a, another cargo of these retrograde carriers (*20*) (fig. S3). Other endogenous proteins that travel along this retrograde route were also affected, including the cation-independent MPR and TGN46, a protein of unknown function that has both Golgi retention and endosome retrieval signals (*21*) (fig. S4). These effects did not simply reflect capture of endosomes on the mitochondria, because both early and late endosomal markers did not relocate (fig. S5). Finally, to confirm that the carriers were moving from endosomes to Golgi, we expressed the golgins in a cell line expressing a CD8-MPR chimera that recycles efficiently from the surface to the Golgi via endosomes (*22*). When CD8 antibodies were bound to the surface and followed after endocytosis, the carriers containing the antibodies could be captured by the mitochondrial golgins early after initiation of uptake; this finding indicates that the carriers were moving from endosomes to the Golgi (fig. S6).

The above experiments used golgins that were constitutively targeted to mitochondria

MRC Laboratory of Molecular Biology, Cambridge CB2 0QH, UK.
*Corresponding author. E-mail: sean@mrc-lmb.cam.ac.uk

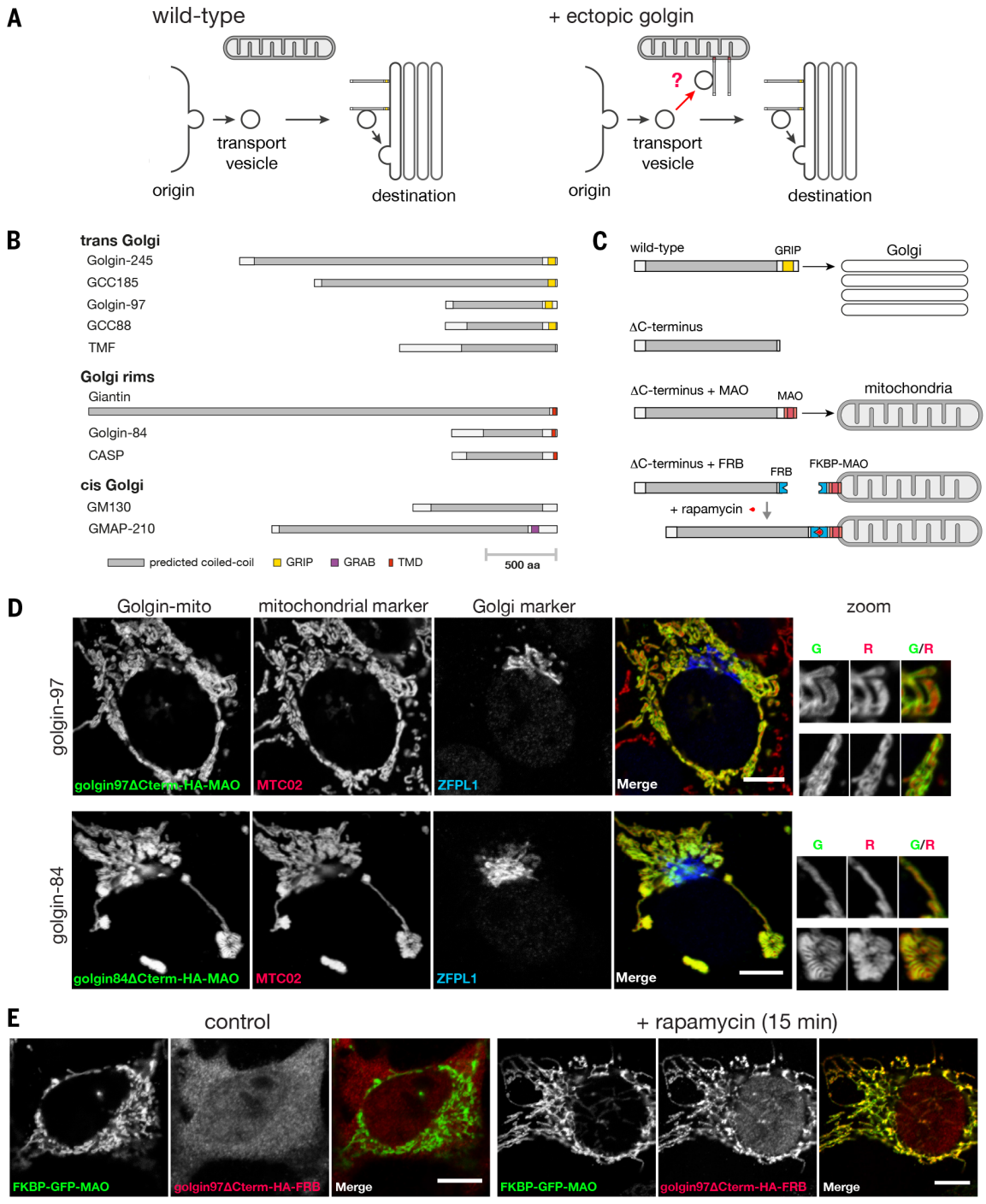

Fig. 1. Strategy for relocation of the golgins to mitochondria. (**A**) An in vivo assay for golgin tethering activity. Normally vesicles from various origins move to find the Golgi. If a particular class of vesicles can be captured by a specific golgin, then presenting that golgin on mitochondria should allow ectopic capture of that class of vesicle. (**B**) The 10 human golgin coiled-coil proteins that have orthologs outside of vertebrates. (**C**) Scheme for relocating golgins to mitochondria in a constitutive or inducible manner, illustrated for the GRIP domain protein golgin-97. The C-terminal transmembrane domain of monoamine oxidase (MOA) is sufficient for targeting to the outer mitochondrial membrane (*40*). Inducible relocation was performed using the rapamycin-controlled heterodimerization domains from FKBP and FRB (*41*). (**D**) COS cells expressing representative golgin-mito fusion proteins stained for a hemagglutinin (HA) epitope located between the golgin and the organelle targeting motif. Costaining for a mitochondrial marker, MTC02, and a Golgi marker, ZFPL1 (cis), indicates correct relocation of each of the golgins to the outer membrane of the mitochondria. Representative regions of mitochondria are magnified (Golgi marker omitted, therefore showing green and red channels only). Scale bars, 10 μm. (**E**) COS cells coexpressing reroutable golgin-97 with FKBP-GFP-MAO with or without 200 nM rapamycin treatment for 15 min. Reroutable golgin-97 was detected by staining for a HA epitope tag between the golgin and the FRB domain. Scale bars, 10 μm.

in transiently transfected cells, and so the golgins required 24 to 36 hours to accumulate to readily detectable levels. When the golgins were instead acutely located to mitochondria by means of the rapamycin-dependent inducible system, we observed a rapid relocation of the retrograde cargo such as CD-MPR and Vti1a within 15 min of addition of rapamycin (Fig. 2C and fig. S3B). This relocation was seen

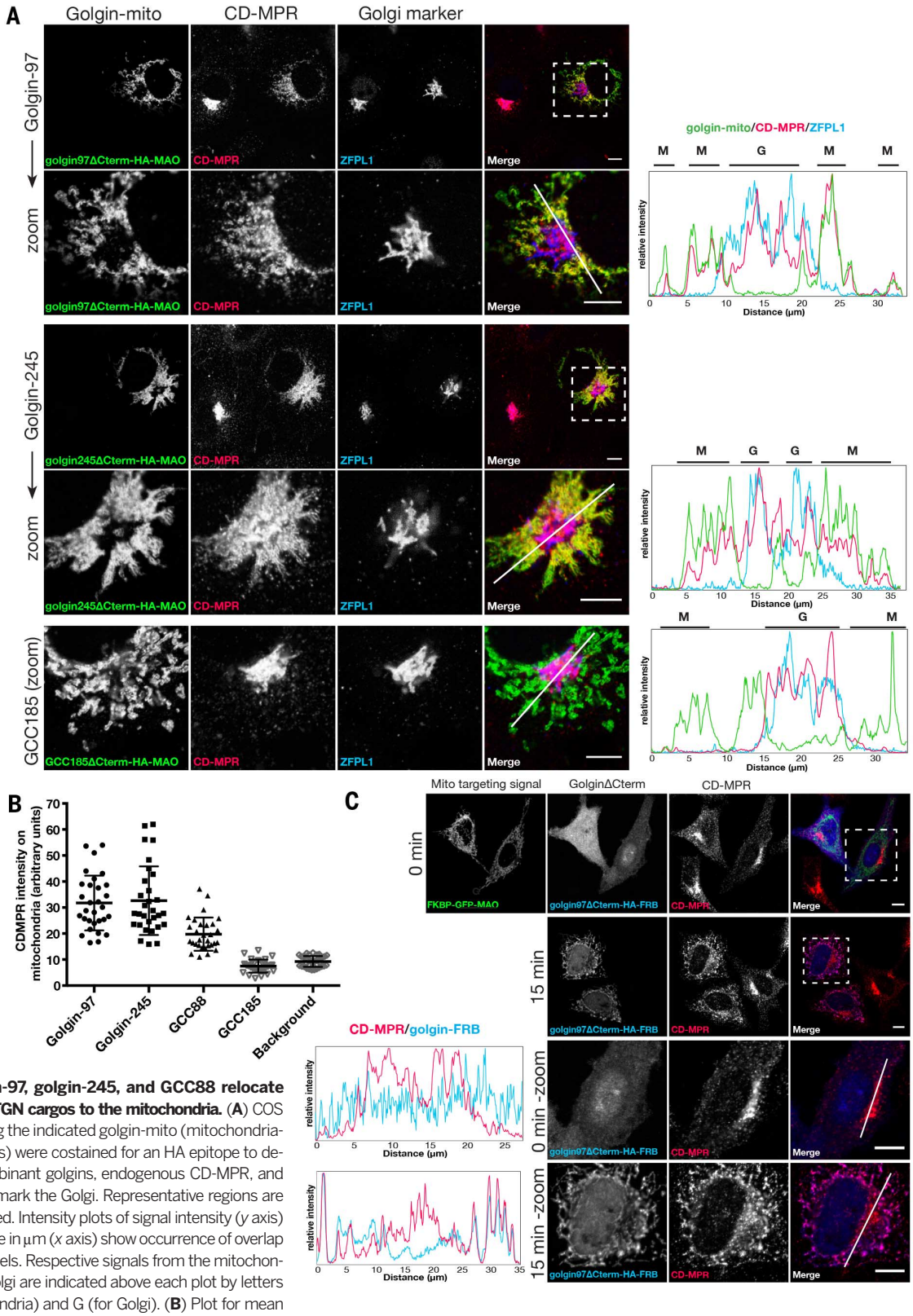

Fig. 2. Golgin-97, golgin-245, and GCC88 relocate endosome-to-TGN cargos to the mitochondria. (**A**) COS cells expressing the indicated golgin-mito (mitochondria-targeted golgins) were costained for an HA epitope to detect the recombinant golgins, endogenous CD-MPR, and ZFPL1 (cis) to mark the Golgi. Representative regions are shown magnified. Intensity plots of signal intensity (*y* axis) against distance in μm (*x* axis) show occurrence of overlap between channels. Respective signals from the mitochondria and the Golgi are indicated above each plot by letters M (for mitochondria) and G (for Golgi). (**B**) Plot for mean CD-MPR labeling intensity within the mitochondria segment (the golgins) or elsewhere in the cell (background labeling); $N \geq 30$. (**C**) COS cells coexpressing reroutable golgin-97 with FKBP-GFP-MAO were treated with 200 nM rapamycin for 0 or 15 min and costained for endogenous CD-MPR. Intensity plot as in (A). Scale bars, 10 μm.

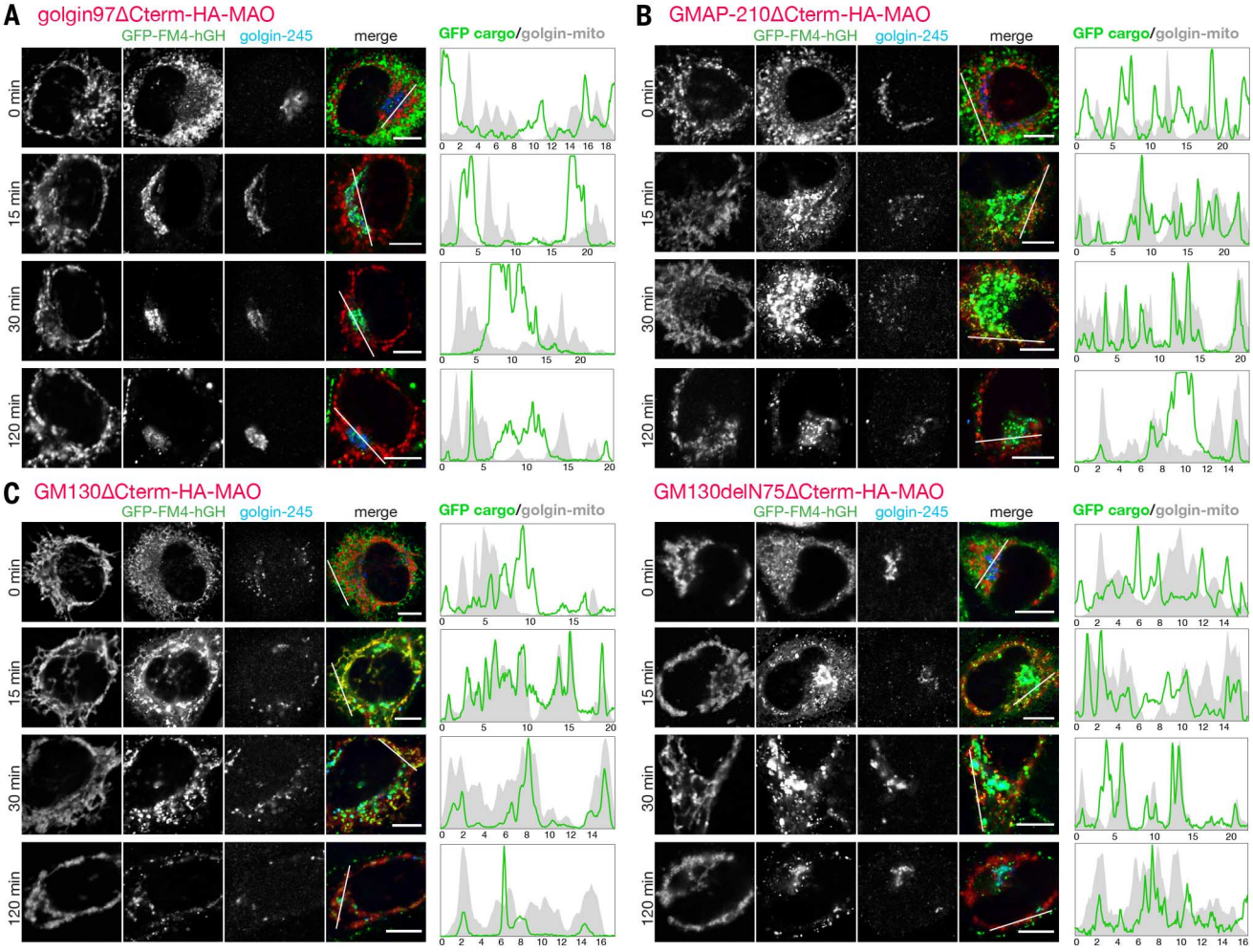

Fig. 3. GMAP210 and GM130 capture ER-derived cargo on mitochondria. (**A** to **C**) C1-HeLa cells expressing GFP-FM4-hGH cargo and transiently expressing mitochondria-targeted golgin-97 (A), GMAP210 (B), GM130 (C), or GM130delN75 (C) were subjected to a secretion assay by treatment with 0.5 μM D/D solubilizer at 37°C and fixed at the indicated time points. The number 75 in GM130delN75 represents the number of the first residue in the fragment. Transfected C1 cells were permeabilized and costained for an HA epitope (to detect the recombinant golgins) and a Golgi marker, golgin-245 (trans). Intensity plots of signal intensity (*y* axis) against distance in μm (*x* axis) show occurrence of overlap between channels. Scale bars, 10 μm.

with the same three GRIP domain golgins, which suggests that the effect is a direct consequence of the ectopic location of the golgins (fig. S7).

Capture of ER-to-Golgi carriers

A second major class of carriers that arrive at the Golgi are those that deliver newly made secreted and membrane proteins from the ER. Proteins leave the ER from exit sites found both adjacent to the Golgi and scattered throughout the cytoplasm, and from the latter sites carriers move along microtubules to reach the Golgi (*23*). To follow these carriers, we made use of a green fluorescent protein (GFP)–tagged secreted protein that accumulates in the ER until released by a small molecule (*24*). Upon release, the reporter relocates to the Golgi within 10 to 15 min and then leaves for the surface; this behavior was not perturbed by the mitochondrial forms of 8 of the 10 golgins tested (Fig. 3A). However, for the golgins GM130 and GMAP-210, we observed association of GFP-labeled structures with mitochondria (Fig. 3, B and C). This association appeared to gradually reduce after an initial peak; to quantify this, we used live cell imaging to compare the GFP-labeled cargo to mCherry-labeled mitochondrial golgins in individual cells over time (figs. S8 to S11). Quantification revealed that GM130 and GMAP-210 caused an association of ER-derived carriers with mitochondria that was specific but also transient, presumably reflecting the carriers being captured and then eventually released, perhaps by being pulled away by the motors that move them toward the Golgi (Fig. 4A).

The two golgins able to capture pre-Golgi carriers are both found on the cis side of the Golgi, consistent with a role in ER-to-Golgi traffic (*25*, *26*). GM130 interacts via its N-terminal 74 residues with the tethering factor p115 (*18*). A mitochondrial form of GM130 lacking residues 1 to 74 no longer relocated p115 to mitochondria and showed reduced Golgi fragmentation (Fig. 3C and fig. S2). Nonetheless, this construct could still transiently capture ER-derived carriers, which suggests that GM130 has some vesicle tethering activity independent of p115 and also indicates that the ectopic capture of ER-derived cargo is not simply a consequence of Golgi fragmentation (Figs. 3C and 4A). To strengthen the latter conclusion, we also followed ER-derived cargo in cells in which the Golgi had been fragmented by depolymerizing microtubules. Despite the Golgi being fragmented, capture was not observed with a control golgin but could be clearly detected for GM130 (Fig. 4, B to D, and movies S1 and S2).

Capture of carriers containing Golgi residents

The Golgi stack is surrounded by vesicles that are thought to recycle Golgi resident proteins back to earlier parts of the stack as the cisternae mature, and it has also been proposed that some may carry secretory cargo forward through the stack (*27*). We thus looked for relocation of Golgi resident proteins by the relocated golgins. With

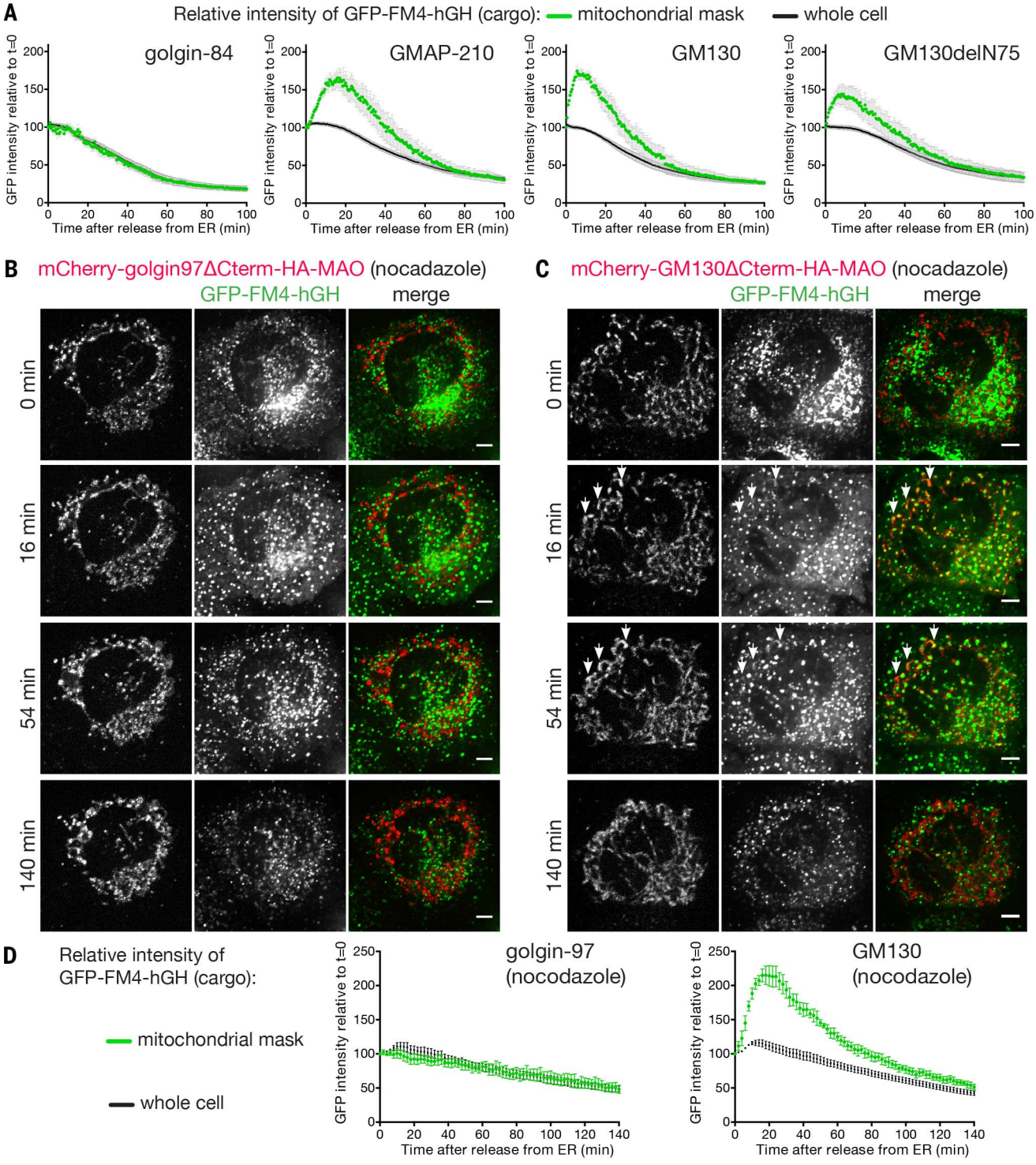

Fig. 4. Live cell imaging of ectopic capture of ER-derived carriers by GMAP210 and GM130. (**A**) Graphs of GFP fluorescence (*y* axis) against time (*x* axis) demonstrate time courses for secretion of the GFP-FM4-hGH reporter by C1 cells that were transiently expressing mitochondria-targeted golgins. Average GFP fluorescence intensity over the entire cell (whole cell) or the mitochondrial region (mitochondria) was determined for several cells over time, with the results presented as percentages of the fluorescence intensity at $t = 0$. Data are means ± SEM; golgin-84 ($N = 5$), GMAP-210 ($N = 7$), GM130 ($N = 6$), and GM130delN75 ($N = 7$). Stills from a representative data set from each are shown in figs. S8 to S11. (**B** and **C**) C1-HeLa cells transiently expressing mitochondria-targeted mCherry-golgin-97 (B) or mCherry-GM130 (C) were pretreated with 0.5 μM nocodazole for 3 hours to depolymerize microtubules prior to being incubated at 37°C for the indicated times with a mix of nocodazole and D/D solubilizer to induce secretion of the GFP-FM4-hGH reporter. Images were acquired every 2 min for 140 min (movies S1 and S2). Transient association of GFP-FM4-hGH with mitochondria can be seen for GM130 (illustrated by arrowheads) but not for golgin-97. Scale bars, 5 μm. (**D**) Quantitation of the relative association of the GFP-FM4-hGH reporter with mitochondria over time in nocodazole-treated cells as in (B) and (C). Data are means ± SEM ($N = 4$ for both).

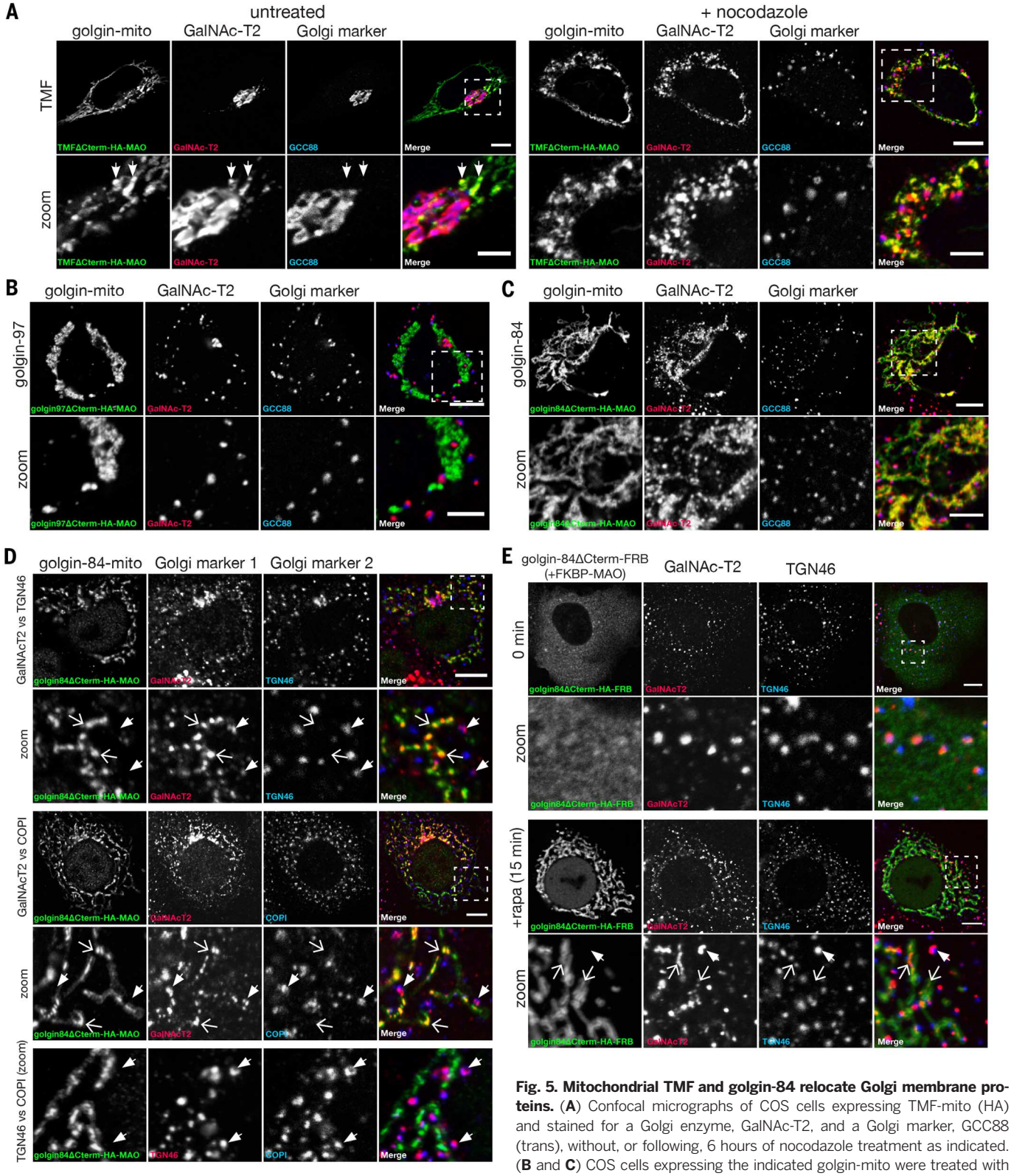

Fig. 5. Mitochondrial TMF and golgin-84 relocate Golgi membrane proteins. (**A**) Confocal micrographs of COS cells expressing TMF-mito (HA) and stained for a Golgi enzyme, GalNAc-T2, and a Golgi marker, GCC88 (trans), without, or following, 6 hours of nocodazole treatment as indicated. (**B** and **C**) COS cells expressing the indicated golgin-mito were treated with nocodazole for 6 hours and costained for GalNAc-T2 and a Golgi marker, GCC88 (trans). (**D**) COS cells expressing golgin-84-mito were treated with 0.5 μM nocodazole for 6 hours and labeled for two of the endogenous Golgi proteins GalNAcT2, TGN46, or COPI as indicated. In all cases, solid arrows indicate Golgi ministacks positive for both Golgi markers, with these being distinct from mitochondria; open arrows indicate structures on mitochondria positive for GalNAcT2 but not the other marker. (**E**) COS cells coexpressing golgin-84ΔCterm-FRB and FKBP-MAO were treated with 0.5 μM nocodazole for 3 hours followed by 200 nM rapamycin (and nocodazole) to direct dimerization and then fixed as indicated and stained for endogenous GalNAcT2 and TGN46. Solid arrows indicate Golgi ministacks positive for both markers; open arrows indicate GalNAcT2 captured onto mitochondria after 15 min. Scale bars, 10 μm.

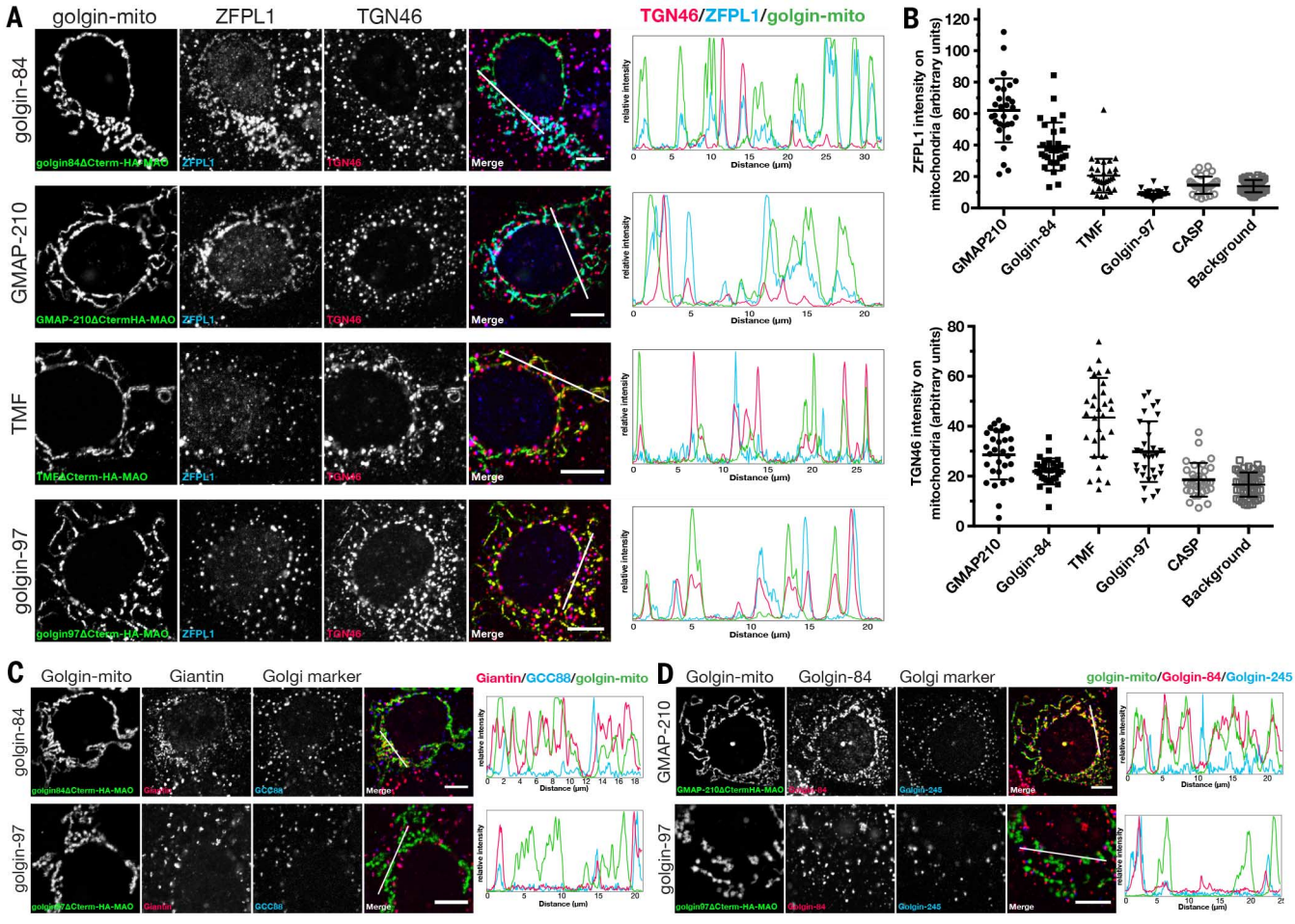

Fig. 6. TMF, golgin-84, and GMAP210 exhibit specificity in the capture of cis-Golgi and trans-Golgi residents. (**A**) COS cells expressing the indicated golgin-mito were treated with nocodazole for 6 hours and costained for two transmembrane Golgi markers, ZFPL1 (cis) and TGN46 (trans). Intensity plots of signal intensity (*y* axis) against distance in μm (*x* axis) show occurrence of overlap between channels. (**B**) Quantitation of mean intensity of ZFPL1 signal and TGN46 signal within the HA-positive mitochondria segment (the golgins) or whole cell (background), $N \geq 30$. (**C** and **D**) COS cells expressing the indicated golgin-mito were treated with nocodazole for 6 hours and costained for either of the transmembrane golgins, giantin or golgin-84, and a Golgi marker, GCC88. Intensity plots of signal intensity (*y* axis) against distance in μm (*x* axis) show occurrence of overlap between the markers. Scale bars, 10 μm (magnified boxes, 5 μm).

ectopic TMF, the endogenous Golgi enzyme GalNAc-T2 could be detected on mitochondria as well as on the Golgi, but unlike the carriers described above, this accumulation was only seen on those mitochondria near the Golgi stack (Fig. 5A). This may reflect the fact that intra-Golgi carriers do not need to move far from the Golgi, and so most only encounter the few mitochondria that are close to the stack, whereas carriers coming to the Golgi from the ER and endosomes can travel long distances along microtubules and hence pass many mitochondria. To increase the probability of intra-Golgi carriers encountering mitochondria, we used nocodazole to remove microtubules and thus scatter the Golgi into many ministacks located throughout the cytoplasm and thus in the proximity of many more mitochondria. In such cells, we could see robust relocation of GalNAc-T2 to mitochondria by TMF (Fig. 5A) as well as by golgin-84 and GMAP-210, but not by any other golgin (Fig. 5, B and C, and fig. S12). Analysis of further Golgi markers confirmed that the ministacks are distinct from the GalNAc-T2 captured on mitochondria, because the markers from different cisternae are much closer to each other than to the GalNAc-T2 on the mitochondria (Fig. 5D). Finally, after acute relocalization of golgin-84 to mitochondria by means of the rapamycin-based dimerization, GalNAc-T2 could be clearly detected on mitochondria after 15 min, indicating that this capture in nocodazole-treated cells is unlikely to be due to an indirect effect arising over many hours (Fig. 5E).

We next examined a range of different Golgi resident membrane proteins in nocodazole-treated cells and again found relocation by specific golgins, with strikingly different patterns seen for different residents. The cis-Golgi membrane protein ZFPL1 (*28*) was efficiently relocated by golgin-84 and GMAP-210, and to a lesser extent by TMF, but was unaffected by the other seven golgins (Fig. 6A and fig. S13). In contrast, the TGN resident protein TGN46 was relocated by TMF but not by golgin-84 or GMAP-210 (Fig. 6A). Quantitation of colocalization with mitochondria confirmed these differential relocations (Fig. 6B). TGN46 has two targeting signals: one in its cytoplasmic tail that mediates retrieval from endosomes (hence TGN46 is in the endosome-to-Golgi carriers captured by the GRIP golgins), and a second transmembrane signal that confers retention in the trans-Golgi, probably by directing recycling within the stack (*21*).

The golgins giantin, CASP, and golgin-84 are themselves Golgi resident membrane proteins; if Golgi cisternae were to undergo maturation, then these three golgins would have to recycle to earlier cisternae in transport vesicles. Indeed, endogenous giantin was relocated to mitochondria by golgin-84 and GMAP-210, and although golgin-84 could not be tested with itself, it was also relocated by GMAP-210 (Fig. 6, C and D, and fig. S14). It is possible that these golgins interact directly to mediate tethering, but this remains to be determined. Taken together, these results show that three of the golgins are able to relocate resident membrane proteins of the Golgi to mitochondria. This presumably reflects the capture

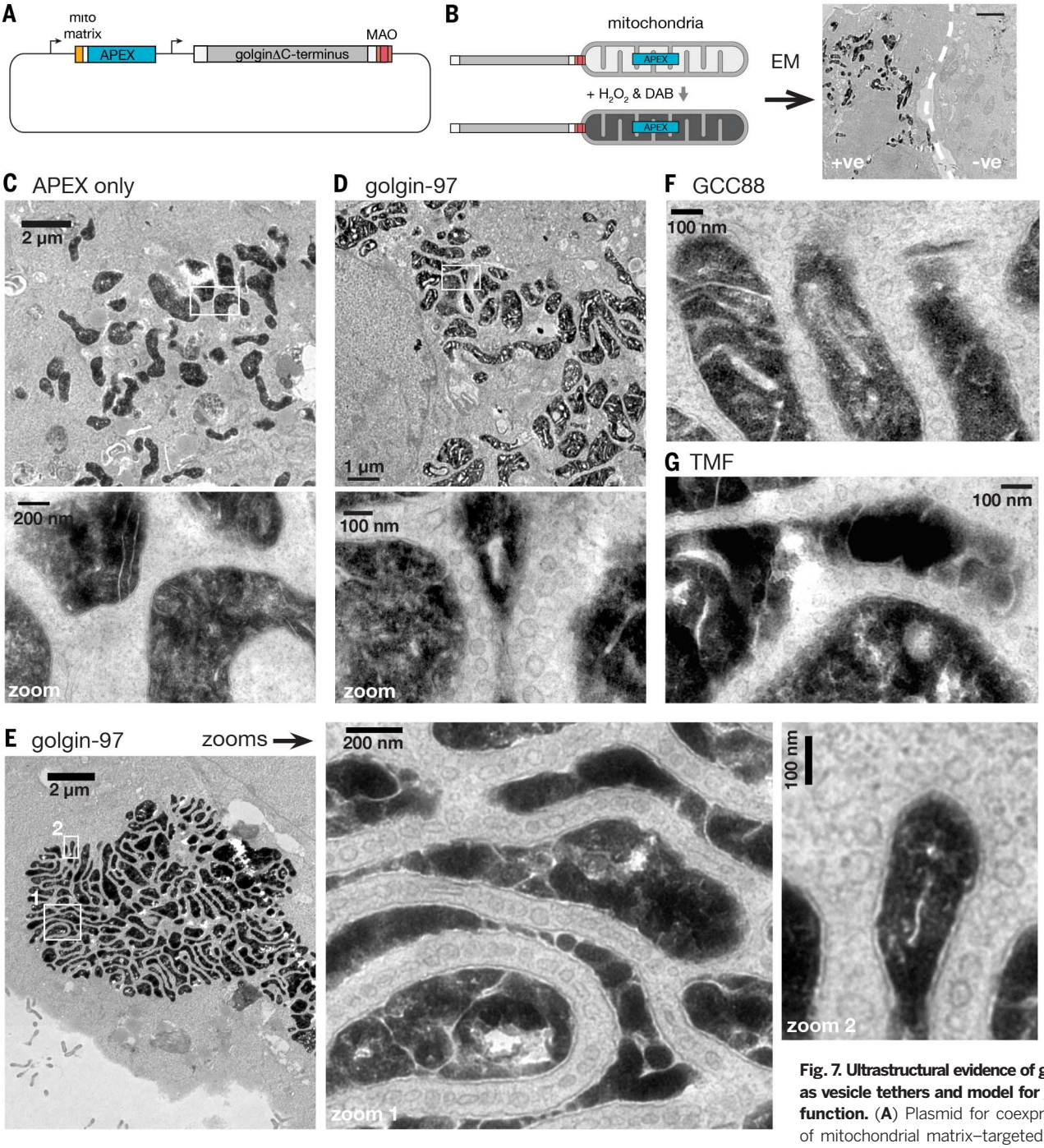

Fig. 7. Ultrastructural evidence of golgins as vesicle tethers and model for golgin function. (**A**) Plasmid for coexpression of mitochondrial matrix–targeted APEX and golgin-mito. (**B**) Strategy for identifying cells labeled by APEX-catalyzed oxidation of DAB. Scale bar, 2 μm. (**C**) Electron micrograph of a COS cell transfected with a plasmid expressing mito matrix–APEX alone. (**D** to **G**) Electron micrographs of COS cells coexpressing mito matrix–APEX and either golgin-97–mito [(D) and (E)], GCC88-mito (F), or TMF-mito (G). In all cases, membranous vesicles can be seen accumulating around the mitochondria.

of carrier vesicles containing these proteins, with the pattern of proteins captured varying between individual golgins.

Electron microscopy reveals carrier capture by golgin-coated mitochondria

In the experiments described above, endogenous membrane proteins were found to be relocated to mitochondria by specific golgins. If this is the case, then membrane-bound carriers accumulating around mitochondria should be detectable by electron microscopy (EM). To identify transfected cells, we expressed the mitochondrial golgins from a bicistronic plasmid that also expressed a form of APEX peroxidase that is targeted to the mitochondrial matrix (Fig. 7A). This peroxidase directs the precipitation of diaminobenzidine to form a dark deposit that is visible in EM sections (*29*) (Fig. 7B). We initially examined the effect of coexpressing golgin-97, which we had found to efficiently capture endosome-derived proteins. In these cells, the mitochondria were surrounded by circular and oval membrane profiles that were absent from control cells expressing APEX alone (Fig. 7, C and D). The structures were typically 60 to 80 nm in diameter and often accumulated between adjacent mitochondria, but could also be seen around isolated parts of the mitochondrial surface.

A

		cis		rims				trans			
		GM130	GMAP-210	Giantin	CASP	Golgin-84	TMF	Golgin-97	Golgin-245	GCC88	GCC185
ER-derived cargo	eGFP-F_M4-hGH	✓	✓	x	x	x	x	x	x	x	x
Golgi residents	ZFPL1	x	✓	x	x	✓	small effect	x	x	x	x
	Giantin	x	✓	n.t.	x	✓	✓	x	x	x	x
	Golgin-84	x	✓	x	x	n.t.	small effect	x	x	x	x
	GalNAc-T2	x	✓	x	x	✓	✓	x	x	x	x
	ST6Gal1-myc	x	x	x	x	x	✓	x	x	x	x
	TGN46	x	x	x	x	x	✓	✓	✓	✓	x
Endosome-to-Golgi cargo	CDMPR	x	x	x	x	x	x	✓	✓	✓	x
	CIMPR	x	x	x	x	x	x	✓	✓	✓	x
	Vti1a	x	x	x	x	x	x	✓	✓	✓	x

B

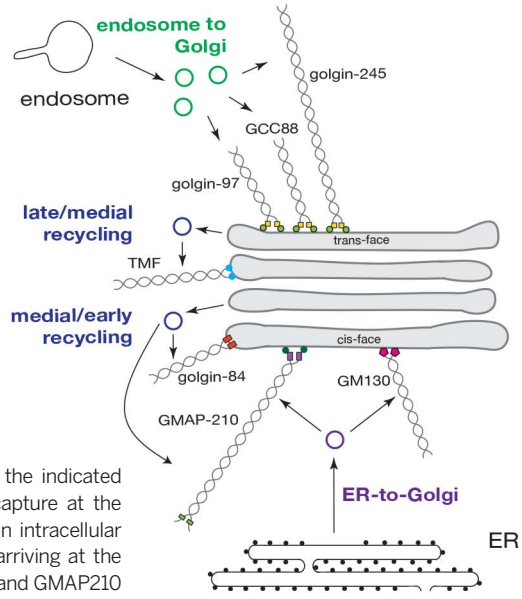

Fig. 8. Summary of golgin tethering activities. (**A**) Summary of results of relocation of the indicated membrane proteins by the panel of 10 golgins that were tested. Check mark indicates capture at the mitochondria in the majority of cells examined; X indicates absence of detectable effect on intracellular distribution. (**B**) Schematic of how golgins appear to tether the different sets of vesicles arriving at the Golgi. Golgin-97, golgin-245, and GCC88 capture endosome-to-TGN carriers; TMF, golgin-84, and GMAP210 mediate intra-Golgi transport, with the latter two having a preference for early Golgi residents; GMAP210 and GM130 capture ER-to-Golgi carriers.

Such membrane capture was also observed with other golgins that can relocate membrane proteins, including GCC88, TMF, GMAP-210, golgin-245, and golgin-84 (Fig. 7, F and G, and fig. S15). In contrast, we did not observe membranes accumulating around mitochondria coated with giantin or GCC185, consistent with their lack of effect on any of the markers tested (fig. S16). The tendency for the captured tubulovesicular structures to accumulate between mitochondria is presumably a result of their simultaneous engagement with golgins attached to adjacent mitochondria. This "zippering" effect resulted in clustering of mitochondria and explains the striped appearance of golgins on mitochondrial clusters that we had observed by immunofluorescence (Fig. 1D). In some cells, the mitochondrial clustering was so effective that all were collected together, separated by lines of captured vesicles that were often at a regular spacing between the mitochondria (Fig. 7E).

Discussion

Multiple classes of intracellular transport vesicles deliver cargo specifically to the Golgi apparatus. Our results show that relocation of specific golgin coiled-coil proteins is sufficient to redirect these specific classes of vesicles to an ectopic location (Fig. 8A). This provides clear in vivo evidence for at least seven of the golgins being bona fide vesicle tethers. However, the golgins not only capture vesicles but also can clearly distinguish among vesicles of different origins. This implies that the location of golgins specifies the point of vesicle tethering, and indicates that the machinery that recruits the golgins to specific cisternae of the Golgi helps to define their identity as the correct target organelle for incoming vesicles (Fig. 8B). This does not preclude other factors such as SNARE complex formation also making a contribution to the specificity of membrane traffic, but at least in this case, SNARE complex formation does not appear to be necessary for recognition of the destination organelle.

Our studies also reveal a degree of redundancy within the golgins; subsets of golgins apparently share tethering activity. For instance, golgin-97, golgin-245, and GCC88 all capture endosome-to-Golgi cargo, and GM130 and GMAP-210 both capture ER-to-Golgi carriers. This partial redundancy would be consistent with the proposal that they act collectively to surround different regions of the Golgi with docking sites for particular vesicle types (*30*). Such a model would be loosely analogous to the capture of cytoplasmic-to-nuclear cargo by the multiple FG repeat proteins of the nuclear pore (*31*). Three of the 10 golgins (CASP, GCC185, and giantin) did not show tethering activity in our assay; it is possible that they have other roles such as microtubule organization, as has been suggested for GCC185 (*14*). However, it is also possible that they can act as tethers, but only in conjunction with other golgins or after Golgi-specific modification (*32*, *33*).

The fact that golgins can distinguish different classes of carrier vesicle implies that each class displays one or more unique features that allow it to be recognized. There are a range of plausible candidates for these vesicle features, such as the Rab guanosine triphosphatases (*30*, *34*, *35*). Indeed, further proteins may bind directly to the golgins to help capture the vesicle even if the golgins are themselves sufficient to nucleate a functional tethering entity. However, irrespective of what else is involved in completing the entire tether, our findings should make it easier to identify and isolate specific classes of carrier vesicles. These key mediators of traffic are small and normally short-lived, but the ectopic golgins cause these carriers to accumulate in a docked state; this allows their contents to be readily probed by immunolabeling and also suggests routes to isolation for proteomic analysis. In the case of the Golgi, our studies are already informative: Trans-Golgi residents preferred TMF, whereas cis- and medial Golgi residents preferred golgin-84 and GMAP-210. Because the golgins were presented in the same way (i.e., on mitochondria), this finding indicates that vesicles from different parts of the stack must display different golgin-binding features, and hence their destination within the stack is directed at least in part by molecular interactions and not simply by spatial proximity. This may be important for allowing the structure of the Golgi to vary between tissues and yet still maintain cisternal identity. In addition, the finding that GMAP-210 can bind both ER-derived vesicles and those containing Golgi residents raises the intriguing possibility that it could act as a scaffold for the assembly of new cisternae. As such, our findings not only reveal that golgins are sufficient to confer specificity to the tethering of Golgi-destined vesicles but also provide new tools to investigate the organization of membrane traffic in this complex and much-debated organelle (*36*).

Materials and methods

Plasmids

C-terminally truncated golgins were provided by A. Gillingham [human GMAP210, golgin-84, and CASP (*33*, *37*)] or PCR-amplified from full-length cDNAs kindly provided by others [human GCC88, GCC185, and golgin-245 from P. Gleeson (*38*); human golgin-97 from F. Barr; mouse TMF and rat GM130 from M. Lowe; human giantin from A. Linstedt (*39*)]. Human MAO-A C-terminal TMD (481-528) was PCR-amplified from human cDNA.

Truncated golgins were as follows: GCC88ΔC-term (1-Ala^{718}); GCC185ΔC-term (1-Ser^{1535}); golgin-97ΔC-term (1-Val^{681}); golgin-245ΔC-term (1-Gly^{2163});

TMFΔC-term (1-Thr^{779}); giantinΔC-term (1-Cys^{3213}); golgin-84ΔC-term (1-Ala^{677}); CASPΔC-term (1-Arg^{618}); GM130ΔC-term (1-Leu^{872}); GM130delN75ΔC-term (Met^{75}-Leu^{872}); GMAP-210ΔC-term (1-Leu^{1756}).

GolginΔC-term-GAGAGA linker-HA-MAO, golginΔC-term-GAGAGA (or GAGAGS) linker-HA-FRB, mCherry-GAGAGA (or GSGSGS) linker-golginΔC-term-GAGAGA linker-MAO, FKBP-GFP-MAO, and FKBP-flag-MAO were cloned into COS cell expression vector containing the cytomegalovirus promoter. Bicistronic plasmids for coexpression of mito-APEX [Addgene #42607 (*29*)] and golginΔC-term-GAGAGA linker-HA-MAO were generated in pcDNA3.1+ (Clontech) from the respective monocistronic plasmids.

Antibodies

Antibodies used in this study included mouse CD-MPR [22d4, Developmental Studies Hybridoma Bank (DSHB)]; mouse CD8 (UCHT4, Sigma); rabbit CLASP1 (gift from A. Akhamanova); rat β′COP [23C (TCP-1)]; mouse EEA1 (610457, BD Biosciences); mouse ERGIC-53 (ALX-804-602-C100, Enzo Life Sciences); mouse GalNAc-T2 (UH-4, gift from U. Mandel and H. Clausen), rabbit GCC88 (HPA021323, Sigma); rabbit GCC185 (HPA035849, Sigma); rabbit giantin (HPA011008, Sigma); rabbit GM130 (1837-1, Epitomics); mouse GM130 (610823, BD Biosciences); mouse golgin-245 (611281, BD Biosciences); rabbit golgin-84 (HPA000992, Sigma); rabbit HA (Y-11, Santa Cruz Biotechnology); rat HA (3F10, Roche); mouse LAMP1 (H4A3, DSHB); mouse MTC02 (ab3298, Abcam); mouse p115 (612260, BD Biosciences); sheep TGN46 (AHP500, AbD serotec); rabbit TMF (HPA008729, Sigma); mouse Vti1a (611220, BD Biosciences); and rabbit ZFPL1 (HPA014909, Sigma).

Cell culture, transient transfections, and treatments

COS-7 cells, CD8-CIMPR HeLa cells (*22*), C1-HeLa cells expressing eGPF-FM4-hGH (*24*), and mouse embryonic fibroblasts (MEFs) were cultured in Dulbecco's modified Eagle's medium (DMEM; Invitrogen) supplemented with 10% fetal calf serum (FCS) and penicillin/streptomycin at 37°C and 5% CO_2.

COS-7 cells and MEFs were transiently transfected with Fugene6 (Promega), and HeLa cell lines with Xtreme Gene 9 (Roche), according to the manufacturers' recommendations. Cells plated on six-well plates were transfected 10 to 18 hours after plating when cells had reached 50 to 80% confluency. After the transfection mixtures were applied, cells were analyzed 24 to 48 hours after transfection.

To induce heterodimerization of FKBP and FRB domains, we treated cells coexpressing fusion proteins with each of these domains at 37°C for various incubation times with rapamycin (Sigma; 200 nM from 2.74 mM stock in DMSO). To depolymerize microtubules, we treated cells at 37°C for 2 to 6 hours with nocodazole (Sigma, 1 μM from a 1 mM stock in DMSO). To induce secretion in C1-HeLa cells, we treated cells with D/D solubilizer (Clontech, 0.5 μM) at 37°C for various incubation times (*24*).

HeLa cells stably expressing the CD8-CIMPR reporter construct (*22*) were transfected with golgin-mito constructs 24 to 48 hours before the internalization assay and plated onto multispot microscope slides 12 to 36 hours after transfection. Slides were incubated at 4°C for 20 min to stop all trafficking and washed with phosphate-buffered saline (PBS). Mouse antibody to CD8 (Sigma) was applied in DMEM for 30 min at 4°C to bind onto the cell surface. After two washes with PBS, antibody uptake was induced by replacing PBS with prewarmed DMEM followed by incubation at 37°C prior to fixation with 4% formaldehyde in PBS.

Immunofluorescence and live cell imaging

COS-7 cells, HeLa cells, and MEFs were fixed with 4% formaldehyde in PBS for 30 min, permeabilized in 0.5% Triton X-100 for 10 min, and blocked in blocking buffer (20% FCS, 0.5% Tween-20 in PBS) for 30 min. Primary and secondary antibodies were applied in blocking buffer for 1 hour; cells were washed twice with PBS and mounted under a cover slip in Vectashield mounting medium (Vector Labs). Images were acquired with a Zeiss LSM780 confocal microscope using a 63× Apochromat oil-immersion objective.

Quantitation of mitochondrial capture in fixed cells was performed with Imaris 7.4.0 (Bitplane). First, the mitochondria and Golgi regions of each transfected cell were segmented by the HA staining pattern and ZFPL1 staining, respectively. Next, the latter segment was subtracted from the former segment to create a new mitochondria segment that had excluded any overlapping Golgi regions. Mean intensity of the molecule of interest on this segment was determined as an arbitrary, but relative, value. Background staining levels were obtained by quantifying mean signal levels on a whole cell segment subtracting the Golgi segment.

HeLa cells stably expressing GFP-FM4-hGH [C1-HeLa (*24*)] were seeded onto four-well chambers (Lab-Tek) in complete medium. Before imaging, 10 mM HEPES (Sigma) was applied to the cells. Live cells were imaged at 37°C using a 100× oil objective on a Nikon Eclipse Ti inverted microscope equipped with an Andor Revolution XD system and a Yokogawa CSU-X1 and an Andor iXon EMCCD camera. Quantitation of transient association of GFP-FM4-hGH with mitochondria decorated with golgins was as for fixed cells, except the mitochondria were segmented using the mCherry fluorescence. At each time point of a movie, two sets of mean signal intensity of the molecule of interest were obtained, one from the mitochondria segment and the other from the whole cell segment.

APEX and electron microscopy

Cells grown on glass-bottom petri dishes (MatTek) were fixed at room temperature with 2% glutaraldehyde (EM grade, Agar Scientific) in 0.1 M cacodylate buffer, pH 7.4 (CB). Cells were then incubated on ice for 30 to 60 min, rinsed twice with chilled CB, and blocked with 50 mM glycine in CB on ice for 10 min. To start the APEX-catalyzed oxidation of 3,3-diaminobenzidine (DAB), we added a freshly prepared solution of DAB free base (0.5 mg/ml; Sigma) in HCl and 0.03% (10 mM) H_2O_2 (Sigma) to the cells. Formation of reaction product (a brownish precipitate) was monitored by light microscopy. After 15 min, the reaction was halted by washing the cells twice with chilled CB. Samples were postfixed with 1% osmium tetroxide in CB on ice for 1 hour, washed five times with distilled water, and dehydrated in an ascending ethanol series (30%, 50%, 70%, 90%, 100%) at room temperature. The dehydrated samples were infiltrated and embedded in CY212 resin. Areas containing brown precipitates were excised and mounted on dummy blocks and sectioned parallel to the substratum. Pale gold 70-nm sections were contrasted with saturated aqueous uranyl acetate and Reynolds lead citrate. Electron micrographs were recorded at 80 kV or 120 kV on a FEI Tecnai Spirit TEM.

REFERENCES AND NOTES

1. R. Jahn, R. H. Scheller, SNAREs—Engines for membrane fusion. *Nat. Rev. Mol. Cell Biol.* **7**, 631–643 (2006). doi: 10.1038/nrm2002; pmid: 16912714
2. T. Söllner *et al.*, SNAP receptors implicated in vesicle targeting and fusion. *Nature* **362**, 318–324 (1993). doi: 10.1038/362318a0; pmid: 8455717
3. J. A. McNew *et al.*, Compartmental specificity of cellular membrane fusion encoded in SNARE proteins. *Nature* **407**, 153–159 (2000). doi: 10.1038/35025000; pmid: 11001046
4. R. Willett *et al.*, COG complexes form spatial landmarks for distinct SNARE complexes. *Nat. Commun.* **4**, 1553 (2013). doi: 10.1038/ncomms2535; pmid: 23462996
5. J. R. C. Whyte, S. Munro, Vesicle tethering complexes in membrane traffic. *J. Cell Sci.* **115**, 2627–2637 (2002). pmid: 12077354
6. M. G. Waters, S. R. Pfeffert, Membrane tethering in intracellular transport. *Curr. Opin. Cell Biol.* **11**, 453–459 (1999). doi: 10.1016/S0955-0674(99)80065-9; pmid: 10449330
7. I.-M. Yu, F. M. Hughson, Tethering factors as organizers of intracellular vesicular traffic. *Annu. Rev. Cell Dev. Biol.* **26**, 137–156 (2010). doi: 10.1146/annurev.cellbio.042308.113327; pmid: 19575650
8. B. S. Glick, A. Nakano, Membrane traffic within the Golgi apparatus. *Annu. Rev. Cell Dev. Biol.* **25**, 113–132 (2009). doi: 10.1146/annurev.cellbio.24.110707.175421; pmid: 19575639
9. B. Goud, P. A. Gleeson, TGN golgins, Rabs and cytoskeleton: Regulating the Golgi trafficking highways. *Trends Cell Biol.* **20**, 329–336 (2010). doi: 10.1016/j.tcb.2010.02.006; pmid: 20227882
10. I. Barinaga-Rementeria Ramirez, M. Lowe, Golgins and GRASPs: Holding the Golgi together. *Semin. Cell Dev. Biol.* **20**, 770–779 (2009). doi: 10.1016/j.semcdb.2009.03.011; pmid: 19508854
11. S. Munro, The golgin coiled-coil proteins of the Golgi apparatus. *Cold Spring Harb. Perspect. Biol.* **3**, a005256 (2011). doi: 10.1101/cshperspect.a005256; pmid: 21436057
12. J. Malsam, A. Satoh, L. Pelletier, G. Warren, Golgin tethers define subpopulations of COPI vesicles. *Science* **307**, 1095–1098 (2005). doi: 10.1126/science.1108061; pmid: 15718469
13. G. Drin, V. Morello, J.-F. Casella, P. Gounon, B. Antonny, Asymmetric tethering of flat and curved lipid membranes by a golgin. *Science* **320**, 670–673 (2008). doi: 10.1126/science.1155821; pmid: 18451304
14. A. Efimov *et al.*, Asymmetric CLASP-dependent nucleation of noncentrosomal microtubules at the trans-Golgi network. *Dev. Cell* **12**, 917–930 (2007). doi: 10.1016/j.devcel.2007.04.002; pmid: 17543864
15. C. Preisinger *et al.*, YSK1 is activated by the Golgi matrix protein GM130 and plays a role in cell migration through its substrate 14-3-3ζ. *J. Cell Biol.* **164**, 1009–1020 (2004). doi: 10.1083/jcb.200310061; pmid: 15037601
16. Y. Elkis *et al.*, Testosterone deficiency accompanied by testicular and epididymal abnormalities in TMF$^{-/-}$ mice. *Mol. Cell. Endocrinol.* **365**, 52–63 (2013). doi: 10.1016/j.mce.2012.09.003; pmid: 23000399

17. P. Smits *et al*., Lethal skeletal dysplasia in mice and humans lacking the golgin GMAP-210. *N. Engl. J. Med.* **362**, 206–216 (2010). doi: 10.1056/NEJMoa0900158; pmid: 20089971
18. N. Nakamura, M. Lowe, T. P. Levine, C. Rabouille, G. Warren, The vesicle docking protein p115 binds GM130, a cis-Golgi matrix protein, in a mitotically regulated manner. *Cell* **89**, 445–455 (1997). doi: 10.1016/S0092-8674(00)80225-1; pmid: 9150144
19. T. Braulke, J. S. Bonifacino, Sorting of lysosomal proteins. *Biochim. Biophys. Acta* **1793**, 605–614 (2009). doi: 10.1016/j.bbamcr.2008.10.016; pmid: 19046998
20. F. Mallard *et al*., Early/recycling endosomes-to-TGN transport involves two SNARE complexes and a Rab6 isoform. *J. Cell Biol.* **156**, 653–664 (2002). doi: 10.1083/jcb.200110081; pmid: 11839770
21. S. Ponnambalam, C. Rabouille, J. P. Luzio, T. Nilsson, G. Warren, The TGN38 glycoprotein contains two non-overlapping signals that mediate localization to the trans-Golgi network. *J. Cell Biol.* **125**, 253–268 (1994). doi: 10.1083/jcb.125.2.253; pmid: 8163544
22. M. N. J. Seaman, Cargo-selective endosomal sorting for retrieval to the Golgi requires retromer. *J. Cell Biol.* **165**, 111–122 (2004). doi: 10.1083/jcb.200312034; pmid: 15078902
23. A. Budnik, D. J. Stephens, ER exit sites—Localization and control of COPII vesicle formation. *FEBS Lett.* **583**, 3796–3803 (2009). doi: 10.1016/j.febslet.2009.10.038; pmid: 19850039
24. D. E. Gordon, L. M. Bond, D. A. Sahlender, A. A. Peden, A targeted siRNA screen to identify SNAREs required for constitutive secretion in mammalian cells. *Traffic* **11**, 1191–1204 (2010). doi: 10.1111/j.1600-0854.2010.01087.x; pmid: 20545907
25. N. Nakamura *et al*., Characterization of a cis-Golgi matrix protein, GM130. *J. Cell Biol.* **131**, 1715–1726 (1995). doi: 10.1083/jcb.131.6.1715; pmid: 8557739
26. C. Infante, F. Ramos-Morales, C. Fedriani, M. Bornens, R. M. Rios, GMAP-210, A cis-Golgi network-associated protein, is a minus end microtubule-binding protein. *J. Cell Biol.* **145**, 83–98 (1999). doi: 10.1083/jcb.145.1.83; pmid: 10189370
27. B. S. Glick, A. Luini, Models for Golgi traffic: A critical assessment. *Cold Spring Harb. Perspect. Biol.* **3**, a005215 (2011). doi: 10.1101/cshperspect.a005215; pmid: 21875986
28. C.-F. Chiu *et al*., ZFPL1, a novel ring finger protein required for cis-Golgi integrity and efficient ER-to-Golgi transport. *EMBO J.* **27**, 934–947 (2008). doi: 10.1038/emboj.2008.40; pmid: 18323775
29. J. D. Martell *et al*., Engineered ascorbate peroxidase as a genetically encoded reporter for electron microscopy. *Nat. Biotechnol.* **30**, 1143–1148 (2012). doi: 10.1038/nbt.2375; pmid: 23086203
30. R. Sinka, A. K. Gillingham, V. Kondylis, S. Munro, Golgi coiled-coil proteins contain multiple binding sites for Rab family G proteins. *J. Cell Biol.* **183**, 607–615 (2008). doi: 10.1083/jcb.200808018; pmid: 19001129
31. S. Wälde, R. H. Kehlenbach, The part and the whole: Functions of nucleoporins in nucleocytoplasmic transport. *Trends Cell Biol.* **20**, 461–469 (2010). doi: 10.1016/j.tcb.2010.05.001; pmid: 20627572
32. J. V. Reddy *et al*., A functional role for the GCC185 golgin in mannose 6-phosphate receptor recycling. *Mol. Biol. Cell* **17**, 4353–4363 (2006). doi: 10.1091/mbc.E06-02-0153; pmid: 16885419
33. A. K. Gillingham, A. C. Pfeifer, S. Munro, CASP, the alternatively spliced product of the gene encoding the CCAAT-displacement protein transcription factor, is a Golgi membrane protein related to giantin. *Mol. Biol. Cell* **13**, 3761–3774 (2002). doi: 10.1091/mbc.E02-06-0349; pmid: 12429822
34. B. Short, A. Haas, F. A. Barr, Golgins and GTPases, giving identity and structure to the Golgi apparatus. *Biochim. Biophys. Acta* **1744**, 383–395 (2005). doi: 10.1016/j.bbamcr.2005.02.001; pmid: 15979508
35. A. Satoh, Y. Wang, J. Malsam, M. B. Beard, G. Warren, Golgin-84 is a rab1 binding partner involved in Golgi structure. *Traffic* **4**, 153–161 (2003). doi: 10.1034/j.1600-0854.2003.00103.x; pmid: 12656988
36. S. Emr *et al*., Journeys through the Golgi—Taking stock in a new era. *J. Cell Biol.* **187**, 449–453 (2009). doi: 10.1083/jcb.200909011; pmid: 19948493
37. A. K. Gillingham, A. H. Y. Tong, C. Boone, S. Munro, The GTPase Arf1p and the ER to Golgi cargo receptor Erv14p cooperate to recruit the golgin Rud3p to the cis-Golgi. *J. Cell Biol.* **167**, 281–292 (2004). doi: 10.1083/jcb.200407088; pmid: 15504911
38. M. R. Luke, L. Kjer-Nielsen, D. L. Brown, J. L. Stow, P. A. Gleeson, GRIP domain-mediated targeting of two new coiled-coil proteins, GCC88 and GCC185, to subcompartments of the trans-Golgi network. *J. Biol. Chem.* **278**, 4216–4226 (2003). doi: 10.1074/jbc.M210387200; pmid: 12446665
39. A. D. Linstedt, H. P. Hauri, Giantin, a novel conserved Golgi membrane protein containing a cytoplasmic domain of at least 350 kDa. *Mol. Biol. Cell* **4**, 679–693 (1993). doi: 10.1091/mbc.4.7.679; pmid: 7691276
40. J. Mitoma, A. Ito, Mitochondrial targeting signal of rat liver monoamine oxidase B is located at its carboxy terminus. *J. Biochem.* **111**, 20–24 (1992). pmid: 1318879
41. J. R. Silvius, P. Bhagatji, R. Leventis, D. Terrone, K-ras4B and prenylated proteins lacking "second signals" associate dynamically with cellular membranes. *Mol. Biol. Cell* **17**, 192–202 (2006). doi: 10.1091/mbc.E05-05-0408; pmid: 16236799

ACKNOWLEDGMENTS

We thank A. Akhmanova, F. Barr, H. Clausen, P. Gleeson, A. Linstedt, M. Lowe, U. Mandel, M. Robinson, and M. Seaman for generous provision of reagents; G. Howard for help with electron microscopy; and A. Gillingham, R. Hegde, B. Nichols, and K. Röper for comments on the manuscript. Supported by the UK Medical Research Council (MRC file reference no. U105178783). The data are presented in the main manuscript and the supplementary materials.

SUPPLEMENTARY MATERIALS

www.sciencemag.org/content/346/6209/1256898/suppl/DC1
Figs. S1 to S16
Movies S1 and S2

3 June 2014; accepted 2 October 2014
10.1126/science.1256898

RESEARCH ARTICLES

TOPOLOGICAL MATTER

Observation of Majorana fermions in ferromagnetic atomic chains on a superconductor

Stevan Nadj-Perge,[1]* Ilya K. Drozdov,[1]* Jian Li,[1]* Hua Chen,[2]* Sangjun Jeon,[1] Jungpil Seo,[1] Allan H. MacDonald,[2] B. Andrei Bernevig,[1] Ali Yazdani[1]†

Majorana fermions are predicted to localize at the edge of a topological superconductor, a state of matter that can form when a ferromagnetic system is placed in proximity to a conventional superconductor with strong spin-orbit interaction. With the goal of realizing a one-dimensional topological superconductor, we have fabricated ferromagnetic iron (Fe) atomic chains on the surface of superconducting lead (Pb). Using high-resolution spectroscopic imaging techniques, we show that the onset of superconductivity, which gaps the electronic density of states in the bulk of the Fe chains, is accompanied by the appearance of zero-energy end-states. This spatially resolved signature provides strong evidence, corroborated by other observations, for the formation of a topological phase and edge-bound Majorana fermions in our atomic chains.

Topological superconductors are a distinct form of matter that is predicted to host boundary Majorana fermions (*1*–*3*). These quasi-particles are the emergent condensed matter analogs of the putative elementary spin-1/2 particles originally proposed by Ettore Majorana (*4*) with the intriguing property of being their own antiparticles. Supersymmetric theories in particle physics and some models for dark matter in cosmology motivate an ongoing search for free Majorana particles (*5*, *6*). The search for Majorana quasi-particle (MQP) bound states in condensed matter systems is motivated in part by their potential use as topological qubits to perform fault-tolerant computation aided by their non-Abelian characteristics (*7*, *8*). Spatially separated pairs of MQP pairs can be used to encode information in a nonlocal fashion, making them more immune to quantum decoherence. Early proposals for the detection of MQPs were based on the properties of superfluid ^{3}He, on exotic fractional quantum Hall states, or on correlated superconductors (*9*–*12*). The focus in the past few years has shifted to the search for these exotic fermions in weakly interacting synthetic systems in which proximity to a conventional Bardeen-Cooper-Schrieffer (BCS) superconductor is used in concert with other electronic properties to create the topological phase that hosts MQPs.

The idea that MQPs can be engineered in the laboratory grew from the theoretical observation that proximity-induced superconductivity on the surface state of a topological insulator is topological in nature (*13*). Pairing on a spinless Fermi surface (*1*), created in this case by the spin-momentum locking of topological surface states, must be effectively p-wave to satisfy the pair–wave function antisymmetry requirement and is therefore topological. This approach was later extended to systems in which a semiconductor nanowire with strong spin-orbit interactions in a parallel magnetic field is in contact with a superconductor (*14*, *15*). Experimental efforts to implement the nanowire proposal have uncovered evidence for a zero-bias peak (ZBP) in tunneling spectroscopy studies of hybrid superconductor-semiconductor nanowire devices, as expected in the presence of the MQP states of a topological superconductor (*16*–*19*). However, the ZBPs detected in such devices could also be caused by the Kondo effect or disorder (*20*–*24*). A key disadvantage of the nanowire studies is that they lack the ability to spatially resolve ZBP features in order to demonstrate that they are localized at the boundary of a gapped superconducting phase. Here we introduce a method of fabricating one-dimensional (1D) topological superconductors and detecting their MQPs that achieves both spatial and spectral resolution.

Magnetic atomic chains as a platform for topological superconductivity

Magnetic atom chains on the surface of a conventional s-wave superconductor have been proposed to provide a versatile platform for the realization of topological superconductors (*25*). This platform lends itself to the detection of MQPs by scanning tunneling microscopy (STM). In the absence of intrinsic spin-orbit coupling, previous theoretical work (*25*–*30*) has shown that a topological phase emerges in an atomic chain when its magnetic atoms have a spatially modulated spin arrangement—for example, a spin helix. The spin texture of the chains emulates the combination of spin-orbit and Zeeman interactions required to create a topological phase. Helical spin configurations are, however, much less common in atomic chains than simple ferromagnetic and antiferromagnetic ones or may be more influenced by disorder (*31*). We therefore explore an alternate, more realizable scenario by placing an Fe chain on the surface of Pb (Fig. 1A). We will show that the essential ingredients for topological superconductivity in this scenario are the ferromagnetic interaction between Fe atoms realized at the Fe-Fe bond distance and the strong spin-orbit interaction in superconducting Pb (*32*). Our approach is related to earlier proposals for topological superconductivity using half-metal ferromagnets or metallic chains placed in contact with superconductors in the presence of spin-orbit interactions (*33*–*35*).

To illustrate the key ingredient of our approach, we first consider an idealized ferromagnetic chain of Fe atoms described by a tight-binding model calculation [section 1 of (*36*)]. We use hopping parameters appropriate for d orbitals of bulk Fe to compute the band structure of a freely suspended linear Fe chain (Fig. 1B). The large exchange interaction results in a fully occupied majority spin band with the Fermi level (E_F) residing in the minority spin bands. Coupling the Fe chain to a BCS superconductor with strong spin-orbit interaction (such as Pb), we find that the spin-orbit interactions lift many of the degeneracies in the chain's band structure shown in Fig. 1B, while at the same time allowing for the occurrence of p-wave superconductivity [section 1 of (*36*)]. Because only the Fe d-bands will be strongly spin-polarized, other bands are unlikely to influence the topological character of the system, whether they reside mainly on the Fe chains or on the substrate. Notably, for large exchange interaction, topological superconductivity is ubiquitous to the type of band structure shown in Fig. 1B—occurring for nearly all values of the chemical potential [Fig. 1C and (*36*) for details]. In this idealized situation, the number of minority spin bands that cross the Fermi level is almost always odd, making the presence of MQPs at the ends of the chains almost guaranteed.

We consider another idealized situation for topological superconductivity by modeling a ferromagnetic chain embedded in a 2D superconductor, which allows us to identify its signatures in STM measurements [section 2 of (*36*)]. The spatially resolved density of states (DOS) of this 2D model at positions on the chain differs from that of a BCS superconductor by the presence of Yu-Shiba-Rusinov in-gap states (Fig. 1, C and D) (*37*–*41*). These calculations also exhibit the spatial and spectroscopic signatures of MQPs at the chain ends (Fig. 1, D and E). Other more realistic models for our experimental system are also worth exploring (see below), and nontopological phases can occur for some chain geometries. These model studies of proximity-induced superconductivity

[1]Joseph Henry Laboratories and Department of Physics, Princeton University, Princeton, NJ 08544, USA. [2]Department of Physics, University of Texas at Austin, Austin, TX 78712, USA.
*These authors contributed equally to this work. †Corresponding author. E-mail: yazdani@princeton.edu

on Fe chains demonstrate that topological states can be identified using STM by establishing (i) ferromagnetism on the chain, (ii) spin-orbit coupling in the host superconductor (or at its surface), (iii) a superconducting gap in the bulk of the chain, and finally (iv) a localized ZBP due to MQPs at the ends of the chain. One can overconstrain these conditions by providing evidence that the system has an odd number of band crossings at E_F. The disappearance of edge-localized ZBPs when the underlying superconductivity is suppressed provides an additional check to show that the MQP signature is associated with superconductivity and not with other phenomena, such as the Kondo effect (*20*–*22*).

Ferromagnetic Fe atomic chains on the Pb(110) surface

To fabricate an atomic chain system on the surface of a superconductor with strong spin-orbit coupling, we used a Pb(110) single crystal, which we prepared with cycles of in situ sputtering and annealing. Following submonolayer evaporation of Fe on the Pb surface at room temperature and light annealing, STM images (temperature was 1.4 K for all experiments reported here) show large atomically ordered regions of the Pb(110) surface, as well as islands and chains of Fe atoms that have nucleated on the surface (Fig. 2A). The islands appear to provide the seed from which chains self-assemble following the anisotropic structure of the underlying surface. Depending on growth conditions, we find Fe chains as long as 500 Å, usually with an Fe island in the middle (inset, Fig. 2A). In longer chains, the ends are separated from the islands in the middle by atomically ordered regions that are 200 Å long. High-resolution STM images show that the chains (with an apparent height of ~2 Å) are centered between the atomic rows of Pb(110), display weak atomic corrugation (5 to 10 pm), and strain the underlying substrate (Fig. 2, B to D). Approximate periodicities of 4.2 and 21 Å measured on the chain show that the Fe chain has a structure that is incommensurate with that of the underlying Pb surface. To identify the atomic structure of our chains, we performed density functional theory (DFT) calculations of Fe on the Pb(110) surface; these calculations show that strong Fe-Pb bonding results in a partially submerged zigzag chain of Fe atoms between Pb(110) atom rows [Fig. 2, E and F; see section 3 of (*36*) for DFT details]. From these calculations, we find that among several candidate structures with the experimental periodicity, a three-layer Fe zigzag chain partially submerged in Pb has the lowest energy and gives contours of constant electron density most consistent with our STM images.

We use a combination of spectroscopic and spin-polarized measurements to demonstrate that Fe atomic chains on Pb(110) satisfy the criteria [conditions (i) to (iv) above] required to demonstrate a 1d topological superconductor. First, we discuss spin-polarized STM studies that show experimental evidence for ferromagnetism on the Fe chains and strong spin-orbit coupling on the Pb surface (Fig. 3, A to C). Using Cr STM tips, which have been prepared using controlled indentation of the tip into Fe islands, we measured tunneling conductance (dI/dV) at a low bias voltage (V = 30 mV) as a function of magnetic field perpendicular to the surface on both chains and on the Pb substrate (Fig. 3, A and B). We validated our preparation of spin-polarized tips by also performing experiments on Co on Cu(111), now a standard system (*40*) for verifying spin-polarized STM capabilities, in situ during the same experimental runs. The spin-polarized measurements on the Fe chains show hysteresis loops characteristic of tunneling between two ferromagnets with the field switching only one of them (at ~0.25 T) (*42*, *43*). The strength of the spin-polarized STM signal varies along the chain, probably due to the electronic and structural properties of our zigzag Fe chains. We find that tunneling with the same tip on the Pb(110) surface far from the Fe chains also shows field-dependent conductance. In contrast to the asymmetric behavior observed on the chains, the field dependence on the substrate is symmetric with field, as expected for tunneling into nonmagnetic Pb, but still shows the switching behavior that is due to magnetization reversal of the tip. Similar tunneling magnetoresistance curves have previously been reported for tunneling from a ferromagnet into semiconductors and have been attributed to spin-polarized tunneling in the presence of strong spin-orbit interactions (*44*). The field-dependent signal on Pb is consistent with a preference for spins to be in the plane of the surface, in which case further polarization of the tip's magnetization perpendicular to the surface suppresses tunneling conductance. The size of this signal depends on the orientation of the tip's magnetization relative to that of the spins at the surface. This observation is consistent with a Rashba-like ($k \cdot \sigma$, where k is the electron's momentum and σ is the spin) spin-orbit coupling at the Pb(110) surface upon which our ferromagnetic Fe chain is self-assembled.

Our DFT calculations confirm that the zigzag Fe chains in Pb(110) are ferromagnetic [section 3 of (*36*)], as expected given that the distance between the Fe atoms is close in that of bulk Fe. These calculations also demonstrate that Fe chains on Pb have an exchange energy J of ~2.4 eV and a magnetic anisotropy energy (1.4 meV

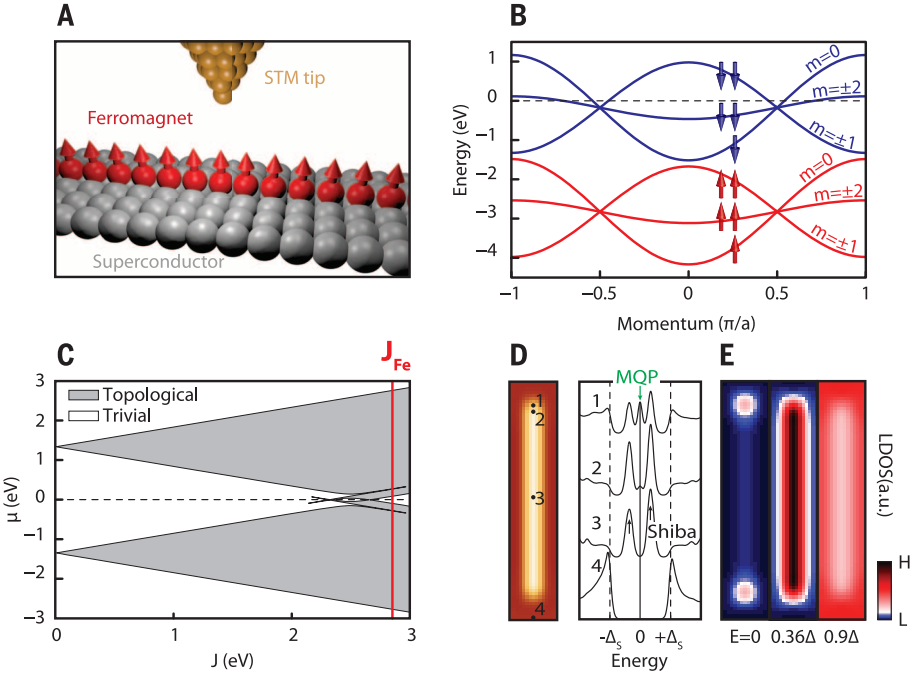

Fig. 1. Topological superconductivity and Majorana fermions in ferromagnetic atomic chains on a superconductor. (**A**) Schematic of the proposal for MQP realization and detection: A ferromagnetic atomic chain is placed on the surface of strongly spin-orbit–coupled superconductor and studied using STM. (**B**) Band structure of a linear suspended Fe chain before introducing spin-orbit coupling or superconductivity. The majority spin-up (red) and minority spin-down (blue) d-bands labeled by azimuthal angular momentum m are split by the exchange interaction J (degeneracy of each band is noted by the number of arrows). a, interatomic distance. (**C**) Regimes for trivial and topological superconducting phases are identified for the band structure shown in (B) as a function of exchange interaction in presence of SO coupling. The value J for Fe chains based on DFT calculations is noted [sections 1 and 3 of (*36*)]. μ is the chemical potential. (**D**) Model calculation of the local density of states (LDOS) of the atomic chain embedded in a 2D superconductor [section 2 of (*36*)]. The left panel shows an image of the chain and the locations at which the LDOS is represented in the right panel; the LDOS curves are offset for clarity. In-gap (Shiba) and zero-energy (MQP) features in LDOS are noted. (**E**) Spatially resolved LDOS calculated at various energies noted at the bottom using the same model. Red (or blue) indicates regions of the high (or low) LDOS. a.u., arbitrary units.

per Fe atom) that is large enough to suppress thermal fluctuations in the magnetic configuration. The large anisotropy also implies that very large fields are required to switch the chain's magnetization orientation, consistent with our finding that low fields only reorient the tip's magnetization.

Our model studies demonstrate that topological superconductivity occurs when an odd number of 1D bands cross the Fermi energy. We now focus on obtaining information on the electronic structure of our Fe chains from STM spectroscopy. As shown in Fig. 3D, the Fe chain contribution to the DOS has two distinct peaks separated by ~0.9 eV, one above and the other below E_F. To understand the origin of this double-peak structure, we have carried out a number of model calculations, including those based on tight binding and DFT for our specific zigzag Fe structures identified by comparing DFT to STM images (Fig. 2, C to F). The results of these calculations, for both suspended and Pb-embedded chains [sections 3 and 4 in (*36*)], indicate that E_F for such a system lies in the Fe minority bands and that the double-peak structure is related to structure-specific features of the minority-band bonding pattern. Moreover, the tight-binding model that reproduces the experimentally observed double-peak structure (Fig. 3E) shows the number of band crossings at E_F to be odd [phase diagram in section 4 in (*36*)]. Although momentum-resolved DOS measurements with the scanning tunneling microscope will be required to more directly probe the band structure of the chains, the correspondence between model calculations and the measured DOS is very suggestive that the band structure of these chains is consistent with topological superconductivity. All of the chains we examined in search for MQPs share the above structural and electronic characteristics.

Superconductivity on Fe atomic chains and signatures of MQP

We use high-resolution spectroscopy and spectroscopic mapping, with both normal and superconducting tips, to establish the signature of both the pairing gap on our Fe chains and of the MQP at their ends at low temperatures (1.4 K) (Figs. 4 and 5). In Fig. 4, we show spatially resolved spectra, as well as spectroscopic maps with a normal tip, on both the substrate and the Fe chain. Examining the spectra away from the Fe chain on the Pb surface, we resolved a superconducting gap that can be modeled with the thermally broadened (T = 1.4 K) BCS DOS with Pb's bulk pairing gap (Δ_s = 1.36 meV) (Fig. 4A, lowest curve). In the middle of the chains, spatially resolved spectroscopic measurements show the formation of features in the Pb gap, with asymmetric edges at roughly ±1 meV, which evolve to include a sharp ZBP that is prominently detected about 10 to 20 Å from the ends of the chain. Figure 4, B to E, shows such ZBPs at two ends of the same chain that grow out of an Fe island. Approaching the island, the spectra on both sides of the chain also show enhanced low-energy DOS, but at these locations, the structure of the chains is not known [example in fig. S14 in (*36*)]. Spectroscopic maps in Fig. 4F allow us to visualize the spatial structure of excitations at different energies and clearly show the localized nature of the ZBPs at one end of the chain and the delocalized nature of the excitations at higher energies throughout the chain. These maps also resolve the spatially modulated decay of the ZBP away from the chain ends that is anticipated from model calculations [section 2 of (*36*)]. Our ability to correlate the location of the ZBP with the end of our atomic chains is one of the main experimental requirements for interpreting that this feature is associated with the predicted MQP of a topological superconductor. We have confirmed the robust observation of ZBPs at the end of multiple chains (more than 10), measured with different tips, on different experimental runs with freshly prepared Pb and Fe chains [see section 5 of (*36*) for more examples].

To obtain more precise information about the pairing gap induced on the Fe chains, we have also carried out spectroscopic measurements with superconducting tips, prepared in situ by contacting a W tip with the Pb surface (Fig. 5). Away from the Fe chains, the spectra measured with these tips show the behavior expected for tunneling between two superconductors, with sharp peaks at energies corresponding to the sum of the BCS gaps on the tip Δ_T and the substrate Δ_S (Fig. 5A). The singularity in DOS at the gap edge in this case allows us to resolve finer features within the thermally broadened DOS of our chains. At the end of the chains, spectroscopy with the superconducting tips shows a sharp peak at $|eV| = \Delta_T$

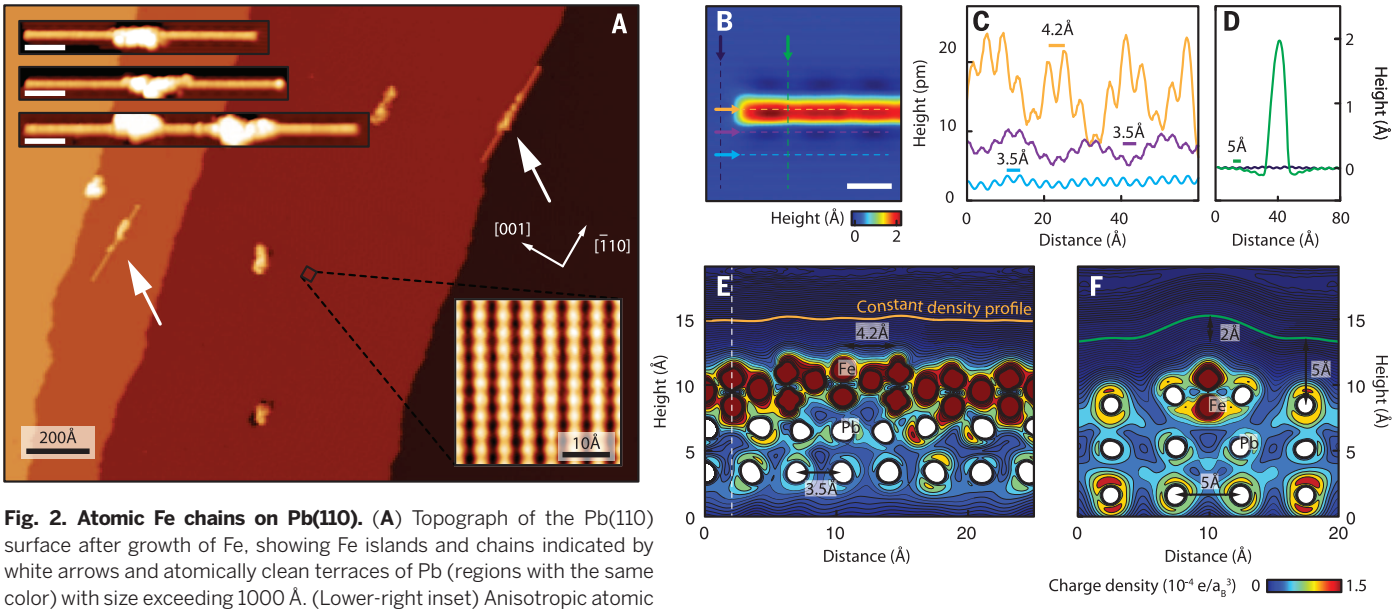

Fig. 2. Atomic Fe chains on Pb(110). (**A**) Topograph of the Pb(110) surface after growth of Fe, showing Fe islands and chains indicated by white arrows and atomically clean terraces of Pb (regions with the same color) with size exceeding 1000 Å. (Lower-right inset) Anisotropic atomic structure of the Pb(110) surface with interatomic distances in the two directions, a = 4.95 Å and $a/\sqrt{2}$ = 3.5 Å, as expected for the face-centered cubic crystal structure. (Upper-left insets) images of several atomic Fe chains and the islands from which they grow (scale bars, 50 Å). (**B**) Fine-scale topograph. The color-coded lines correspond to the line traces in (C) and (D). Scale bar, 20 Å. (**C**) Cross section of the image in (B) along the chain measured on top of the chain (light brown) and along two different lines next to the chains (purple and blue), showing atomic corrugation of the chain and strain induced in the substrates. Both are influenced by the incommensurate placement of the Fe atoms in Pb. (**D**) Apparent STM height profile on the substrate (black) and across the atomic chain (green). (**E** and **F**) Atomic structure of the zigzag chain, as calculated using DFT [section 3 of (*36*)] along (E) and across (F) the chain. The Fe chain structure that has the lowest energy in the DFT calculations matches the structural features in the STM measurements [(B) to (D)]. a_B is the Bohr radius. All measurements were carried out at 1.4 K.

(where eV is energy) corresponding to the peaks at these locations identified as ZBPs when measured with the normal tips (Fig. 5B). Spectroscopic maps with the superconducting tip at this energy also show this feature to be the most pronounced at the end of the chains (Fig. 5D, middle panel), as expected for bound MQPs. At other locations in the middle (bulk) of the chains (Fig. 5, C and D), this signature of MQPs is greatly suppressed, but there are sharp peaks at higher energies $|eV| > \Delta_T$ that can be attributed to the edge of a pairing gap at about 200 to 300 μeV. Using a model calculation of scattering of electrons in an Fe chain from a Pb(110) surface, we estimate that the effective Rashba spin-orbit interaction strength induced on the chain by the Pb substrate [section 6 of (*36*)] is ~0.11 eV-Å. The use of this value in our simple linear chain calculation (Fig. 1, B and C) yields a value for the p-wave gap of ~100 μeV, which is qualitatively consistent with our experimental results [section 1 of (*36*)]. Separate calculations for an embedded zigzag structure using Pb's bulk atomic spin-orbit coupling also yield a similar value [section 4 of (*36*)]. The qualitative agreement between the theoretical and experimental estimates of the p-wave gap is notable considering the many uncertainties that we have not taken into account; for instance, surface relaxation, surface dipole, lattice mismatch, and modification of s-wave pair potentials near the surface of Pb. The size of this pairing gap is also consistent with the low-energy background tunneling conductance (50% of the normal state) observed at 1.4 K in the middle of the wire with the normal tip, as shown in Fig. 4 [see also section 9 of (*36*) for more details]. We also note that our experiments are in a regime where coupling strength between the scanning tunneling microscope tip and the MQP at the end of our chains is small in energy, as compared to the thermal energy, resulting in the suppression of the zero-bias conductance ($1.3 \times 10^{-4}\ e^2/h$, where e is the electron charge and h is Planck's constant, as shown in Fig. 4) from the ideal value of $2e^2/h$ (*45*). Evidence for a gap in the middle of our chains, with a value that is in line with model calculations, together with ZBPs at their ends completes the list of experimental observations required to conclude that superconductivity on our ferromagnetic atomic chains is topological in nature.

Finally, we comment on the particle-hole asymmetric features at energies above the minimum gap of our chain measured with normal tips (near ±1 meV) throughout the chain (shown in Fig. 4). These features in the spectra are reproducible and reminiscent of the band of Yu-Shiba-Rusinov in-gap states found in the 2D model calculation of Fig. 1D. Our DFT calculations show that there is substantial charge transfer from the Pb substrate to the Fe chain, resulting in a linear dipole-moment density (per angstrom) of 0.02 e·Å perpendicular to the Pb surface. As in the case of isolated magnetic impurities, this potential makes tunneling into and out of the in-gap states asymmetric (see also results of simulations in Fig. 1D that include such a potential) (*40*, *41*). These in-gap states also change approaching the end of our chains; however, they are always distinct in energy from the ZBP we associate with the MQP, even at the end of the chain [see fig. S14 in (*36*), for example].

Experimental checks for interpretations other than MQPs

To address alternatives to the MQP interpretation of the ZBP, we have carried out a number of control experiments. First, we examine the possibility of the ZBP being due to a Kondo resonance, which has been raised in the context of semiconductor nanowire experiments where there is experimental evidence for a Kondo effect (*21*, *22*). To address this issue, we have carried out experiments in weak magnetic fields (0.1 T) that suppress superconductivity in the Pb substrate. All features associated with the gap in the middle of the chains and the ZBP at their ends disappear in the absence of superconductivity in Pb [section 7 of (*36*)]. If the ZBPs at the ends of the chains were due to the Kondo effect, we expect that increasing the DOS near E_F in the normal state would only enhance the ZBP rather than suppress it. The importance of superconductivity to the formation of the ZBP also rules out alternative scenarios in which such peaks appear due to disorder effects. Second, our spin-polarized STM measurements do not show substantial magnetization change at the end of the chain, which discounts the unlikely scenario in which the pairing gap at the end of the chain is strongly suppressed and therefore gives an apparent ZBP. Third, structural and potential defects in our substrate cannot produce in-gap states (including ZBPs) in accordance with Anderson's theorem and previous experiments, which show that, for conventional s-wave superconductors, in-gap states are not induced by nonmagnetic adsorbates or step edges (*40*, *41*).

Finally, we have found very short Fe chains (~30 to 40 Å) in which the ZBPs are strongly suppressed [section 8 of (*36*)]. This observation suggests that coupling the end states to each other suppresses the signatures we are associating with MQPs. Although more detailed length-dependence experiments are needed to characterize the decay

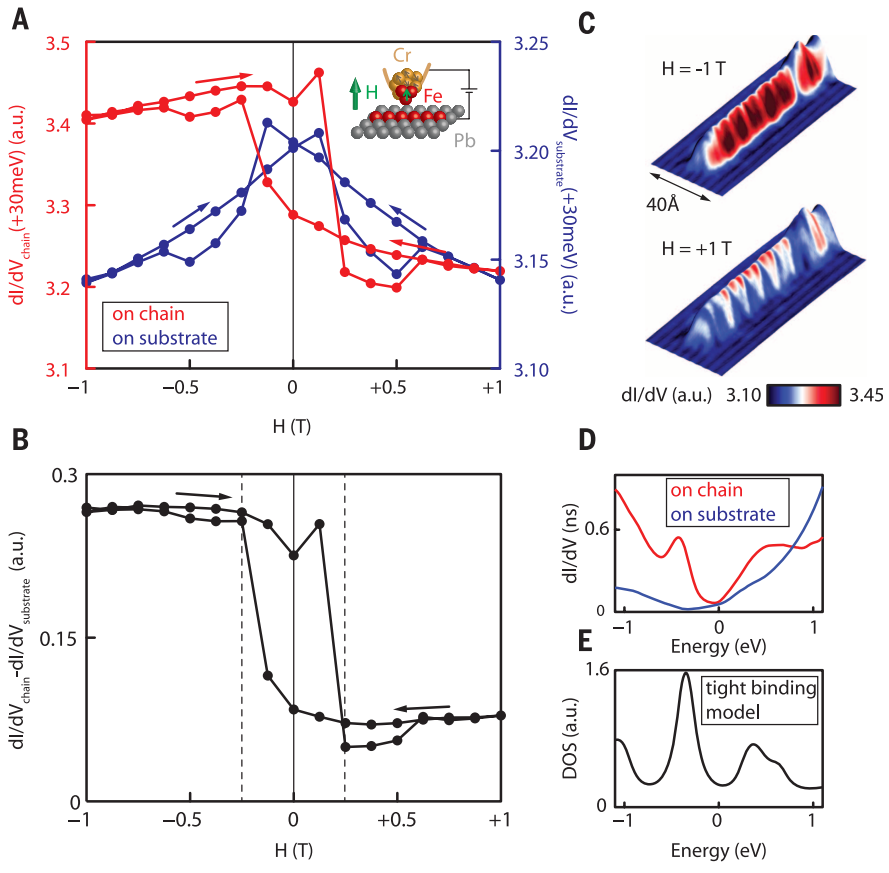

Fig. 3. Spin-polarized measurements and normal state characterization of ferromagnetic chains. (**A**) Spatially average (over a region of ~100 Å) STM tunneling conductance as a function out-of-plane applied magnetic field H on the atomic chain and the substrate measured with a spin-polarized bulk Cr/Fe tip. The inset shows a schematic of the measurement (set point voltage V = 30 mV, current I = 0.75 nA). Tip switching occurs at ±0.25 T. (**B**) Difference between conductance on and off the chain shown in (A). (**C**) Topography of the chain colorized by the conductance at ±1 T from low (dark blue) to high conductance (dark red). (**D**) STM point spectra of the atomic chain and the substrate. (**E**) DOS computed using a tight-binding model of a zigzag Fe chain, as described in section 4 of (*36*).

length of MQP end states more quantitatively, this experiment establishes that our ZBPs are not associated with disorder at the end of our chains. More specifically, our model calculations show the wave function of the MQP at one end of our hybrid chain-superconductor system to have a combination of power-law decay (on the Fermi length scale) and an exponential decay (related to the p-wave pairing's coherence length) as a function of distance from the end of the chains [section 2 of (*36*)] (*46*). Our experimentally observed decay of the ZBP over 15 to 20 Å (Figs. 4 and 5) is probably associated with the power-law decay and the effective Fermi wavelength in our chain and is consistent with the suppression of the MQP signatures in chains of twice that length. The small ZBP splitting that may be present even in our longest chains is smaller than our energy resolution, which is ~100 to 200 μeV for measurements with the superconducting tip. Besides the coupling between the MQPs on either side of a chain, there are situations in which multiple channels on the chain can give rise to multiple MQP at the same end of the chain [section 2 of (*36*)]. Generically, a perturbation can couple and split these MQPs, unless they are protected by a symmetry [see, for example, (*47*)] of the system, resulting in the absence of topological superconductivity. Ultimately, the splitting of our MQPs needs to be experimentally tested using higher-resolution measurements. Our ability to characterize splitting is limited by thermal broadening (1.4 K), which accounts for the width of the experimental features and contributes to the background tunneling conductance at zero bias—so-called quasi-particle poisoning of MQP [section 9 of (*36*)]. Future studies will require millikelvin STM measurements, a capability that has already been demonstrated in experiments on other exotic superconductors (*48*). Overall, based on the results of these control experiments together with the observation of all four enumerated experimental signatures, we conclude that our results are consistent with the realization of a topological superconducting state with localized MQPs.

Outlook

The experimental system described here demonstrates a platform for future experiments to manipulate MQPs and to realize other related 1D or 2D topological superconducting phases. An obvious extension of our experiments is to 2D islands of ferromagnetic films on the surface of Pb. Provided that these films are thin enough, a few monolayers as in our chains, pairing could be stabilized at a reasonable temperature and the edges of these islands could harbor propagating Majorana modes. The detailed structure of such modes, whether they can be chiral or fully in-gap, depends on the spin-orbit coupling configuration. Searching for other systems with both even and odd numbers of band crossings at E_F on Pb can be used to further test the concept behind our studies and should show both topological and nontopological superconducting phases. Although the phase with the even number of crossings at the E_F is not topological, it is a model system to form the Fulde-Ferrell-Larkin-Ovchinnikov (FFLO) phase that has a modulated gap structure with a periodicity related to (in the simplest case) the difference between the two Fermi points (1D) or circles (2D) (*49*, *50*). STM spectroscopic mapping can be used to characterize the modulated gap structure of this system and provide evidence for an FFLO phase.

Ultimately, manipulation of MQPs is required to demonstrate braiding and the non-Abelian characteristics of these quasi-particles. We have recently proposed that application of a parallel magnetic field to ringlike magnetic atomic structures fabricated on a thin film superconductor can be used to generate edges between trivial and topological regions with MQP in such rings (*51*). The rotation of the parallel magnetic field (that does not perturb superconductivity in thin films) can then be used to manipulate and braid MQPs in ringlike atomic structures. This proposal applies to both the spin-helix arrangement of magnetism as well as to the ferromagnetic chains studied here. In addition to manipulating MQPs, a parallel field applied to a chain on a thin film superconductor can also be used to drive the chains between topological and trivial superconducting

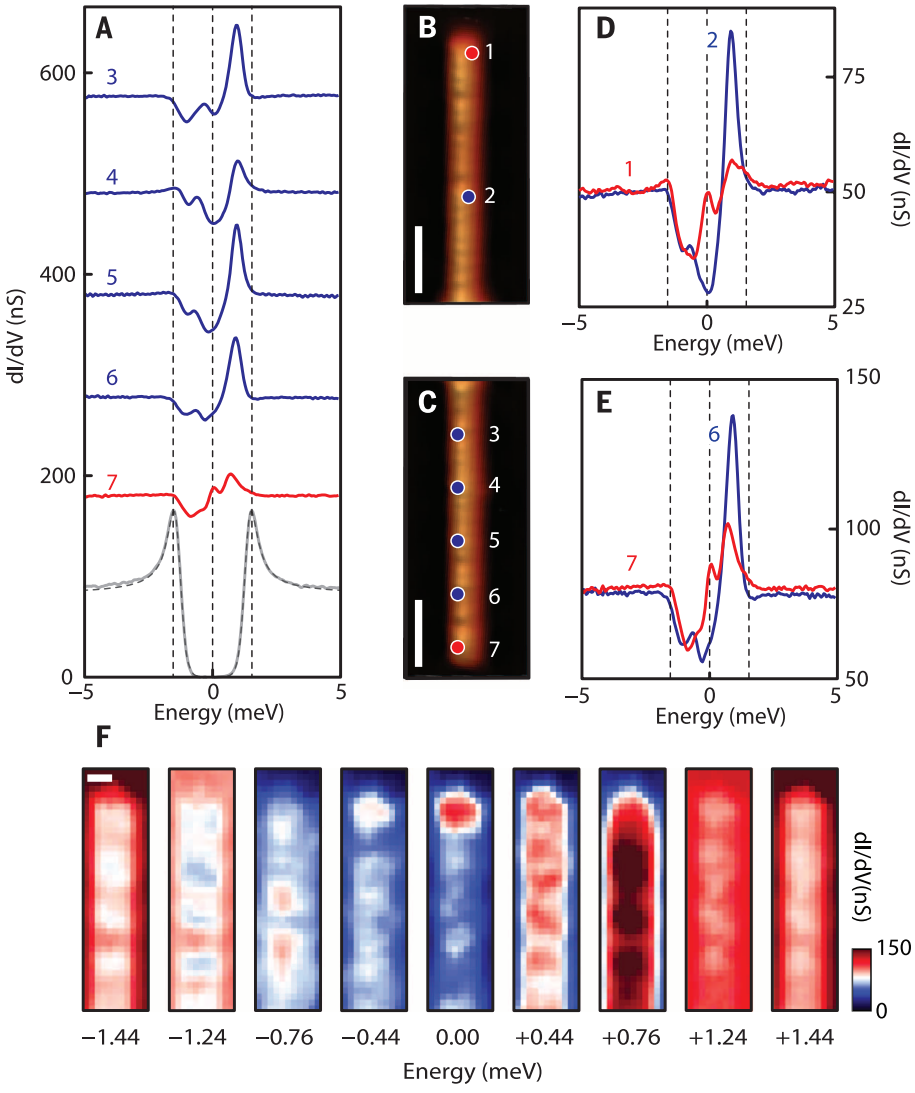

Fig. 4. Spectroscopic mapping of atomic chains and ZBPs. (**A**) STM spectra measured on the atomic chain at locations corresponding to those indicated in (B) and (C). For clarity, the spectra are offset by 100 nS. The red spectrum shows the ZBP at one end of the chain. The gray trace measured on the Pb substrate can be fit using thermally broadened BCS DOS (dashed gray line, fit parameters Δ_s = 1.36 meV, T = 1.45 K). (**B** and **C**) Zoom-in topography of the upper (B) and lower end (C) of the chain and corresponding locations for spectra marked (1 to 7). Scale bars, 25 Å. (**D** and **E**) Spectra measured at marked locations, as in (B) and (C). (**F**) Spatial and energy-resolved conductance maps of another Fe atomic chain close to its end, which shows similar features in point spectra as in (A). The conductance map at zero bias (middle panel) shows increased conductance close to the end of the chain. Scale bar, 10 Å. We note that the localization length of the MQP observed here is a factor of 10 or smaller in length than the distance from the end to the islands that form in the middle of the chains.

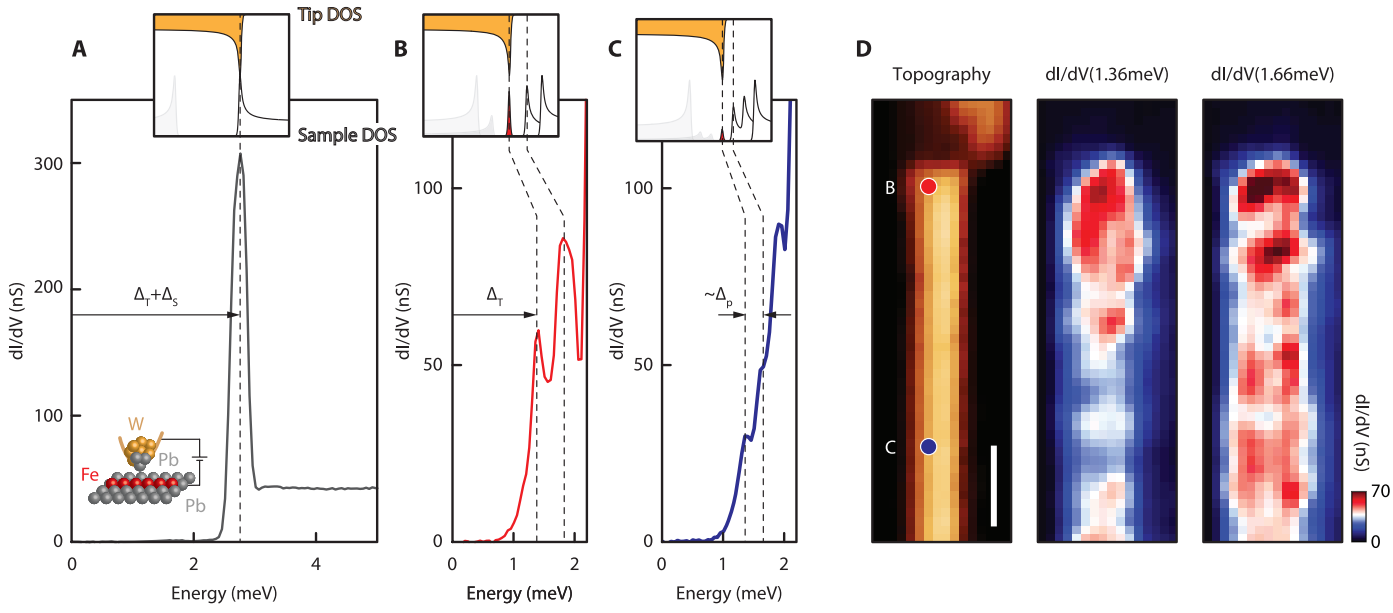

Fig. 5. High–energy resolution spectra obtained using a superconducting tip. (**A**) Point spectra on the superconducting substrate (with a gap of Δ_S) using the superconducting tip (with a gap of Δ_T) shows a peak at $\Delta_T + \Delta_S$. The inset shows alignment of the BCS DOS for the tip and the sample as a function of bias, which results in the conductance at $\Delta_T + \Delta_S$ and suppressed conductance at lower voltages. (**B**) STM spectra at the end of the Fe chain showing a peak at Δ_T, which corresponds to the ZBP. The inset shows schematics of the DOS alignment between the tip and the sample. The shape of the spectra and the higher peak indicate that the ZBP resides in a gap even at the end of the wire. (**C**) Point spectra in the middle of the Fe atomic chain showing a peak at Δ_T + 300 μV, signaling the approximate value of the effective p-wave gap Δ_p in the bulk of the chain. The inset shows a schematic of suppressed ZBP and edge of a Δ_p in the DOS. (**D**) Topographic image of the atomic chain and spatially resolved conductance maps for $|eV_1| = \Delta_T = 1.36$ meV and $|eV_2| = \Delta_T + 0.3$ meV. The left image indicates where the point spectra in (B) and (C) are taken. Scale bar, 20 Å.

phases. Ultimately, atomic manipulation techniques with the scanning tunneling microscope can be used to fabricate complex magnetic structures in which MQP may be engineered and manipulated.

REFERENCES AND NOTES

1. A. Y. Kitaev, *Physics-Uspekhi* **44**, 131–136 (2001).
2. J. Alicea, *Rep. Prog. Phys.* **75**, 076501 (2012).
3. C. W. J. Beenakker, *Annu. Rev. Condens. Matter Phys.* **4**, 113–136 (2013).
4. E. Majorana, *Nuovo Cim.* **14**, 171–184 (1937).
5. F. Wilczek, *Nat. Phys.* **5**, 614–618 (2009).
6. D. Wark, *Nature* **510**, 224–225 (2014).
7. A. Y. Kitaev, *Ann. Phys.* **303**, 2–30 (2003).
8. C. Nayak, S. H. Simon, A. Stern, M. Freedman, S. Das Sarma, *Rev. Mod. Phys.* **80**, 1083–1159 (2008).
9. M. M. Salomaa, G. E. Volovik, *Phys. Rev. B* **37**, 9298–9311 (1988).
10. G. Moore, N. Read, *Nucl. Phys. B* **360**, 362–396 (1991).
11. N. Read, D. Green, *Phys. Rev. B* **61**, 10267–10297 (2000).
12. D. A. Ivanov, *Phys. Rev. Lett.* **86**, 268–271 (2001).
13. L. Fu, C. L. Kane, *Phys. Rev. Lett.* **100**, 096407 (2008).
14. R. M. Lutchyn, J. D. Sau, S. Das Sarma, *Phys. Rev. Lett.* **105**, 077001 (2010).
15. Y. Oreg, G. Refael, F. von Oppen, *Phys. Rev. Lett.* **105**, 177002 (2010).
16. V. Mourik *et al.*, *Science* **336**, 1003–1007 (2012).
17. A. Das *et al.*, *Nat. Phys.* **8**, 887–895 (2012).
18. M. T. Deng *et al.*, *Nano Lett.* **12**, 6414–6419 (2012).
19. A. D. K. Finck, D. J. Van Harlingen, P. K. Mohseni, K. Jung, X. Li, *Phys. Rev. Lett.* **110**, 126406 (2013).
20. J. Liu, A. C. Potter, K. T. Law, P. A. Lee, *Phys. Rev. Lett.* **109**, 267002 (2012).
21. E. J. H. Lee *et al.*, *Phys. Rev. Lett.* **109**, 186802 (2012).
22. H. O. H. Churchill *et al.*, *Phys. Rev. B* **87**, 241401 (2013).
23. D. I. Pikulin, J. P. Dahlhaus, M. Wimmer, H. Schomerus, C. W. J. Beenakker, *New J. Phys.* **14**, 125011 (2012).
24. G. Kells, D. Meidan, P. W. Brouwer, *Phys. Rev. B* **86**, 100503 (2012).
25. S. Nadj-Perge, I. K. Drozdov, B. A. Bernevig, A. Yazdani, *Phys. Rev. B* **88**, 020407 (2013).
26. F. Pientka, L. I. Glazman, F. von Oppen, *Phys. Rev. B* **88**, 155420 (2013).
27. J. Klinovaja, P. Stano, A. Yazdani, D. Loss, *Phys. Rev. Lett.* **111**, 186805 (2013).
28. B. Braunecker, P. Simon, *Phys. Rev. Lett.* **111**, 147202 (2013).
29. M. M. Vazifeh, M. Franz, *Phys. Rev. Lett.* **111**, 206802 (2013).
30. S. Nakosai, Y. Tanaka, N. Nagaosa, *Phys. Rev. B* **88**, 180503 (2013).
31. Y. Kim, M. Cheng, B. Bauer, R. M. Lutchyn, S. Das Sarma, *Phys. Rev. B* **90**, 060401(R) (2014).
32. A. Yazdani, "Visualizing topological quantum states: From Dirac to Majorana fermions," presentation at Nobel Symposium on New Forms of Matter: Topological Insulators and Superconductors, Högberga Gård, Lidingö, Sweden, 13 to 15 June 2014.
33. M. Duckheim, P. W. Brouwer, *Phys. Rev. B* **83**, 054513 (2011).
34. S. B. Chung, H. J. Zhang, X. L. Qi, S. C. Zhang, *Phys. Rev. B* **84**, 060510(R) (2011).
35. A. C. Potter, P. A. Lee, *Phys. Rev. B* **85**, 094516 (2012).
36. Materials and methods are available as supplementary materials on *Science* Online.
37. L. Yu, *Acta Phys. Sin.* **21**, 75–91 (1965).
38. H. Shiba, *Prog. Theor. Phys.* **40**, 435–451 (1968).
39. A. I. Rusinov, *Sov. Phys. JETP Lett.* **29**, 1101–1106 (1969).
40. A. Yazdani, B. A. Jones, C. P. Lutz, M. F. Crommie, D. M. Eigler, *Science* **275**, 1767–1770 (1997).
41. A. Balatsky, I. Vekhter, J.-X. Zhu, *Rev. Mod. Phys.* **78**, 373–433 (2006).
42. M. Bode, M. Getzlaff, R. Wiesendanger, *Phys. Rev. Lett.* **81**, 4256–4259 (1998).
43. O. Pietzsch, A. Kubetzka, M. Bode, R. Wiesendanger, *Phys. Rev. Lett.* **92**, 057202 (2004).
44. J. Moser *et al.*, *Phys. Rev. Lett.* **99**, 056601 (2007).
45. K. T. Law, P. A. Lee, T. K. Ng, *Phys. Rev. Lett.* **103**, 237001 (2009).
46. A. A. Zyuzin, D. Rainis, J. Klinovaja, D. Loss, *Phys. Rev. Lett.* **111**, 056802 (2013).
47. C. Fang, M. J. Gilbert, B. A. Bernevig, *Phys. Rev. Lett.* **112**, 106401 (2014).
48. B. B. Zhou *et al.*, *Nat. Phys.* **9**, 474–479 (2013).
49. A. I. Larkin, Y. N. Ovchinnikov, *Sov. Phys. JETP* **20**, 762 (1965).
50. P. Fulde, R. A. Ferrell, *Phys. Rev.* **135**, A550–A563 (1964).
51. J. Li, T. Neupert, B. A. Bernevig, A. Yazdani, http://arxiv.org/abs/1404.4058 (2014).

ACKNOWLEDGMENTS

We thank F. von Oppen, L. Glazman, D. Loss, A. Stern, J. Alicea, M. Franz, R. Lutchyn, C.-K. Shih, B. Feldman, M. Randeria, P. Lee, and N. P. Ong for helpful discussions. The work at Princeton University has been primarily supported by Majorana Basic Research Challenge grant through ONR-N00014-14-1-0330, ONR-N00014-11-1-0635, ONR- N00014-13-10661, NSF–Materials Research Science and Engineering Center programs through the Princeton Center for Complex Materials DMR-0819860, and NSF CAREER DMR-095242. Work at the University of Texas at Austin was supported by ONR-N00014-14-1-0330 and the Welch Foundation grant TBF1473. This project was also made possible using the facilities at Princeton Nanoscale Microscopy Laboratory supported by grants through NSF-DMR-1104612, ARO-W911NF-1-0262, ARO-MURI program W911NF-12-1-0461, U.S. Department of Energy Office of Basic Energy Sciences, DARPA-SPWAR Meso program N6601-11-1-4110, Laboratory for Physical Sciences and ARO-W911NF-1-0606, and the W. Keck Foundation. A.Y., B.A.B., and Princeton University have filed a provisional patent related to this work. S.N.-P. acknowledges support of the European Union Marie Curie program (IOF 302937); J.L. acknowledges support of the Swiss National Science Foundation; and A.Y. acknowledges the hospitality of the Aspen Center for Physics, supported under NSF grant PHYS-1066293.

SUPPLEMENTARY MATERIALS

www.sciencemag.org/content/346/6209/602/suppl/DC1
Materials and Methods
Supplementary Text
Figs. S1 to S16
Table S1
References (*52*–*59*)

28 July 2014; accepted 19 September 2014
Published online 2 October 2014;
10.1126/science.1259327

GENE REGULATION

Structural basis for microRNA targeting

Nicole T. Schirle, Jessica Sheu-Gruttadauria, Ian J. MacRae*

MicroRNAs (miRNAs) control expression of thousands of genes in plants and animals. miRNAs function by guiding Argonaute proteins to complementary sites in messenger RNAs (mRNAs) targeted for repression. We determined crystal structures of human Argonaute-2 (Ago2) bound to a defined guide RNA with and without target RNAs representing miRNA recognition sites. These structures suggest a stepwise mechanism, in which Ago2 primarily exposes guide nucleotides (nt) 2 to 5 for initial target pairing. Pairing to nt 2 to 5 promotes conformational changes that expose nt 2 to 8 and 13 to 16 for further target recognition. Interactions with the guide-target minor groove allow Ago2 to interrogate target RNAs in a sequence-independent manner, whereas an adenosine binding-pocket opposite guide nt 1 further facilitates target recognition. Spurious slicing of miRNA targets is avoided through an inhibitory coordination of one catalytic magnesium ion. These results explain the conserved nucleotide-pairing patterns in animal miRNA target sites first observed over two decades ago.

MicroRNAs (miRNAs) are small [~22 nucleotides (nt)] RNAs with regulatory roles in plants and animals. miRNAs function within RNA-induced silencing complexes (RISCs), which contain a member of the Argonaute protein family (*1*). Argonaute uses the miRNA as a guide for identifying complementary target mRNAs, which then leads to silencing of the targeted messages via translational repression and degradation (*2*). More than 1000 miRNAs are encoded in the human genome, and over 50% of mammalian protein-coding genes contain a conserved miRNA target site (*3*). Consequently, miRNAs contribute to diverse physiological processes in mammals, including epithelial regeneration (*4*), cardiac function (*5*), ovulation (*6*), and the progression of cancer (*7*).

Perfect complementarity between miRNAs and their targets is not necessary for silencing, and some miRNA nucleotides are more important than others (*8*, *9*). Specifically, pairing to the miRNA "seed region" (nt 2 to 7 or 2 to 8, from the 5′ end) is the most evolutionarily conserved feature of miRNA targets in animals (*10*–*14*). Crystal structures of human Argonaute proteins show nt 2 to 6 of the guide RNA bound in a prearranged A-form conformation, which was proposed to minimize the entropic cost associated with forming a stable duplex with target RNAs (*15*–*17*). However, nucleotides outside of the seed region in these structures were mostly disordered, and no structure of any eukaryotic Argonaute bound to a target RNA has been reported.

Guide RNAs are threaded through the N-PAZ channel

Structural insights into eukaryotic Argonaute proteins have been thwarted by the challenge of separating Argonaute from copurifying cellular RNAs (*15*, *18*). Although a protocol for purifying RNA-free Ago2 has been reported (*19*), the

Department of Integrative Structural and Computational Biology, The Scripps Research Institute, La Jolla, CA 92037, USA.
*Corresponding author. E-mail: macrae@scripps.edu

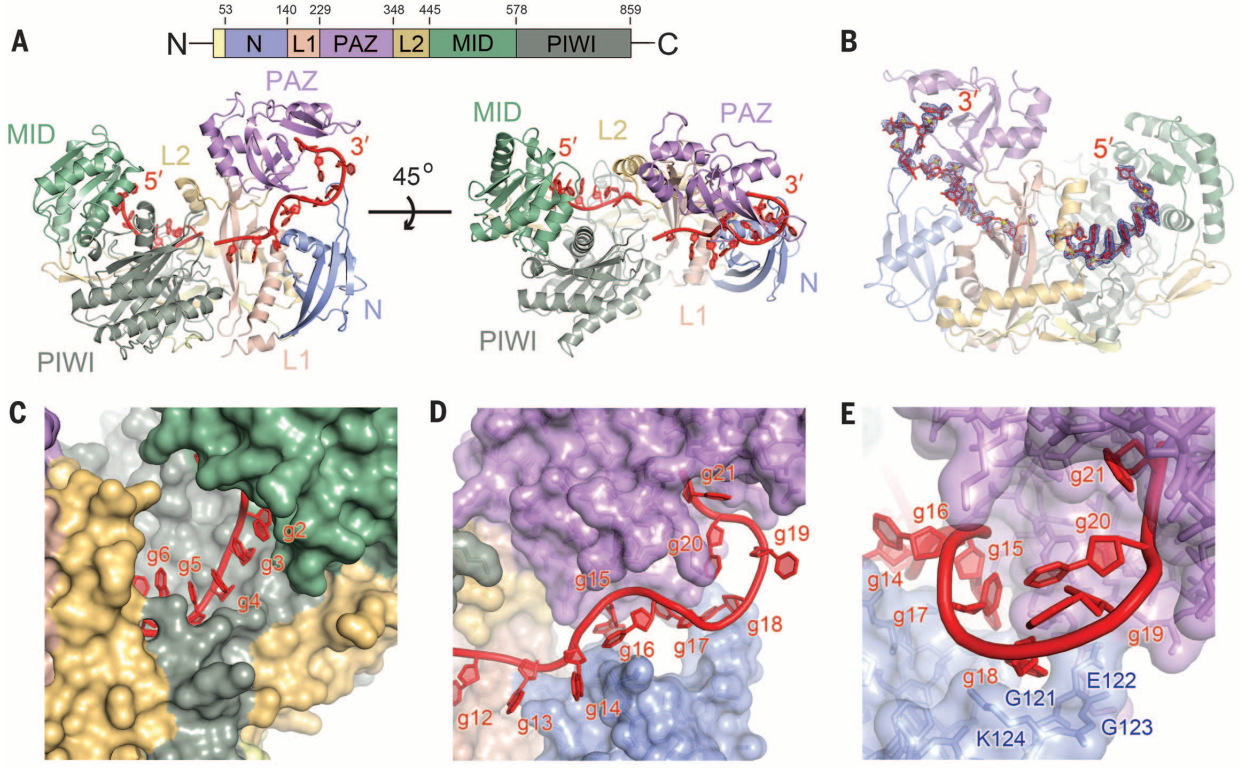

Fig. 1. Structure of the Ago2-guide complex. (**A**) Schematic of the Ago2 primary sequence. Front and top views of human Ago2 bound to a defined guide RNA (red). Ago2 contains a large central cleft between two lobes (N-PAZ and MID-PIWI) connected by two linker domains (L1 and L2). (**B**) Guide RNA omit map contoured at 2σ (blue mesh). (**C**) Nucleotides g2–g5 are exposed, whereas Ago2 occludes nucleotides g6 and g7. (**D**) The 3′ half of the guide is threaded through the N-PAZ channel. (**E**) View down the N-PAZ channel.

method generates relatively small amounts of material and is difficult to reproduce. As an alternative, we adapted a biochemical method for purifying RISC loaded with a specified guide from cell lysates (*20*) to produce milligram quantities of recombinant Ago2 bound to a defined 21-nt guide RNA. The ratio of Ago2 protein to guide RNA in the purified samples is 1:1.2 ± 0.2, and pre–steady-state kinetics showed that 99.0 ± 8.6%

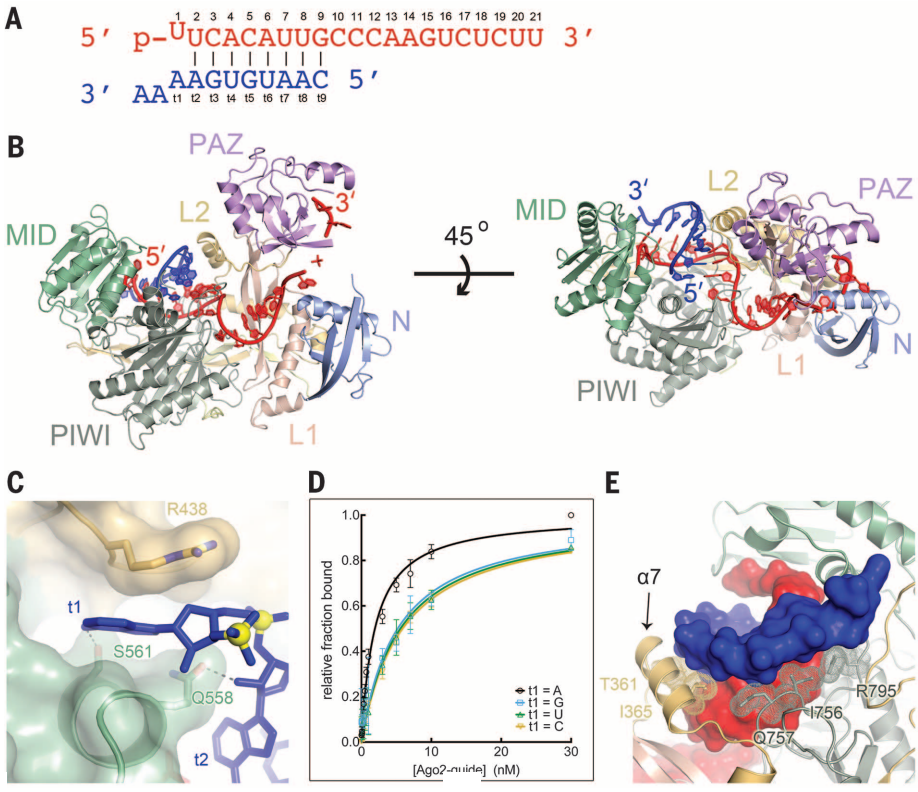

Fig. 2. Structure of Ago2 bound to seed-matched target RNAs. (**A**) Sequences of guide (red) and target RNAs (blue). (**B**) Front and top views of Ago2 bound to guide and target RNAs. (**C**) Binding pocket for t1 adenine between L2 and MID domains. (**D**) Equilibrium binding data for target RNAs bearing different t1 nucleotides. Mean values from ≥ three independent replicates ± SE shown. (**E**) Ago2 interrogates the guide-target minor groove. Protein is shown as a ribbon, RNA in surface representation, and interacting side-chains as sticks with dots. Helix-7 (α7) is indicated with the arrow.

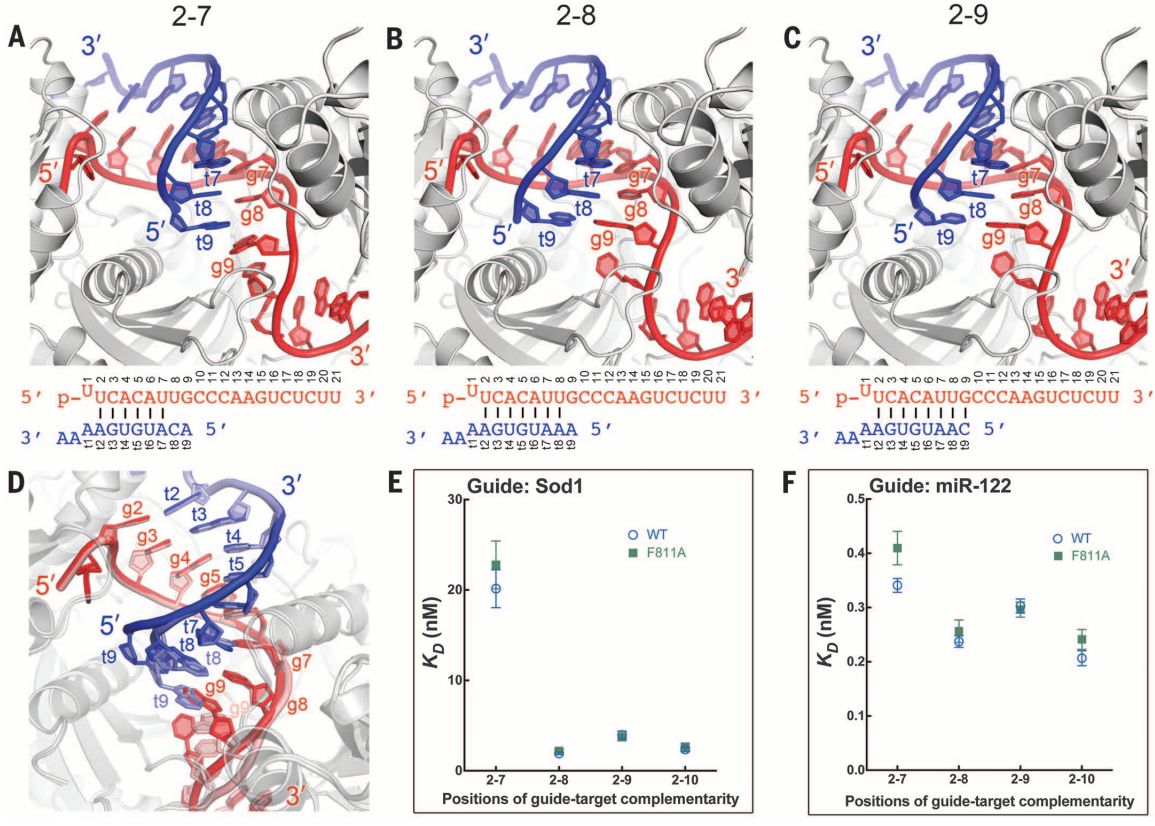

Fig. 3. Structural analysis of seed-pairing. (**A** to **C**) Ago2-guide-target complexes with pairing to (A) g2–g7, (B) g2–g8, or (C) g2–g9. (**D**) Alignment of g2–g9 structure (guide, red; target, blue) with g2–g7 structure (guide, pink; target, light blue). (**E** and **F**) Dissociation constants of wild type (WT) and F811A Ago2 proteins binding target RNAs with various degrees of guide complementarity. Ago2 was loaded with guide RNAs derived from either (E) Sod1 or (F) miR122. Mean of independent triplicates, ±SEM.

of the Ago2 molecules are catalytically active against the specified target RNA (fig. S1).

Guide-selected Ago2 samples crystallized in a condition similar to that used to determine structures of human Ago1 and Ago2 (*15*, *19*). However, in contrast to previous structures, we observed unambiguous electron density for most of the guide RNA, with only four guide (g) nucleotides (nt g8–g11) disordered (Fig. 1, A and B). The guide 5′ end is anchored in the Ago2 MID (middle) domain, and nucleotides g2–g7 are splayed in a helical conformation (Fig. 1C). Nucleotides g12–g20 extend from the center of the protein to the 3′ nucleotide–binding site in the PAZ [P-element-induced whimpy testes (PIWI)/Argonaute/Zwille] domain (*21*). Nucleotides g14–g18 are threaded through a narrow channel formed between the PAZ and N domains of Ago2 (Fig. 1D). The channel ends at g18, where the RNA turns and extends into the 3′ binding pocket. Consistent with the ability of Ago2 to bind guide RNAs of any nucleotide sequence, the majority of contacts are made through hydrogen bonds and salt linkages to the RNA sugar-phosphate backbone (fig. S2). Base-stacking between g14–g18 is completely disrupted by interactions with the N-PAZ channel, and the Watson-Crick edges of g15, g17, and g18 face the interior of the complex (Fig. 1D). Therefore, in the observed conformation, interactions with Ago2 prevent the 3′ half of the guide RNA from base-pairing with complementary targets.

The ordered guide RNA was accompanied by a reduction in the relative temperature factors in the Ago2 N domain compared with previous structures (fig. S3). Improvements in the electron density map allowed us to observe amino acid residues 119 to 125, which fold into a hairpin loop that forms the end of the N-PAZ channel and directs the guide 3′ end into the PAZ domain through contacts to g18 (Fig. 1E). An expansion of positively charged residues in the analogous loop in *Arabidopsis* Ago4, Ago6, and Ago9 has been proposed as an explanation for how these Agos preferentially retain longer (~24 nt) guide RNAs (*22*). The improved map also revealed an error surrounding residues 110 to 118 in our original Ago2 structures (*15*) that was propagated to subsequent structures of human Ago1 and Ago2 (figs. S4 and S5) (*16*, *19*).

Structural basis for miRNA target recognition

We determined crystal structures of guide-selected Ago2 bound to short target RNAs (11 nt) with complementarity to nucleotides g2–g7, g2–g8, or g2–g9. The target RNAs included an adenosine nucleotide in the t1 position (the target nucleotide opposite g1) and two nucleotides 3′ of t1 (Fig. 2A). Target RNAs bound the complex through Watson-Crick pairing with the seed, forming an A-form duplex in the front half of the Ago2 central cleft (Fig. 2B and fig. S6). The t1-adenine inserts into a narrow pocket between the MID and L2 domains of Ago2 where Ser^{561} hydrogen bonds to the adenine N6 amine (Fig. 2C). The pocket appears to specifically recognize adenosine nucleotides because a target RNA with a t1-A bound Ago2 with almost threefold higher affinity than equivalent targets with U, G, or C t1 nucleotides (Fig. 2D). This may explain why t1 adenosines enhance miRNA-mediated repression and are conserved in many mammalian miRNA target sites (*3*, *11*). No electron density was apparent for the two nucleotides 3′ of t1, indicating that Ago2 does not make defined contacts to target RNAs downstream of miRNA binding sites.

Ago2 makes several hydrogen bonds/salt linkages to seed paired target RNAs (fig. S7), but the major mode of recognition by the protein appears to be shape complementarity to the minor

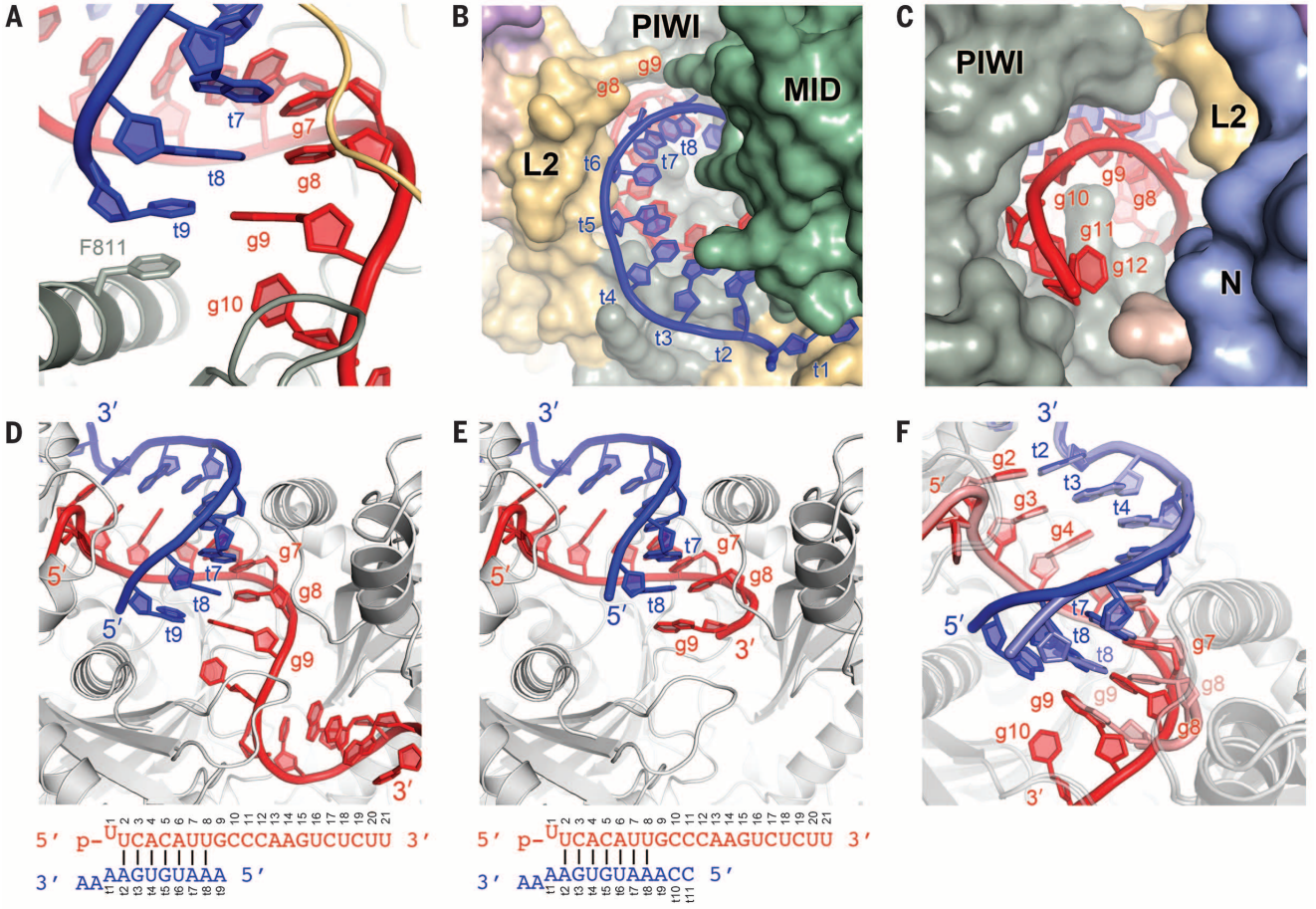

Fig. 4. Ago2 restricts guide-target pairing beyond the seed. (**A**) F811 stacks against t9 of short target RNAs. (**B** and **C**) The central cleft viewed from the (B) MID and (C) N domain, showing narrowing of the cleft after g8 (g13–g16 omitted for clarity). (**D** and **E**) Ago2-guide complex bound to target RNAs paired to g2–g8 that end at (D) t9 or (E) t11. (**F**) Superposition of structures in (D) and (E).

groove of the guide-target duplex. Aliphatic segments of residues R795, I756, and Q757 within the PIWI domain and I365 and T361 on helix-7 of the L2 domain line the minor groove, making extensive hydrophobic and van der Waals interactions with positions 2 to 7 of the guide-target duplex (Fig. 2D). These minor groove contacts may explain why G:U wobble base pairs, in which the guanine unpaired exocyclic amino alters minor groove shape and electrostatic potential (*23*), reduce Argonaute target affinity, and are not commonly observed in miRNA target sites (*13*, *24*, *25*). (Single-letter abbreviations for the amino acid residues are as follows: A, Ala; C, Cys; D, Asp; E, Glu; F, Phe; G, Gly; H, His; I, Ile; K, Lys; L, Leu; M, Met; N, Asn; P, Pro; Q, Gln; R, Arg; S, Ser; T, Thr; V, Val; W, Trp; and Y, Tyr. In the mutants, other amino acids were substituted at certain locations; for example, F811A indicates that phenylalanine at position 811 was replaced by alanine.)

In contrast to positions 2 to 7, Ago2 does not contact the minor groove at positions 8 and 9, suggesting that the protein is more tolerant of mismatches in this region (Fig. 3, A to C). Indeed, the guide-target duplex with g8–g9 mismatches has distortions away from A-form due to staggering of the mismatched bases (Fig. 3A). The distortions are limited to positions 8 and 9, indicating that pairing status at g8 and g9 does not perturb guide-target duplex structure in positions 2 to 7 (Fig. 3D). However, binding experiments show that pairing to g8 can substantially contribute to the affinity of Ago2 for target RNAs (Fig. 3E and fig. S8). An unrelated guide RNA displayed a smaller difference between the affinities for g2–g7 and g2–g8 complementary target RNAs, revealing that the degree to which pairing to g8 influences target affinity is dependent on the seed sequence (Fig. 3F).

Narrowing of the central cleft restricts pairing past g8

Although complementarity to g8 increased the affinity of Ago2 for target RNAs, extending complementarity to g9 and g10 did not enhance affinity further (Fig. 3, E and F). In fact, both sequences displayed a modest decrease in affinity for targets complementary to g2–g9 compared with g2–g8, indicating that pairing to g9 is actually detrimental to stability of the Ago2-guide-target complex. t9 stacks against F811 in the 2 to 9 paired structure (Fig. 4A). However, an F811A mutation did not markedly alter the affinity for full-length target RNAs (Fig. 3, E and F). Moreover, the complex lacks sufficient space necessary to accommodate target nucleotides beyond t9 (Fig. 4, B and C), and the t9 nucleotide was disordered in crystals containing a longer target RNA, which included mismatches to g11 (Fig. 4, D and E). We conclude that the observed conformation of Ago2 can only accommodate pairing to g9 when using short targets that end at t9 (such as those used to facilitate crystallization), and that pairing to g9 on longer targets (such as those in the 3′ UTR of a mRNA) requires further opening of the Ago2 central cleft. We suggest that opening the cleft involves conformational changes responsible for the decrease

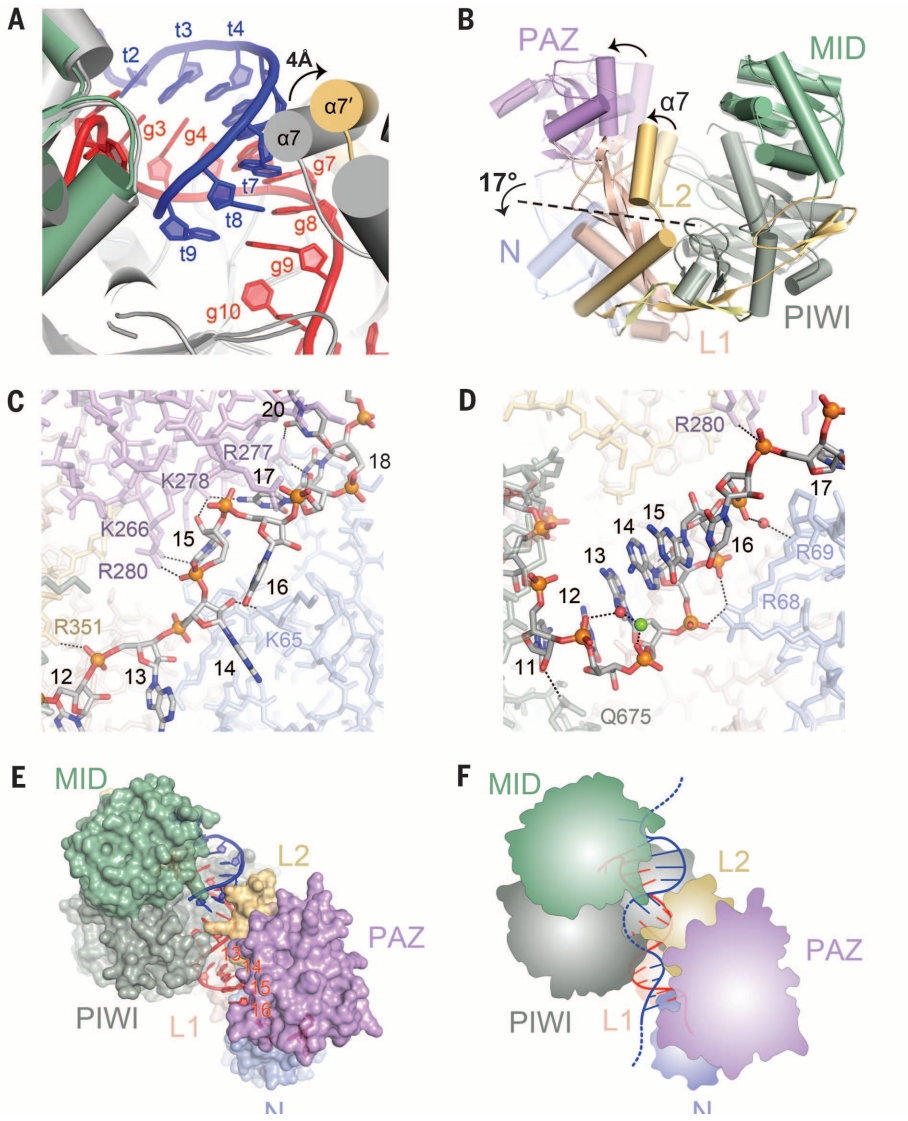

Fig. 5. Comparison of Ago2-guide and Ago2-guide-target structures. (**A**) Helix-7 (α7) shifts to accommodate pairing to target RNAs. The Ago2-guide structure (gray) aligned to the Ago2-guide-target structure (colored). (**B**) The PAZ domain and helix-7 move as a rigid body. Superposition of protein components from Ago2-guide (semitransparent) and Ago2-guide-target (opaque) structures. Arrows indicate movement from guide-only to guide-target structures. Dashed line marks hinge in the L1/L2 domains. (**C** and **D**) Contacts to the guide RNA supplemental region in the (C) guide-only and (D) target-bound structures. (**E**) The supplemental region (g13–g16) adopts an exposed helical conformation in the Ago2-guide-target structure. (**F**) Illustrated model for seed plus supplemental pairing.

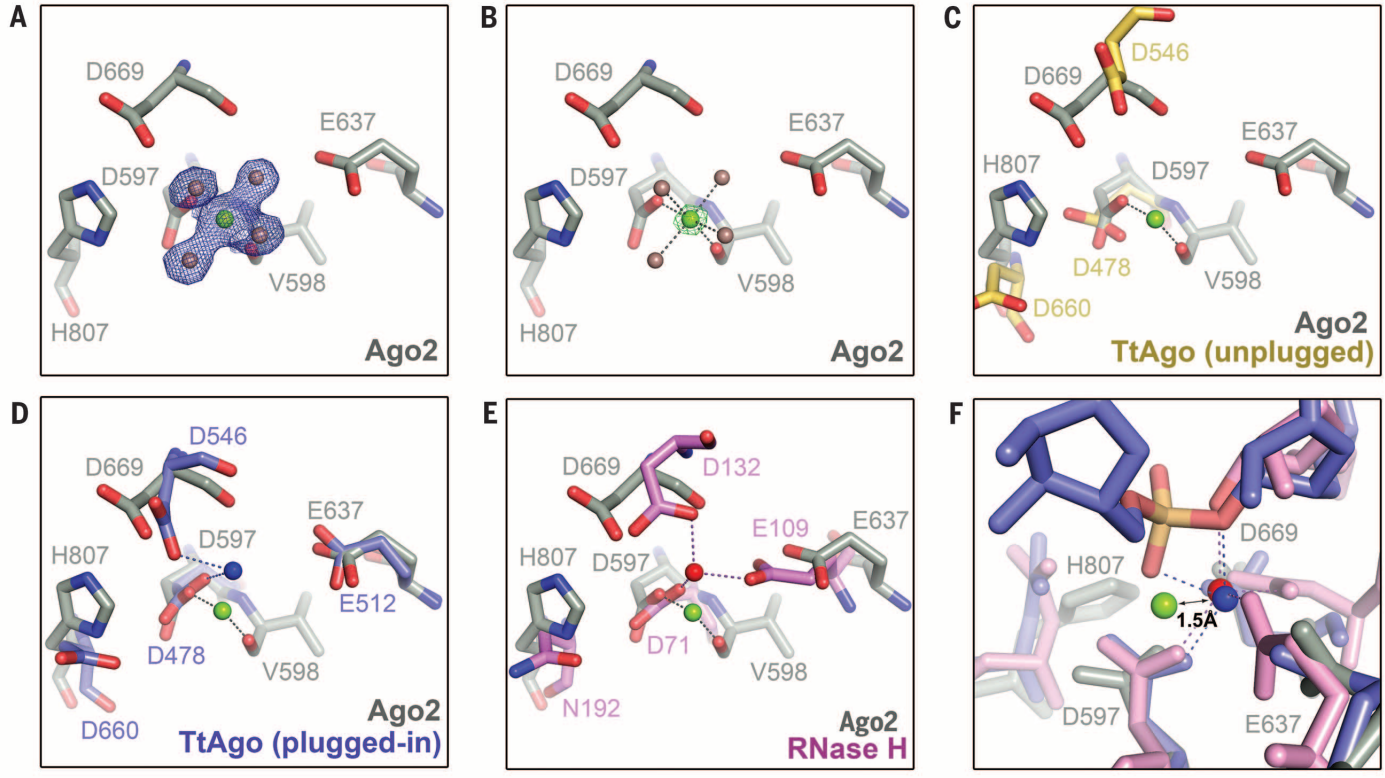

Fig. 6. Inactive magnesium ion in the Ago2 active site. (**A** and **B**). Magnesium ion (green) is bound to the D597 carboxylate side chain, the V598 main chain carbonyl, and four water molecules (brown spheres). $2F_o$-F_c map (blue mesh) was contoured at 1.5σ (A), and F_o-F_c magnesium omit map (green mesh) was contoured at 15σ (B). (**C**) Active site of Ago2 (gray) aligned with unplugged active site of TtAgo (yellow) (PDB ID 3DLH). (**D**) Ago2 active site aligned with plugged-in TtAgo (blue) (PDB ID 3HVR). Metals ions are shown as spheres. (**E**) Ago2 active site aligned with *Bacillus halodurans* RNase H (pink with red magnesium ion; PDB ID 2G8H). (**F**) Alignment of Ago2 (gray with green magnesium), TtAgo (blue), and *B. halodurans* RNase H (pink) shows the Ago2 magnesium shifted 1.5 Å from the active position.

in target affinity associated with pairing to g9. This model may explain why complementarity beyond g8 is not a well-conserved feature of vertebrate miRNA targets sites (*11*).

A structural model for miRNA targeting

Structures of human Ago1 and Ago2 and yeast Ago1 indicate that in the absence of target RNA, eukaryotic Argonaute proteins kink their guide RNAs at the end of the seed region (*15*–*18*). The kink appears to be stabilized by helix-7, which inserts a hydrophobic residue (I365 in Ago2) between g6 and g7. In moving from the guide-only to the target-bound conformation, helix-7 shifts ~4 Å to interact with the minor groove of the guide-target duplex (Fig. 5A). The movement of helix-7 is required to avoid steric clashes with target nt t6 and t7 and is therefore necessary for target pairing beyond g5 (fig. S9). Movement of helix-7 also releases the constraints on the guide RNA, relaxing the kink and allowing g6 and g7 to adopt an A-form conformation for target pairing. Thus, the guide and protein act synergistically to recognize target RNAs; movement of helix-7 to accommodate targets beyond g5 also releases g6 and g7, facilitating the additional base pairing. Formation of these base pairs generates a guide-target duplex with a minor groove that provides a new binding surface for helix-7, stabilizing the opened conformation. Conversely, mismatches or G:U wobble pairs would present a distorted minor groove to helix-7, which would then be more likely to shift back toward the guide RNA and displace the mispaired target.

Seed pairing opens the N-PAZ channel for supplemental pairing

Superimposing guide-only and guide-target structures of Ago2 indicates that helix-7 and the PAZ domain move as a discrete rigid body relative to the MID, PIWI, and N domains (Fig. 5B). The hinge for this conformational change resides in the base of helix-7 and extends across the β-sheet in the L1 domain. We suggest that the movements in helix-7, induced by seed pairing, are propagated to positional shifts in the PAZ domain, leading to a widening of the N-PAZ channel. Mutation of F181, which resides in the hinge, inhibits small RNA duplex unwinding during RISC-loading (*26*), suggesting that related conformational changes are involved in passenger strand removal.

Widening of the N-PAZ channel is accompanied by repositioning of the 3′ half of the guide RNA, with g11–g16 shifting to adopt a near A-form conformation (Fig. 5, C and D). Helical stacking is disrupted after g16 by P67 of the N domain, and electron density for g17–g19 is weak, which is indicative of conformational heterogeneity. However, density for g20 and g21 is visible, with the 3′ end of the guide bound to the PAZ domain. The Watson-Crick faces of g13–g16, which can supplement repression of target sites with weak seed pairing (*27*), are splayed out toward the solvent in a manner reminiscent of the seed region in guide-only structures (Fig. 5D). We suggest that seed pairing is coupled to a rearrangement in the 3′ half of the guide that facilitates target interactions in the supplemental region. Nucleotides g12 and g13 are partially occluded by a PIWI domain loop (residues 602 to 608), indicating that target pairing to the supplemental region may nucleate at g14–g16 and extend back into the central cleft. We suggest that target RNAs paired to the seed may exit the central cleft and extend over the middle of the PIWI domain to pair with the supplemental region on the other side (Fig. 5, E and F). This would allow the complex to maximize guide-target interactions while avoiding the topological issues and entropic costs associated with wrapping the target and guide RNAs around each other within the central cleft (*3*). Consistent

with this model, complementarity to g9–g12 is not correlated with miRNA-mediated repression (*27*), and the affinity of mouse Ago2 for a fully complementary target RNA is less than that of a similar target that pairs only to the seed and supplemental regions (*24*).

An inactivated magnesium ion in the slicer active site

In addition to miRNA-mediated repression, Ago2 can silence targets by catalyzing an endonucleolytic "slicing" reaction (*28*, *29*). Slicing is more specific than miRNA-mediated repression because target cleavage requires extensive complementarity between guide and target RNAs (*25*, *30*, *31*). Slicing specificity in *T. thermophilus* Argonaute (TtAgo) is achieved through a conformational switch involving insertion of a catalytic "glutamate finger" into the active site, triggered by extensive guide-target pairing (*32*). Although it is possible that human Ago2 undergoes similar conformational transitions, the equivalent glutamate residue (E637) is inserted into the active site in all available Ago2 structures, irrespective of target pairing status (fig. S10). Therefore, the mechanisms underlying slicing specificity in humans are less clear.

We observed electron density for a metal ion in the active site of guide-selected Ago2 (Fig. 6, A and B). The metal is coordinated to four water molecules, the carboxylate side chain of D597, and the main chain carbonyl of V598, with a coordination geometry (octahedral) and interatomic distances (2.1 Å) characteristic of a magnesium ion (*33*). Comparison with TtAgo suggests that the magnesium is the functional equivalent of catalytic metal "B" in TtAgo guide-target structures (Fig. 6, C and D) (*32*). However, the coordination of metal B in TtAgo differs from that in Ago2; in TtAgo, the metal is chelated by the carboxylate groups of D478 and D546 (equivalent to D597 and D669 in Ago2, respectively), with no interactions to the main chain (*32*). Comparison with structures of bacterial ribonuclease H (RNase H) indicates that metal B in TtAgo is in a conserved, cleavage-compatible position (Fig. 6, D and E). We therefore suggest that the magnesium observed in Ago2 is in an inactivated position, stabilized by coordination to the main chain carbonyl of V598.

We propose that chelating to the scissile phosphate in complementary target RNAs induces a ~1.5 Å shift in the position of the magnesium into an active coordination similar to that observed in TtAgo and RNase H (Fig. 6F). The shift likely involves an exchange of the main chain carbonyl bond for a bond to catalytic residue D669 (*28*), mediated by D659. We suggest that precise positioning of the scissile phosphate is required to move the metal ion into the activated position, which is consistent with the observation that guide-target mismatches near the cleavage site can dramatically reduce catalytic activity (*24*, *30*, *34*–*36*). This model also explains how structural elements in the PIWI and N domains, which likely influence positioning of the guide-target duplex within the central cleft, contribute substantially to slicing activity (*16*, *17*, *37*).

Discussion

The structures presented here show Ago2 in two distinct conformational states: one in which the majority of the guide RNA is sequestered from target pairing, and a second with the full seed and supplemental regions exposed. Although the RNAs in previous structures of human Ago1 and Ago2 were mostly disordered, the proteins crystallized in conformations similar to the guide-sequestered structure reported here, indicating that this is a well-populated conformation (*15*–*17*, *19*). We propose that the guide-sequestered state limits spurious interactions with cellular RNAs by confining pairing potential to guide nt g2–g5 (Fig. 1C). In this model, Ago2 primarily uses g2–g5 to identify candidate target sites (fig. S11), which are then further interrogated by g6–g7 and helix-7. Target interactions can be stabilized further still by pairing to g8 and/or g13–g16 and through interactions with t1 adenine nucleotides, which may also facilitate the initial identification of target sites (*11*). This stepwise targeting model is similar to the mechanism of nucleic acids annealing in free solution, in which extended duplex structures are nucleated by small segments (3 to 4 base pairs) of complementarity (*38*).

The observations that Ago2 is loaded with small RNA duplexes (*39*–*41*) and cleaves target RNAs with extensive complementarity (*28*, *29*) indicate that the protein adopts at least one additional conformational state with a widened central cleft to accommodate guide-target pairing beyond g8. Extended target pairing probably requires release of the guide 3′ end from the PAZ domain, as in TtAgo (fig. S12) (*32*, *42*). Furthermore, the identification of miRNA target sites with central or 3′ complementarity and limited seed pairing suggests that the protein may adopt additional stable conformational states (*43*–*45*). However, because 80% of miRNA-target interactions appear to function through seed pairing (*44*), it is likely that the structures presented here represent the majority of miRNA targeting events in human cells.

REFERENCES AND NOTES

1. S. M. Hammond, S. Boettcher, A. A. Caudy, R. Kobayashi, G. J. Hannon, *Science* **293**, 1146–1150 (2001).
2. D. P. Bartel, *Cell* **116**, 281–297 (2004).
3. D. P. Bartel, *Cell* **136**, 215–233 (2009).
4. R. R. Chivukula *et al.*, *Cell* **157**, 1104–1116 (2014).
5. M. Xin, E. N. Olson, R. Bassel-Duby, *Nat. Rev. Mol. Cell Biol.* **14**, 529–541 (2013).
6. H. Hasuwa, J. Ueda, M. Ikawa, M. Okabe, *Science* **341**, 71–73 (2013).
7. A. Lujambio, S. W. Lowe, *Nature* **482**, 347–355 (2012).
8. R. C. Lee, R. L. Feinbaum, V. Ambros, *Cell* **75**, 843–854 (1993).
9. B. Wightman, I. Ha, G. Ruvkun, *Cell* **75**, 855–862 (1993).
10. E. C. Lai, *Nat. Genet.* **30**, 363–364 (2002).
11. B. P. Lewis, C. B. Burge, D. P. Bartel, *Cell* **120**, 15–20 (2005).
12. B. P. Lewis, I. H. Shih, M. W. Jones-Rhoades, D. P. Bartel, C. B. Burge, *Cell* **115**, 787–798 (2003).
13. J. Brennecke, A. Stark, R. B. Russell, S. M. Cohen, *PLOS Biol.* **3**, e85 (2005).
14. A. Krek *et al.*, *Nat. Genet.* **37**, 495–500 (2005).
15. N. T. Schirle, I. J. MacRae, *Science* **336**, 1037–1040 (2012).
16. C. R. Faehnle, E. Elkayam, A. D. Haase, G. J. Hannon, L. Joshua-Tor, *Cell Reports* **3**, 1901–1909 (2013).
17. K. Nakanishi *et al.*, *Cell Reports* **3**, 1893–1900 (2013).
18. K. Nakanishi, D. E. Weinberg, D. P. Bartel, D. J. Patel, *Nature* **486**, 368–374 (2012).
19. E. Elkayam *et al.*, *Cell* **150**, 100–110 (2012).
20. C. F. Flores-Jasso, W. E. Salomon, P. D. Zamore, *RNA* **19**, 271–279 (2013).
21. J. B. Ma, K. Ye, D. J. Patel, *Nature* **429**, 318–322 (2004).
22. C. Poulsen, H. Vaucheret, P. Brodersen, *Plant Cell* **25**, 22–37 (2013).
23. G. Varani, W. H. McClain, *EMBO Rep.* **1**, 18–23 (2000).
24. L. M. Wee, C. F. Flores-Jasso, W. E. Salomon, P. D. Zamore, *Cell* **151**, 1055–1067 (2012).
25. J. G. Doench, P. A. Sharp, *Genes Dev.* **18**, 504–511 (2004).
26. P. B. Kwak, Y. Tomari, *Nat. Struct. Mol. Biol.* **19**, 145–151 (2012).
27. A. Grimson *et al.*, *Mol. Cell* **27**, 91–105 (2007).
28. J. Liu *et al.*, *Science* **305**, 1437–1441 (2004).
29. F. V. Rivas *et al.*, *Nat. Struct. Mol. Biol.* **12**, 340–349 (2005).
30. S. M. Elbashir, J. Martinez, A. Patkaniowska, W. Lendeckel, T. Tuschl, *EMBO J.* **20**, 6877–6888 (2001).
31. J. G. Doench, C. P. Petersen, P. A. Sharp, *Genes Dev.* **17**, 438–442 (2003).
32. G. Sheng *et al.*, *Proc. Natl. Acad. Sci. U.S.A.* **111**, 652–657 (2014).
33. H. Zheng *et al.*, *Nat. Protoc.* **9**, 156–170 (2014).
34. T. Holen, M. Amarzguioui, M. T. Wiiger, E. Babaie, H. Prydz, *Nucleic Acids Res.* **30**, 1757–1766 (2002).
35. M. Amarzguioui, T. Holen, E. Babaie, H. Prydz, *Nucleic Acids Res.* **31**, 589–595 (2003).
36. B. Haley, P. D. Zamore, *Nat. Struct. Mol. Biol.* **11**, 599–606 (2004).
37. J. Hauptmann *et al.*, *Nat. Struct. Mol. Biol.* **20**, 814–817 (2013).
38. P. D. Ross, J. M. Sturtevant, *Proc. Natl. Acad. Sci. U.S.A.* **46**, 1360–1365 (1960).
39. C. Matranga, Y. Tomari, C. Shin, D. P. Bartel, P. D. Zamore, *Cell* **123**, 607–620 (2005).
40. T. A. Rand, S. Petersen, F. Du, X. Wang, *Cell* **123**, 621–629 (2005).
41. P. J. Leuschner, S. L. Ameres, S. Kueng, J. Martinez, *EMBO Rep.* **7**, 314–320 (2006).
42. Y. Wang *et al.*, *Nature* **461**, 754–761 (2009).
43. C. Shin *et al.*, *Mol. Cell* **38**, 789–802 (2010).
44. S. Grosswendt *et al.*, *Mol. Cell* **54**, 1042–1054 (2014).
45. A. Helwak, G. Kudla, T. Dudnakova, D. Tollervey, *Cell* **153**, 654–665 (2013).

ACKNOWLEDGMENTS

We are grateful to P. D. Zamore and J. R. Williamson for generous advice and scientific insights. Diffraction data were collected at beam lines 11-1 and 12-2 at the Stanford Synchrotron Radiation Lightsource and 24-ID-E at the Advanced Photon Source, supported by National Institute of General Medical Sciences grant P41 GM103403 and U.S. Department of Energy contract DE-AC02-06CH11357. N.T.S. is a predoctoral fellow of the American Heart Association and an Achievement Rewards for College Scientists (ARCS) scholar. The work was supported by NIH grant R01 GM104475 to I.J.M. Coordinates of the Ago2-guide and guide-target complexes have been deposited in the Protein Data Bank (PDB) (4W5N, 4W5O, 4W5Q, 4W5R, and 4W5T).

SUPPLEMENTARY MATERIALS

www.sciencemag.org/content/346/6209/608/suppl/DC1
Materials and Methods
Supplementary Text
Figs. S1 to S13
Tables S1 and S2
References
Movies S1 and S2

30 June 2014; accepted 29 August 2014
10.1126/science.1258040

REPORTS

NUCLEAR PHYSICS

Momentum sharing in imbalanced Fermi systems

O. Hen,[1]* M. Sargsian,[2] L. B. Weinstein,[3] E. Piasetzky,[1] H. Hakobyan,[4,5] D. W. Higinbotham,[6] M. Braverman,[1] W. K. Brooks,[4] S. Gilad,[7] K. P. Adhikari,[3] J. Arrington,[8] G. Asryan,[5] H. Avakian,[6] J. Ball,[9] N. A. Baltzell,[8] M. Battaglieri,[10] A. Beck,[1,11] S. May-Tal Beck,[1,11] I. Bedlinskiy,[12] W. Bertozzi,[7] A. Biselli,[13] V. D. Burkert,[6] T. Cao,[14] D. S. Carman,[6] A. Celentano,[10] S. Chandavar,[15] L. Colaneri,[16] P. L. Cole,[6,17,18] V. Crede,[19] A. D'Angelo,[16,20] R. De Vita,[10] A. Deur,[6] C. Djalali,[14,21] D. Doughty,[6,22] M. Dugger,[23] R. Dupre,[24] H. Egiyan,[6] A. El Alaoui,[8] L. El Fassi,[3] L. Elouadrhiri,[6] G. Fedotov,[14,25] S. Fegan,[10] T. Forest,[17] B. Garillon,[24] M. Garcon,[9] N. Gevorgyan,[5] Y. Ghandilyan,[5] G. P. Gilfoyle,[26] F. X. Girod,[6] J. T. Goetz,[15] R. W. Gothe,[14] K. A. Griffioen,[27] M. Guidal,[24] L. Guo,[2,6] K. Hafidi,[8] C. Hanretty,[28] M. Hattawy,[24] K. Hicks,[15] M. Holtrop,[29] C. E. Hyde,[3] Y. Ilieva,[14,30] D. G. Ireland,[31] B. I. Ishkanov,[25] E. L. Isupov,[25] H. Jiang,[14] H. S. Jo,[24] K. Joo,[32] D. Keller,[28] M. Khandaker,[17,33] A. Kim,[34] W. Kim,[34] F. J. Klein,[18] S. Koirala,[3] I. Korover,[1] S. E. Kuhn,[3] V. Kubarovsky,[6] P. Lenisa,[35] W. I. Levine,[36] K. Livingston,[31] M. Lowry,[6] H. Y. Lu,[14] I. J. D. MacGregor,[31] N. Markov,[32] M. Mayer,[3] B. McKinnon,[31] T. Mineeva,[32] V. Mokeev,[6,24,37] A. Movsisyan,[35] C. Munoz Camacho,[24] B. Mustapha,[8] P. Nadel-Turonski,[6] S. Niccolai,[24] G. Niculescu,[38] I. Niculescu,[38] M. Osipenko,[10] L. L. Pappalardo,[35,39] R. Paremuzyan,[5,29] K. Park,[6,34] E. Pasyuk,[6] W. Phelps,[2] S. Pisano,[40] O. Pogorelko,[12] J. W. Price,[41] S. Procureur,[9] Y. Prok,[3,28] D. Protopopescu,[31] A. J. R. Puckett,[32] D. Rimal,[2] M. Ripani,[10] B. G. Ritchie,[23] A. Rizzo,[16] G. Rosner,[31] P. Roy,[19] P. Rossi,[6] F. Sabatié,[9] D. Schott,[30] R. A. Schumacher,[36] Y. G. Sharabian,[6] G. D. Smith,[42] R. Shneor,[1] D. Sokhan,[31] S. S. Stepanyan,[34] S. Stepanyan,[6] P. Stoler,[43] S. Strauch,[14,30] V. Sytnik,[4] M. Taiuti,[44] S. Tkachenko,[28] M. Ungaro,[6] A. V. Vlassov,[12] E. Voutier,[45] N. K. Walford,[18] X. Wei,[6] M. H. Wood,[14,46] S. A. Wood,[6] N. Zachariou,[14] L. Zana,[29,42] Z. W. Zhao,[28] X. Zheng,[28] I. Zonta,[16] Jefferson Lab CLAS Collaboration†

The atomic nucleus is composed of two different kinds of fermions: protons and neutrons. If the protons and neutrons did not interact, the Pauli exclusion principle would force the majority of fermions (usually neutrons) to have a higher average momentum. Our high-energy electron-scattering measurements using ^{12}C, ^{27}Al, ^{56}Fe, and ^{208}Pb targets show that even in heavy, neutron-rich nuclei, short-range interactions between the fermions form correlated high-momentum neutron-proton pairs. Thus, in neutron-rich nuclei, protons have a greater probability than neutrons to have momentum greater than the Fermi momentum. This finding has implications ranging from nuclear few-body systems to neutron stars and may also be observable experimentally in two-spin–state, ultracold atomic gas systems.

Many-body systems composed of interacting fermions are common in nature, ranging from high-temperature superconductors and Fermi liquids to atomic nuclei, quark matter, and neutron stars. Particularly intriguing are systems that include a short-range interaction that is strong between unlike fermions and weak between the same type of fermions. Recent theoretical advances show that even though the underlying interaction can be very different, these systems share several universal features (*1*–*4*). In all of these systems, this interaction creates short-range–correlated (SRC) pairs of unlike fermions with a large relative momentum ($k_{rel} > k_F$) and a small center-of-mass momentum ($k_{tot} < k_F$), where k_F is the Fermi momentum of the system. This pushes fermions from low momenta ($k < k_F$, where k is the fermion momentum) to high momenta ($k > k_F$), creating a "high-momentum tail."

In atomic nuclei, SRC pairs have been studied using many different reactions, including pick-up, stripping, and electron and proton scattering. The results of these studies highlighted the importance of correlations in nuclei, which lead to a high-momentum tail and decreased occupancy of low-lying nuclear states (*5*–*13*).

Recent experimental studies of balanced (symmetric) interacting Fermi systems, with an equal number of fermions of the two kinds, confirmed these predictions of a high-momentum tail populated almost exclusively by pairs of unlike fermions (*8*–*11*, *14*–*16*). These experiments were carried out using very different Fermi systems: protons and neutrons in atomic nuclei and two-spin–state, ultracold atomic gases. These systems span more than 15 orders of magnitude in Fermi energy from 10^6 to 10^{-9} eV and exhibit different short-range interactions [predominantly a strong tensor interaction in the nuclear systems (*8*, *9*, *17*, *18*) and a tunable Feshbach resonance in the atomic system (*14*, *15*)]. For cold atoms, Tan (*1*–*3*) showed that the momentum density decreases as C/k^4 for large k. The scale factor, C, is known as Tan's contact and describes many properties of the system (*4*). Similar pairing of nucleons in nuclei with $k > k_F$ was also predicted in (*19*).

In this work, we extend these previous studies to imbalanced (asymmetric) nuclear systems, with unequal numbers of the different fermions. When there is no interaction, the Pauli exclusion principle pushes the majority fermions (usually neutrons) to a higher average momentum. Including a short-range interaction introduces a new universal feature: the probability for a fermion to have momentum $k > k_F$ is greater for the minority than for the majority fermions. This is because the short-range interaction populates the high-momentum

[1]Tel Aviv University, Tel Aviv 69978, Israel. [2]Florida International University, Miami, FL 33199, USA. [3]Old Dominion University, Norfolk, VA 23529, USA. [4]Universidad Técnica Federico Santa María, Casilla 110-V Valparaíso, Chile. [5]Yerevan Physics Institute, 375036 Yerevan, Armenia. [6]Thomas Jefferson National Accelerator Facility, Newport News, VA 23606, USA. [7]Massachusetts Institute of Technology, Cambridge, MA 02139, USA. [8]Argonne National Laboratory, Argonne, IL 60439, USA. [9]Commissariat à l'Energie Atomique et aux Energies Alternatives, Centre de Saclay, Irfu/Service de Physique Nucléaire, 91191 Gif-sur-Yvette, France. [10]Istituto Nazionale di Fisica Nucleare (INFN), Sezione di Genova, 16146 Genova, Italy. [11]Nuclear Research Center Negev, P.O. Box 9001, Beer-Sheva 84190, Israel. [12]Institute of Theoretical and Experimental Physics, Moscow, 117259, Russia. [13]Fairfield University, Fairfield, CT 06824, USA. [14]University of South Carolina, Columbia, SC 29208, USA. [15]Ohio University, Athens, OH 45701, USA. [16]INFN, Sezione di Roma Tor Vergata, 00133 Rome, Italy. [17]Idaho State University, Pocatello, ID 83209, USA. [18]Catholic University of America, Washington, DC 20064, USA. [19]Florida State University, Tallahassee, FL 32306, USA. [20]Università di Roma Tor Vergata, 00133 Rome, Italy. [21]University of Iowa, Iowa City, IA 52242, USA. [22]Christopher Newport University, Newport News, VA 23606, USA. [23]Arizona State University, Tempe, AZ 85287-1504, USA. [24]Institut de Physique Nucléaire ORSAY, Orsay, France. [25]Skobeltsyn Institute of Nuclear Physics, Lomonosov, Russia. [26]University of Richmond, Richmond, VA 23173, USA. [27]College of William and Mary, Williamsburg, VA 23187-8795, USA. [28]University of Virginia, Charlottesville, VA 22901, USA. [29]University of New Hampshire, Durham, NH 03824-3568, USA. [30]The George Washington University, Washington, DC 20052, USA. [31]University of Glasgow, Glasgow G12 8QQ, UK. [32]University of Connecticut, Storrs, CT 06269, USA. [33]Norfolk State University, Norfolk, VA 23504, USA. [34]Kyungpook National University, Daegu 702-701, Republic of Korea. [35]INFN, Sezione di Ferrara, 44100 Ferrara, Italy. [36]Carnegie Mellon University, Pittsburgh, PA 15213, USA. [37]Moscow State University, Moscow, 119234, Russia. [38]James Madison University, Harrisonburg, VA 22807, USA. [39]Universitá di Ferrara, 44122 Ferrara, Italy. [40]INFN, Laboratori Nazionali di Frascati, 00044 Frascati, Italy. [41]California State University, Dominguez Hills, Carson, CA 90747, USA. [42]Edinburgh University, Edinburgh EH9 3JZ, UK. [43]Rensselaer Polytechnic Institute, Troy, NY 12180-3590, USA. [44]Università di Genova, 16146 Genova, Italy. [45]Laboratoire de Physique Subatomique et de Cosmologie, Universite Joseph Fourier, CNRS/IN2P3, Institut National Polytechnique, Grenoble, France. [46]Canisius College, Buffalo, NY 14208, USA.

***Corresponding author. E-mail: or.chen@mail.huji.ac.il** †The collaboration on this paper consists of all listed authors. There are no additional collaborators.

tail with equal numbers of majority and minority fermions, thereby leaving a larger fraction of majority fermions in low-momentum states ($k < k_F$) (see Fig. 1). In neutron-rich nuclei, this increases the average proton momentum and may even result in protons having higher average momentum than neutrons, inverting the momentum sharing in imbalanced nuclei from that in noninteracting systems. Theoretically, this can happen because of the tensor part of the nucleon-nucleon interaction, which creates predominantly spin-1, isospin-0 neutron-proton (np) SRC pairs (*17*, *18*).

Here we identify SRC pairs in the high-momentum tail of nuclei heavier than carbon with more neutrons (N) than protons (Z) (i.e., $N > Z$). The data show the universal nature of SRC pairs, which even in lead (N/Z = 126/82) are still predominantly np pairs. This np-pair dominance causes a greater fraction of protons than neutrons to have high momentum in neutron-rich nuclei.

The data presented here were collected in 2004 in Hall B of the Thomas Jefferson National Accelerator Facility using a 5.014-GeV electron beam incident on ^{12}C, ^{27}Al, ^{56}Fe, and ^{208}Pb targets. We measured electron-induced two-proton knockout reactions (Fig. 2). The CEBAF Large Acceptance Spectrometer (CLAS) (*20*) was used to detect the scattered electron and emitted protons. CLAS uses a toroidal magnetic field and six independent sets of drift chambers, time-of-flight scintillation counters, Cerenkov counters, and electromagnetic calorimeters for charged-particle identification and trajectory reconstruction (Fig. 2) (*16*).

We selected events in which the electron interacts with a single fast proton from an SRC pair in the nucleus (*9*, *16*) by requiring a large four-momentum transfer $Q^2 = \vec{q}^{\,2} - (\omega/c)^2 > 1.5$ GeV$^2/c^2$ [where $\vec{q}$ and ω are the three-momentum and energy, respectively, transferred to the nucleus and c is the speed of light] and Bjorken scaling parameter $x_B = Q^2/(2m_N \cdot \omega) > 1.2$ (where m_N is the nucleon mass). To ensure selection of events in which the knocked-out proton belonged to an SRC pair, we further required missing momentum $300 < |\vec{p}_{miss}| < 600$ MeV/c, where $\vec{p}_{miss} = \vec{p}_p - \vec{q}$ with $\vec{p}_p$ the measured proton momentum. We suppressed contributions from inelastic excitations of the struck nucleon by limiting the reconstructed missing mass of the two-nucleon system $m_{miss} < 1.1$ GeV/c^2. In each event, the leading proton that absorbed the transferred momentum was identified by requiring that its momentum $\vec{p}_p$ is within 25° of $\vec{q}$ and that $|\vec{p}_p|/|\vec{q}| \geq 0.6$ (*16*, *21*).

When a second proton was detected with momentum greater than 350 MeV/c, it was emitted almost diametrically opposite to $\vec{p}_{miss}$ (see fig. S19). The observed backward-peaked angular distributions are very similar for all four measured

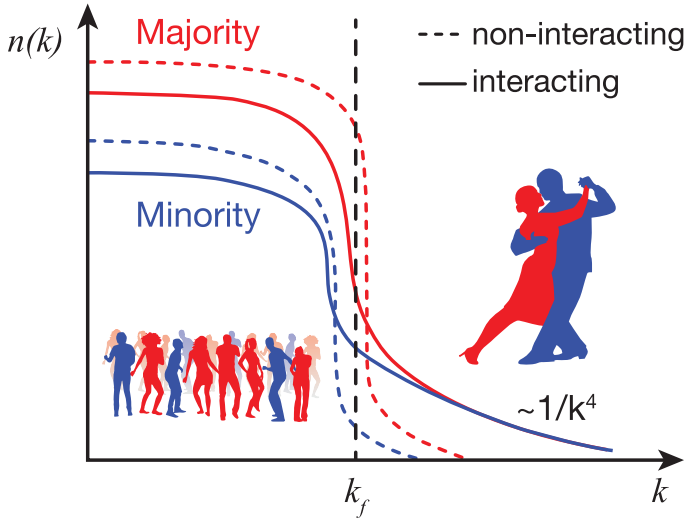

Fig. 1. Schematic representation of the momentum distribution, $n(k)$, of two-component imbalanced Fermi systems. Red and blue dashed lines show the noninteracting system, whereas the solid lines show the effect of including a short-range interaction between different fermions. Such interactions create a high-momentum tail ($k > k_F$, where k_F is the Fermi momentum of the system). This is analogous to a dance party with a majority of girls, where boy-girl interactions will make the average boy dance more than the average girl.

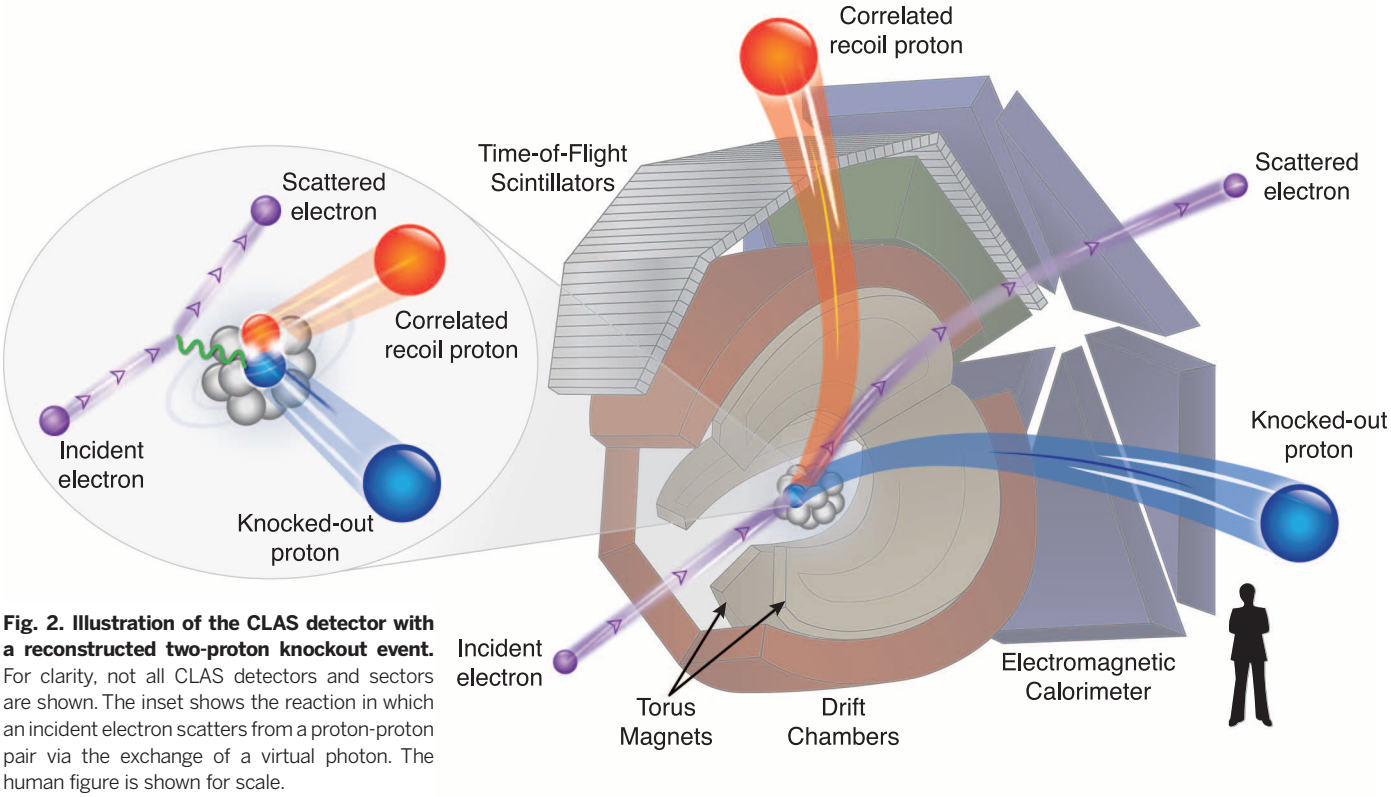

Fig. 2. Illustration of the CLAS detector with a reconstructed two-proton knockout event. For clarity, not all CLAS detectors and sectors are shown. The inset shows the reaction in which an incident electron scatters from a proton-proton pair via the exchange of a virtual photon. The human figure is shown for scale.

nuclei. This backward peak is a strong signature of SRC pairs, indicating that the two emitted protons were largely back-to-back in the initial state, having a large relative momentum and a small center-of-mass momentum (*8*, *9*). This is a direct observation of proton-proton (pp) SRC pairs in a nucleus heavier than ^{12}C.

Electron scattering from high–missing-momentum protons is dominated by scattering from protons in SRC pairs (*9*). The measured single-proton knockout ($e,e'p$) cross section (where e denotes the incoming electron, e' the measured scattered electron, and p the measured knocked-out proton) is sensitive to the number of pp and np SRC pairs in the nucleus, whereas the two-proton knockout ($e,e'pp$) cross section is only sensitive to the number of pp-SRC pairs. Very few of the single-proton knockout events also contained a second proton; therefore, there are very few pp pairs, and the knocked-out protons predominantly originated from np pairs.

To quantify this, we extracted the $[A(e,e'pp)/A(e,e'p)]/[^{12}C(e,e'pp)/^{12}C(e,e'p)]$ cross-section double ratio for nucleus A relative to ^{12}C. The double ratio is sensitive to the ratio of np-to-pp SRC pairs in the two nuclei (*16*). Previous measurements have shown that in ^{12}C nearly every high-momentum proton ($k > 300$ MeV/$c > k_F$) has a correlated partner nucleon, with np pairs outnumbering pp pairs by a factor of ~20 (*8*, *9*).

To estimate the effects of final-state interactions (reinteraction of the outgoing nucleons in the nucleus), we calculated attenuation factors for the outgoing protons and the probability of the electron scattering from a neutron in an np pair, followed by a neutron-proton single-charge exchange (SCX) reaction leading to two outgoing protons. These correction factors are calculated as in (*9*) using the Glauber approximation (*22*) with effective cross sections that reproduce previously measured proton transparencies (*23*), and using the measured SCX cross section of (*24*). We extracted the cross-section ratios and deduced the relative pair fractions from the measured yields following (*21*); see (*16*) for details.

Figure 3 shows the extracted fractions of np and pp SRC pairs from the sum of pp and np pairs in nuclei, including all statistical, systematic, and model uncertainties. Our measurements are not sensitive to neutron-neutron SRC pairs. However, by a simple combinatoric argument, even in ^{208}Pb these would be only $(N/Z)^2 \sim 2$ times the number of pp pairs. Thus, np-SRC pairs dominate in all measured nuclei, including neutron-rich imbalanced ones.

The observed dominance of np-over-pp pairs implies that even in heavy nuclei, SRC pairs are dominantly in a spin-triplet state (spin 1, isospin 0), a consequence of the tensor part of the nucleon-nucleon interaction (*17*, *18*). It also implies that there are as many high-momentum protons as neutrons (Fig. 1) so that the fraction of protons above the Fermi momentum is greater than that of neutrons in neutron-rich nuclei (*25*).

In light imbalanced nuclei ($A \leq 12$), variational Monte Carlo calculations (*26*) show that this results in a greater average momentum for the minority component (see table S1). The minority component can also have a greater average momentum in heavy nuclei if the Fermi momenta of protons and neutrons are not too dissimilar. For heavy nuclei, an np-dominance toy model that quantitatively describes the features of the momentum distribution shown in Fig. 1 shows that in imbalanced nuclei, the average proton kinetic energy is greater than that of the neutron, up to ~20% in ^{208}Pb (*16*).

The observed np-dominance of SRC pairs in heavy imbalanced nuclei may have wide-ranging implications. Neutrino scattering from two nucleon currents and SRC pairs is important for the analysis of neutrino-nucleus reactions, which are used to study the nature of the electro-weak interaction (*27*–*29*). In particle physics, the distribution of quarks in these high-momentum nucleons in SRC pairs might be modified from that of free nucleons (*30*, *31*). Because each proton has a greater probability to be in a SRC pair than a neutron and the proton has two u quarks for each d quark, the u-quark distribution modification could be greater than that of the d quarks (*19*, *30*). This could explain the difference between the weak mixing angle measured on an iron target by the NuTeV experiment and that of the Standard Model of particle physics (*32*–*34*).

In astrophysics, the nuclear symmetry energy is important for various systems, including neutron stars, the neutronization of matter in core-collapse supernovae, and r-process nucleosynthesis (*35*). The decomposition of the symmetry energy at saturation density ($\rho_0 \approx 0.17$ fm^{-3}, the maximum density of normal nuclei) into its kinetic and potential parts and its value at supranuclear densities ($\rho > \rho_0$) are not well constrained, largely because of the uncertainties in the tensor component of the nucleon-nucleon interaction (*36*–*39*). Although at supranuclear densities other effects are relevant, the inclusion of high-momentum tails, dominated by tensor-force–induced np-SRC pairs, can notably soften the nuclear symmetry energy (*36*–*39*). Our measurements of np-SRC pair dominance in heavy imbalanced nuclei can help constrain the nuclear aspects of these calculations at saturation density.

Based on our results in the nuclear system, we suggest extending the previous measurements of Tan's contact in balanced ultracold atomic gases to imbalanced systems in which the number of atoms in the two spin states is different. The large experimental flexibility of these systems will allow observing dependence of the momentum-sharing inversion on the asymmetry, density, and strength of the short-range interaction.

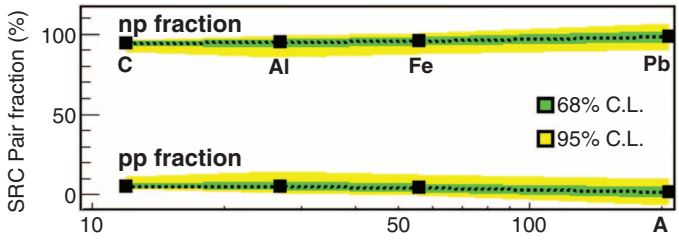

Fig. 3. The extracted fractions of np (top) and pp (bottom) SRC pairs from the sum of pp and np pairs in nuclei. The green and yellow bands reflect 68 and 95% confidence levels (CLs), respectively (*9*). np-SRC pairs dominate over pp-SRC pairs in all measured nuclei.

REFERENCES AND NOTES

1. S. Tan, *Ann. Phys.* **323**, 2952–2970 (2008).
2. S. Tan, *Ann. Phys.* **323**, 2971–2986 (2008).
3. S. Tan, *Ann. Phys.* **323**, 2987–2990 (2008).
4. E. Braaten, in *Lecture Notes in Physics* (Springer, Berlin, 2012), vol. 836, p. 193.
5. L. Lapikás, *Nucl. Phys. A.* **553**, 297–308 (1993).
6. K. I. Blomqvist *et al*., *Phys. Lett. B* **421**, 71–78 (1998).
7. R. Starink *et al*., *Phys. Lett. B* **474**, 33–40 (2000).
8. E. Piasetzky, M. Sargsian, L. Frankfurt, M. Strikman, J. W. Watson, *Phys. Rev. Lett.* **97**, 162504 (2006).
9. R. Subedi *et al*., *Science* **320**, 1476–1478 (2008).
10. K. Sh. Egiyan *et al*., *Phys. Rev. Lett.* **96**, 082501 (2006).
11. N. Fomin *et al*., *Phys. Rev. Lett.* **108**, 092502 (2012).
12. V. R. Pandharipande, I. Sick, P. K. A. deWitt Huberts, *Rev. Mod. Phys.* **69**, 981–991 (1997).
13. J. Arrington, D. W. Higinbotham, G. Rosner, M. Sargsian, *Prog. Part. Nucl. Phys.* **67**, 898–938 (2012).
14. J. T. Stewart, J. P. Gaebler, T. E. Drake, D. S. Jin, *Phys. Rev. Lett.* **104**, 235301 (2010).
15. E. D. Kuhnle *et al*., *Phys. Rev. Lett.* **105**, 070402 (2010).
16. Materials and methods are available as supplementary materials on *Science* Online.
17. R. Schiavilla, R. B. Wiringa, S. C. Pieper, J. Carlson, *Phys. Rev. Lett.* **98**, 132501 (2007).
18. M. M. Sargsian, T. V. Abrahamyan, M. I. Strikman, L. L. Frankfurt, *Phys. Rev. C* **71**, 044615 (2005).
19. L. Frankfurt, M. Strikman, *Phys. Rep.* **160**, 235–427 (1988).
20. B. A. Mecking *et al*., *Nucl. Inst. Meth. A* **503**, 513–553 (2003).
21. O. Hen *et al*., *Phys. Lett. B* **722**, 63–68 (2013).
22. I. Mardor, Y. Mardor, E. Piasetsky, J. Alster, M. M. Sargsyan, *Phys. Rev. C* **46**, 761–767 (1992).
23. D. Dutta, K. Hafidi, M. Strikman, *Prog. Part. Nucl. Phys.* **69**, 1–27 (2013).
24. J. L. Friedes, H. Palevsky, R. Stearns, R. Sutter, *Phys. Rev. Lett.* **15**, 38–41 (1965).
25. M. M. Sargsian, *Phys. Rev. C* **89**, 034305 (2014).
26. R. B. Wiringa, R. Schiavilla, S. C. Pieper, J. Carlson, *Phys. Rev. C* **89**, 024305 (2014).
27. L. Fields *et al*., *Phys. Rev. Lett.* **111**, 022501 (2013).
28. G. A. Fiorentini *et al*., *Phys. Rev. Lett.* **111**, 022502 (2013).
29. Neutrino-Nucleus Interactions for Current and Next Generation Neutrino Oscillation Experiments, Institute for Nuclear Theory (INT) workshop INT-13-54W, University of Washington, Seattle, WA, 3 to 13 December 2013.
30. O. Hen, D. W. Higinbotham, G. A. Miller, E. Piasetzky, L. B. Weinstein, *Int. J. Mod. Phys. E* **22**, 133017 (2013).
31. L. B. Weinstein *et al*., *Phys. Rev. Lett.* **106**, 052301 (2011).
32. G. P. Zeller *et al*., *Phys. Rev. Lett.* **88**, 091802 (2002).
33. G. P. Zeller *et al*., *Phys. Rev. Lett.* **90**, 239902 (2003).
34. I. C. Cloët, W. Bentz, A. W. Thomas, *Phys. Rev. Lett.* **102**, 252301 (2009).
35. J. M. Lattimer, Y. Lim, *Astrophys. J.* **771**, 51 (2013).
36. A. Carbone, A. Polls, A. Rios, *Europhys. Lett.* **97**, 22001 (2012).
37. I. Vidana, A. Polls, C. Providencia, *Phys. Rev. C* **84**, 062801(R) (2011).
38. C. Xu, A. Li, B. A. Li, *J. Phys. Conf. Ser.* **420**, 012090 (2013).
39. B.-A. Li, L.-W. Chen, C. M. Ko, *Phys. Rep.* **464**, 113–281 (2008).

ACKNOWLEDGMENTS

This work was supported by the U.S. Department of Energy (DOE) and the National Science Foundation, the Israel Science Foundation, the Chilean Comisión Nacional de Investigación Científica y Tecnológica, the French Centre National de la

Recherche Scientifique and Commissariat a l'Energie Atomique, the French-American Cultural Exchange, the Italian Istituto Nazionale di Fisica Nucleare, the National Research Foundation of Korea, and the UK's Science and Technology Facilities Council. Jefferson Science Associates operates the Thomas Jefferson National Accelerator Facility for the DOE, Office of Science, Office of Nuclear Physics under contract DE-AC05-06OR23177. The raw data from this experiment are archived in Jefferson Lab's mass storage silo.

SUPPLEMENTARY MATERIALS

www.sciencemag.org/content/346/6209/614/suppl/DC1
Materials and Methods
Figs. S1 to S30
Tables S1 to S8
References (*40*–*51*)

2 June 2014; accepted 2 October 2014
Published online 16 October 2014;
10.1126/science.1256785

VOLCANOLOGY

A large magmatic sill complex beneath the Toba caldera

K. Jaxybulatov,[1,2,3] N. M. Shapiro,[3]* I. Koulakov,[1,2] A. Mordret,[3] M. Landès,[3] C. Sens-Schönfelder[4]

An understanding of the formation of large magmatic reservoirs is a key issue for the evaluation of possible strong volcanic eruptions in the future. We estimated the size and level of maturity of one of the largest volcanic reservoirs, based on radial seismic anisotropy. We used ambient-noise seismic tomography below the Toba caldera (in northern Sumatra) to observe the anisotropy that we interpret as the expression of a fine-scale layering caused by the presence of many partially molten sills in the crust below 7 kilometers. This result demonstrates that the magmatic reservoirs of present (non-eroded) supervolcanoes can be formed as large sill complexes and supports the concept of the long-term incremental evolution of magma bodies that lead to the largest volcanic eruptions.

The size and type of a volcanic eruption depend on the processes that occur in the magmatic reservoirs in Earth's crust. In particular, the largest eruptions require the building of extended pools of viscous gas-rich magma within the crust (*1*–*3*). In the present study, we investigated the magmatic system that produced one of the strongest eruptions in the Quaternary: the Toba event that occurred 74,000 years ago in northern Sumatra, Indonesia (Fig. 1), and emitted at least 2800 cubic kilometers of volcanic material (*4*). This catastrophe is believed to have affected the global climate and to have had a strong impact on the biosphere (*4*, *5*). The event was preceded during the previous 2 million years by at least four other eruptions in nearby locations that had volcano explosivity indices above 7 (*4*). The generation of this exceptional sequence of eruptions could be possible with the existence of a very large magma reservoir in the crust that formed over a long period of time (>1 million years) (*6*). Considering the relatively short period of time that has passed since the main Toba event, the structures that were responsible for the formation and functioning of this reservoir are expected to be well preserved in the Sumatra crust to date. Combined with previous geophysical investigations, the new data presented here provide us with information about the structure of the Toba volcano-magmatic complex and help us to better understand the internal structure and ascent mechanism of large magma volumes through the crust before their super-eruptions.

Geological observations of eroded and exposed past volcanoes and geodynamic models indicate that volcano-magmatic reservoirs evolve over long periods of time and grow in small increments, with the formation of dykes or sills (*2*, *3*, *7*–*9*). However, the exact mechanisms involved in the ascent and emplacement of the magma in the crust beneath active volcanoes are not yet completely understood, mainly because of the lack of detailed information about the structures of volcano-magmatic complexes below volcanoes in their most productive phase. Large-scale images of zones affected by melts can be obtained with magneto-telluric methods (*10*) and with seismic tomography (*11*). Some signatures of large crustal intrusions can also be detected by receiver functions (*12*). However, the individual dykes or sills within magmatic complexes that have metric or decametric thicknesses (*7*) cannot be deduced from geophysical imaging alone, and as layered intrusions, their interpretation requires additional geological information (*13*).

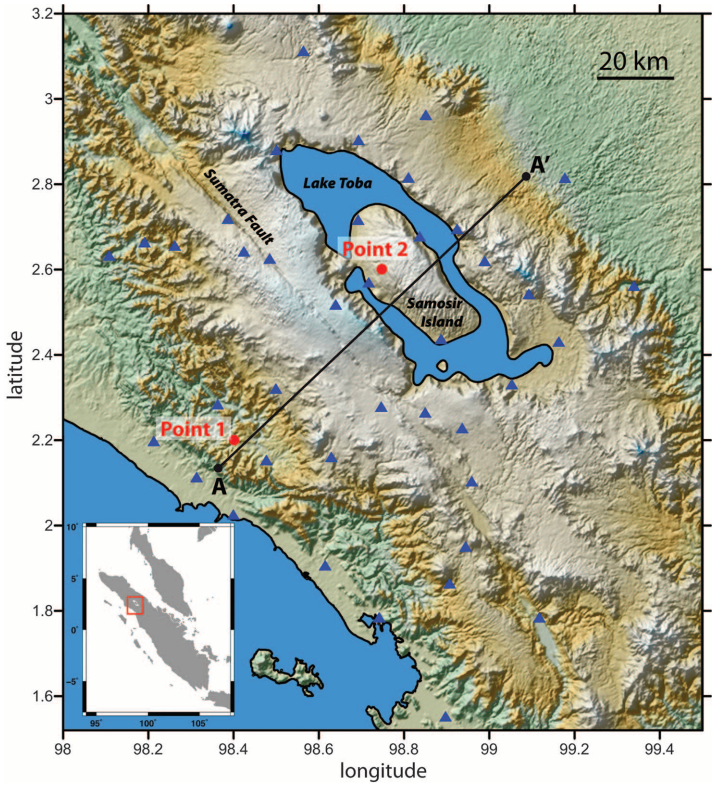

Fig. 1. Topographic map of the Lake Toba region. Blue triangles, locations of the seismic stations; black line, profile for cross sections shown in Fig. 3; red circles, locations where 1D inversion is illustrated in figs. S6 and S8. (Inset) Location of the Lake Toba region within northern Sumatra.

[1]Trofimuk Institute of Petroleum Geology and Geophysics, Siberian Branch of Russian Academy of Sciences, Prospekt Koptyuga, 3, Novosibirsk 630090, Russia. [2]Novosibirsk State University, 2, Pirogova Street, Novosibirsk 630090, Russia. [3]Institut de Physique du Globe de Paris, Sorbonne Paris Cité, CNRS (UMR 7154), 1 rue Jussieu, 75238 Paris, Cedex 5, France. [4]GFZ German Research Centre for Geosciences, Telegrafenberg 14473 Potsdam, Germany.
*Corresponding author. E-mail: nshapiro@ipgp.fr

Fine-scale layering in dyke or sill complexes affects the macromechanical properties of the crustal material, which results in anisotropy that can be measured with seismic waves. For example, the faster velocities of vertically propagating *P* waves below the Merapi volcano (Java, Indonesia) (*14*) were attributed to the presence of dykes with dominantly vertical orientations. Alternatively, the horizontal layering that is typical for sill complexes would result in so-called radial anisotropy (vertical transversely isotropic media with a vertical slow axis of symmetry) (*15*). This type of anisotropy is well known in the upper mantle, where it is mainly associated with mineralogical preferential orientation caused by the strain in response to large-scale mantle flow (*16*). Similar processes are believed to produce the radial anisotropy that has been observed recently within the crust in tectonically active regions (*17*, *18*). Transverse isotropy is also well known in sedimentary rock (*19*).

One of the methods used to estimate radial anisotropy is the measurement and simultaneous inversion of dispersion curves of Rayleigh and Love surface waves (*16*). Inferring information about crustal structure generally requires dispersion measurements at periods <20 s, which are now possible with methods based on the correlation of ambient seismic noise (*20*). We have applied noise-based surface-wave seismic tomography to study the structure of the middle and upper crust below the Toba caldera and its surrounding areas (*21*). Recent seismological studies (*22*–*25*) have indicated the presence of low–seismic-velocity anomalies beneath the Toba caldera that might be associated with sediments filling the caldera at its shallowest levels and with magma or partly molten portions in the deeper crust and mantle. However, because of poor vertical resolution, these seismic images have not provided indications to date about how these magma bodies might have been emplaced within the crust.

We processed continuous records from 40 seismic stations that were installed around Lake Toba (*25*) between May and October 2008 (Fig. 1) to compute the cross-correlations of ambient seismic noise (fig. S1). The resulting waveforms were used to measure group velocities of fundamental-mode Rayleigh and Love waves (*26*) at periods between 3 and 19 s. We then regionalized these measurements to obtain two-dimensional (2D) maps (Fig. 2) of the distribution of group velocities (*27*). A 3D model of the distribution of the shear speeds within the crust (Fig. 3) was constructed via inverting regionalized dispersion curves with a neighborhood algorithm (*21*, *28*).

For Rayleigh waves (Fig. 2, A and B, and fig. S9) at all periods, the group velocity distributions show the prominent low-velocity anomaly beneath Samosir Island, which is located in the central part of the Toba caldera. These images are similar to those previously obtained with the same data set but slightly different data processing and inversion (*25*), and they are consistent with the body wave tomography (*24*). For Love waves, the strong low-velocity anomaly is also observed for short periods that correspond to shallower depths (Fig. 2C), although its amplitude strongly decreases at long periods that are affected by deeper structures (Fig. 2D). To explain this difference between Rayleigh and Love waves, there is the need to introduce radial anisotropy (transverse isotropy with a vertical symmetry axis) with a horizontally polarized shear wave speed (V_{SH}) that is greater than the vertically polarized shear wave speed (V_{SV}). This anisotropy is required at depths >7 km (figs S6 to S8) below the Toba caldera, whereas outside this region, the data can be explained through an isotropic middle crust.

The radial anisotropy within the middle crust below the Toba caldera (fig. S9) can be explained by a large layered intrusion complex that is dominated by horizontally oriented sills (Fig. 3D). We have estimated the possible macromechanical properties of such media via the modeling of seismic velocities in random layered structures (*15*, *21*). We compared the modeling results with the average shear wave speeds V_{SV} and V_{SH} observed below the Toba caldera at depths between 7 and 20 km (~3.0 and ~3.35 km/s, respectively). We also used the regional tomographic model (*24*) that is based on records from earthquakes that were mainly located below the Toba caldera (i.e., on the nearly vertical rays) to deduce the average speed of the vertically propagating *P* waves (V_{PV}), which was approximately 5.3 km/s. After testing numerous random structures whose properties were based on the known seismic speeds of plutonic rock (*29*, *30*) and on typical thicknesses of sills (*7*), we found that the observed strong radial anisotropy and low V_{SV} can be explained by the presence of molten fractions in some sills (table S1), which is in agreement with geodynamic models (*2*).

Fast magma displacements and strong explosions during super-eruptions might destroy the dominant horizontal stratification in the uppermost crust. Based on our tomography images, we hypothesize that the observed nearly isotropic low-velocity anomaly above 7 km in depth beneath the caldera (Fig. 3D, red area above dotted line) represents the medium that was affected by the most recent Toba eruption, 74,000 years ago.

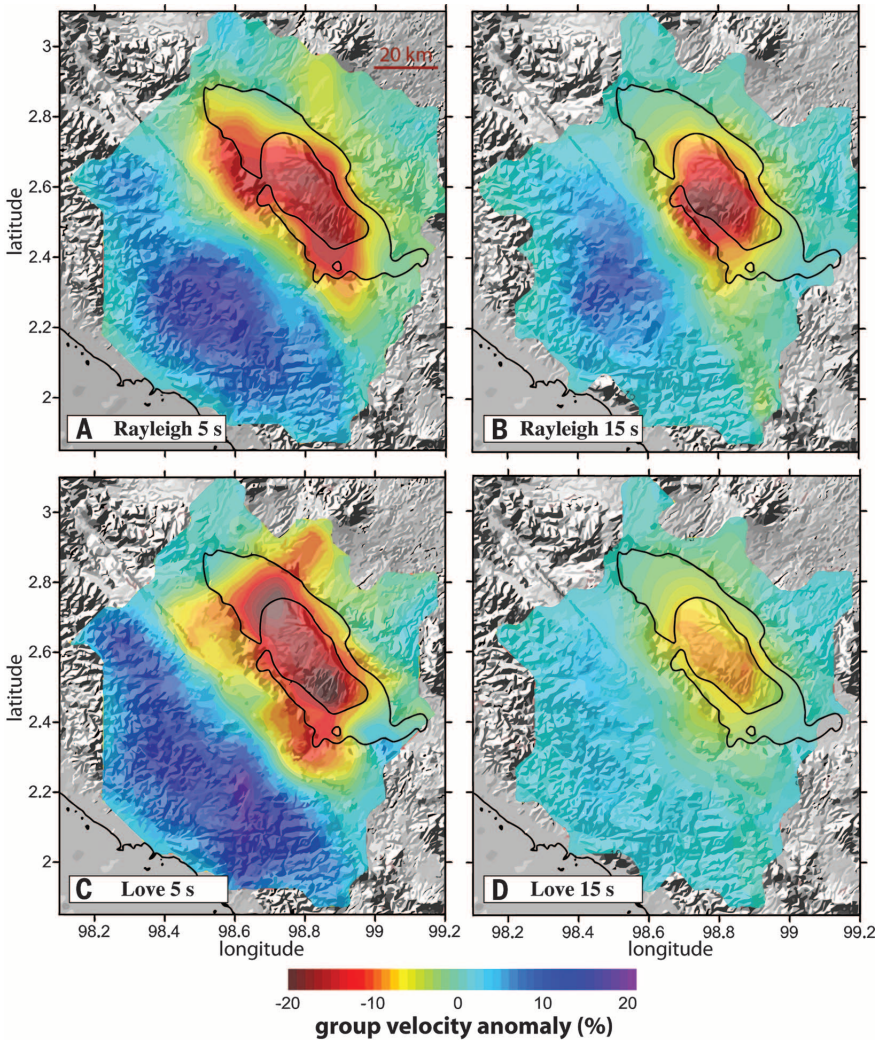

Fig. 2. Group velocity maps of the Rayleigh and Love waves derived from the ambient noise tomography. Colors plotted on top of the shaded relief show group velocity anomalies relative to average values at every period. (**A** and **B**) show Rayleigh wave maps, and (**C** and **D**) show Love wave maps.

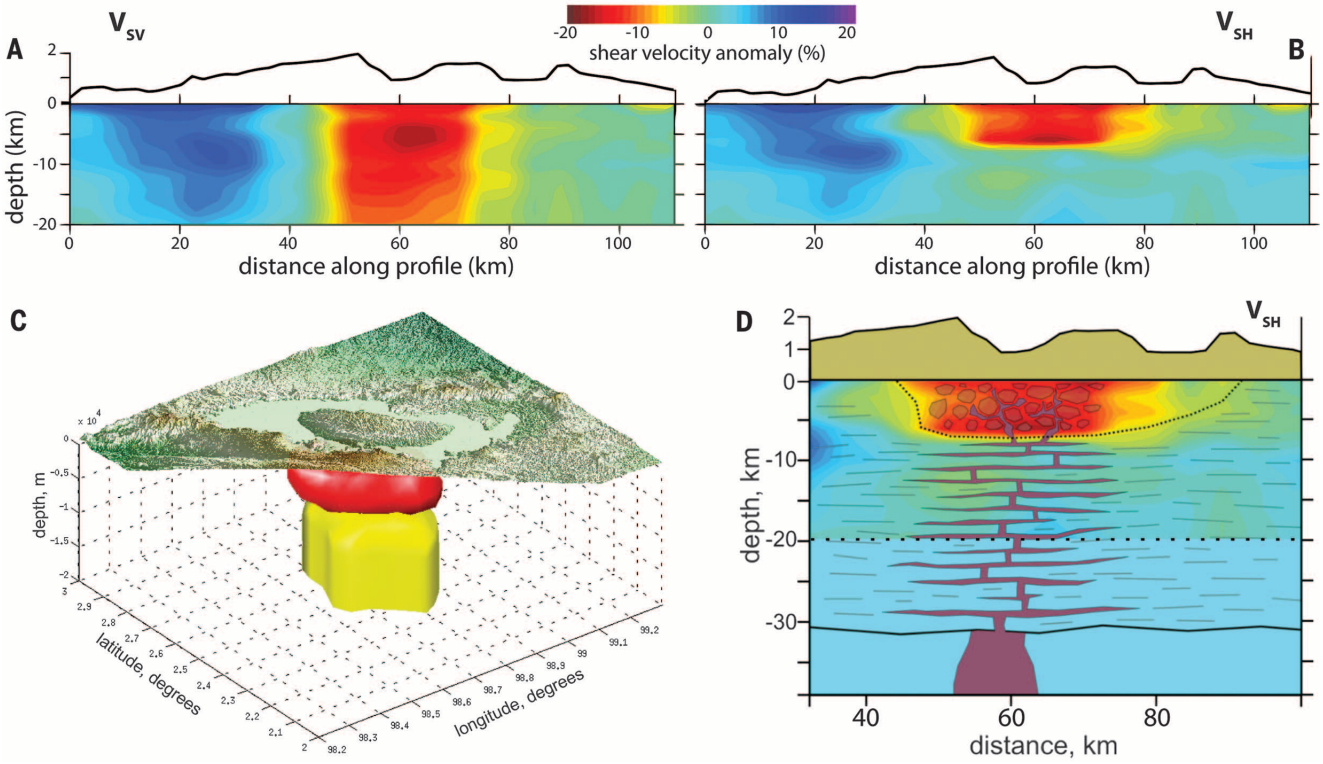

Fig. 3. 3D shear velocity model below the Toba caldera and its interpretation. (**A**) Distribution of V_{SV} in vertical cross section along profile A-A' of Fig. 1. The topography is vertically exaggerated. (**B**) Similar to (A), but for V_{SH}. (**C**) 3D iso-surface representation of the tomographic model. Red surface, low (<–10%) Voigt average speed anomaly; yellow surface, region with strong (>10%) radial anisotropy [$\xi = 2 \times 100\% \times (V_{SH} - V_{SV})/(V_{SH} + V_{SV})$]. Vertically exaggerated topography is shown on the top. (**D**) Schematic interpretation of the velocity structure for the Toba caldera complex superimposed on the distribution of the V_{SH} (shown above 20 km in depth). The anisotropy below 7 km in depth appears to be due to a layered magmatic intrusion dominated by horizontally oriented sills. Dotted line, the low-velocity area below the caldera that might have been affected by the super-eruption 74,000 years ago and where the horizontal stratification would not be preserved.

Below 7 km in depth, the strong horizontal anisotropy corresponds to the preserved sill complex in the middle crust.

The evidence obtained for significant crustal anisotropy, together with the information derived on Toba from other geophysical studies, provides the key to an understanding of the magma intrusion mechanisms that are related to large caldera-forming eruptions. These large-scale volcanic events, such as that of Toba 74,000 years ago, should be preceded by a massive ascent of a large volume of magma. A plausible scenario is that this magma was accumulated incrementally over long periods of time and mainly in the form of successive sill-type intrusions, as suggested by geodynamic models (*2*, *3*, *7*, *8*, *31*). This resulted in the formation of a large layered intrusion complex in the crust. The preferential horizontal orientation of the layers within this sill complex containing a significant amount of melt leads to the observed radial anisotropy. We argue, therefore, that observations of such anisotropy can be used to image and to characterize parts of the crust where the partially molten magma is accumulated before future eruptions.

REFERENCES AND NOTES

1. O. Bachmann, G. Bergantz, *Elements* **4**, 17–21 (2008).
2. C. Annen, J.-D. Blundy, R. S. J. Sparks, *J. Petrol.* **47**, 505–539 (2006).
3. C. Annen, *Earth Planet. Sci. Lett.* **284**, 409–416 (2009).
4. C. A. Chesner, *Quat. Int.* **258**, 5–18 (2012).
5. F. J. Gathorne-Hardy, W. E. H. Harcourt-Smith, *J. Hum. Evol.* **45**, 227–230 (2003).
6. J. E. Gardner, P. W. Layer, M. J. Rutherford, *Geology* **30**, 347–350 (2002).
7. C. Michaut, C. Jaupart, *Tectonophysics* **500**, 34–49 (2011).
8. A. Gudmundsson, *Tectonophysics* **500**, 50–64 (2011).
9. B. Taisne, C. Jaupart, *J. Geophys. Res.* **114**, B09203 (2009).
10. G. J. Hill *et al.*, *Nat. Geosci.* **2**, 785–789 (2009).
11. J. M. Lees, *J. Volcanol. Geotherm. Res.* **167**, 37–56 (2007).
12. X. Peng, E. D. Humphreys, *J. Geophys. Res.* **103**, 7171–7186 (1998).
13. J. W. Shervais, S. K. Vetter, B. B. Hanan, *Geology* **34**, 365–368 (2006).
14. I. Koulakov, A. Jakovlev, B. G. Luehr, *Geochem. Geophys. Geosyst.* **10**, Q02011 (2009).
15. G. W. Postma, *Geophysics* **20**, 780–806 (1955).
16. G. Ekström, A. M. Dziewonski, *Nature* **394**, 168–172 (1998).
17. N. M. Shapiro, M. H. Ritzwoller, P. Molnar, V. Levin, *Science* **305**, 233–236 (2004).
18. M. P. Moschetti, M. H. Ritzwoller, F. Lin, Y. Yang, *Nature* **464**, 885–889 (2010).
19. Z. Wang, *Geophysics* **67**, 1423–1440 (2002).
20. N. M. Shapiro, M. Campillo, L. Stehly, M. H. Ritzwoller, *Science* **307**, 1615–1618 (2005).
21. Information on materials and methods is available on *Science* Online.
22. R. Masturyono *et al.*, *Geochem. Geophys. Geosyst.* **2**, 1014 (2001).
23. K. Sakaguchi, H. Gilbert, G. Zandt, *Geophys. Res. Lett.* **33**, L20305 (2006).
24. I. Koulakov, T. Yudistira, B. G. Luehr, P. Wandono, *Geophys. J. Int.* **177**, 1121–1139 (2009).
25. J. Stankiewicz, T. Ryberg, C. Haberland, D. Fauzi, D. Natawidjaja, *Geophys. Res. Lett.* **37**, L17306 (2010).
26. G. D. Bensen *et al.*, *Geophys. J. Int.* **169**, 1239–1260 (2007).
27. M. Barmin, M. H. Ritzwoller, A. L. Levshin, *Pure Appl. Geophys.* **158**, 1351–1375 (2001).
28. A. Mordret, M. Landès, N. M. Shapiro, S. Singh, P. Roux, *Geophys. J. Int.* **198**, 1514–1525 (2014).
29. T. M. Brocher, *Bull. Seismol. Soc. Am.* **98**, 950–968 (2008).
30. K. Wohletz, G. Heiken, *Volcanology and Geothermal Energy* (Univ. of California Press, Berkeley, CA, 1992).
31. E. Chaussard, F. Amelung, *Geophys. Res. Lett.* **39**, L21311 (2012).

ACKNOWLEDGMENTS

All of the data used in this study (doi:10.14470/2N934755) were acquired with instruments from the GFZ instrument pool (GIPP) and distributed by the GFZ-GEOFON data center. Computations in this study were performed using the High-Performance Computing infrastructure S-CAPAD at the Institute de Physique du Globe de Paris, which is supported by the Île-de-France region (via the SEASAME program), France-Grille (http://www.france-grilles.fr), and the CNRS MASTODONS program. The work of K.J., A.M., and N.M.S. was supported by the European Union through the European Research Council advanced grant project 227507 Whisper and for C.S.-S. by the Federal Ministry of Education and Research (BMBF) project MIIC (grant no. 03G0736A). I.K. was supported by the Russian Science Foundation (grant no. 14-17-00430). M.L. was supported by the French project DataScale. We acknowledge C. Jaupart (Institut de Physique du Globe de Paris) for helpful discussions.

SUPPLEMENTARY MATERIALS

www.sciencemag.org/content/346/6209/617/suppl/DC1
Materials and Methods
Figs. S1 to S10
Table S1
References (*32*–*43*)

10 July 2014; accepted 1 October 2014
10.1126/science.1258582

NANOMATERIALS

Influence of the support on surface rearrangements of bimetallic nanoparticles in real catalysts

Núria J. Divins,[1] Inma Angurell,[2] Carlos Escudero,[3] Virginia Pérez-Dieste,[3] Jordi Llorca[1]*

Catalysts used for heterogeneous processes are usually composed of metal nanoparticles dispersed over a high–surface-area support. In recent years, near-ambient pressure techniques have allowed catalyst characterization under operating conditions, overcoming the pressure gap effect. However, the use of model systems may not truly represent the changes that occur in real catalysts (the so-called material gap effect). Supports can play an important role in the catalytic process by providing new active sites and may strongly affect both the physical and chemical properties of metal nanoparticles. We used near-ambient pressure x-ray photoelectron spectroscopy to show that the surface rearrangement of bimetallic (rhodium-palladium) nanoparticles under working conditions for ethanol steam reforming with real catalysts is strongly influenced by the presence of a reducible ceria support.

The structure of heterogeneous catalysts is dynamic and depends on the composition of the surrounding environment. Thus, both their surface structure and composition may be modified when the gaseous conditions change, in order to adapt their electronic properties and geometry to the new surrounding environment. Some structures and active phases only exist under reaction conditions and can differ from those identified under ultrahigh-vacuum (UHV) conditions (*1*, *2*). Thus, the study of catalytic systems under real operating conditions is essential to identify the active species at work, because the restructuring driven by the environment may induce strong changes in both the properties and behavior of catalysts (*3*, *4*). The advent of several in situ surface-sensitive techniques has allowed the characterization of surfaces under controlled atmospheres that can closely reproduce the working conditions of these systems (*5*). In this work, we used synchrotron-based ambient-pressure x-ray photoelectron spectroscopy (AP-XPS) to monitor both the surface restructuring and chemical state of two systems: (i) unsupported model $Rh_{0.5}Pd_{0.5}$ nanoparticles (NPs) and (ii) $Rh_{0.5}Pd_{0.5}$ NPs supported on CeO_2 powder (which constitutes a real catalyst). Both systems were exposed to reducing, oxidizing, and ethanol steam reforming (ESR) conditions to produce hydrogen. Three photon energies were chosen (670, 875, and 1150 eV) in order to perform a depth-profile study of both systems to infer the environment-induced rearrangement and the development of a core-shell structure.

RhPd NPs were first studied by AP-XPS at the Advanced Light Source (Berkeley, USA) in a seminal work by Tao *et al.* under NO, O_2, H_2, and NO + CO environments to investigate the surface rearrangement of this bimetallic system in relevant reactions applied to pollution abatement (*6*). These authors used unsupported model NPs about 15 nm in diameter and found that a core-shell structure developed under the reducing and oxidizing environments tested. This finding showed that surface rearrangements in bimetallic systems occurred under different atmospheres, although no support was used. At the same time, the RhPd system shows excellent performance in ESR ($C_2H_5OH + 3\ H_2O \rightarrow 6\ H_2 + 2\ CO_2$) when supported over CeO_2 (*7*, *8*). This reaction represents a very attractive route to obtain hydrogen from both a renewable and widespread source (bioethanol) without net CO_2 emissions and is currently being intensively researched (*9*, *10*).

The synergic effect exerted by the support on the catalytic performance of metal NPs has been extensively studied, and immense effort has been made to elucidate the exact mechanisms involved in the metal-support interaction (*11*–*16*). Nonetheless, most of the fundamental work has been conducted in model systems such as single crystals, thin films, or isolated NPs. These systems lack some important features found in real catalysts, such as a high surface area, different types of defects, exposed planes and anchoring sites, the presence of reactive hydroxyl groups, the ability to activate certain reactants, etc., which all play an important role in the catalytic processes. We overcame this problem by directly studying a $Rh_{0.5}Pd_{0.5}/CeO_2$ real catalyst pellet in the AP-XPS experiments. By combining the results obtained from the AP-XPS studies with bench catalytic tests in a model system (unsupported $Rh_{0.5}Pd_{0.5}$ NPs) and in our real catalytic system ($Rh_{0.5}Pd_{0.5}/CeO_2$), we showed that the CeO_2 support exerts a prominent role on the surface rearrangement of the bimetallic NPs, which in turn has a strong effect on the catalytic performance. The CeO_2 support is crucial for the ESR reaction, not only for activating the water molecule and avoiding carbon deposition because of its remarkable oxygen storage-release capability (*17*–*19*), but also by

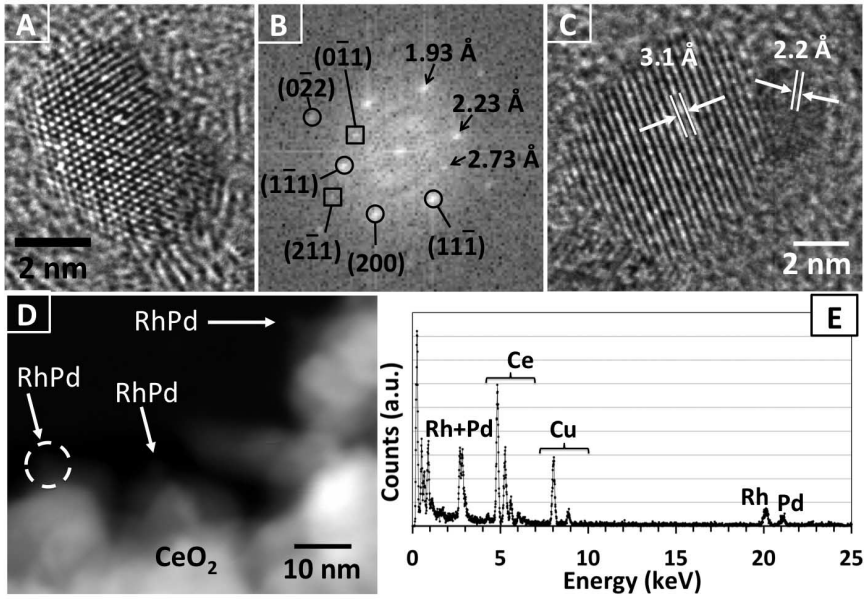

Fig. 1. The characterization of the unsupported $Rh_{0.5}Pd_{0.5}$ NPs and the $Rh_{0.5}Pd_{0.5}/CeO_2$ catalyst by TEM techniques revealed the presence of isolated alloy NPs. (**A**) HRTEM image of a representative $Rh_{0.5}Pd_{0.5}$ NP as prepared. (**B**) Fourier transform image of the NP shown in (A). (**C**) HRTEM image of the $Rh_{0.5}Pd_{0.5}/CeO_2$ catalyst. (**D**) STEM image of the $Rh_{0.5}Pd_{0.5}/CeO_2$ catalyst. (**E**) EDX spectrum recorded in the region encircled in (D) (the Cu signal is due to the TEM grid).

[1]Institute of Energy Technologies and Centre for Research in NanoEngineering, Technical University of Catalonia, Diagonal 647, 08028 Barcelona, Spain. [2]Department of Inorganic Chemistry, University of Barcelona, Martí i Franquès 1, 08028 Barcelona, Spain. [3]ALBA Synchrotron Light Source, Carretera BP 1413 Km. 3.3, 08290 Cerdanyola del Vallès, Barcelona, Spain.
*Corresponding author. E-mail: jordi.llorca@upc.edu

altering the oxidation states together with the surface reorganization of the noble metal atoms under reaction conditions.

The model $Rh_{0.5}Pd_{0.5}$ NPs were prepared by using a variation of a previously published procedure (*20*), followed by an extraction process with dodecanethiol in toluene (*21*, *22*). Figure 1A shows a representative high-resolution transmission electron microscopy (HRTEM) image of a model $Rh_{0.5}Pd_{0.5}$ NP. The mean diameter of the model $Rh_{0.5}Pd_{0.5}$ NPs determined by TEM analysis was 4 ± 1 nm. Rh and Pd were alloyed; the Fourier transform (FT) image (Fig. 1B) shows reflections at 1.93 and 2.23 Å that can be indexed to the (200) and (111) planes of a RhPd alloy, respectively, and reflections forbidden by selection rules in face-centered cubic Rh and Pd [(011) and (211) planes] (*23*). The $Rh_{0.5}Pd_{0.5}/CeO_2$ catalyst (3 weight % metal) was prepared by incipient wetness impregnation from a toluene solution containing the model $Rh_{0.5}Pd_{0.5}$ NPs followed by calcination at 573 K for 6 hours. Figure 1C shows a HRTEM image of a $Rh_{0.5}Pd_{0.5}$ NP supported on a CeO_2 crystallite. The pre-formed $Rh_{0.5}Pd_{0.5}$ NPs were well dispersed on the ceria support and maintained their original size. The respective interplanar spacings measured for CeO_2 and for the metal NPs (Fig. 1C) closely match the theoretical values of CeO_2 (111) at 3.12 Å and Pd-Rh (111) at 2.25 to 2.20 Å. The bimetallic nature of the metal particles was confirmed by energy-dispersive x-ray spectroscopy (EDX) on individual nanoparticles. Figure 1E shows the EDX analysis performed on the region encircled in Fig. 1D, which corresponds to a scanning transmission electron microscopy (STEM) image of the sample. All of the NPs analyzed showed Rh and Pd signals consistent with an atomic Rh/Pd ratio of 1.0 ± 0.2.

As expected, the catalytic performance of $Rh_{0.5}Pd_{0.5}/CeO_2$ for ESR was superior to that of the model $Rh_{0.5}Pd_{0.5}$ NPs (*22*) (fig. S1). At 1050 K, at a steam-to-carbon ratio (S/C) of 3 and space velocity of 2.04×10^{-4} ml of liquid/(milligrams of catalyst × minutes), the amount of hydrogen produced by $Rh_{0.5}Pd_{0.5}/CeO_2$ doubled that achieved by the model $Rh_{0.5}Pd_{0.5}$ NPs (28 versus 15 ml/min). In addition, the product distribution obtained was notably different in both systems. Following (*7*), the ESR over noble metals supported on reducible oxides follows three steps: (i) ethanol decomposition ($C_2H_5OH \rightarrow H_2 + CO + CH_4$); (ii) water-gas shift (WGS, $CO + H_2O \Leftrightarrow H_2 + CO_2$); and (iii) methane steam reforming (MSR, $CH_4 + H_2O \Leftrightarrow 3\ H_2 + CO$). The much higher CO_2 concentration attained by the $Rh_{0.5}Pd_{0.5}/CeO_2$ than that obtained by the unsupported NPs (15.9 versus 1.8% at 1050 K) shows promotion of the WGS reaction (step 2) by CeO_2, as already reported (*24*). In the case of the unsupported NPs, the lack of WGS promotion was confirmed by the presence of large quantities of CO in the reformate stream (31.1 versus 12.3% for $Rh_{0.5}Pd_{0.5}/CeO_2$). Additionally, methane concentration was lower in the case of the real catalyst (11.0 versus 14.7% for the model NPs), indicating that MSR (step 3) also took place to a greater degree in the presence of the CeO_2 support. These two effects led to higher hydrogen production for the $Rh_{0.5}Pd_{0.5}/CeO_2$ system than for the model NPs, thus demonstrating the essential role of the ceria support for ESR. After ESR performance, field emission scanning electron microscopy (FESEM) and HRTEM showed RhPd NPs of similar size, 6 ± 1 nm, in both samples (fig. S2).

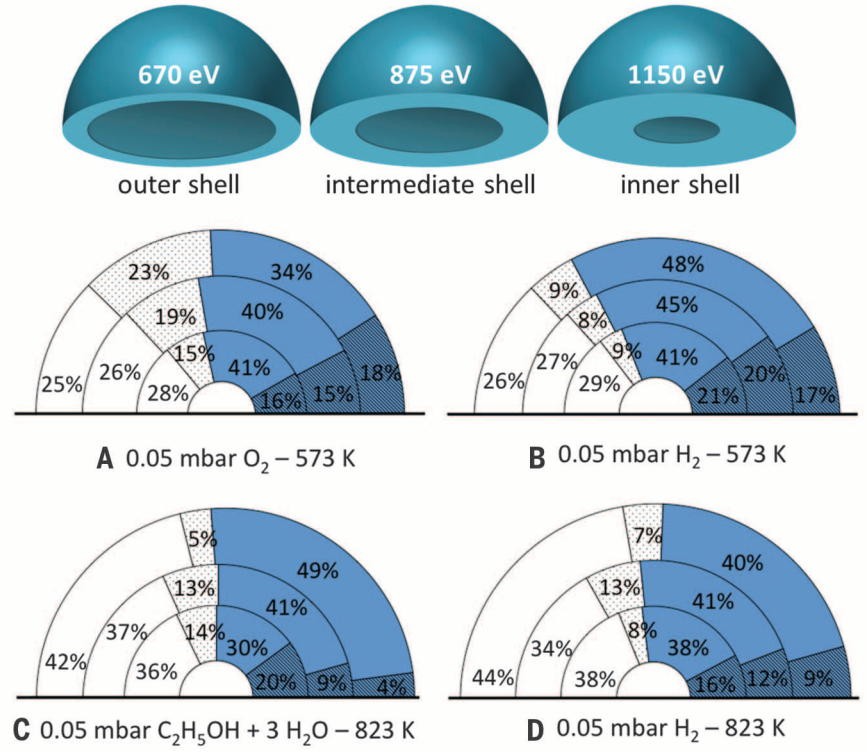

Fig. 2. Atomic fractions of Pd and Rh calculated for the model $Rh_{0.5}Pd_{0.5}$ NPs. The top row shows the three different volumes sampled. Semicircles below show the atomic fractions of Pd (depicted in blue) and Rh (depicted in white), where the dashed regions correspond to the oxidized fraction of each metal. The outer semicircle corresponds to the atomic fractions obtained with hν = 670 eV, the intermediate semicircle corresponds to hν = 875 eV, and the inner semicircle corresponds to hν = 1150 eV. (**A** to **D**) show the different gaseous environments.

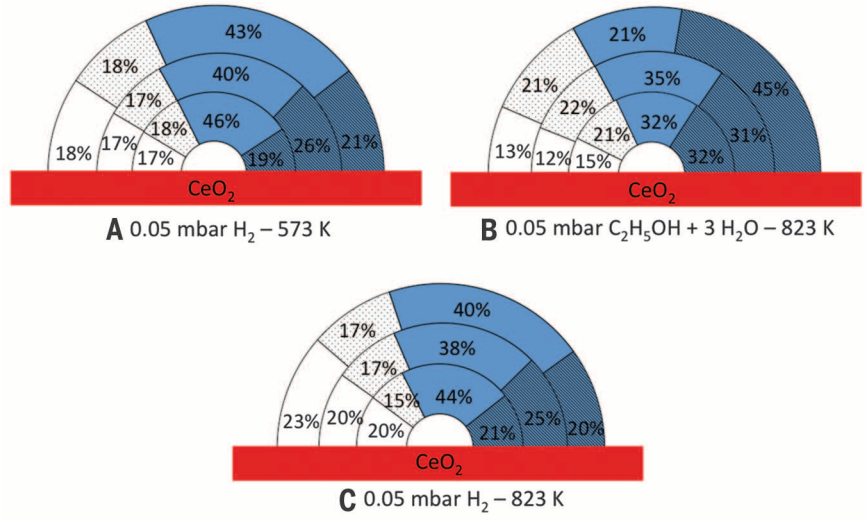

Fig. 3. Atomic fractions of Pd and Rh calculated for the $Rh_{0.5}Pd_{0.5}/CeO_2$ catalyst. Semicircles show the atomic fractions of Pd (depicted in blue) and Rh (depicted in white), where the dashed regions correspond to the oxidized fraction of each metal. The outer semicircle corresponds to the atomic fractions obtained with hν = 670 eV, the intermediate semicircle corresponds to hν = 875 eV, and the inner semicircle corresponds to hν = 1150 eV. (**A** to **C**) show the different gaseous environments.

The AP-XPS experiments were carried out at the CIRCE beamline of the ALBA synchrotron light source (*25*), at a sample pressure of 0.05 mbar. The sequence was as follows: (i) O_2 at 573 K, (ii) H_2 at 573 K, (iii) ethanol and water (S/C = 3) at 823 K, and (iv) H_2 at 823 K. Three different photon energies (hυ) of 670, 875, and 1150 eV were used in each case to obtain XP spectra of Rh 3d, Pd 3d, O 1s, C 1s, and Ce 3d (the latter excited only by hυ = 1150 eV). The chosen photon energies account for inelastic mean free paths (IMFPs) of Rh 3d and Pd 3d photoelectrons of ~0.7, 0.9, and 1.2 nm, respectively (*26*), which allowed us to perform a depth-profile study of the $Rh_{0.5}Pd_{0.5}$ NPs. For a spherical $Rh_{0.5}Pd_{0.5}$ NP 4 nm in diameter, the volumes defined by these IMFPs from the exterior surface represent approximately 25, 34, and 44% of their total volume, respectively (*22*).

Figure 2 shows the percentage atomic ratios between Rh and Pd, together with their oxidation states calculated from the XP spectra recorded for the model $Rh_{0.5}Pd_{0.5}$ NPs under the different gaseous environments tested and the three photon energies monitored (*22*). In each figure, the three regions shown symbolize the results obtained for each sampling depth. During the first treatment (calcination at 573 K, O_2 atmosphere, Fig. 2A), the model NPs showed a Pd/Rh ratio near unity and did not show substantial differences at the different depths studied. The Pd atomic fraction in the outer region (excited at 670 eV) was 0.52 ± 0.03, whereas for the inner region (excited at 1150 eV), it was 0.57 ± 0.03. Pd was highly reduced at all depths with concentrations of metallic Pd of 65 to 72%. Rh was also reduced in all the layers, but to a lesser extent (51 to 65%). For both metals, oxidation increased toward the NP surface.

Upon reduction with H_2 at 573 K (for catalyst activation, see Fig. 2B and fig. S4), Pd segregated toward the surface, with a Pd atomic fraction of about 0.65 ± 0.03. This result fully agrees with the work of Tao *et al.* (*6*), where a migration of Pd atoms toward the surface during H_2 exposure was also reported. At the same time, Rh experienced a strong reduction, and ~75% of both metals was present in the metallic state. After H_2 activation of the sample, we studied the ESR process by dosing ethanol and water directly inside the analysis chamber at 823 K. Under ESR (Fig. 2C), the NPs restructured as Rh atoms migrated toward the surface; again the atomic ratio of Rh and Pd was ~1:1. Furthermore, the outer region of the $Rh_{0.5}Pd_{0.5}$ NPs further reduced, and approximately 90% of Rh and Pd was found in their metallic state, which is ascribed to the reducing effect of the hydrogen generated during the ESR reaction at 823 K. This effect was corroborated by studying the $Rh_{0.5}Pd_{0.5}$ NPs under pure H_2 at the same temperature (Fig. 2D and fig. S5). At this temperature, the noble metals did not undergo substantial changes as compared with the previous ESR environment.

A different scenario results when the model $Rh_{0.5}Pd_{0.5}$ NPs are supported on CeO_2 (Fig. 3). For the real $Rh_{0.5}Pd_{0.5}/CeO_2$ catalyst, the reduction treatment at 573 K resulted in a Pd-rich surface with Pd atomic fractions of about 0.65 (Fig. 3A and fig. S4). This value is similar to that found for the unsupported NPs under the same environment (Fig. 2B). However, under ESR conditions at 823 K, there was no migration of Rh or Pd. The atomic fraction of both noble metals remained approximately constant at the same values as in the previous reducing treatment for all depths; for the unsupported NPs, surface Pd enrichment that occurred during catalyst activation was reversed during the ESR reaction. Most importantly, both metals became more oxidized (Fig. 3B), whereas for unsupported NPs, the metals were predominantly reduced (Fig. 2C). Furthermore, Pd developed a core-shell structure of oxidation states, as seen in Fig. 4 as a large oxidized Pd component in the outer shell of the $Rh_{0.5}Pd_{0.5}/CeO_2$ catalyst. Taking into account that the region sampled at 670 eV corresponds only to the outer shell, whereas the region sampled at 875 eV corresponds to the weighted contribution of the outer shell and the intermediate shell, the strong decrease of the Pd oxidation fraction observed in the 875-eV region of the supported NPs indicates that the Pd oxidation is strongly confined to the NPs surface. It is likely that the activation of water by CeO_2, as deduced from the catalytic results, creates –OH groups at the catalyst surface, thus leading to the oxidation of the outermost layers of the NPs. This remarkable difference indicates that the interaction of the metal NPs with the ceria support plays a key role in reactions catalyzed by the RhPd alloy NPs by limiting the reorganization of the metals under reaction conditions ("quenching effect") and by providing active oxygen atoms to the metals at the surface of the NPs. Figure 4 shows the Pd 3d, Rh 3d, and O 1s XP spectra recorded for both the model $Rh_{0.5}Pd_{0.5}$ NPs and the $Rh_{0.5}Pd_{0.5}/CeO_2$ catalyst under ESR conditions at 823 K. The photoemission lines of the noble metals of the real catalyst contain, in all cases, an additional component with respect to the unsupported NPs at ~308.7 and 337.8 eV for Rh $3d_{5/2}$ and Pd $3d_{5/2}$, respectively, which is ascribed to the metal-support interaction discussed above (*27*). The O 1s spectra of the $Rh_{0.5}Pd_{0.5}/CeO_2$ showed three spectral features: the component at low binding energy

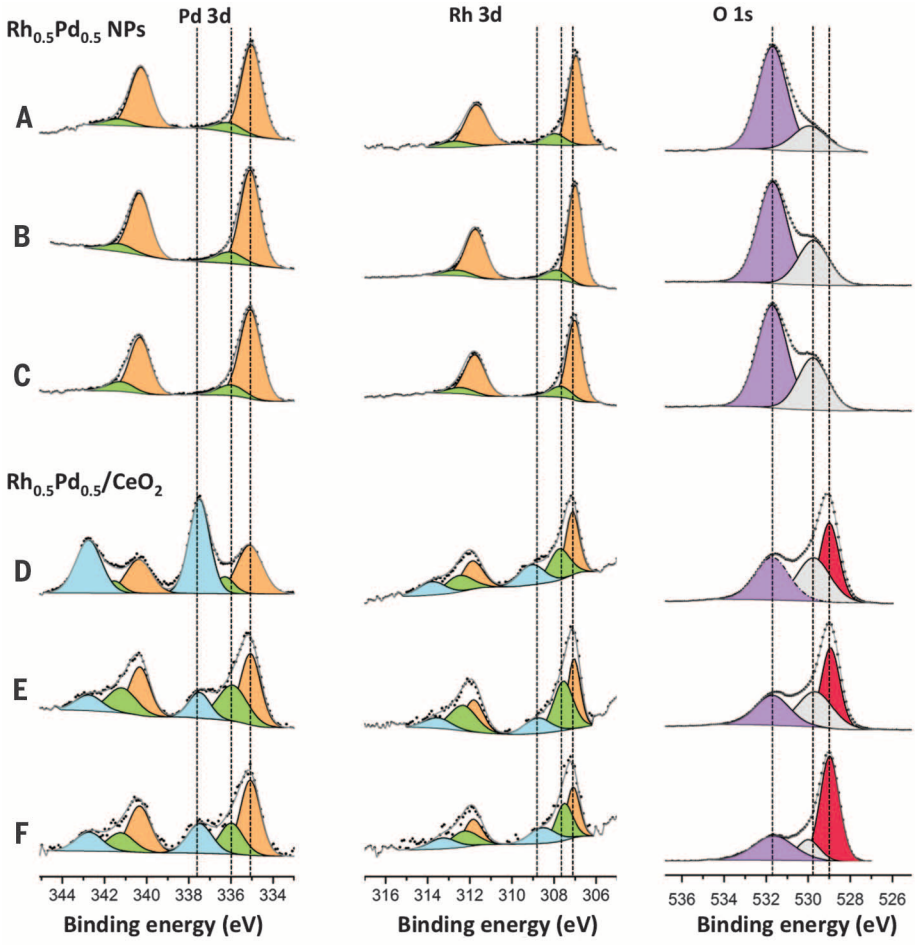

Fig. 4. Ambient pressure x-ray photoelectron spectra of Pd 3d, Rh 3d, and O 1s. The spectra were recorded for both the model $Rh_{0.5}Pd_{0.5}$ NPs (**A** to **C**) and the $Rh_{0.5}Pd_{0.5}/CeO_2$ catalyst (**D** to **F**) under ESR conditions at 823 K. The photon energies used were 670 eV [(A) and (D)], 875 eV [(B) and (E)], and 1150 eV [(C) and (F)]. The sample pressure was 0.05 mbar. The O 1s regions in (B), (C), (E), and (F) correspond in kinetic energy scale to the metal regions in (A), (B), (D), and (E), respectively.

(529.1 eV) has been ascribed to O-Ce, the component at 530 eV to O-metals (Rh and/or Pd), and the component at 531.8 eV to –OH groups present on the surface of the catalyst (Fig. 4, D to F, O 1s) (*28*, *29*). The ratio between the area of the O-Ce peak and the –OH peak increases as the photon energy increases; i.e., as the sampling depth increases, which highlights the sensitivity to different depths of the chosen photon energies and the presence of the –OH groups on the surface of the $Rh_{0.5}Pd_{0.5}/CeO_2$ catalyst. The same trend is observed for the unsupported NPs, where the ratio between the O-metal peak and the –OH peak also increases when the photon energy is increased (Fig. 4, A to C, O 1s). In this case, the O 1s high-binding-energy component could be related to hydroxyl groups interacting with water molecules (*30*), because they almost do not participate in the ESR reaction (fig. S1), and the –OH groups do not affect the oxidation state of the metals (Fig. 2 C), because the inner shells are the most oxidized ones.

Finally, the oxidation state of both metals in the $Rh_{0.5}Pd_{0.5}/CeO_2$ catalyst very nearly recovered the values of the first reducing treatment at lower temperature (Fig. 3A) during the reduction with pure H_2 at the reaction temperature (823 K, Fig. 3C and fig. S5), unlike the model NPs, and again this points to the stabilizing effect of the ceria support. Analysis of the oxidation state of cerium (performed only with hυ = 1150 eV, fig. S3) reveals variations depending on the gaseous environment and temperature (*22*). Under H_2 and 573 K, the Ce^{3+}/Ce^{4+} atomic ratio was 0.63. The ratio decreased to 0.58 during the ESR reaction at 823 K, in accordance with the oxidation experienced by the noble metals, and it strongly increased up to 0.83 under H_2 at 823 K.

In the absence of a support, the model NPs were more strongly reduced for all the environments tested, and the reduction temperature affected the amount of metallic phase found in Rh and Pd. Compared with the unsupported NPs, the capability of CeO_2 as a support to activate water and to donate oxygen atoms determined the oxidation states of the noble metals under the same reaction conditions. In addition, the interaction between the ceria support and the metal nanoparticles prevented reorganization of the Rh and Pd atoms. We have thus demonstrated the pivotal role of the metal-support interaction in the reorganization of metal atoms in supported bimetallic catalysts under operating conditions and shown that this effect has a strong influence on the catalytic performance. Keeping this in mind, it should be noted that AP-XPS studies (and other studies) carried out on unsupported model systems may not provide reliable information on supported real catalysts. For this reason, it is very important to also take into account the influence of the support in spite of the experimental difficulties often encountered.

REFERENCES AND NOTES

1. F. F. Tao, M. Salmeron, *Science* **331**, 171–174 (2011).
2. S. Zafeiratos *et al.*, *J. Catal.* **269**, 309–317 (2010).
3. D. E. Starr, H. Bluhm, Z. Liu, A. Knop-Gericke, M. Hävecker, in *In-situ Characterization of Heterogeneous Catalysts*, J. A. Rodriguez, J. C. Hanson, P. J. Chupas, Eds. (Wiley, New York, 2013), pp. 315–343.
4. D. E. Starr, Z. Liu, M. Hävecker, A. Knop-Gericke, H. Bluhm, *Chem. Soc. Rev.* **42**, 5833–5857 (2013).
5. C. Escudero, M. Salmeron, *Surf. Sci.* **607**, 2–9 (2013).
6. F. Tao *et al.*, *Science* **322**, 932–934 (2008).
7. H. Idriss *et al.*, *ChemSusChem* **1**, 905–910 (2008).
8. N. J. Divins, E. López, Á. Rodríguez, D. Vega, J. Llorca, *Chem. Eng. Process. Process Intensif.* **64**, 31–37 (2013).
9. G. A. Deluga, J. R. Salge, L. D. Schmidt, X. E. Verykios, *Science* **303**, 993–997 (2004).
10. J. Llorca, V. Cortés Corberán, N. J. Divins, R. O. Fraile, E. Taboada, in *Renewable Hydrogen Technologies*, L. M. Gandía, G. Arzamendi, P. M. Diéguez, Eds. (Elsevier, Amsterdam, 2013), pp. 135–169.
11. F. Aksoy *et al.*, *Nucl. Instruments Methods Phys. Res. Sect. A Accel. Spectrometers Detect. Assoc. Equip.* **645**, 260–265 (2011).
12. K. Mudiyanselage *et al.*, *Angew. Chem. Int. Ed. Engl.* **52**, 5101–5105 (2013).
13. C. Wen *et al.*, *ACS Nano* **6**, 9305–9313 (2012).
14. A. Caballero *et al.*, *Chem. Commun. (Camb.)* **46**, 1097–1099 (2010).
15. C. Mattevi *et al.*, *J. Phys. Chem. C* **112**, 12207–12213 (2008).
16. A. Bruix *et al.*, *J. Am. Chem. Soc.* **134**, 8968–8974 (2012).
17. A. Trovarelli, *Catal. Rev.* **38**, 439–520 (1996).
18. H. Song, L. Zhang, R. Watson, D. Braden, U. Ozkan, *Catal. Today* **129**, 346–354 (2007).
19. H. Idriss, *Platin. Met. Rev.* **48**, 105–115 (2004).
20. X. Peng, Q. Pan, G. L. Rempel, S. Wu, *Catal. Commun.* **11**, 62–66 (2009).
21. J. C. Garcia-Martinez, R. M. Crooks, *J. Am. Chem. Soc.* **126**, 16170–16178 (2004).
22. See the supplementary materials.
23. Y. Qi *et al.*, *Nanoscale* **6**, 7012–7018 (2014).
24. C. Wheeler, *J. Catal.* **223**, 191–199 (2004).
25. V. Pérez-Dieste *et al.*, *J. Phys. Conf. Ser.* **425**, 072023 (2013).
26. C. J. Powell, A. Jablonski, *NIST Electron Inelastic-Mean-Free-Path Database - Version 1.2* (National Institute of Standards and Technology, Gaithersburg, MD, 2010).
27. Y. Zhu *et al.*, *ACS Catal.* **3**, 2627–2639 (2013).
28. M. M. Natile, A. Glisenti, *Surf. Sci. Spectra* **13**, 17–30 (2006).
29. C. Force, E. Roman, J. M. Guil, J. Sanz, *Langmuir ACS J. Surf. Colloids* **23**, 4569–4574 (2007).
30. H. Sánchez Casalongue *et al.*, *Nat. Commun.* **4**, 2817 (2013).

ACKNOWLEDGMENTS

This work has been funded through grant MINECO ENE2012-36368. J.L. is grateful to the ICREA Academia program.

SUPPLEMENTARY MATERIALS

www.sciencemag.org/content/346/6209/620/suppl/DC1
Materials and Methods
Figs. S1 to S5
References (*31*–*33*)

30 June 2014; accepted 2 October 2014
10.1126/science.1258106

EARLY SOLAR SYSTEM

Early accretion of water in the inner solar system from a carbonaceous chondrite–like source

Adam R. Sarafian,[1]* Sune G. Nielsen,[1] Horst R. Marschall,[1,2,3] Francis M. McCubbin,[4] Brian D. Monteleone[1]

Determining the origin of water and the timing of its accretion within the inner solar system is important for understanding the dynamics of planet formation. The timing of water accretion to the inner solar system also has implications for how and when life emerged on Earth. We report in situ measurements of the hydrogen isotopic composition of the mineral apatite in eucrite meteorites, whose parent body is the main-belt asteroid 4 Vesta. These measurements sample one of the oldest hydrogen reservoirs in the solar system and show that Vesta contains the same hydrogen isotopic composition as that of carbonaceous chondrites. Taking into account the old ages of eucrite meteorites and their similarity to Earth's isotopic ratios of hydrogen, carbon, and nitrogen, we demonstrate that these volatiles could have been added early to Earth, rather than gained during a late accretion event.

Hydrogen is vitally important in cosmochemical and geochemical processes. For example, water (H_2O) plays a critical role in plate tectonics on Earth (*1*) and has likely shaped the surface of Mars (*2*). Despite the abundance of water on Earth and evidence of water on the Moon, Mars, and the asteroid 4 Vesta (*2*–*4*), these planetary bodies are often thought to have accreted dry (*5*–*8*). This prompts two key questions: Where did the water come from? And when was it present in the inner solar system? The answers may reveal information about accretion processes in terrestrial planets. Additionally, the extent and importance of lateral water transport throughout the history of the solar system are debatable (*9*, *10*).

The source of water in planetary bodies can be investigated by measuring the ratio between the isotopes of hydrogen (deuterium, D or ^2H, and hydrogen, ^1H) because different regions of the

[1]Department of Geology and Geophysics, Woods Hole Oceanographic Institution, Woods Hole, MA 02543, USA. [2]Department of Earth and Planetary Sciences, American Museum of Natural History, New York, NY 10024, USA. [3]School of Earth Sciences, University of Bristol, Bristol BS8 1RJ, UK. [4]Institute of Meteoritics, University of New Mexico, Albuquerque, NM 87131, USA.
*Corresponding author. E-mail: asarafian@whoi.edu

solar system vary widely in measured D/H ratios (*11*). Thus, determining D/H ratios in meteorites with well-known ages and planetary origins can help constrain the timing of water delivery to accreting planetary bodies. Such analysis provides an ideal opportunity to study the provenance of water in bodies throughout the solar system, including Earth, the Moon, Mars, and the asteroid belt (*12*–*14*).

Eucrites, a class of asteroidal basaltic meteorites, can provide unique information about the timing of water delivery to planets because most of these rocks crystallized 4559 to 4547 million years ago (Ma), or ~8 to 20 million years after the first solids in the solar system, calcium- and aluminum-rich inclusions (CAIs) (*15*, *16*). Eucrites belong to the howardite-eucrite-diogenite group of meteorites (HEDs) that are derived from the asteroid belt, dominantly from the asteroid Vesta (*17*–*19*). Determining the source of water in eucrites can constrain the time at which water existed in the inner solar system, because these ancient rocks are some of the oldest igneous rocks in the solar system. However, until recently it was believed that eucrites were completely anhydrous and therefore could provide no insight into the D/H ratio of Vesta (*4*, *6*).

Here, we report the concentration and isotopic composition of structurally bound water in the mineral apatite [$Ca_5(PO_4)_3(OH,F,Cl)$] from five different basaltic eucrite samples: Juvinas, Pasamonte, Cachari, Stannern, and Pecora Escarpment (PCA) 91078 (figs. S1 and S2). We measured the D/H and water contents simultaneously in situ using a Cameca 1280 ion microprobe. The water concentration in these apatites ranges from 668 to 2624 μg/g, which agrees with calculated water contents from electron probe measurements (table S1) (*4*, *20*). We measured δD values ranging from −231 per mil (‰) to −37‰ (Table 1) (*21*). No systematic variation in D/H exists between samples or between different apatite grains in the same meteorite (Fig. 1). The weighted mean hydrogen isotopic composition for eucritic apatite from the five different investigated samples is δD = −162 ± 127‰ (2σ; n = 11).

There are three processes that could have modified the hydrogen isotopic composition of the apatite we analyzed from that of the parental magma: (i) hydrous degassing before or during apatite crystallization, (ii) equilibrium stable isotope fractionation between hydrous phases and melt, and (iii) contamination or assimilation of exogenous H or D, presumably from the regolith of Vesta. Degassing is unlikely due to the small observed spread in δD with the relatively large spread of water contents of the analyzed apatite (*22*, *23*). Apatite is the only hydrous mineral phase in eucrites, and stable isotope fractionation between apatite and melt is expected to be small (~20‰) at high temperature; thus, apatite-melt fractionation should be minor relative to the variation in δD observed (*24*). Contamination by exogenic H from solar wind and/or by D produced during spallation processes is unlikely, because apatites have young exposure ages, high water contents, and a small range of δD across

Table 1. Hydrogen isotope and water analyses of apatite and epoxy.

Sample	δD (‰) ± 2σ	H_2O (μg/g) ± 2σ
PCA 91078 ap1	−141 ± 40	804 ± 60
PCA 91078 ap2	−109 ± 53	668 ± 52
Pasamonte ap1	−53 ± 29	2207 ± 153
Pasamonte ap2	−216 ± 25	1630 ± 584
Pasamonte ap3	−200 ± 34	1545 ± 295
Juvinas ap1	−223 ± 21	1781 ± 152
Juvinas ap2	−179 ± 29	1594 ± 107
Stannern ap1	−107 ± 38	2624 ± 182
Stannern ap2	−37 ± 68	2390 ± 157
Stannern ap3	−75 ± 36	1595 ± 107
Cachari ap1	−158 ± 24	932 ± 62
PCA 91078 epoxy	−174 ± 9	140,000 ± 9000
Weighted mean apatite	−162 ± 127	1748 ± 1689

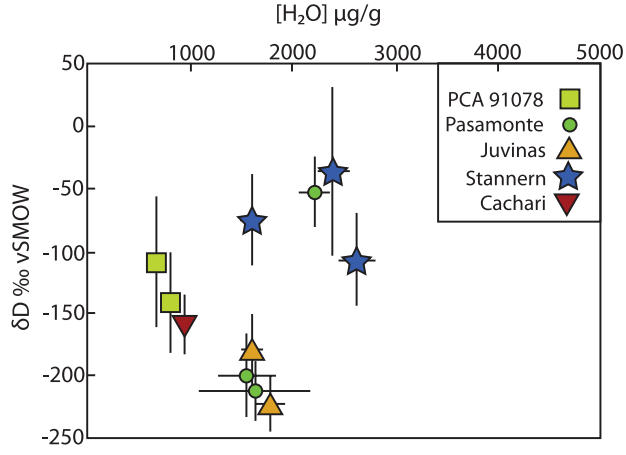

Fig. 1. Hydrogen isotopes versus water content of eucrite apatites. Note the large variation in water content that contrasts with a small range in the hydrogen isotopic compositions. Error bars are 2σ; where error bars are not present, they are smaller than the symbol.

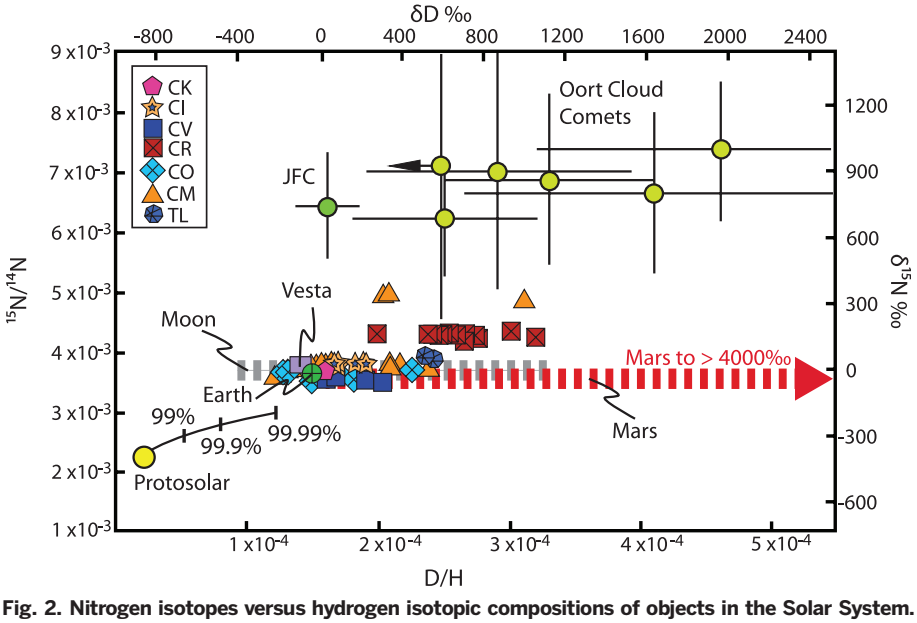

Fig. 2. Nitrogen isotopes versus hydrogen isotopic compositions of objects in the Solar System. Note that the fields for the Moon and Mars are large; these represent all D/H data because of a lack of consensus about the hydrogen isotopic compositions for the bulk Moon and Mars. For carbonaceous chondrites, ice in equilibrium with bulk clays has δD values of ~ −400‰ to 100‰ (*12*). Early carbonaceous chondrite ice could be another source of water for the inner solar system. The degassing model line originating at protosolar values does not intersect Vesta, Earth, or the Moon. See (*20*) for details and data. [Figure modified from (*3*, *28*)]

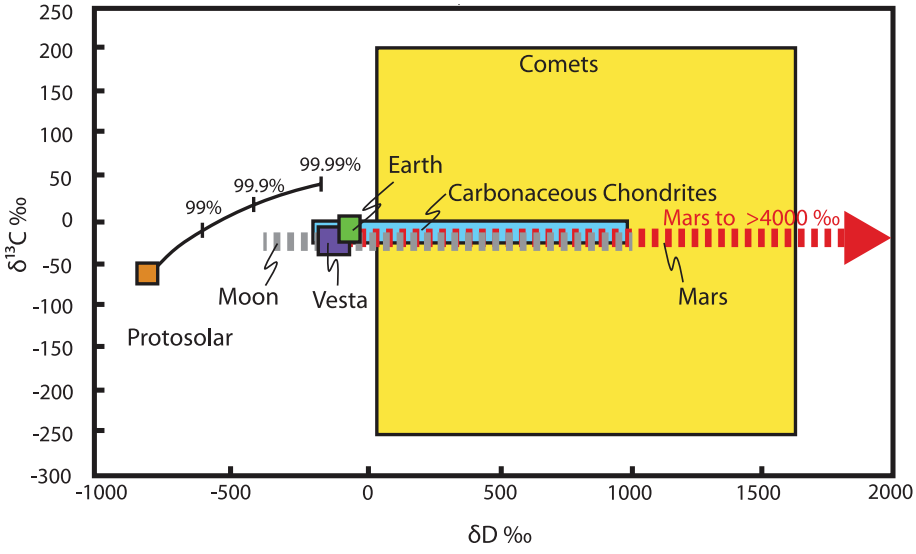

Fig. 3. Carbon versus hydrogen isotopes. Note that Earth, the Moon, and Vesta plot within the carbonaceous chondrite field. Because carbon isotopes vary from −250‰ to 200‰ in comets, C isotopes are not useful for excluding comets as a source of C for inner solar system bodies. The degassing line originating from the protosolar point assumes minimal C isotope fractionation and maximal H fractionation. See (*20*) for details and data.

exposure ages and metamorphic grades (*20*). We conclude that none of these processes have substantially affected the H isotopic compositions measured in the present study (*20*).

On the basis of the weighted mean δD of the apatites we analyzed, the δD value of eucrite magmatic water is −162‰, which is the value we adopt for bulk Vesta (*20*). This value is within the combined uncertainties of the value for the bulk Earth (~ −90‰) (*22*) and possibly the Moon (~ +90‰; Fig. 2) (*3*, *23*). The fact that Earth and Vesta have indistinguishable δD values suggests that they have the same source of water. Our new D/H data, in combination with published bulk nitrogen (N) isotope data for eucrites, shows that the most likely common source of volatiles for Earth and eucrites (Vesta) is carbonaceous chondrites (*13*, *25*). Note that N isotopes exclude the Jupiter family comets as a potential source of water for Earth and Vesta. Nitrogen isotopes also exclude Oort cloud comets as a source of water for the inner solar system planetary bodies as well. Kinetic isotope fractionation during both accretion and magmatic processes would not allow the H and N isotope systems as currently measured on Earth and Vesta to have evolved from the material implied by the signature of the Jupiter family comets or of the Oort cloud comets (Fig. 2). Although we propose that carbonaceous chondrites provided water for the inner solar system, there is evidence to show that at least Earth accreted from a heterogeneous mixture of hydrous and anhydrous materials, which rules out carbonaceous chondrites as the only terrestrial building blocks (*8*).

The hypothesis that inner solar system water came from a carbonaceous chondrite source is further supported by bulk carbon (C) isotope data. The C isotopic compositions of Earth and Vesta are very similar and overlap with that of carbonaceous chondrites but not with the solar composition (Fig. 3). Thus, the isotopic compositions of three different volatile elements as well as their concentration ratios for Earth and Vesta are consistent with the composition of carbonaceous chondrites.

Earth and Vesta have indistinguishable H, C, and N isotopic compositions, and thus likely have the same volatile source. This source must have had an H isotopic composition similar to or lower than the values measured in our samples, because possible magmatic fractionation processes could only lead to a relative enrichment and not a depletion in deuterium (*20*). One important reservoir that has low D/H and low $^{15}N/^{14}N$ is the Sun (Fig. 2), which could theoretically be an alternative source of volatiles in the inner solar system, assuming that such a solar-derived reservoir would have been later altered by a secondary degassing process. Our model for degassing uses the most conservative input values, which lead to the largest isotope fractionations for N and H isotopes and reflect degassing of a 1:1 mixture of NH_4 and H_2. It is evident that degassing alone cannot realistically evolve solar H and N isotope ratios to values measured in Vesta (Fig. 2). Degrees of degassing in excess of 99.99% are required to evolve N and H isotope ratios of the Sun to ratios close to those of the inner solar system. Additionally, if this extreme degassing also involved volatile loss of C, then C isotopes would significantly disagree with a solar source of volatiles because the solar C isotopic composition would become heavier than that of Earth, the Moon, or Vesta (Fig. 3). It is highly unlikely that accretion and degassing would strongly fractionate H and N isotopes yet would allow C isotopes on Vesta to remain isotopically light. Consequently, we rule out a solar source of volatiles for the bodies in the inner solar system.

The H, C, and N isotopic similarities between eucrites, Earth, and potentially the Moon allow us to place important limits on the timing of water delivery to the inner solar system. Earth cannot provide timing of water delivery because it is currently geologically active. The Moon likely accreted its water at or before ~200 million years after CAIs, or around 4367 Ma (*3*, *23*), but such a constraint is not very rigorous, given that all the planets in the inner solar system are thought to have fully accreted by this time. Eucrites provide a substantially earlier data point, which suggests that the source of Earth's water was present in the inner solar system very early, ~8 to 20 million years after CAIs (*15*, *16*). This evidence moves back the time at which the terrestrial water reservoir is thought to exist and have been available for accretion. Additionally, this reservoir was present between 1 and 2.4 AU and perhaps throughout the inner solar system. Late-stage addition of water to planets from outer parts of the solar system is therefore unlikely to have affected the water budgets of inner solar system bodies. Thus, the bulk of the highly volatile elements H, C, and N now present in Earth and the asteroid belt most likely arrived from a local source (i.e., carbonaceous chondrite–like material) very early in solar system history. The limited variation in δD over a large range of heliocentric distances (1 to 2.4 AU) supports the notion of a uniform source of water in the inner solar system. Our findings cannot preclude a late addition of water for Earth with a carbonaceous chondrite–like D/H, but the observation indicates that a late addition of water is not necessary.

Our geochemical results are in agreement with several dynamic solar system models for planetary water delivery. These models indicate that carbonaceous chondritic planetesimals delivered water during primary accretion of Earth (*9*, *26*, *27*). In addition, it is believed that Earth's water condensed in the outer asteroid belt and giant planet regions and was then transported to Earth by dynamical processes related to giant planet migration (*27*). The implications are that (i) the migration of water in the inner solar system must have started by 8 to 20 million years after CAIs, or (ii) water was always present in the inner solar system, in which case no water migration is needed to satisfy the H isotopic composition of terrestrial planets (*10*).

REFERENCES AND NOTES

1. I. Campbell, S. Taylor, *Geophys. Res. Lett.* **10**, 1061–1064 (1983).
2. M. H. Carr, J. W. Head III, *Earth Planet. Sci. Lett.* **294**, 185–203 (2010).
3. A. E. Saal, E. H. Hauri, J. A. Van Orman, M. J. Rutherford, *Science* **340**, 1317–1320 (2013).
4. A. R. Sarafian, M. F. Roden, A. E. Patiño Douce, *Meteorit. Planet. Sci.* **48**, 2135–2154 (2013).
5. F. Albarède, *Nature* **461**, 1227–1233 (2009).
6. J. J. Papike, *Rev. Mineral.* **43**, 7-01–7-10 (1998).
7. P. Lucey *et al.*, *Rev. Mineral. Geochem.* **60**, 83–219 (2006).
8. M. Schönbächler, R. W. Carlson, M. F. Horan, T. D. Mock, E. H. Hauri, *Science* **328**, 884–887 (2010).
9. A. Morbidelli, J. I. Lunine, D. P. Obrien, S. N. Raymond, K. J. Walsh, *Annu. Rev. Earth Planet. Sci.* **40**, 251–275 (2012).

10. H. King *et al.*, *Earth Planet. Sci. Lett.* **300**, 11–18 (2010).
11. F. Robert, D. Gautier, B. Dubrulle, *Space Sci. Rev.* **92**, 201–224 (2000).
12. C. M. Alexander *et al.*, *Science* **337**, 721–723 (2012).
13. F. Robert, *Science* **293**, 1056–1058 (2001).
14. L. Hallis, G. Taylor, K. Nagashima, G. Huss, *Earth Planet. Sci. Lett.* **359–360**, 84–92 (2012).
15. Q. Zhou *et al.*, *Geochim. Cosmochim. Acta* **110**, 152–175 (2013).
16. K. Misawa, A. Yamaguchi, K. Hiroshi, *Geochim. Cosmochim. Acta* **69**, 5847–5861 (2005).
17. R. N. Clayton, N. Onuma, T. K. Mayeda, *Earth Planet. Sci. Lett.* **30**, 10–18 (1976).
18. T. B. McCord, J. B. Adams, T. V. Johnson, *Science* **168**, 1445–1447 (1970).
19. H. Y. McSween Jr., D. W. Mittlefehldt, A. W. Beck, R. G. Mayne, T. J. McCoy, in *The Dawn Mission to Minor Planets 4 Vesta and 1 Ceres* (Springer, New York, 2012), pp. 141–174.
20. See supplementary materials on *Science* Online.
21. $\delta D = \{[(D/H_{unknown})/(D/H_{VSMOW})] - 1\} \times 1000$, where VSMOW = Vienna standard mean ocean water.
22. Z. D. Sharp, F. M. McCubbin, C. K. Shearer, *Earth Planet. Sci. Lett.* **380**, 88–97 (2013).
23. R. Tartèse *et al.*, *Geology* **42**, 363–366 (2014).
24. T. Chacko, D. R. Cole, J. Horita, *Rev. Mineral. Geochem.* **43**, 1–81 (2001).
25. Y. Miura, N. Sugiura, *Antarctic Meteor. Res.* **6**, 338 (1993).
26. A. Morbidelli *et al.*, *Meteorit. Planet. Sci.* **35**, 1309–1320 (2000).
27. D. P. O'Brien, K. J. Walsh, A. Morbidelli, S. N. Raymond, A. M. Mandell, *Icarus* **239**, 74–84 (2014).

ACKNOWLEDGMENTS

We thank the anonymous reviewers; K. Righter, D. Ebel, C. Agee, and T. McCoy for sample allocations; and N. Shimizu and G. Gaetani for their immense help. Supported by NASA graduate fellowship NNX13AR90H (A.R.S.), an Andrew W. Mellon Foundation Award for Innovative Research (S.G.N.), and NASA Cosmochemistry Program award NNX11AG76G (F.M.M.). Secondary ion mass spectrometry analyses were made at the Northeast National Ion Microprobe Facility (NENIMF) at the Woods Hole Oceanographic Institution (WHOI). NENIMF acknowledges support from the NSF Instrumentation and Facilities Program, Division of Earth Sciences, and from WHOI. Data are presented in the main text of the manuscript and the supplementary materials.

SUPPLEMENTARY MATERIALS

www.sciencemag.org/content/346/6209/623/suppl/DC1
Materials and Methods
Supplementary Text
Figs. S1 and S2
Table S1
References (*28*–*81*)

30 May 2014; accepted 29 September 2014
10.1126/science.1256717

NEURODEVELOPMENT

Dendrite morphogenesis depends on relative levels of NT-3/TrkC signaling

William Joo,[1,2] Simon Hippenmeyer,[1]* Liqun Luo[1,2]†

Neurotrophins regulate diverse aspects of neuronal development and plasticity, but their precise in vivo functions during neural circuit assembly in the central brain remain unclear. We show that the neurotrophin receptor tropomyosin-related kinase C (TrkC) is required for dendritic growth and branching of mouse cerebellar Purkinje cells. Sparse TrkC knockout reduced dendrite complexity, but global Purkinje cell knockout had no effect. Removal of the TrkC ligand neurotrophin-3 (NT-3) from cerebellar granule cells, which provide major afferent input to developing Purkinje cell dendrites, rescued the dendrite defects caused by sparse TrkC disruption in Purkinje cells. Our data demonstrate that NT-3 from presynaptic neurons (granule cells) is required for TrkC-dependent competitive dendrite morphogenesis in postsynaptic neurons (Purkinje cells)—a previously unknown mechanism of neural circuit development.

Neurotrophins regulate the survival, differentiation, and plasticity of peripheral and central neurons (*1*–*3*). The mammalian neurotrophin family signals through three tropomyosin-related kinase (Trk) receptors, as well as the p75 neurotrophin receptor (p75NTR). Whereas brain-derived neurotrophic factor (BDNF) has been intensely studied, much less is known about neurotrophin-3 (NT-3) and its receptor, TrkC, despite their widespread expression in the developing and adult brain (*4*, *5*). The lack of central brain cell death in mice lacking NT-3 and TrkC contrasts starkly with the severe reductions in sensory and sympathetic neurons and suggests survival-independent functions (*6*, *7*). NT-3 functions in dendrite morphogenesis in brain slice culture and in proprioceptive axon patterning (*8*–*10*). However, evaluating the roles of NT-3/TrkC signaling in the central brain in vivo has been hindered by the early postnatal lethality of NT-3 or TrkC knockout mice and the limited cellular resolution of phenotypic analyses (*7*, *11*).

To study the cell-autonomous function of TrkC in mouse neural development, we used mosaic analysis with double markers (MADM) (*12*, *13*) with a null allele of *trkC* that removes all isoforms of the receptor (*14*), and a pan-neural *Nestin-Cre* line (*15*) to drive recombination throughout the brain. Thus, in an otherwise heterozygous animal ($trkC^{+/-}$), Cre/*loxP*-mediated mitotic recombination between homologous chromosomes sparsely labels wild-type ($trkC^{+/+}$) and homozygous mutant ($trkC^{-/-}$) cells in distinct colors (figs. S1A and S2). In these animals, sparse $trkC^{-/-}$ cells were labeled with green fluorescent protein (GFP) (green), $trkC^{+/+}$ cells with tdTomato (red), and $trkC^{+/-}$ cells with both GFP and tdTomato (yellow). Cells without recombination, which remained colorless, were all $trkC^{+/-}$. Although survival of central brain cells was not apparently affected by sparse *trkC* removal (figs. S2 and S3A), consistent with previous observations (*6*, *7*), we observed a distinctive Purkinje cell dendrite phenotype (Fig. 1).

Both $trkC^{+/+}$ and $trkC^{+/-}$ Purkinje cells extended complex dendritic arbors that spanned the entire molecular layer of the cerebellum (Fig. 1A, left and middle). In contrast, arbors from $trkC^{-/-}$ cells failed to reach the pial surface (65 out of 72 cells; Fig. 1A, right). These stunted arbors exhibited normal dendritic spine density (fig. S3B), but spanned only ~75% of the molecular layer (Fig. 1B). To determine when the $trkC^{-/-}$ dendrite phenotype emerges, we compared $trkC^{+/+}$ and $trkC^{-/-}$ cells between postnatal day 7 (P7) and P21, when Purkinje cells normally elaborate their dendrites and begin to form synapses (Fig. 1C and fig. S4). Although indistinguishable from control cells at P7 and P10, $trkC^{-/-}$ cells exhibited reduced dendritic arbor height, branch number, and total dendrite length compared to $trkC^{+/+}$ cells by day 14 (Fig. 1, C and D, and fig. S4). Growth and branching phenotypes persisted in 3-month-old animals (Fig. 1, C and D, and fig. S4), indicating that loss of TrkC caused a morphogenesis defect rather than a developmental delay. Furthermore, the most distal dendritic branches were preferentially lost in $trkC^{-/-}$ cells (fig. S3C). Uniparental disomies (*13*) (fig. S5) and fluorescent markers (fig. S6) did not affect Purkinje cell dendrite phenotypes. Thus, our mosaic analysis suggested that TrkC is required cell-autonomously for proper Purkinje cell dendrite growth and branching.

Although Trk signaling normally requires the tyrosine kinase domain (*16*), TrkC also has a kinase-independent role in synaptogenesis (*17*). To determine whether dendritic arborization relies on kinase activity, we examined MADM mice harboring a conditional allele in which *loxP* sites flank an exon encoding part of the TrkC kinase domain (*18*). Here, *Nestin-Cre* mediated interchromosomal recombination within the MADM cassettes, and also excised this exon to generate a "kinase-dead" allele ($trkC^{KD}$; fig. S1B). At P21, Purkinje cells homozygous for this allele ($trkC^{KD/KD}$) exhibited dendrite height, branch number, and total dendritic length phenotypes

[1]Howard Hughes Medical Institute and Department of Biology, Stanford University, Stanford, CA 94305, USA. [2]Neurosciences Program, Stanford University, Stanford, CA 94305, USA.
*Present address: Institute of Science and Technology Austria, 3400 Klosterneuburg, Austria. **†Corresponding author. E-mail: lluo@stanford.edu**

comparable to those of *trkC*$^{-/-}$ cells (Fig. 2). Thus, proper dendritic arborization requires TrkC kinase activity.

Because perturbing TrkC in a sparse population (0.5 to 1%) of Purkinje cells disrupted their dendritic arbors, we examined how TrkC ablation from all Purkinje cells affects dendrite morphology. Calbindin immunostaining labels Purkinje cells and their dendrites, which normally span the entire molecular layer of the cerebellum (Fig. 3A). *trkC* conditional knockout using Purkinje cell–specific *pcp2-Cre* (*19*) (fig. S1C) did not reduce Purkinje cell dendrite height compared to controls (Fig. 3, A and B). To analyze dendrite branching in more detail, we used MADM cassettes to sparsely label Purkinje cells in the Purkinje cell–specific *trkC* conditional knockout background. In this context, *pcp2-Cre* removed *trkC* from all Purkinje cells, but GFP and tdTomato were reconstituted only in a sparse subset (5 to 10%) of Purkinje cells through interchromosomal recombination

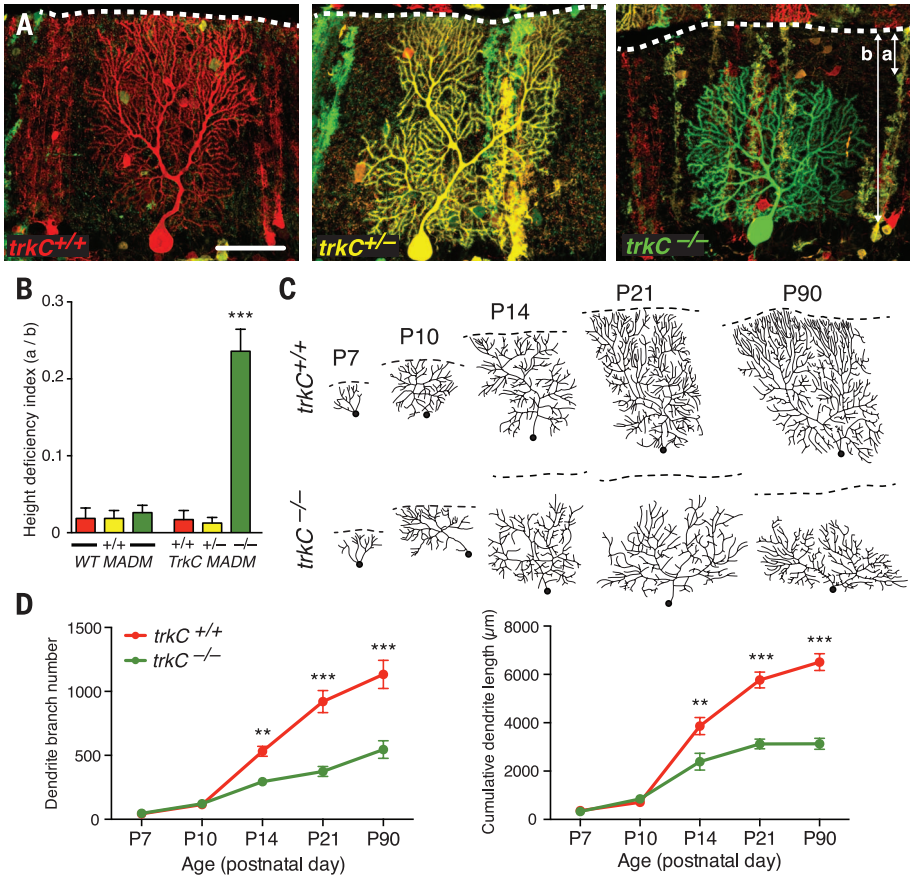

Fig. 1. TrkC is cell-autonomously required for Purkine cell dendritic arborization. (**A**) Postnatal day 21 (P21) red *trkC*$^{+/+}$ and yellow *trkC*$^{+/-}$ Purkinje cell dendritic arbors span the entire molecular layer of the cerebellar cortex. In contrast, *trkC*$^{-/-}$ Purkinje cell dendritic arbors are shorter and fail to reach the pial surface (dashed white lines). Short (a) and long (b) arrows indicate distance from pial surface to top of arbor and molecular layer span, respectively. Scale bar, 50 μm. (**B**) Quantifications of height deficiency index (*a*/*b*) for *WT MADM* and *trkC MADM*. Here and in subsequent figures, all values are means ± SEM. *** $P < 0.001$, one-way analysis of variance (ANOVA) with Tukey's multiple comparisons test. (**C**) Traces of Purkinje cell dendritic arbors between P7 and P90. Dashed lines indicate the external granule layer margin in P7–P10, or the pial surface in P14–90. Dots indicate primary branch start point. (**D**) Quantification of dendrite branch number (left) and cumulative dendrite length (right). Red, *trkC*$^{+/+}$; green, *trkC*$^{-/-}$. ** $P < 0.01$, *** $P < 0.001$, two-way ANOVA with Bonferroni's multiple comparisons test. See table S1 for additional information including *N* for each experiment.

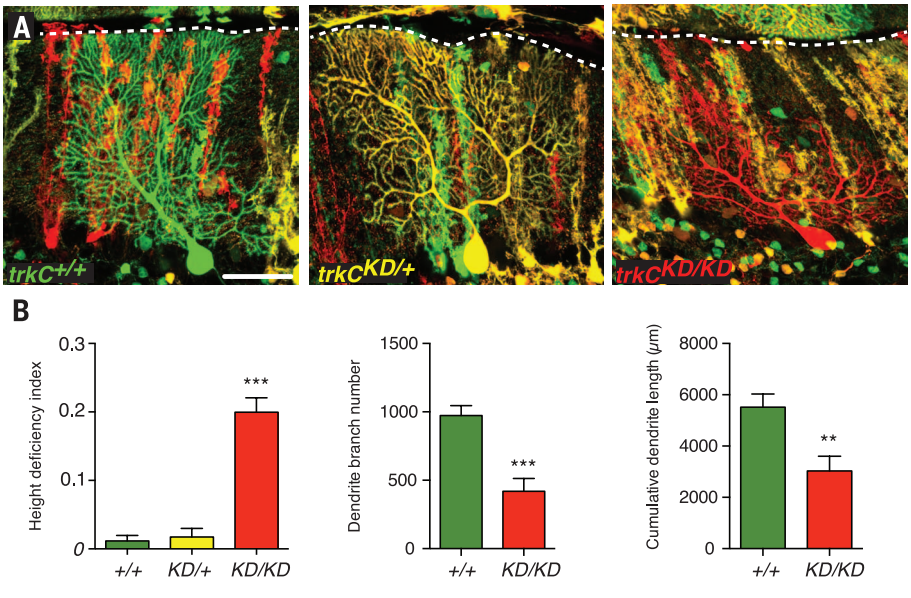

Fig. 2. Dendritic arborization requires TrkC kinase activity. (**A**) Analogous to *trkC*$^{-/-}$ arbors (Fig. 1), *trkC*$^{KD/KD}$ arbors are shorter than those of *trkC*$^{+/+}$ and *trkC*$^{KD/+}$ cells at P21 and fail to reach the pial surface. (**B**) Quantifications of height deficiency index (*** $P < 0.001$, one-way ANOVA with Tukey's multiple comparisons test), branch number, and cumulative dendrite length (** $P < 0.01$, *** $P < 0.001$, unpaired *t* test) as in Fig. 1. Also see table S1.

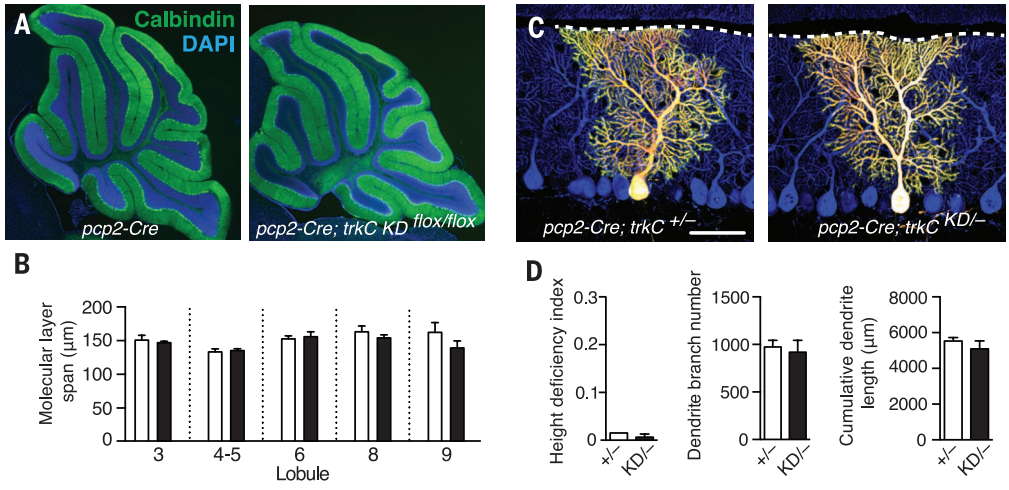

Fig. 3. Normal dendrite morphogenesis when all Purkinje cells lack TrkC. (**A**) Calbindin staining labels Purkinje cells and their dendrites (green). Removing *trkC* from all Purkinje cells (right) does not cause global reductions in dendrite height relative to controls (left) at P21. (**B**) Molecular-layer thickness across multiple lobules was similar for control *pcp2-Cre*$^{+/-}$ (white) and *pcp2-Cre*$^{+/-}$*;trkC KD*$^{flox/flox}$ (black) mice. No significant differences, two-way ANOVA with Tukey's multiple comparisons test. (**C**) *trkC*$^{KD/-}$ Purkinje cells do not exhibit dendrite height or branching defects relative to *trkC*$^{+/-}$ cells. (**D**) Quantifications of height deficiency index, branch number, and cumulative length as in Fig. 1 (no significant differences, unpaired *t* test). Also see table S1. DAPI, 4´,6-diamidino-2-phenylindole

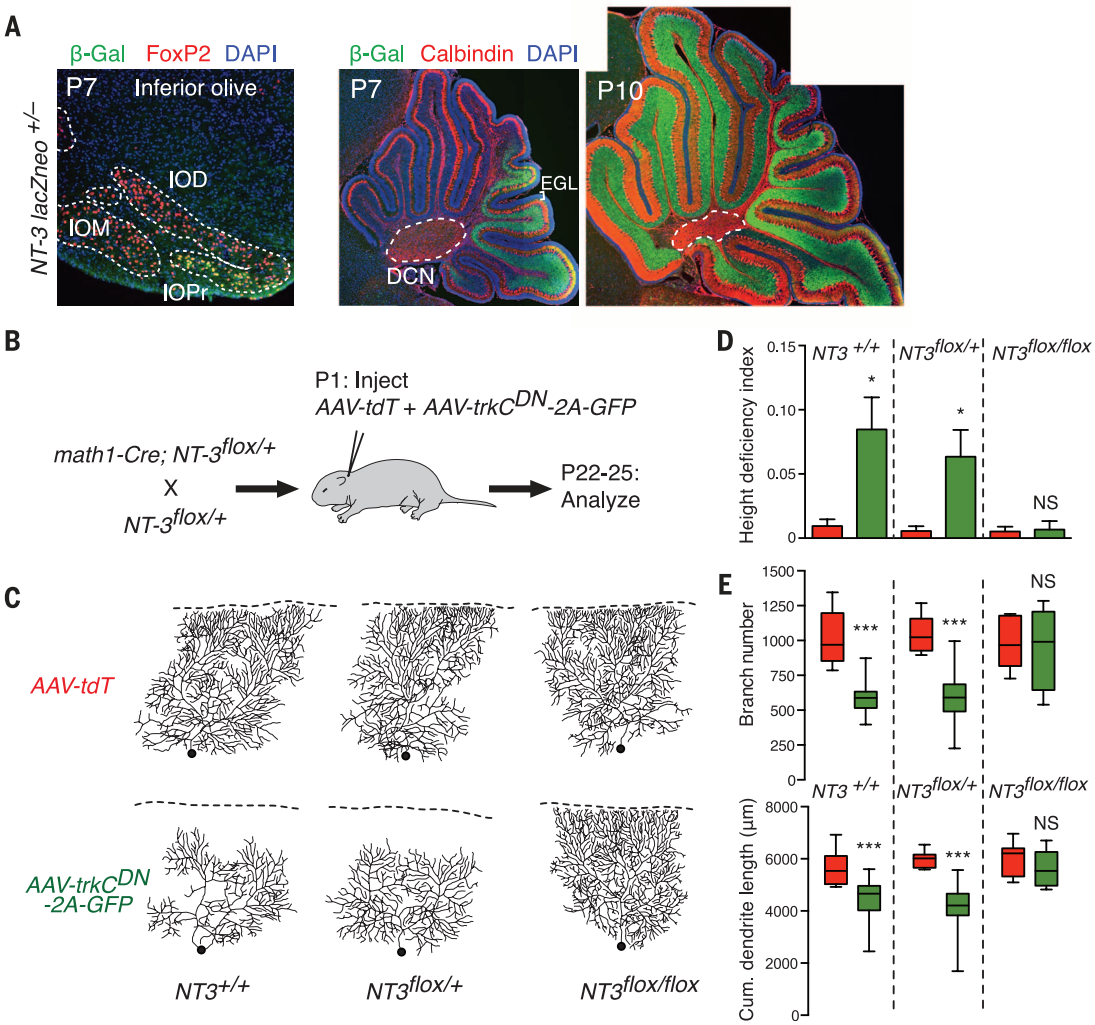

Fig. 4. Testing NT-3/TrkC-dependent competition. (**A**) β-Gal staining reports NT-3 expression patterns in a *NT-3*$^{lacZneo/+}$ knock-in mouse (green). Left: coronal section of the mouse medulla at P7. FoxP2 staining labels inferior olive neurons (red). β-Gal is present in a subset of neurons in the inferior olive principal nucleus (IOPr), but not in the medial or dorsal nuclei (IOM, IOD). Middle and right: At P7, β-Gal is enriched in granule cells of posterior folia. By P10, β-Gal is present in all folia. No signal was detectable in the external granular layer (EGL, bracket), which contains granule cell progenitors. Likewise, no signal was detectable in Purkinje cells or the deep cerebellar nuclei (DCN, dashed line), the postsynaptic targets of Purkinje cells. (**B**) Schematic of a viral approach to test relative NT-3/TrkC signaling in dendrite morphogenesis. Viruses encoding either tdTomato (*AAV-tdT*) or a dominant-negative TrkC together with GFP (*AAV-trkC*^{DN}*-2A-GFP*) were coinjected into *math1-Cre;NT-3*$^{flox/flox}$, *math1-Cre;NT-3*$^{flox/+}$, or control *math1-Cre* mice at P1. tdT or GFP/TrkC^{DN}-expressing Purkinje cells were analyzed 21 to 24 days after injection. (**C**) Dendritic arbors of tdT or GFP/TrkC^{DN}-expressing Purkinje cells. In *math1-Cre;NT-3*$^{+/+}$ or *math1-Cre;NT-3*$^{flox/+}$ mice, TrkC^{DN}-expressing cells exhibited decreased arbor complexity much like that of MADM *trkC*$^{-/-}$ cells (Fig. 1). However, in *math1-Cre;NT-3*$^{flox/flox}$ animals, dendrite defects were rescued to wild-type levels. (**D**) Quantification of height deficiency index. *$P < 0.05$, one-way ANOVA with Tukey's multiple comparisons test. (**E**) Quantification of tdT and GFP/TrkC^{DN} dendritic branch number (top) and cumulative length (bottom). Boxes indicate the mean (middle line) and 25 to 75% range, while whiskers indicate maximum and minimum values. ***$P < 0.001$, two-way ANOVA with Sidak's multiple comparisons test. Also see table S1.

(fig. S1D). Such individually labeled *trkC*$^{KD/-}$ Purkinje cells exhibited normal dendrite height, branching, and length (Fig. 3, C and D). Thus, in contrast to sparse MADM-based knockout of TrkC, TrkC ablation from all Purkinje cells did not disrupt dendritic arborization.

Differences in the timing of *trkC* removal are unlikely to account for the distinct outcomes of global and sparse knockout (Figs. 1 to 3). *pcp2-Cre* mediated recombination in nearly all Purkinje cells by P7 and markedly reduced *trkC* mRNA levels in Purkinje cells by P10 (fig. S7), well before dendrite phenotypes emerge at P14. A more likely interpretation is that the observed dendrite defects depend on the sparseness of *trkC* deletion. This raised the possibility of a competitive mechanism (*20*), in which dendrite morphogenesis depends on relative differences in TrkC signaling between neighboring Purkinje cells.

We next investigated the expression pattern of NT-3, the ligand for TrkC (*16*), using a *lacZ* knock-in reporter in the *NT-3* locus (*21*). The *lacZ* product β-galactosidase (β-Gal) was transiently expressed at P7 (but not at P14) in a small subset of inferior olive neurons, which extend climbing fibers to Purkinje cell dendrites (Fig. 4A, left). β-Gal was also expressed in cerebellar granule cells, which send parallel fibers to provide major inputs to Purkinje cell dendrites, but was undetectable in the external granular layer, which contains granule cell progenitors (Fig. 4A, middle and right). This suggests that postmitotic granule cells express NT-3 after migrating to the internal granular layer. Although restricted to granule cells in posterior folia at P7 (Fig. 4A, middle), β-Gal was expressed in all folia by P10 (Fig. 4A, right), coinciding with the time window of TrkC-dependent dendritic development (Fig. 1, C and D). Purkinje cell dendrite morphogenesis likely relies on NT-3 produced around or after P10, as dendrite phenotypes of sparse *trkC*$^{-/-}$ Purkinje cells were equally severe in anterior and posterior folia (fig. S8). Given that β-Gal was undetectable in the deep cerebellar nuclei, the postsynaptic targets of Purkinje cells (Fig. 4A), presynaptic granule cells are the best candidate cellular source of NT-3.

Conditional knockout of NT-3 from granule cell progenitors using *math1-Cre* (*22*) did not affect Purkinje cell dendrite height (fig. S9), branch number, or total length (Fig. 4, B to E). This is consistent with the absence of dendrite phenotypes in Purkinje cell–specific *trkC* knockout (Fig. 3). We next devised a method to investigate NT-3/TrkC signaling in a competitive context (Fig. 4B). Adeno-associated virus serotype 8 (AAV8) preferentially transduces Purkinje cells when injected into neonatal mice (*23*). We exploited this tropism to cotransduce two AAV vectors, the first expressing tdTomato as a control, and the second expressing a dominant-negative TrkC construct (fig. S10) together with GFP (TrkC^{DN}-2A-GFP). We achieved sparse labeling (~0.5%) by controlling the titer and volume of neonatal injections (fig. S11). In P21 mice, TrkC^{DN}-expressing GFP-positive Purkinje cells exhibited reduced dendrite height, branch number, and total length relative to control, tdTomato-expressing Purkinje cells (Fig. 4, C to E, left columns). This viral approach thus corroborated results from MADM-based sparse knockout.

To test sparse TrkC loss-of-function in the absence of NT-3, we neonatally transduced AAV viruses into conditional knockout mice in which *math1-Cre* removes NT-3 from all granule cells (Fig. 4B). In heterozygous (*NT-3*$^{flox/+}$) conditional knockout animals, TrkC^{DN}-expressing GFP-positive Purkinje cells still exhibited reduced branching number and length compared to tdTomato-positive control cells (Fig. 4, C to E, middle columns). However, in homozygous (*NT-3*$^{flox/flox}$) conditional knockout animals, the dendrite phenotypes of TrkC^{DN}-expressing cells were completely suppressed (Fig. 4, C to E, right columns). Thus, granule cell–derived NT-3 is necessary for TrkC-dependent competitive dendrite morphogenesis in Purkinje cells.

In summary, although Purkinje cell dendrite development can proceed in the absence of NT-3 or TrkC, our data indicate that relative intercellular differences in NT-3/TrkC signaling can profoundly modulate dendrite morphogenesis. Specifically, Purkinje cells with lower TrkC levels relative to their neighbors exhibit reduced dendritic arbor complexity. Future studies should elucidate how Purkinje cells compare TrkC levels, and how such intercellular comparisons contribute to normal circuit function. For example, heterogeneous TrkC activation during development may diversify Purkinje cell dendrite complexity, or homeostatically adjust dendrite branching rates to ultimately equalize Purkinje cell participation in the cerebellar circuit. Furthermore, NT-3/TrkC may cooperate with other signals to regulate dendrite development. Although p75NTR likely acts as a receptor for paracrine signals during competitive axon stabilization and pruning (*24*, *25*), we found that sparse *trkC* knockout phenotypes persisted in *p75*$^{-/-}$ mice (fig. S12), suggesting alternative mechanisms. Indeed, TrkC/NT-3 signaling may mediate competition by enhancing neuronal activity or synaptogenesis, both of which are known to modulate dendritic arborization (*26*, *27*). In one scenario, differential TrkC/NT-3 signaling may drive competitive parallel fiber synapse formation and locally stabilize Purkinje cell dendritic branches. Consistent with this idea, each parallel fiber forms synapses with only a subset of Purkinje cells along its trajectory (*28*), whereas TrkC can mediate postsynaptic differentiation (*17*) and NT-3 can be anterogradely transported and released from central neuron presynaptic terminals (*29*).

According to the classic neurotrophic theory, developing axons compete for limiting amounts of neurotrophic factors from their target tissues, which signal retrogradely to support neuronal survival and axon growth (*30*, *31*). Our findings expand this paradigm and suggest that growing dendrites analogously require anterograde NT-3 from their presynaptic partners during competitive dendrite growth.

REFERENCES AND NOTES

1. E. J. Huang, L. F. Reichardt, *Annu. Rev. Neurosci.* **24**, 677–736 (2001).
2. H. Park, M. M. Poo, *Nat. Rev. Neurosci.* **14**, 7–23 (2013).
3. V. Nikoletopoulou *et al.*, *Nature* **467**, 59–63 (2010).
4. P. C. Maisonpierre *et al.*, *Neuron* **5**, 501–509 (1990).
5. L. Tessarollo *et al.*, *Development* **118**, 463–475 (1993).
6. L. Minichiello, R. Klein, *Genes Dev.* **10**, 2849–2858 (1996).
7. I. Silos-Santiago, A. M. Fagan, M. Garber, B. Fritzsch, M. Barbacid, *Eur. J. Neurosci.* **9**, 2045–2056 (1997).
8. A. K. McAllister, D. C. Lo, L. C. Katz, *Neuron* **15**, 791–803 (1995).
9. A. K. McAllister, L. C. Katz, D. C. Lo, *Neuron* **18**, 767–778 (1997).
10. T. D. Patel *et al.*, *Neuron* **38**, 403–416 (2003).
11. P. Ernfors, K. F. Lee, J. Kucera, R. Jaenisch, *Cell* **77**, 503–512 (1994).
12. H. Zong, J. S. Espinosa, H. H. Su, M. D. Muzumdar, L. Luo, *Cell* **121**, 479–492 (2005).
13. S. Hippenmeyer, R. L. Johnson, L. Luo, *Cell Reports* **3**, 960–967 (2013).
14. L. Tessarollo *et al.*, *Proc. Natl. Acad. Sci. U.S.A.* **94**, 14776–14781 (1997).
15. P. H. Petersen, K. Zou, J. K. Hwang, Y. N. Jan, W. Zhong, *Nature* **419**, 929–934 (2002).
16. E. J. Huang, L. F. Reichardt, *Annu. Rev. Biochem.* **72**, 609–642 (2003).
17. H. Takahashi *et al.*, *Neuron* **69**, 287–303 (2011).
18. X. Chen *et al.*, *Neuron* **46**, 13–21 (2005).
19. X. M. Zhang *et al.*, *Genesis* **40**, 45–51 (2004).
20. C. N. English, A. J. Vigers, K. R. Jones, *Proc. Natl. Acad. Sci. U.S.A.* **109**, 19456–19461 (2012).
21. I. Fariñas, K. R. Jones, C. Backus, X. Y. Wang, L. F. Reichardt, *Nature* **369**, 658–661 (1994).
22. V. Matei *et al.*, *Dev. Dyn.* **234**, 633–650 (2005).
23. D. A. Gibson *et al.*, *Neuron* **81**, 1040–1056 (2014).
24. L. Cao *et al.*, *Curr. Biol.* **17**, 911–921 (2007).
25. K. K. Singh *et al.*, *Nat. Neurosci.* **11**, 649–658 (2008).
26. C. M. Niell, M. P. Meyer, S. J. Smith, *Nat. Neurosci.* **7**, 254–260 (2004).
27. H. Cline, K. Haas, *J. Physiol.* **586**, 1509–1517 (2008).
28. L. Li *et al.*, *PLOS ONE* **5**, e11503 (2010).
29. C. A. Altar, P. S. DiStefano, *Trends Neurosci.* **21**, 433–437 (1998).
30. R. Levi-Montalcini, *Science* **237**, 1154–1162 (1987).
31. L. S. Zweifel, R. Kuruvilla, D. D. Ginty, *Nat. Rev. Neurosci.* **6**, 615–625 (2005).

ACKNOWLEDGMENTS

We thank D. Ginty, L. Tessarollo, and D. Rowitch for mouse lines; the Stanford Gene Vector and Virus Core for AAV production; P. Mehlen and S. Tauszig-Delamasure for advice on cell culture experiments; B. Weissbourd for assistance with in situ hybridization; and T. Clandinin and members of the Luo Lab for helpful discussions and comments on the manuscript. W.J. was supported by the Stanford Neurosciences Graduate Program, the Lorraine Kendall Predoctoral Fellowship Fund, and an NIH National Research Service Award Predoctoral Fellowship (5 F31 NS071697). This research was also supported by an NIH grant (R01-NS050835). L.L. is an investigator of the Howard Hughes Medical Institute. The supplementary materials contain additional data. Stanford University holds a patent on the MADM technology (U.S. Patent 7,282,621) that is described in this paper. The MADM mice are available at the Jackson Laboratory. There is no restriction on sharing all materials with nonprofit organizations. Commercial use of the mice requires a license from Stanford. Please contact Kirsten Leute at kirsten.leute@stanford.edu for more information.

SUPPLEMENTARY MATERIALS

www.sciencemag.org/content/346/6209/626/suppl/DC1
Materials and Methods
Figs. S1 to S12
Table S1
References (*32*–*41*)

21 July 2014; accepted 1 October 2014
10.1126/science.1258996

WILDLIFE DISEASE

Recent introduction of a chytrid fungus endangers Western Palearctic salamanders

A. Martel,[1]* M. Blooi,[1,2]† C. Adriaensen,[1]† P. Van Rooij,[1]† W. Beukema,[3] M. C. Fisher,[4] R. A. Farrer,[5] B. R. Schmidt,[6,7] U. Tobler,[6,7] K. Goka,[8] K. R. Lips,[9] C. Muletz,[9] K. R. Zamudio,[10] J. Bosch,[11] S. Lötters,[12] E. Wombwell,[13,14] T. W. J. Garner,[14] A. A. Cunningham,[14] A. Spitzen-van der Sluijs,[15] S. Salvidio,[16] R. Ducatelle,[1] K. Nishikawa,[17] T. T. Nguyen,[18] J. E. Kolby,[19] I. Van Bocxlaer,[20] F. Bossuyt,[20] F. Pasmans[1]

Emerging infectious diseases are reducing biodiversity on a global scale. Recently, the emergence of the chytrid fungus *Batrachochytrium salamandrivorans* resulted in rapid declines in populations of European fire salamanders. Here, we screened more than 5000 amphibians from across four continents and combined experimental assessment of pathogenicity with phylogenetic methods to estimate the threat that this infection poses to amphibian diversity. Results show that *B. salamandrivorans* is restricted to, but highly pathogenic for, salamanders and newts (Urodela). The pathogen likely originated and remained in coexistence with a clade of salamander hosts for millions of years in Asia. As a result of globalization and lack of biosecurity, it has recently been introduced into naïve European amphibian populations, where it is currently causing biodiversity loss.

Emerging infectious diseases play an important role in the ongoing sixth mass extinction (*1*). Fungi comprise a greater threat relative to other taxonomic classes of pathogens and have recently caused some of the most severe die-offs and extinctions among a wide range of organisms (*2*). The classical cause of amphibian chytridiomycosis (*Batrachochytrium dendrobatidis*) has resulted in extensive disease and declines in a wide variety of amphibian species across the three orders [i.e., frogs and toads (Anura), salamanders and newts (Urodela), and caecilians (Gymnophiona)] (*2*). Recently, a second highly pathogenic chytrid fungus (*B. salamandrivorans*) emerged as a novel form of amphibian chytridiomycosis and extirpated fire salamander populations in northern Europe (*3*, *4*) in a region where *B. dendrobatidis* is in a state of stable coexistence with the amphibian communities (*5*).

To predict the potential impact of *B. salamandrivorans* on amphibian diversity more broadly, we first estimated its host range by experimentally exposing 35 species from the three amphibian orders (10 anurans, 24 urodelans, and 1 caecilian) to controlled doses of 5000 zoospores for 24 hours (*3*) (table S1). Except for five urodelan taxa for which wild-caught specimens were used, all other experimental animals were captive bred. With the exception of four urodelan taxa, all experimental animals derived from a single source population. After exposure, animals were monitored daily for clinical signs until at least 4 weeks after exposure. Infection loads were assessed weekly using quantitative polymerase chain reaction (qPCR) on skin swabs (*6*), and histopathology was performed on all specimens that died. Our results show that colonization by *B. salamandrivorans* was limited to Urodela, whereas none of the anuran and caecilian species became infected (Fig. 1, squares). Alarmingly, 41 out of 44 of the Western Palearctic salamanders (Salamandridae and Plethodontidae) rapidly died after infection with *B. salamandrivorans*. The propensity of *B. salamandrivorans* to infect these species was confirmed by its ability to successfully invade the skin of several urodelan, but none of the anuran, species. This was demonstrated with an immunohistochemical staining of the abdominal skin of amphibians after exposure to 10,000 zoospores for 24 hours (table S1 and fig. S1).

To estimate the current range of *B. salamandrivorans* infections, we used qPCR to screen 5391 wild amphibian individuals from four continents for the presence of *B. salamandrivorans* DNA in their skin (*6*) (tables S2 and S3). In accordance with the results of the experimentally determined host range, infections were detected only in urodeles. Furthermore, the detection of *B. salamandrivorans* DNA (all sequences were 100% identical with GenBank accession number KC762295) was limited to East Asia (Thailand, Vietnam, and Japan) in the absence of obvious disease, and Europe (Netherlands and Belgium) where it is associated with severe disease outbreaks [Netherlands, 2010 (*3*, *4*), and Belgium, 2013 (Eupen, N50°37′23″; E6°05′19″) and 2014 (Robertville, N50°27′12″; E6°06′11″)]. These findings suggest long-term endemism in Asia and a recent incursion in Europe.

We used the results of our infection experiments as a proxy for classifying amphibians into four categories of response to *B. salamandrivorans*: resistant, tolerant, susceptible, and lethal (Fig. 1, squares). Although the limited number of source populations used does not allow estimation of within-species variation, responses to infection were highly consistent within a given population. Lethal responses were observed in specimens from both captive-bred (10 of 19 taxa) and wild (2 of 5 taxa) urodelans. Our infection experiments indicated three Asian salamanders (*Cynops pyrrhogaster*, *Cynops cyanurus*, and *Paramesotriton deloustali*) as potential reservoirs. Seven specimens of these species were capable of limiting clinical disease and either persisted with infection for up to at least 5 months with recurring episodes of clinical disease, or even totally cleared the infection (table S1 and fig. S2). The combined evidence of natural occurrence and experimental maintenance of *B. salamandrivorans* infections indicates that at least these three species may function as a reservoir in Asia.

To investigate whether these amphibian communities may have constituted a reservoir of infection in the past, we estimated when *B. salamandrivorans* diverged from *B. dendrobatidis* and used present-day patterns of susceptibility to reconstruct amphibian susceptibility through time. Our Bayesian estimates of divergence time with a broad prior calibration range resulted in a mean estimate of 67.3 million years ago (Ma) (fig. S3) and a 95% highest posterior density interval of 115.3 to 30.3 Ma, indicating that *B. salamandrivorans* diverged from *B. dendrobatidis* in the Late Cretaceous or early Paleogene (Fig. 1, gray bar). Maximum parsimony and maximum likelihood ancestral reconstructions (Fig. 1) of amphibian susceptibility suggest that the potential of being a reservoir evolved in the ancestors of modern Asian newts between 55 and 34 Ma in the Paleogene (Fig. 1, orange

[1]Department of Pathology, Bacteriology and Avian Diseases, Faculty of Veterinary Medicine, Ghent University, Salisburylaan 133, B-9820 Merelbeke, Belgium. [2]Centre for Research and Conservation, Royal Zoological Society of Antwerp, Koningin Astridplein 26, Antwerp, Belgium. [3]CIBIO/InBIO, Centro de Investigação em Biodiversidade e Recursos Genéticos da Universidade do Porto, Instituto de Ciências Agrárias de Vairão, Rua Padre Armando Quintas, Vairão, Portugal. [4]Department of Infectious Disease Epidemiology, Imperial College London, Norfolk Place, London W2 1PG, UK. [5]Genome Sequencing and Analysis Program, The Broad Institute of MIT and Harvard, Cambridge, MA 02142, USA. [6]Koordinationsstelle für amphibien- und reptilienschutz in der Schweiz (KARCH), Passage Maximilien-de-Meuron 6, 2000 Neuchâtel, Switzerland. [7]Institut für Evolutionsbiologie und Umweltwissenschaften, Universität Zürich. Winterthurerstrasse 190, 8057 Zürich, Switzerland. [8]Invasive Alien Species Research Team, National Institute for Environment Studies, 16-2 Onogawa, Tsukuba, Ibaraki 305-8506, Japan. [9]Department of Biology, University of Maryland, College Park, MD 20742, USA. [10]Department of Ecology and Evolutionary Biology, Cornell University, Ithaca, NY 14853, USA. [11]Museo Nacional de Ciencias Naturales, Consejo Superior de Investigaciones cientificas (CSIC), José Gutiérrez Abascal 2, 28006 Madrid, Spain. [12]Biogeography Department, Trier University, 54286 Trier, Germany. [13]Durrell Institute of Conservation and Ecology, University of Kent, Kent CT2 7NR, UK. [14]Institute of Zoology, Zoological Society of London, London NW1 4RY, UK. [15]Reptile, Amphibian and Fish Conservation the Netherlands (RAVON), Post Office Box 1413, 6501 BK Nijmegen, Netherlands. [16]Department of Earth Science, Environmental and Life (Di.S.T.A.V.), University of Genova, Corso Europa 26, I-16132 Genova, Italy. [17]Graduate School of Human and Environmental Studies, Kyoto University, Yoshida Nihonmatsu-cho, Sakyo-ku, Kyoto 606-8501, Japan. [18]Vietnam National Museum of Nature, Vietnam Academy of Science and Technology, 18 Hoang Quoc Viet, Cau Giay, Hanoi, Vietnam. [19]James Cook University, One Health Research Group, School of Public Health, Tropical Medicine and Rehabilitation Sciences, Townsville, Queensland, Australia. [20]Amphibian Evolution Lab, Biology Department, Vrije Universiteit Brussel, Pleinlaan 2, 1050 Brussels, Belgium.
***Corresponding author. E-mail: an.martel@ugent.be** †These authors contributed equally to this work.

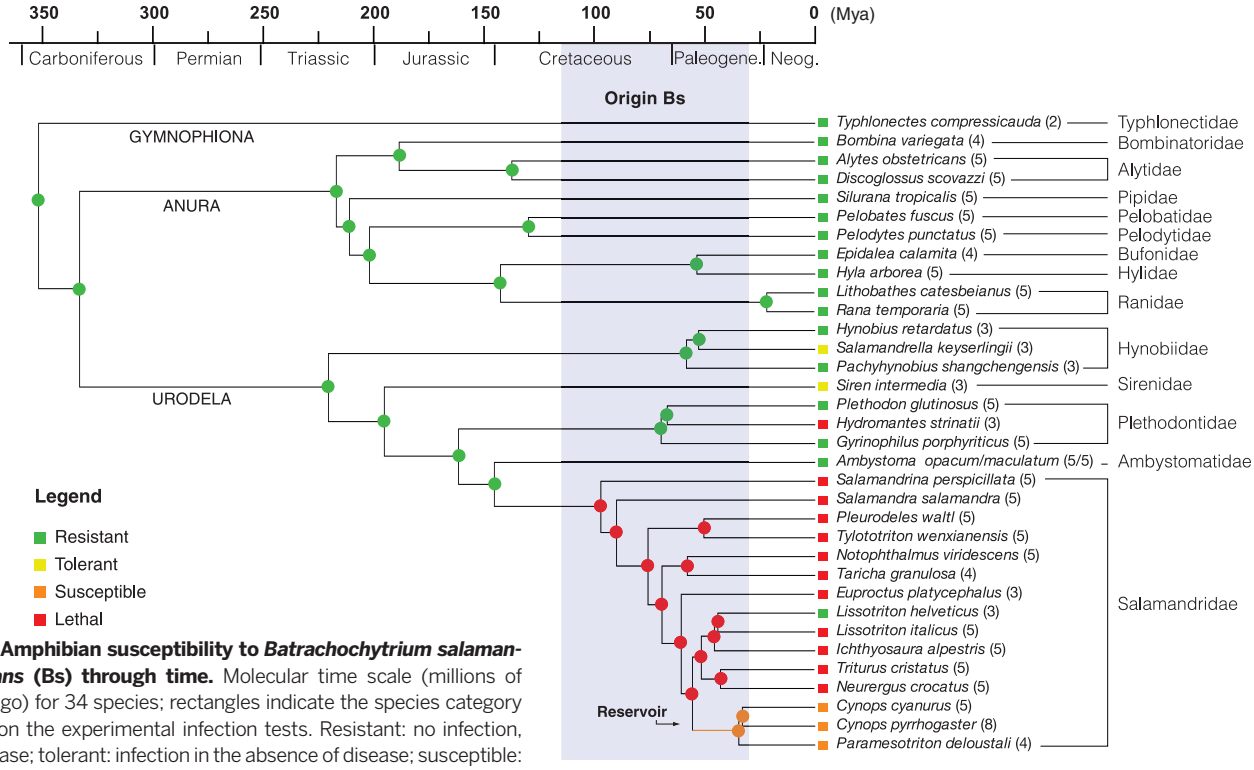

Fig. 1. Amphibian susceptibility to *Batrachochytrium salamandrivorans* (Bs) through time. Molecular time scale (millions of years ago) for 34 species; rectangles indicate the species category based on the experimental infection tests. Resistant: no infection, no disease; tolerant: infection in the absence of disease; susceptible: infection resulting in clinical disease with possibility of subsequent recovery; lethal: infection resulting in lethal disease in all infected animals. Colored dots on nodes indicate the results of the maximum likelihood ancestral reconstructions ($P > 0.95$). The clade of susceptible Asian salamanders that originated in the early Paleogene is indicated in orange. The 95% highest posterior density for time of divergence between *B. salamandrivorans* and *B. dendrobatidis* is indicated in gray.

branch), shortly after the origin of their pathogen. These ancestors reached Asia after withdrawal of the Turgai Sea (*7*), suggesting that Asia has been a natural reservoir for *B. salamandrivorans* for the past 30 million years. Our detection of *B. salamandrivorans* in a >150-year-old museum sample of the Asian newt *Cynops ensicauda* (table S4, RMNH RENA 47344) is consistent with this reservoir hypothesis.

Given the discontinuity of the global distribution of *B. salamandrivorans*, introduction from Asia into Europe must have been human-mediated. Asian salamanders and newts are being traded internationally in large numbers annually (for instance, more than 2.3 million individuals of *Cynops orientalis* were imported into the United States from 2001 to 2009) (*8*). To assess the potential of *B. salamandrivorans* spread by captive amphibians, we tested 1765 skin samples from amphibians in pet shops in Europe, London Heathrow Airport, and an exporter in Hong Kong (tables S5 and S6) and 570 samples from other captive amphibians (tables S7 and S8) for *B. salamandrivorans*. We found three positive samples from captive individuals of the Asian newt species *Tylototriton vietnamensis*, two of which were imported to Europe in 2010. Furthermore, our transmission experiments showed that *B. salamandrivorans* can effectively be transmitted across multiple urodelan species (e.g., from *Cynops pyrrhogaster* to *Salamandra salamandra*, fig. S4) by direct contact, demonstrating the potential for pathogen spillover.

Our infection experiments show that *B. salamandrivorans* is lethal to at least some of the New World salamandrid species (genera *Taricha* and *Notophthalmus*). Although these combined genera contain only seven species, together they have a widespread distribution and are often very abundant. The outcome of exposure of three lineages of plethodontids (a family comprising 66% of global urodelan diversity) to *B. salamandrivorans* ranged from a lack of any detectable infection (*Gyrinophilus*), to transient skin invasion (*Plethodon*) and lethal infection (*Hydromantes*), making it likely that other species in this large family are vulnerable.

Our study demonstrates that the process of globalization with its associated human and animal traffic can rapidly erode ancient barriers to pathogen transmission, allowing the infection of hosts that have not had the opportunity to establish resistance. Thus, pathogens, such as those we describe here, have the potential to rapidly pose a threat of extinction.

REFERENCES AND NOTES

1. D. B. Wake, V. T. Vredenburg, *Proc. Natl. Acad. Sci. U.S.A.* **105** (suppl. 1), 11466–11473 (2008).
2. M. C. Fisher *et al.*, *Nature* **484**, 186–194 (2012).
3. A. Martel *et al.*, *Proc. Natl. Acad. Sci. U.S.A.* **110**, 15325–15329 (2013).
4. A. Spitzen-van der Sluijs *et al.*, *Amphib.-reptil.* **34**, 233–239 (2013).
5. A. Spitzen-van der Sluijs *et al.*, *Conserv. Biol.* **28**, 1302–1311 (2014).
6. M. Blooi *et al.*, *J. Clin. Microbiol.* **51**, 4173–4177 (2013).
7. P. Zhang, T. J. Papenfuss, M. H. Wake, L. Qu, D. B. Wake, *Mol. Phylogenet. Evol.* **49**, 586–597 (2008).
8. A. Herrel, A. van der Meijden, *Herpetol. J.* **24**, 103–110 (2014).

ACKNOWLEDGMENTS

We thank M. Schenkel and J. Beukema for providing samples and the National Museum of Natural History–Naturalis, Leiden, Netherlands, for providing museum specimens. We thank the many amphibian breeders (including S. Bogaerts, M. Sparreboom, H. Janssen, F. Maillet, A. Jamin, and S. Voitel) who provided offspring to conduct the infection experiments. Financial support was partly provided by the Dutch Ministry of Economic Affairs and by the UK Department for Environment, Food and Rural Affairs, project grant FC1195. M.B. is funded by a Dehousse grant from the Royal Zoological Society of Antwerp. P.V.R. is funded by Ghent University Special Research Fund (BOF13/PDO/130). F.P. and T.W.J.G. are funded by the Morris Animal Foundation (D12z0-002). M.C.F. and T.W.J.G. are funded by the UK Natural Environment Research Council (NERC). R.A.F. is supported by the Wellcome Trust. U.T. and B.R.S. are funded by the Vontobel Stiftung, Janggen-Pöhn Stiftung, Basler Stiftung für biologische Forschung, Stiftung Dr. Joachim De Giacomi, Zoo Zürich, Grün Stadt Zürich, European Union of Aquarium Curators, and Zürcher Tierschutz. J.B. is funded by Fundación General CSIC and Banco Santander. E.W. is funded by Economic and Social Research Council (ESRC)-NERC Interdisciplinary Ph.D. studentship. A.A.C. is supported by a Royal Society Wolfson research merit award. K.N. is funded by grants from the Ministry of Education, Science and Culture, Japan (nos. 20770066 and 23770084) and Japan Society for the Promotion of Science (JSPS) AA Core-to-Core program Type B. Asia-Africa Science Platforms. T.T.N. is funded by the JSPS RONPAKU program. F.B. is supported by European Research Council Starting Grant 204509 [project Tracing Antimicrobial Peptides and Pheromones in the Amphibian Skin (TAPAS)]. I.V.B is supported by a postdoctoral Fellowship from the Fonds voor Wetenschappelijk Onderzoek Vlaanderen (FWO). All data described in the paper are presented in the supplementary materials.

SUPPLEMENTARY MATERIALS

www.sciencemag.org/content/346/6209/630/suppl/DC1
Materials and Methods
Figs. S1 to S5
Tables S1 to S10
References (*9*–*39*)

3 July 2014; accepted 8 September 2014
10.1126/science.1258268

BEHAVIORAL ECONOMICS

Avoiding overhead aversion in charity

Uri Gneezy,[1,2]* Elizabeth A. Keenan,[1] Ayelet Gneezy[1]

Donors tend to avoid charities that dedicate a high percentage of expenses to administrative and fundraising costs, limiting the ability of nonprofits to be effective. We propose a solution to this problem: Use donations from major philanthropists to cover overhead expenses and offer potential donors an overhead-free donation opportunity. A laboratory experiment testing this solution confirms that donations decrease when overhead increases, but only when donors pay for overhead themselves. In a field experiment with 40,000 potential donors, we compared the overhead-free solution with other common uses of initial donations. Consistent with prior research, informing donors that seed money has already been raised increases donations, as does a $1:$1 matching campaign. Our main result, however, clearly shows that informing potential donors that overhead costs are covered by an initial donation significantly increases the donation rate by 80% (or 94%) and total donations by 75% (or 89%) compared with the seed (or matching) approach.

Imagine you are the head of a charity organization and you have just secured funds from a generous private donor to help launch a new fundraising campaign. How can you use this initial donation to maximize contributions from other potential donors? Traditionally, charities have used these financial gifts to solicit additional donations in two primary ways: (i) announcing the initial donation as seed money or (ii) using it in a "matching model" in which the charity uses the initial funds to match every new dollar donated. Here we propose a third alternative: using the initial donation to cover a charity's overhead costs (i.e., administrative and fundraising costs), thereby allowing all subsequent donations to be overhead-free and to go directly to the cause.

Researchers have extensively studied the two traditional uses of initial large donations—seed money and matching grants—and found them both to be effective in increasing donor contributions (*1*). Publicly announcing seed money increases the number of people who donate and the amount they give (*2*). Furthermore, seed money that covers a greater percentage of the total campaign goal results in a significant increase in contributions compared with seed money that covers a smaller percentage of the campaign goal (*3*). Consistent with theoretical predictions regarding the potential of seed money in fundraising (*4*), this increase in contributions has been attributed to social comparison (*5*–*7*) and to "goal gradient helping," whereby the closer a fundraising campaign comes to meeting its goal, the more likely people are to donate (*8*, *9*).

A parallel line of research shows that, like seed money, announcing a matching grant can increase the fraction of people who choose to donate and the amount they give, both in the laboratory (*10*–*12*) and in the field (*13*, *14*), though the matching level ($1:$1, $2:$1, or $3:$1) does not affect giving.

Our investigation focuses on a different aspect of fundraising campaigns: how donated funds will be used. Overhead ratios, measured by the proportion of donated funds spent on nonprogrammatic costs such as administrative and fundraising costs, have emerged as an important efficiency indicator for nonprofit organizations (*15*). Charity evaluators, such as Charity Navigator and CharityWatch, assign ratings to charities based largely on their relative spending on overhead, and evidence suggests that overhead-related measures may guide donation decisions, such that higher overhead spending decreases giving. In particular, it has been shown that donors strongly prefer charities with low overhead despite cost effectiveness, in part because overhead ratios are easier to evaluate (*16*, *17*).

Moreover, an examination of actual charitable giving data reveals a negative correlation between the amount donated and the amount organizations spend on administrative and fundraising costs, suggesting that individuals are sensitive to how charities spend their funds (*18*). As a result of individuals' aversion to large overhead expenditures, charities are increasingly under pressure to spend less on overhead and more on direct program costs. Ironically, reducing overhead spending has a negative impact on charities' ability to initiate fundraising campaigns, invest in long-term planning, and sufficiently support overall infrastructure, which ultimately undermines efforts to serve their causes effectively (*19*–*21*). The pressure from donors on charities to lower fundraising and overhead costs leads to several other negative consequences, such as underreporting of fundraising and overhead costs by charities and a tendency to only fund programs with low(er) overhead costs (*22*–*24*).

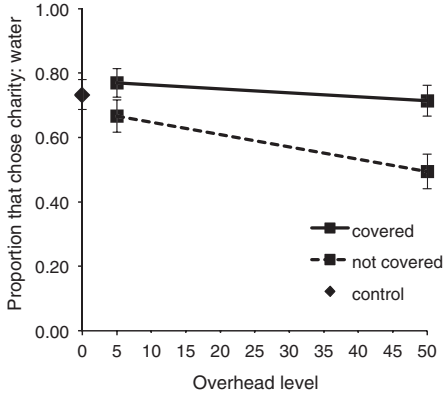

Fig. 1. Proportion of participants that chose charity: water by overhead level and by whether or not someone else covered the overhead. Error bars are ±1 SEM.

It is important to note that from a theoretical perspective, basing donation decisions on overhead is wrong. As the literature argues, donors should not care about levels of overhead costs (*25*, *26*). If donors are interested in efficiency, they should compare different funds producing the same good and select the one producing the good at acceptable quality at the lowest price. However, donors typically do not know the quality, nor the price, of the good produced. Instead, donors should look at changes in overhead costs rather than levels of costs (*25*).

In this paper, we test whether designating early large gifts to cover overhead costs increases donors' willingness to contribute to a charity. From an economic perspective, designating initial large gifts as seed money or using them to cover overhead costs is the same. Charities are interested in maximizing the total funds raised and are agnostic about whether overhead costs are covered by initial donations or are shared by all donors. Consumers, however, seem to have clear, strong preferences: They want their donations to be put to "good" use—in other words, for direct program costs.

We began our empirical investigation with a laboratory experiment that had three goals. First, we sought empirical support for our assertion above that an increase in overhead costs associated with a donation decreases giving. Existing evidence is limited, and it is important to document it in a scientific investigation. Second, we wanted to gain insight into what drives overhead aversion. Our third goal was to test our proposed solution in a controlled environment.

We recruited 449 undergraduates from a public university in southern California (35.19% female, mean age = 21.56) to complete a study for class credit in the spring of 2014. Using a between-participants design (see the supplementary materials for a detailed description of materials and methods), we randomly assigned participants

Table 1. The number of people who chose to donate by treatment and by amount donated.

Donation amount	Control	Seed	Match	Overhead
$20	297	396	373	726
$50	36	52	41	86
$100	3	27	27	43

[1]Rady School of Management, University of California San Diego, 9500 Gilman Drive, La Jolla, CA 92093, USA. [2]Center for Research in Experimental Economics and Political Decision Making (CREED), University of Amsterdam, 1018 WB, Amsterdam, Netherlands.
*Corresponding author. E-mail: ugneezy@ucsd.edu

to one of five treatments. All participants were presented with two charities: (i) Kids Korps USA, described as "a nonprofit organization that engages young people in volunteerism and teaches them about leadership and civic responsibility," and (ii) charity: water, described as "a nonprofit organization that brings clean and safe drinking water to people in developing nations."

In all five treatments, we asked participants to decide which of the two charities should receive a $100 donation. Participants were informed that we would randomly choose the decision of one participant and implement it (i.e., make his or her specific donation), making decisions consequential. Participants were also told that there was no overhead associated with donations made to Kids Korps. For charity: water, we manipulated two aspects of the overhead associated with donations. First, we varied the overhead level associated with participants' donations. In treatment one, there was no overhead; in treatment two, the overhead associated with the donation was 5% (i.e., we sent $95 to charity: water if participants chose it); and in treatment three, the overhead was 50%. Note that if a participant chose charity: water, the organization was paid $100 in treatment one, $95 in treatment two, and $50 in treatment three. Our dependent measure was the proportion of donations given to charity: water. All studies reported here were designed such that they do not involve deception (i.e., we actually changed the overhead associated with a donation as described).

The results of the first three treatments support our assertion regarding overhead aversion. The majority of participants in the no-overhead treatment (73.33%) donated to charity: water. The proportion of participants who donated to charity: water in the 5%-overhead treatment decreased to 66.67%, though not significantly using a test of proportion (z = 0.98, P = 0.33). When overhead costs were 50%, only 49.43% of participants chose to donate to charity: water, which is significantly lower than the proportions observed in the no-overhead (z = 3.27, P < 0.01) and 5%-overhead (z = 2.32, P = 0.02) treatments. Probit regressions confirm the above results (see supplementary text and table S1). Estimated marginal effects show that participants in the 50% overhead treatment are 24% (or 17%) less likely to choose charity: water compared with those in the no-overhead (or 5%-overhead) treatment.

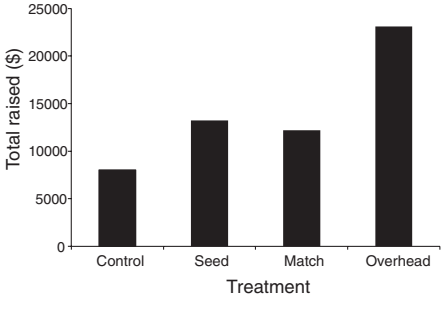

Fig. 2. Total amount raised by treatment.

Although not surprising, these results provide some of the first experimental evidence for the existence of overhead aversion. As noted above, the laboratory experiment was also designed to help us understand why people do not like overhead, which could guide future fundraising campaigns and allow organizations to increase contributions without lowering their overhead costs.

We can think of two main reasons for donors' overhead aversion. The first is that high overhead might imply that an organization is inefficient or even corrupt. In other words, potential donors may use a charity's overhead spending as a signal of the likelihood that the charity will deliver on its promises. The second possible explanation for why overhead plays such an important role in donors' behavior relates to the impact the donor wants to have on the cause she supports, often referred to in the literature on philanthropy as "efficacy" (*27*). Considered in the context of mental accounting (*28*), the utility potential donors receive from their donation might depend on the donation frame. In particular, individuals might feel that they made a greater impact when they know they are helping the cause directly as opposed to when their contribution pays the salary of a charity's staff member. This explanation is consistent with the theory of impact philanthropy, which proposes that donors are motivated by the opportunity to personally make a difference (*29*). According to this model, the impact philanthropist would prefer to target a specific charitable cause rather than overhead, because her perceived impact is greater.

To test which of the two potential explanations drives the overhead aversion observed in our data, our laboratory experiment included two additional treatments. Treatments four and five were similar to treatments two and three, respectively, with one important difference: In addition to providing information regarding the overhead associated with donations to charity: water (5% and 50%), we informed participants that "someone else already covered this cost for your contribution, so for every dollar you'll donate the entire $1 will go to 'charity: water.'"

If overhead is used as a signal of efficiency, then we should not observe a difference in overhead aversion between treatments two and four or treatments three and five, as the quality of this signal is the same. If, however, the observed overhead aversion is driven by a decrease in the perceived personal impact the donor experiences with respect to her donation, then the proportion of individuals choosing to donate to charity: water in treatments four and five would be similar to that observed in the no-overhead treatment (treatment one). After all, the personal impact of the donation on the cause is the same.

The results of all five treatments are presented in Fig. 1. As can be seen, the results reject the efficiency explanation and are in line with the personal impact explanation. In treatment five, at 50% covered overhead, 71.43% of participants donated to charity: water, which is not different from donations in treatment one (no overhead, z = 0.29, P = 0.77) and is significantly higher than those in treatment three (50% uncovered overhead, z = 3.00, P < 0.01). See table S1 for probit regression results that also include demographic (gender, age, donation frequency, and familiarity with the charity) controls.

The results of the laboratory experiment demonstrate that individuals are sensitive to overhead levels. As overhead increased, the proportion of individuals choosing to donate decreased significantly. Moreover, the effect disappeared when someone else covered the (same) overhead costs, suggesting that this aversion is driven by individuals' need to feel that their personal donation has a positive impact on the cause. Finally, the results provide initial support for our proposed solution: Offering individuals an overhead-free donation opportunity while holding overhead costs constant significantly increased donations to charity: water as if there was no overhead at all.

Although the charities we used in our experiment were real charities and participants' choices were consequential, our experiment was conducted with undergraduate students in a laboratory setting. Ultimately, however, we wanted to test the effect of an overhead-free donation opportunity on actual donations. To that end, we conducted a large field experiment with a foundation that specializes in education (*30*). The foundation purchased the right to send a one-time donation request letter to 40,000 potential U.S. donors who donated to similar causes in the preceding 5 years. Participation was limited to U.S. addresses; however, the charity does not have information regarding these donors' demographics. All letters were mailed on the same day during the spring of 2013 and included a nonstamped return envelope as well as a single-page solicitation. Participants were randomly assigned to one of four treatments: control, seed, match, or overhead (N = 10,000 participants per treatment).

We informed participants in the control treatment about the foundation's new initiative to promote educational projects in different locations in the United States and that the program cost per location was $20,000. Participants were not given a specific geographical location for the project and were told that the foundation is interested in sponsoring as many projects for which it can raise money.

Participants were asked to give $20, $50, or $100. The pledge form included the following statement: "Our goal in this campaign is to raise money for the projects. Implementing each project costs $20,000. Your tax-deductible gift makes a difference. Enclosed is…" Participants were asked to check a box to indicate their donation amount.

The letter in the seed treatment further informed participants that the foundation had already secured $10,000 for the project from a private donor. The added text read, "A private donor who believes in the importance of the project has given this campaign seed money in the amount of $10,000. Your tax-deductible gift makes a difference. Enclosed is…"

We told participants in the match condition that a donor had offered a matching grant of up to $10,000 and that the matching rate would be

$1:$1. The added text read, "A private donor who believes in the importance of the project has given this campaign a matching grant in the amount of $10,000. The matching grant will match every dollar given by donors like you with a dollar, up to a total of $20,000…"

Finally, we told participants in the overhead treatment that a donor had given a $10,000 grant to cover all of the overhead costs associated with raising the funds needed for the project. The added text read "A private donor who believes in the importance of the project has given this campaign a grant in the amount of $10,000 to cover all the overhead costs associated with raising the needed donations…"

Result 1, donation rate: Overall, 336 individuals (3.36%) in the control treatment donated (fig. S1). This number increased to 475 (4.75%) in the seed treatment, and the difference is significant using a test of proportion ($z = 4.98$, $P < 0.001$). In the match treatment, 441 (4.41%) chose to donate, which is significantly higher than donation rates in the control treatment ($z = 3.84$, $P < 0.001$) but not statistically different from donation rates in the seed treatment ($z = 1.15$, $P = 0.25$). Response rate in the overhead treatment was 855 (8.55%), higher than any of those observed in the other three treatments ($z = 15.51$, 10.78, and 11.89 for the difference from control, seed, and match, respectively; all $P < 0.001$).

Result 2, amount donated: Most individuals donated $20 (see Table 1), and the $20 donations also accounted for most of the money collected (74% in control, 60% in seed, 61% in match, and 63% in overhead). In the overhead treatment, 726 (7.26%) individuals donated $20, which is significantly greater than the proportion of individuals who donated $20 in the control (297, 2.97%), seed (396, 3.96%), and match (373, 3.73%) treatments ($z = 13.77$, 10.14, and 10.95, respectively; all $P < 0.001$). In addition, although the proportions of individuals who donated $20 in the seed and match treatments are not significantly different from each other ($z = 0.85$, $P = 0.40$), they are significantly greater than the proportion of individuals who donated $20 in the control treatment ($z = 3.83$ and 2.99 for the difference from control, respectively; all $P < 0.01$). This pattern persists with respect to $50 donations: 86 (0.86%) individuals in the overhead treatment donated $50, which is significantly greater than in the control (36, 0.36%), seed (52, 0.52%), and match (41, 0.41%) treatments ($z = 4.54$, 2.90, and 4.01, respectively; all $P < 0.01$). The difference in the proportion of individuals choosing to donate $50 in each of the latter three treatments was not significant (all $P > 0.05$). Finally, 43 (0.43%) participants donated $100 in the overhead treatment, which is significantly greater than the number of participants who donated $100 in the control (3, 0.03%, $z = 5.90$, $P < 0.001$), seed (27, 0.27%) and match (27, 0.27%) treatments (both $z = 1.92$, both $P = 0.05$). Finally, although the proportions of individuals who donated $100 in the seed and match treatments are not significantly different from each other, they are significantly greater than the proportion of individuals who donated $100 in the control treatment (all $z = 4.39$, all $P < 0.001$).

Overall, the campaign raised $8040 through the control treatment (mean donation $M = \$0.80$, $SD = 4.82$ per solicitation) (Fig. 2). The amount raised in the seed treatment [$13,220 ($M = \$1.32$, $SD = 7.36$ per solicitation)] was 64% higher than that in the control treatment. An intention-to-treat analysis revealed that this difference was significant [$t(19998) = 5.89$, $P < 0.001$]. The amount collected in the match treatment was $12,210, 52% more than in the control treatment [$t(19998) = 4.85$, $P < 0.001$, $M = \$1.22$, $SD = 7.12$ per solicitation]. This amount was not significantly different from the amount collected in the seed treatment [$t(19998) = 0.99$, $P = 0.32$]. Finally, the foundation raised $23,120 ($M = \$2.31$, $SD = 9.39$ per solicitation) in the overhead treatment—a significant increase relative to the control [188%, $t(19998) = 14.29$, $P < 0.001$], seed [75%, $t(19998) = 8.30$, $P < 0.001$], and match [89%, $t(19998) = 9.26$, $P < 0.001$] treatments.

Conditional on giving, the average amounts donated in the seed, match, and overhead treatments ($27.83, $27.69, $27.04, respectively) are significantly greater than the amount donated in the control treatment ($23.93; all $P < 0.01$); however, they are not statistically different from each other. Hence, the difference between the control and the other three treatments results from both the extensive margin (i.e., the number of people who choose to donate) and the intensive margin (i.e., the amount given by donors). In contrast, the difference in total amount donated between the seed, match, and overhead treatments comes from the extensive margin only. We did not predict this result, which could be an important aspect to study in future research.

It is important to note that field experiments are a major tool in finding a "treatment effect" (i.e., changes between treatments) rather than the actual size of the effect. For example, converging evidence shows that adding a match offer to the solicitation increases giving, but the specific levels differ across experiments and sometimes even within an experiment. In one such experiment (*13*), the authors report an overall difference of 19% (compared with the 52% increase we report in this paper) but find that adding a matching grant affected only some groups of donors, not all. On the other hand, a paper testing the effect of seed money (*3*) finds that an increase in seed money from 10 to 67% increases giving sixfold (compared with the increase of 64% in our experiment). Despite these different effect sizes, which are driven by factors such as the different characteristics of the groups of potential donors and participants used in different experiments, the treatment effect is similar.

The results of our field and laboratory experiments support the importance of perceived personal impact in the decision to donate. The notion of perceived personal impact relates to the theory of "warm glow," which suggests that impure altruism guides an individual's decision to give (*31*): Donors care not only about helping the cause but also about how doing so makes them feel (*32*) and the way it reflects on their self-identity (*33*–*36*). In the context of our overhead result, impure altruism would predict that the warm glow a donor experiences when helping the recipient of the donation is greater than the warm glow he or she receives from helping to cover the charity's overhead costs.

Recently, nonprofit organizations have been trying to convince donors to place less weight on overhead cost information. In an open letter to the donors of America (*37*), the executives of three leading U.S. charity evaluators argue that "The percent of charity expenses that go to administrative and fundraising costs—commonly referred to as 'overhead'—is a poor measure of a charity's performance." An important effort in this direction is being led by Dan Pallotta, a founder of multiday charity events such as 3-day cancer walks, who proclaims (*38*), "It's no wonder that the public demands low overhead instead of impact. We've never told them that the two things are not correlated."

In this paper, we propose one way to bypass individuals' reluctance to donate due to overhead-related concerns: overhead-free donations. A prominent example of this approach is charity: water, a nonprofit that has split into two separate organizations: "charity: water," which accepts donations that go entirely to program expenses, and "The Well," which fundraises for charity: water and has its costs paid for by larger wealthy donors.

An open question that we cannot address with the current data regards the overall effect of using the overhead-free method for donations. Is it going to increase overall giving to charities or simply shift giving from other charities? Furthermore, this method could exacerbate the unpopularity of overhead costs among donors, causing a race to the bottom among nonprofit organizations soliciting gifts to cover overhead costs. Another question we cannot address fully with the current data is whether the mere mention of overhead triggers changes in behavior compared with a situation in which overhead is not mentioned at all. Is it better to draw donors' attention to the existence of overhead or to ignore it altogether? The answer to this question may depend on donors' lay expectations or beliefs about overhead as well as the value they put on transparency in organizations. This would be an important question to address in future research.

Finally, we would like to note that we are not suggesting halting efforts to explain the importance of overhead costs and how they can be used to improve the effectiveness of charities. However, we believe such efforts entail a prolonged uphill battle that may ultimately prove futile. Instead, to increase current charitable giving, we propose an approach that simultaneously addresses individuals' concerns and increases overall giving. This method allows organizations to focus their efforts on convincing a handful of big donors that their money is best spent on overhead, which supports the development and maintenance of strong infrastructure, rather than trying to change the perceptions of the general public.

REFERENCES AND NOTES

1. L. Vesterlund, in *The Nonprofit Sector*, R. Steinberg, W. W. Powell, Eds. (Yale Univ. Press, New Haven, CT, ed. 2, 2006).
2. D. Rondeau, J. A. List, *Exp. Econ.* **11**, 253–267 (2008).
3. J. A. List, D. Lucking-Reiley, *J. Polit. Econ.* **110**, 215–233 (2002).
4. J. Andreoni, *J. Polit. Econ.* **106**, 1186–1213 (1998).
5. R. Croson, J. Shang, *Exp. Econ.* **11**, 221–233 (2008).
6. B. S. Frey, S. Meier, *Am. Econ. Rev.* **94**, 1717–1722 (2004).
7. J. Potters, M. Sefton, L. Vesterlund, *Econ. Theory* **33**, 169–182 (2007).
8. C. E. Cryder, G. Loewenstein, H. Seltman, *J. Exp. Soc. Psychol.* **49**, 1078–1083 (2013).
9. L. Vesterlund, *J. Public Econ.* **87**, 627–657 (2003).
10. C. C. Eckel, P. J. Grossman, *J. Public Econ.* **87**, 681–701 (2003).
11. C. C. Eckel, P. J. Grossman, *Nonprofit Volunt. Sector Q.* **33**, 271–289 (2004).
12. C. C. Eckel, P. J. Grossman, R. M. Johnston, *J. Public Econ.* **89**, 1543–1560 (2005).
13. D. Karlan, J. A. List, *Am. Econ. Rev.* **97**, 1774–1793 (2007).
14. S. Meier, *J. Eur. Econ. Assoc.* **5**, 1203–1222 (2007).
15. W. P. Barrett, Most charitable bang for the donor's buck. *Forbes*, 30 November 2011; www.forbes.com/sites/williampbarrett/2011/11/30/most-charitable-bang-for-the-donors-buck-2/.
16. J. Baron, E. Szymanska, in *The Science of Giving: Experimental Approaches to the Study of Charity*, D. M. Oppenheimer, C. Y. Olivola, Eds. (Psychology Press, New York, 2011), chap. 13.
17. L. Caviola, N. Faulmüller, J. A. C. Everett, J. Savulescu, G. Kahane, *Judgm. Decis. Mak.* **9**, 303–316 (2014).
18. D. Tinkelman, K. Mankaney, *Nonprofit Volunt. Sector Q.* **36**, 41–64 (2007).
19. A. G. Gregory, D. Howard, *Stanford Soc. Innovation Rev.* **Fall**, 49–53 (2009).
20. J. D. Lecy, E. A. M. Searing, *Nonprofit Volunt. Sec. Q.* 10.1177/0899764014527175 (2014).
21. K. Wing, M. A. Hager, "Getting what we pay for: Low overhead limits nonprofit effectiveness," *Brief No. 3* (The Urban Institute, Washington, DC, 2004).
22. T. H. Pollak, "What we know about overhead costs in the nonprofit sector," *Brief No. 1* (The Urban Institute, Washington, DC, 2004).
23. K. Wing, M. A. Hager, "The quality of financial reporting by nonprofits: Findings and implications," *Brief No. 4* (The Urban Institute, Washington, DC, 2004).
24. M. A. Hager, T. Flack, "The pros and cons of financial efficiency standards," *Brief No. 5* (The Urban Institute, Washington, DC, 2004).
25. W. Bowman, *Nonprofit Volunt. Sector Q.* **35**, 288–310 (2006).
26. R. Steinberg, in *The Economics of Non Profit Institutions: Studies in Structure and Policy*, S. Rose-Ackerman, Ed. (Oxford Univ. Press, New York, 1986), pp. 347–364.
27. R. Bekkers, P. Wiepking, *Nonprofit Volunt. Sector Q.* **40**, 924–973 (2011).
28. R. Thaler, *J. Econ. Behav. Organ.* **1**, 39–60 (1980).
29. B. Duncan, *J. Public Econ.* **88**, 2159–2180 (2004).
30. As is common in running experiments with organizations, we signed a nondisclosure agreement that limits the amount of information we can give regarding the procedure.
31. J. Andreoni, *Econ. J.* **100**, 464–477 (1990).
32. A. Imas, *J. Public Econ.* **114**, 14–18 (2014).
33. G. A. Akerlof, R. E. Kranton, *Q. J. Econ.* **115**, 715–753 (2000).
34. D. Ariely, A. Bracha, S. Meier, *Am. Econ. Rev.* **99**, 544–555 (2009).
35. R. Bénabou, J. Tirole, *Am. Econ. Rev.* **96**, 1652–1678 (2006).
36. A. Gneezy, U. Gneezy, G. Riener, L. D. Nelson, *Proc. Natl. Acad. Sci. U.S.A.* **109**, 7236–7240 (2012).
37. A. Taylor, J. Harold, K. Berger, "The overhead myth: Letter to the donors of America" (2013); http://overheadmythcom.b.presscdn.com/wp-content/uploads/2013/06/GS_OverheadMyth_Ltr_ONLINE.pdf).
38. D. Pallotta, *Uncharitable: How Restraints on Nonprofits Undermine Their Potential* (Tufts Univ. Press, Lebanon, NH, 2008).

ACKNOWLEDGMENTS

Funding was provided by the John Templeton Foundation through the Science of Philanthropy Initiative. The data reported in this paper are archived in the Harvard Dataverse Network at http://dx.doi.org/10.7910/DVN/27366. We thank the reviewers for valuable comments that helped to improve the manuscript.

SUPPLEMENTARY MATERIALS

www.sciencemag.org/content/346/6209/632/suppl/DC1
Materials and Methods
Supplementary Text
Fig. S1
Table S1
Additional Data Tables S1 and S2

26 March 2014; accepted 25 September 2014
10.1126/science.1253932

EARTH HISTORY

Low Mid-Proterozoic atmospheric oxygen levels and the delayed rise of animals

Noah J. Planavsky,[1]*† Christopher T. Reinhard,[2]*† Xiangli Wang,[1,3] Danielle Thomson,[4] Peter McGoldrick,[5] Robert H. Rainbird,[6] Thomas Johnson,[3] Woodward W. Fischer,[7] Timothy W. Lyons[8]

The oxygenation of Earth's surface fundamentally altered global biogeochemical cycles and ultimately paved the way for the rise of metazoans at the end of the Proterozoic. However, current estimates for atmospheric oxygen (O_2) levels during the billion years leading up to this time vary widely. On the basis of chromium (Cr) isotope data from a suite of Proterozoic sediments from China, Australia, and North America, interpreted in the context of data from similar depositional environments from Phanerozoic time, we find evidence for inhibited oxidation of Cr at Earth's surface in the mid-Proterozoic (1.8 to 0.8 billion years ago). These data suggest that atmospheric O_2 levels were at most 0.1% of present atmospheric levels. Direct evidence for such low O_2 concentrations in the Proterozoic helps explain the late emergence and diversification of metazoans.

It remains unclear whether the appearance and diversification of animals are linked to a change in environmental oxygen (O_2) levels or if this dramatic shift in the structure and complexity of the biosphere simply reflects the timing of genetic and/or developmental innovation independent of any environmental control (*1*–*4*). Quantitative constraints on O_2 levels during the mid-Proterozoic [1.8 to 0.8 billion years ago (Ga)]—the long interval leading up to the Cambrian explosion in animal life (*5*, *6*)—are required to compare atmospheric oxygen levels with the absolute O_2 requirements for metazoan physiology (*3*, *5*). Such a comparison is essential for delineating the potential role of Earth's oxygen cycle in the early evolution of animal life.

The appearance of terrestrial red-beds and the disappearance of detrital pyrite beds indicate oxidative processes in terrestrial environments after ~2.4 Ga and a permanent rise in atmospheric O_2 concentrations above the very low values characteristic of the Archean atmosphere (<0.001% of the present atmospheric level or PAL) (*6*, *7*). However, these observations provide only a crude lower estimate for mid-Proterozoic atmospheric O_2 of ~1% PAL. The most widely accepted upper limit on mid-Proterozoic atmospheric O_2 is ~40% PAL, which is an estimate based on the inferred temporal and spatial extent of anoxia in the Proterozoic ocean combined with steady-state physicochemical models of ocean ventilation (*8*, *9*).

Chromium (Cr) isotopes may provide a much needed additional constraint on Proterozoic O_2 levels (*10*). Chromium exists in two primary redox states at Earth's surface—oxidized Cr(VI) and reduced Cr(III). Because Cr within the crust is hosted within rock-forming minerals predominantly as Cr(III), the initial Cr reservoir for terrestrial weathering will be stable under reducing conditions. In addition, Cr undergoes only limited fractionation during typical non-redox–dependent transformations (*11*–*13*), but the oxidation and reduction of Cr induce large isotope fractionations. At equilibrium, Cr(VI) species will be enriched in the heavy isotope, ^{53}Cr, by over 6‰ relative to the parent Cr(III) reservoir (*13*), although environmental fractionations are likely kinetic and are unlikely to reach this full equilibrium value (*12*, *14*). Chromium oxidation occurs predominantly through the dissolution of Cr(III)-bearing minerals in terrestrial soils and subsequent reaction with manganese (Mn) oxides [e.g.,

[1]Department Geology and Geophysics, Yale University, CT, USA. [2]School of Earth and Atmospheric Sciences, Georgia Institute of Technology, GA, USA. [3]Department of Geology, University of Illinois, Champaign, IL, USA. [4]Department of Earth Science, Carleton University, Ottawa, ON, Canada. [5]Centre for Ore Deposit and Exploration Science, University of Tasmania, TAS, Australia. [6]Geological Survey of Canada, Ottawa, ON, Canada. [7]Division of Geological and Planetary Sciences, California Institute of Technology, Pasadena, CA, USA. [8]Department of Earth Sciences, University of California, Riverside, CA, USA. ***Corresponding author. E-mail: noah.planavsky@yale.edu (N.J.P.); chris.reinhard@eas.gatech.edu (C.T.R.)** †These authors contributed equally to this work.

(*15*–*17*)], the occurrence of which in modern environments is linked specifically to the presence of free environmental O_2. This process yields dissolved Cr(VI) oxyanion species (CrO_4^{2-} and $HCrO_4^-$) that are significantly more soluble and mobile than Cr(III). However, during transport within and away from weathering environments, isotopically light Cr(VI) can be selectively reduced and immobilized (*12*, *14*, *18*). As a result, the net effect of redox reactions will be to produce a highly mobile CrO_4^{2-} reservoir with positive δ^{53}Cr values. In contrast, igneous systems are characterized by a very narrow range of Cr isotope ratios (reported as δ^{53}Cr values), with an average value of −0.12‰ (±0.101 2 SDs) (*19*). It is expected that the Cr cycle on a reducing Earth surface would be dominated by mobilization, transport, and burial of less mobile Cr(III) with minimal fractionation from igneous silicate Earth.

Although Cr isotope data have been used to examine the broad-scale oxygenation of Earth's atmosphere (*10*, *20*), these initial surveys did not examine the billion-year interval before the evolution of animals. We targeted several mid-Proterozoic sedimentary successions to fill major gaps in the sedimentary Cr isotope record of this interval. To isolate redox conditions in terrestrial settings, we explored shallow, nearshore iron-rich marine units that are most likely to capture terrigenous weathering signals and lack measurable contributions from contemporaneous hydrothermal systems. We focused on samples from the 1.7-Ga Chuanlinggou Formation in China, the ~1.65-Ga Freedom Formation in the United States, the 1.45-Ga Sherwin Formation in Australia, and the ~0.9-Ga Aok Formation in Canada (*21*). The targeted samples comprise granular deposits that are sedimentologically and geochemically equivalent to Phanerozoic (<542-million-year-old) nearshore iron-rich deposits—rocks commonly referred to as ironstones (Fig. 1)—and formed in marginal marine or deltaic settings genetically similar to iron-rich portions of the modern Amazon delta (*22*). For comparison, we also determined the Cr isotope composition of a suite of analogous Phanerozoic ironstones, deposited between ~0.445 and 0.090 Ga, to provide a comparative view of Cr isotope systematics in nearshore iron-rich sedimentary units that formed beneath an atmosphere independently and unequivocally constrained to have been well-oxygenated.

Understanding petrographic context and postdepositional history is essential to interpret Cr isotope data. Chromium with either crustal or highly fractionated δ^{53}Cr values can be introduced into a rock unit during burial diagenesis, given that both oxidizing groundwaters and reduced basinal brines commonly lead to secondary metal enrichment [e.g., (*23*, *24*)]. To gauge whether the examined samples record primary (depositional) or secondary Cr isotope signatures, we studied the samples using standard petrography and laser ablation–inductively coupled plasma mass spectrometry (LA-ICP-MS) trace-element mapping. Notably, the selected samples lack obvious textural or geochemical evidence for secondary mineralization. Chromium resides predominantly in iron-rich sedimentary grains (e.g., concentrically coated iron ooids), rather than detrital Cr-rich grains (e.g., chromite) or diagenetic chemical cements (Fig. 2). This observation is consistent with Cr acquisition by sorption during sedimentation of precursor ferric oxides. In addition, preservation of fine-scale sedimentary textures in the ironstones, such as laminations in coated grains (Fig. 1 and fig. S1), is commonly observed and suggests limited fluid-rich alteration and recrystallization. Therefore, we are confident that our selected ironstone samples record depositional signals and thus can be used to track environmental Cr cycling.

All of the examined mid-Proterozoic ironstones have δ^{53}Cr values indistinguishable from those of igneous sources (−0.124‰, ±0.101 2 SDs, Fig. 2A). This range is in marked contrast to that of the examined Phanerozoic ironstones, which have consistently positive δ^{53}Cr values indicative of oxidative Cr cycling. Phanerozoic ironstone samples with a stronger detrital contribution have less-fractionated, near-igneous Cr isotopes values (Fig. 2A), which is an important factor controlling the wide range of δ^{53}Cr values seen in Phanerozoic ironstones. In contrast, the mid-Proterozoic ironstones, despite being characterized by a broad range in authigenic Cr enrichment, show little to no isotopic offset from bulk silicate Earth—with no correlation between authigenic Cr enrichment and δ^{53}Cr values (Fig. 2A). This set of observations is most parsimoniously explained by the onset of a significant Cr(VI) exit channel from the terrestrial realm in the interval between the mid-Proterozoic and Phanerozoic data [e.g., (*25*)].

To test the hypothesis of a diminished Earth surface Cr redox cycling during mid-Proterozoic time, we sought an independent Cr archive in shales. Shales can also develop large authigenic Cr enrichments, marked by significantly higher Cr/Ti ratios than that of bulk crust. Authigenic Cr enrichment in fine-grained sediments and sedimentary rocks (shales) is thought to reflect processes similar to that in ironstones: coprecipitation and scavenging of particle-reactive Cr(III) phases or sorption and sequestration of dissolved Cr(VI) (*26*). Phanerozoic and latest Proterozoic shales commonly show large authigenic Cr

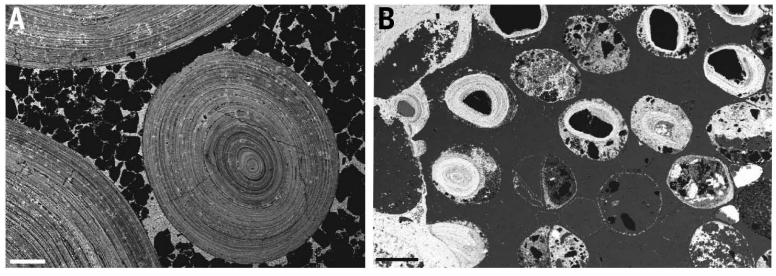

Fig. 1. Back-scatter electron micrographs of representative samples of ironstones. (**A**) the 1.45-Ga Sherwin Formation in northwestern Australia and (**B**) the 0.44-Ga Red Mountain Formation in southeastern United States. Samples are composed largely of hematite-coated grains and quartz sand. Fine concentric laminations of authigenic hematite are apparent. Scale bars, 200 μm.

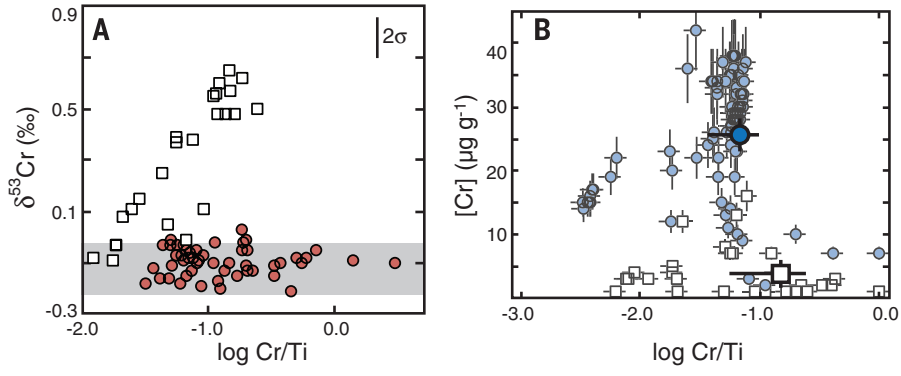

Fig. 2. Chromium isotope values and Cr/Ti ratios. (**A**) Phanerozoic (white squares) and Proterozoic (red circles) ironstones. The gray bar demarcates the igneous Cr isotope range, while the error bar in the top right denotes uniform external reproducibility (2σ). Phanerozoic and Proterozoic samples show a similar range in Cr/Ti ratios but markedly different Cr isotope trajectories. The trend defined by the Phanerozoic results from mixing between a crustal and an ^{53}Cr-enriched authigenic Cr component, providing a clear signal for an oxidative Cr cycle. (**B**) In situ Cr and Ti concentrations for representative mid-Proterozoic ironstones. Hematitic sedimentary grains are shown as blue circles; hematite cements, as white squares. Error bars in (B) denote uncertainty in measured concentrations of 15%, propagated into calculated Cr/Ti values (see supplementary materials). Large filled points denote the average values (±95% confidence interval) for grains (blue) and cements (white).

enrichments, whereas mid-Proterozoic shales are marked by Cr/Ti ratios similar to bulk crustal values (*26*). This relationship is consistent with widely reducing conditions and inventory drawdown in the earlier mid-Proterozoic ocean and/or smaller terrestrial-to-marine Cr fluxes (*26*). We observe a large range of δ^{53}Cr values for Phanerozoic-age Cr-enriched shales (Fig. 3). Most notably, we also find an increase in Cr enrichment and a wide range of δ^{53}Cr values in the ~0.8- to 0.75-Ga shales from the upper Wynniatt Formation in the Shaler Supergroup in Arctic Canada (*27*). The Wynniatt Formation yielded samples with markedly positive δ^{53}Cr values (peak values >2 ‰), which clearly indicate the operation of an oxidative surface Cr cycle at that time. The large Cr enrichments in these shales also suggest that a fully oxidative Cr cycle was in place (*25*, *26*). Therefore, the coupled shale and ironstone record suggests that there was a major change in Cr cycling by at least 0.75 Ga.

We propose that the observed shifts in the shale and ironstone Cr records between ~0.8 and 0.75 Ga were caused by a rise in environmental O_2 concentrations. Further, we suggest that the minimal Cr isotope fractionation observed during mid-Proterozoic time results from a general lack of Cr redox cycling. Although it is difficult to quantify the minimum amount of O_2 needed to induce and preserve large Cr isotope fractionations in marine chemical sediments, we estimate a range for this threshold by considering how ambient O_2 levels affect rates of Mn oxidation, which in turn affect Cr oxidation. Briefly, we use a kinetic model in which the relative amount of Cr(III) oxidation during weathering is governed by the availability of Mn(III,IV) species. Even with a wide range of ambient chemistries, Mn-oxide phases, and oxidation mechanisms (*21*), we find that extensive Mn-Cr redox cycling occurs at markedly low environmental O_2 levels (<0.1% PAL; Fig. 4). Thus, to explain the mid-Proterozoic Cr isotope data, we hypothesize that atmospheric partial oxygen pressure (pO_2) levels were at times, if not persistently, extremely low.

Minimum estimates for Proterozoic atmospheric pO_2 levels have been notoriously difficult to establish. Specifically, traditionally used lower estimates for pO_2 values (>1% PAL), derived from paleosols (*9*), are likely to overestimate minimum atmospheric oxygen partial pressures due either to the use of extremely high [and likely incorrect; e.g., (*28*)] atmospheric CO_2 concentrations (in steady-state calculations) or because they neglect microbial iron oxidation (in kinetic-transport models). Further, there is a paucity of mid-Proterozoic paleosols (*7*), preventing direct, time-equivalent comparison between our results and the paleosol record. We note, however, previous suggestions on the basis of petrography and major-element geochemistry that the ~1.1-Ga Sturgeon Falls paleosol records a lack of terrestrial Mn oxidation—consistent with our Cr isotope data (*29*).

Others have suggested active environmental Cr redox cycling before our estimate of ~750 Ga (*10*, *20*). Although each report must be evaluated individually, the presence of possible earlier periods of extensive Cr oxidation is consistent with atmospheric oxygen levels that were highly dynamic during the Precambrian and indicates that the traditional image of a unidirectional rise in atmospheric pO_2 is likely overly simplistic (*30*). Instability in atmospheric oxygen levels would be expected in a system characterized by very low O_2 partial pressures and thus potentially very short response times for the atmospheric oxygen reservoir. Dynamics aside, it seems clear that there is a first-order difference in the nature of Earth-surface Cr cycling between the mid-Proterozoic and the late-Proterozoic/Phanerozoic.

Under previous estimates of atmospheric pO_2 during the mid-Proterozoic (1% PAL < pO_2 < 40% PAL), there was potentially sufficient atmospheric oxygen for the earliest sessile and mobile animals to thrive well in advance of their ostensible emergence (*3*). However, our preferred maximum pO_2 estimate for mid-Proterozoic time

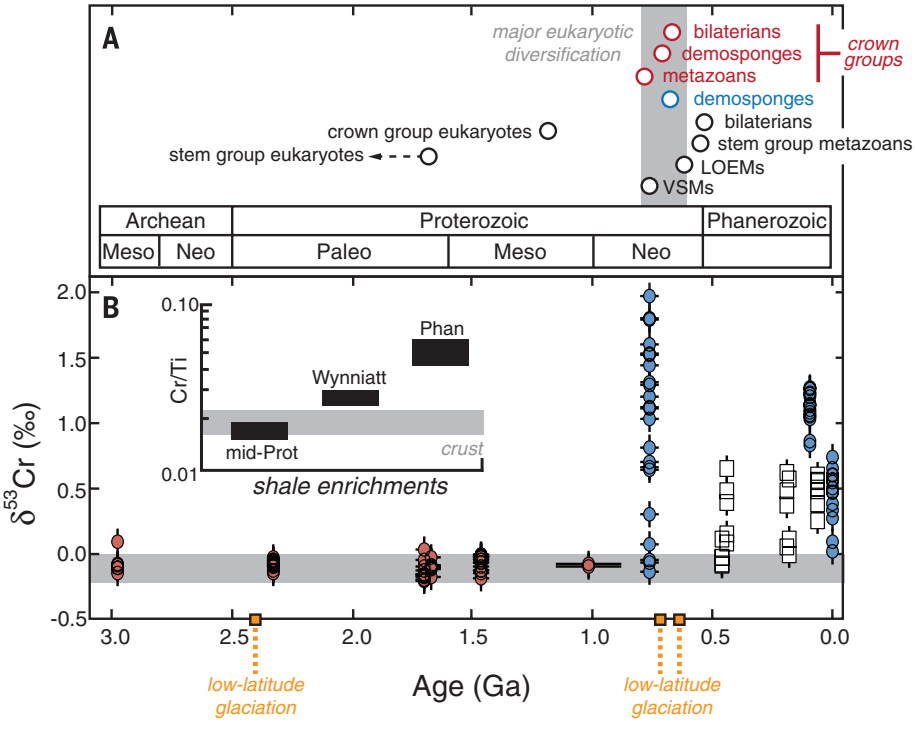

Fig. 3. Summary of sedimentary chromium isotope data in the context of major events in biological evolution. (**A**) Shown are approximate dates for the first appearance of various eukaryotic groups (*2*, *31*, *32*) in the body fossil record (open white circles), the molecular fossil record (open blue circle), and best estimates from molecular clock techniques for the emergence of major crown groups (open red circles). Also shown are the appearances of large ornamented Ediacaran microfossils (LOEMs) and vase-shaped microfossils (VSMs). The vertical gray field denotes an interval of major eukaryotic diversification. (**B**) Shown are Precambrian ironstone data (filled red circles), Phanerozoic ironstone data (white squares), and shale/mudstone data (filled blue circles) (n = 171). Horizontal gray field denotes the range for the isotopic composition of high-temperature Cr sources. Vertical error bars denote external reproducibility; horizontal error bars denote uncertainty in age constraints (error bars are smaller than symbol size when not shown). Inset shows a summary of the Cr enrichment record from anoxic shales, with boxes showing the average Cr/Ti value (±95% confidence interval) for each interval [data for mid-Proterozoic (mid-Prot) and Phanerozoic (Phan) from (*26*); data for the ~0.8- to 0.75-Ga Wynniatt Formation from this study]. Horizontal gray field in the inset denotes the range of Cr/Ti values for upper continental crust.

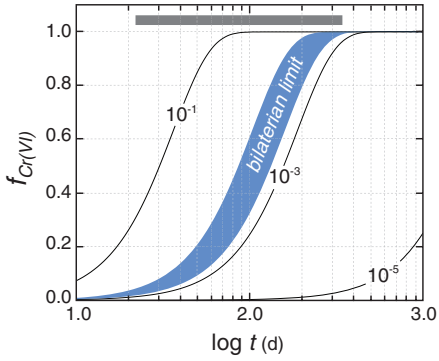

Fig. 4. Results from a kinetic model for Cr(III)-Mn(II) oxidation. Curves show the normalized fractional conversion of initial Cr(III) to Cr(VI) as a function of time in an oxidant-limited Mn-Cr system, with contours labeled according to atmospheric pO_2 (relative to the PAL). The blue field denotes values established from metabolic theory to be limiting for the last common ancestor of bilaterians (*3*), with the range encompassing organisms limited by pure diffusion and those that have a simple circulatory system. The dark gray bar shows an approximate range for the residence time of modern soil pore fluids.

(<0.1% PAL) is below theoretical estimates for the minimum O_2 requirements of the last common ancestor of bilaterians, measured limits at which bilaterians are found in the modern oceans, and threshold estimates for earlier diverging metazoan phyla (*3*, *4*). In addition, it is possible that existing theoretical estimates of biological O_2 thresholds are biased toward low values, as they neglect the metabolic requirements of different life-history stages and synergistic physiological effects. In any case, our results suggest a temporal overlap between the appearance of stable environments favorable for animal life and the divergence of basal metazoan clades—which, according to recent estimates [e.g., (*2*)], occurred between ~0.8 and 0.7 Ga (Fig. 3). Though the emergence and eventual ecological dominance of animal life must, at its core, be tied to genetic and developmental innovations, our results implicate Earth's oxygen cycle as a crucial factor shaping the evolutionary landscape from which animal life emerged and help explain the delayed appearance of animals in the late Proterozoic.

REFERENCES AND NOTES

1. N. J. Butterfield, *Geobiology* **7**, 1–7 (2009).
2. D. H. Erwin *et al.*, *Science* **334**, 1091–1097 (2011).
3. E. A. Sperling, G. P. Halverson, A. H. Knoll, F. A. Macdonald, D. T. Johnston, *Earth Planet. Sci. Lett.* **371-372**, 143–155 (2013).
4. D. B. Mills *et al.*, *Proc. Natl. Acad. Sci. U.S.A.* **111**, 4168–4172 (2014).
5. J. L. Payne *et al.*, *Photosynth. Res.* **107**, 37–57 (2011).
6. H. D. Holland, *Philos. Trans. R. Soc. Lond. B Biol. Sci.* **361**, 903–915 (2006).
7. R. Rye, H. D. Holland, *Am. J. Sci.* **298**, 621–672 (1998).
8. D. E. Canfield, *Annu. Rev. Earth Planet. Sci.* **33**, 1–36 (2005).
9. L. R. Kump, *Nature* **451**, 277–278 (2008).
10. R. Frei, C. Gaucher, S. W. Poulton, D. E. Canfield, *Nature* **461**, 250–253 (2009).
11. A. S. Ellis, T. M. Johnson, T. D. Bullen, *Environ. Sci. Technol.* **38**, 3604–3607 (2004).
12. T. M. Johnson, T. D. Bullen, in *Geochemistry of Non-Traditional Stable Isotopes (Mineralogical Society of America,* Chantilly, VA, 2004), vol. 55, chap. 9, pp. 289–318.
13. E. A. Schauble, G. R. Rossman, H. P. J. Taylor Jr., *Chem. Geol.* **205**, 99–114 (2004).
14. S. Zink, R. Schoenberg, M. Staubwasser, *Geochim. Cosmochim. Acta* **74**, 5729–5745 (2010).
15. R. Bartlett, B. James, *J. Environ. Qual.* **8**, 31 (1979).
16. S. E. Fendorf, *Geoderma* **67**, 55–71 (1995).
17. J. Kotaś, Z. Stasicka, *Environ. Pollut.* **107**, 263–283 (2000).
18. A. S. Ellis, T. M. Johnson, T. D. Bullen, *Science* **295**, 2060–2062 (2002).
19. R. Schoenberg, S. Zink, M. Staubwasser, F. von Blanckenburg, *Chem. Geol.* **249**, 294–306 (2008).
20. S. A. Crowe *et al.*, *Nature* **501**, 535–538 (2013).
21. Materials and methods and full model details are available on *Science* Online.
22. R. C. Aller, J. E. Mackin, R. T. Cox Jr., *Cont. Shelf Res.* **6**, 263–289 (1986).
23. A. C. Brown, *Econ. Geol.* **100**, 765 (2005).
24. D. Leach *et al.*, *Econ. Geol.* **100**, 561 (2005).
25. K. O. Konhauser *et al.*, *Nature* **478**, 369–373 (2011).
26. C. T. Reinhard *et al.*, *Proc. Natl. Acad. Sci. U.S.A.* **110**, 5357–5362 (2013).
27. D. van Acken, D. Thomson, R. H. Rainbird, R. A. Creaser, *Precambrian Res.* **236**, 124–131 (2013).
28. N. D. Sheldon, *Precambrian Res.* **147**, 148–155 (2006).
29. E. A. Zbinden, H. D. Holland, C. R. Feakes, S. K. Dobos, *Precambrian Res.* **42**, 141–163 (1988).
30. T. W. Lyons, C. T. Reinhard, N. J. Planavsky, *Nature* **506**, 307–315 (2014).
31. G. D. Love *et al.*, *Nature* **457**, 718–721 (2009).
32. A. H. Knoll, *Cold Spring Harb. Perspect. Biol.* **6**, a016121 (2014).

ACKNOWLEDGMENTS

N.J.P., C.T.R., X.W., T.J, and T.W.L. acknowledge funding from NASA Exobiology Program. N.J.P., C.T.R., and T.W.L. acknowledge funding from the NSF-ELT program. C.T.R. acknowledges an O.K. Earl fellowship from the California Institute of Technology. R.H.R. and D.T. acknowledge funding from a National Science and Engineering Research Council of Canada Discovery Grant and by Natural Resources Canada's GEM Program. P.McG. acknowledges funding through the Australian Research Council's Centres of Excellence Program and thanks S. Gilbert for expert help with the LA-ICPMS work. We are indebted to A. Bekker, B. Maynard, A. Hofmann, K. Konhauser, J. Owens, C. Li, and G. Love for discussion and samples. Full data tables are in the supplementary materials.

SUPPLEMENTARY MATERIALS

www.sciencemag.org/content/346/6209/635/suppl/DC1
Materials and Methods
Supplementary Text
Figs. S1 to S5
Table S1
References (*33*–*106*)
Databases S1 and S2

7 July 2014; accepted 30 September 2014
10.1126/science.1258410

CHEMICAL BIOLOGY

A bump-and-hole approach to engineer controlled selectivity of BET bromodomain chemical probes

Matthias G. J. Baud,[1,2]*† Enrique Lin-Shiao,[1,2]*‡ Teresa Cardote,[1]* Cynthia Tallant,[2]§ Annica Pschibul,[1] Kwok-Ho Chan,[1] Michael Zengerle,[1] Jordi R. Garcia,[1] Terence T.-L. Kwan,[2] Fleur M. Ferguson,[2] Alessio Ciulli[1,2]||

Small molecules are useful tools for probing the biological function and therapeutic potential of individual proteins, but achieving selectivity is challenging when the target protein shares structural domains with other proteins. The Bromo and Extra-Terminal (BET) proteins have attracted interest because of their roles in transcriptional regulation, epigenetics, and cancer. The BET bromodomains (protein interaction modules that bind acetyl-lysine) have been targeted by potent small-molecule inhibitors, but these inhibitors lack selectivity for individual family members. We developed an ethyl derivative of an existing small-molecule inhibitor, I-BET/JQ1, and showed that it binds leucine/alanine mutant bromodomains with nanomolar affinity and achieves up to 540-fold selectivity relative to wild-type bromodomains. Cell culture studies showed that blockade of the first bromodomain alone is sufficient to displace a specific BET protein, Brd4, from chromatin. Expansion of this approach could help identify the individual roles of single BET proteins in human physiology and disease.

The Bromo and Extra-Terminal (BET) proteins Brd2, Brd3, Brd4, and Brdt play key roles in transcriptional regulation by controlling networks of genes involved in cellular proliferation and cell-cycle regulation as part of multiprotein complexes. Misregulation of BET protein activity has been linked to disease states, notably in NUT-midline carcinoma and other cancers (*1*). Key to the activity of BET proteins are paired, highly homologous bromodomains present in their amino-terminal regions (Fig. 1A) that direct recruitment to nucleosomes by specifically binding to acetylated lysines within histone tails. Elucidation of the complex biological processes controlled by BET proteins would benefit greatly from chemical probes that allow perturbation of individual bromodomains with high selectivity.

Potent cell-active small molecules based on a triazolodiazepine scaffold including I-BET (*2*), JQ1 (*3*), and GW841819X (*4*) (Fig. 1B) were recently discovered that bind to the acetyl-lysine (KAc) binding pocket of BET bromodomains [dissociation constant (K_d) 50 to 370 nM for I-BET] (Fig. 1C, table S1, and fig. S1). These molecules display activity in vivo (*5*) against NUT-midline carcinoma (*6*), multiple myeloma (*7*), mixed-lineage leukemia (*8*), and acute myeloid leukemia (*9*, *10*). Several compounds, including I-BET, are now in clinical trials (*11*). These and other inhibitors developed to date are pan-selective for the BET members relative to other bromodomains (*3*) but show poor selectivity within the subfamily (Fig. 1C). Lack of selectivity confounds association of the pharmacology of BET bromodomain inhibitors to a particular target, which has fueled interest in finding more selective inhibitors. However, it is not clear which BET bromodomains should be

[1]Division of Biological Chemistry and Drug Discovery, College of Life Sciences, University of Dundee, James Black Centre, Dow Street, Dundee, DD1 5EH, UK. [2]Department of Chemistry, University of Cambridge, Lensfield Road, Cambridge CB2 1EW, UK.
*These authors contributed equally to this work. †Present address: Medical Research Council Laboratory of Molecular Biology, Francis Crick Avenue, Cambridge Biomedical Campus, Cambridge CB2 0QH, UK. ‡Present address: Biochemistry and Molecular Biophysics Graduate Group, Perelman School of Medicine, University of Pennsylvania, Philadelphia, PA 19104, USA. §Present address: Nuffield Department of Clinical Medicine, Structural Genomics Consortium, University of Oxford, Old Road Campus, Roosevelt Drive, Oxford OX3 7DQ, UK. **||Corresponding author. E-mail: a.ciulli@dundee.ac.uk**

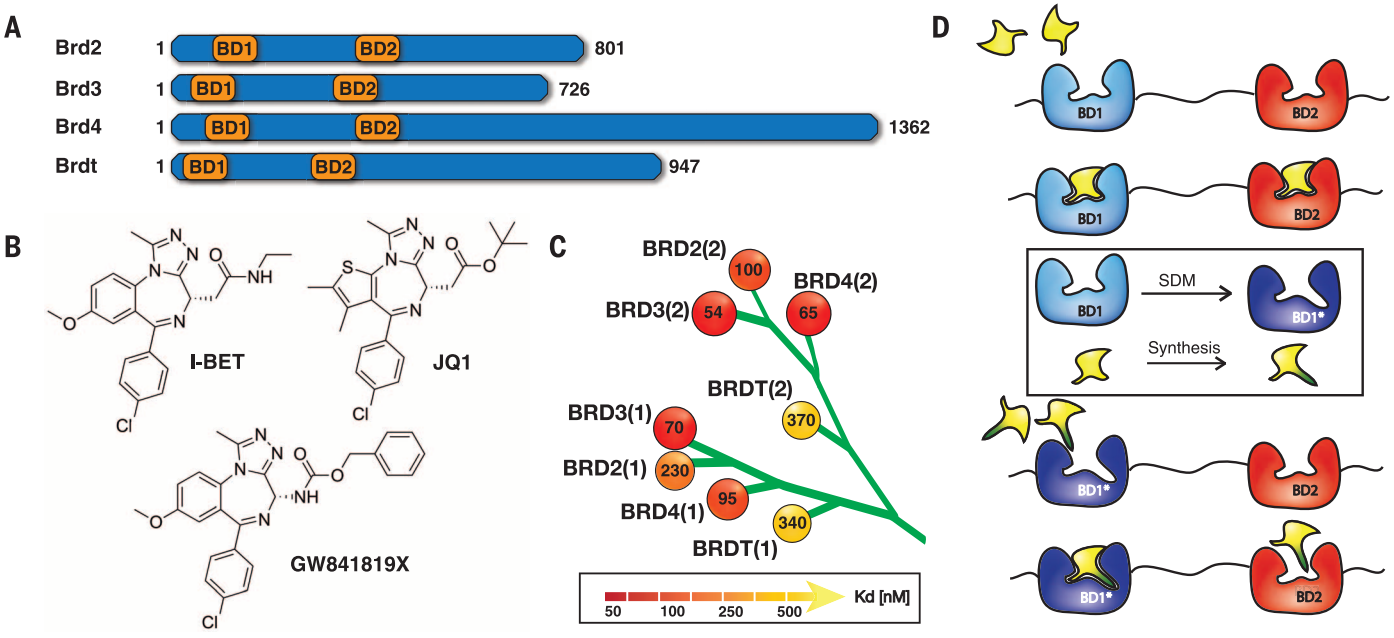

Fig. 1. BET bromodomains, pan-selective inhibitors, and bump-and-hole approach. (**A**) Domain organization of BET proteins. The name and length of the proteins are shown together with the position of their first and second bromodomains. (**B**) Chemical structures of BET bromodomain inhibitors I-BET, JQ1, and GW841819X that share a common triazolodiazepine scaffold. (**C**) Dissociation constants (K_d, in nanomolar) determined by means of ITC are shown for I-BET binding to the eight individual BET bromodomains distributed as subfamily branch in a human bromodomain phylogenetic tree. (**D**) Rationale for a bump-and-hole approach to engineer selectivity of BET bromodomain inhibitors.

the target of such an effort, and the high structural conservation and sequence identity of their KAc-binding sites hamper achievement of single-target selectivity.

To address these problems, we hypothesized that a chemical genetic approach could be devised based on engineered shape complementarity between the bromodomain and a small-molecule inhibitor, allowing systematic generation of an orthogonal high-affinity protein-ligand variant pair. In a "bump-and-hole" strategy conceptually related to that developed to selectively target the adenosine 5′-triphosphate–binding site of protein kinases (*12*, *13*), a conserved hydrophobic residue on the bromodomain would be mutated to a smaller residue to generate a "hole" on the protein. The mutant would then be specifically targeted with analogs of a known ligand bearing a sterically bulky "bump" that can be accommodated by the pocket engineered on the mutant protein. Wild-type (WT) bromodomains would then bind the bulky analog more weakly as a result of a steric clash between the bump and the naturally occurring residue (Fig. 1D).

We first inspected sequence alignments of the BET bromodomains (Fig. 2A) and their crystal structures with bound I-BET, JQ1, and GW841819X (Fig. 2B and fig. S2) to identify a suitable position for mutagenesis. These analyses revealed a leucine residue [L94 in Brd4(1)] from the ZA loop that is strictly conserved throughout the BET subfamily and forms side-chain hydrophobic contacts with the inhibitors, thus providing a general strategy. To introduce a hole that could accommodate bumped ligands, we mutated leucine to an alanine (L/A). All L/A mutants displayed melting temperatures (T_m) above 40°C and thermal shifts (ΔT_m) within +1° and –3°C relative to wild type in differential scanning fluorimetry (DSF) (table S2) and showed overall similar binding profiles toward multi-acetylated histone H4 peptides compared with that of the respective wild type, by means of biolayer interferometry (BLI) (fig. S3). Representative L/A mutants of both bromodomains of

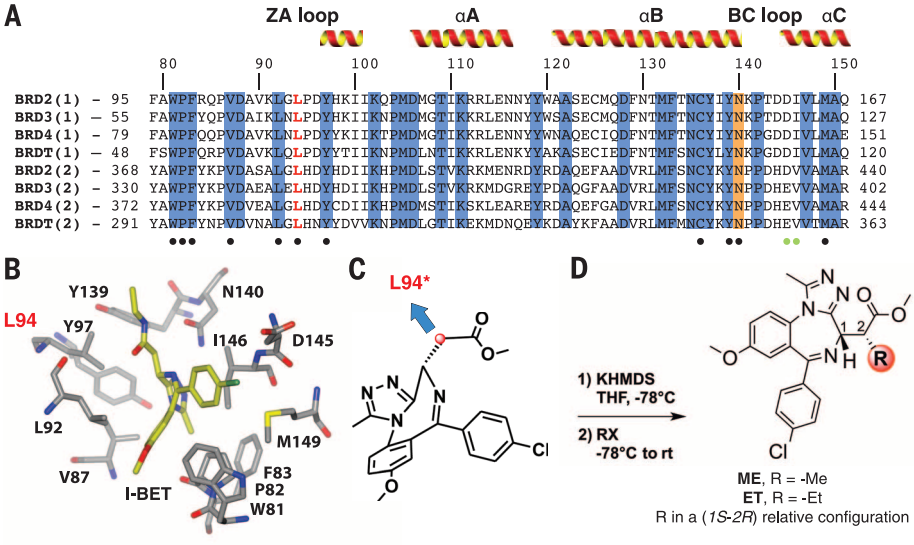

Fig. 2. Identification of L94 as mutational position and bumped ligand design. (**A**) Sequence alignment of the eight BET bromodomains. Conserved residues (blue) and a conserved asparagine (orange) that directly hydrogen bonds to acetyl-lysine are highlighted, and positions of α-helices are shown. Conserved and nonconserved residues making contacts with I-BET are highlighted with black and green dots, respectively. The targeted leucine residue is highlighted in red. The sequence numbering shown on top of the alignment is for Brd4(1). (**B**) Stick representation of I-BET (yellow carbons) and binding site residues of Brd4(1) [PDB 3P5O (*2*)]. L94 is highlighted in red. (**C**) Chemical structure of a methylester derivative of I-BET and position selected for derivatization to target a hole introduced by mutation at L94. (**D**) Synthetic route to introduce bumps at position 2 of the methylester side chain. R, alkyl; X, I; KHDMS = potassium bis(trimethylsilyl)amide.

Brd2 and Brd4 as well as singly and doubly mutated tandem constructs retained the ability to bind to a tetra-acetylated H4 peptide in isothermal titration calorimetry (ITC), showing K_d within five- to ninefold (first bromodomain) and 0.3- to 1.6-fold (second bromodomain) relative to that of the wild type (table S3). Furthermore, singly and doubly mutated full-length Brd4 constructs conditionally expressed with tetracycline could restore c-Myc mRNA levels in a background of small interfering RNA knockdown of endogenous Brd4 in U2OS osteosarcoma cells (fig. S4). Together, these results demonstrate that L/A mutants of BET bromodomains are stable, retain KAc-specific histone binding, and can substitute for WT functionality.

Analyses of crystal structures suggested that functionalization of the side chain methylene of I-BET (Fig. 2C, red carbon) could provide a desired bump to fill the hole introduced by the L/A mutation. Docking studies suggested optimal substitutions to be in a (*R*)-configuration (Fig. 2D and fig. S5). To minimize alteration in electrostatics and physicochemical properties of the ligand scaffold, a methylester analog of I-BET was functionalized with alkyl groups at the R position (Fig. 2D). Compounds **ME** (R = methyl) and **ET** (R = ethyl) were synthesized and tested by means of DSF and ITC to determine whether they are more selective for L/A than for WT proteins (Fig. 3, A and B). Ligand **ME** bound to WT Brd2(1) and Brd2(2) with K_d of 1.5 and 0.3 μM, respectively, which are a seven- and threefold weaker binding than I-BET as a result of introducing the bump. **ME** displayed K_d of 17 and 22 nM (ΔT_m of 7.9° and 9.3°C, respectively) against the corresponding L/A mutants, which are a 90- and 14-fold stronger binding relative to wild type. This promising selectivity profile was improved upon introducing a bulkier ethyl group. Compound **ET** showed K_ds of 74 and 86 nM (ΔT_m of 7.6° and 8.1°C) against Brd2(1)$_{L110A}$ and Brd2(2)$_{L383A}$, respectively, which are 120- and 200-fold increases in affinity compared with wild type (K_d, 9 and 17 μM) (Fig. 3, A and B).

To validate our design strategy, we solved high-resolution structures of Brd2(2)$_{L383A}$ apoprotein (apo) and in complex with **ME** and **ET** using x-ray crystallography (table S4 and figs. S6 to S8). The L/A mutant retained the same overall fold as the wild type (root mean square deviation of backbone atoms = 0.22 Å) (fig. S6). As predicted by docking, bumped ligands adopt the same binding mode as that of I-BET and JQ1 (fig. S8, A and B), positioning the respective methyl and ethyl substituents toward the hole introduced by the L/A mutation (Fig. 3, C and D, and fig. S8C). In particular, the ethyl group of **ET** achieves optimal shape complementarity with the engineered pocket (Fig. 3D) and desired steric clash against the Leu side chain present in the wild type (fig. S8D).

We next profiled selectivity across the entire BET bromodomain subfamily by characterizing the binding of **ET** to all WT and L/A mutant proteins by means of DSF (table S5) and ITC (Fig. 3, E and F, table S5, and fig. S9). **ET** induced high thermal stabilization of all L/A mutants, with ΔT_m ranging from 5.4° to 13.4°C, while stabilizing all WT proteins by less than 3°C (table S5). Pleasingly, **ET** maintained high binding affinity toward all L/A mutants, with K_d ranging from 36 to 200 nM (Fig. 3F) and large favorable binding enthalpies ΔH from −8 to −22 kcal/mol (table S5). Crucially, **ET** was notably less potent against WT bromodomains, with K_d ranging from 6 to 19 μM (Fig. 3E). A complete profile of **ET** binding affinity for L/A versus the wild type shows that binding selectivity of up to 540-fold and no less than 30-fold (average of 160-fold) is afforded across the subfamily (table S6). Taken together, these

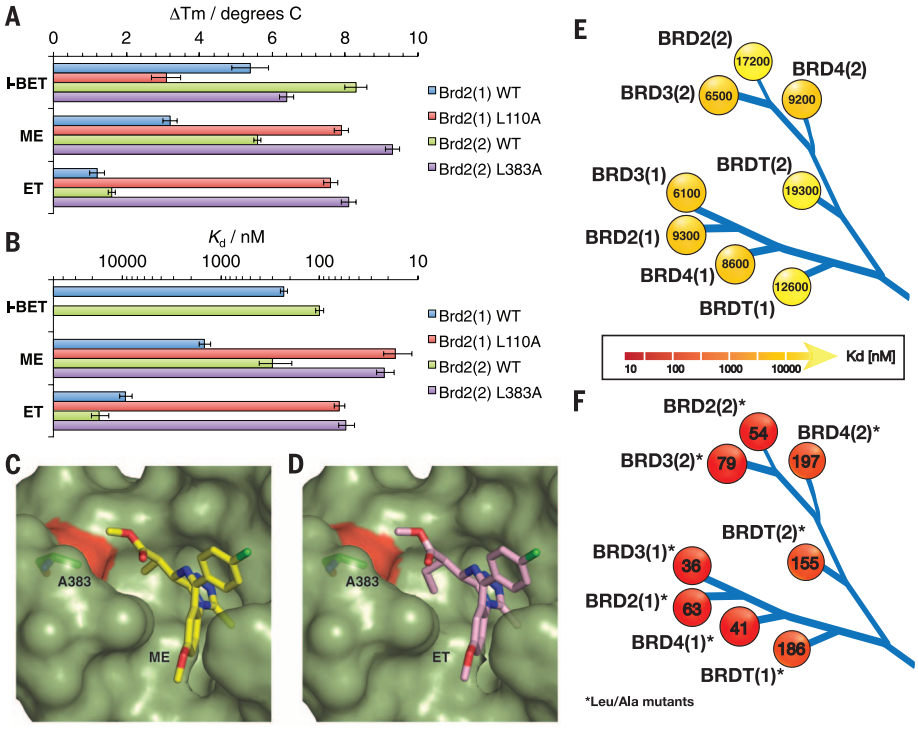

Fig. 3. Bumped ligand ET binds to engineered L/A bromodomains with high selectivity. (**A**) Thermal stabilization (ΔT_m, in degrees Celsius) of WT Brd2 bromodomains and their L/A mutants by I-BET, **ME**, and **ET** measured by means of DSF. The data shown are mean ± SD of three measurements. (**B**) Dissociation constants (K_d, in nanomolar) determined by means of ITC for I-BET binding to WT and for **ME** and **ET** binding to WT and L/A mutant Brd2 bromodomains. The error bars reflect the quality of the fit between the nonlinear least-squares curve and the experimental points. (**C** and **D**) Cocrystal structures of Brd2(2)L383A (green, surface representation) in complex with **ME** [(C) stick, yellow carbons] and **ET** [(D) stick, pink carbons]. The L/A mutation is shown in red, and A383 is shown as stick, green carbons. (**E** and **F**) Affinity profile (K_d, in nanomolar) of **ET** binding to (E) wild-type and (F) L/A mutant BET bromodomains measured by means of ITC.

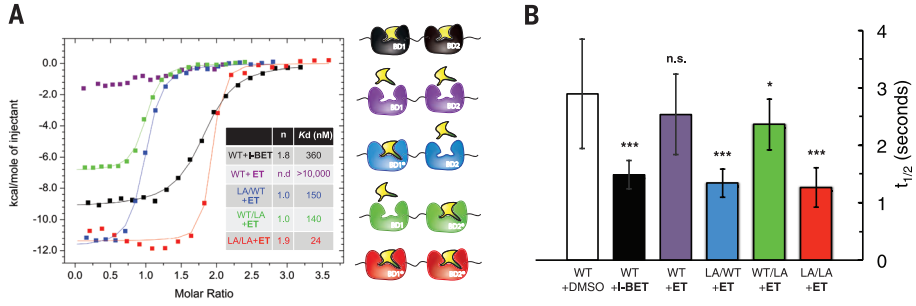

Fig. 4. ET is highly selective for L/A BET bromodomains in vitro and in cells. (**A**) ITC titrations of I-BET against WT tandem bromodomain construct of Brd2 (black) and of **ET** against the wild type (purple) and the same construct containing the L/A mutation in the first only (blue), second only (green), and both first and second bromodomains (red) at 30°C. Stoichiometry *n* and dissociation constants K_d are given in the inset table. (**B**) Evaluation of the selectivity of **ET** in human osteosarcoma cells (U2OS) cells by using FRAP. Quantitative comparison of half-time of fluorescence recovery are shown for cells transfected with full-length human green fluorescent protein (GFP)–Brd4 and treated with dimethyl sulfoxide (white, vehicle control) or 1 μM I-BET (black), and for cells expressing wild type (purple), L/A-WT (blue), WT-L/A (green), or double L/A (red) GFP-Brd4 and treated with 1 μM **ET**. The data shown represent the mean ± SEM (n = 16 to 21 biological replicates). Statistical significance was determined with one-tailed *t* tests: *P < 0.05; **P < 0.01; ***P < 0.001; n.s. not significant.

results demonstrate that our orthogonal **ET** and L/A mutant pairs achieve tailored high selectivity at the level of individual bromodomains.

To further demonstrate the feasibility of targeting the L/A mutation selectively, we characterized binding affinities and stoichiometries of **ET** within the context of a tandem bromodomain construct of Brd2 using ITC (Fig. 4A). In contrast to I-BET (K_d = 360 nM and expected stoichiometry of 2:1), no binding of **ET** to wild type was observed (K_d > 10 μM). The inactivity of **ET** against WT was further evidenced by its inability to induce upregulation of p21 mRNA levels, as reporter of downstream c-Myc activity (*14*), when compared with I-BET treatment in U2OS cells (fig. S10). However, **ET** exhibited K_d of 140 to 150 nM for the two single L/A mutants and 24 nM for the double mutant, with the expected 1:1 and 2:1 stoichiometries, respectively, confirming potent and selective targeting of mutant versus WT bromodomain (Fig. 4A).

To assess probe selectivity inside cells, we developed fluorescence recovery after photobleaching (FRAP) assays in U2OS cells transfected with full-length human Brd4. Control treatment with 1 μM I-BET accelerated the fluorescence recovery of the photobleached nuclear region of cells transfected with wild type (Fig. 4B, black, and fig. S11) relative to vehicle (Fig. 4B, white), indicating displacement of Brd4 from chromatin, as reported with JQ1 (*3*). As expected, exposure with 1 μM **ET** against wild type showed no significant reduction of recovery times relative to vehicle-treated cells (Fig. 4B, purple). Crucially, exposure of 1 μM **ET** against a double L(94,387)/A mutant showed recovery times comparable with the I-BET control in FRAP assays (Fig. 4B, red), and similarly fast recoveries were seen when the first domain only was mutated (Fig. 4B, blue) but not the second (Fig. 4B, green). Together, our data show that **ET** retains selectivity in cells and suggest that blockade of the first domain alone is sufficient to displace Brd4 from chromatin.

We describe a bump-and-hole approach to engineer controlled selectivity onto small-molecule modulation of BET bromodomains. We demonstrate that mutation of a conserved leucine residue within the bromodomain can be targeted by an ethyl derivative of I-BET with high potency and BET-subfamily selectivity in vitro and in cells. We also show proof of concept of applying orthogonal bromodomain:ligand pairs to dissect the role of individual bromodomains of Brd4 in chromatin binding. Future application of this approach could help identify which BET bromodomain target would be the most relevant therapeutic target in a given disease condition. To this end, recent advances in site-specific nuclease technologies for targeted genome engineering by use of clustered regulatory interspaced short palindromic repeat (CRISPR)/Cas9-based RNA-guided DNA endonucleases, among others (*15*, *16*), have opened up the possibility of systematically generating knock-in mutants in cells and living rodents (*17*). If a desired selectivity cannot be achieved at the KAc-binding site of WT bromodomains, it could be achieved instead by targeting allosteric sites or by modulating other specific protein-protein interactions of BET multiprotein complexes. Last, our approach could be extended to engineer selective chemical control within other subfamilies of the human bromodomain phylogenetic tree.

REFERENCES AND NOTES

1. A. C. Belkina, G. V. Denis, *Nat. Rev. Cancer* **12**, 465–477 (2012).
2. E. Nicodeme *et al.*, *Nature* **468**, 1119–1123 (2010).
3. P. Filippakopoulos *et al.*, *Nature* **468**, 1067–1073 (2010).
4. C. W. Chung *et al.*, *J. Med. Chem.* **54**, 3827–3838 (2011).
5. R. K. Prinjha, J. Witherington, K. Lee, *Trends Pharmacol. Sci.* **33**, 146–153 (2012).
6. GlaxoSmithKline, "A study to investigate the safety, pharmacokinetics, pharmacodynamics, and clinical activity of GSK525762 in subjects with NUT midline carcinoma (NMC)," ClinicalTrials.gov identifier NCT01587703; available at www.clinicaltrials.gov/show/NCT01587703.
7. J. E. Delmore *et al.*, *Cell* **146**, 904–917 (2011).
8. M. A. Dawson *et al.*, *Nature* **478**, 529–533 (2011).
9. J. Zuber *et al.*, *Nature* **478**, 524–528 (2011).
10. J. A. Mertz *et al.*, *Proc. Natl. Acad. Sci. U.S.A.* **108**, 16669–16674 (2011).
11. P. Filippakopoulos, S. Knapp, *Nat. Rev. Drug Discov.* **13**, 337–356 (2014).
12. K. Shah, Y. Liu, C. Deirmengian, K. M. Shokat, *Proc. Natl. Acad. Sci. U.S.A.* **94**, 3565–3570 (1997).
13. A. C. Bishop *et al.*, *Nature* **407**, 395–401 (2000).
14. F. Lamoureux *et al.*, *Nat. Commun.* **5**, 3511 (2014).
15. L. Cong *et al.*, *Science* **339**, 819–823 (2013).
16. P. Mali *et al.*, *Science* **339**, 823–826 (2013).
17. T. Gaj, C. A. Gersbach, C. F. Barbas 3rd, *Trends Biotechnol.* **31**, 397–405 (2013).

ACKNOWLEDGMENTS

We thank S. Knapp, O. Fedorov, and their team for constructs, assistance with BLI, and discussions; S. Swift for assistance with the Light Microscopy Facility; C. Conte, E. Griffis, V. Cowling, and M. Peggie for materials and discussions; and D. Chirgadze for assistance with the Crystallographic X-ray Facility. This work was supported by awards to A.C. from the UK Biotechnology and Biological Sciences Research Council (BBSRC, grant BB/J001201/1 and David Phillips Fellowship BB/G023123/1). E.L.S. and A.P. were supported by European Commission Erasmus work placement grants. Microscopy and biophysics were supported by Wellcome Trust strategic awards to the University of Dundee (097945/Z/11/Z and 100476/Z/12/Z, respectively). The University of Dundee and the authors have filed patent applications (GB1320994.5 and GB1401001.1) related to the use of the bump-and-hole BET bromodomain chemical probes and mutant pairs for examining the biological function of BET bromodomain proteins. Coordinates and structure factors have been deposited with the Protein Data Bank (PDB) under accession code 4QEU [$Brd2(2)_{L383A}$ apo], 4QEV (in complex with **ME**), and 4QEW (in complex with **ET**).

SUPPLEMENTARY MATERIALS

www.sciencemag.org/content/346/6209/638/suppl/DC1
Materials and Methods
Supplementary Text
Figs. S1 to S11
Tables S1 to S6
References (*18*–*36*)

17 December 2013; accepted 1 October 2014
10.1126/science.1249830

INNATE IMMUNITY

A Spaetzle-like role for nerve growth factor β in vertebrate immunity to *Staphylococcus aureus*

Lucy Hepburn,[1,2]* Tomasz K. Prajsnar,[3,4,5]* Catherine Klapholz,[1,2] Pablo Moreno,[1] Catherine A. Loynes,[5,6] Nikolay V. Ogryzko,[5] Karen Brown,[1,2,7] Mark Schiebler,[1,2] Krisztina Hegyi,[1,2]† Robin Antrobus,[1] Katherine L. Hammond,[5,6] John Connolly,[3,4] Bernardo Ochoa,[8] Clare Bryant,[9] Michael Otto,[10] Bas Surewaard,[11] Suranjith L. Seneviratne,[12] Dorothy M. Grogono,[2,7] Julien Cachat,[13] Tor Ny,[14] Arthur Kaser,[2] M. Estée Török,[2] Sharon J. Peacock,[2,15] Matthew Holden,[15,16] Tom Blundell,[8] Lihui Wang,[17] Petros Ligoxygakis,[17] Liliana Minichiello,[18] C. Geoff Woods,[1,19] Simon J. Foster,[3,4] Stephen A. Renshaw,[3,5,6]‡ R. Andres Floto[1,2,7]‡

Many key components of innate immunity to infection are shared between *Drosophila* and humans. However, the fly Toll ligand Spaetzle is not thought to have a vertebrate equivalent. We have found that the structurally related cystine-knot protein, nerve growth factor β (NGFβ), plays an unexpected Spaetzle-like role in immunity to *Staphylococcus aureus* infection in chordates. Deleterious mutations of either human NGFβ or its high-affinity receptor tropomyosin-related kinase receptor A (TRKA) were associated with severe *S. aureus* infections. NGFβ was released by macrophages in response to *S. aureus* exoproteins through activation of the NOD-like receptors NLRP3 and NLRP4 and enhanced phagocytosis and superoxide-dependent killing, stimulated proinflammatory cytokine production, and promoted calcium-dependent neutrophil recruitment. *TrkA* knockdown in zebrafish increased susceptibility to *S. aureus* infection, confirming an evolutionarily conserved role for NGFβ-TRKA signaling in pathogen-specific host immunity.

Staphylococcus aureus causes a range of serious infections, including skin ulceration, osteomyelitis, pneumonia, and septicaemia (*1*, *2*). Several evolutionarily conserved components of antistaphylococcal immunity have been identified using *Drosophila* as a model organism (*3*, *4*). One of the key mediators of immunity to Gram-positive bacteria in *Drosophila* is the soluble protein Spaetzle which, when activated by Spaetzle processing enzyme (SPE) upon

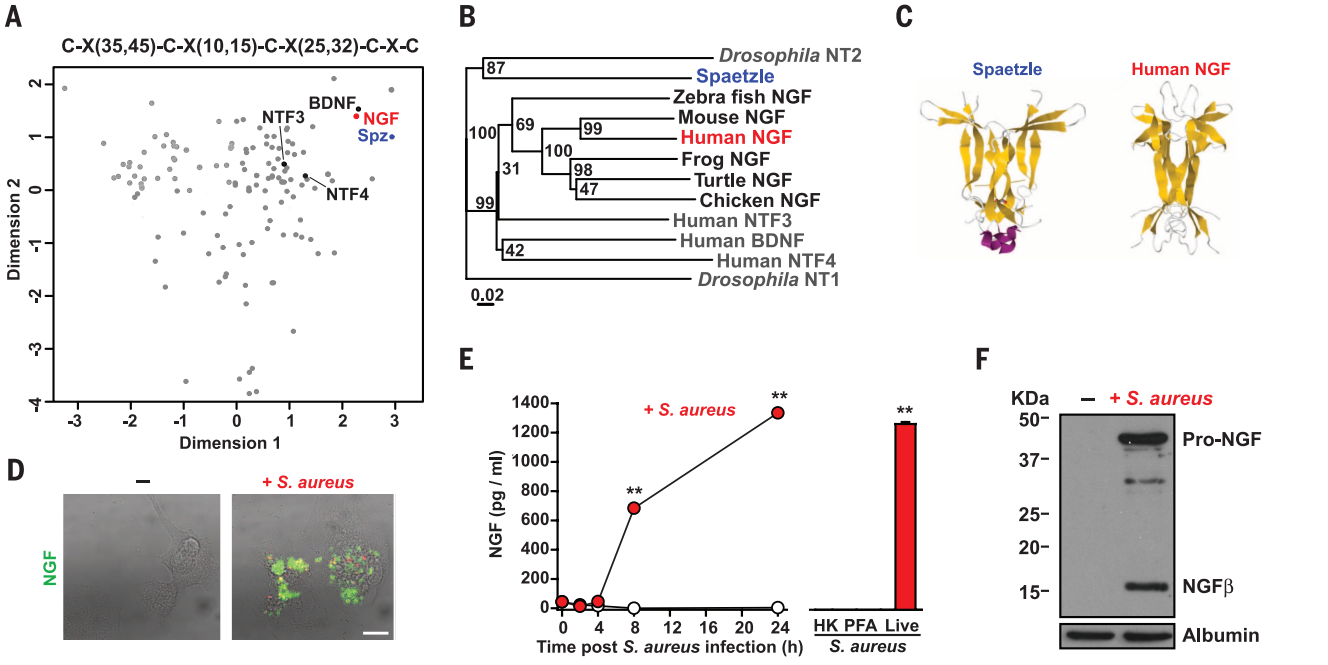

Fig. 1. NGFβ is implicated in antistaphylococcal immunity and is released from macrophages after *S. aureus* infection. (**A**) Bioinformatic identification of potential human orthologs of *Spaetzle*. The human proteome was searched using a PROSITE pattern to find soluble proteins potentially containing a >10-membered cystine-knot domain, which were then subjected to multifactorial analysis, incorporating structural prediction of disulphide bond formation with other structural and sequence parameters (see supplementary materials for details) to identify NGF (red) as the closest human ortholog to Spaetzle (Spz, blue). The other human neurotrophins [BDNF, neurotrophic factor 3 (NTF3), and NTF4 (black)] are also highlighted. (**B**) Phylogenetic alignment of vertebrate neurotrophic factors (NGF, BDNF, and NTF 3 and 4), *Drosophila* neurotrophin (NT) 1 and 2, and the *Drosophila* immune regulator Spaetzle, with bootstrap values. (**C**) Dimeric protein structures (from the Protein Data Bank) of Spaetzle and human NGFβ. (**D**) Intracellular staining of NGFβ (green) in primary human macrophages uninfected (left) or infected (right) with *S. aureus* (SH1000) (red) and then treated with monensin for 14 hours to prevent secretion. Scale bar, 5 μm. (**E**) Time course of NGFβ release from primary human macrophages after infection with *S. aureus*. NGFβ secretion requires live bacteria because heat-killed (HK) or paraformaldehyde (PFA)–killed *S. aureus* do not trigger NGFβ release. (**F**) Release of pro-NGF and NGFβ from differentiated THP-1 cells upon infection with *S. aureus* for 12 hours. *$P \leq 0.05$; **$P \leq 0.005$. All experiments were carried out in at least triplicate and are representative of at least three independent repeats.

infection, triggers effector immunity in an autocrine and paracrine manner through Toll receptor activation (*3*, *5*–*8*). To detect potential vertebrate equivalents of Spaetzle, we searched the human proteome using a relatively tolerant PROSITE pattern [C-X(35,45)-C-X(10,15)-C-X(25,32)-C-X-C; modified from (*9*)] to identify 166 soluble proteins potentially containing a >10-membered cystine knot domain (see the supplementary materials). We identified the neurotrophin nerve growth factor β (NGFβ) as a possible vertebrate ortholog of Spaetzle (Fig. 1, A and B). NGFβ regulates the survival, differentiation, and function of central and peripheral neurons (*10*, *11*), predominantly through activation of its high-affinity receptor, tropomyosin-related kinase receptor A (TRKA). Like Spaetzle, NGFβ is generated by enzymatic cleavage of a precursor proprotein to form a biologically active cystine-knot dimer (*11*) (Fig. 1C). Because NGFβ is implicated in the modulation of inflammation in non-neuronal cells (*12*–*14*), we asked whether NGFβ could play a Spaetzle-like role in coordinating vertebrate immunity to *S. aureus*.

Deleterious biallelic mutations in the genes encoding NGFβ (*NGF*) (*15*, *16*) or TRKA (*NTRK1*) (*17*) lead to a profound congenital sensory and autonomic neuropathy [termed hereditary sensory and autonomic neuropathy (HSAN) 4 and 5]. We found that these individuals also had frequent severe *S. aureus* infections of skin, teeth, joints, and bone (fig. S1), suggesting a pathogen-specific immune defect. To further explore the role of NGFβ in staphylococcal immunity, we measured its release from primary human macrophages obtained from healthy individuals. Infection of cells with live, but not killed, *S. aureus* stimulated de novo synthesis and secretion of both pro-NGF and mature NGFβ (Fig. 1, D to F). We found considerable variation in NGFβ stimulation by clinical isolates of *S. aureus*. Clones triggering lower levels of NGFβ were associated with increased all-cause patient mortality (fig. S1), again suggesting a protective role for NGFβ during *S. aureus* infection. The exact mechanisms generating mature NGFβ remain unclear, but it is likely that endogenous and exogenous host proteases [such as furins (*18*), matrix metalloproteinase (MMP) 7, and plasmin (*19*)], as well as bacterial proteases (fig. S1), combine to cleave pro-NGF during *S. aureus* infection, suggesting similarities with the regulation of Spaetzle processing (*20*).

We next examined whether other bacterial species were also able to stimulate NGFβ release from macrophages. Although a low-level response was seen with some other bacteria (such as

[1]Cambridge Institute for Medical Research, University of Cambridge, UK. [2]Department of Medicine, University of Cambridge, UK. [3]Krebs Institute, University of Sheffield, Western Bank, Sheffield, S10 2TN, UK. [4]Department of Molecular Biology and Biotechnology, University of Sheffield, Western Bank, Sheffield, S10 2TN, UK. [5]Bateson Centre, University of Sheffield, Western Bank, Sheffield, S10 2TN, UK. [6]Department of Infection and Immunity, University of Sheffield, Western Bank, Sheffield, S10 2TN, UK. [7]Cambridge Centre for Lung Infection, Papworth Hospital, Cambridge, UK. [8]Department of Biochemistry, University of Cambridge, UK. [9]Department of Veterinary Medicine, University of Cambridge, UK. [10]Laboratory of Human Bacterial Pathogenesis, National Institute of Allergy and Infectious Diseases (NIAID), National Institutes of Health (NIH), Bethesda, USA. [11]Department of Medical Microbiology, University Medical Centre, Utrecht, Netherlands. [12]Department of Clinical Immunology, Royal Free Hospital London, UK. [13]Department of Pathology and Immunology, Geneva University, Switzerland. [14]Department of Medical Biochemistry and Biophysics, Umea University, Sweden. [15]Wellcome Trust Sanger Institute, Hinxton, UK. [16]School of Medicine, University of St. Andrews, UK. [17]Biochemistry Department, Oxford University, UK. [18]Pharmacology Department, Oxford University, UK. [19]Department of Medical Genetics, University of Cambridge, UK.
*These authors contributed equally to this work. †Deceased.
‡Corresponding author. E-mail: arf27@cam.ac.uk (R.A.F.); s.a.renshaw@sheffield.ac.uk (S.A.R.)

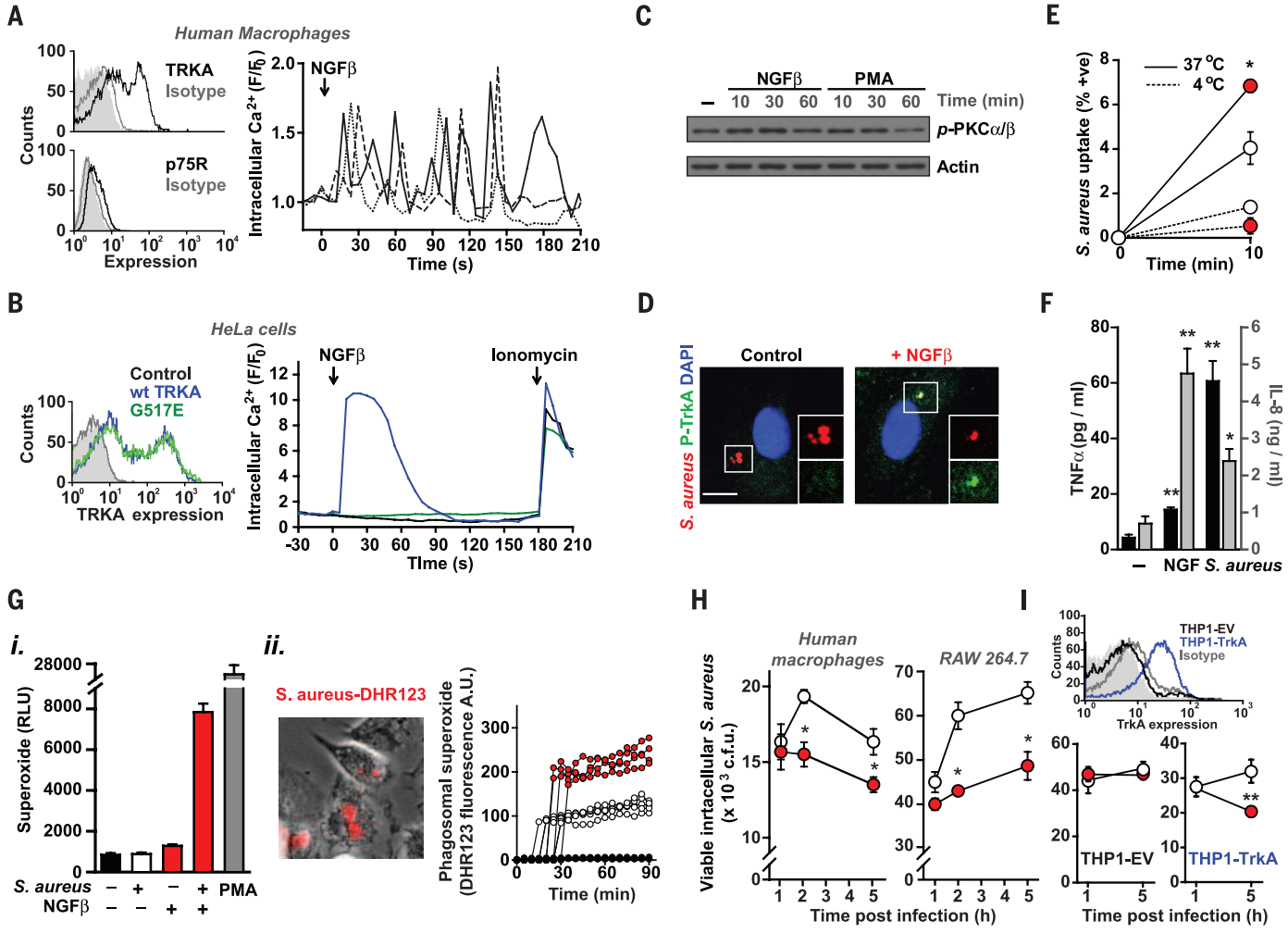

Fig. 2. Effects of NGFβ-TRKA signaling in human macrophages. (**A**) Addition of NGFβ (250 ng/ml; 9.25 μM) triggers sustained calcium oscillations in Fluo3-loaded primary human macrophages (detected by single-cell confocal imaging). Three representative recordings normalized for starting fluorescence (F/F_0) are shown. (Inset) Surface expression of TRKA and p75R (black) compared with isotype control (dark gray) or unstained cells (gray fill) on primary human macrophages. (**B**) Single-cell calcium signaling in GCamp3-expressing HeLa cells transfected with wild-type TRKA (blue), HSAN4-associated TRKA mutation (G517E; green) or empty vector (black) in response to NGFβ (250 ng/ml; 9.25 μM). (Inset) Surface expression of TRKA in transfected HeLa cells. (**C**) TRKA signaling in macrophages triggered rapid activation of calcium-dependent PKC isoforms. (**D**) Colocalization of intracellular phospho-TRKA (green) with red fluorescent protein (RFP)–labeled *S. aureus* (SH1000; red) in primary human macrophages treated for 30 min with 100 ng/ml (3.7 μM) NGFβ. (**E** and **F**) Addition of NGFβ to primary human macrophages increased (E) phagocytosis of RFP-labeled *S. aureus* and (F) release of TNFα and IL-8 (measured after 24 hours). (**G**) (i) Luminol-based detection of superoxide in response to *S. aureus*, NGFβ, or phorbol 12-myristate 13-acetate (PMA). (ii) The generation of phagosomal superoxide, monitored by DHR123-labeled heat-killed *S. aureus*, is increased in cells treated with the TRKA-specific agonist gambogic amide (250 nM; red) compared with vehicle (white; $P < 0.005$) or bacteria without cells (black). Four representative fluorescence traces from individual cells are shown for each group. (**H** and **I**) TRKA activation (by gambogic amide; 250 nM) enhanced intracellular killing of *S. aureus* in (H) primary human macrophages (left) and the mouse macrophage cell line RAW 264.7 (right) and (I) TRKA-transfected (blue), but not control (black), THP-1 cells. (Inset) Surface TRKA expression in THP-1 cells transfected with TRKA (blue) or empty vector (black) compared with isotype control (gray) and unstained cells (gray fill). All experiments were carried out in at least triplicate and are representative of at least three independent repeats.

Enterococcus faecalis), only *S. aureus* effectively triggered NGFβ release (fig. S1). Indeed, the closely related skin commensal *Staphylococcus epidermidis* was unable to stimulate NGFβ production effectively, suggesting that macrophages can discriminate between pathogenic and nonpathogenic staphylococcal species. Furthermore, macrophages only secreted NGFβ and not other neurotrophins [brain-derived growth factor (BDNF), NT3, and NT4] in response to infection (fig. S1). Thus, NGFβ may act as a specific and sensitive signal for *S. aureus* infection in man, potentially explaining the clinical phenotype of patients with HSAN 4 and 5 and suggesting a nonredundant and pathogen-specific role for NGFβ in innate immunity.

We then explored the cellular pathways triggering NGFβ generation. Rather than involving conventional surface pattern recognition receptors, *S. aureus* elicits NGFβ production through activation of nucleotide–binding and oligomerization domain (NOD)–like receptors (NLRs) (fig. S2), a well-recognized consequence of infection with this bacteria (*21*), and suggests an additional potential role for NGFβ during tissue damage.

To define the bacterial components responsible for NGFβ release from macrophages, we screened the Nebraska library of *S. aureus* transposon mutants (*22*) for their ability to stimulate NGFβ release from THP-1 cells. This identified a number of genes involved in bacterial cell wall synthesis, macromolecular transport, metabolism, and cellular regulation (fig. S3 and table S1), including the *saeR/saeS* 2 component gene system and autolysin, which regulate exoprotein

and peptidoglycan release, respectively (*23*, *24*). As expected, a number of purified *S. aureus*–derived exoproducts (protein A, peptidoglycan, and α-haemolysin) were able to stimulate NGFβ release in a proteinase K–dependent manner (fig. S3). Because most single exoprotein deletion mutants were still capable of stimulating NGFβ release, suggesting redundancy (fig. S4), we turned to comparative mass spectroscopy of conditioned media from wild-type and *saeS*-mutant *S. aureus* to define further bacterial components mediating NGFβ release (fig. S4) and identified alpha phenol–soluble modulins (α-PSMs), a recently described family of secreted peptides capable of membrane rupture (*25*), as putative factors (fig. S4). Thus, multiple *S. aureus* exoproteins can stimulate NGFβ release from macrophages. We asked whether this regulatory mechanism might be evolutionarily conserved to control Spaetzle production in *Drosophila*. Intriguingly, although the regulation of Spaetzle activity has focused on its SPE-mediated activation (*26*), pro-Spaetzle levels in *Drosophila* phagocytes (S2 cells) were stimulated by wild-type but not *saeR*-mutant *S. aureus*, by conditioned media, and by peptidoglycan (fig. S4), mirroring our results with NGFβ.

We then evaluated the effects of NGFβ on macrophage function. Primary human macrophages, which have constitutively high surface expression of TRKA but not the low-affinity NGF receptor p75, responded to NGFβ with sustained calcium signaling (Fig. 2A), which could be reconstituted in HeLa cells expressing wild-type TRKA but not the HSAN5-associated mutation G517E (Fig. 2B). TRKA signaling in macrophages also triggered rapid activation of calcium-dependent protein kinase C (PKC) isoforms (Fig. 2C), as well as other recognized components of TRKA signaling observed in neuronal cells (table S2). Because TRKA is thought to continue signaling after internalization, thereby permitting signal transmission along axons (*27*), we examined whether phagosomal TRKA activation might occur and found persistent tyrosine phosphorylation of TRKA within *S. aureus*–containing phagosomes (Fig. 2D). Functionally, TRKA activation led to enhanced phagocytosis (Fig. 2E), proinflammatory cytokine release from uninfected cells (Fig. 2F), and increased *S. aureus*–induced phagosomal superoxide generation (Fig. 2G). TRKA activation also enhanced intracellular killing of *S. aureus* in human and mouse macrophages (Fig. 2H) and in TRKA-transfected, but not control, THP-1 cells (Fig. 2I). This increased killing was dependent on intact receptor signaling (because it was not observed in cells from HSAN4 patients) and was principally mediated through enhanced superoxide generation (fig. S5) and autophagy (fig. S6). TRKA-dependent effector responses also depended on intact TLR signaling, because intracellular killing in *S. aureus*–infected cells and cytokine production in uninfected cells were abrogated in *Myd88*$^{-/-}$ and *Trif*$^{-/-}$ macrophages (fig. S7), suggesting an evolutionarily conserved interaction between cystine knot proteins and Toll family receptors.

We next determined the role of NGFβ-TRKA in human neutrophils, which are critical components of the host response to *S. aureus* infection (*28*). Neutrophils constitutively expressed TRKA (Fig. 3A) and released NGFβ in response to live *S. aureus* and peptidoglycan (Fig. 3B). As seen in macrophages, NGFβ stimulated neutrophils to generate superoxide (Fig. 3C) and secrete

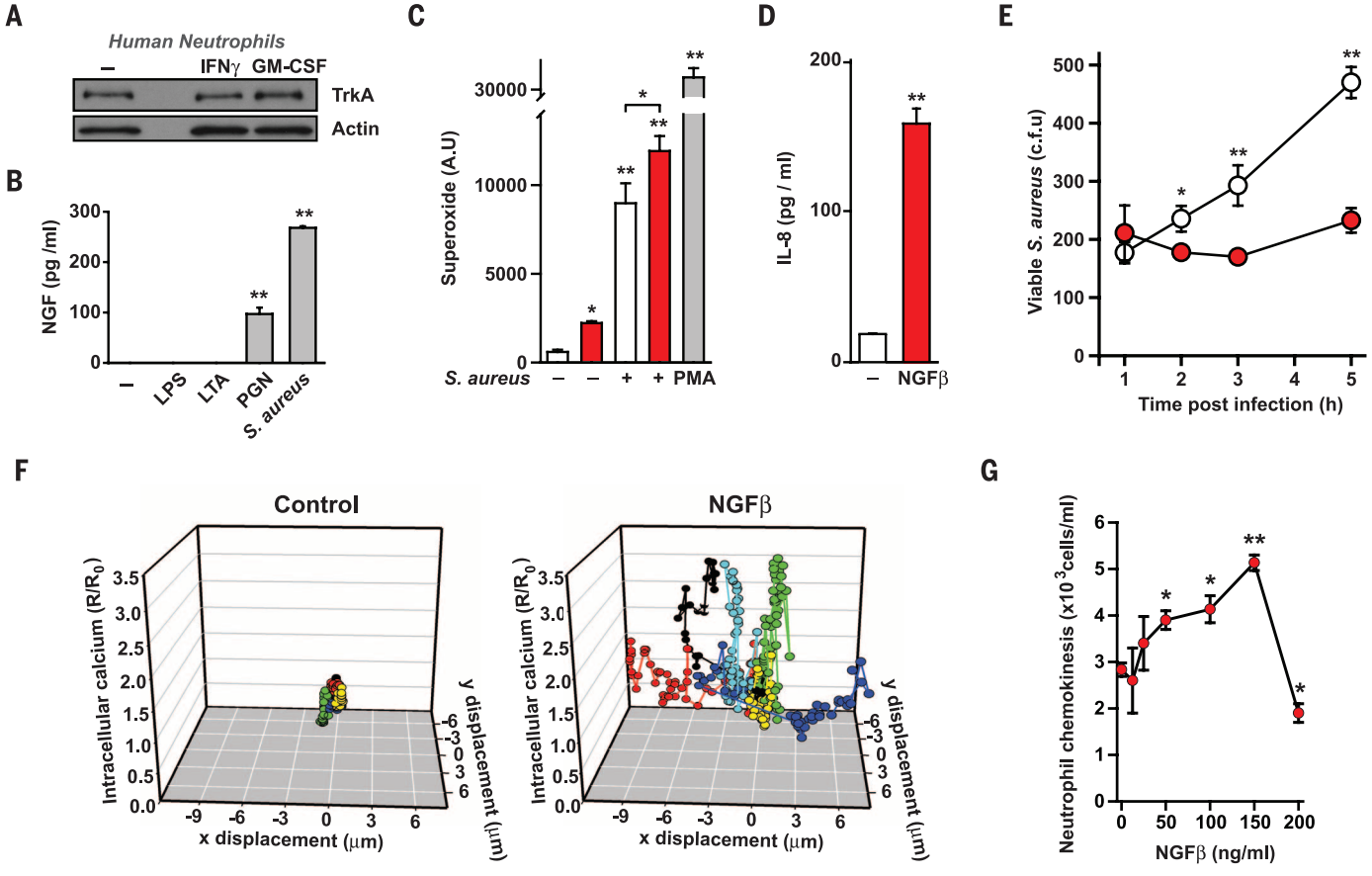

Fig. 3. NGFβ-TRKA signaling stimulates functional activation of neutrophils. (**A**) TRKA expression on untreated, IFN-γ (10 ng/ml) or granulocyte-macrophage colony-stimulating factor (100 ng/ml)–primed primary human neutrophils. (**B**) Neutrophils secrete NGFβ in response to live *S. aureus*, peptidoglycan (PGN) but not lipopolysaccharide (LPS; 100 ng/ml) or lipoteichoic acid (LTA; 5 μg/ml). (**C** and **D**) Neutrophils generate superoxide (C) and release interleukin-8 (IL-8) (D) in response to *S. aureus*, PMA, and/or NGFβ (red). (**E**) Killing of *S. aureus* by human neutrophils is enhanced by treatment with NGFβ (100 ng/ml; red) compared with control (white). (**F**) Representative plots of *x*-*y* displacement and calcium levels in individual neutrophils after addition of vehicle (control) or NGFβ. (**G**) Chemokinesis of human neutrophils assessed using a transwell assay in response to increasing concentrations of NGFβ. $*P \leq 0.05$; $**P \leq 0.005$. All experiments were carried out in at least triplicate and are representative of at least three independent repeats.

proinflammatory cytokines (Fig. 3D) and enhanced intracellular killing of *S. aureus* (Fig. 3E). NGFβ also stimulated chemokinesis and chemotaxis in a TRKA- and calcium-dependent manner (Fig. 3, F and G, movie S1, and fig. S8), suggesting that NGFβ may be an important chemotactic signal for neutrophil recruitment to sites of *S. aureus* infection.

To establish whether NGFβ-TRKA signaling represents a critical, evolutionarily conserved component of vertebrate immunity to *S. aureus* infection, we examined its role during in vivo infection of zebrafish. Effective morpholino knockdown of *trkA* was confirmed by immunohistochemistry, where we observed the expected loss of trkA protein in the forebrain and nose of zebrafish larvae (Fig. 4A). Knockdown of *trkA* had a major effect on the host response to *S. aureus*: *trkA* morphants were more susceptible to *S. aureus* infection than controls, a phenotype that could be rescued by concomitant injection of morpholino-resistant *trkA* RNA (Fig. 4B) and was only partially rescued in a transgenic line expressing trkA specifically in macrophages (fig. S9), suggesting the critical importance of trkA signaling in other cells (such as neutrophils). Bacterial counts in *trkA*-deficient fish rose faster and remained significantly higher than in controls (Fig. 4C). We then explored the relationship between the ability of bacteria to stimulate NGFβ release from macrophages and the in vivo effect of silencing trkA expression during infection (Fig. 4D). We observed a greater effect of *trkA* knockdown in fish infected with

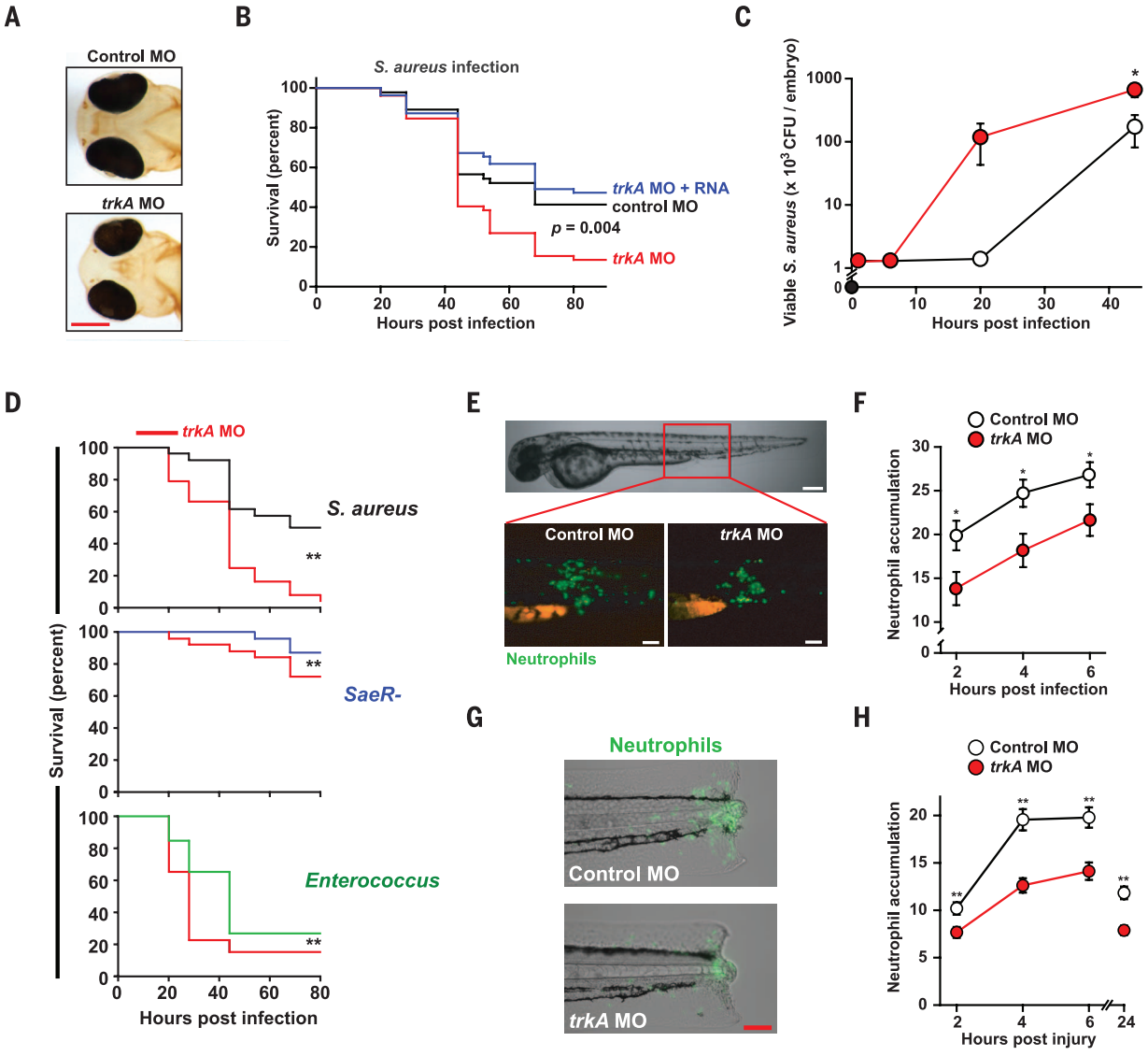

Fig. 4. Disruption of NGFβ-TrkA signaling compromises *S. aureus* immunity in vivo. (**A**) Reduced TrkA protein expression (assessed by immunohistochemistry) in the forebrain and nose of 72 hours post-infection zebrafish larvae injected with *trkA*-targeted (bottom) but not control (top) morpholinos. (**B**) Kaplan-Meier survival curves of fish infected with *S. aureus*. *TrkA* morphants (red) were more susceptible to *S. aureus* infection than controls (black) and could be rescued by concomitant injection of morpholino-resistant *trkA* RNA (blue). *N* of at least 45 fish per group performed as three independent experiments. (**C**) Numbers of viable *S. aureus* were significantly greater in *trkA* morphant (red) than control (white) fish, assessed as colony-forming units (CFU) per embryo. (**D**) Morpholino *trkA* knockdown (red) caused a greater effect on mortality in fish infected with wild-type (SH1000) *S. aureus* (black) compared to animals infected with bacteria less able to trigger NGFβ release from macrophages: the *saeR*–*S. aureus* mutant (causing a mild infection; blue) and *Enterococcus faecalis* (causing a severe infection; green). (**E** to **H**) Reduced migration of green fluorescent protein–tagged neutrophils to sites of *S. aureus* infection [(E) and (F)] or sterile inflammation [(G) and (H)] in *trkA* morphants (red) compared with controls (white). Representative images at 4 hours after infection (E) (scale bar: brightfield, 200 μm; fluorescence, 100 μm) or tail injury (G) (scale bar, 100 μm). *N* of at least 32 fish per group performed as three independent experiments. $^{*}P \le 0.05$; $^{**}P \le 0.005$; $^{***}P \le 0.0005$. Unless otherwise stated, data shown are representative of at least three independent experiments.

wild-type (SH1000) *S. aureus* compared to animals infected with bacteria less able to trigger NGFβ release from macrophages: the *saeR–S. aureus* mutant (causing a mild infection) and *Enterococcus* (causing a severe infection). Furthermore, *trkA* knockdown compromised neutrophil migration to sites of *S. aureus* infection (Fig. 4, E and F) as well as sterile inflammation (Fig. 4, G and H), supporting a role for NGFβ as an "alarmin" for both *S. aureus* infection and nonspecific tissue damage.

In summary, our results indicate a critical role for NGFβ-TRKA signaling in controlling vertebrate innate immunity during *S. aureus* infection. It is also conceivable that other vertebrate cystine-knot proteins might play similar roles to NGFβ for other bacterial pathogens. The recent finding that Spaetzle also functions as a neurotrophin in *Drosophila* (*29*) suggests an evolutionarily conserved dual function for cystine-knot proteins in both nerve development and antistaphylococcal immunity and may explain stimulation of aberrant nerve growth by soft-tissue infection by *S. aureus* (*30*). Our findings reveal pleotropic effects of the NGFβ-TRKA pathway that may particularly influence innate immunity to *S. aureus* infection, suggesting that, potentially, person-to-person variability in phagocyte secretion of, or response to, NGFβ may influence vulnerability to *S. aureus* infection and may provide opportunities for therapeutic intervention, particularly in multidrug-resistant disease.

REFERENCES AND NOTES

1. F. D. Lowy, *N. Engl. J. Med.* **339**, 520–532 (1998).
2. G. E. Thwaites *et al.*, *Lancet Infect. Dis.* **11**, 208–222 (2011).
3. B. Lemaitre, J. Hoffmann, *Annu. Rev. Immunol.* **25**, 697–743 (2007).
4. L. M. Stuart, R. A. Ezekowitz, *Nat. Rev. Immunol.* **8**, 131–141 (2008).
5. J. A. Hoffmann, *Nature* **426**, 33–38 (2003).
6. S. Valanne, J.-H. Wang, M. Rämet, *J. Immunol.* **186**, 649–656 (2011).
7. M. P. Belvin, K. V. Anderson, *Annu. Rev. Cell Dev. Biol.* **12**, 393–416 (1996).
8. A. N. Weber *et al.*, *Nat. Immunol.* **4**, 794–800 (2003).
9. U. A. Vitt, S. Y. Hsu, A. J. Hsueh, *Mol. Endocrinol.* **15**, 681–694 (2001).
10. S. Cohen, R. Levi-Montalcini, *Proc. Natl. Acad. Sci. U.S.A.* **42**, 571–574 (1956).
11. M. V. Sofroniew, C. L. Howe, W. C. Mobley, *Annu. Rev. Neurosci.* **24**, 1217–1281 (2001).
12. L. Aloe, R. Levi-Montalcini, *Brain Res.* **133**, 358–366 (1977).
13. U. Otten, P. Ehrhard, R. Peck, *Proc. Natl. Acad. Sci. U.S.A.* **86**, 10059–10063 (1989).
14. S. C. Bischoff, C. A. Dahinden, *Blood* **79**, 2662–2669 (1992).
15. E. Einarsdottir *et al.*, *Hum. Mol. Genet.* **13**, 799–805 (2004).
16. O. P. Carvalho *et al.*, *J. Med. Genet.* **48**, 131–135 (2011).
17. A. Rotthier, J. Baets, V. Timmerman, K. Janssens, *Nat. Rev. Neurol.* **8**, 73–85 (2012).
18. N. G. Seidah, S. Benjannet, S. Pareek, M. Chrétien, R. A. Murphy, *FEBS Lett.* **379**, 247–250 (1996).
19. M. A. Bruno, A. C. Cuello, *Proc. Natl. Acad. Sci. U.S.A.* **103**, 6735–6740 (2006).
20. L. El Chamy, V. Leclerc, I. Caldelari, J. M. Reichhart, *Nat. Immunol.* **9**, 1165–1170 (2008).
21. R. Muñoz-Planillo, L. Franchi, L. S. Miller, G. Núñez, *J. Immunol.* **183**, 3942–3948 (2009).
22. P. D. Fey *et al.*, *MBio* **4**, e00537-12 (2013).
23. M. A. Benson, S. Lilo, T. Nygaard, J. M. Voyich, V. J. Torres, *J. Bacteriol.* **194**, 4355–4365 (2012).
24. W. Vollmer, B. Joris, P. Charlier, S. Foster, *FEMS Microbiol. Rev.* **32**, 259–286 (2008).
25. A. Peschel, M. Otto, *Nat. Rev. Microbiol.* **11**, 667–673 (2013).
26. I. H. Jang *et al.*, *Dev. Cell* **10**, 45–55 (2006).
27. C. L. Howe, J. S. Valletta, A. S. Rusnak, W. C. Mobley, *Neuron* **32**, 801–814 (2001).
28. K. M. Rigby, F. R. DeLeo, *Semin. Immunopathol.* **34**, 237–259 (2012).
29. B. Zhu *et al.*, *PLOS Biol.* **6**, e284 (2008).
30. I. M. Chiu *et al.*, *Nature* **501**, 52–57 (2013).

ACKNOWLEDGMENTS

We thank S. Clegg and E. Henderson for help with patient samples, R. Mifsud and D. Cusens for initial phylogenetic and functional analysis, A. Segal for provision of *Nod2*$^{-/-}$ mouse bone marrow, and the aquarium staff of the Bateson Centre, University of Sheffield for zebrafish husbandry. This work was supported by The Wellcome Trust [Senior Clinical Research Fellowship to R.A.F. (084953), project grant to S.J.F./S.A.R. (089981), The Medical Research Council, UK (Research center grant (G0700091), Senior Clinical Fellowship to S.A.R. (G0701932)], Papworth Hospital and the National Institute for Health Research Cambridge Biomedical Research Centre, and the Intramural Research Program of NIAID, NIH.

SUPPLEMENTARY MATERIALS

www.sciencemag.org/content/346/6209/641/suppl/DC1
Figs. S1 to S9
Movie S1
Databases S1 and S2
References (*31*–*64*)

14 July 2014; accepted 2 October 2014
10.1126/science.1258705

PLANT GENETICS

A Y-chromosome–encoded small RNA acts as a sex determinant in persimmons

Takashi Akagi,[1,2] Isabelle M. Henry,[1] Ryutaro Tao,[2]* Luca Comai[1]*

In plants, multiple lineages have evolved sex chromosomes independently, providing a powerful comparative framework, but few specific determinants controlling the expression of a specific sex have been identified. We investigated sex determinants in the Caucasian persimmon, *Diospyros lotus,* a dioecious plant with heterogametic males (XY). Male-specific short nucleotide sequences were used to define a male-determining region. A combination of transcriptomics and evolutionary approaches detected a Y-specific sex-determinant candidate, *OGI*, that displays male-specific conservation among *Diospyros* species. *OGI* encodes a small RNA targeting the autosomal *MeGI* gene, a homeodomain transcription factor regulating anther fertility in a dosage-dependent fashion. This identification of a feminizing gene suppressed by a Y-chromosome–encoded small RNA contributes to our understanding of the evolution of sex chromosome systems in higher plants.

Sexuality promotes and maintains genetic diversity in eukaryotic organisms. The characterization of sex chromosomes revealed evolutionary mechanisms governing sexuality in animals (*1*–*3*). However, most plant sex chromosomes, which could be present in up to 5% of species (*4*, *5*), remain poorly characterized (*5*–*8*). Dioecy, the separation of sex organs among male and female individuals, can be controlled by a heterogametic male system comparable to that of mammals and based on X and Y chromosomes, or on the X-to-autosome ratio (*5*–*8*). Species with heterogametic females, such as those of birds (ZW system), are less common (*8*). Studies of Y-chromosome structure and evolution in *Silene latifolia* (*9*–*11*), papaya (*Carica papaya*) (*12*–*15*), and date palm (*16*) have revealed a heterochromatic nonrecombining region controlling sex determination, a feature shared by loci controlling other sexual characters such as asexual reproduction via apomixis and the inability to self-fertilize via self-incompatibility systems (*7*). For Y-linked sex determination, as for apomixis, it has been challenging to identify genetic determinants in this heterochromatic context. A theoretical model postulates that two changes must occur during the transition from hermaphroditism to dioecy: a recessive mutation resulting in male sterility and a dominant female-suppressing mutation (*8*, *17*).

The *Diospyros* genus, within the Ebanaceae (Ericales), contains mostly tree species, including the economically important persimmons (*D. kaki*, *D. virginiana*, and *D. lotus*) and ebony (*D. ebenum*). Dioecy may predate the divergence of the *Diospyros* genus (*18*) and possibly even the origin of the Ebenaceae (35 to 65 million years ago) (*18*–*20*). Male flowers have fertile stamens but rudimentary, arrested carpels and are organized in a three-flower cyme. Female flowers display developed but defective anthers that normally do not produce pollen grains (fig S1, A to P). Although a single female flower is formed per inflorescence, lateral aborted flower primordia are often visible on the flower pedicel (fig. S1, Q and R).

We used de novo whole-genome sequencing and transcriptome approaches to characterize the sex determination system in the diploid *D. lotus*, located to a single sex determination (SD) locus on the Y chromosome (*21*).

[1]Department of Plant Biology and Genome Center, University of California Davis, Davis, CA, USA. [2]Laboratory of Pomology, Graduate School of Agriculture, Kyoto University, Kyoto, Japan.
***Corresponding author. E-mail: rtao@kais.kyoto-u.ac.jp (R.T.); lcomai@ucdavis.edu (L.C.)**

To identify male-specific sequences, genomic sequencing libraries were constructed from *D. lotus*, segregating F_1 sibling trees (*21*). Libraries pooled according to sex were sequenced to an estimated 45 to 50× coverage (Fig. 1A). Every 35–base pair (bp) subsequence (35-mer or k-mer) present in these sequencing reads was cataloged, and reads including significant male-pool–specific k-mers (MSKs) (Fig. 1B) were used for in silico assembly (methods 2 and 3) of 5100 contigs putatively located on the Y chromosome. We discarded those in which potential Y-specific polymorphisms perfectly matched reads from one or more female samples, which suggests that they are probably located in a region of active recombination (fig. S2). Integrating and expanding the remaining contigs resulted in ~800 contigs located on putative male-specific regions of the Y chromosome (MSYs, fig. S3) and amounting to a total length of ~1 Mb (Fig. 1C).

To identify genes expressed during the differentiation of male androecia and female gynoecia, RNA-Seq was performed on tissue from mixed buds, including floral organ primordia, from nine males and nine females from the F_1 used for the genomic analysis, and their parents. We followed three complementary approaches to interpret these expression data: (i) we mapped the reads to the MSY genomic contigs; (ii) we seeded assembly with the reads, including male-specific

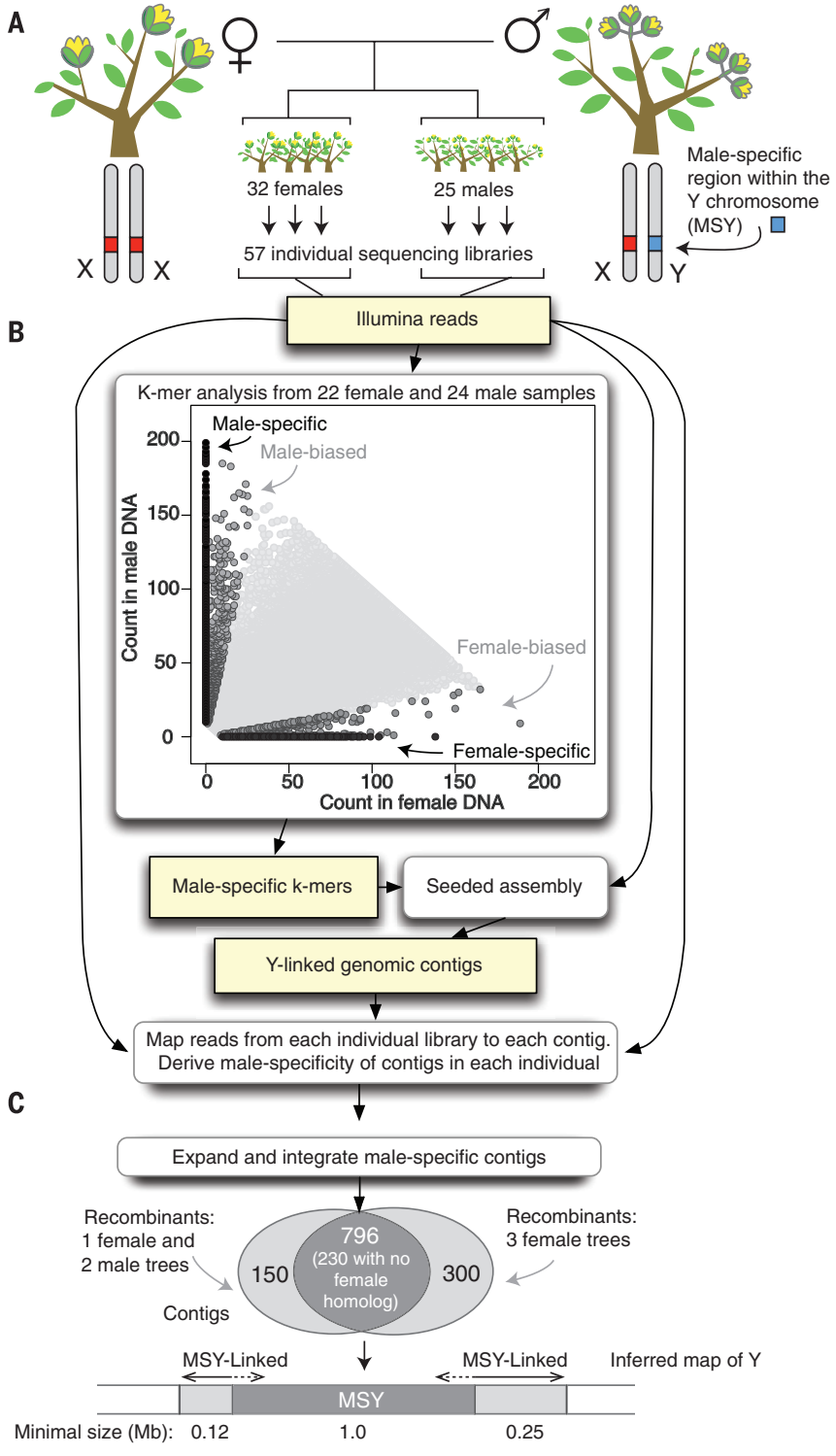

Fig. 1. Identification of male-specific sequences from genomic sequence reads. (**A**) Genomic sequencing libraries were created from *D. lotus* segregating F_1 sibling trees. (**B**) Reads from samples of the same gender were pooled and searched for the presence of gender-specific 35-bp k-mers (see inset graph). Reads including MSKs were assembled to generate Y-linked genomic contigs. (Inset graph) Distribution of gender-specific or -biased k-mers (35 bp). (**C**) Expected organization of the assembled contigs within the MSY locus and surrounding regions. Different numbers of individuals in (A) and (B) reflect availability through sexual maturity in the sib-family.

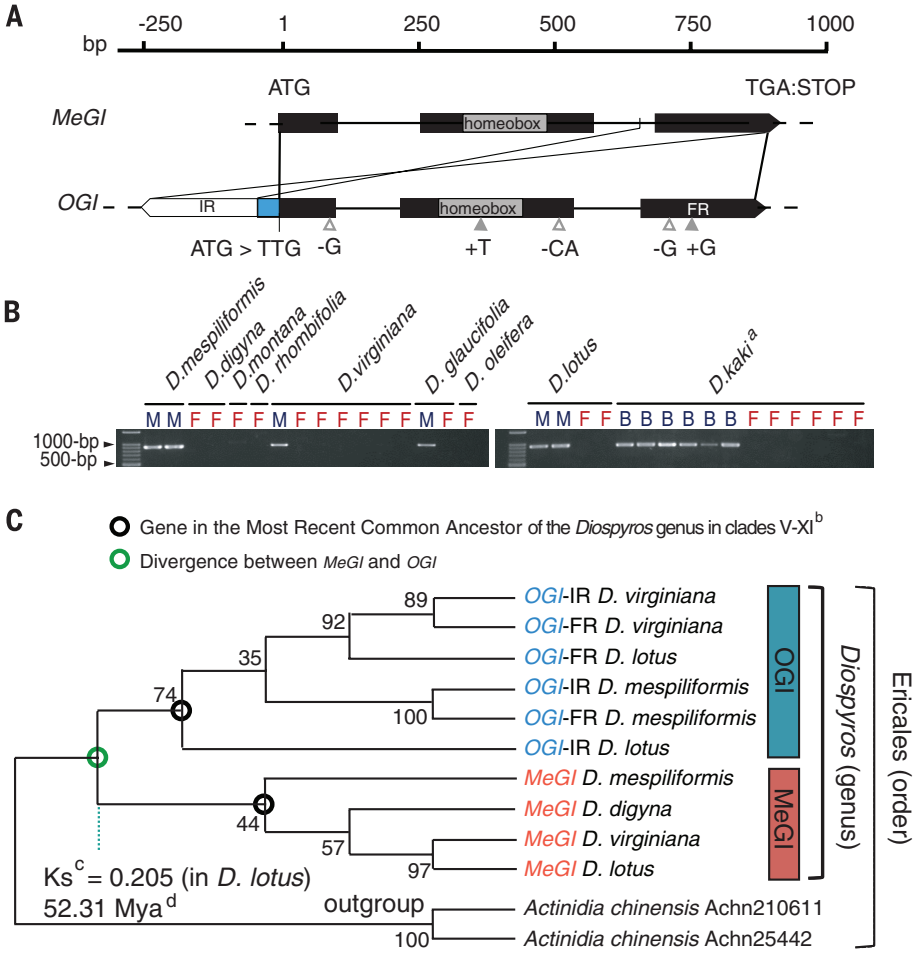

Fig. 2. Sequence and expression analysis of *OGI* and *MeGI*. (**A**) Comparative structure of the *OGI* and *MeGI* genes. White and gray triangles in the *OGI* coding regions indicate disruptive deletions and insertions, respectively. Homeobox domains are noted. The blue region in *OGI* bears no homology to the *MeGI* sequences. (**B**) PCR amplification of the *OGI* gene in males (M) and females (F) of *Diospyros* species. ([a]) In hexaploid *D. kaki*, monoecious (B) cultivars bear both male and female flowers. (**C**) Maximum likelihood–based phylogenetic tree of the *OGI* (blue) forward (FR) and inverted (IR) repeat sequences and the corresponding region from the *MeGI* (red) sequence, from various *Diospyros* species. One-tenth values of bootstraps from 1000 replicates are indicated on the branches. ([b]) Taxa cover a substantial portion of the *Diospyros* genus (*18*, *20*). ([c]) Ks value from the codon frame of the *MeGI* gene used to estimate ([d]) the timing of divergence between *MeGI* and *OGI* (method 8), to at least 52 million years ago, before the origin of the *Diospyros* genus.

cDNA k-mers (methods 2 and 4, fig. S4); and (iii) we assembled a draft of the transcriptome and identified genes that were differentially expressed between male and female individuals (method 6). Most of the expressed (reads per kilobase of sequence per million mapped reads) > 1.0) gene fragments isolated from (i) and (ii) were identical, even though they were derived independently, suggesting that we had successfully identified the majority of the sequences associated with MSYs (fig. S5). After integration of the genes identified using those two approaches, 22 candidate genes underlying the SD locus were identified (table S1).

We identified 62 genes that were differentially expressed between male and female samples [false discovery rate (FDR) < 0.01, table S2], seven of which were MSY-linked. We focused on a pair of class I homeodomain transcription factors, because the first gene, which we named *OGI* (Japanese for "male tree"), exhibits male-specific expression in developing buds, is a Y-specific SD candidate with no homologous sequence in the female genomic reads, and its coding sequence presents multiple disruptive stop codons. The second gene, which we named *MeGI* (Japanese for "female tree"), is not MSY-linked and is thus located on an autosomal region, but exhibited female-biased bud- and flower-specific expression (fig. S6, A and B) (FDR = 1×10^{-05}, table S2). Moreover, these two genes are monophyletic orthologs of the barley *Vrs1* gene (fig. S7). In barley, mutation of *Vrs1* lifts the developmental inhibition on the lateral flowers, resulting in fully fertile three-flower inflorescences instead of a single central fertile flower and two rudimentary lateral spikelets (*22*, *23*). This mutant is architecturally similar to the male flowers of *D. lotus*, whereas wild-type barley architecture resembles that of female *D. lotus* flowers (fig. S1, Q and R). *OGI* sequence analysis predicted the presence of a hairpin structure, with high similarity to the homologous region of the *MeGI* gene (Fig. 2A and fig. S8).

Despite multiple disruptive mutations, the *OGI* gene sequence and male specificity are highly conserved in the *Diospyros* genus (Fig. 2B). Phylogenetic analyses suggest that the establishment of *OGI* predated *Diospyros* radiation (Fig. 2C and fig. S9) and that suppressed recombination maintained *OGI* on the Y chromosome for tens of millions of years. The nucleotide substitution patterns within the *OGI* repeats suggest lineage-independent coevolution (fig. S10), which is consistent with selective pressure maintaining a conserved double-stranded RNA structure. Furthermore, sequence analysis of ~150 kb surrounding *OGI* revealed highly repetitive sequences and the presence of male-specific regions (fig. S11), similar to MSY regions from other species (*3*, *14*). In contrast, divergence between the X and Y alleles of the other 21 SD candidates suggests that they were established more recently than dioecy within this genus (*18*, *20*) (figs. S9 and S12, table S3, and text S1 and S2). In conclusion, evolutionary inference supported *OGI* as the best SD candidate.

There is no proven method for *D. lotus* transformation, but it is expected to take several years. Therefore, we elected to functionally characterize *OGI* and *MeGI* in other systems instead. Transient coexpression assays in tobacco (*Nicotiana benthamiana*) demonstrated that overexpression of *OGI* suppressed the expression of *MeGI* (fig. S13A) (P = 0.00082, Student's t test), suggesting that *OGI* can repress *MeGI* in plants.

Three of 11 *Arabidopsis thaliana* plants independently transformed with *MeGI* driven by the constitutive CaMV35S promoter (table S4) exhibited stunted growth and sterile androecia, occasionally producing nonfunctional pollenlike grains (Fig. 3, A to I), whereas carpels could produce fertile seeds upon cross-pollination (Fig. 3, J and K). The other eight *A. thaliana* transformants carrying the same overexpression construct were not stunted and were typically male-fertile (Fig. 3L, fig. S14, and table S4) but also displayed *MeGI* mRNA incomplete splicing, resulting in low expression of the functional *MeGI* transcript (P = 0.0017, Student's t test; Fig. 3, M and N). Similarly, in *N. tabacum*, 5 out of 12 plants transformed with *MeGI* driven by its native promoter exhibited low pollen germination (P < 0.005, Student's t test)

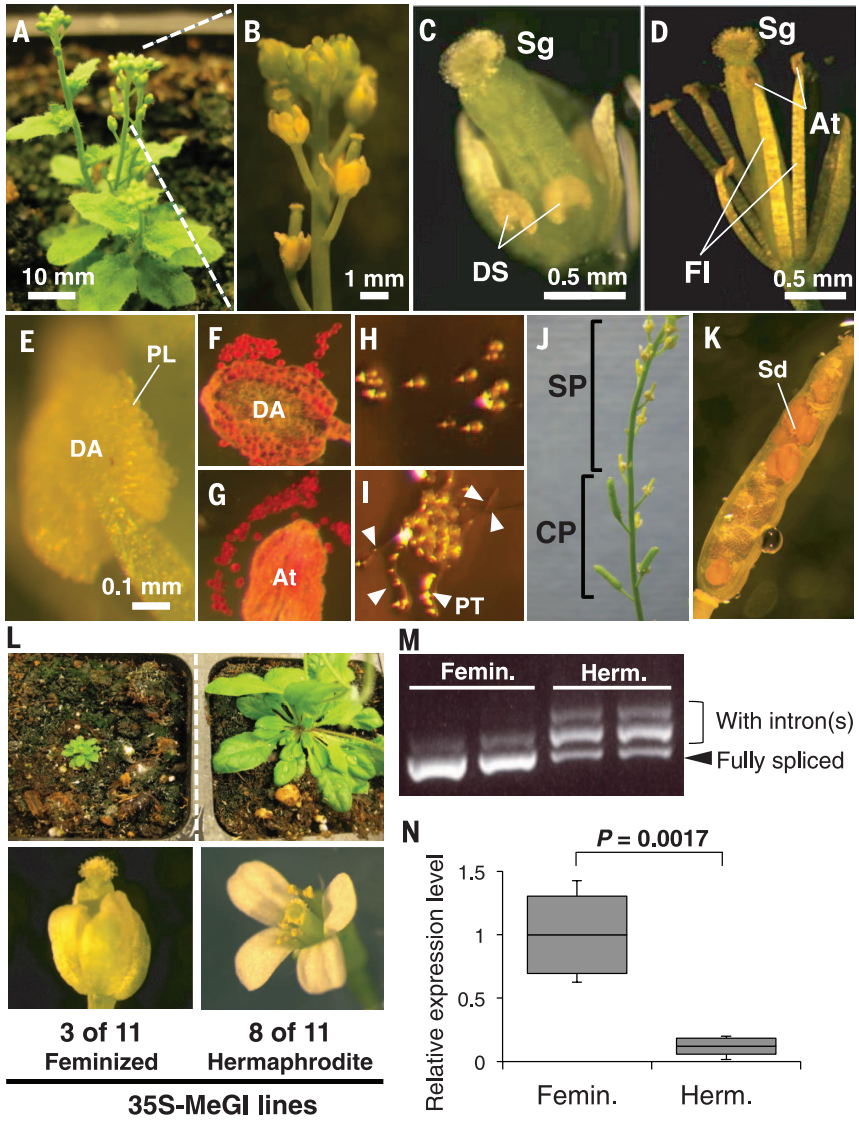

Fig. 3. Phenotypes of *A. thaliana* plants overexpressing *MeGI* under the control of the CaMV-35S promoter. (A) to (K) Severe feminized and stunted phenotypes. (**A**) Whole plants at 62 days after germination. (**B**) Defective development of stamens and petals. (**C** and **D**) Dissected flowers (without petals and sepals) of 35S-MeGI (C) and control (D). Sg, stigma; DS, defective stamens; St, stamens; At, anthers; Fl, filaments. (**E**) Pollenlike grains (PL) sometimes produced from defective anthers (DA) in fully mature flowers. (**F** and **G**) Positive vital staining of pollen(-like) grain from the 35S-MeGI (F) and control (G) plants. (**H** and **I**) Pollen tube (PT) formation assay for 35S-MeGI (H, negative) and control (I, positive) plants. (**J** and **K**) Silique elongation and seed (Sd) formation after cross-pollination using wild-type (Col-0) pollen (CP) but not after self-pollination (SP). (L) to (N) Comparison of stunted and feminized (Femin.), and WT-like and hermaphroditic (Herm.) 35S-MeGI lines. (**L**) Representative phenotypes. (**M** and **N**) Polymerase chain reaction (PCR) amplification of genomic *MeGI* sequence (M), including both introns (Fig. 2A) and quantitative PCR (N) corresponding to fully spliced *MeGI*. *MeGI* transcripts in hermaphroditic plants exhibited incomplete splicing (M), resulting in at least a two- to threefold reduction in functional transcript levels (N).

and shorter androecia, whereas carpels remained normal (fig. S15). Taken together, the phenotypes observed in transgenic *A. thaliana* and *N. tabacum* were consistent with the morphology of female flowers in *D. lotus* (fig. S1). Furthermore, the association of male sterility with higher expression of *MeGI* in persimmon and in transgenic *Arabidopsis* suggested that *MeGI* may be a dosage-dependent growth inhibitor that can sterilize androecia. The *OGI* RNA hairpin structure suggested a role for RNA interference in *MeGI* repression. To test this hypothesis, we analyzed small RNA. *OGI* production of male-specific 21-bp small RNAs was high in buds and low in flowers. *MeGI*-specific small RNAs accumulated in the buds and flowers of males only, consistent with *OGI* triggering transitive and persistent small RNA production from *MeGI* (Fig. 4A and figs. S6C and S13B).

Our data suggest a model for sex determination in *Diospyros*, in which *OGI*, or *Oppressor of MeGI,* represses the expression of the feminizing *Male Growth Inhibitor* gene, *MeGI,* in male flowers (Fig. 4B). *OGI*'s role as a dominant suppressor of feminization could be consistent with the Su^F gene model (*17*) for the establishment of dioecy. There is no evidence that *MeGI* promotes gynoecia formation. Instead, evidence from *MeGI* expression in hermaphroditic *Arabidopsis* supports a feminizing role through androecia sterilization. Mechanisms affecting gynoecia formation in *Diospyros* are still missing in this model, and an additional Y-linked locus may be required, as postulated by the two-mutation model for the evolution of dioecy (*8*, *17*). Alternatively, a single master regulator of sex determination, such as *SRY* in humans, may be sufficient (*2*, *8*, *24*). Together with findings that a W-encoded Piwi-interacting RNA determines sex in silkworms (*25*), our results suggest that RNA-based sex-determining mechanisms may be present in other systems as well. The involvement of small RNAs in sex determination might explain why they have been difficult to identify so far. Our discovery in *Diospyros* of a small-RNA–based repressor encoded by the Y chromosome and acting on a transcription factor that affects another fertility provides a plausible sex-determination mechanism and an exciting starting point for comparison with other dioecious systems.

REFERENCES AND NOTES

1. B. Charlesworth, *Curr. Biol.* **6**, 149–162 (1996).
2. D. Bachtrog, *Curr. Opin. Genet. Dev.* **16**, 578–585 (2006).
3. D. Bachtrog, *Nat. Rev. Genet.* **14**, 113–124 (2013).
4. C. Yampolsky, H. Yampolsky, *Bibl. Genet.* **3**, 1–62 (1922).
5. R. Ming, J. Wang, P. H. Moore, A. H. Paterson, *Am. J. Bot.* **94**, 141–150 (2007).
6. C. Ainsworth, *Ann. Bot.* **86**, 211–221 (2000).
7. R. Ming, A. Bendahmane, S. S. Renner, *Annu. Rev. Plant Biol.* **62**, 485–514 (2011).
8. D. Charlesworth, *J. Exp. Bot.* **64**, 405–420 (2013).
9. R. Bergero, S. Qiu, A. Forrest, H. Borthwick, D. Charlesworth, *Genetics* **194**, 673–686 (2013).
10. N. Blavet *et al.*, *BMC Genomics* **13**, 226 (2012).
11. E. Kejnovsky, B. Vyskot, *Cytogenet. Genome Res.* **129**, 250–262 (2010).
12. Z. Liu *et al.*, *Nature* **427**, 348–352 (2004).
13. A. R. Gschwend *et al.*, *Proc. Natl. Acad. Sci. U.S.A.* **109**, 13716–13721 (2012).
14. J. Wang *et al.*, *Proc. Natl. Acad. Sci. U.S.A.* **109**, 13710–13715 (2012).
15. R. Aryal, R. Ming, *Plant Sci.* **217-218**, 56–62 (2014).
16. E. Cherif *et al.*, *New Phytol.* **197**, 409–415 (2013).
17. B. Charlesworth, D. Charlesworth, *Am. Nat.* **112**, 975–997 (1978).

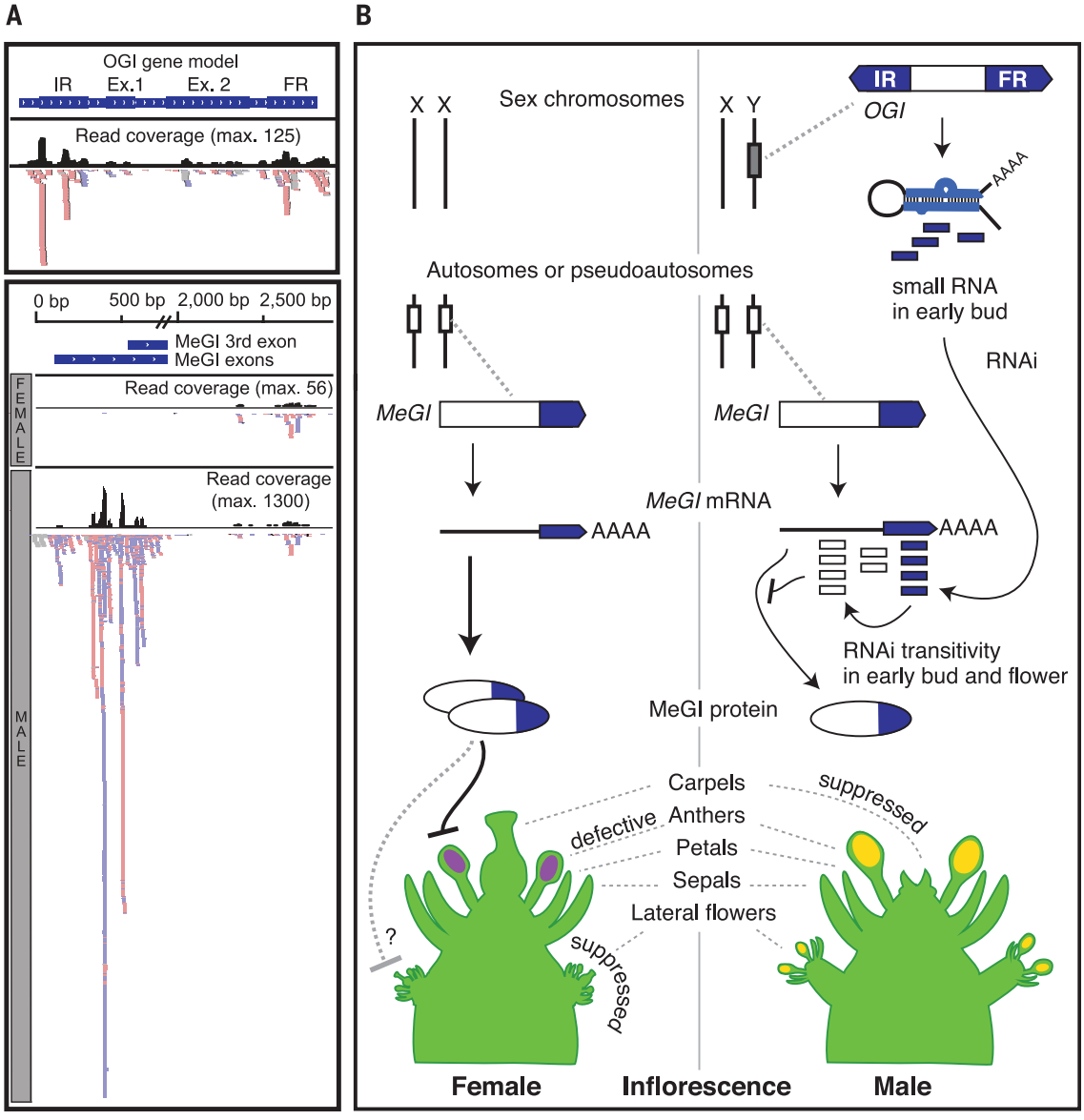

Fig. 4. Functional analysis of *OGI* and *MeGI*. (**A**) Small-RNA sequencing of developing male and female buds and read mapping to *OGI* (top) and *MeGI* (bottom) sequences. The *OGI* gene model and *MeGI* cDNA are shown on top. Coverage distributions and read mapping in the forward (pink) and reverse (blue) direction are shown for male reads for *OGI* and both male and female reads for *MeGI*. No female reads mapped to *OGI*. (**B**) Chromosomal map of *OGI* and *MeGI*, with a model of their interaction and potential function in female (left) and male (right) flower development. RNAi, RNA interference. The model omits a mechanism for male suppression of gynoecia. A second, dominant Y-linked gene could exist. Alternatively, under a single sex-determination model, *OGI*-mediated repression of *MeGI* might limit the gynoecia.

18. S. Duangjai, B. Wallnöfer, R. Samuel, J. Munzinger, M. W. Chase, *Am. J. Bot.* **93**, 1808–1827 (2006).
19. D. C. Christophel, J. F. Basinger, *Nature* **296**, 439–441 (1982).
20. B. Turner *et al.*, *Mol. Phylogenet. Evol.* **69**, 740–763 (2013).
21. T. Akagi *et al.*, *J. Jpn. Soc. Hortic. Sci.* **83**, 214–221 (2014).
22. T. Komatsuda *et al.*, *Proc. Natl. Acad. Sci. U.S.A.* **104**, 1424–1429 (2007).
23. S. Sakuma *et al.*, *New Phytol.* **197**, 939–948 (2013).
24. A. E. Quinn, S. D. Sarre, T. Ezaz, J. A. Marshall Graves, A. Georges, *Biol. Lett.* **7**, 443–448 (2011).
25. T. Kiuchi *et al.*, *Nature* **509**, 633–636 (2014).

ACKNOWLEDGMENTS

We thank M. Lieberman and K. Ngo for bioinformatics support, the University of California Davis Genome Center DNA Technologies Core for sequencing support, and the U.S. Department of Agriculture's Agricultural Research Service for providing plant samples from various *Diospyros* species. Supported by a Grant-in-Aid from the Japan Society for the Promotion of Science (JSPS) fellows (to T.A.); a Grant-in-Aid for Young Scientists (A) (no. 26712005 to T.A.) and for Challenging Exploratory Research (no. 26660025 to R.T.) from JSPS; a University of California Davis Genome Center seed grant (to I.M.H.); and the Office of Science (Biology and Environmental Research) of the U. S. Department of Energy (grant DE-SC0007183 to L.C.). All sequence data generated in the context of this manuscript have been deposited in the appropriate NCBI database: Illumina and PacBio reads in the Short Read Archives (SRA) database (SRA ID SRP045872), RNA-Seq reads and associated statistics in the Gene Expression Omnibus (GEO: GSE61386) database (BioProject ID PRJNA261435), and the OGI and MeGI genomic sequences obtained from various *Diospyros* species were submitted to GenBank (IDs KM408638 to KM408642). The Whole Genome Shotgun (WGS) project has been deposited at DDBJ/EMBL/GenBank under the accession no. JRBH00000000. The version described in this paper is version JRBH01000000. The Transcriptome Shotgun Assembly (TSA) project has been deposited at DDBJ/EMBL/GenBank under the accession no. GBSJ00000000. The version described in this paper is the first version, GBSJ01000000. The authors declare no competing financial interests. T.A., I.M.H., and L.C. designed the experiments. T.A. performed the experiments. T.A. and I.M.H. analyzed the data. R.T. initiated the study and maintained the KK persimmon sib-family. T.A. drafted the manuscript. All authors participated in data interpretation, edited the manuscript, and approved the final manuscript. Correspondence and requests for materials should be addressed to R.T. (rtao@kais.kyoto-u.ac.jp) and L.C. (lcomai@udavis.edu).

SUPPLEMENTARY MATERIALS

www.sciencemag.org/content/346/6209/646/suppl/DC1
Materials and Methods
Supplementary Text S1 and S2
Figs. S1 to S15
Tables S1 to S7
References (*26*–*46*)

10 June 2014; accepted 26 September 2014
10.1126/science.1257225

Human Heart Cell Model

Identifying potential cardiotoxicity as early as possible in the drug development process can reduce the risk of costly program failures and minimize health risks. Cytiva Plus provides a high-fidelity human heart cell model that is available in quantities compatible with screening, enabling earlier and more confident prioritization of compounds. Conveniently cryopreserved in quantities to match a range of applications, Cytiva Plus cardiomyocytes are ready-for-use in multi-electrode arrays, impedance, and high-content analysis applications for compound safety profiling. The cardiomyocytes are produced in a way that reflects native human heart cell development, without engineering techniques that could alter expression levels of relevant genes. This makes Cytiva Plus a dependable and reproducible biologically relevant cell model that supports the measurement of electrophysiological, structural, and functional cell changes, and demonstrates expected pharmacological responses to reference compounds. Cytiva Plus enables compound profiling based on multiple cardiotoxicity indications for more integrated risk assessment and mechanistic investigations.

GE Healthcare
For info: 800-526- 3593
www.gelifesciences.com/cytivaplus

Micro-Volume Probes

New micro-volume probes are designed for the accurate and reliable measurement of solutions in volumes as low as 150 µL. The micro-volume probes are available in two variants: the 4 mm probe with a 120 mm reach and the 6 mm probe has a 180 mm reach. The specific designs of each of the probes ensure their suitability for use in test tubes and small vessels, while the small shaft diameters allow for accurate readings in sample volumes as small as 150 µL and 200 µL respectively. Both probes are made from glass and can be used with any of the bench conductivity meters supplied by Jenway. The new probes are the latest addition to Jenway's extensive selection of conductivity equipment, designed to suit all kinds of laboratories and applications.

Jenway
For info: +44-(0)-1785-812121
www.jenway.com

High-Content Confocal Screening System

The Opera Phenix is a next generation, confocal, high-content screening system that enables scientists to perform the most challenging applications with greater speed and sensitivity. Scientists will benefit from the Opera Phenix system's ability to discriminate phenotypes of complex cellular models, such as primary cells and 3-D tissues, which are highly indicative of human physiology. More accurate characterization will enable scientists to gain insights into the causes of transformation of normal cells to cancerous cells, or the impact of a treatment on cancer cells. The Opera Phenix system's innovative optical design solves the challenges that many scientists have faced with traditional high-content imaging systems. The system's patented Synchony Optics design carefully controls excitation to eliminate unwanted crosstalk in the sample, resulting in better sensitivity without reducing speed. Researchers can quickly and easily turn the high-quality data into robust, quantitative results using the Harmony High-Content Imaging and Analysis Software.

PerkinElmer
For info: 877-754-6973
www.perkinelmer.com

Peroxidase Staining Systems

The ImmPRESS Excel Amplified Peroxidase Staining Systems are complete staining kits optimized for immunohistochemistry where additional sensitivity is required. These polymer based systems generate precise, sharp antigen localization in cell and tissue preparations with little to no background interference. Kit components include BLOXALL Blocking Solution to abolish endogenous peroxidase activity, a species specific amplifier antibody, ImmPRESS Excel peroxidase polymer reagent, and ImmPACT DAB *Eqv* substrate. Provided as ready-to-use, prediluted reagents, the kits offer added convenience to the end-user and contain sufficient reagent to stain approximately 150 sections. Current formats are for the detection of mouse or rabbit primary antibodies: ImmPRESS Excel Anti-Mouse IgG Staining Kit and ImmPRESS Excel Anti-Rabbit IgG Staining Kit.

Vector Laboratories
For info: 650-697-3600
www.vectorlabs.com

Color Calibration System

Take the guesswork out of adjusting color settings on your lab equipment. Now you can calibrate your computer monitors and brightfield microscope images and know that you are seeing and evaluating colors consistently. Datacolor Chromacal Color Calibration System is an innovative new approach to standardizing color in microscopy imaging systems. The system consists of three components to establish a color profile for the microscopy system: proprietary software, color calibration, microscope slide, computer monitor, and calibration sensor. The system enables users to establish and preserve the color integrity of their digital images from transmitted, brightfield microscopy. The Chromacal software uses an image from a special calibration slide to establish a microscope system-specific color profile and applies that industry-standard profile to your specimen images. All original images are preserved. "Chromacal-ibrated" images are saved separately with amended metadata.

Electron Microscopy Science
For info: 800-523-5874
www.emsdiasum.com/microscopy

Electronically submit your new product description or product literature information! Go to www.sciencemag.org/products/newproducts.dtl for more information.

Newly offered instrumentation, apparatus, and laboratory materials of interest to researchers in all disciplines in academic, industrial, and governmental organizations are featured in this space. Emphasis is given to purpose, chief characteristics, and availability of products and materials. Endorsement by *Science* or AAAS of any products or materials mentioned is not implied. Additional information may be obtained from the manufacturer or supplier.

OLYMPUS®

Your Vision, Our Future

Expanding Your Vision™

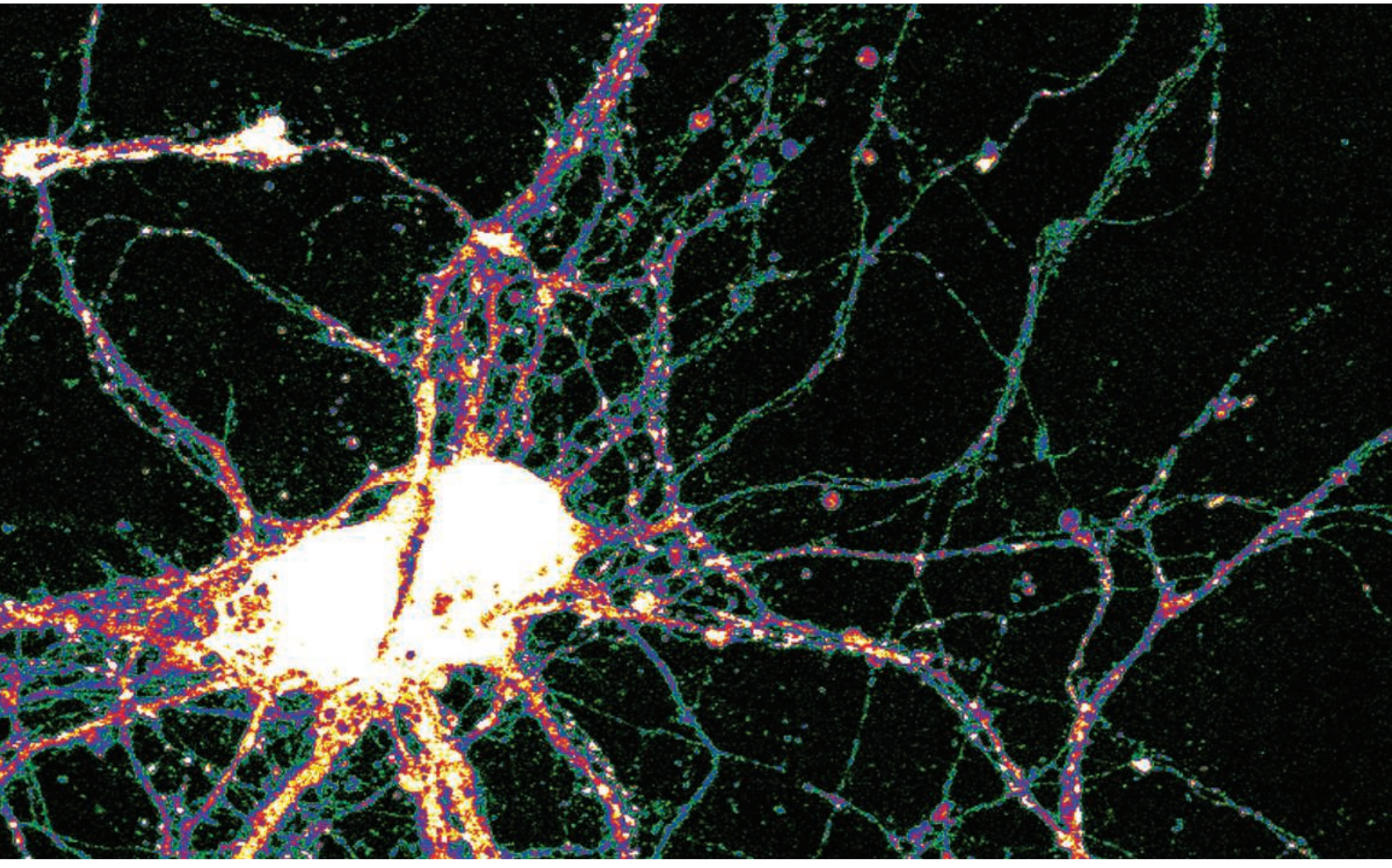

At Olympus, we help you see more.

With an eye on detail and a focus on quality, we are here to aide in your discoveries and advance your research. Olympus has the wide range of imaging solutions you require, built with optical excellence and proven application expertise.

Let us work with you in discovering what is to come.

Your Science Matters™

For further information, please visit: **YourScienceMatters.com**

OLYMPUS
48 Woerd Avenue, Waltham, MA 02453, 800-446-5967

Life Science

NOW YOU CAN SEE ANY RNA™.

Advanced RNA *in situ* Hybridization for any gene with RNAscope® technology.

Be Amazed.

Proprietary RNAscope® *in situ* hybridization (ISH) assay enables:

- Quantitative, sensitive and specific molecular detection with morphological context
- Visualization of virtually any mRNA or long noncoding RNA in any species
- 2-week turnaround for probe design

Learn more at www.acdbio.com

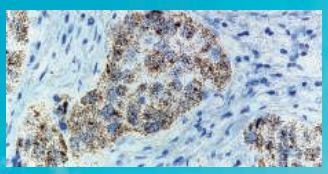

HER2 expression in human breast cancer FFPE tissue using RNAscope® 2.0 HD Reagent Kit-BROWN

ACD
Advanced Cell Diagnostics

AACR American Association for Cancer Research

ANNUAL MEETING

2015 | PHILADELPHIA

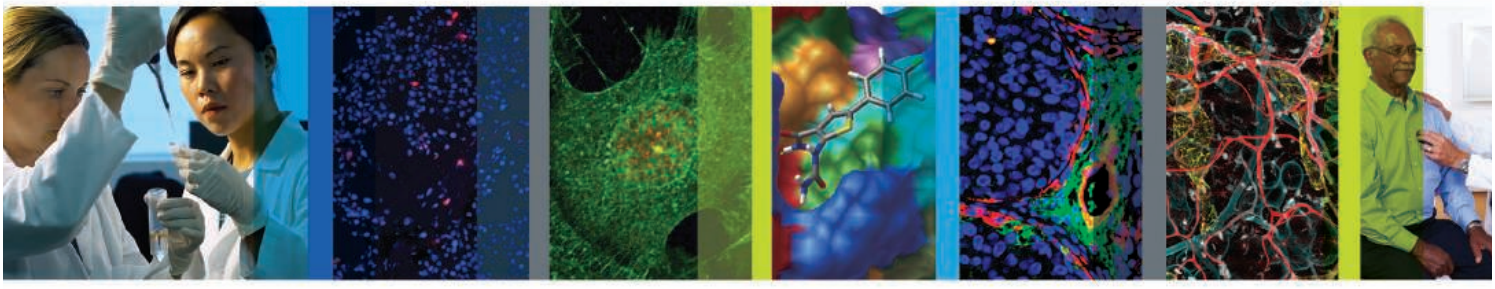

Bringing Cancer Discoveries to Patients

APRIL 18-22, 2015
PENNSYLVANIA CONVENTION CENTER
PHILADELPHIA, PA

Join us in Philadelphia

for the most comprehensive cancer research meeting in the world... the AACR Annual Meeting 2015!

Connect with the international cancer research community to foster new collaborations, learn about cutting-edge advances, and obtain feedback on your research.

This must-attend meeting covers every aspect of cancer – from epidemiology, molecular biology, and clinical studies to prevention, survivorship, and patient advocacy.

Submit your abstract today. Every abstract that is accepted for publication in the *Proceedings of the AACR* is presented at the meeting, and all abstracts are considered for oral presentations in minisymposia.

Submit your abstract by December 3, 2014!

Register Today!
Take advantage of the lowest rates available.

Become a Member!
Join the AACR and receive a discount on registration.

We look forward to welcoming you to our hometown of Philadelphia, PA!

WWW.AACR.ORG

TRANSLATE NEUROSCIENCE DISCOVERIES INTO THERAPEUTICS

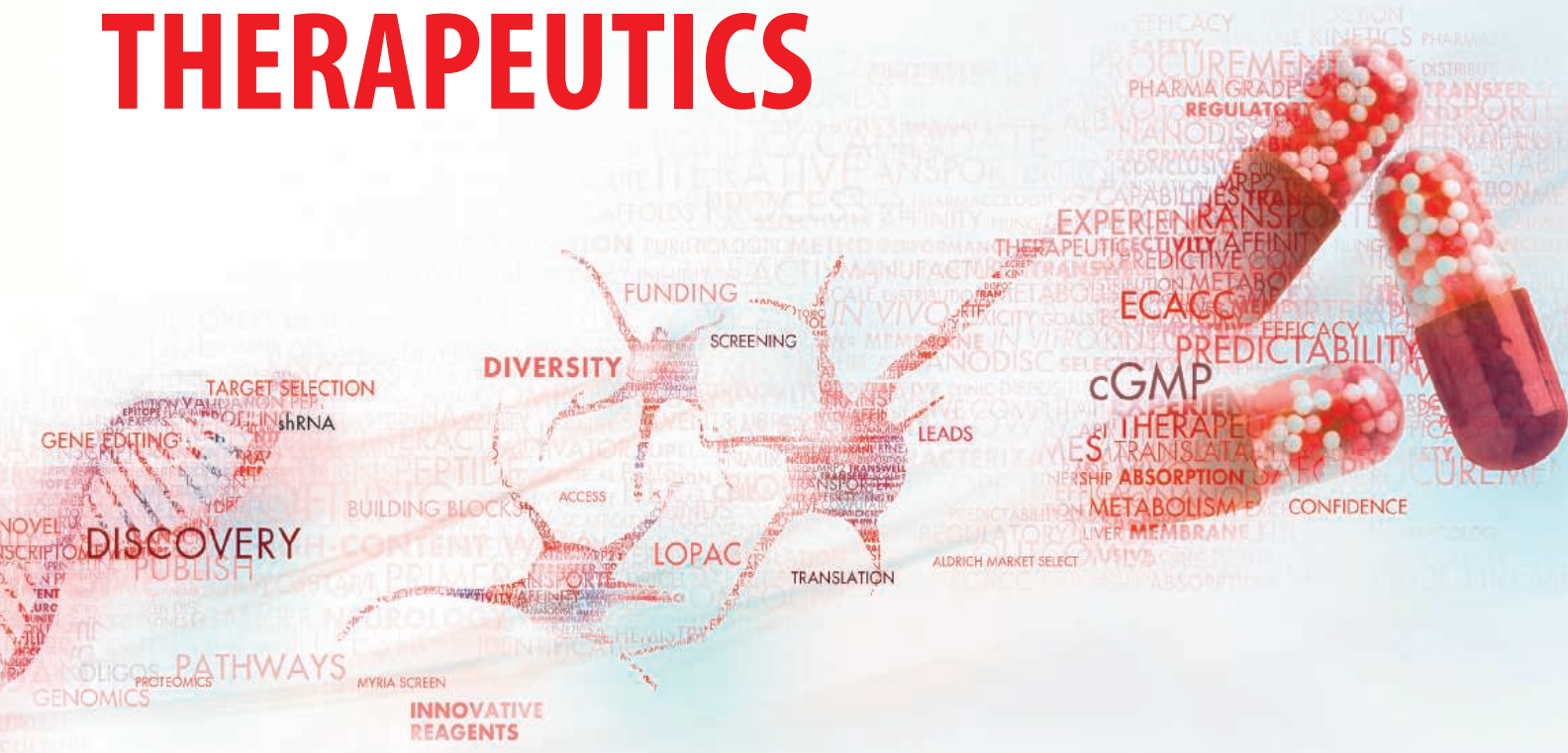

Technology targeted to your Neuroscience research

- Enable the discovery of novel targets and pathways with quality reagents and cutting-edge gene editing technology
- Create diverse and unique compounds with the largest portfolio of building blocks, catalysts and reagents
- Accelerate novel compound discovery with a chemically diverse array of compounds and screening libraries

TRANSLATIONAL RESEARCH SOLUTIONS

Download our apps for more information

sigma-aldrich.com/sfn

SIGMA® | ALDRICH® | SUPELCO® | SAFC®

82642
1104

SIGMA-ALDRICH®

Inter / depend / play / connect / link / act

INDIANA UNIVERSITY
NETWORK SCIENCE INSTITUTE

The new Indiana University Network Science Institute unites 100+ researchers at IU—building on their world-renowned multidisciplinary expertise toward further scientific understanding of the complex networked systems of our world. Through pioneering new approaches in mapping, representing, visualizing, modeling, and analyzing diverse complex networks across levels and disciplines, IU will lead the way.

At IU we keep track of the big picture—ever-changing and interconnected. We're laying the groundwork for innovative research and discovery in the area of network science.

Visit us at **iuni.iu.edu**

IUNI

AAAS 2015 ANNUAL MEETING

12–16 FEBRUARY • SAN JOSE, CA

INNOVATIONS, INFORMATION, AND IMAGING

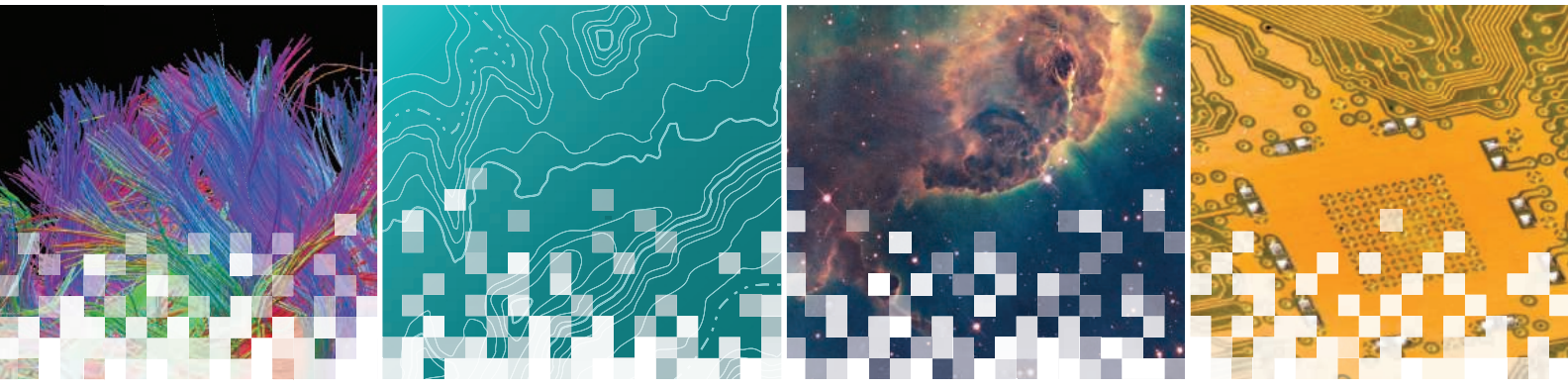

Plenary Lectures

A highlight of the AAAS Annual Meeting, plenary speakers share important advances in science, technology, and education.

Daphne Koller
President and Co-Founder,
Coursera

The Online Revolution: Learning Without Limits

Friday, 13 February
5:00–6:00 p.m.

Karl Deisseroth
D.H. Chen Professor of Bioengineering,
Stanford University

Optical Descontruction of Fully-Assembled Biological Systems

Sunday, 15 February
5:00–6:00 p.m.

David Baker
Professor of Biochemistry,
University of Washington

Post-Evolutionary Biology: Design of Novel Protein Structures, Functions, and Assemblies

Saturday, 14 February
5:00–6:00 p.m.

Neil Shubin
Professor, Organismal Biology and Anatomy,
University of Chicago

Finding Your Inner Fish

Monday, 16 February
8:30–9:30 a.m.

www.aaas.org/meetings

Investments Boost Neurotechnology Career Prospects

The past few years have seen some extraordinary activity in the neuroscience field. High-profile advances, from the Allen Brain Atlas to the Brainbow mouse, have injected an air of excitement into the study of the brain—an atmosphere that has been amplified by big funding initiatives in the United States and abroad. For budding neuroscientists, it's heady days—at least if you've got a knack for technology development, programming, and engineering. But it will take more than raw skill to land a job.

See the full story on page 653.

Upcoming Features

Nanotechnology Careers—Nov. 14 ■ *Regional Focus: Europe—Nov. 28* ■ *Regional Focus: Asia—Dec. 12*

eppendorf & Science

PRIZE FOR NEURO BIOLOGY

Congratulations
to Dr. Eiman Azim
Columbia University

And the Winner is...

Eppendorf & Science Prize for Neurobiology
Congratulations to Eiman Azim on winning the 2014 Eppendorf & Science Prize. Dr. Azim's work has provided fundamental new insights into the neural mechanisms that enable skilled limb movements to be both smooth and precise. His research has provided direct support for long-standing theories about the roles of internal feedback pathways within the central nervous system and external feedback from the muscles in regulating fine motor control.

The annual US$25,000 Eppendorf & Science Prize for Neurobiology honors scientists, like Dr. Azim, for their outstanding contributions to neurobiology research based on methods of molecular and cell biology. Eiman Azim is the 13th recipient of this international award. He will be presented with the Prize at a ceremony held during the week of the 2014 Annual Meeting of the Society for Neuroscience in Washington, DC.

You Could Be Next.
If you are 35 years of age or younger and currently performing neurobiology research, you could be next to win the 2015 Prize. Deadline for entries is June 15, 2015.

Learn more at: www.eppendorf.com/prize

eppendorf

Science AAAS

Time For An Upgrade?

Cyto-ID® Autophagy Detection Kit

Rapid | Specific | Quantitative

The Cyto-ID® Autophagy Detection Kit is a no-transfection quantitative assay for monitoring detoxification activity by promoting the autophagic pathway in live cells. Suitable for flow cytometry and microscopy, the assay facilitates high-throughput screening of activators and inhibitors of autophagy. The Cyto-ID® Autophagy Detection Kit includes a patent-pending dye that selectively stains pre-autophagosomes, autophagosomes, and autolysosomes (autophagolysosomes), with minimal staining of lysosomes. Discover Enzo's complete portfolio of Cellestial® assays for live cell analysis.

scientists ***enabling*** scientists.™

www.enzolifesciences.com

Enzo® Life Sciences

Time For An Upgrade?

Cyto-ID® Autophagy Detection Kit

Rapid | Specific | Quantitative

The Cyto-ID® Autophagy Detection Kit is a no-transfection quantitative assay for monitoring detoxification activity by promoting the autophagic pathway in live cells. Suitable for flow cytometry and microscopy, the assay facilitates high-throughput screening of activators and inhibitors of autophagy. The Cyto-ID® Autophagy Detection Kit includes a patent-pending dye that selectively stains pre-autophagosomes, autophagosomes, and autolysosomes (autophagolysosomes), with minimal staining of lysosomes. Discover Enzo's complete portfolio of Cellestial® assays for live cell analysis.

scientists ***enabling*** scientists.™

www.enzolifesciences.com

Enzo® Life Sciences

Sequencing power for every scale.

The HiSeq X Ten contains 10 sequencing systems.

NEW HiSeq X™ Ten

Population power.
$1000 human genome and extreme throughput for population-scale sequencing.

HiSeq® 2500

Production power.
Power and efficiency for large-scale genomics.

NEW NextSeq™ 500

Flexible power.
Desktop speed and simplicity for whole-genome, exome, transcriptome sequencing, and more.

MiSeq®

Focused power.
Desktop speed and simplicity for targeted and small-genome sequencing.

MiSeqDx™

Focused Dx power.
The first and only FDA-cleared *in vitro* diagnostic next-generation sequencing system.

Find the right sequencer to fit your every need. www.illumina.com/power

illumina®

EMD MILLIPORE

Issues with your tissues?
Process all your slides in a SNAP for streamlined IHC.

Variability – it's the challenge you face in traditional immunohistochemistry (IHC) experiments. If you're handling slides manually, using pap pens, pipetting, dipping and pouring, you risk slide-to-slide process variability, which may affect your results.

Experience a controlled vacuum force that removes solutions evenly from all your slides at once – in seconds.

Experience minimal slide handling, with blocking, washing, antibody and staining solutions contacting your tissues in self-contained reservoirs.

The SNAP i.d.® 2.0 system has been delighting Western blot users for years. Now we've applied its power to IHC.

Enhance your research with the SNAP i.d.® 2.0 system.
www.emdmillipore.com/IHC

EMD Millipore is a division of Merck KGaA, Darmstadt, Germany

EMD MILLIPORE

Suit(Ab)le Antibodies

We're selective. We're specific. We're scientists. We create the antibodies that are most relevant for today's research needs.

As a thoughtful producer, we take a selective approach to offering the best antibodies for each target. Our team of R&D scientists combs research and collaborates with leading institutions to identify only the most relevant antibodies for your research. Our expertise combines the pioneering work of Chemicon® and Upstate®, but our wisdom doesn't stop there. We constantly review, assess and determine which antibodies are the most suitable – those which provide the right level and type of data. It is our job to understand your needs so we can offer you the best of the best.

Put the most suitable antibodies to work for you.
www.emdmillipore.com/Ab

EMD Millipore is a division of
Merck KGaA, Darmstadt, Germany

BS-GEN-13-09105 03/2014

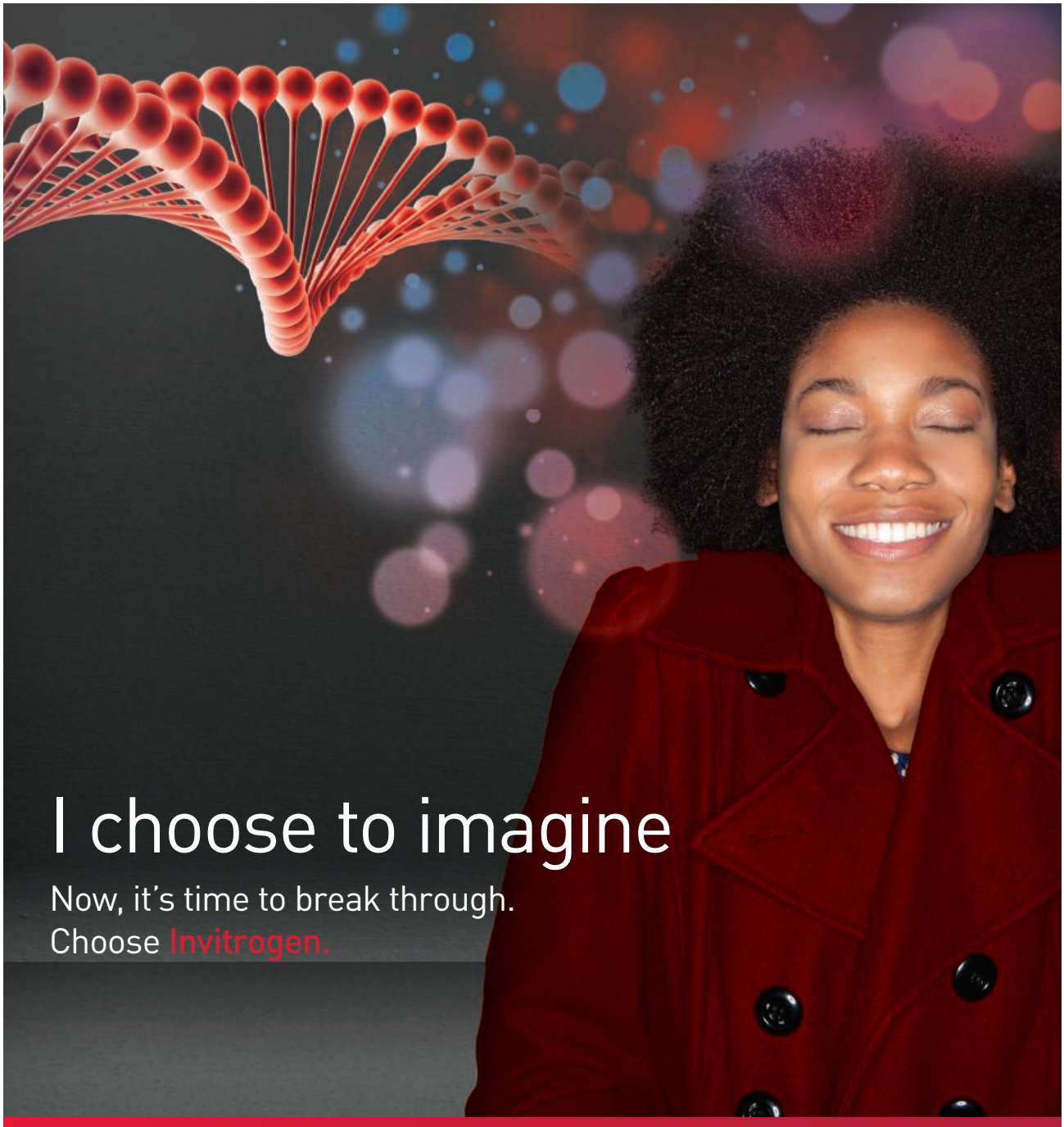

Discover the innovations that drive your breakthroughs at **lifetechnologies.com/invitrogen**

life technologies

A Thermo Fisher Scientific Brand

100 YEARS
OF EXPERT-CURATED CONTENT FOR 50 YEARS.

WE'RE THE STEWARDS OF THE INFORMATION THAT MATTERS MOST TO YOU.

CARING
FOR THE RESEARCH COMMUNITY'S MOST IMPACTFUL CONTENT

Web of Science™ connects publications and researchers through citations and controlled indexing. With 50 years of cumulative expertise and continuous innovation, Thomson Reuters Web of Science is the global standard for finding and connecting scholarly content across disciplines and around the world. In fact, it's the only database that effectively translates the collective wisdom of the best researchers in each field into a dataset that makes that knowledge available to all.

An integral part of the evolution of search, today the Web of Science offers you:

- **Cover-to-cover** indexing with an objective evaluation process to meet the highest standards
- **Comprehensive** and relevant coverage
- **Cited reference search** to track prior research and monitor current developments
- The ability to **identify** hidden patterns, gaining insight into emerging research trends

Visit us at **go.thomsonreuters.com/50years** to learn about all of our offerings.

50th Anniversary Science Citation Index®

THOMSON REUTERS™

BUT NOTHING COUNTS LIKE THE COUNTESS® II FL AUTOMATED CELL COUNTER

You see the potential in every sample, in every cell. In your work, simplicity, affordability, and flexibility mean more time for discovery.

Count cells in a whole new light with the quantifiably brilliant Countess® II FL Automated Cell Counter.

Everything counts at **lifetechnologies.com/countessII**

life technologies

A Thermo Fisher Scientific Brand

A NEW PERSPECTIVE TO

cancer metabolism research

XF technology provides the easiest and most comprehensive assessment of cancer cell metabolism, measuring glucose and glutamine metabolism, and fatty acid oxidation of cancer cells in a microplate, in real time!

— Kacey Caradonna, Ph.D.,
Application Scientist,
Seahorse Bioscience

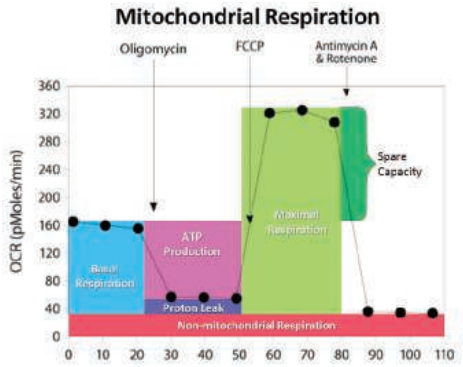

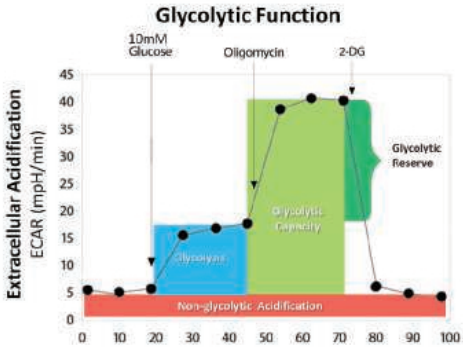

The NEW XFp Extracellular Flux Analyzer

With the XFp Analyzer, it is easier than ever to perform functional metabolic measurements in live cells in your own lab. The XFp is designed to perform standard metabolic assays reliably and consistently on your precious samples. The compact format of the XFp Analyzer and XF stress tests make this new platform ideal for pairwise comparisons to validate your genomic or proteomic data.

See what's possible.

Scan this QR code to view videos and see what the XF^e Analyzer can achieve.
Visit **www.seahorsebio.com/science** for more information!

Seahorse Bioscience

BOUNDARY-BREAKING
ACOUSTIC FOCUSING CYTOMETRY

Introducing the Attune® NxT Acoustic Focusing Cytometer—a high-performance package that's flexible enough for any lab

The Attune® NxT Acoustic Focusing Cytometer combines unmatched precision, speed, and sensitivity, in a modular design that can grow with you. With up to 4 lasers and 14 colors, the Attune® NxT cytometer is designed to accommodate most experimental design needs and lab budgets. Boundaries, beware.

See the next big thing in flow cytometry at
lifetechnologies.com/attune

life technologies
A Thermo Fisher Scientific Brand

Human Heart Cell Model

Identifying potential cardiotoxicity as early as possible in the drug development process can reduce the risk of costly program failures and minimize health risks. Cytiva Plus provides a high-fidelity human heart cell model that is available in quantities compatible with screening, enabling earlier and more confident prioritization of compounds. Conveniently cryopreserved in quantities to match a range of applications, Cytiva Plus cardiomyocytes are ready-for-use in multi-electrode arrays, impedance, and high-content analysis applications for compound safety profiling. The cardiomyocytes are produced in a way that reflects native human heart cell development, without engineering techniques that could alter expression levels of relevant genes. This makes Cytiva Plus a dependable and reproducible biologically relevant cell model that supports the measurement of electrophysiological, structural, and functional cell changes, and demonstrates expected pharmacological responses to reference compounds. Cytiva Plus enables compound profiling based on multiple cardiotoxicity indications for more integrated risk assessment and mechanistic investigations.

GE Healthcare
For info: 800-526- 3593
www.gelifesciences.com/cytivaplus

Micro-Volume Probes

New micro-volume probes are designed for the accurate and reliable measurement of solutions in volumes as low as 150 µL. The micro-volume probes are available in two variants: the 4 mm probe with a 120 mm reach and the 6 mm probe has a 180 mm reach. The specific designs of each of the probes ensure their suitability for use in test tubes and small vessels, while the small shaft diameters allow for accurate readings in sample volumes as small as 150 µL and 200 µL respectively. Both probes are made from glass and can be used with any of the bench conductivity meters supplied by Jenway. The new probes are the latest addition to Jenway's extensive selection of conductivity equipment, designed to suit all kinds of laboratories and applications.

Jenway
For info: +44-(0)-1785-812121
www.jenway.com

High-Content Confocal Screening System

The Opera Phenix is a next generation, confocal, high-content screening system that enables scientists to perform the most challenging applications with greater speed and sensitivity. Scientists will benefit from the Opera Phenix system's ability to discriminate phenotypes of complex cellular models, such as primary cells and 3-D tissues, which are highly indicative of human physiology. More accurate characterization will enable scientists to gain insights into the causes of transformation of normal cells to cancerous cells, or the impact of a treatment on cancer cells. The Opera Phenix system's innovative optical design solves the challenges that many scientists have faced with traditional high-content imaging systems. The system's patented Synchony Optics design carefully controls excitation to eliminate unwanted crosstalk in the sample, resulting in better sensitivity without reducing speed. Researchers can quickly and easily turn the high-quality data into robust, quantitative results using the Harmony High-Content Imaging and Analysis Software.

PerkinElmer
For info: 877-754-6973
www.perkinelmer.com

Peroxidase Staining Systems

The ImmPRESS Excel Amplified Peroxidase Staining Systems are complete staining kits optimized for immunohistochemistry where additional sensitivity is required. These polymer based systems generate precise, sharp antigen localization in cell and tissue preparations with little to no background interference. Kit components include BLOXALL Blocking Solution to abolish endogenous peroxidase activity, a species specific amplifier antibody, ImmPRESS Excel peroxidase polymer reagent, and ImmPACT DAB *Eqv* substrate. Provided as ready-to-use, prediluted reagents, the kits offer added convenience to the end-user and contain sufficient reagent to stain approximately 150 sections. Current formats are for the detection of mouse or rabbit primary antibodies: ImmPRESS Excel Anti-Mouse IgG Staining Kit and ImmPRESS Excel Anti-Rabbit IgG Staining Kit.

Vector Laboratories
For info: 650-697-3600
www.vectorlabs.com

Color Calibration System

Take the guesswork out of adjusting color settings on your lab equipment. Now you can calibrate your computer monitors and brightfield microscope images and know that you are seeing and evaluating colors consistently. Datacolor Chromacal Color Calibration System is an innovative new approach to standardizing color in microscopy imaging systems. The system consists of three components to establish a color profile for the microscopy system: proprietary software, color calibration, microscope slide, computer monitor, and calibration sensor. The system enables users to establish and preserve the color integrity of their digital images from transmitted, brightfield microscopy. The Chromacal software uses an image from a special calibration slide to establish a microscope system-specific color profile and applies that industry-standard profile to your specimen images. All original images are preserved. "Chromacal-ibrated" images are saved separately with amended metadata.

Electron Microscopy Science
For info: 800-523-5874
www.emsdiasum.com/microscopy

Electronically submit your new product description or product literature information! Go to www.sciencemag.org/products/newproducts.dtl for more information.

The 2015 Keystone Symposia Neurobiology Conferences

Neuroinflammation in Diseases of the Central Nervous System

January 25–30, 2015
Sagebrush Inn and Conference Center | Taos, New Mexico | USA
Scientific Organizers: Richard M. Ransohoff, Christopher K. Glass and V. Hugh Perry
www.keystonesymposia.org/15A5
Deadlines: Discounted Registration – Nov 24, 2014 (abstracts also still accepted online through this date)

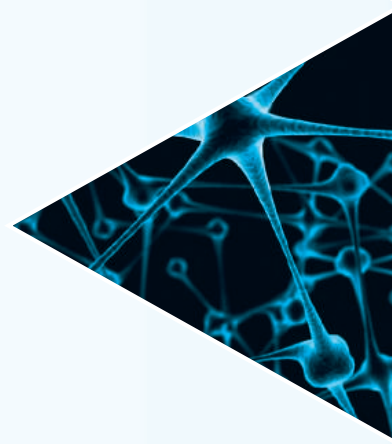

Neuroepigenetics

February 22–26, 2015
Eldorado Hotel & Spa | Santa Fe, New Mexico | USA
Scientific Organizers: Hongjun Song and Li-Huei Tsai
www.keystonesymposia.org/15B5
Deadlines: Abstract – Nov 19, 2014; Discounted Registration – Dec 18, 2014

Optogenetics

March 12–16, 2015
Westin Downtown Denver | Denver, Colorado | USA
Scientific Organizers: Edward S. Boyden, Klaus M. Hahn and Chandra Tucker
www.keystonesymposia.org/15C5
Deadlines: Discounted Abstract/Scholarship – Nov 12, 2014; Abstract – Dec 11, 2014; Discounted Registration – Jan 13, 2015

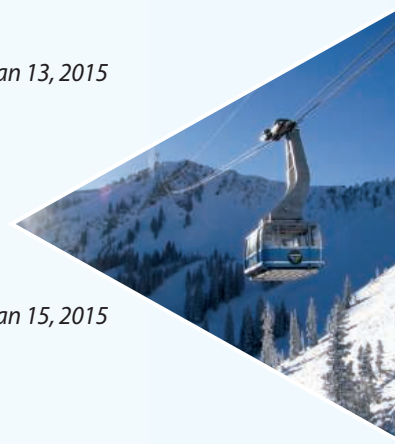

Pathways of Neurodevelopmental Disorders

March 16–20, 2015
Granlibakken Resort | Tahoe City, California | USA
Scientific Organizers: Randi J. Hagerman, Mustafa Sahin and Paul J. Hagerman
www.keystonesymposia.org/15C8
Deadlines: Discounted Abstract/Scholarship – Nov 18, 2014; Abstract – Dec 16, 2014; Discounted Registration – Jan 15, 2015

Neural Control of Metabolic Physiology and Diseases

April 12–17, 2015
Snowbird Resort | Snowbird, Utah | USA
Scientific Organizers: Dongsheng Cai and Martin G. Myers, Jr.
www.keystonesymposia.org/15D4
Deadlines: Discounted Abstract/Scholarship – Dec 4, 2014; Abstract – Jan 13, 2015; Discounted Registration – Feb 12, 2015

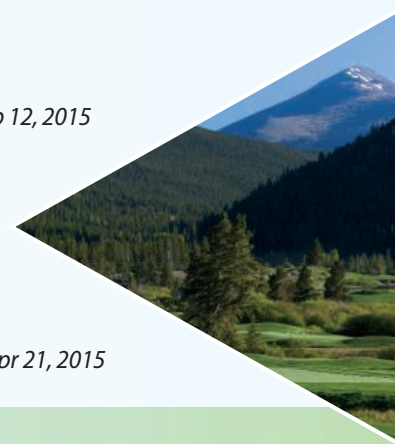

Autophagy

June 19–24, 2015
Beaver Run Resort | Breckenridge, Colorado | USA
Scientific Organizers: Eric H. Baehrecke and Jayanta Debnath
www.keystonesymposia.org/15E6
Deadlines: Discounted Abstract/Scholarship – Feb 17, 2015; Abstract – Mar 17, 2015; Discounted Registration – Apr 21, 2015

Submitting an abstract represents an excellent way of participating in the conference via a poster presentation and possible selection for a short talk. Scholarships are available for graduate students and postdoctoral fellows. For full program, speaker, abstract and scholarship details, visit **www.keystonesymposia.org/neuro**.

KEYSTONE SYMPOSIA™
on Molecular and Cellular Biology
Accelerating Life Science Discovery

At CST, if it's not specific, it doesn't ship.

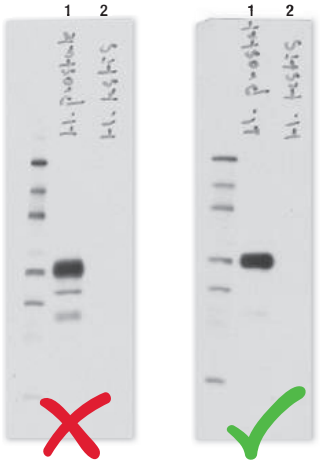

WB analysis of extracts from human prostate and testis using two development samples at 1:1000 dilution.

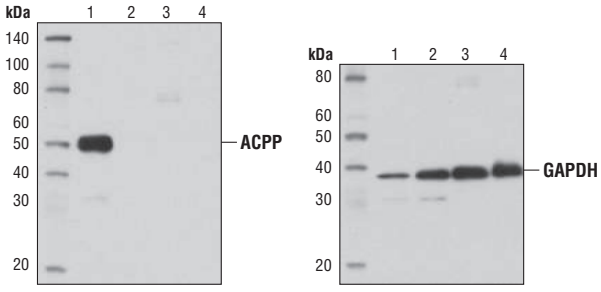

Prostatic Acid Phosphatase (D3Y5P) Rabbit mAb #12861: WB analysis of extracts from human prostate, testis, liver, and spinal cord using #12861 (left) and GAPDH (D16H11) XP® Rabbit mAb #5174 loading control (right) demonstrating prostate-specific expression of ACPP.

1 - Human Prostate Tissue
2 - Human Testis Tissue
3 - Human Liver
4 - Human Spinal Cord.

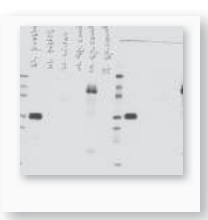

Skeptical? See the whole film at
www.cellsignal.com/wbskeptical

WB IP IHC IF F ChIP

For Research Use Only. Not For Use In Diagnostic Procedures.

14PADIHC_NONE0152ENG_02

Cell Signaling TECHNOLOGY®

Science Careers Advertising

For full advertising details, go to ScienceCareers.org and click For Employers, or call one of our representatives.

Tracy Holmes
Worldwide Associate Director
Science Careers
Phone: +44 (0) 1223 326525

THE AMERICAS

E-mail: advertise@sciencecareers.org
Fax: 202 289 6742

Tina Burks
Phone: 202 326 6577

Nancy Toema
Phone: 202 326 6578

Marci Gallun
Sales Administrator
Phone: 202 326 6582

Online Job Posting Questions
Phone: 202 312 6375

EUROPE / INDIA / AUSTRALIA / NEW ZEALAND / REST OF WORLD

E-mail: ads@science-int.co.uk
Fax: +44 (0) 1223 326532

Axel Gesatzki
Phone: +44 (0) 1223 326529

Sarah Lelarge
Phone: +44 (0) 1223 326527

Kelly Grace
Phone: +44 (0) 1223 326528

JAPAN

Katsuyoshi Fukamizu (Tokyo)
E-mail: kfukamizu@aaas.org
Phone: +81 3 3219 5777

Hiroyuki Mashiki (Kyoto)
E-mail: hmashiki@aaas.org
Phone: +81 75 823 1109

CHINA / KOREA / SINGAPORE / TAIWAN / THAILAND

Ruolei Wu
Phone: +86 186 0082 9345
E-mail: rwu@aaas.org

ScienceCareers
FROM THE JOURNAL SCIENCE AAAS

ScienceCcareers.org

Careers in Nanotechnology

Special Career Feature

November 14, 2014

Ads accepted until November 10, if space is still available.

There's only one Science

This feature examines the professional landscape for scientists, engineers, and clinicians who endeavor to better understand how nanotechnology can impact biological systems.

Why you should advertise in this issue of *Science*:

Reach: Your job ad is seen by 570,400 readers around the globe

Bonus distributions to:
Materials Research Society
November 30 – December 5, Boston, MA

To book your ad: advertise@sciencecareers.org

THE AMERICAS
202-326-6582

JAPAN
+81 3 3219 5777

EUROPE/ROW
+44 (0) 1223 326500

CHINA / KOREA / SINGAPORE / TAIWAN
+86 186 0082 9345

ScienceCareers
FROM THE JOURNAL SCIENCE AAAS

Produced by the *Science*/AAAS Custom Publishing Office. | ScienceCareers.org

Investments Boost Neurotechnology Career Prospects

The past few years have seen some extraordinary activity in the neuroscience field. High-profile advances, from the Allen Brain Atlas to the Brainbow mouse, have injected an air of excitement into the study of the brain—an atmosphere that has been amplified by big funding initiatives in the United States and abroad. For budding neuroscientists, it's heady days—at least if you've got a knack for technology development, programming, and engineering. But it will take more than raw skill to land a job. **By Jeffrey M. Perkel**

Mark Cembrowski was a graduate student in applied mathematics with a taste for neurobiology at Northwestern University when he discovered a way to marry his two interests.

Two of his math professors were collaborating with physiologist Joshua Singer, also at Northwestern, who was keen to model the biology of a retinal cell called the AII amacrine interneuron. "Josh wanted someone to come in and build a model of single AII cells to try and understand how the AII works as an input/output device," Cembrowski explains. So, he joined Singer's team.

But models are only as good as their input data, and very quickly, Cembrowski says, he realized he needed more of it. Specifically patch-clamp electrophysiology data. And he was going to have to collect it himself.

Patch clamping isn't easy even for seasoned neuroscientists, let alone an applied mathematician who'd never set foot in a biology lab. "I was the worst of the worst," he concedes. "I broke a lot of things getting started."

Still, he persevered, and in 2012 published his first electrophysiology paper. "My whole perspective on this just flipped 180 degrees," he says. "When I found the confidence and the ability to do these experimental techniques, I felt like I was on top of the world."

As it turns out, researchers like Cembrowski are atop the neuroscience world, too, where research opportunities increasingly blend traditional neurobiology with technology development.

That marriage of disciplines underlies President Obama's recently announced Brain Research through Advanced Innovative Neurotechnologies (BRAIN) initiative. Seeded with $110 million from the U.S. National Institutes of Health (NIH), the National Science Foundation, and the Defense Advanced Research Projects Agency, the initiative has a heavy focus on technology development, says **Tom Insel**, director of the National Institute of Mental Health (NIMH), one of four NIH institutes that together contributed $40 million to the pot.

"This is a unique investment," Insel says. "It's not to expand all of neuroscience, but it's to invest in the area of tool development specifically, which is sometimes difficult to do with RO1 grant funding."

In particular, he says, the initiative will support a new breed of neuroscientist, one trained not as a classical brain researcher but as a physicist or mathematician, computer scientist or engineer—researchers who may never have received NIH funding before. "One of the measures of success for me with the BRAIN Initiative is, when I see the pay plan of who's going to be funded, I'm hoping that I will not recognize most of the names," he says.

One name that won't be on the list is Cembrowski, who is still in training. Upon graduating with a Ph.D. in applied mathematics, he joined **Nelson Spruston**'s lab at the Howard Hughes Medical Institute's Janelia Farm Research Campus, a private research institute with a heavy focus on neurobiology. There, he pivoted again and again, from electrophysiology to RNA-sequencing data analysis, to anatomy and histology, and thence to behavioral analysis. "No technique is an island," he explains. "There's always other techniques that one can adopt as a way of validating and extending what you've done previously."

"This is a guy who just knows no boundaries," Spruston says. "He's going to go out and learn what he needs to learn to answer the questions that he wants to answer. And this is to me the phenotype of the successful neuroscientist these days."

Collecting techniques

So how can one develop that phenotype? Certainly, a solid technical background doesn't hurt. Popular flavors *du jour* include connectomics, functional magnetic resonance imaging (fMRI), and optogenetics.

But it's not the acquisition of techniques per se that matters, most say, so much as the willingness to try new things, coupled with sufficient neurobiology expertise to understand what questions to ask. continued>


Eve Marder

ILLUSTRATION: AGSANDREW/SHUTTERSTOCK.COM; PHOTO: MIKE LOVETT

Upcoming Features

Nanotechnology Careers—November 14 ■ *Regional Focus: Europe—November 28* ■ *Regional Focus: Asia—December 12*

"We don't hire assistant professors because they know technique *x*, but because they are working on an interesting problem," says **Eve Marder**, a professor of neuroscience at Brandeis University. "We totally expect that in five or 10 years, they might be using a completely different technology."

Ed Boyden, a chemist and physicist turned electrical engineer who co-developed optogenetics, echoes that sentiment. "Skills are certainly good to have. But maybe even more important than having skills is having the ability to pick up new skills," he says. After all, today's hot technology is tomorrow's dinosaur.

In this era of "big data," strong computational skills and informatics expertise also are increasingly valuable for neuroscience success, says **David Van Essen**, alumni endowed professor of neurobiology at the Washington University School of Medicine and co-principal investigator (PI) of the Human Connectome Project (HCP). "That doesn't mean that they have to write new programs themselves," he says, "but they have to be comfortable with using computers in increasingly sophisticated ways."

Marder says her students inevitably become proficient in MATLAB. So, too, do researchers working with **Moritz Helmstaedter**, a connectomics expert and director of the Max Planck Institute for Brain Research in Frankfurt, Germany.

Helmstaedter says that in his experience, the best skillset for neuroscience in general, and connectomics in particular, is a background in physics. "That's almost always a convincing feature," he says, "because somebody who has that kind of background and is interested in neuroscience, very rarely fails on you." But barring that, he continues, interest in quantitative analysis is a must.

The brain, he notes, is a biological machine "of un-understood complexity," inevitably requiring sophisticated number crunching and quantitative approaches rarely found in pure biology. "Data is so massive that analysis has to be quantitative, of course, but also it has to involve high-dimensional pattern recognition. And these are topics that you have to have a very quantitative background for."

Such quantitative prowess can even help researchers leverage public datasets they didn't generate. **Van Wedeen**, another HCP PI at the Massachusetts General Hospital (MGH) Martinos Center for Biomedical Engineering, says the proliferation of neuroscience resources, such as those put out by the HCP and Allen Brain Atlas, can pay unexpected dividends for young researchers who lack the funds to collect such data themselves. In particular, they allow researchers to test-drive radical ideas and pivot to new areas of focus. "They enable everyone, young and old alike, to pursue hypotheses that are not heavily driven by preceding work," he says.

"Our students are expected to become sophisticates in digital signal processing, statistics, neurophysiology, electronics, measurement, and experimental design, simultaneously."
— Mark Cohen

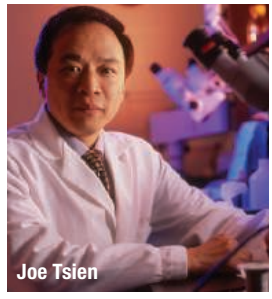

Joe Tsien

Spruston says that the postdocs he hires generally aren't afraid to take something apart and reassemble it, or write their own software rather than using off-the-shelf solutions. In part, he says, that's because he wants people who are "very quantitatively adept." But also it's because industry leaders tend to be people who understand a technology well enough to improve upon it. "If you just keep doing what you were doing five years ago or 10 years ago, it won't pay off in the same way as it will if you're on top of the technological advances as they happen."

Continuing education

One way neuroscientists can hone their technical edge is to take off-major courses in physics or engineering (if they are still in graduate school) or postdoc in a lab that can teach them new techniques.

But the burgeoning emphasis on technology development means that career development isn't just about teaching old neuroscientists new tricks; it's also about educating engineers, physicists, and computer scientists in the basics of neuroscience. **Joe Tsien**, co-director of the Brain and Behavior Discovery Institute at Georgia Regents University, has several computer scientists and physicists in his lab. "It's easier from my own experience to train these people to do the biology than to train the biologists [as] computer scientists," he says.

Some universities have begun offering graduate training specifically focused on neurotechnology, among them the Massachusetts Institute of Technology (MIT) Center for Neurobiological Engineering. Boyden, who codirects that center, says traditional neuroscience graduate programs typically focus on hypothesis-driven research—asking and answering "profound, deep mysteries of the brain." The MIT center, in contrast, "is about building tools."

"We really want to build technologies that enable us to answer questions that people might not even be able to ask right now," Boyden explains.

Martin Monti, assistant professor of psychology at the University of California, Los Angeles (UCLA), took a different path to boost his technological *bona fides*. In 2008, while a postdoc in the Medical Research Council Cognition and Brain Sciences Unit at the University of Cambridge, United Kingdom, Monti spent two weeks in sunny California at the UCLA Semel Neuro-Imaging Training Program (NITP).

NITP is a federally funded project whose agenda is "to take people with training that's nontraditional for neuroscience—engineers, mathematicians, statisticians, physicists, and so on—and to bring them up to speed on neuroimaging, a science that needs those sorts of technologies," says **Mark Cohen**, who directs the program. "It includes both a traditional one-year fellowship program open to UCLA graduate students, and

PHOTOS: (FROM TOP) PHIL JONES; MARC ROSEBORO PHOTOGRAPHY (MROSEBOR@UCLA.EDU)

"In this era of 'big data,' strong computational skills and informatics expertise also are increasingly valuable for neuroscience success."
— David Van Essen

Featured Participants

Brain and Behavior Discovery Institute, Georgia Regents University
www.gru.edu/mcg/discovery/bbdi

Brandeis University
www.brandeis.edu

Janelia Farm Research Campus
janelia.org

Max Planck Institute for Brain Research
www.brain.mpg.de/home.html

MGH Martinos Center for Biomedical Engineering
www.nmr.mgh.harvard.edu

MIT Center for Neurobiological Engineering
web.mit.edu/cnbe

National Institute of Mental Health
www.nimh.nih.gov

Northwestern University
www.northwestern.edu

UCLA Semel NeuroImaging Training Program
www.brainmapping.org/NITP

Washington University School of Medicine
medicine.wustl.edu

Additional Resources

BRAIN Initiative
www.nih.gov/science/brain

Human Brain Project
www.humanbrainproject.eu

Human Connectome Project
www.humanconnectome.org

a two-week immersive summer course in advanced magnetic resonance imaging methods and applications."

Limited to 35 or 36 attendees at all academic ranks, "the summer program combines classroom lectures, laboratory exercises, and a team-based research experience," says Cohen, "some of which result in publications and lasting collaborations."

The program also has a complementary agenda, he adds, which is to take people in more traditional neuroscience fields "and get them down and deep with the nitty-gritty of the technologies that we use in imaging, including math, physics, electrical engineering, and other things that are crucial to an understanding of the field."

According to Cohen, NITP—which is one of just three such programs around the country (the others are at MGH and the University of Pittsburgh)—offers its students a rare opportunity in interdisciplinary training. "Our students are expected to become sophisticates in digital signal processing, statistics, neurophysiology, electronics, measurement, and experimental design, simultaneously. Neuroimaging has become an unusually demanding high-technology field, and few places are equipped to offer these students the training that they need to become broad participants."

Monti already had substantial experience with fMRI when he signed up for NITP, he says, but was looking for a deeper understanding of the technology. The course, he says, "completely changed the way in which I understand experiments and analyze data," he says. He discovered he'd only scratched the surface of how fMRI works and what it can do—knowledge that he says helps him design better experiments, and may have boosted his career prospects.

Of course, a one- or two-week training course isn't going to make or break a resume, says **Robert Savoy**, an instructor in radiology at Mass General who runs several of the short-term training programs at the MGH Martinos Center. "This is not a degree-granting program," he says. "It isn't even CME [continuing medical education credit]-granting." But it is nevertheless valuable. Says Monti, "[NITP] certainly gave me a huge advantage in terms of talking about and conceiving experiments. Even just that made me a better candidate than many other people for any postdoc or faculty position."

A brain research brain drain?

There's no denying there's some big money in neuroscience these days. The BRAIN Initiative will dole out some $110 million in funding in its first year—about 2% of the $5.5 billion the NIH will spend this year on neuroscience overall, according to Insel—and President Obama has requested $200 million for 2015. A recent report by a working group of the Advisory Committee to the Director of the NIH, has recommended a subsequent investment of $4.5 billion over 10 years. The European Research Council spent some €250 million (~US$323 million) on neuroscience research in 2012. More recently, the European Union earmarked €1 billion (US$1.3 billion) toward the controversial Human Brain Project.

Such spending will undoubtedly produce new job opportunities at all levels of research, from technicians to postdocs to principal investigators. But the BRAIN Initiative, at least, says Insel, isn't a job program per se. "This is really about creating tools and resources for the broad community of people who want to study the brain."

China, too, is investing heavily in the brain, says Tsien, who in addition to his position in Georgia also is honorary chief scientist at the Brain Decoding Center at the BanNa Biomedical Research Institute in Yunnan Province, China. With comparatively fewer labs and scientists vying for research dollars, he estimates funding rates in China are "probably [around] 30%." In contrast, just 17.5% of RO1 applications were funded in 2013, according to the NIH. As a result, Tsien says, he is seeing a "fundamental shift," with many foreign postdocs who once would try to stay in the United States now heading home. "The vast majority go back to their country because there are more opportunities there."

Similarly, Helmstaedter says he has seen an increase in applicants from the United States for group leadership positions at the Max Planck Institute. "One hears about bad funding, but to [hear] that somebody would consider going to Europe from the United States, which for a long time was the place to do research, that's amazing," he says.

How that situation will evolve, of course, is anybody's guess. But neuroscience, at least, seems to be on the upswing. Says Spruston, "I think, if I were a student or a postdoc, I'd be encouraged about what's happening in the field now."

Jeffrey M. Perkel is a freelance science writer based in Pocatello, Idaho.

DOI: 10.1126/science.opms.r1400148

Department of Neuroscience

The **Department of Neuroscience** invites applications for two **Full Associate/Assistant Professors** in Computational and Theoretical Neuroscience. One position will be joint with the Department of Computer Science and a separate position will be joint with the Department of Mathematics. This search is part of a multi-faculty hiring initiative in Computational and Theoretical Neuroscience with the aim of building existing strengths in the field to create a Computational and Theoretical Neuroscience Center.

Those interested whose work intersects with computer science approaches and include, but are not limited to, information and complexity theory, computational modeling, computational geometry, statistics, machine learning, robotics, graphical models, stochastic processes, coding theory, and data mining should go to **http://services.cs.utexas.edu/recruit/faculty/frontmatter/checklist.html** for application instructions.

Those interested whose work intersects with mathematical approaches and include, but are not limited to, dynamical systems, partial differential equations, algebraic geometry, statistics, information theory, stochastic processes, and applied and computational topology should go to **https://academicjobsonline.org/ajo/jobs/4726** for application instructions.

The University of Texas at Austin is an Equal Opportunity Employer. Qualified women and minorities are encouraged to apply; a background check will be conducted on applicants selected.

VCU

The **Department of Anatomy and Neurobiology** on the **Medical College of Virginia Campus of Virginia Commonwealth University** is currently offering two tenure-track positions at all faculty ranks. The department currently has 15 full-time neuroscience faculty who are supported by substantial extramural support. Additionally, their research efforts are assisted by an advanced and expansive bioimaging core. These positions are supported by state funds and will be offered to individuals with solid extramural funding and an outstanding publication record that complements the research directions of the department in glial cell biology, neuroplasticity, and traumatic brain injury. The successful candidate will also be expected to come with graduate and professional student teaching expertise related to one of the department's core activities in either the area of gross anatomy, histology, or neuroscience. Applicants should possess a PhD, MD, or DDS degree or equivalent with demonstrated experience working in and fostering a diverse faculty, staff and student environment or a commitment to do so as a faculty member at VCU. The available positions offer attractive salaries and start-up packages with appropriate laboratory space. Review of the applications will begin immediately and the positions will remain open until filled.

Interested candidates should send a curriculum vitae, a letter of intent outlining their research and scholarly accomplishments, and the name, address, telephone number, and email address of three references. Application materials must be electronically submitted to **anatrecruit@vcu.edu**.

Virginia Commonwealth University is an Equal Opportunity/Affirmative Action Employer. Women, minorities, and persons with disabilities are encouraged to apply.

The **Department of Biological Science** at Florida State University invites applications for a **tenure-track assistant professor** position in the broad area of **Immunology**, including but not limited to structural immunology, innate immunity, mucosal/microbiome immunity, neuroimmunology, immunology of cancer, and developmental immunology. We are seeking candidates who will establish an extramurally funded research program and will participate in undergraduate and graduate education. The Department of Biological Science is a group of 43 integrated faculty. The Cell and Molecular Biology area within the department has existing strengths in structural biology, virology/microbiology, genomics, developmental biology, and neuroscience. Excellent research facilities include: a state of the art imaging facility with a Titan Krios electron microscope, hybridoma facility, flow cytometry facility, next generation sequencing facility, and mass spectrometry facility. Additionally, faculty have access to the newly formed Center for Genomics and Personalized Medicine and the National High Magnet Field Laboratory.

Apply at **http://jobs.fsu.edu** (Job ID **38006**). Applicant should submit in a single pdf: (1) a cover letter, (2) curriculum vitae, and (3) a research statement. Additionally, three confidential, independent letters of support are required to be sent to **immunology.search@bio.fsu.edu**. Priority will be given to completed applications received by **December 7, 2014**. Review of applications will continue until the position is filled. Questions about the position may be directed to: **tang@bio.fsu.edu**.

Florida State University is an Equal Opportunity/Access/Affirmative Action/Pro Disabled and Veteran Employer.

http://www.hr.fsu.edu/PDF/Publications/diversity/EEO_Statement.pdf

The UC Davis MIND Institute, School of Medicine, and the Genome Center invite applications for a tenure-track faculty position at the Assistant or Associate level in the area of human genetics and genomics. Applicants interested in genomic approaches to autism or related disorders who employ large-scale, technology-driven approaches that complement existing strengths at UC Davis are particularly encouraged to apply. Ideal candidates would combine bioinformatics with wet bench approaches in human studies. Candidates should be strongly motivated by the biological and medical importance of their research and should value the opportunity to work in close collaboration with both clinical and research faculty.

The UC Davis MIND Institute (Medical Investigation of Neurodevelopmental Disorders) is a collaborative international research center, committed to the awareness, understanding, prevention, care, and cures of neurodevelopmental disorders. Its mission is to find effective treatments and cures for autism and other neurodevelopmental disorders. The MIND Institute is an administrative unit within the UC Davis School of Medicine. The UC Davis Genome Center integrates experimental and computational approaches to address key problems at the forefront of genomics. The Center faculty build on and enhance the unique strengths and unmatched breadth of the life sciences on the UC Davis campus.

Candidates may be at the junior or mid-career level. At the midcareer level, we invite applications from prominent scientists with distinguished records of research, including extramural funding, teaching, and leadership in genomics. At the junior level, we invite applications from candidates whose accomplishments in innovative research and commitments to teaching demonstrate their potential to develop into the future leaders in human genetics and genomics.

This position requires a Ph.D., M.D./Ph.D., or equivalent. The appointment will be at the Assistant or Associate Professor level in an appropriate academic department in the School of Medicine. The position will remain open until filled. For fullest consideration, applicants should submit a letter of application, a curriculum vitae, statements of research and teaching interests, and the names of at least five references to the UC Davis Recruit Website **https://recruit.ucdavis.edu/apply/JPF00399** by **December 1, 2014**.

The University of California is an Affirmative Action/Equal Opportunity Employer.

CUNY The City University of New York

CUNY ADVANCED SCIENCE RESEARCH CENTER

Director of Neuroscience

The ASRC seeks a dynamic and innovative scientist with demonstrated leadership and research accomplishments in neuroscience to serve as Professor and Director of Neuroscience. The position will be a tenured faculty member and program administrator. The successful candidate will be expected to engage in teaching and research; oversee the Neuroscience program; lead researchers in collaborative projects and activities; lead the continued acquisition of external funding; recruit new faculty; and ensure compliance with federal research guidelines and University policies. Applicants must be accomplished and respected researchers in an area of neuroscience with a solid record of scholarly activities and possess appropriate credentials for a senior faculty appointment at one of the CUNY colleges. Successful candidates will be scientists of outstanding merit and accomplishment with active, funded research programs in neuroscience or a closely related area; strong leadership qualities; familiarity with multi-disciplinary programs; interest in promoting research collaborations and diverse academic activities; ability to foster collaboration among scientists; and ability to identify promising new areas for basic research applications. The director will have the opportunity to recruit new faculty into related areas in neuroscience. Exceptional candidates may be appointed as a Distinguished and/or Einstein Professor. Ph.D. in a life science, engineering, or closely-related science area required.

To apply and to seek further information visit:
asrc.cuny.edu/jobs
CUNY Advanced Science Research Center
85 St. Nicholas Terrace, New York, NY 10031

We are committed to enhancing our diverse academic community by actively encouraging people with disabilities, minorities, veterans, and women to apply. We take pride in our pluralistic community and continue to seek excellence through diversity and inclusion. EO/AA Employer.

Institut Pasteur

Creation of new research groups in the department of Neuroscience at Institut Pasteur

The Department of Neuroscience at Institut Pasteur launches a call for junior, mid-career and senior group leaders.

Institut Pasteur is located in central Paris and offers an outstanding and unparalleled research environment through its state-of-the-art research laboratories with integral biological services capability, cutting-edge scientific equipment, and technologically-advanced platforms.

Within this campus, the major focus of the Department of Neuroscience is the elucidation of genetic (and epigenetic), molecular, cellular and circuit mechanisms underlying the neural basis of behavior. Further information can be found on the Departmental website: **http://www.pasteur.fr/en/research/neuroscience**. Detailed descriptions on the Institute and on-campus facilities could be found at http://www.pasteur.fr/en.

We encourage applications from outstanding individuals interested in the development, plasticity, computational and pathophysiology of sensory and cognitive circuits in mammalian brain (rodents to humans). Applications will be evaluated on the basis of scientific excellence. Highly attractive packages to match the experience of the candidate will be provided, including institutional salaries (Principal investigator, technician, secretary, post-doctoral fellows), a substantial contribution to running costs and equipment, access to on campus state-of-the-art technology core facilities, as well as support for relocation expenses and administrative issues.

Applicants should provide a letter of intent (LOI) to constitute a in a single PDF file (in order):

1. A brief introductory letter
2. A Curriculum Vitae, 10 most important publications and a full publication list
3. A description of past and present research activities (up to 2 pages with 1.5 spacing; Times 11 or Arial 10 font size).
4. The proposed research project (up to 2 pages with 1.5 spacing; Times 11 or Arial 10 font size).

A pdf copy of the LOI should be electronically submitted to **neuroloi@pasteur.fr** no later than **December 30, 2014** by 5:00 pm (Central European Time). Shortlisted applicants will be notified by e-mail by **February 1st 2015**. A complete application will be requested and due for submission by **mid-March 2015**. Applicants will be invited for interview to take place end of **April 2015**.

Massachusetts Institute of Technology

Come work with us!

Tenure Track Faculty

The Department of Brain & Cognitive Sciences (BCS) (http://bcs.mit.edu) and **The Picower Institute for Learning & Memory at MIT** (http://picower.mit.edu/) are looking to hire up to three (3) tenure-track faculty at the assistant professor level who work in one or more of the following three (3) areas:

i) *Computational* approaches to intelligence, cognition or neuroscience; an experimental component to the candidate's research would be viewed as a positive but is not necessary. An affiliation with Electrical Engineering and Computer Science, the Computer Science and Artificial Intelligence Laboratory (CSAIL), or other allied departments is possible.

ii) *Molecular & cellular:* The Picower Institute is searching for a candidate studying development, function or plasticity of neuronal circuits at the cellular, circuit, and/or systems levels using a multi-faceted approach combining different methodologies and levels of analysis. Candidates with strong cellular/molecular training who are studying development of brain circuits or using stem cell technologies are particularly encouraged to apply.

iii) *Human cognition and/or cognitive neuroscience* using behavioral methods, especially in the areas of language and/or cognitive development OR using fMRI/neuroscience methods.

Successful applicants are expected to develop and lead independent, internationally competitive research programs and to share in our commitment to excellence in undergraduate and graduate education by teaching courses and mentoring graduate and undergraduate research. PhD must be completed by start day of employment and some postdoctoral training is preferred.

Please submit application materials – cover letter, CV, statement of research and teaching interests and representative reprints – online at https://academicjobsonline.org/ajo/jobs/4202. Please state research area in cover letter. To help direct the application, applicants should indicate which of the three areas listed above is their main research area by answering the mandatory questions included in the application. In addition, please arrange to have three letters of recommendation submitted online. Review of applications will begin on November 1, 2014.

MIT is an affirmative action employer, and we encourage applications from women and underrepresented minorities.

http://web.mit.edu

McGOVERN INSTITUTE
FOR BRAIN RESEARCH AT MIT

Call for Nominations: Scolnick Prize in Neuroscience

The McGovern Institute for Brain Research is accepting nominations for the 12th annual Edward M. Scolnick Prize in Neuroscience. The Prize recognizes an outstanding discovery or significant advance in the field of neuroscience. The prize is $100,000. The recipient presents a public lecture at MIT, hosted by the McGovern Institute and followed by a dinner in Spring 2015.

Nomination Deadline: December 15, 2014

Nomination procedures: Candidates for the award must be nominated by individuals affiliated with universities, hospitals, medicals schools, or research institutes, with a background in neuroscience. Self-nomination is not permitted. Each nomination should include: 1. A biosketch or CV of the nominee; 2. A letter of nomination with a summary and analysis of the major contributions of the nominee to the field of neuroscience. 3. Up to two representative reprints will be accepted.

Selection Procedure: Members of the selection committee and faculty affiliated with MIT are not eligible. Announcement of the award recipient will be made in January 2015. Recipient must attend all events to be awarded the prize.

Past Scolnick Prize Recipients: 2004: Dr. Masakazu Konishi, Caltech, **2005:** Dr. Judith L. Rapoport, NIMH/NIH, **2006:** Dr. Michael E. Greenberg, HMS, **2007:** Dr. David Julius, UCSF, **2008:** Dr. Michael Davis, Emory University, **2009:** Dr. Jeremy Nathans, Johns Hopkins University, **2010:** Drs. Lily and Yuh-Nung Jan, UCSF, **2011:** Dr. Bruce McEwen, The Rockefeller University, **2012:** Dr. Roger Nicoll, UCSF, **2013:** Dr. Thomas Jessell, Columbia University, **2014:** Dr. Huda Zoghbi, Baylor College of Medicine

Send nomination packet to: Attn: Scolnick Prize Nomination McGovern Institute for Brain Research Massachusetts Institute of Technology 77 Massachusetts Avenue 46-3160 Cambridge, MA 02139; or e-mail: **gwolf@mit.edu**. For more information: visit website: **http://mcgovern.mit.edu**

Memorial Sloan-Kettering Cancer Center

The Sarcoma Medical Oncology Service in the Department of Medicine of Memorial Sloan Kettering Cancer Center is seeking an outstanding **scientist/physician-scientist** with expertise in drug development/discovery and translational research. The successful candidate will be have a research program directed at translational sarcoma research and lead the Jennifer Linn Laboratory of New Drug Development in Sarcoma and Rare Cancers that will interface with the Hospital's sarcoma disease management team. Applicants should have a significant record of research accomplishment, and a proven ability to collaborate with translational physicians on clinically relevant projects. Candidates may have scientific background in any relevant translational field including stem cell biology, epigenetics, metabolomics, cell signaling, etc. Research applicable to sarcoma is desirable but not necessary, but work in the Linn Laboratory will be directed to Sarcoma and rare unidentified cancers.

Interested applicants should forward a cover letter, curriculum vitae, statement of research interests, and list of references to **David Spriggs, M.D, Head of the Solid Tumor Oncology Division, Memorial Sloan Kettering Cancer Center, 300 E 66th Street, 13th Floor, New York, NY 10065**, faxes will be accepted at **646-888-4270** and emails should be sent to **rodrigc4@mskcc.org**.

Memorial Sloan Kettering Cancer Center is an Equal Opportunity Employer with a strong commitment to enhancing the diversity of its faculty and staff. Women and applicants from diverse racial, ethnic and cultural backgrounds are encouraged to apply.

WASHINGTON STATE UNIVERSITY

The School of Biological Sciences at Washington State University, Pullman, Washington, invites applications for a full-time, non-tenure track, Clinical Assistant Professor position in **human biology** to begin 16 August 2015. The successful candidate will be expected to apply innovative strategies to develop and teach online undergraduate courses that support a proposed BS in Biology to be offered through our Global Campus. Courses are likely to include human physiology, human anatomy, human nutrition, developmental biology, and medical terminology. Participation in service needs is an expectation, and scholarship, either on pedagogy or a disciplinary specialty, is expected for promotion in this position. The primary service role may be academic advising for pre-medical and pre-dental students with undergraduate majors in biology and zoology. Our hire will be expected to advance the WSU commitment to diversity and multiculturalism among the faculty, staff, and students.

To apply visit **www.wsujobs.com** and upload application materials that include a cover letter, Curriculum Vitae, names and contact information for three references, a teaching statement that addresses the applicant's experience in teaching online courses, and up to three relevant publications. The reference letters will be automatically requested and obtained from the reference provider through our online application system. For information on the position candidates may contact **Dr. Larry Hufford** (**hufford@wsu.edu**).

Washington State University is an Equal Opportunity/Affirmative Action Educator and Employer.

FOCUS ON NEUROSCIENCE

Memorial Sloan-Kettering Cancer Center

2015 Position Postdoctoral Fellow/Faculty in Germline Cancer Genomics

The Clinical Genetics Service in the Department of Medicine at Memorial Sloan Kettering Cancer Center has an opening for a post-doctoral fellow or laboratory track faculty level applicant. The focus of the laboratory is on use of next generation genomic tools to discover novel cancer predisposition genes/alleles (see e.g. PMID: 24013638; PMID: 23544012). Studies will be conducted using computational analysis of primary exome- or genome- level germline data in cancer-affected kindreds/cohorts using family based, linkage, population based analytical strategies. Prior bench experience in molecular biology is desirable.

A curriculum vitae should be sent to **Kenneth Offit, M.D., MPH, Chief, Clinical Genetics Service, Memorial Sloan-Kettering Cancer Center, 1275 York Avenue, Box 192, New York, NY 10065**; e-mail: **offitk@mskcc.org**.

Memorial Sloan-Kettering Cancer Center is an Equal Opportunity Employer with a strong commitment to enhancing the diversity of its faculty and staff. Women and applicants from diverse racial, ethnic and cultural backgrounds are encouraged to apply.

ASSISTANT OR ASSOCIATE PROFESSOR EXPERIMENTAL PHYSICS (Tenure-Track)

The Department of Physics at the City College of New York has a tenure-track faculty position in Experimental Physics with a starting date of August 26th, 2015. The position is at the entry level but higher rank and salary will be considered for exceptionally qualified candidates.

The successful candidate must have a strong research record and outstanding promise for future accomplishments in one or several of the following fields: quantum photonics, experimental quantum information processing, quantum metrology and nanoscale sensing, solid-state quantum physics, spin physics, and quantum spintronics. The successful candidate is expected to have or generate an active research program and obtain independent external funding. The candidate will also be required to participate in undergraduate and graduate teaching, mentor graduate students and help in the growth of our graduate program.

Candidates should have a PhD in physics or a related discipline and at least one year of postdoctoral experience, significant achievements or outstanding potential in research, and evidence of and commitment to excellence in teaching. Reviewing of applications will start on December 1st, 2014 and will continue until the position is filled.

To be considered for this position, you must include your resume, a statement of teaching philosophy, a brief (3-page limit) statement of research interests, and the names and addresses of at least three references.

To apply, please view the job posting **(Job ID 11626)** at **http://www.cuny.edu/employment/jobsearch.html**, and follow all instructions.

The City College of New York

Northeastern University
College of Engineering

With **44** tenure-track hires since 2011, **8** federally-funded research centers, and a bioengineering department established in **2013**, Northeastern's College of Engineering is in a period of dynamic growth. Our emphasis on interdisciplinary, use-inspired research—tied to Northeastern's unique history of industry collaboration via the university's signature cooperative education program—enables partnerships with academic institutions, medical research centers, and companies near our centrally located Boston campus and around the globe.

The college seeks outstanding faculty candidates, with emphasis on bio-related, interdisciplinary expertise.

Successful applicants will lead internationally recognized research programs aligned with one or more of the college's strategic research initiatives. Particular consideration will be given to candidates at the associate or full professor level; exceptional candidates at the assistant professor level will also be considered.

Learn more and apply at coe.neu.edu/faculty/positions

Northeastern is an Affirmative Action/Equal Opportunity educator and employer committed to excellence through diversity.

The Institute for Genomic Biology (IGB) at the University of Illinois at Urbana-Champaign is proud to announce

THE CARL R. WOESE POSTDOCTORAL FELLOWSHIP PROGRAM

In 1977, Carl R. Woese overturned one of the major dogmas of biology with his discovery of the Archaea, the third domain of life. The methods he utilized involving ribosomal RNA have become the standard approach used to identify and classify all organisms today. As a faculty member of the University of Illinois for nearly 50 years and a founding member of the Institute for Genomic Biology, we honor the legacy of Carl R. Woese with the establishment of the Woese Fellowship.

The Woese Fellows will be truly exceptional young scholars who have completed their Ph.D. within the last several years, and are at the forefront of their field in evolution and the emergence of life, or other rapidly developing areas of quantitative biology and genomics. Woese Fellows will combine a quantitative outlook on biology with creative, possibly interdisciplinary, approaches to deep scientific questions, and will be able to take advantage of the stimulating IGB environment to carry out independent and collaborative research in a field of genomic biology. Woese Fellows will typically spend two to three years conducting research in one or more of the several research themes in the Institute. An annual salary of $55,000 will be provided, with a yearly stipend of $10,000 to be used in support of research.

The closing date for all positions is February 1, 2015.
Fellows will be announced on or about April 1, 2015.
To apply, please visit http://go.illinois.edu/woesefellow.

The University of Illinois is an Affirmative Action/Equal Opportunity Employer. The Institute for Genomic Biology is a pioneer in advancing life sciences research with program areas in systems biology, cellular and metabolic engineering, and genome technology. Visit www.igb.illinois.edu for additional information.

Stanford SCHOOL OF EARTH SCIENCES | Environmental Earth System Science

FACULTY POSITION IN WATER and LAND RESOURCES

The Department of Environmental Earth System Science at Stanford University seeks an innovative scholar for a junior level, tenure-track, faculty appointment in the area of freshwater and land resources.

We seek a broad-thinking, multi-disciplinary scientist employing hydrological, ecological, and/or other appropriate approaches for the study and management of coupled freshwater and land systems. Preference will be given to an individual focusing on regional to large-system scales. We expect development of a vigorous research program employing strong analytical, computational, and/or measurement methods. The successful candidate will also be expected to teach classes in freshwater/land-system processes and resources as well as mentor students at the graduate and undergraduate levels.

Each applicant is asked to provide a cover letter describing research and teaching experience as well as future plans in these areas, curriculum vitae, and a list of three referees who may be contacted for letters of recommendation. Please submit the requested materials at: **https://academicjobsonline.org/ajo/jobs/4923**. Review of applications will begin on **December 15, 2014**, and will continue until the position is filled. Questions related to your submission may be directed to **maslin@stanford.edu**.

Stanford University is an Equal Opportunity Employer and is committed to increasing the diversity of its faculty. It welcomes applications from women and minority groups, as well as others who would bring additional dimensions to the university's research and teaching missions.

Research Opportunities in Luxembourg. See what's behind it.

PEARL
LUXEMBOURG'S RESEARCH PROGRAMME FOR INTERNATIONALLY RECOGNISED SENIOR RESEARCHERS

Interested in establishing a high-profile research programme? Through our research programme PEARL (financial contribution up to EUR 5 million) we give you the opportunity to transfer your research programme to a research institution in Luxembourg.

ATTRACT
LUXEMBOURG 'S RESEARCH PROGRAMME FOR OUTSTANDING YOUNG RESEARCHERS FROM ALL OVER THE WORLD

Interested in doing scientific research at a high level in an international environment? Our research programme ATTRACT will allow you to set up your independent research team within a research institution in Luxembourg which will offer you attractive career opportunities. Funding up to EUR 2 million.

More information about ATTRACT and PEARL as well as the other funding opportunities offered by the National Research Fund Luxembourg can be found on the FNR's website.

Go and see what's behind on **www.fnr.lu/pearl** and **www.fnr.lu/attract**

For an overview on research in Luxembourg, have a look at **www.innovation.public.lu**

Fonds National de la Recherche Luxembourg
INVESTIGATING FUTURE CHALLENGES

UNC SCHOOL OF MEDICINE

Assistant Professor

The University of North Carolina announces an appointment in the Department of Ophthalmology in the UNC School of Medicine

The Department of Ophthalmology in the UNC School of Medicine is seeking to fill a tenure-track position at the rank of Assistant Professor with an outstanding PhD and/or MD scientist. The candidate would also be eligible for a basic science affiliation in the Department of Cell Biology and Physiology. The ideal candidate will have demonstrated the potential to establish or has established an independent, creative research program in the area of stem cell neurobiology with the aim of developing a program in retinal cell regeneration. The qualified candidate must have an M.D. or a Ph.D. degree in an appropriate discipline and have a strong track record of publications that demonstrates creativity and breadth of experience and potential. Candidates will also be expected to contribute to the research and graduate training in the Department of Cell Biology and Physiology. For additional information contact: **Donald L. Budenz, MD, MPH, Professor and Chairman, Department of Ophthalmology, UNC-CH, Department of Ophthalmology, 5151 Bioinformatics Bldg, CB# 7040, Chapel Hill, NC 27599-7040, dbudenz@med.unc.edu., phone: 919-966-5296, fax: 919-966-1908**.

To apply for this position all applicants must apply on line at: **http://unc.peopleadmin.com/postings/48079**. Apply deadline is **November 30, 2014**. Please include a cover letter, CV, a detailed statement of research program and interests, and the names and contact information or four references.

UNC-CH is an Equal Opportunity Employer.

The UC Davis Genome Center, Comprehensive Cancer Center, and College of Biological Sciences invite applications for a tenure track faculty position at the intersection of human cancer genetics and bioinformatics. Applicants interested in computational approaches to cancer who employ large-scale, data-driven methods that complement existing strengths at UC Davis are particularly encouraged to apply. Ideal candidates will combine basic and clinical bioinformatics studies. Candidates should be strongly motivated by the biological and medical importance of their research and should value the opportunity to work in close collaboration with both clinical and research faculty.

The UC Davis Genome Center integrates experimental and computational approaches to address key problems at the forefront of genomics. The UC Davis Comprehensive Cancer Center's mission is to lower the mortality from cancer, focusing on reducing cancer health disparities, and delivering innovative clinical trials to our patients, informed by clinical genomics combined with basic science discoveries. The multidisciplinary faculty of both Centers build on and enhance the unique strengths and unmatched breadth of the life sciences on the UC Davis campus.

Candidates may be at any academic level. At the senior level, we invite applications from prominent scientists with distinguished records of research, including extramural funding, teaching, and leadership in cancer genomics and bioinformatics. At the junior level, we invite applications from candidates with outstanding accomplishments in innovative research and a commitment to teaching that demonstrates their potential to develop into future leaders in cancer genomics and bioinformatics.

This position requires a Ph.D., M.D./Ph.D., or equivalent degree. The appointment will be at the Assistant, Associate or Full Professor level in the Department of Molecular and Cellular Biology in the College of Biological Sciences. The position will remain open until filled. For fullest consideration, applicants should submit a letter of application, a curriculum vitae, statements of research and teaching interests, and the names of at least five references to the UC Davis Recruit Website **https://recruit.ucdavis.edu/apply/JPF00406** by **December 1, 2014**.

The University of California is an Affirmative Action/Equal Opportunity Employer.

MINERVA

The Minerva Schools at KGI

The Minerva Schools at KGI (the Keck Graduate Institute) are designed to prepare students to become innovators and leaders in a wide variety of disciplines. Our aim is to reinvent higher education at every level, from how we define the curriculum to how we teach. All teaching is done using the Minerva Active Learning Forum cloud-based software, which supports real-time, synchronous seminars (ranging from 15-19 students) with high levels of faculty-student interaction. All Minerva classes are seminars that use active learning to help students learn to think critically, think creatively, and communicate effectively about the material, and to develop knowledge on their own; no traditional information transmission per se occurs during class.

We seek both half-time and full-time faculty at the Assistant Professor, Associate Professor, and Professor level; all faculty must have a Ph.D. or comparable degree, and must be comfortable with new technology, passionate about undergraduate teaching, flexible, and willing to embrace innovative pedagogical approaches based on the science of learning.

Email the following to **facultyapplications@minerva.kgi.edu**

- A cover letter explaining why you believe you would be a good fit to teach a specific Minerva course.
- A current C.V.
- The names of, and contact information for, three people who will write a letter of recommendation; we are particularly interested in people who can attest to the quality of your teaching, your general quality of mind, and your openness to new pedagogical approaches.
- In addition, please have your three recommenders send their letters to facultyapplications@minerva.kgi.edu with your name in the subject line.

Applications should be submitted by **30 November 2014**.

See www.minerva.kgi.edu for more information.

Bioengineering Faculty Position

The **California Institute of Technology** invites applications for a tenure-track professorial position in the Division of Biology and Biological Engineering. Bioengineering research at Caltech focuses on the application of engineering principles to the design, analysis, construction, observation and manipulation of biological systems, and on the discovery and application of new engineering principles inspired by the properties of biological systems.

Applications are invited in any area of bioengineering research. Candidates with strong commitments to research and teaching excellence are encouraged to apply. Preference will be given to candidates at the Assistant Professor level; however, consideration will also be given to more senior applicants. Initial appointments at the assistant professor level are for four years, and are contingent upon completion of the Ph.D. degree.

The Bioengineering Option (http://www.be.caltech.edu) includes faculty from the Divisions of Biology and Biological Engineering (http://www.bbe.caltech.edu), Chemistry and Chemical Engineering (http://www.cce.caltech.edu), Engineering and Applied Science (http://www.eas.caltech.edu), and Physics, Mathematics, and Astronomy (http://www.pma.caltech.edu).

Please submit online application at **http://bbe.caltech.edu/Positions** and include a brief cover letter; curriculum vitae; relevant publications, a description of proposed research; and a statement of teaching interests. Instructions will be given for submission of letters of reference when you apply on-line. The **application deadline is December 1, 2014**. Applicants must also commit to **attend a recruiting symposium at Caltech on February 24-25, 2015**, where they will present their research and future directions.

EOE of Minorities/Females/Protected Vets/Disability.

Full Professor and Associate Professor Positions, School of Energy, Soochow University, China

Description: 10 full professor or principal investigator (PI) and 20 associate professor positions are available at School of Energy of Soochow University. The School of Energy focuses on researches in areas related to science and technology of new energy. Research includes but not limited to one of the following areas:

(A) Various type of chemical, physical and biological batteries, supercapacitors, and fuel cells
(B) Nano energy materials
(C) Photovoltaic materials and cells
(D) Carbon capture and storage
(E) Photosynthesis
(F) Other advanced science and technology in renewable energy

Qualifications: Candidates must have a Ph.D degree in chemistry, physics, material science or related fields; at least 2 years of post doctoral experience is preferred; he/she should be able to conduct advanced and collaborative research, either in industrials or academics; high publication record is desirable; he/she should be able to obtain public and private research fundings in China.

Employment Term: Soochow University is located in the heart of beautiful Suzhou city in Jiangsu province, China. The University has recently experienced a rapid expansion with the enrollment of high level scholars. Successful candidates will be highly compensated based on experience.

Applications: Interested candidates should send in complete CVs to Prof. Gao at gaolijun@suda.edu.cn and Prof. Liu at zfliu@pku.edu.cn

Faculty Positions Available at The IAS and The MRI, Wuhan University, Wuhan, China

Two newly founded institutes at Wuhan University in China, the Institute for Advanced Studies (IAS) and the Medical Research Institute (MRI), cordially invite applications for ~50 each, open-rank faculty positions in Biology, Chemistry, Physics, Material Sciences, and Medical Sciences.

All applicants must have a Ph. D or MD and a successful postdoctoral experience. Successful candidates will be expected to establish an active research program in relevant disciplines. We offer internationally competitive recruitment packages.

The applicants should submit, electronically, a full CV, a research statement and contact information of three referees in a single PDF file to wdgyy@whu.edu.cn (for IAS positions) or shuoffice@whu.edu.cn (for MRI positions).

Applications that apply for both institutes at the same time will not be accepted and further processed.

http://hr.whu.edu.cn/

Tenure-Track position at the Assistant/Associate/Full Professor level in Anesthesiology and Neuroscience

Jiangsu Province Key Laboratory of Anesthesiology **(State Key Laboratory Cultivation Base for Anesthesiology)** at Xuzhou Medical College (http://www.xzmc.edu.cn) invites applications from scientists for a tenure-track position at the rank of Assistant/Associate/Full Professor level in Anesthesiology or related field. Applicants must have a Ph.D. and/or M.D. degree, postdoctoral training. We are particularly interested in candidates who is with research training in the field of anesthesiology and neuroscience and can use cutting edge approaches involving electrophysiological, genetic, cellular, molecular, or behavioral techniques to address key problems related to Anesthesiology, especial in 1) Pain, 2) Post operative cognitive dysfunction (POCD) and 3) Mechanisms of anesthetics and its neuronal toxic. The successful candidate is expected to develop and/or maintain an independent program of research with external funding.

The College and Department provide a very supportive research environment with excellent resources conducive to developing a successful research program. Laboratory space is also exceptional, with Jiangsu Province Key Laboratory of Anesthesiology located in a two-year old 45000 sq. foot, state-of-the-art animal research building.

Please submit a letter of application, cv, a research statement, sample publications, and provide three letters of reference to: rsc@xzmc.edu.cn and caojl0310@aliyun.com. Questions about the position should be directed to Professor Jun-Li Cao, Director, Jiangsu Province Key Laboratory of Anesthesiology, at caojl0310@aliyun.com or to Yuan-Dong Li, Human Resources, at rsc@xzmc.edu.cn

Faculty Positions available at Hohai University, Nanjing, China

Hohai University invites applications for faculty positions at the assistant, associate, or full professor level in the area of engineering, science, economics, management, liberal arts, and law. Applicants should have a doctoral degree from a prestigious university. For the complete job announcements and directions on how to apply, visit: rsc.hhu.edu.cn or contact the Department of human resource at 86-25-83786205.

Hohai University, founded in 1915, wins its worldwide reputation on the research of Water Science& Civil Engineering&Environment Engineering. It is a National key university of China, and among the universities of the National "*211 Project*" and Innovation Bases of the National "*985 Project*". Hohai University aims to be a research oriented university.

ILLINOIS
UNIVERSITY OF ILLINOIS AT URBANA-CHAMPAIGN

Faculty Positions in Stream Ecology and Ecohydrology
Department of Natural Resources and Environmental Sciences

The Department of Natural Resources and Environmental Sciences invites applications for two tenure-track positions at the **ASSISTANT PROFESSOR** level expected to begin August 16, 2015. These positions are part of a campus initiative centered on Energy and the Environment and a campus-based cluster hire in Water and Land Sustainability (http://provost.illinois.edu/communication/clusterhiring.html).

The **Stream Ecology** hire will be expected to establish a research program that could include (but not be limited to) topics such as nutrient cycling, effects of agricultural runoff and nutrient input on ecosystem services of streams, links between riparian areas and stream ecosystems, ecological restoration of aquatic habitats, or impacts of climate change on sustainability of stream ecosystems. Emphasis on mitigating the negative impacts of increasing human populations on aquatic ecosystems, the conservation of ecological integrity, and defining land use impacts on stream resources or water quality would also be of interest. Full details at **http://go.illinois.edu/F1400154**

The **Ecohydrology** hire will be expected to establish a research program with an emphasis on coupled hydrological and ecological processes involving water, energy, and material fluxes at scales ranging from watersheds to regions. The ideal candidate will combine field-based methods, data-model integration, and data-assimilation of temporal and spatial data to improve understanding and prediction of coupled processes at multiple scales and in the context of global environmental change. Full details at **http://go.illinois.edu/F1400171**

A Ph.D. is required at the time of appointment and postdoctoral experience is preferred. Successful candidates will be expected to develop an externally funded research program and teach at undergraduate and graduate levels.

Please visit **https://jobs.illinois.edu/** to view the complete position announcements and application instructions. For full consideration all requested application information must be received by **December 1, 2014**.

Illinois is an EEO Employer/Vet/Disabled
www.inclusiveillinois.illinois.edu

PENNSTATE HERSHEY
College of Medicine

FACULTY POSITION IN BIOCHEMISTRY, MOLECULAR BIOLOGY, AND GENETICS

The Department of Biochemistry and Molecular Biology at the Penn State University College of Medicine is expanding under the new leadership of Dr. James R. Broach. The Department invites applications from outstanding scientists with Ph.D., M.D., or equivalent degrees for a full-time tenure-track position. We seek candidates at the Assistant Professor level who have an active highly competitive independent research program or who show a strong potential to develop such a program. We are looking for candidates in the areas of molecular biology, genetics, epigenetics, and/or genomics. Candidates will have the opportunity to participate in Penn State's medical genomics program through the new Institute for Personalized Medicine.

For additional information, please visit the following website:
http://www2.med.psu.edu/biochemistry/

Applicants should submit a curriculum vitae and a brief statement of research plans to **www.psu.job**, **position #53894** and arrange for three letters of reference to be sent to Faculty Search Committee, **biochem_apply@hmc.psu.edu**. Application should be received prior to **November 15, 2014**.

Penn State is committed to Affirmative Action, Equal Opportunity and the diversity of its workforce.

UNIVERSITY AT ALBANY
State University of New York

Assistant Professor in Ecology and Evolution of Infectious Diseases (2 positions)

The Department of Biological Sciences (**http://www.albany.edu/biology**), University at Albany, invites applications for two tenure-track positions at the Assistant Professor level. The Department seeks candidates whose research will advance conceptual understanding of ecological and evolutionary aspects of infectious diseases. Possible research themes may include, but are not limited to, microbial/viral pathogen transmission and spread, host-pathogen interactions, vector biology or pathogen variation and evolution. Applicants should have wide interests in disease biology and the ability to interact with a diverse faculty working across many research areas. Opportunities for collaboration include faculty in the Life Sciences (**http://www.albany.edu/lifesciences**), the RNA Institute (**http://www.albany.edu/rna**) and the School of Public Health (**http://www.albany.edu/sph**), as well as the New York State Department of Health (**http://www.wadsworth.org**).

Successful candidates will contribute to the Department's graduate program in Ecology and Evolutionary Biology (EEB). The successful candidates will be expected to teach at the undergraduate and graduate levels in courses appropriate to their expertise and to establish a sustained, externally funded research program. Initial salary and startup funds are competitive.

Applicants must have a Ph.D. from a university accredited by the U.S. Department of Education or an internationally recognized accrediting organization, post-doctoral experience, and a strong publication record. To apply, submit a CV, selected reprints (no more than 5), a statement of research interests and future plan, a statement of teaching interests and a minimum of three letters of reference. Applicants must address in the application, their ability to work with a culturally diverse population. Materials are accepted on-line at

http://albany.interviewexchange.com/candapply.jsp?JOBID=53990

The University at Albany is an EO/AA/IRCA/ADA Employer

ILLINOIS
UNIVERSITY OF ILLINOIS AT URBANA-CHAMPAIGN

Faculty Positions in Stream Ecology and Ecohydrology
Department of Natural Resources and Environmental Sciences

The Department of Natural Resources and Environmental Sciences invites applications for two tenure-track positions at the **ASSISTANT PROFESSOR** level expected to begin August 16, 2015. These positions are part of a campus initiative centered on Energy and the Environment and a campus-based cluster hire in Water and Land Sustainability (http://provost.illinois.edu/communication/clusterhiring.html).

The **Stream Ecology** hire will be expected to establish a research program that could include (but not be limited to) topics such as nutrient cycling, effects of agricultural runoff and nutrient input on ecosystem services of streams, links between riparian areas and stream ecosystems, ecological restoration of aquatic habitats, or impacts of climate change on sustainability of stream ecosystems. Emphasis on mitigating the negative impacts of increasing human populations on aquatic ecosystems, the conservation of ecological integrity, and defining land use impacts on stream resources or water quality would also be of interest. Full details at **http://go.illinois.edu/F1400154**

The **Ecohydrology** hire will be expected to establish a research program with an emphasis on coupled hydrological and ecological processes involving water, energy, and material fluxes at scales ranging from watersheds to regions. The ideal candidate will combine field-based methods, data-model integration, and data-assimilation of temporal and spatial data to improve understanding and prediction of coupled processes at multiple scales and in the context of global environmental change. Full details at **http://go.illinois.edu/F1400171**

A Ph.D. is required at the time of appointment and postdoctoral experience is preferred. Successful candidates will be expected to develop an externally funded research program and teach at undergraduate and graduate levels.

Please visit **https://jobs.illinois.edu/** to view the complete position announcements and application instructions. For full consideration all requested application information must be received by **December 1, 2014**.

Illinois is an EEO Employer/Vet/Disabled
www.inclusiveillinois.illinois.edu

UNIVERSITY AT ALBANY
State University of New York

Assistant Professor in Ecology and Evolution of Infectious Diseases (2 positions)

The Department of Biological Sciences (**http://www.albany.edu/biology**), University at Albany, invites applications for two tenure-track positions at the Assistant Professor level. The Department seeks candidates whose research will advance conceptual understanding of ecological and evolutionary aspects of infectious diseases. Possible research themes may include, but are not limited to, microbial/viral pathogen transmission and spread, host-pathogen interactions, vector biology or pathogen variation and evolution. Applicants should have wide interests in disease biology and the ability to interact with a diverse faculty working across many research areas. Opportunities for collaboration include faculty in the Life Sciences (**http://www.albany.edu/lifesciences**), the RNA Institute (**http://www.albany.edu/rna**) and the School of Public Health (**http://www.albany.edu/sph**), as well as the New York State Department of Health (**http://www.wadsworth.org**).

Successful candidates will contribute to the Department's graduate program in Ecology and Evolutionary Biology (EEB). The successful candidates will be expected to teach at the undergraduate and graduate levels in courses appropriate to their expertise and to establish a sustained, externally funded research program. Initial salary and startup funds are competitive.

Applicants must have a Ph.D. from a university accredited by the U.S. Department of Education or an internationally recognized accrediting organization, post-doctoral experience, and a strong publication record. To apply, submit a CV, selected reprints (no more than 5), a statement of research interests and future plan, a statement of teaching interests and a minimum of three letters of reference. Applicants must address in the application, their ability to work with a culturally diverse population. Materials are accepted on-line at

http://albany.interviewexchange.com/candapply.jsp?JOBID=53990

The University at Albany is an EO/AA/IRCA/ADA Employer

ASSISTANT PROFESSOR

Integrative Ecoimmunology

The Department of Biological Sciences at The University of Alabama invites applications for a tenure-track faculty position at the rank of **Assistant Professor** in **Integrative Ecoimmunology**. We seek applicants whose research focuses on mechanisms driving changes in host physiology and behavior in response to parasites or pathogens under ecologically relevant contexts. Applicants should use broadly integrative approaches including, but not limited to, molecular, cellular, and physiological methods to characterize host immune responses, hormonal modulation of immune responses, disease susceptibility in a social context, parasite/pathogen manipulation of host behavior and physiology, and life history evolution. Candidates that utilize field-based approaches and/or laboratory-based investigations using model or non-model systems are encouraged to apply. The successful candidate will be expected to establish an extramurally funded and internationally recognized research program in Ecoimmunology. Teaching responsibilities will include basic undergraduate courses in biology, immunology, and graduate courses in the successful candidate's area of expertise.

Candidates must have a Ph.D. in the Biological Sciences or related field, postdoctoral (or equivalent job) experience, demonstrated excellence in research, and a commitment to excellence in teaching and the training of undergraduate and graduate students. Queries regarding additional details should be addressed to the chair of the search committee: Dr. Ryan L. Earley at **rlearley@as.ua.edu**.

To apply, go to **https://facultyjobs.ua.edu/postings/36161**, complete the online application (Job #0809244), and upload: (1) an application letter with a list of three to five references (including contact information); (2) CV; (3) statement of research interests and goals; and (4) statement of teaching interests and philosophy. Letters of reference will be requested by the search committee as appropriate. Consideration of applications will begin 1 December 2014, and will continue until the position is filled. Prior to hiring, the final candidate will be required to pass a pre-employment background investigation. The anticipated start date is August 16, 2015.

Additional information about the Department of Biological Sciences and this available position can be found on our website at **http://bsc.ua.edu**. Applications from women and members of traditionally under-represented groups in Biology are especially encouraged.

The University of Alabama is an equal-opportunity educational institution/employer.

THE UNIVERSITY OF ALABAMA®
THE CAPSTONE OF HIGHER EDUCATION

ASSISTANT PROFESSOR

Invertebrate Systematics

The Department of Biological Sciences at The University of Alabama invites applications for a tenure-track faculty position at the rank of **Assistant Professor** in **Systematic Invertebrate Biology** to begin August 2015. All taxonomic groups of invertebrates will be considered. Applicants whose research integrates modern genomic approaches to study the taxonomy, systematics, biogeography, and evolution of invertebrates are encouraged to apply. The successful applicant will be expected to establish an active independent research program, attract extramural funding, and must be committed to excellence in teaching and mentoring undergraduate and graduate students. In addition, the successful applicant will be expected to curate the invertebrate collection maintained by the Department of Biological Sciences and must provide evidence of curatorial experience and/or other relevant abilities. The invertebrate collection at The University of Alabama contains significant holdings of freshwater mussels, freshwater decapods, and marine invertebrates. Individuals interested in diversifying this actively growing collection are encouraged to apply. Candidates must have a Ph.D. in the Biological Sciences or a related field and postdoctoral (or equivalent job) experience.

A complete application includes (1) an application letter with a list of at least four references (including contact information); (2) CV; (3) statement of research interests and goals; and (4) statement of teaching interests and philosophy. Letters of reference will be requested by the search committee as appropriate. To apply, go to **https://facultyjobs.ua.edu/postings/36132**, complete the online application (Job #0809229), and upload all requested documents. Questions about the position may be addressed to Dr. Phil Harris (**pharris@bama.ua.edu**; 205-348-1831). Consideration of applications will begin December 1, 2014 and will continue until the position is filled. For more information about the department, visit our website at **http://bsc.ua.edu**. Prior to hiring, the final candidate will be required to pass a pre-employment background investigation. The anticipated start date is August 16, 2015.

Additional information about the Department of Biological Sciences and this available position can be found on our website at **http://bsc.ua.edu**. Applications from women and members of traditionally under-represented groups in Biology are especially encouraged.

The University of Alabama is an equal-opportunity educational institution/employer.

THE UNIVERSITY OF ALABAMA®
THE CAPSTONE OF HIGHER EDUCATION

POSITIONS OPEN

THE UNIVERSITY OF ARIZONA

POSTDOCTORAL/RESEARCH ASSOCIATE POSITIONS in Human and/or Mouse Immunology

A postdoctoral position is available to qualified applicants in the laboratory of **Dr. Janko Nikolich-Zugich** in the Department of Immunobiology, College of Medicine, University of Arizona. For description of laboratory interests and publications, see **website: http://immunobiology.arizona.edu/faculty/janko-nikolich-zugich-md-phd.**

Qualified applicants will investigate T cell function and homeostasis in health, viral diseases, vaccination and aging in a human and/or mouse model. Cellular immunology training is essential for this position and background in inflammation is advantageous.

Research in the Department and the University is supported by state-of-the-art core facilities including animal housing, FACS, DNA, Microarrays, Proteomics and Imaging. University of Arizona is amongst the top 20 public research and education universities, boasting excellent departments and Centers, as well as lively campus culture, and life and a blossoming recreation center. It is located in sunny Tucson, a city with a vibrant multicultural population of approximately 900,000, a strong economy and business opportunities. Tucson is surrounded by a majestic desert and mountains rising to more than 9,000 feet. Interested individuals should send inquiries/curriculum vitae and arrange for three letters of reference to be sent to:

Janko Nikolich-Zugich, M.D., Ph.D.
Head, Department of Immunobiology
E-mail: nikolich@email.arizona.edu

FORENSIC SCIENCE

The Chemistry Department and the National Center for Forensic Science at the University of Central Florida (UCF) anticipate hiring a nine-month, tenure-track **ASSISTANT, ASSOCIATE,** or **FULL PROFESSOR** in forensic science effective fall 2015. Minimum qualifications at the Assistant Professor level are a Ph.D. in chemistry or appropriately related field from an accredited institution, at least one year of postdoctoral research or equivalent experience and a demonstrated track record of research productivity in forensic science. Candidates for appointment as Associate or Full Professor will exhibit a track record of competitive funding for forensic science research. Specialization in forensic toxicology is of specific interest; however, applications in all areas of forensic science are welcome. A candidate hired at the Assistant Professor level will be expected to develop an externally funded, nationally competitive research program. State-of-the art laboratory space and a competitive startup package can be expected. A successful candidate at any level will contribute to teaching in both the undergraduate and graduate programs. The Chemistry Department at UCF offers B.S. Chemistry, B.S. Forensic Science, M.S. Chemistry, M.S. Forensic Science, and Ph.D. Chemistry degrees. The National Center for Forensic Science at UCF is an internationally recognized leader in forensic science research. The University of Central Florida, located in Orlando, FL, is the nation's second largest university with over 60,000 students and is continuing to build internationally recognized research programs. Applicants must apply online at **website: http://www.jobswithucf.com** and submit letter of application, curriculum vita, description of research plans, teaching philosophy and interests, and names of at least three references. Please arrange to have three letters of reference sent to **e-mail: chemstaff@ucf.edu.** Please indicate in the subject line "Forensic Science Search". Review of applications will begin December 1, 2014 and continue until the position is filled. *UCF is an Equal Opportunity/Affirmative Action Employer. All qualified applicants are encouraged to apply, including minorities, women, veterans, and individuals with disabilities. As a Florida public university, UCF makes all application materials and selection procedures available to the public upon request.*

ENVIRONMENTAL CHEMISTRY

The Chemistry Department at the University of Central Florida anticipates hiring a nine-month, tenure-track **ASSISTANT PROFESSOR** effective fall 2015 with specialization in Environmental Chemistry. We seek broadly trained, collaborative environmental chemists having strong analytical skills and who focus on coastal upland and/or nearshore (wetland, estuarine, or marine) systems or organisms that reside therein. Potential research areas include, but are not restricted to: biogeochemistry, climate change, environmental toxicology, atmospheric, aquatic or soil chemistry, and/or sea-level rise.

The University of Central Florida is strategically investing in interdisciplinary studies of Coastal Systems. This year we are searching for a cluster of five tenure-track faculty in Chemistry (1), Biology (2), and Civil & Environmental Engineering (2). Those who are hired should be interested in interdisciplinary collaborative research in one or more of the other fields. These hires are part of 200 new faculty positions to be hired university-wide in 2015–16, with more hires anticipated in coming years.

Minimum qualifications are a Ph.D. in chemistry or closely related field from an accredited institution, and at least one year of postdoctoral research experience with demonstrated track record of research productivity. It is expected the candidate will teach at both the undergraduate and graduate levels, and develop externally funded, nationally competitive research. State-of-the art laboratory space and a competitive startup package can be expected.

The Department of Chemistry (**website: http://www.chemistry.cos.ucf.edu**) at UCF offers B.S. Chemistry, B.S. Forensic Science, M.S. Chemistry, M.S. Forensic Science, and Ph.D. Chemistry degrees. The successful candidate may be considered for secondary joint appointments in either the Department of Civil, Environmental, and Construction Engineering or the Department of Biology.

The University of Central Florida, located in Orlando, FL, is the nation's second largest university with over 60,000 students and is continuing to build internationally recognized programs in chemical and forensic sciences. Applicants must apply online at **website: http://www.jobswithucf.com** and submit letter of application, curriculum vita, and description of instructional development or research plans, teaching philosophy and interests, and names of at least three references. Please arrange to have three letters of reference sent to **e-mail: chemstaff@ucf.edu.** Please indicate in the subject line "Environmental Chemistry Search". Review of applications will begin December 1, 2014 and continue until the position is filled. *UCF is an Equal Opportunity/Affirmative Action Employer. All qualified applicants are encouraged to apply, including minorities, women, veterans, and individuals with disabilities. As a Florida public university, UCF makes all application materials and selection procedures available to the public upon request.*

FACULTY POSITION IN NEUROSCIENCE

The Department of Cell Biology and Neuroscience at Montana State University (MSU) invites applications for a tenure-track position at any rank. We seek an established neuroscientist who uses novel approaches to study the nervous system. Successful candidates will have a vigorous, innovative, externally funded (e.g., NIH, NSF) research program with international recognition, an excellent publication record, a strong track record of leadership and collaboration, and an interest in teaching at the undergraduate and graduate level. Salary support for the nine-month academic year is provided and grant funding can be used to supplement both the academic year and summer salary. Recent initiatives at MSU include a new Center for Mental Health Research and Recovery and those with an interest in psychiatric disease and program building are encouraged to apply. To apply, submit curriculum vitae, a two-page summary of research accomplishments and future plans, and the names and contact information of three references in PDF format to **e-mail: cbn@cns.montana.edu.** Review of applications will begin on December 1, 2014. See **websites: http://www.montana.edu/cbn** and **http://www.montana.edu/jobs/faculty** for more information. *Montana State University is an Affirmative Action/Equal Opportunity Employer. We strongly encourage women, racial/ethnic/gender minorities, persons with disabilities, and veterans to apply.*

CARL MOORE ENDOWED CHAIR in Chemistry and Biochemistry Loyola University Chicago

The Department of Chemistry and Biochemistry invites applications for the Carl Moore Endowed Chair beginning fall 2015. Preference is for an appointment at the rank of **PROFESSOR,** although advanced **ASSOCIATE PROFESSORS** will also be considered. Applicants from all research areas of chemistry or biochemistry will be considered but analytical biochemistry is of particular interest. A Ph.D. degree in chemistry, biochemistry, or in a closely related field is required. The successful candidate will be expected to have a tenured appointment and an externally funded research program as well as highly cited publications. The incumbent will be expected to maintain an internationally recognized and a competitive externally funded research program, leading to continued publications and funding opportunities. This appointment will be accompanied by a reduced teaching load. The Department offers Ph.D., M.S., and ACS approved B.S. degrees. For more details about the department, visit **website: http://www.luc.edu/chemistry.** Candidates should complete an online application at **website: http://www.careers.luc.edu,** with a cover letter, a curriculum vitae, and a description of research and teaching interests. Applicants should provide the names and e-mail addresses of three individuals prepared to speak to their professional qualifications. Review of applications will begin on November 30, 2014 and applications will be accepted until the position is filled. *Applications from women, minorities, veterans, and persons with disabilities are especially encouraged. Loyola University Chicago is An Equal Opportunity/Affirmative Action Employer.*

FACULTY POSITION in Mesenchymal Progenitor, Differentiation, or Stem Cell Biology

Duke University's Departments of Orthopaedic Surgery and Cell Biology invite applications for a tenure-track faculty position in the field of mesenchymal progenitor cell biology. The ideal candidate will have a Ph.D. or MD, and significant postdoctoral or faculty experience. They should have a record of outstanding scientific accomplishments and a well-developed research plan in a relevant research discipline such as: embryonic or induced stem cells; multipotent cells; differentiation to mesenchymal lineages; de-differentiation; and/or the use of cells for diagnosis, modeling disease, repair, or regeneration. An appointment at any academic level is available depending on the expertise and track record of the successful candidate. The successful candidate will complement and enhance our substantial existing strengths in cell biology, orthopaedics, sarcoma, bioengineering, developmental biology, and musculoskeletal research. We expect the successful candidate to initiate and maintain an original, competitive, and independently funded research program. Interested candidates should submit application materials including a cover letter, curriculum vitae, statement of accomplishments and future research goals (two-page limit), electronic reprints of up to three recent articles, and arrange to have up to three letters of reference provided. The closing date for applications is December 15, 2014. Materials should be addressed to **Benjamin Alman,** Chair of Orthopaedic Surgery, and submitted electronically by **e-mail: tim.riddle@duke.edu.**

Duke University is an Affirmative Action/Equal Opportunity Employer committed to providing employment opportunity without regard to an individual's age, color, disability, genetic information, gender, gender identity, national origin, race, religion, sexual orientation, or veteran status.

WORKING LIFE

By **George F. Gao** *and* **Yong Feng**

On the ground in Sierra Leone

When you arrive in Sierra Leone, things look pretty normal. Life goes on as usual in many respects. In Freetown, the streets are still busy, and people still go to the market. In the villages, people are doing the same things they always do: sitting and chatting, wandering, playing football. But there is nothing normal about the work we are doing here. ¶ We have been in Sierra Leone for more than a month, with a China-based team running a mobile testing laboratory and a holding center for Ebola cases. When you arrive at a clinic or a holding center here, you see immediately how devastating Ebola is and how inadequate the resources are. The local public health system is weak. People die in fields outside of clinics. Many more die inside their homes.

With 4868 deaths from 9911 cases as of 22 October, according to the World Health Organization, the Ebola outbreak in West Africa—including Guinea, Sierra Leone, and Liberia—shows no signs of diminishing.

Getting Ebola under control is a problem for the world because, as we have seen, viruses do not require a visa to travel. Cases have surfaced in Senegal, Nigeria, and Mali, and Ebola has even extended its reach to Europe and North America. Ebola was long thought to affect only people living in poverty, so it has been neglected by the world. We have too few virologists and vaccinologists working in relevant areas and too little money invested in relevant research. Even if we get this outbreak under control soon—and we believe we will—the world will remain vulnerable to future outbreaks of Ebola and other infections as long as developed countries, with their enormous financial resources, fail to deal with these neglected diseases.

The entire country of Sierra Leone has fewer than 100 registered doctors. In one village of 9000 people, there is no doctor and no way of triaging cases in a timely manner. And because of a lack of facilities, patients—suspected, probable, or even confirmed—cannot be removed immediately and have to be kept in the community or at home, waiting for beds to open up.

The need for material aid is great, but the need for manpower is even larger and more urgent. West Africa needs doctors to run treatment and holding centers; virologists to do laboratory diagnostics; epidemiologists to dissect the major factors affecting the outbreak, which would lead to effective public health measures; public health workers to help implement these measures; and educators to work with the public and improve communications. Only when all this has been implemented in a coordinated way are we likely to see the transmission chain in West Africa cut; hopefully this will happen before Ebola becomes a big problem elsewhere. All this is needed now, on the ground, in every community and village.

"A younger generation ... must be trained to specialize in African communicable diseases."

Looking to the future, we call on the world to build up an effective public health system in West Africa. The first and obvious need is for strong government leadership to coordinate the region's public health affairs. But more is needed: A younger generation from developed countries must be trained to specialize in African communicable diseases. Some of these people must set up and run training programs for younger West Africans.

We urge young scientists planning their careers to consider studying communicable diseases, especially highly pathogenic ones like Ebola or Lassa fever. Research must be driven not merely by scientists' interests but by the desire—the urgent need—to find solutions for real-world problems. Younger scientists are needed to work in labs in the developed countries but also here on the ground, to talk with the local people, understand their needs and pain, and work bravely to fight deadly viruses like Ebola. ■

George F. Gao is deputy director general of the Chinese Center for Disease Control and Prevention. Yong Feng is director of the Division of African Affairs in the Department of International Cooperation at China's National Health and Family Planning Commission.

ILLUSTRATION: ROBERT NEUBECKER